STATE - PLANE ANALYSIS OF RESONANT CONVERTERS

by

Ramesh Oruganti

Dissertation submitted to the Faculty of the

Virginia Polytechnic Institute and State University

in partial fulfillment of the requirements for the degree of

Doctor of Philosophy

in

Electrical Engineering

APPROVED:

Fred C. Lee, Chairman

Dan Y. Chen

Douglas K. Lindner

Lee W. Johnson

Krishnan Ramu

20 March, 1987

Blacksburg, Virginia

STATE - PLANE ANALYSIS OF RESONANT CONVERTERS

by

Ramesh Oruganti

Fred C. Lee, Chairman

Electrical Engineering

(ABSTRACT)

State-plane technique was adopted for analysis of a class of resonant dc to dc power converters. A comprehensive method was developed to understand the complex operation of a resonant converter, identify its operating modes along with their regions of occurrence and determine the dc characteristics of the converter in each mode. The method was shown by application to a series resonant converter (SRC), a parallel resonant converter (PRC) and the family of quasi resonant converters (QRCs). Several major conclusions were experimentally verified.

By suitably modifying the method, the effect of parasitic losses on the performance of a SRC was also studied. The operating regions where significant deviations in dc characteristics occurred due to losses were also identified. In addition, from the mode and dc analysis of a PRC, a novel resonant buck converter with dc gain almost insensitive to load variations was proposed.

Generalized mode and dc analysis applicable to all QRC topological variations were performed using state-plane diagrams. Four sets of mode and dc analyses were shown to be adequate to characterize the steady-state operation of nearly a hundred QRC variations. This simplified the understanding and analysis of these converters. Also, two simple circuit rules were introduced using which several QRC topological variations were generated and evaluated based on relative component stresses.

The state-plane technique was also used to understand and evaluate different control methods of a SRC. The occurrence of large, undesirable tank energy surges with analog-signal-to-discrete-time-interval-converter (ASDTIC) control was investigated and explained using state-plane trajectories. A new control method called "optimal trajectory control", which attempts to achieve the fastest response possible was proposed. By exploiting the structure of SRC state portrait, the tank energy is always kept within bounds with this control. Experimental implementation was discussed in detail along with experimental oscillograms which confirm the predicted fast response.

Acknowledgements

I wish to thank Professor F. C. Lee for his encouragement and support during the course of this research work and also for providing me the opportunity to work in the area of resonant power converters. Special thanks are also due to Drs. D. Y. Chen, L. W. Johnson, D. K. Lindner and K. Ramu for their contributions as members of my doctoral committee and for their suggestions regarding the final documentation.

I also acknowledge the support provided by NASA Lewis Research Center, Cleveland, OH, through the grants NAG 3-405 and NAG 3-551 to Virginia Polytechnic and State University.

I sincerely thank for painstakingly editing a large part of the manuscript. I also thank for his assistance during the experimental work on the control of a series resonant converter.

I would like to take this opportunity to thank two of my fellow graduate students and for several free-wheeling discussions which made my stay at Virginia Tech both stimulating and enjoyable.

I am greatly indebted to for volunteering to draw several figures in the report at short notice. But for her untiring and enthusiastic help the completion of this dissertation would have taken a much longer duration.

With a deep sense of gratitude I thank my friend for his considerable help in preparing the final document despite his own busy schedule. The friendly and concerned support he provided helped me and my family meet several challenges along the way. Thank you, .

During the hectic final days when this document was put together, there were several voluntary offers of help from friends for which I am truly grateful. I would like to particularly thank and

for their concern and help.

A special thanks is due to my brother O. Prabhakar who has been keenly interested in my career over the years. His support made it possible for me to begin my studies at Virginia Tech.

With love, I thank my parents Mrs. O. Saraswathi and Mr. O. V. Subbaramiah for the many sacrifices they made in bringing up the children under not so easy circumstances. Their abiding faith in me and my abilities has always been a source of confidence and inspiration to me. I owe my love of learning to my father and no one will be more pleased with my obtaining the doctoral degree than he.

I thank my children and for being the way they are and hope to be available to them more in the future.

My wife, , has helped in several ways in preparing this dissertation. I am thankful to her for her care, support and understanding during the years of my Ph.d work. Without her loving and stabilizing influence in my life, this work would not have been possible.

I dedicate this dissertation to my wife, , my children, and , and to the memory of

Table of Contents

Introduction **1**

1.1 Background 1

1.2 Literature Survey 3

1.3 Present Work 9

1.3.1 Motivation And Objective 9

1.3.2 Method Of Analysis 9

1.3.3 Major Results 10

1.3.4 Outline Of Report 12

DC Analysis Of Series Resonant Converter **13**

2.0 Symbols Of Variables 13

2.1 Introduction 16

2.2 Ideal State-Plane Analysis 17

2.2.1 Circuit Operation 17

2.2.2 Assumptions 22

2.2.3 Topological Modes 22

2.2.4 State Portrait Development 25

2.2.5 Steady-State Trajectories 30
2.2.5.1 CCM Operation Below Resonant Frequency 33
2.2.5.2 DCM Operation Below Half Of Resonant Frequency 35
2.2.5.3 DCM Operation When Load Voltage Equals Supply Voltage 37
2.2.5.4 CCM Operation Above Resonant Frequency 43
2.2.6 Ideal Regions Of Operation 44
2.3 Results Of DC Analysis 48
2.4 Conclusions 59

Effect Of Parasitic Losses On Series Resonant Converter 60
3.0 Symbols Of Variables 60
3.1 Introduction 61
3.2 State Plane Analysis 62
3.2.1 Modeling the Losses 62
3.2.2 Trajectory Equation With Loss 64
3.2.2.1 A Special Trajectory Segment 71
3.2.3 Steady-State Trajectories 73
3.3 Upper Load Limit 76
3.3.1 Maximum Power Transfer 80
3.4 Results Of DC Analysis 82
3.5 Experimental Results 87
3.6 Conclusions 94

Methods Of Control For Series Resonant Converter 98
4.0 Symbols Of Variables 98
4.1 Introduction 99
4.2 Existing Methods Of Control 101
4.2.1 ASDTIC Control 102
4.2.1.1. Simulation Of SRC With ASDTIC Control 102

4.2.2 Frequency Control 104
4.2.3 Capacitor-Voltage Control 104
4.2.4 Diode-Conduction-Angle Control 106
4.3 State-Plane Analysis 106
4.3.1 Control Methods 110
4.3.1.1 Capacitor-Voltage Control 110
4.3.1.2 Frequency Control 111
4.3.1.3 ASDTIC Control 113
4.3.1.4 Diode-Conduction-Angle Control 114
4.3.1.5 Transistor-Conduction-Angle Control 115
4.3.1.6 Optimal Trajectory Control 115
4.3.2 DC Gain Characteristics 116
4.3.3 Limits On Dynamic Performance Of Resonant Converters 116
4.4 Performance Of Control Methods 121
4.4.1 Performance Criteria 123
4.4.1.1 Stability 123
4.4.1.2 Response To Control Change 124
4.4.1.3 Load Increase / Short-Circuit 124
4.4.1.4 Control Range 125
4.4.2 Performance Evaluation 125
4.4.2.1 ASDTIC Control 125
4.4.2.2 Transistor-Conduction-Angle Control 127
4.4.2.3 Capacitor-Voltage Control 129
4.4.2.4 Frequency Control 129
4.4.2.5 Diode-Conduction-Angle Control 133
4.4.2.6 Optimal Trajectory Control 136
4.4.3 Summary 139
4.5 Implementation Of Optimal Trajectory Control 142
4.5.1 Computation Of Feedback Variable 143
4.5.2 Power Circuit 144

4.5.3 Control Circuit 146
4.5.4 Scaling The Variables 150
4.5.5 Experimental Performance 155
4.6 Conclusions 161

DC Analysis Of Parallel Resonant Converter 162
5.0 Symbols Of Variables 162
5.1 Introduction 165
5.2 Ideal State-Plane Analysis 168
5.2.1 Resonant Topological Modes 168
5.2.2 State Portrait Development 169
5.2.3 Steady-State Trajectories 174
5.2.4 Forced Commutation Trap Zones 179
5.2.5 Nonresonant Topological Modes 179
5.2.5.1 Inductor Charging Intervals: 179
5.2.5.2 Capacitor Discharge Intervals: 181
5.2.5.3 Discontinuous Operation Interval: 185
5.3 Complete Mode Analysis 185
5.3.1 Construction Of CCM Steady-State Trajectories 185
5.3.2 Method Of Mode Analysis 187
5.3.3 Mode Definitions 188
5.3.4 PRC Base-Drive Strategies 188
5.3.5 Load Current Equals Zero 190
5.3.6 Load Current In Range A 190
5.3.6.1 NonCCM Trajectories With Intersection-1 192
5.3.6.2 NonCCM Trajectories With Intersection-2 197
5.3.7 Load Current In Range B 199
5.3.8 Load Current In Range C 202
5.3.9. Results Of Mode Analysis 202

5.4 Results Of DC Analysis 208
5.5 Experimental Results 216
5.5.1 Existence Of The Modes 216
5.5.2 Mode Boundaries 227
5.5.3 DC Characteristics 234
5.6 Novel Resonant Buck Converter 237
5.6.1 Circuit Derivation 237
5.6.2 Features Of Resonant Buck Converter 241
5.7 Conclusions 241

State-Plane Analysis Of Quasi-Resonant Converters 244
6.0 Symbols Of Variables 244
6.1 Introduction 246
6.2 Basic Quasi-Resonant Converters 247
6.3 Intervals Of Operation 249
6.3.1 Resonant Interval Analysis 253
6.3.1.1 Basic ZCS QRCs 254
6.3.1.2 Basic ZVS QRCs 255
6.4 Normal Mode (Mode-1) Steady-State Trajectories 256
6.4.1 Mode-1 Operation In ZCS QRCs 262
6.4.2 Mode-1 Operation in ZVS Converters 263
6.5 Load Ranges of Quasi-Resonant Converters 264
6.5.1 Buck Converter 265
6.5.2 Boost Converter 265
6.5.3 Buck-Boost Converter 266
6.5.4 Boost-Buck Converter 266
6.5.5 Discussion 267
6.6 Effect Of Frequency Variation 267

6.6.1 Half-Wave ZCS Converters 268
6.6.2 Full-Wave ZCS Converters 268
6.6.3 Half-Wave ZVS Converters 271
6.6.4 Full-Wave ZVS Converters 271
6.7 Results Of DC Analysis 274
6.7.1 Mode Boundaries 274
6.7.2 DC Characteristics 274
6.8 QRC - Topological Variations 277
6.8.1 The Shift Rules 283
6.8.1.1 Inductor Shift Rule 283
6.8.1.2 Capacitor Shift Rule 287
6.8.2 QRC Topological Variations 291
6.8.3 Evaluation Of QRC Variations 303
6.8.3.1 ZCS Resonant Buck Converters 303
6.8.3.2 A Few ZVS Resonant Boost-Buck Variations 310
6.8.3.3 QRC Topologies With Low Component Stresses 316
6.9 Summary And Conclusion 320

Conclusions And Future Work 321

References 325

Ideal Analysis Of SRC 329
A.1 CCM Analysis Below Resonance 329
A.1.1 Switching Boundary 331
A.1.2 Analysis Of A Steady-State Trajectory 332
A.1.3 Parameter Values Under Limiting Conditions 339
A.2 Type-2 DCM Analysis 342
A.3 CCM Analysis above Resonance 345

A.3.1 Switching Boundary 345
A.3.2 Analysis Of A Steady-State Trajectory 347
A.3.3 Parameter Values Under Limiting Conditions 350
A.4 Type-1 DCM Analysis 351
A.5 SRC Design Curves 354
A.6 Numerical Examples 365
A.6.1 Example 1 365
A.6.2 Example 2 366
A.6.2.1 Design 1 368
A.6.2.2 Design 2 369
A.6.2.3 Comparison Of Design 1 and Design 2 370
A.7 Program Listings 371
A.7.1 DC Analysis - CCM Below Resonance 371
A.7.2 DC Analysis - Type-2 DCM 371
A.7.3 DC Analysis - CCM Above Resonance 372
A.7.4 DC Analysis Given Operating Frequency 372
A.7.5 Trajectory Plots - Steady-State 373
A.7.6 Trajectory Plots - Control Analysis 375
A.7.7 Subroutines 377

Analysis Of SRC With Loss 382
B.1 Type - 2 DCM 382
B.2 Type-1 DCM 386
B.3 CCM 389
B.4 Program Listings 395
B.4.1 CCM Analysis Below Resonance 395
B.4.2 DC Characteristics Given Operating Frequency 395
B.4.3 Trajectory Plots - State Portrait 396

B.4.4 Trajectory Plots - Steady State 397
B.4.5 Trajectory Plots - Steady-State Given Frequency 399
B.4.6 Subroutines 400

Ideal Analysis Of PRC 404
C.1 Mode Boundaries 405
C.1.1 Time Intervals On State-Plane Diagrams 405
C.1.1.1 Resonant intervals (M1, M2, M3 and M4) 405
C.1.1.2 Inductor Charging/Discharging Intervals (M5 and M6) 408
C.1.1.3 Capacitor Charging/Discharging Interval (M7 And M8) 408
C.1.2 Lower CCM Boundary 409
C.1.3 Multiple Region Boundary 410
C.1.4 Boundary Between TM1 And TM2 411
C.1.5 DCM Boundary 413
C.1.6 Boundary Between Intersections-1 And -2 414
C.1.7 Upper CCM Boundary 417
C.1.8 Limit Boundary 418
C.1.9 Results Of Mode Analysis 419
C.2 Ideal DC Analysis 419
C.2.1 CCM Analysis - Intersection-1 419
C.2.1.1 Analysis Of A Steady-State Trajectory 419
C.2.1.2 Applicable Range Of Analysis 427
C.2.2 CCM Analysis - Intersection-2 428
C.2.2.1 Analysis Of A Steady-State Trajectory 428
C.2.2.2 Applicable Range Of Analysis 433
C.2.3. TM1 Analysis - Intersection-1 434
C.2.3.1 Applicable Range Of Analysis 434
C.2.3.2 Analysis Of A Steady-State Trajectory 436
C.2.4. TM2 Analysis 439

C.2.4.1 Applicable Range Of Analysis 439
C.2.4.2 Analysis Of A Steady-State Trajectory 441
C.2.5. DCM Analysis 444
C.2.5.1 Applicable Range Of Analysis 444
C.2.5.2 Analysis Of A Steady-State Trajectory 444
C.2.6.TM1 Analysis - Intersection-2 446
C.2.6.1 Applicable Range Of Analysis 448
C.2.6.2 Analysis Of A Steady-State Trajectory 448
C.2.7 LIMIT Analysis 450
C.3 Design Curves 451
C.4 Numerical Example 451
C.4.1 PRC Design 458
C.4.2 SRC Design 459
C.4.3 Operating Frequency Range 460
C.5 Program Listings 463
C.5.1 Complete DC Analysis 463
C.5.2 Complete DC Analysis - Given Operating Frequency 464
C.5.3 Subroutines 464

Ideal Analyses Of QRCs 469
D.1 Time Intervals On State - Plane Diagrams 470
D.2 Analysis Of QRCs With Half-Wave ZCS 471
D.2.1 Boundary Equations 471
D.2.1.1 Boundary Between Mode 1 And Mode 2 471
D.2.1.2 Boundary Between Mode 2 And Mode 3 473
D.2.1.3 Upper Boundary 473
D.2.2 DC Analysis 474
D.2.2.1 Analysis In Mode 1 474
D.2.2.2 Analysis In Mode 2 476

D.2.2.3 Analysis In Mode 3 478
D.3 Analysis Of QRCs With Full-Wave ZCS 479
D.3.1 Boundary Equations 479
D.3.1.1 Boundary Between Mode 1 And Mode 2 479
D.3.1.2 Upper Boundary 481
D.3.2 DC Analysis 481
D.3.2.1 Analysis In Mode 1 481
D.3.2.2 Analysis In Mode 2 483
D.4 Analysis Of QRCs With Half-Wave ZVS 486
D.4.1 Boundary Equations 486
D.4.1.1 Boundary Between Mode 1 And Mode 2 486
D.4.1.2 Boundary Between Mode 2 And Mode 3 486
D.4.1.3 Upper Boundary 488
D.4.2 DC Analysis 488
D.4.2.1 Analysis In Mode 1 489
D.4.2.2 Analysis In Mode 2 489
D.4.2.3 Analysis In Mode 3 491
D.5 Analysis Of QRCs With Full-Wave ZVS 492
D.5.1 Boundary Equations 492
D.5.1.1 Boundary Between Mode 1 And Mode 2 492
D.5.1.2 Upper Boundary 492
D.5.2 DC Analysis 494
D.5.2.1 Analysis In Mode 1 494
D.5.2.2 Analysis In Mode 2 495
D.6 DC Gain Relationships 496
D.6.1 Buck QRC 497
D.6.2 Boost QRC 497
D.6.3 Buck-Boost QRC 498
D.6.4 Boost-Buck QRC 499
D.7 Program Listings 499

D.7.1 Mode Boundaries 499
D.7.2 DC Characteristics - Half-Wave ZCS 500
D.7.3 DC Charateristics - Full-Wave ZCS 502
D.7.4 DC Characteristics - Half-Wave ZVS 503
D.7.5 DC Characteristics - Full-Wave ZVS 504
D.7.6 Subroutines 506

SPICE2 Simulation Of A Series Resonant Converter 507

E.1 Program Listings 508

Vita 511

List Of Figures

Chapter 2

2.1.	A half-bridge series resonant converter	18
2.2.	Typical waveforms - CCM below resonance	19
2.3.	Typical waveforms - CCM above resonance	20
2.4.	Typical waveforms - Type-2 DCM	21
2.5.	Topological modes	23
2.6.	Common equivalent circuit for different resonant intervals	24
2.7.	State-trajectories during resonant intervals $V_{oN} = 0.5$	27
2.8.	Composite state portrait $V_{oN} = 0.5$	29
2.9.	Set of composite state portraits	31
2.10.	Two asymmetrical steady-state trajectories	32
2.11.	Typical CCM/DCM-2 steady-state trajectories below resonance $V_{oN} = 0.5$	34
2.12.	Set of steady-state trajectories below resonance	36
2.13.	A steady-State trajectory with "multiple" resonant cycle operation	38
2.14.	Ideal steady-state trajectories in DCM-2 $V_{oN} = 0.5$	39
2.15.	SPICE2 simulation of effect of finite Q in DCM-2 $V_o = 150$ V and $Q = 20$	40
2.16.	Type-1 DCM trajectories	41
2.17.	Typical waveforms - Type-1 DCM	42
2.18.	Typical CCM steady-state trajectories above resonance $V_{oN} = 0.5$	45
2.19.	Set of steady-state trajectories above resonance	46
2.20.	Ideal regions of SRC operation	47
2.21.	Ideal design curves for a SRC - $0 < \omega_N < 0.5$	52
2.22.	Ideal design curves for a SRC - $0.5 < \omega_N < 1.0$	54
2.23.	Ideal design curves for a SRC - $1.0 < \omega_N < 1.5$	56
2.24.	SRC ideal dc characteristics	58

Chapter 3

3.1.	Common equivalent circuit for different resonant intervals	63
3.2.	Trajectory for conduction angle π	72
3.3.	Composite state portrait with loss - ζ = 1/30 and V_{oN} = 0.5	74
3.4.	CCM/DCM-2 steady-state trajectories for $\omega_N < 1$, V_{oN} = 0.5, ζ = 1/30	75
3.5.	Typical steady-state trajectories with loss	77
3.6.	Maximum energy trajectory at $\omega = \omega_D$	78
3.7.	Effect of losses on maximum output current and output voltage	81
3.8.	Maximum power output as function of damping factor	83
3.9.	Regions of SRC operation below resonance - with loss	84
3.10.	Design parameters vs normalized frequency - with loss; ζ = .025	85
3.11.	DC characteristics for $\omega_N < 1$ - with loss	88
3.12.	DC characteristics for $\omega_N < 1$ - without loss	89
3.13.	Experimental SRC circuit	91
3.14.	Drive circuit for the power MOSFET	92
3.15.	Experimental verification of analysis	93
3.16.	Experimental trajectories in different modes	95
3.17.	Experimental waveforms corresponding to Figure 3.16	96

Chapter 4

4.1.	Functional Block Diagrams	100
4.2.	Control waveforms for SRC control	103
4.3.	Simulation of SRC with ASDTIC control	105
4.4.	SRC steady-state trajectory under CCM	107
4.5.	Control of SRC - Block diagrams	109
4.6.	Control laws on state plane	112
4.7.	DC gain characteristics - Normalized output current versus normalized control input	117

4.8.	Limits on dynamic performance of SRC	119
4.9.	Partial computer flowchart for state-plane study of control methods	122
4.10.	ASDTIC control problems viewed on state plane	126
4.11.	Unstable response of transistor-conduction-angle control	128
4.12.	Response for step control change	130
4.13.	Transient under short circuit	131
4.14.	Capacitor-voltage control - Response trajectories	132
4.15.	Frequency control - Response trajectories	134
4.16.	Diode-conduction-angle control - Response trajectories	135
4.17.	Explanatory diagram for operation of optimal trajectory control	137
4.18.	Optimal trajectory control - Response trajectories	138
4.19.	Response of optimal trajectory control for large control changes	140
4.20.	Experimental power circuit diagram	145
4.21.	Functional block diagram of experimental control circuit	147
4.22.	Optimal trajectory control circuit diagram	148
4.23.	Typical control waveforms of optimal trajectory control	151
4.24.	Circuit for introducing step-control change	156
4.25.	Transient response for step-change in control - Optimal trajectory control	158
4.26.	Transient response for step-control change - Frequency control	159
4.27.	Transient Performance for large changes in tank energy	160

Chapter 5

5.1.	A half-bridge parallel resonant converter (PRC)	166
5.2.	Resonant topological modes of a PRC	170
5.3.	Common equivalent circuit for different resonant intervals	171
5.4.	Continuous-conduction mode (CCM) waveforms - $I_{oN} < 1$, $\omega_N < 1$	172
5.5.	State trajectories under different resonant topological modes ($I_{oN} = 0.5$)	175
5.6.	Composite state portrait of a PRC ($I_{oN} = 0.5$)	176
5.7.	CCM steady-state trajectories - $I_{oN} < 1$	177
5.8.	CCM waveforms for Fig. 5.7 (b) - $I_{oN} < 1$, $\omega_N > 1$	178

5.9.	Forced commutation trap zones	180
5.10.	Explanatory diagram for inductor charging/discharging interval	182
5.11.	Nonresonant topological modes - equivalent circuit diagrams	183
5.12.	Nonresonant topological modes - state-plane trajectories	184
5.13.	State-plane construction of CCM trajectories	186
5.14.	Base-drive strategies	189
5.15.	Steady-State trajectories for $I_{oN} = 0$	191
5.16.	NonCCM operation for $I_{oN} < 1$ below ω_{LOW} - strategy - 1	193
5.17.	NonCCM operation for $I_{oN} < 1$ below ω_{LOW} - strategy - 2	195
5.18.	Discontinuous-conduction mode (DCM) waveforms for Fig. 5.17(e)	196
5.19.	NonCCM operation for $I_{oN} < 1$ above ω_{HIGH}	198
5.20.	TM1 waveforms for Fig. 5.19 (b)	200
5.21.	CCM steady-state trajectories - $0 < I_{oN} < \sqrt{2}$	201
5.22.	NonCCM operation for $1 < I_{oN} < \sqrt{2}$ below ω_{LOW}	203
5.23.	NonCCM operation for $1 < I_{oN} < \sqrt{2}$ above ω_{HIGH}	204
5.24.	Steady-state trajectories for $I_{oN} > \sqrt{2}$ below ω_{MAX}	205
5.25.	Steady-State trajectories for $I_{oN} > \sqrt{2}$ above ω_{MAX}	206
5.26.	Operating regions of a PRC	209
5.27.	Features of PRC operating regions	210
5.28.	Ideal DC characteristics of a PRC - Below resonant frequency	213
5.29.	Ideal DC characteristics of a PRC - Above resonant frequency	214
5.30.	Complete Ideal DC characteristics of a PRC	215
5.31.	Experimental PRC circuit - power circuit	217
5.32.	Controller circuit diagram	218
5.33.	Explanatory diagram for the experimental verification of PRC modes	220
5.34.	Oscillograms of experimental trajectories under Strategy-2 with $I_o = 0.5$ A ($I_{oN} = 0.517$) - line 'a' of Fig. 5.33	221
5.35.	Waveforms corresponding to Fig. 5.34	222
5.36.	Oscillograms of experimental trajectories under Strategy-1 with $I_o = 1.0$ A ($I_{oN} = 1.034$) - line 'b' of Fig. 5.33	223
5.37.	Waveforms corresponding to Fig. 5.36	224

5.38.	Oscillograms of experimental trajectories under Strategy-1 with I_o = 1.5 A (I_{oN} = 1.551) - line 'c' of Fig. 5.33	225
5.39.	Waveforms corresponding to Fig. 5.38	226
5.40.	Experimental mode boundaries - ω_{LOW} and ω_{HIGH}	228
5.41.	Experimental boundaries - ω_{MUL}, ω_{MAX} and ω_{LIMIT}	229
5.42.	Experimental boundaries - Natural commutation region and ω_{DISC}	230
5.43.	Explanatory diagrams for reduction in natural commutation region	232
5.44.	Explanatory diagrams for deviation observed in ω_{DISC} boundary	233
5.45.	Experimental DC characteristics - Below resonant frequency	235
5.46.	Experimental DC characteristics - Above resonant frequency	236
5.47.	State-plane derivation of the resonant buck converter	238
5.48.	Tank waveforms for Fig. 5.47 (b)	239
5.49.	Circuit derivation of the novel resonant buck converter	240
5.50.	Theoretical DC characteristics of the novel resonant buck converter	242

Chapter 6

6.1.	Resonant switches	248
6.2.	Basic quasi-resonant converters	250
6.3.	Equivalent circuits during different intervals of operation	251
6.4.	Common steady-state trajectories in mode-1	257
6.5.	Common waveforms for QRCs with half-wave ZCS	258
6.6.	Common waveforms for QRCs with full-wave ZCS	259
6.7.	Common waveforms for QRCs with half-wave ZVS	260
6.8.	Common waveforms for QRCs with full-wave ZVS	261
6.9.	Effect of frequency variation - QRCs with half-wave ZCS	269
6.10.	Effect of frequency variation - QRCs with full-wave ZCS	270
6.11.	Effect of frequency variation - QRCs with half-wave ZVS	272
6.12.	Effect of frequency variation - QRCs with full-wave ZVS	273
6.13.	Operating regions of QRCs	275
6.14.	Diode voltage charateristics of QRCs	278

6.15.	DC gain charateristics of QRCs with ZCS	279
6.16.	DC gain charateristics of QRCs with ZVS	281
6.17.	Inductor shift rule	284
6.18.	Capacitor shift rule	288
6.19.	Resonant buck converter variations	293
6.20.	Resonant boost converter variations	295
6.21.	Resonant buck-boost converter variations	297
6.22.	Resonant boost-buck converter variations	299
6.23.	Mode-1 state plane diagrams of resonant buck converters with ZCS	304
6.24.	Comparison of full-wave ZCS resonant buck converters	307
6.25.	Mode-1 state plane diagrams of a few ZVS resonant boost-buck converters	311
6.26.	Comparison of half-wave ZVS resonant boost-buck converters	312
6.27.	Mode-1 steady-state trajectories for QRCs with low component stress	317
6.28.	Quasi-resonant converters with low component stress	318

Appendix A

A.1	Ideal CCM operation below resonance - Analysis diagram	330
A.2	Ideal type-2 DCM operation - Analysis diagram	340
A.3	Ideal CCM operation above resonance - Analysis diagram	346
A.4	Ideal type-1 DCM operation - Analysis diagram	352
A.5	Ideal design curves for a SRC - $0 < \omega_N < 0.5$	355
A.6	Ideal design curves for a SRC - $0.5 < \omega_N < 1.0$	358
A.7	Ideal design curves for a SRC - $1.0 < \omega_N < 1.5$	361
A.8	SRC ideal DC characteristics	364

Appendix B

B.1	Type-2 DCM operation with loss - Analysis diagram	383
B.2	Type-1 DCM operation with loss - Analysis diagram	387
B.3	CCM operation below resonance with loss - Analysis diagram	390
B.4	CCM analysis with loss given R, ζ, and V_{oN} - computer flowchart	393
B.5	CCM analysis with loss given ω_N, ζ and V_{oN} - computer flowchart	394

Appendix C

C.1	Operation at boundary frequencies - Analysis diagrams	406
C.2	PRC boundaries of operation - Strategy-1	420
C.3	CCM operation in intersection-1 - Analysis diagram	421
C.4	CCM operation in intersection-2 - Analysis diagram	429
C.5	TM1 operation in intersection-1 - Analysis diagram	435
C.6	TM2 operation - Analysis diagram	440
C.7	DCM operation - Analysis diagram	445
C.8	TM1 operation in intersection-2 - Analysis diagram	447
C.9	Ideal design curves for a PRC - CCM below resonance ($I_{oN} \leq 1$)	452
C.10	Ideal design curves for a PRC - CCM above resonance ($I_{oN} < 1$)	454
C.11	Ideal DC characteristics of a PRC - below and above resonant frequency	456
C.12	Complete ideal DC characteristics of a PRC	457

Appendix D

D.1	QRCs with half-wave ZCS - Analysis diagrams	472
D.2	QRCs with full-wave ZCS - Analysis diagrams	480
D.3	QRCs with half-wave ZVS - Analysis diagrams	487
D.4	QRCs with full-wave ZVS - Analysis diagrams	493

List Of Tables

2.1	SRC - Summary of Equations	49
4.1	SRC - Evaluation of Control Methods	141
5.1	PRC - Operating Modes	207
5.2	PRC - Regions	211
6.1	QRC - Intervals of Operation	252
6.2	DC Gains of Quasi-Resonant Converters	276
6.3	Comparison of Full-Wave ZCS Resonant Buck Converters	315
6.4	Comparison of a few Half-Wave ZVS Resonant Boost-Buck Converters	319
A.1	SRC - Parameters under Limiting Conditions	341

Chapter 1

Introduction

1.1 Background

Power electronics, in a broad sense, is concerned with the processing of given electrical power into output suitable for specific load or loads, using static electronic devices and means. The conditioning may involve meeting the requirements of frequency, which includes dc, number of phases and magnitudes of voltage or current, imposed by the load. Additional demands may exist on the quality of the processed power. These include factors such as harmonic content, output regulation and response to control and load changes.

Like many other areas of engineering, power electronics is an applications-driven field. The continued demands for smaller, lighter and yet efficient power processing equipment have been the main motivating factors behind the introduction of new circuit topologies and the development of new power semiconductor devices.

Almost all power electronic circuits utilize electronic switches, which modulate the input supply waveform and generate ac waveforms internal to the circuit. A power transformer is needed in many

applications, to change the voltage level, or to provide electrical isolation, or both. Also, a low pass filter is usually required at the output to eliminate the internal ac waveform. The size of a transformer or a filter circuit is reduced considerably when a higher operating frequency is used. This is the reason for the progressively higher internal frequencies which have been used in power electronic equipment over the years.

The switch dissipates energy both during the turn-on process and the turn-off process. Thus the total power loss in the switch depends on the number of switching operations in a second and hence increases rapidly with the internal switching frequency. It is essential that the switching loss of an intrinsically fast device, such as a power MOSFET (metal-oxide-semiconductor field effect transistor), be limited in a circuit, in order to utilize such a switch at a high frequency without sacrificing the efficiency. Resonant converters aim at reduction or elimination of either the turn-on loss or the turn-off loss or both, by suitably shaping the switch waveforms, using resonant phenomenon.

During the turn-on process, the voltage across the switch reduces to zero, while the current builds from zero to the value dictated by the external circuit. The overlap of these two transitions for a finite interval, during which the electronic switch stays in its active region, accounts for the turn-on loss. While reducing the turn-on interval will reduce this loss, there are limitations imposed by the device and its drive circuit.

Those resonant converters which reduce the turn-on loss do so by a)reducing the switch voltage to zero before the turn-on instant, b)limiting the rate of rise of switch current, or c)by following both (a) and (b) together. As examples, quasi-resonant converters utilizing the zero voltage switching principle [62] follow method (a), quasi-resonant converters operating on the zero current switching principle [61] follow method (b) and series and parallel resonant converters operating above resonant frequency [7] follow method (c).

The loss during turn-off is mainly due to the interruption of the current in the parasitic inductances of the circuit by the power switch. Thus, increasing the speed of the turn-off process can not eliminate the turn-off loss and will, on the other hand, raise the voltage stress across the switch to unacceptable levels.

In order to minimize the turn-off loss, the energy stored in the parasitic inductances at the instant of switching can either a)be diverted away from the switch or b)be reduced in magnitude. Snubber circuits, which are generally dissipative, operate using method (a) by diverting the inductive energy to an energy absorbing device such as a capacitor. Resonant converters based on the principle of zero voltage switching, such as the Class-E amplifier [57], also use method (a), by limiting the rate of rise of the switch voltage after it is turned off.

The inductive energy in the circuit can be minimized (method (b) above) by improving the layout for which there are obvious physical limitations. An alternative way called zero current switching principle is to make the current in the device zero at the switching instant. The latter method is adopted in many resonant converters, such as the series resonant converter when operated below resonant frequency [9], where a resonant cycle ensures the required current zero values at switch-off instants.

The concept of resonant converters has been known for several years [1], as one of the alternatives to commutate a conducting thyristor or thyratron. These devices can not be turned off using their gate drive signals. In these early resonant converters, schemes in which the device current reduces to zero by itself due to resonance were used to commutate conducting devices.

In recent years, the technology of resonant power processors has been the focus of considerable research and development efforts [2 to 39, 44 to 68], though modern power devices, such as bipolar junction transistors [BJTs] or MOSFETs, can be easily turned off through their base or gate terminals. The renewed interest in resonant converters is due to their ability to minimize switching loss and enable converter frequencies to be increased to high levels, as discussed earlier. They represent an important and exciting technological development towards further miniaturization of power electronic equipment.

1.2 Literature Survey

References [1 to 11] present some of the bridge type resonant converter topologies which have been developed over the years. As indicated in Sec. 1.1, early series converters [1] utilized the resonant

principle to commutate a conducting device and these converters were used in such industrial applications as induction heating and melting [2].

Mapham [3] presents a dc to ac inverter topology with good output ac voltage waveform. This can be considered to be the forerunner of the present day dc to ac and dc to dc resonant converters. Myers and Peck [4], Babu [5] and Ranganathan, Ziogas and Stefanovic [6] discuss the operation of the dc to dc parallel resonant converter (PRC), which is somewhat similar to the Mapham converter. The name parallel resonant converter is ambiguous and it will be more accurate to call this circuit as the "parallel load-capacitor link resonant converter". However, for convenience, the term parallel resonant converter is used throughout this report. Myers and Peck [4] operate the PRC above resonant frequency. In this range of operation, the antiparallel diode across the power device is naturally commutated and hence the slow, built-in diode of a power MOSFET can be used as feedback diode in the circuit. The configuration suggested by Myers and Peck also incorporates the transformer leakage inductance as part of the resonant circuit by placing the resonant capacitor on the secondary side of the transformer. The operation of a resonant converter above resonant frequency is also suggested by Steigerwald [7].

Due to similarity in appearances of PRC and dc to dc version of Mapham converter, one may be led to believe that their performances are also similar. However, the location of the resonant inductor in the two topologies is different and this causes crucial differences in their operations. Considering a half-bridge topology, the PRC utilizes a single resonant inductor, whereas the Mapham converter splits the inductor and places one inductor in series with each of the two devices. The operations of the two converters in the discontinuous conduction mode (DCM) of operation are the same. During the normal operation, however, the Mapham converter exhibits an "overlap interval", when a diode and a thyristor conduct together, whereas this overlap interval is absent in the case of the PRC.

A dc to dc resonant converter topology, in which the load was effectively connected in series with the resonant capacitor, was introduced by Schwarz [8]. In the case of the PRC, the load is connected effectively across the resonant capacitor. The ideal dc voltage gain of the topology suggested in [8], however, is unity for all load magnitudes and operating frequencies. Due to this, the converter's output can not be regulated. Schwarz added feedback diodes across the devices to overcome this problem [9] and this is the topology currently referred to as the series resonant converter (SRC).

The PRC and the SRC circuits are two major bridge type resonant converters, with distinct operating characteristics. The operation of an SRC can be approximated by a current source, while that of a PRC by a voltage source. Thus, in a voltage regulator application the PRC is generally the better choice, whereas in applications such as welding where a current output is required the SRC is the preferred topology.

Kassakian [10] derives a current mode converter from the PRC topology, using the duality principle. It is to be noted that Kassakian refers to the PRC topology as the series resonant converter. Kassakian, Goldberg and Moretti [11] also evaluate the merits and demerits of these two topologies. The converter introduced by Kassakian has the lower component stresses, but requires special start-up and shut-down schemes.

Several ingenious schemes have been suggested for using the principle of resonant power conversion for more complex applications, such as dc to low frequency ac. Many of these suggestions are due to Schwarz and Klassens. References [12,13,14,15] show a few of the proposed systems. In these schemes, the input supply feeds an input matrix of power switches and the load circuit is connected to an output matrix of power switches. A resonant circuit forms a single phase high frequency link between the input and output switches. The systems perform basically like dc to dc resonant converters with the input supply and the output load circuit connected in different ways at different operating intervals, as determined by the power switches of the input and the output matrix.

The characteristics of resonant converters in the continuous conduction mode CCM are sensitive to load variations. A large operating frequency range may be required in order to cater to widely varying loads and this is a disadvantage in many cases. Muroyama and Sakakibara [16] and Chen and Bonert [17] present modifications to tank circuits of certain resonant converters, in order to reduce or eliminate this load dependence.

Several authors, [5,6] for example, have obtained the steady-state solutions of resonant converters using computer algorithms. King and Stuart [18,19] and Vorperian and Cuk [20] have both carried out systematic dc analyses of the SRC based on circuit analysis techniques. Vorperian and Cuk have also included a limited dc analysis of PRC in [21].

King and Stuart [18, 19] present their results of CCM analysis in terms of an intermediate parameter, the diode conduction angle. These equations are relatively easy to solve. Another advantage of this method is that once the steady-state solution is obtained, several other parameters, such as the device average currents and conduction angles, can be calculated in a straight-forward manner. Furthermore, King and Stuart use output voltage as the load parameter and this permits their results to be used for any type of load directly.

Vorperian and Cuk [20] brought out the complexity of SRC operation and carried out an exhaustive dc analysis of this converter, under different loads, operating frequencies and modes of operation. The closed-form equations for the ideal dc voltage gain for both SRC [20] and PRC [21] were derived by them. These equations, however, are complex and difficult to solve. Since the load parameter used in the derivation is the load resistor, the dc gain equations presented by them can not be directly used if the load is a back-emf type of load, such as a dc motor or a battery.

Witulski and Erickson [22] have derived from the equations of Vorperian and Cuk [20] for SRC closed-form solutions relating output voltage and current. This method of presenting the dc output characteristics have been termed as "output plane presentation". Johnson and Erickson [23] have also analyzed the PRC and derived equations relating output voltage and current for a few of the modes of PRC operation.

References [4,6,9,24,25,26,27] discuss the different control methods that can be adopted to control resonant converters. Schwarz [9] presents an analog-signal-to-discrete-time-interval-converter (ASDTIC) control. This method has also been called the integral pulse control [25,26]. The aim of this method is to control the tank energy by controlling the half-cycle average tank current. This method, however, results in an unstable system as pointed out by Oruganti and Lee [28,29]. DeHaan [25] and DeHaan and Huisman [26] also confirm that SRC with ASDTIC control is unstable and suggest modifications to make the system stable.

Myers and Peck [4] adopt the easier frequency control method for the PRC, while Robson and Hancock [27] do the same for the SRC. Ranganathan, Ziogas and Stefanovic [6] describe a simple method of control for the PRC, which may be called the "capacitor-voltage control". King and Stuart [24] describe yet another method of control, this time for the SRC, and this method may be called the "diode-

conduction-angle control". Reference [24] also compares frequency control and diode-conduction-angle control based on the ability to withstand overloads, using static characteristics of the converter.

In all the methods of control described above, the frequency of operation has to be changed to compensate for load and supply variations and this is a disadvantage. The converter output can also be varied by controlling a)input to the tank circuit or b)output after the tank circuit. In these methods, the operating frequency can be held constant, though the complexity of the power circuit is increased. An interesting output phase angle control method, which may be called "alpha control", has been proposed by Ranganathan, Ziogas and Stefanovic [30]. Based on this, a modified phase angle control technique called "theta control" has been proposed by Tsai, Oruganti and Lee [31]. Unlike the system in [30], theta control results in a system whose dc characteristics are insensitive to load variations. Another scheme for obtaining controlled low frequency output from two resonant converters by using the beat frequency method has been suggested by Ranganathan, Ziogas and Stefanaovic [32]. Varying the input to the tank circuit has been adopted by several authors including Chen and Bonert [17], Harada and Chen [33], Pitel [34], Turnbull and Tompkins [35].

A few of the publications relate to the dynamics of resonant converter operation. Vorperian and Cuk [21] present a small signal analysis of SRC and PRC under frequency control method. The analysis is based on discrete data approach, though the final results are presented in the frequency domain to facilitate measurement. Simplified frequency domain transfer function expressions are presented by Vorperian [36] when the converters are operated away from the resonant frequency under light load conditions. Verghese, Elbuluk and Kassakian [37] present a generalized discrete data approach for power electronic circuits, and have performed a small signal discrete time analysis on the SRC to illustrate the approach. King and Stuart [38] present a discrete-time model of SRC for the purpose of large-signal dynamic simulation. King and Stuart [39] have also discussed the instability induced in a SRC under certain conditions due to the low frequency resonant circuit formed by the normal tank circuit together with the magnetizing inductance of the output transformer, if used.

Graphical state-plane technique [40] has been used effectively in the analysis and control of nonresonant inverters and converters [41,42,43]. In the case of resonant converters, Kasturi [44] has compared a few dc to ac topologies based on the sensitivity of the peak resonant-capacitor voltage to load variations, using state-plane techniques.

Dougherty [45] presents a simulation of SRC using SUPER-SCEPTRE, which is an electrical analysis program based on the state-variable approach. Kassakian [46] simulates a resonant converter utilizing a hybrid computer program developed to simulate power electronic circuits. Avant and Lee [47] present examples of SRC simulations utilizing an accurate thyristor model named the "J3 SCR model".

References [4,5,27,35,49 to 54] are some of the publications dealing with the design and technology of resonant converters.

Several resonant converters using a single switch have been proposed typically for low power applications. Buchanan and Miller [55] and Miller [56] have proposed a few circuits based on zero current principle. Sokal and Sokal [57] and Redl, Molnar and Sokal [58] have presented class-E amplifiers which operate on the zero voltage switching principle. Liu and Lee [59] isolated the half-wave zero current resonant switch using which they generated a series of quasi-resonant converters similar to the pulse-width modulated (PWM) converters. Oruganti and Lee [60] have proposed a resonant buck converter using a full-wave zero current switch derived from the state-plane analysis of parallel resonant converter. The characteristics of this converter is load independent which is a desirable feature. Liu, Oruganti and Lee [61] present both types of zero current switches and discuss their use in different topologies. Liu and Lee [62] have proposed a series of quasi-resonant converters based on zero-voltage switches, which are duals of zero-current switches. By adopting the zero voltage resonant switching, the operating frequency of QRC could be increased even further. However, zero voltage switch QRCs can not operate below a certain minimum load. Zeng, Chen and Lee [63] have presented variations of zero current switching quasi resonant converters and have compared them on the basis of component stresses. In a development parallel to the present work, Vorperian, Tymerski, Liu and Lee [67,68] have performed a generalized dc analysis (in mode 1 converter operation). They have also carried out ac small signal analyses generating dc and ac models similar to those in transistor analysis.

1.3 Present Work

1.3.1 Motivation And Objective

The operation of a resonant converter under varying load and operating frequency is complex [20]. The analytical techniques based on circuit analysis principles alone [18 to 23] do not directly identify the modes exhibited by a converter under different operating conditions. The existence of the modes and the performance of the converter in each of these modes are not readily apparent from such studies. However, in order to design and use a resonant converter effectively, it is necessary that its characteristics under different operating modes be clearly established. The major objective of the present work is the development of an analytical method applicable to a large class of resonant converters for determining their modes of operation and for establishing the characteristics in each of these modes. The study also aims at the application of the method to specific types of resonant converters in order to determine their characteristics fully.

Simulation of a SRC with ASDTIC control [8,28,29], as part of the present study, revealed that the control of resonant converters is considerably more complex than that of their pulse-width modulated (PWM) counterparts. The dynamics of the SRC often appeared unpredictable, with an irregular sequence of conduction accompanied by large power surges in the tank circuit and current stresses on the components. Another objective of the present study was to investigate the reason for such phenomena and to assess the different control methods which can be used with a SRC.

1.3.2 Method Of Analysis

The approach that was found suitable for the objectives of the study was graphical state plane technique [40]. Using this approach, the operation of the converter is represented visually both under steady state and under limited duration transient conditions. Under steady-state conditions, the method facilitates

qualitative understanding of converter operation including identification of the operating modes. In addition, the technique permits simple geometrical analysis of the state plane diagrams for obtaining the characteristics in each mode.

Under dynamic conditions, the performance of the converter under different control methods can be assessed on the state plane. In particular, the ability of a control method in keeping the circuit component stresses and the tank energy within bounds during transients can be investigated using the graphical state plane technique.

Graphical state plane technique has been used effectively in the analysis and control of nonresonant inverters and converters [41,42,43]. In the case of resonant converters, Kasturi [44] has compared a few dc to ac topologies based on the sensitivity of the peak resonant-capacitor voltage to load variations, using state-plane technique. Verghese, Elbuluk and Kassakian [37] suggest the use of the closed steady-state trajectory of a SRC for graphically determining its dc characteristics. The present study is a parallel development which evolved without reference to the work mentioned in [37].

1.3.3 Major Results

Graphical state-plane technique has been successfully adapted for understanding the operation of certain resonant converters, identifying the operating modes and their applicable regions and establishing the characteristics of the converters in each of the modes. The method of analysis has been presented in this report by actual application to different types of resonant converters - SRC, PRC and the family of QRCs. In addition to the establishment of the method of analysis, the following results specific to each type of resonant converter have also been achieved.

SRC: 1) Mode analysis was performed and the dc characteristics of the converter in each mode was determined using graphical state-plane technique.
2) The effect of parasitic losses, which has been generally ignored in the literature, was incorporated into the graphical analysis. It was shown both experimentally and theoretically that ignoring the losses leads

to poor prediction of SRC performance under certain conditions, whereas by including the losses the characteristics of the converter are predicted more accurately.

3) ASDTIC control was shown to be unstable. The occurrence of large tank energy surges with this control method was explained using state-plane trajectories.

4) A number of control methods, including new ones, were compared on the state plane for performance under conditions such as step control change, step load voltage change and ideal short circuit.

5) Based on the state-plane analysis, a control method which attempts to achieve the fastest possible response called "optimal trajectory control" was proposed. By exploiting the inherent properties of the SRC as revealed by the state-plane analysis, the tank energy is always kept within bounds avoiding the overshoots and surges present with certain other control methods. Experimental results also confirm the excellent performance predicted for this control method.

PRC.: 1) Complete mode analysis, including identification of many hitherto unknown modes, was performed. The complex behavior of the converter under varying load and frequency was analyzed. The dc characteristics of the converter in each of the modes was determined. Experimental results confirm the existence of the various modes. The experimental mode boundaries and dc characteristics are compared with the theoretical predictions.

2) A novel resonant buck converter using a bidirectional switch was proposed based on the state-plane analysis of a PRC. This converter, which is a member of the QRC family, has many attractive features including dc characteristics that are almost load independent.

QRCs: 1) Generalized mode and dc analysis applicable for all members of the QRC family was carried out using state-plane techniques. Although nearly hundred QRC variations exist, it was shown that only four sets of mode and dc analyses - one for each type of resonant switch - are needed. This simplifies the understanding and analysis of these converters considerably.

2) Using two simple circuit rules, named "inductor and capacitor shift rules", a technique for generating many topological variations from given QRC was established. Several topological variations including new ones were generated by application of these rules. By comparing relative component stresses, a few topologies, one for each QRC type, were selected from the point of view of low component stresses.

Most of the work presented in this report have been included by Oruganti and Lee in [64], which is a set of lecture notes dealing with the analysis, design and control of resonant converters. The publications

based on the work presented in this report are [28,29,60,65,66]. The state-plane analysis of the novel resonant buck converter which was included as part of [64,66] has been omitted from the present report because of the inclusion of the generalized QRC analysis.

1.3.4 Outline Of Report

The geometrical analysis of the state-plane diagrams and computer programs for generating the characteristic curves have been placed in the appendixes.

In Chapter 2, the state-plane analysis of a SRC both above and below resonant frequency is presented.

In Chapter 3, the analysis of Chapter 2 is modified to include parasitic losses, for operation below resonant frequency.

The control analysis is carried out in Chapter 4 on the state plane. The new optimal trajectory control is also presented in Chapter 4.

In Chapter 5, an exhaustive dc analysis including mode analysis of a PRC is performed. The novel resonant buck converter is also proposed in this chapter.

Generalized dc analyses applicable for all QRC topologies are carried out in Chapter 6. Also, many QRC topological variations including several new ones are generated and evaluated using two circuit rules.

The quantitative analyses of state-plane diagrams corresponding to SRC (losses ignored), SRC (losses included), PRC and the QRCs are included in Appendixes A, B, C and D, respectively. SPICE2 simulation of SRC with ASDTIC control is briefly described in Appendix E and a typical program listing is also included.

Chapter 2

DC Analysis Of Series Resonant Converter

2.0 Symbols Of Variables

The symbols listed below include those used in Appendix A also. In alphabetical order,

α	-	Diode Conduction Angle
β	-	Transistor Conduction Angle
Δi_L	-	Change in Inductor Current
Δi_{LN}	-	Normalized Change in Inductor Current
ρ	-	Radius of a State Trajectory
θ	-	Angular Interval on State Plane
θ_0	-	Initial Angle on State Plane
ω	-	Operating Frequency
ω_N	-	Normalized Operating Frequency
ω_0	-	Resonant Frequency of the *LC* Circuit
C	-	Value of Resonant Capacitor

d	-	Instantaneous Distance of State from Origin
e_T	-	Instantaneous Resonant Tank Energy
e_{TN}	-	Normalized Instantaneous Tank Energy
E_{TP}	-	Peak Tank Energy
E_{TPN}	-	Normalized Peak Tank Energy
I_{DAV}	-	Average Diode Current
I_{DAVN}	-	Normalized Average Diode Current
I_{DR}	-	RMS Diode Current
I_{DRN}	-	Normalized RMS Diode Current
I_{QAV}	-	Average Transistor Current
I_{QAVN}	-	Normalized Average Transistor Current
I_{QR}	-	RMS Transistor Current
I_{QRN}	-	Normalized RMS Transistor Current
i_L	-	Instantaneous Resonant Inductor Current
I_{LAV}	-	Half-Cycle Average Inductor Current
I_{LAVN}	-	Normalized Half-Cycle Average Inductor Current
i_{LN}	-	Normalized Instantaneous Inductor Current
I_{L0}	-	Initial Inductor Current
I_{L0N}	-	Normalized Initial Inductor Current
I_{LP}	-	Peak Inductor Current
I_{LPN}	-	Normalized Peak Inductor Current
I_{LR}	-	RMS Inductor Current
I_{LRN}	-	Normalized RMS Inductor Current
i_o	-	Instantaneous Output Current (Before Filter)
I_o	-	Output DC Current (After Filter)
i_{oN}	-	Normalized Instantaneous Output Current (Before Filter)
I_{oN}	-	Normalized Output DC Current (After Filter)
I_{XAV}	-	Average Current of Device X
I_{XAVN}	-	Normalized Average Current of Device X
L	-	Value of Resonant Inductor
N_i	-	Current Normalizing Factor
N_v	-	Voltage Normalizing Factor

R	-	Radius of Transistor Trajectory
R'	-	Radius of Diode Trajectory
R_{LOAD}	-	Load Resistance
R_{max}	-	Maximum Radius of Transistor Trajectory
R_{min}	-	Minimum Radius of Transistor Trajectory
R_N	-	Normalized Load Resistance
t	-	Time
T	-	Operating Period
$t_1, t_2, .. t_A, t_B, ..$	-	Particular Instants of Time
t_d	-	Diode Conduction Interval
t_q	-	Transistor Conduction Interval
T_N	-	Angular Operating Period
v_C	-	Instantaneous Resonant Capacitor Voltage
V_{CA}	-	Capacitor Voltage at $t = t_A$
V_{CAN}	-	Normalized Capacitor Voltage at $t = t_A$
V_{CB}	-	Capacitor Voltage at $t = t_B$
V_{CBN}	-	Normalized Capacitor Voltage at $t = t_B$
v_{CN}	-	Normalized Instantaneous Capacitor Voltage
V_{C0}	-	Initial Capacitor Voltage
V_{C0N}	-	Normalized Initial Capacitor Voltage
V_{CP}	-	Peak Capacitor Voltage
V_{CPN}	-	Normalized Peak Capacitor Voltage
V_E	-	Equivalent Driving Voltage
V_{EN}	-	Normalized Equivalent Driving Voltage
V_o	-	Output DC Voltage
v_L	-	Instantaneous Voltage Across Inductor
V_{oN}	-	Normalized Output DC Voltage
V_s	-	Supply DC Voltage
(VS)	-	Volt-Seconds Across Inductor
$(VS)_N$	-	Normalized Volt-Seconds Across Inductor
$(VS)_P$	-	Peak Volt-Seconds Across Inductor
$(VS)_{PN}$	-	Normalized Peak Volt-Seconds Across Inductor

v_{zy} - Instantaneous Voltage at the Input Terminals of Output Rectifier

Z_0 - Characteristic Impedance of Resonant Tank

2.1 Introduction

In this chapter, a detailed steady-state analysis of the series resonant converter (**SRC**) is performed using state-plane analytical techniques. The SRC can be viewed as a piecewise linear system switching between five possible circuit topologies. Based on the possible trajectories on the state plane in the different topological modes a composite state portrait is first established. This state portrait completely characterizes the operation of the converter at an output voltage for all operating conditions.

Closed steady-state trajectories are then constructed on the state plane using the trajectory segments belonging to a state-portrait. These trajectories correspond to different steady-state operating conditions. The operation of the SRC for different loads and operating frequencies is then examined by studying these steady-state trajectory diagrams. In Appendix A, these diagrams are also used to quantitatively analyze converter performance and to derive the equations governing the operation of the converter. Useful design curves have been plotted from these analytical results and these are included in the same appendix along with a few numerical examples.

The analysis in this chapter is performed assuming lossless operation of the converter. In reality, the circuit does possess losses which can affect the performance under certain operating conditions, such as when the frequency of operation is close to resonant frequency. Under such circumstances, the ideal lossless analysis indicates the limit on converter performance. Also, it is more convenient to determine converter operating modes and dc characteristics without assuming losses and then to include the losses, if necessary, to determine the resulting deviations from the ideal performance. Chapter 3 shows such an approach applied to the case of a SRC for operation below resonant frequency when the losses are considered.

2.2 *Ideal State-Plane Analysis*

2.2.1 Circuit Operation

The circuit diagram of a half-bridge series resonant converter is shown in Fig. 2.1. Figure 2.2 shows typical waveforms for operation in the continuous-conduction mode (**CCM**) when the operating frequency is less than the resonant frequency of the tank circuit. Likewise, the waveforms in Fig. 2.3 correspond to typical CCM operation when the operating frequency is above the resonant frequency of the tank. It must be noted that as per the terminologies associated with resonant converters continuous-conduction mode or discontinuous-conduction mode (**DCM**) refers to the tank current, i_L , being either continuous or discontinuous. This is unlike the case with switching regulator analyses, where the terms CCM and DCM usually refer to the nature of output current i_o. In the particular case of a SRC, however, whenever current i_L is continuous, i_o is also continuous; likewise, whenever i_L is discontinuous, i_o is also discontinuous.

In Fig. 2.1, devices Q1 and D1 form a bidirectional switch, SW1, and Q2 and D2 form another bidirectional switch, SW2. Under CCM conditions a square waveform is imposed across points 'zx' in the circuit. Inductor L and capacitor C form the resonant tank circuit. The output load is connected in series with the tank circuit through the output bridge rectifier. Thus, the rectified tank current feeds the load after being filtered by the filter capacitor, C_F. In Figs. 2.2 and 2.3, the current marked as I_{LAV} is the half-cycle average inductor current equal to I_o, the dc current fed to the load. Also, I_{L0} and V_{C0} refer to the values of i_L and v_C, respectively, at the instant when Q1 is turned on. In Fig. 2.2, devices Q1 and Q2 are naturally commutated; whereas in Fig. 2.3, the devices are force commutated.

At sufficiently low frequencies, waveforms corresponding to the DCM operation (also known as type-2 DCM or DCM-2) occur as shown in Fig. 2.4. In this mode of operation the tank current is discontinuous, as indicated by the interval (t_2 to t_3) in Fig. 2.4.

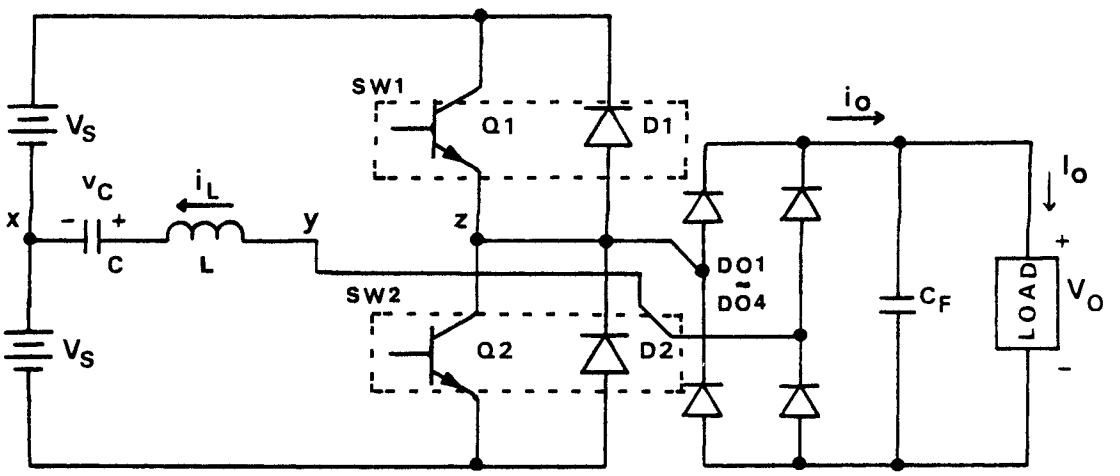

Figure 2.1. A half-bridge series resonant converter

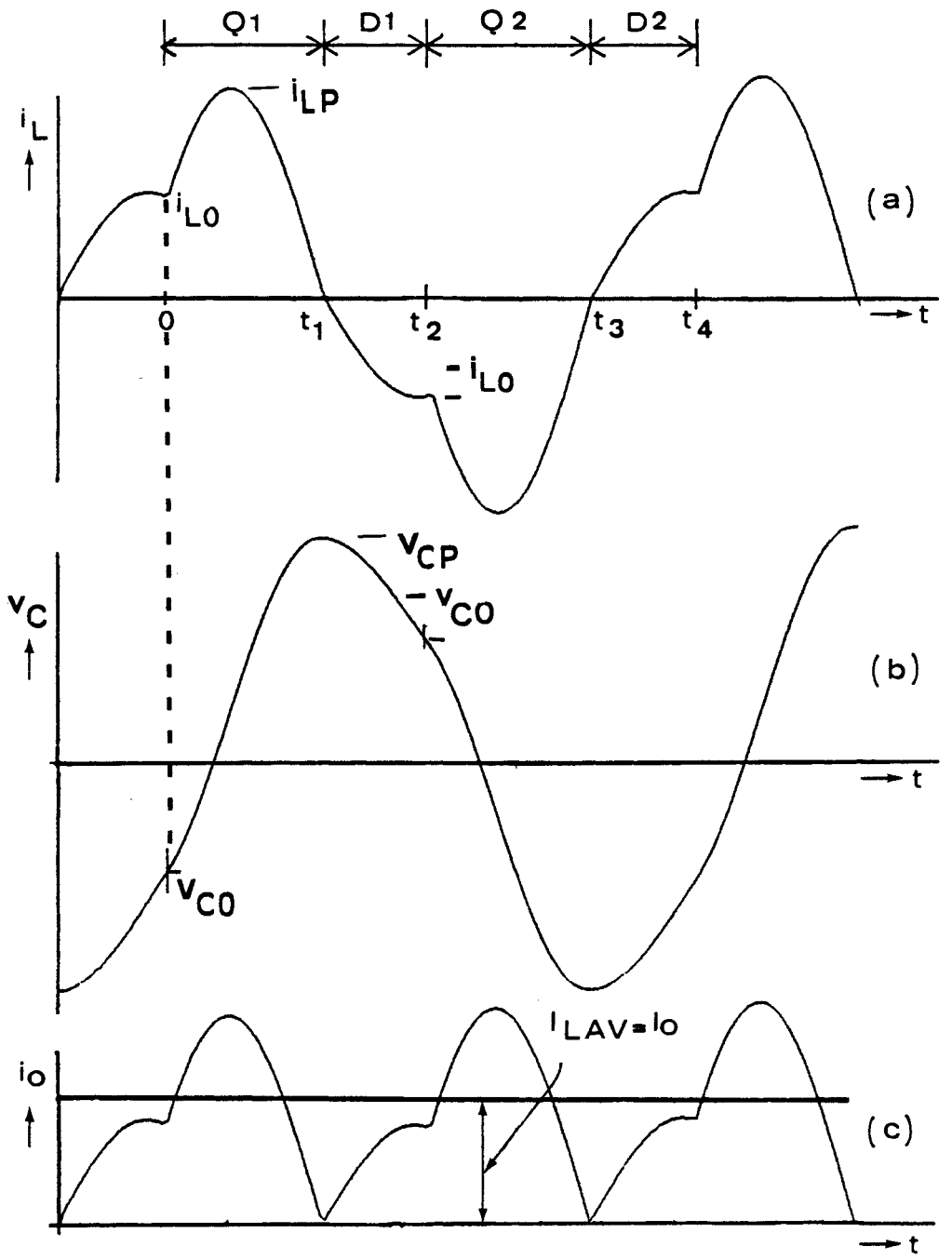

Figure 2.2. Typical waveforms - CCM below resonance

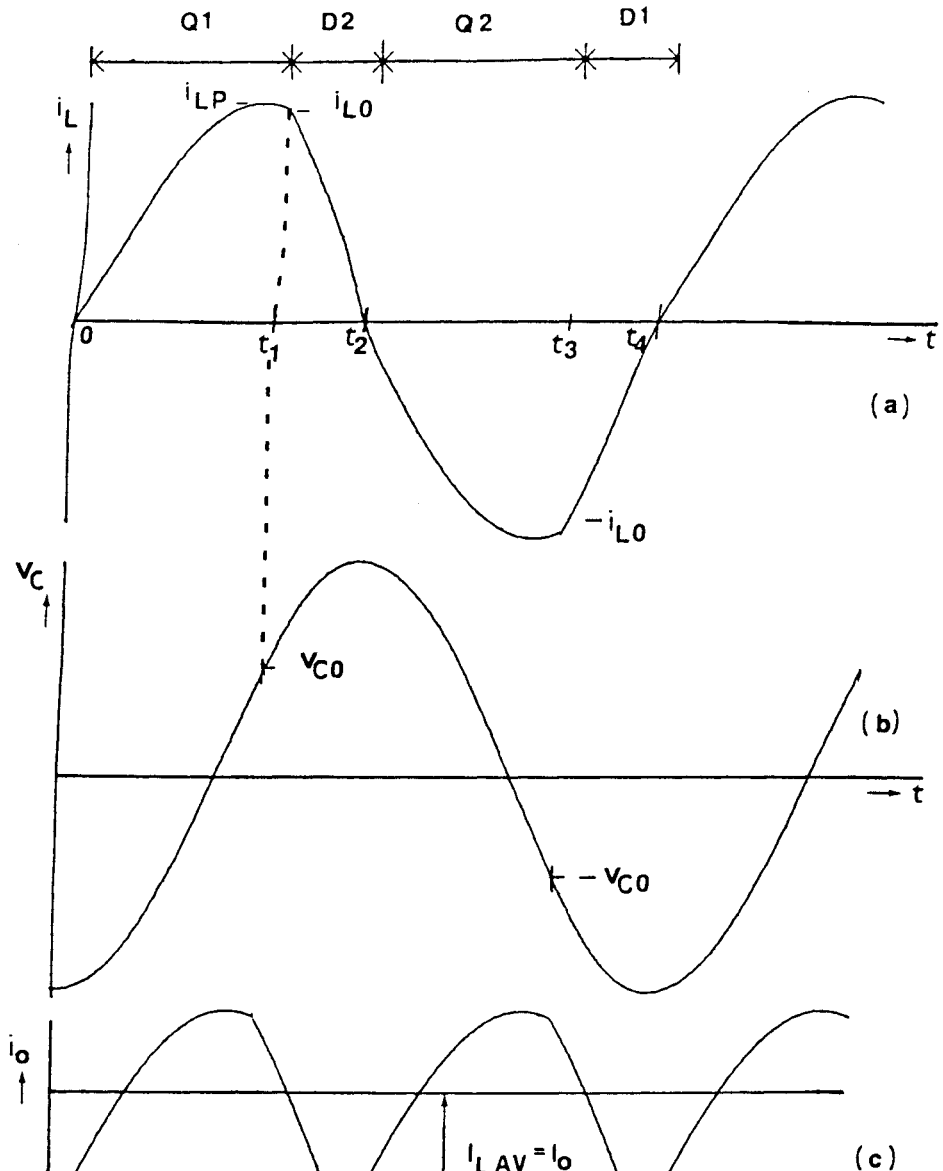

Figure 2.3. Typical waveforms - CCM above resonance

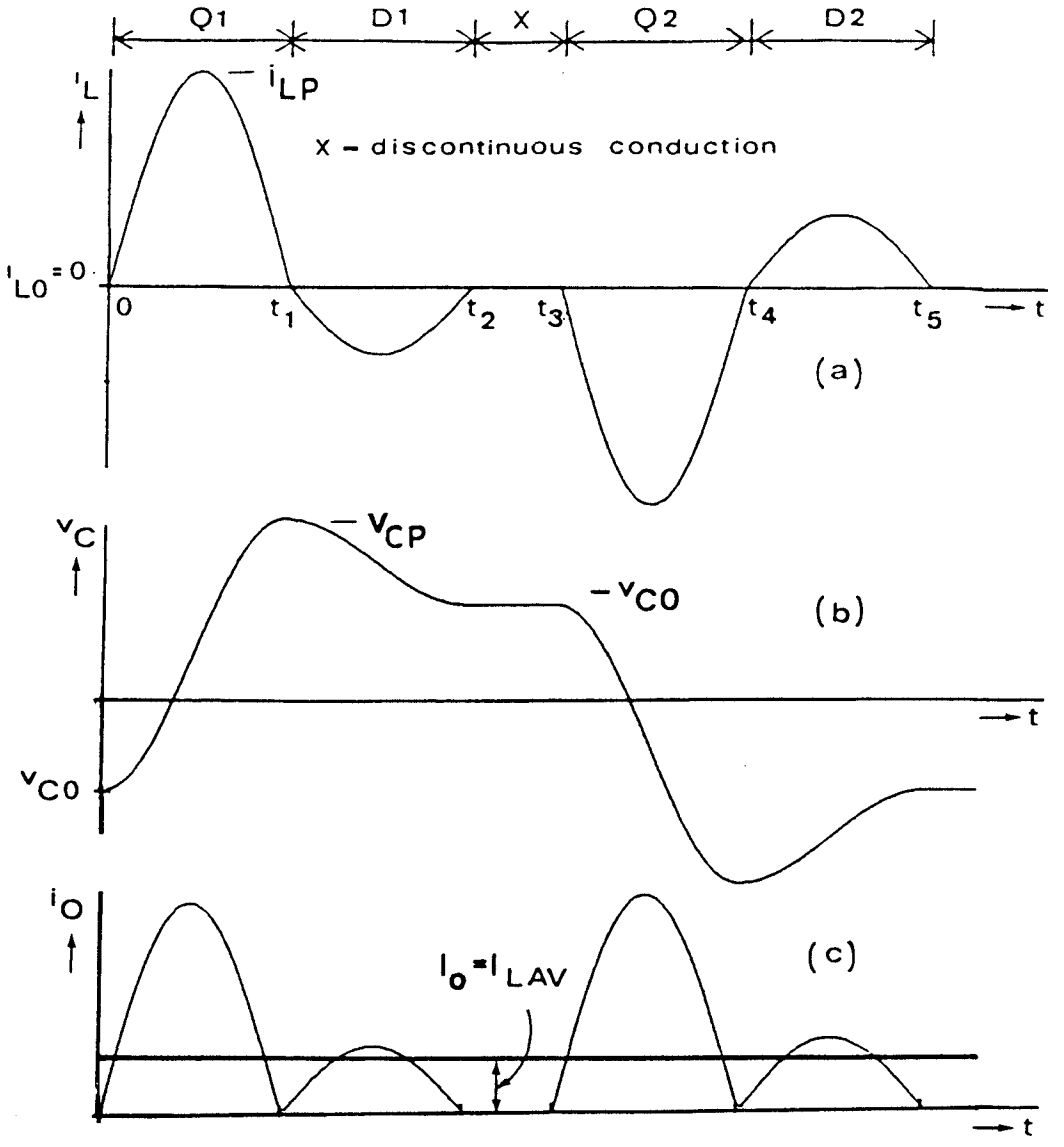

Figure 2.4. Typical waveforms - Type-2 DCM

2.2.2 Assumptions

In Fig. 2.1, three state variables, one corresponding to each of the energy storage elements, L, C and C_F, can be identified. To simplify the analysis, it is assumed that filter capacitor C_F is sufficiently large such that output voltage V_o remains constant for at least one cycle of operation. Under this assumption, number of state variables can be reduced to two, resonant inductor current i_L and resonant capacitor voltage v_C. The behavior of the system can then be studied using graphical state-plane methods. This assumption is justifiable since the operating frequency of the SRC is usually much higher than the corner frequency of the output filter.

A second simplifying assumption is that the circuit losses, including tank, switch and filter losses, are negligible. This results in an ideal lossless resonant circuit with infinite quality factor **Q**. This assumption simplifies the analysis considerably and the basic operating features of the converter are brought out in a clear manner. However, the converter losses do affect the dc characteristics under certain conditions. The mode boundaries, as determined by the ideal analysis, are also altered by the inclusion of losses. The analysis without losses represents the ideal performance that can be obtained from the converter. The effect of losses on the dc performance of a SRC is analyzed in Chapter 3.

2.2.3 Topological Modes

The SRC can be viewed as a piecewise linear system switching between five possible linear modes of operation. Four of these five topological modes are called resonant topological modes. These correspond to intervals when devices Q1, D1, Q2 and D2 conduct as illustrated in Fig. 2.5(a)-(d). The time intervals marked on Fig. 2.5(a)-(d) correspond to those in Fig. 2.2. In the case of a SRC, each resonant topological mode uniquely corresponds to a device conduction. The fifth non-resonant topological mode (see Fig. 2.5(e)) occurs when none of the four devices conduct, as in the interval (t_2 to t_3) in Fig. 2.4. During this interval the inductor current is zero and the capacitor voltage remains constant. The trajectory on the state plane remains at a point. Figure 2.6 shows a common equivalent circuit for the four resonant topological modes along with the corresponding drive voltage, V_E .

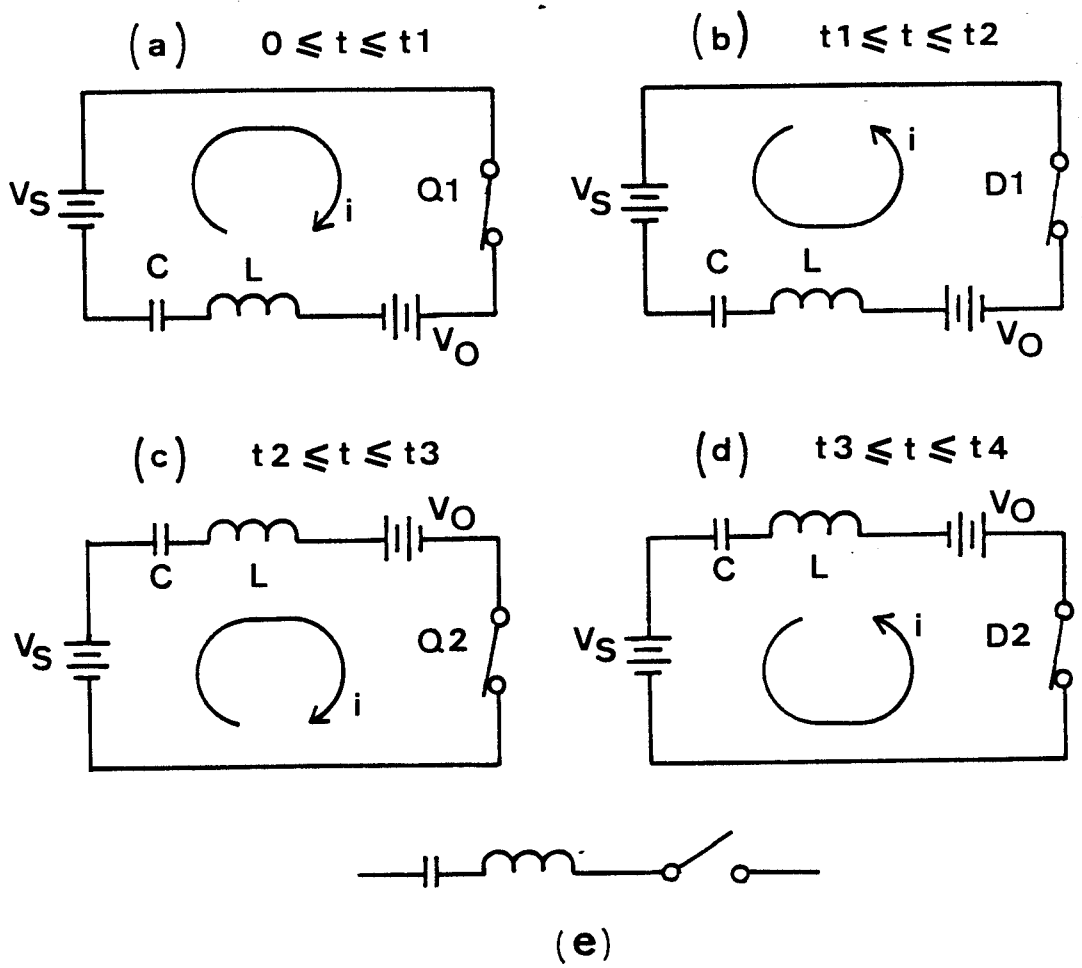

Figure 2.5. Topological modes
a) to d) Resonant e) Nonresonant

CONDUCTION	V_E
Q1	$V_S - V_O$
D1	$V_S + V_O$
Q2	$-V_S + V_O$
D2	$-V_S - V_O$

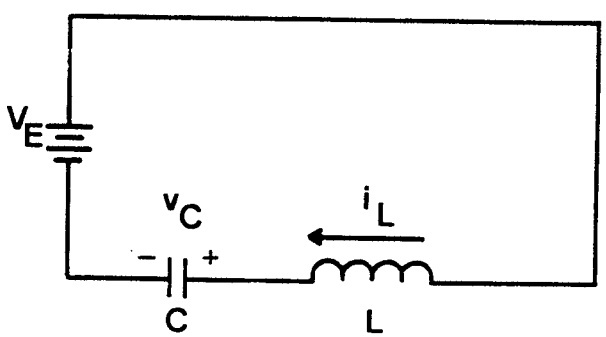

Figure 2.6. Common equivalent circuit for different resonant intervals

2.2.4 State Portrait Development

The network equations for the circuit in Fig. 2.6 are

$$\begin{bmatrix} \dot{v}_C \\ \dot{i}_L \end{bmatrix} = \begin{bmatrix} 0 & \frac{1}{C} \\ \frac{-1}{L} & 0 \end{bmatrix} \begin{bmatrix} v_C \\ i_L \end{bmatrix} + \begin{bmatrix} 0 \\ \frac{1}{L} \end{bmatrix} V_E \tag{2.1}$$

with initial conditions $i_L/_{(t=t_0)} = I_{L0}$ and $v_C/_{(t=t_0)} = V_{C0}$.

The system described by (2.1) has a single equilibrium point at $v_C = V_E$ and $i_L = 0$. The eigen-values are $\pm j/\sqrt{LC}$. The circuit equilibrium is called a center. Solving (2.1),

$$\begin{aligned} v_C - V_E &= I_{L0}Z_0 \sin[\omega_0(t - t_0)] + (V_{C0} - V_E)\cos[\omega_0(t - t_0)] \\ i_L &= I_{L0}\cos[\omega_0(t - t_0)] - \frac{(V_{C0} - V_E)}{Z_0}\sin[\omega_0(t - t_0)] \end{aligned} \tag{2.2}$$

$$\text{where} \qquad Z_0 = \sqrt{\frac{L}{C}} \tag{2.3}$$

is the characteristic impedance (ohms) and

$$\omega_0 = \frac{1}{\sqrt{LC}} \tag{2.4}$$

is the resonant frequency (radians/second). Let

$$\theta = \omega_0 (t - t_0) \tag{2.5}$$

The voltage and current normalizing factors are defined as follows.

$$\begin{aligned} N_v &= \text{Voltage Normalizing Factor} \\ &= V_s = \text{Input Supply Voltage} \end{aligned} \tag{2.6}$$

$$\begin{aligned} N_i &= \text{Current Normalizing Factor} \\ &= \frac{V_s}{Z_0} \end{aligned} \tag{2.7}$$

Normalizing all currents and all voltages with these factors, (2.2) can be written as

$$\begin{aligned} v_{CN} - V_{EN} &= I_{L0N} \sin\theta + (V_{C0N} - V_{EN}) \cos\theta \\ i_{LN} &= I_{L0N} \cos\theta - (V_{C0N} - V_{EN}) \sin\theta \end{aligned} \tag{2.8}$$

The subscript N in (2.8) refers to normalized circuit variables.

By eliminating θ in (2.8) the following equation for the state trajectory is obtained.

$$i_{LN}^2 + (v_{CN} - V_{EN})^2 = I_{L0N}^2 + (V_{C0N} - V_{EN})^2 = \rho^2 \tag{2.9}$$

$$\text{Also,} \qquad \theta = \tan^{-1}\left\{\frac{-i_{LN}}{v_{CN} - V_{EN}}\right\} - \theta_0, \qquad \text{where} \tag{2.10}$$

$$\theta_0 = \tan^{-1}\left\{\frac{-I_{L0N}}{V_{C0N} - V_{EN}}\right\} \tag{2.11}$$

Equations (2.9) and (2.10) express the relationship between normalized state variables i_{LN} and v_{CN}. Equation (2.9) shows that the state trajectories are circles with their centers at

$$v_{CN} = V_{EN}, \qquad i_{LN} = 0 \tag{2.12}$$

and with radius ρ. The magnitude of ρ depends on initial conditions I_{L0N} and V_{C0N}. From (2.5) and (2.10) it can be inferred that the time elapsed between two points on the circular trajectory is proportional to the angle subtended at the center.

Based on (2.9), four sets of trajectories, one for each of the four resonant topological modes, are drawn in Fig. 2.7(a)-(d). Since the devices conduct only in one direction, the trajectories are sets of semicircles, each set extending to only one half of the $v_{CN} - i_{LN}$ plane. In these trajectories, time flows in a clockwise direction. From (2.12), the four centers, marked as M1, M2, M3 and M4 in the figure, are given by

M1	*Q1 interval*	$v_{CN} = 1 - V_{oN},$	$i_{LN} = 0$
M2	*D1 interval*	$v_{CN} = 1 + V_{oN},$	$i_{LN} = 0$
M3	*Q2 interval*	$v_{CN} = -1 + V_{oN},$	$i_{LN} = 0$
M4	*D2 interval*	$v_{CN} = -1 - V_{oN},$	$i_{LN} = 0,$

where V_{oN} refers to the normalized output dc voltage.

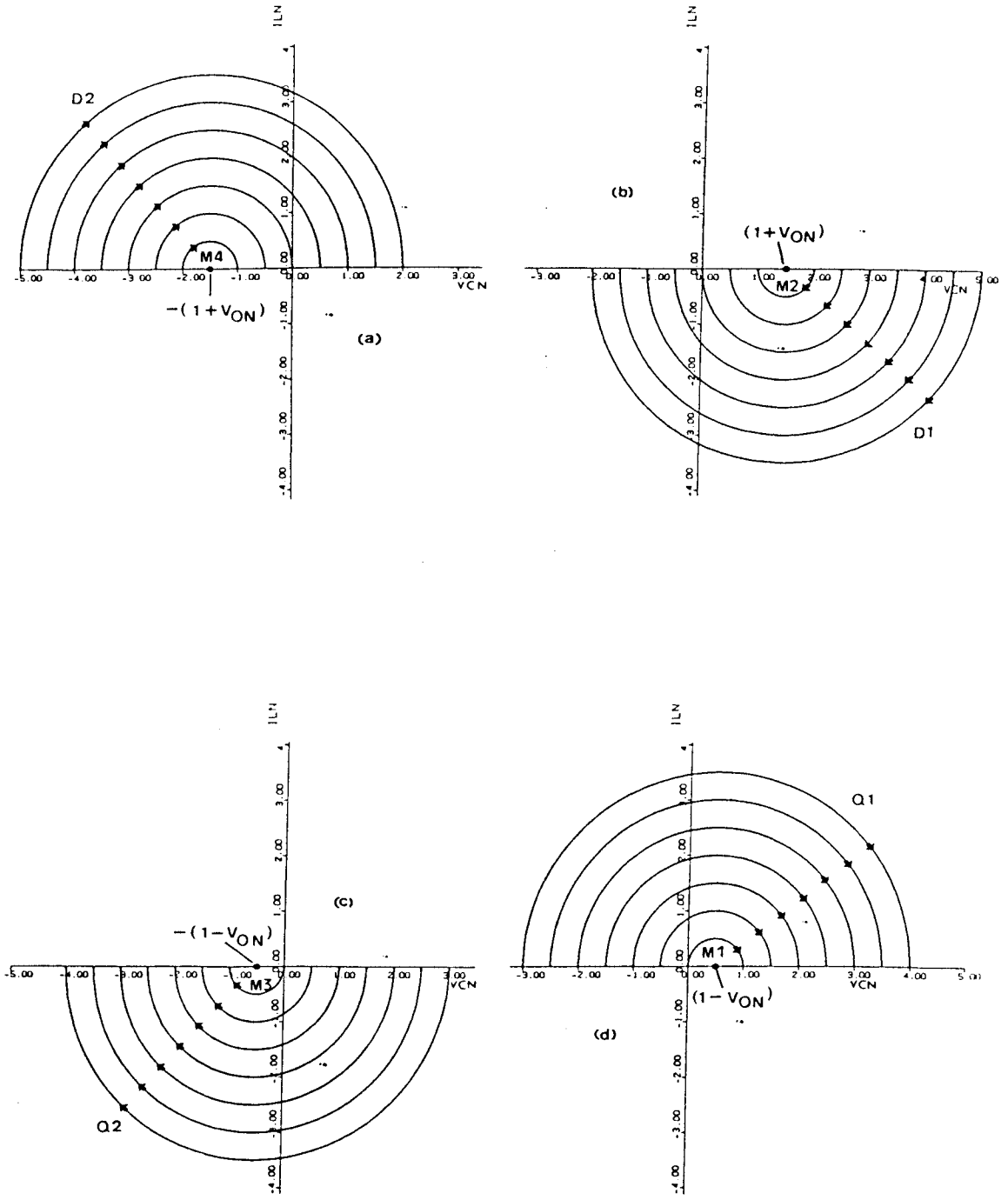

Figure 2.7. State-trajectories during resonant intervals $V_{ON} = 0.5$

a) Q1 trajectories
b) D1 trajectories
c) Q2 trajectories
d) D2 trajectories

By combining the sets of trajectories described above, a composite state portrait, as shown in Fig. 2.8, can be constructed. The state portrait in Fig. 2.8 completely characterizes the SRC at the particular output voltage, which in this case equals $0.5 \times V_s$. It should be observed that the fifth nonresonant topological mode of operation - the discontinuous current interval - occurs when the state comes to rest on the v_{CN} axis of Fig. 2.8 anywhere between the two diode centers, $v_{CN} = -(1 + V_{oN})$ and $v_{CN} = (1 + V_{oN})$.

Instantaneous tank energy e_T is given by

$$e_T = (C\ v_C^2 + L\ i_L^2)/2 \tag{2.13}$$

Normalizing with energy factor $V_s^2 / \omega_0 Z_0$, normalized instantaneous tank energy e_{TN} is given by

$$e_{TN} = (v_{CN}^2 + i_{LN}^2)/2 = d^2/2, \quad \text{where} \tag{2.14}$$

$$d = \sqrt{(v_{CN}^2 + i_{LN}^2)} \tag{2.15}$$

The distance between the current state of the system and the origin is represented by d. Equation (2.14) shows that the instantaneous energy of the tank is proportional to d^2.

From Fig. 2.8 we observe that when Q1 or Q2 conducts, the tank energy increases since the magnitude of d along a state trajectory corresponding to a transistor conduction interval always increases. On the other hand, the conduction of D1 or D2 reduces the tank energy level. This observation has an intuitive appeal since when Q1 or Q2 conducts the tank is charged by the source. In contrast, when D1 or D2 conducts the tank delivers energy both to the source and to the load.

With the aid of state-plane diagrams, the operation of a SRC both under steady-state conditions and under limited-duration transient conditions can be easily identified and analyzed. The state portrayal for a possible trajectory, T, is illustrated in Fig. 2.8.

At t_A, assume device Q2 is already conducting. The system follows a Q2 trajectory with center M3 at $v_{CN} = -1 + V_{oN} = -0.5$. At t_B, the current polarity reverses causing D2 to conduct. Q1 can be turned on at any instant after t_B, and the actual time at which this occurs, t_C in Fig. 2.8, is determined by a given control law. Between t_B and t_C the system follows a D2 trajectory with center M4 at

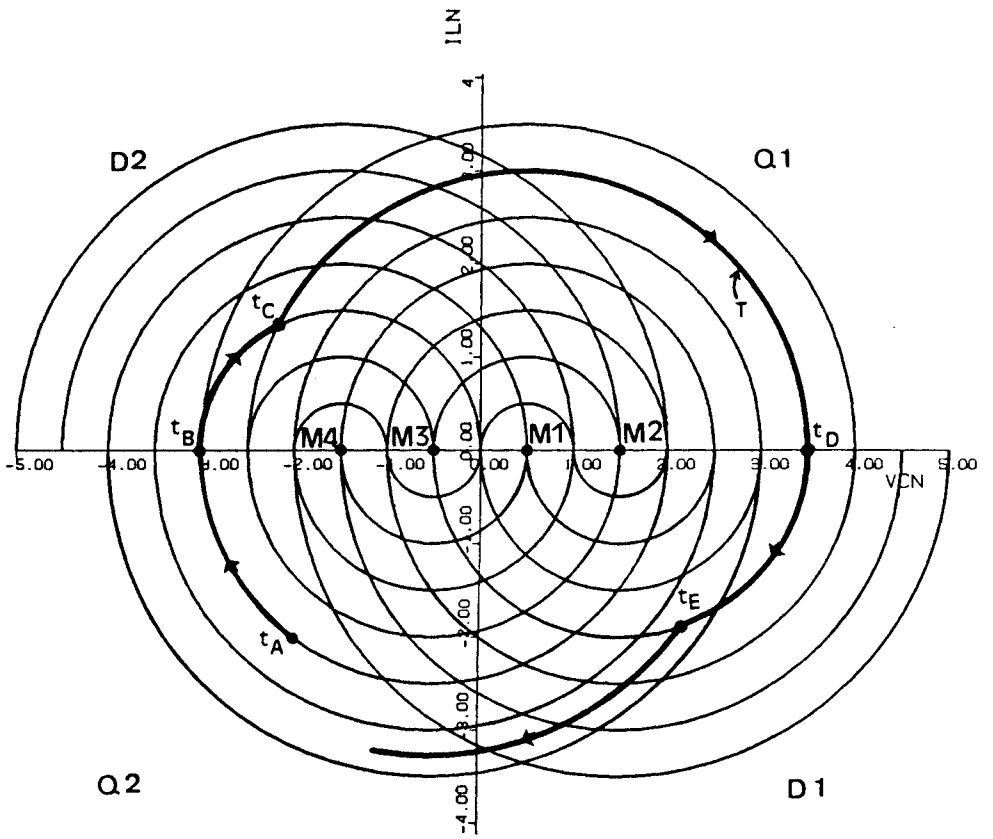

Figure 2.8. Composite state portrait $V_{oN} = 0.5$

$v_{CN} = -1 - V_{oN} = -1.5$. At t_C, Q1 is switched on and, between t_C and t_D, the system follows a Q1 trajectory with center M1 at $v_{CN} = 1 - V_{oN} = 0.5$.

The dramatic effect of control on the circuit variables and the tank energy level can be seen from Fig. 2.8. If Q1 is switched on later than t_C, the system would follow a lower-energy Q1 trajectory than the one marked. On the other hand, if Q1 is switched on earlier than t_C, the system would follow a higher-energy Q1 trajectory. The operation of the system at t_D and t_E is similar to that at t_B and t_C, respectively, with the Q1,D1 pair interchanging roles with the Q2, D2 pair.

Figure 2.9 shows a set of state portraits of a SRC for different load voltages, V_{oN}, from zero to unity in steps of 0.25. As may be observed, at $V_{oN} = 0$, M1 and M2 and, likewise, M3 and M4 coincide. At $V_{oN} = 1$, M1 and M3 coincide at the origin. The rest of this Chapter deals with analysis of the SRC operation under steady-state operating conditions. The dynamic performance of a SRC under different control methods is evaluated in Chapter 4.

2.2.5 Steady-State Trajectories

For a given operating frequency, ω, and load voltage, V_o, a closed steady-state trajectory corresponding to the steady-state waveforms can be drawn on the state plane. The piecewise circular segments of the steady-state trajectory will then belong to the Q1, D1, Q2 and D2 trajectories of the corresponding state portrait. A study of Fig. 2.8 reveals that many different types of closed steady-state trajectories can be created. Figure 2.10 shows two asymmetrical steady-state trajectories in which the two halves of the bridge are turned on for different durations. In Fig. 2.10(a), the conduction sequence is Q1, D2, D1, Q2 and D1 and in Fig, 2.10(b), it is Q1, D1, Q1 and Q2. Each closed trajectory represents a possible operating point of the converter and may be realized when the load voltage corresponds to that of the state portrait and when the devices are switched as per the duration and sequence indicated by the steady-state trajectory. However, all such asymmetrical trajectories are generally not practical and are not investigated in this report.

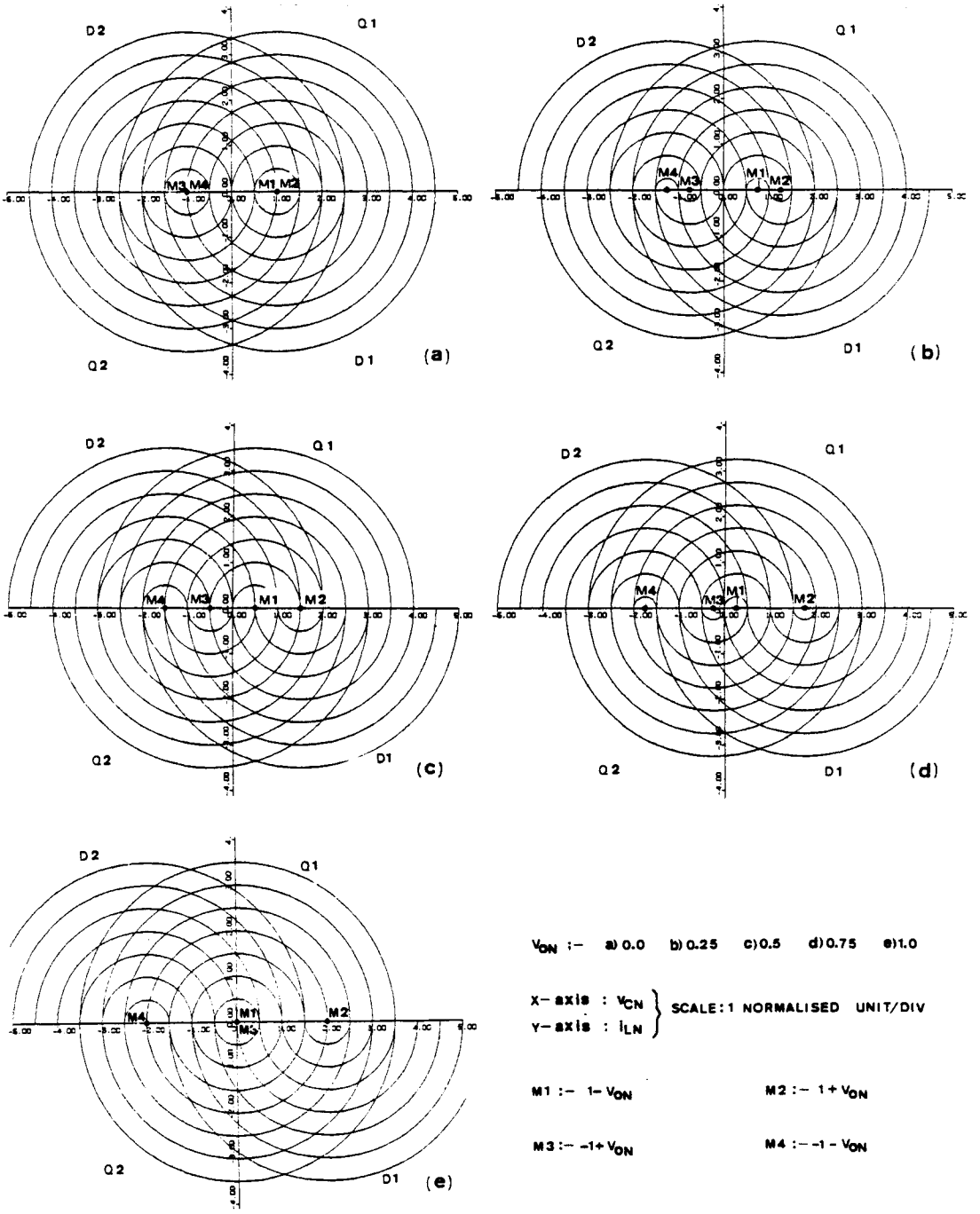

Figure 2.9. Set of composite state portraits

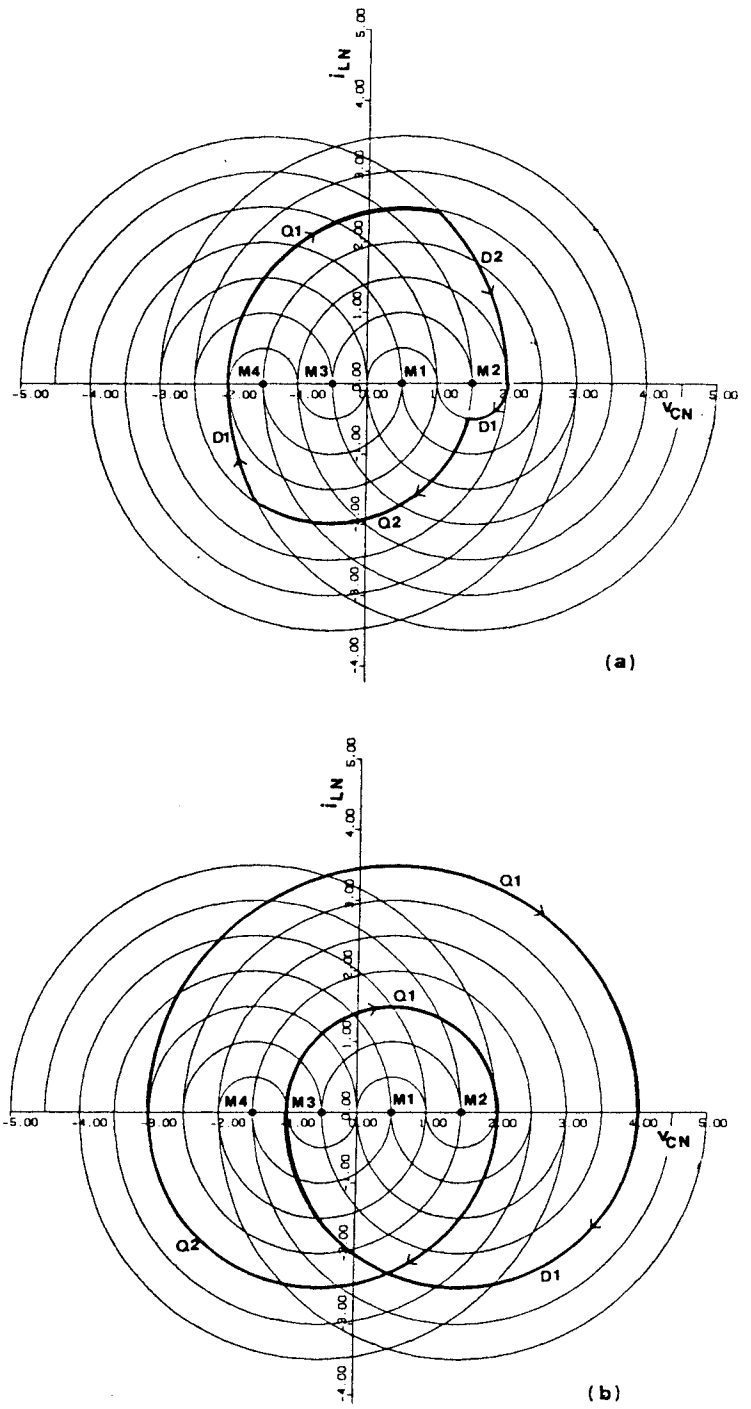

Figure 2.10. Two asymmetrical steady-state trajectories

2.2.5.1 CCM Operation Below Resonant Frequency

Figure 2.11 shows typical CCM steady-state trajectories for operation below resonance. An infinite number of steady-state trajectories exist, each corresponding to a unique frequency, load current and tank energy level. The operating frequency, ω, can be varied from 0.5 to 1.0 times the resonant frequency, ω_0, in this region. The normalized operating frequency is defined by

$$\omega_N = \frac{\omega}{\omega_0} \tag{2.16}$$

Thus, the corresponding range of ω_N is between zero and unity. As the frequency is increased towards resonance, the trajectory size increases along with the load current and tank energy level, as shown in Sec. A.1.3.

Let us now consider a single trajectory marked T in Fig. 2.11. The typical waveforms for this trajectory are as in Fig. 2.2. As can be observed, transistors Q1 and Q2 commutate naturally, whereas diodes D1 and D2 turn off while carrying current. Q1, D1, Q2 and D2 is the sequence of device conduction. α is the diode conduction angle and is proportional to the conduction period of the diode. If t_d is the diode conduction interval, then

$$\alpha = \omega_0 t_d \tag{2.17}$$

Likewise, β is the transistor conduction angle and is proportional to the conduction period of the transistor. If t_q is the transistor conduction interval, then

$$\beta = \omega_0 t_q \tag{2.18}$$

In Fig. 2.11, line S1 (S2) is the steady-state switching boundary between diode D2 (D1) conduction and transistor Q1 (Q2) conduction.

Figure 2.12 shows sets of steady-state trajectories corresponding to values of V_{oN} ranging from 0 to 1 in steps of 0.25. Figure 2.12(a) shows one limiting case when $V_{oN} = 0$. Here, the centers for D1 and Q1 coincide and, likewise, the centers for D2 and Q2 coincide. The switching boundaries, S1 and S2, lie on

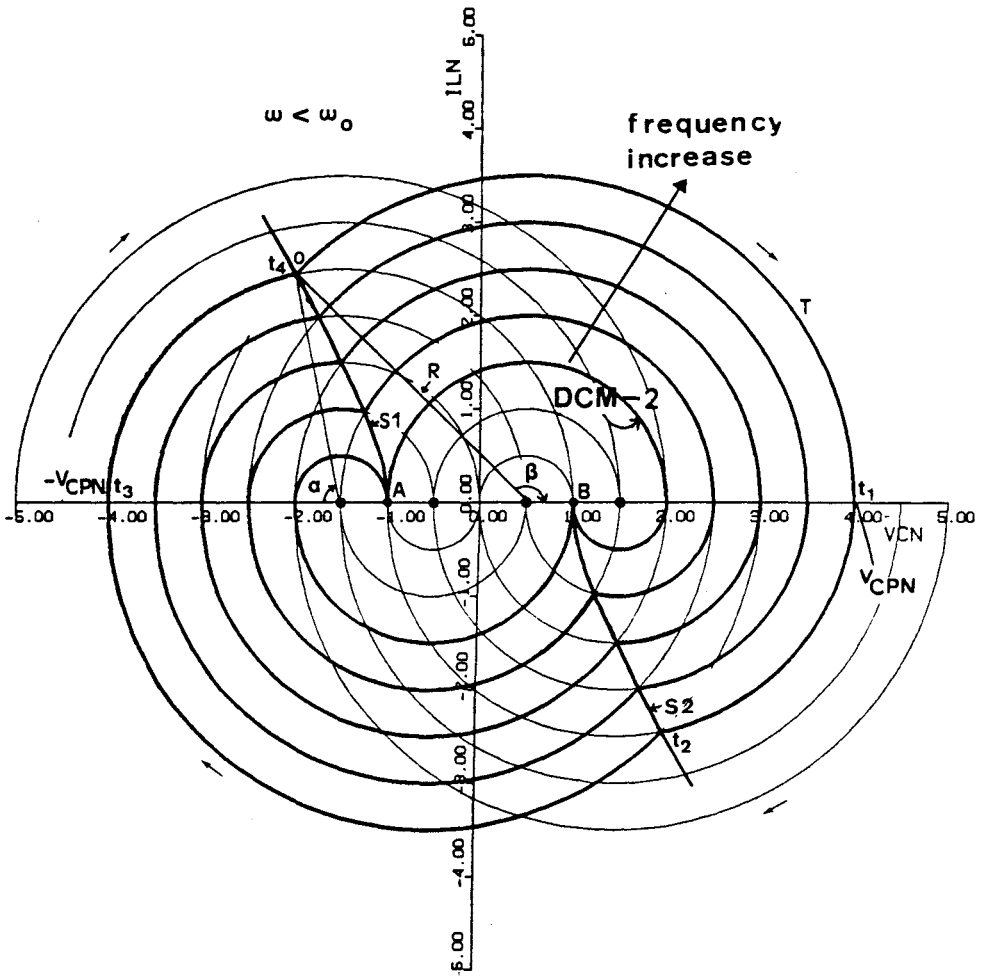

Figure 2.11. Typical CCM/DCM-2 steady-state trajectories below resonance $V_{oN} = 0.5$

the i_{LN} axis. The diode and the transistor conduct equally and, thus, the maximum loading for the diodes occur when the output voltage is zero.

When V_{oN} = 1 the centers for Q1 and Q2 coincide at the origin as shown in Fig. 2.12(e). The switching boundaries, now, lie on the v_{CN} axis. All the steady-state trajectories are concentric circles resembling the ideal oscillations of a lossless LC resonant circuit. The two transistors conduct for an angular duration of π each. This implies that the operating frequency represented by each CCM trajectory in Fig. 2.12(e) equals the tank resonant frequency. Thus, CCM steady-state trajectories exist ideally for V_{oN} = 1 only when ω_N = 1. These steady-state trajectories, however, are not realizable in practice because of circuit losses, and the system will always spiral towards the origin.

2.2.5.2 DCM Operation Below Half Of Resonant Frequency

In Fig. 2.11, if the operating frequency is reduced to 0.5 $\times$ ω_0 , the trajectory marked DCM-2 is reached. Each device conducts for an angle of π. At even lower frequencies of operation, the circuit operates in the DCM mode. The trajectory remains the same for all operating frequencies for a given output voltage. However, additional discontinuous intervals are introduced (fifth topological mode) at points A and B on the trajectory. The waveshapes at different frequencies are similar and differ only in the duration of the interval when all the devices are off (interval t_2 - t_3 in Fig. 2.3). This mode can also be called type-2 DCM or the DCM-2, since two current pulses, one corresponding to a transistor conduction and the other to a diode conduction, occur in each half-cycle of converter operation.

In the above discussion of the DCM mode, it has been implicitly assumed that after D1 (D2) conducts and commutates, Q1 (Q2) is not switched on again. In other words, Q1 (Q2) base drive is presumed to be removed while the antiparallel diode D1 (D2) is conducting. If, however, this was not so, then the DCM as discussed above will not always be present and may be replaced by other more complex modes of operation. These modes have been analyzed extensively in [20]. A typical operation in this region is shown in Fig. 2.13. The device conduction sequence in this case is Q1, D1, Q1, D2, Q2, D2, Q2 and D1. In Fig. 2.13, the bidirectional switch (Q1-D1 or Q2-D2) conducts for a duration longer than a resonant cycle period and, hence, this region of operation may be called the 'multiple' resonant cycle region. Use of state-plane diagrams will make the analysis in this region relatively easy to perform and com-

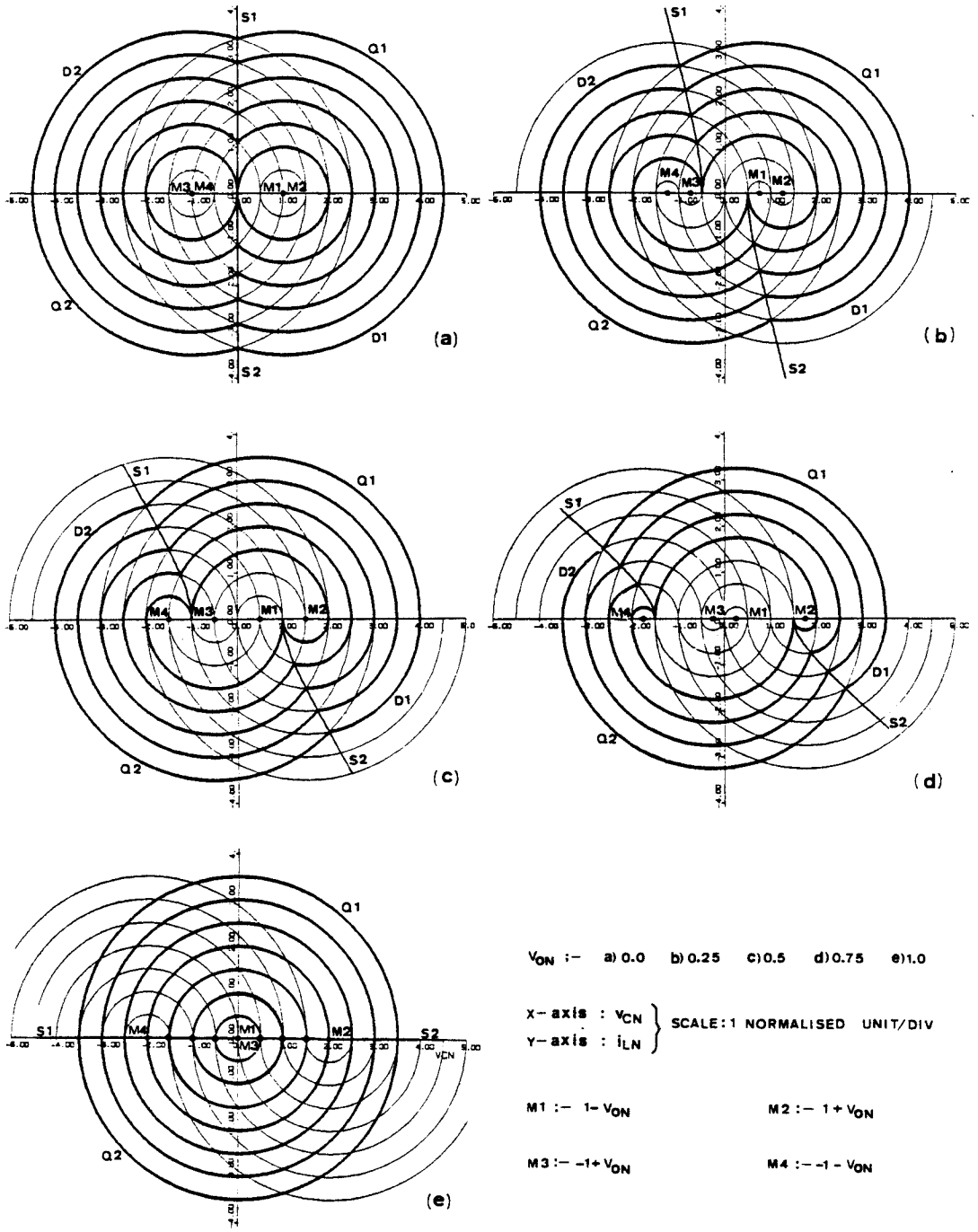

Figure 2.12. Set of steady-state trajectories below resonance

prehend. However, due to the limited practical use of this region of operation, it is not investigated further.

Figure 2.14 shows a phenomenon which occurs in the discontinuous mode of operation. An infinite number of DCM steady-state solutions, each with the same average output current and the same frequency, exist and all except the one marked T are asymmetrical. With the assumption of an ideal tank circuit, the circuit can theoretically stay on any of the trajectories indefinitely. However, with circuit losses, the system would gradually slide from an asymmetrical mode to the symmetrical steady-state trajectory. Figure 2.15 shows a SPICE-2 [48] simulation of this transient phenomenon. The SRC circuit in Appendix E.1 was simulated with an additional series resistance (0.3201 Ω) in the tank circuit to account for the losses. The resulting Q of the tank circuit is 20. The dynamics of this lateral transient depends on the losses in the circuit; the smaller the losses are, the longer the settling time will be. This phenomenon can cause imbalance in the device stresses in the discontinuous mode, particularly when circuit Q is high.

2.2.5.3 DCM Operation When Load Voltage Equals Supply Voltage

In Sec. 2.2.5.1, we noted that for $V_{oN} = 1$, CCM steady-state trajectories exist, even under ideal conditions, only when $\omega_N = 1$. At lower frequencies, the inner circular trajectories, as shown within diode centers M2 and M4 in Fig. 2.12(e), occur. These have been reproduced in Fig. 2.16 for clarity. In Fig. 2.16, all the trajectories are bounded within the diode centers {-2, +2}. Figure 2.17 shows typical waveforms in this mode of operation. The following explanation holds true both for the trajectory marked 'T' in Fig. 2.16 and for the waveforms in Fig. 2.17.

Transistor Q1 is switched on at t=0. It conducts for a duration of π and naturally commutates at $t = t_1$ (point B in Fig. 2.16). Normally the conduction of diode D1 will follow. However, no D1 trajectory leaves point B in Fig. 2.16. In fact, only Q2 trajectories are available for the system at point B. Hence, the circuit stays at this point during interval $\{t_1 - t_2\}$ until Q2 is turned on. Operation during the second half cycle follows in a similar manner.

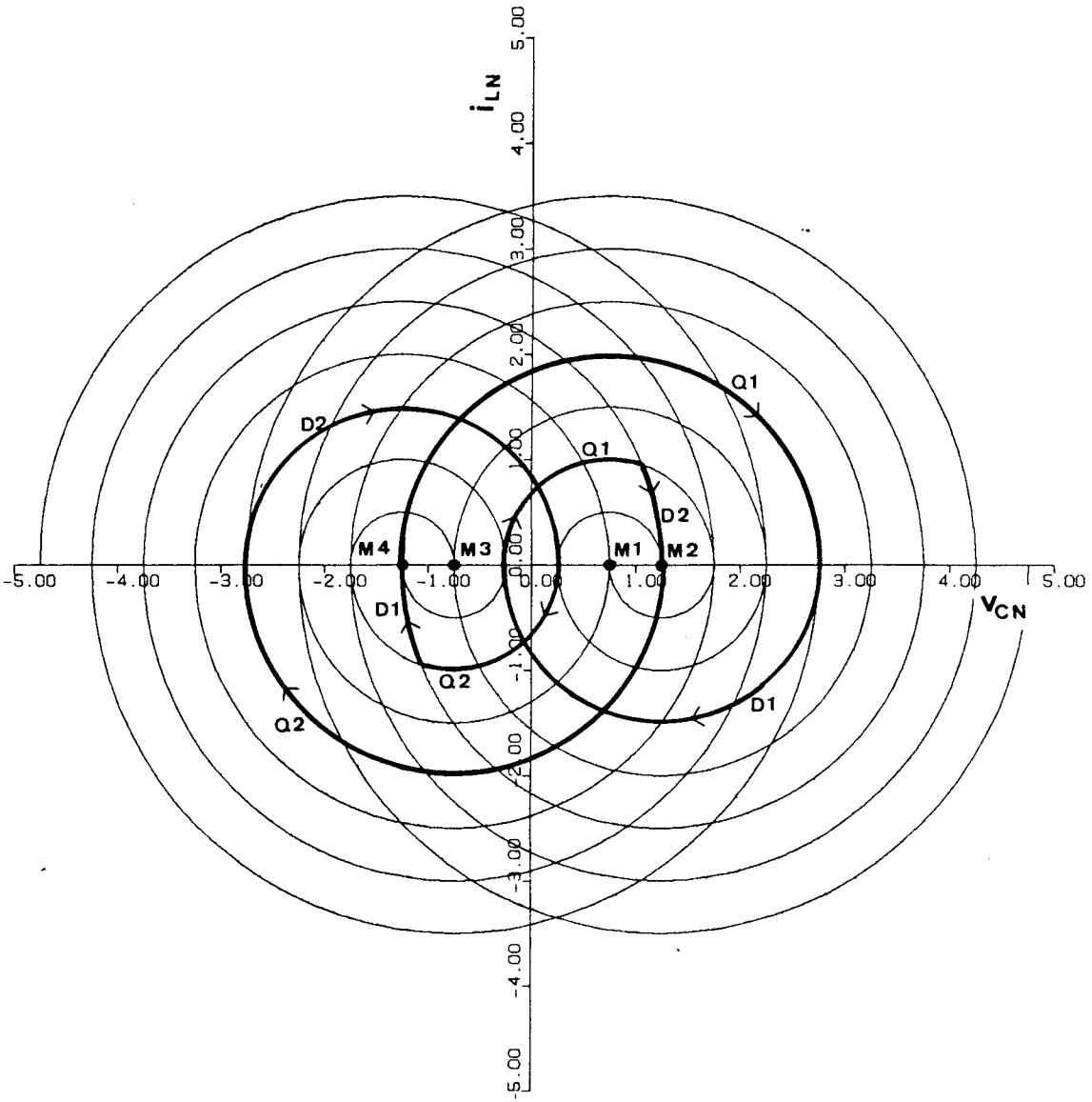

Figure 2.13. A steady-State trajectory with "multiple" resonant cycle operation

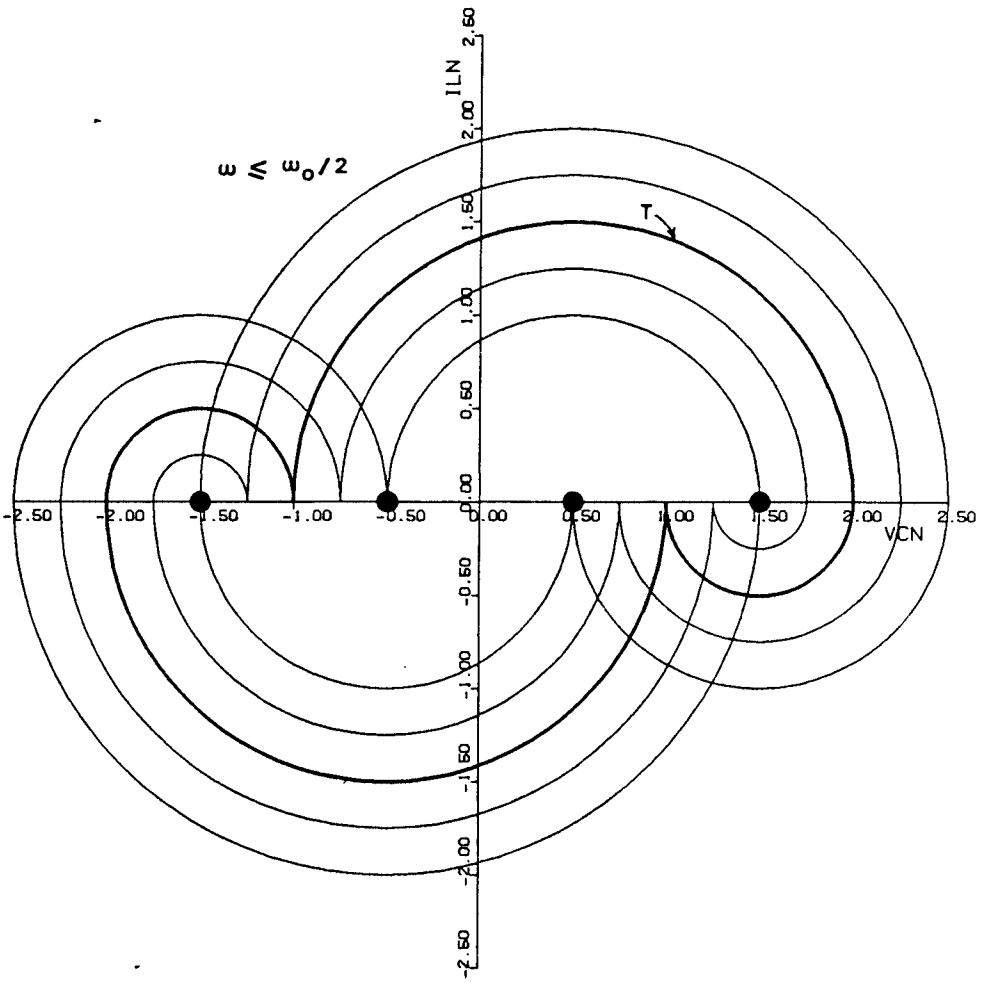

Figure 2.14. Ideal steady-state trajectories in DCM-2 V_{oN} = 0.5

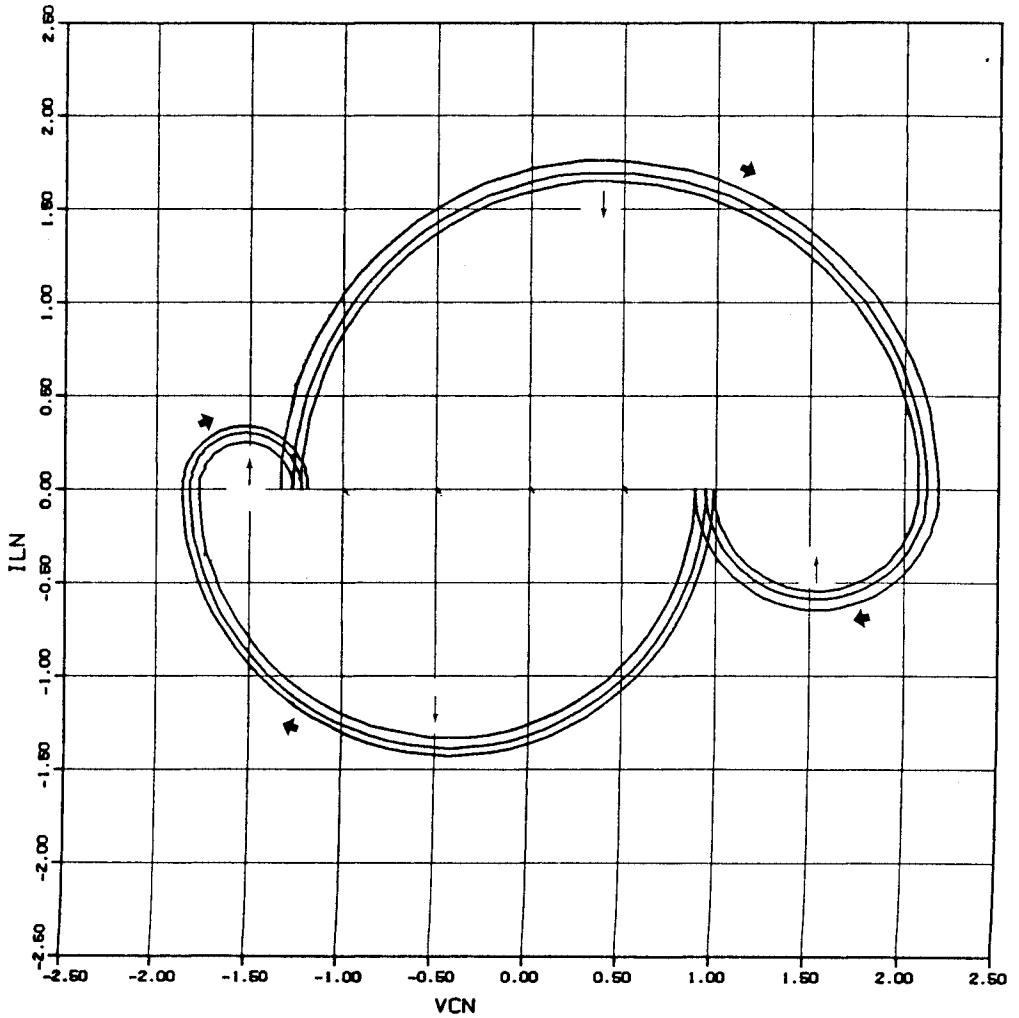

Figure 2.15. SPICE2 simulation of effect of finite Q in DCM-2 V_o = 150 V and Q = 20

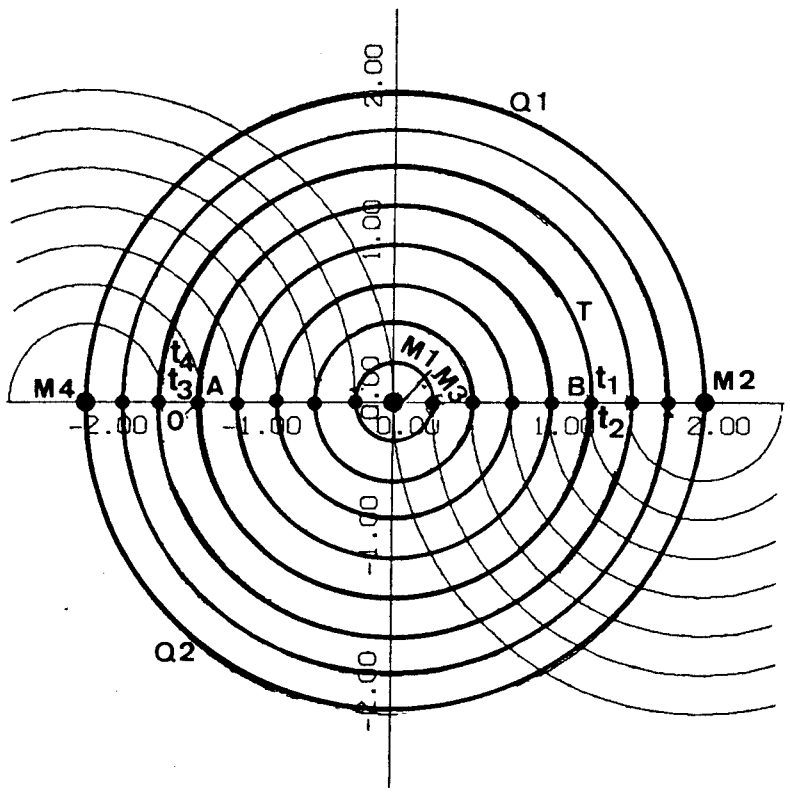

Figure 2.16. Type-1 DCM trajectories

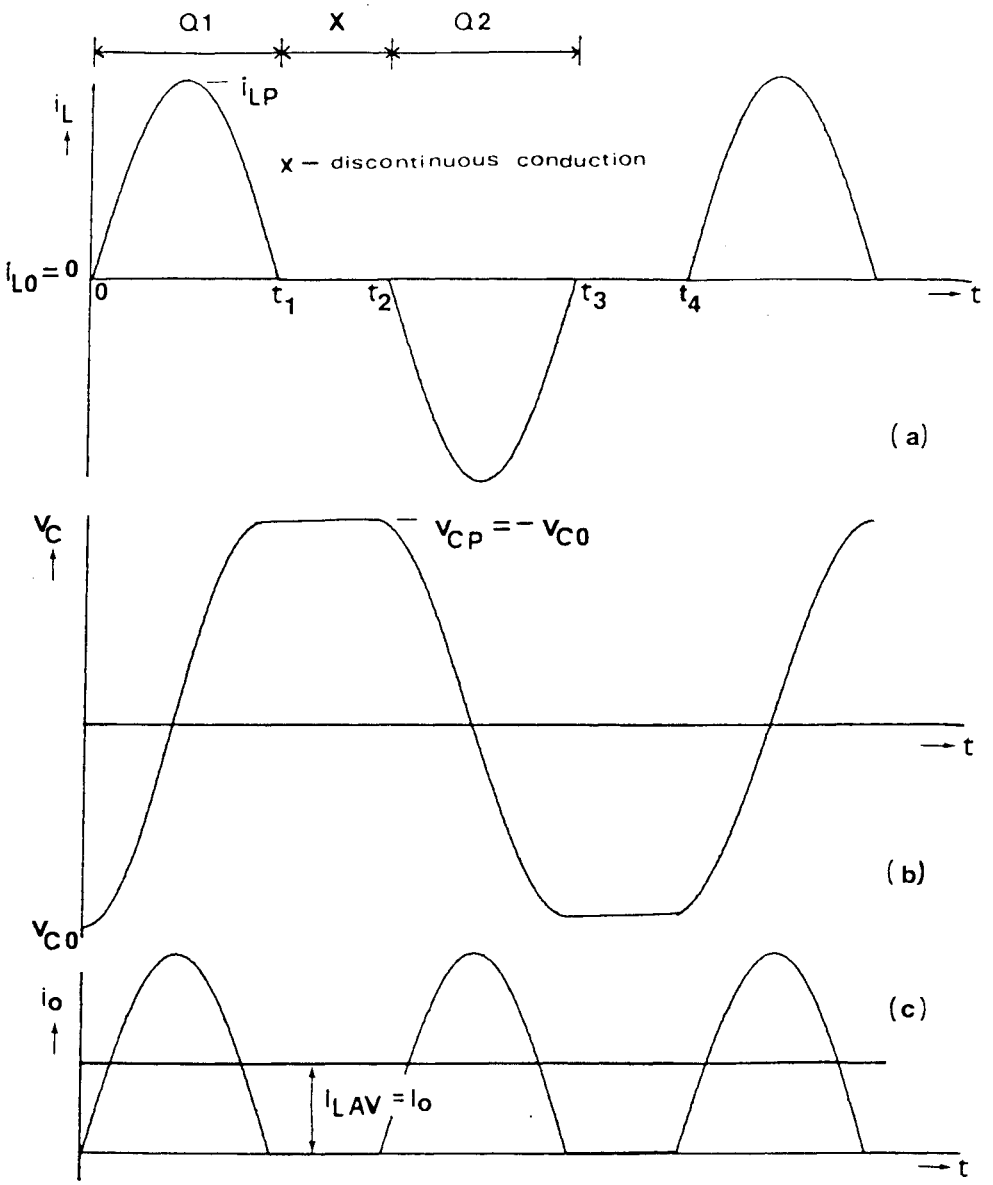

Figure 2.17. Typical waveforms - Type-1 DCM

From another perspective, both diode D1 and transistor Q1 are reverse biased during the interval $\{t_1 - t_2\}$. From Fig. 2.16, at instant t_1, $0 < v_C < 2V_s$. The voltage across Q1 (and D1) is given by $V_s - v_{zy} - v_C$ (see Fig. 2.1). First assume that device Q1 attempts to conduct at instant t_1. Voltage v_{zy} across terminals "zy" in Fig. 2.1 then equals $+ V_o = V_s$. The voltage across Q1 is, therefore, $- v_C$ and thus Q1 is reverse biased. If, on the other hand, diode D1 conducts, $v_{zy} = - V_o = - V_s$. The voltage across D1 (this time from cathode to anode) is then given by $2V_s - v_C$. Since $v_C < 2V_s$, D1 is also reverse biased. Thus, if either Q1 or D1 attempts to conduct, the voltage across 'zy' reverses so as to reverse bias the particular device.

At $t = t_2$, transistor Q2 is switched on and the second half of the operating cycle follows. This mode of operation can also be called type-1 DCM or DCM-1 since one current pulse occurs per each half cycle of circuit operation. The region of occurrence for DCM-1 is $\omega_N < 1$ and $V_{oN} = 1$.

2.2.5.4 CCM Operation Above Resonant Frequency

The output of the converter can also be controlled by increasing the switching frequency above resonance. As pointed out in [7], this mode of operation has certain desirable features.

When the converter is operated in this mode, the power switches are turned on at zero current and the antiparallel diodes are naturally commutated. As a result, fast recovery diodes are not required as is usually the case with the bridge configuration. This feature permits the designer to use a Darlington power transistor with a slow built-in antiparallel diode or power field-effect transistor (FET) with its inherent antiparallel diode to form a composite bidirectional switch for resonant converters. It must be noted that these slow-recovery antiparallel diodes of the BJT and FET, in general, do not meet the requirements of high-frequency applications when used with other types of switching converters.

When the operating frequency is higher than the resonant frequency, the transistor does switch off considerable current. However, since the transistor turns on at zero current and at zero voltage, large capacitors without series resistors can be used as lossless snubbers to alleviate the problem of turn-off stress [7].

Figure 2.18 shows a family of symmetrical CCM steady-state trajectories when V_{oN} = 0.5 for this operating mode. The state portrait on which these are plotted remains the same as for operation below resonance. Once again an infinite number of trajectories exist, each corresponding to a unique frequency, load current and tank energy level. The operating frequency can be varied between resonant frequency and infinity in this region. The trajectory size diminishes along with the load current and tank energy level as the frequency is increased above resonance, as shown in Sec. A.3.3.

Let us now consider a single trajectory marked T in Fig. 2.18. The typical waveforms for this trajectory are as in Fig. 2.3. As can be observed, transistors Q1 and Q2 are force commutated whereas diodes D1 and D2 turn off at zero current. Q1, D2, Q2 and D1 is the sequence of device conduction. Once again α and β are the diode and transistor conduction angles, respectively. Line S1 (S2) in Fig. 2.18 is the steady-state switching boundary between transistor Q1 (Q2) conduction and diode D1 (D2) conduction.

Figure 2.19 shows sets of steady-state trajectories corresponding to values of V_{oN} ranging from 0 to 1 in steps of 0.25. Figure 2.19(a) is a limiting case when V_{oN} = 0. The switching boundaries S1 and S2 lie on the i_{LN} axis. The diode and the transistor conduct equally and, thus, the maximum loading for the diodes occur once again when the output voltage is zero.

When V_{oN} = 1, the switching boundaries lie on the v_{CN} axis. All the steady-state trajectories are concentric circles with two transistors conducting for a duration of π each. These trajectories are identical to the CCM trajectories below resonance in Fig. 2.12(e). The operating frequency of each of the CCM trajectory in Fig. 2.19(e) equals the tank resonant frequency. Thus, for this case, CCM trajectories exist only when ω_N equals unity. No CCM trajectory is possible when the operating frequency exceeds the resonant frequency whenever V_{oN} equals unity.

2.2.6 Ideal Regions Of Operation

Based on the discussions so far, Fig. 2.20 shows the ideal regions of operation of a SRC on the ω_N - V_{oN} plane. The features of this diagram are as follows.

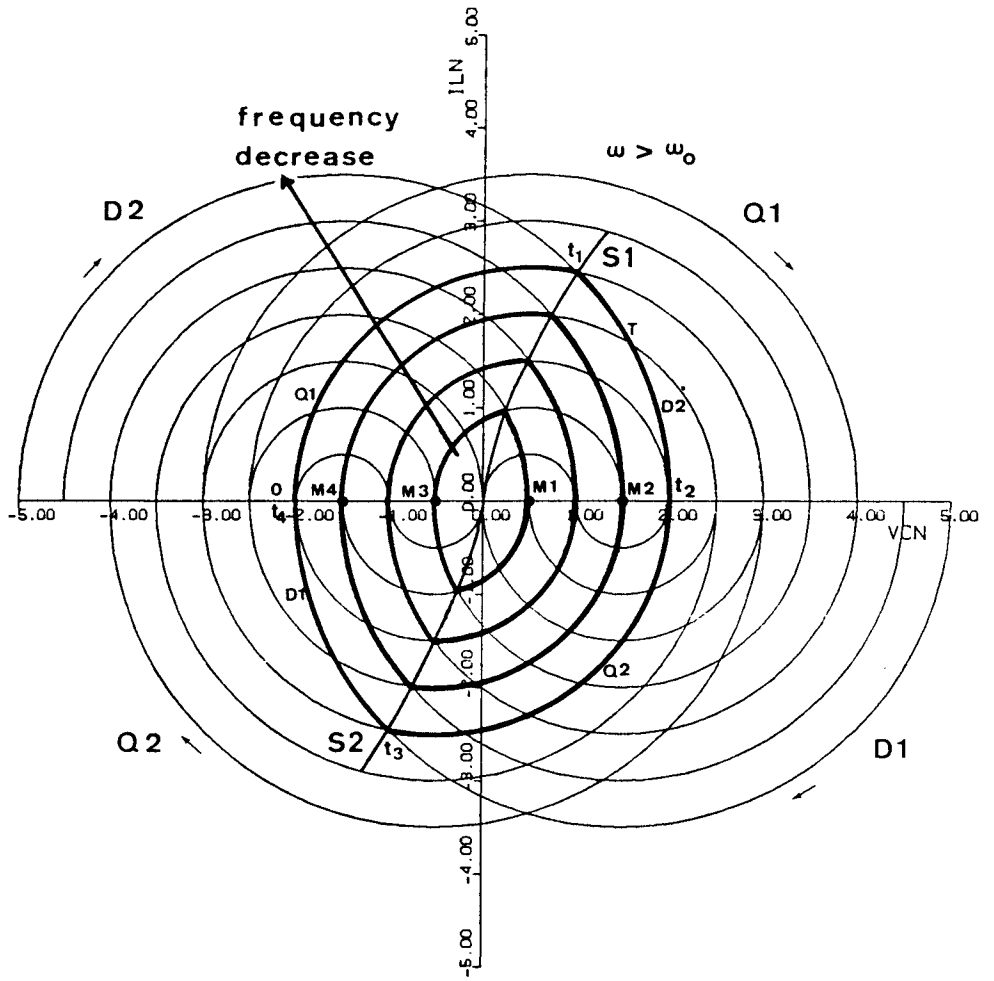

Figure 2.18. Typical CCM steady-state trajectories above resonance $V_{oN} = 0.5$

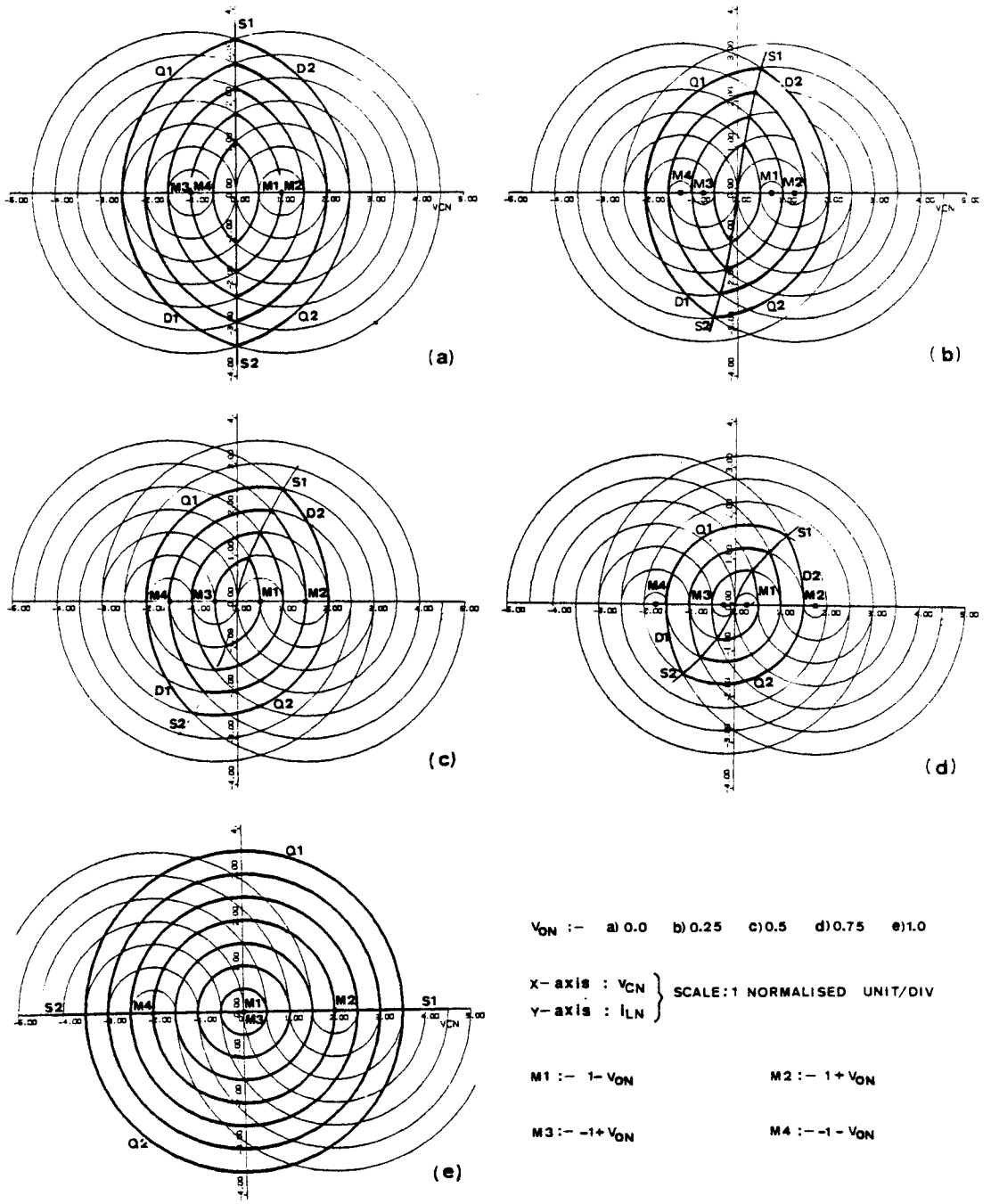

Figure 2.19. Set of steady-state trajectories above resonance

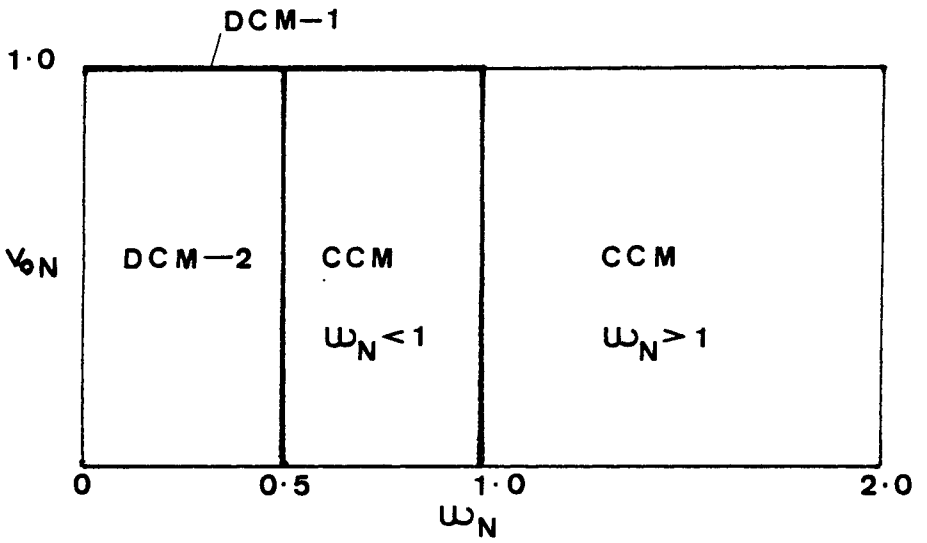

Figure 2.20. Ideal regions of SRC operation

The maximum possible load voltage, V_{oN}, for an SRC is unity. Also, for $\omega_N < 0.5$, the circuit operates in normal DCM (DCM-2) and for $\omega_N > 0.5$, the circuit operates in CCM. Devices Q1 and Q2 are naturally commutated whenever $\omega_N < 1$, whereas they are force commutated for $\omega_N > 1$.

A limit in the operation is reached when the load voltage equals supply voltage ($V_{oN} = 1$). In this case, the circuit generates output current for operating frequencies only up to resonant frequency. Also, CCM operation is possible only at one operating frequency, when ω_N equals unity. At lower operating frequencies, the circuit does not operate in CCM but only in DCM-1.

2.3 Results Of DC Analysis

Under the assumptions made in Sec. 2.2.2 and under the specific conditions of operation, the state-plane trajectories represent the exact operation of the converter. These state-plane diagrams may then be utilized to quantitatively analyze the steady-state properties of the resonant converter. Appendix A presents the details of such an analysis for the different modes of SRC operation identified in Sec. 2.2.5.

The results of the analysis are presented in Table 2.1. For definitions of parameters such as R, V_{CPN} and $(VS)_{PN}$, please refer to Sec. 2.0. Table 2.1 contains equations for useful design parameters such as the device average and rms currents, average and rms inductor currents, peak voltage stress on the resonant capacitor, peak current stress, and maximum volt-seconds applied on the resonant inductor. The switching boundary equations relating the switching-point state variables I_{LON} and V_{CON} for SRC operation in CCM both below and above resonant frequency are given at the bottom of Table 2.1.

In the case of CCM operation, it is assumed that transistor trajectory radius R and normalized load voltage V_{oN} are the known independent variables. This was done since the equations using R and V_{oN} as the independent variables are easy to derive and are and explicit. For the same reason, V_{oN} and ω_N have been assumed to be known for DCM-2 operation and R and ω_N for DCM-1 operation. If a desired circuit parameter is to be expressed in terms of other variables, then it may be done by further manipulation of the equations. An example would be to express the equations for CCM opera-

TABLE-2.1

SRC SUMMARY OF EQUATIONS

Para-meter	DCM - 1 $0 < \omega_N \leq 1$ $V_{oN} = 1$ $0 < R \leq 2$	DCM - 2 $0 < \omega_N \leq 0.5$ $0 \leq V_{oN} < 1$	CCM $0.5 \leq \omega_N < 1$ $0 \leq V_{oN} < 1$ $1 + V_{oN} \leq R < \infty$	CCM $1 < \omega_N < \infty$ $0 \leq V_{oN} < 1$ $1 - V_{oN} \leq R < \infty$
V_{oN}	$V_{oN} = 1$	V_{oN} (Given)	V_{oN} (Given)	V_{oN} (Given)
R	R (Given)	$1 + V_{oN}$	R (Given)	R (Given)
R'	0	$1 - V_{oN}$	$R - 2V_{oN}$	$R + 2V_{oN}$
α	0	π	$\pi - \cos^{-1}\frac{R'^2 + 4 - R^2}{4R'}$	$\cos^{-1}\frac{R'^2 + 4 - R^2}{4R'}$
β	π	π	$\pi - \cos^{-1}\frac{R^2 + 4 - R'^2}{4R}$	$\cos^{-1}\frac{R^2 + 4 - R'^2}{4R}$
T_N	$2\pi/\omega_N$	$2\pi/\omega_N$	$2(\alpha + \beta)$	$2(\alpha + \beta)$
ω_N	ω_N (Given)	ω_N (Given)	$\pi/(\alpha + \beta)$	$\pi/(\alpha + \beta)$
V_{CON}	$-R$	$-2V_{oN}$	$-V_{oN}(R + 1 - V_{oN})$	$V_{oN}(R - 1 + V_{oN})$
I_{LON}	0	0	$R \sin\beta$	$R \sin\beta$
V_{CPN}	R	2	$R + 1 - V_{oN}$	$R - 1 + V_{oN}$
I_{LPN}	R	$1 + V_{oN}$	R	R, $\beta \geq \pi/2$ I_{LON}, $\beta \leq \pi/2$
$(VS)_{PN}$	$2R$	$2(1 + V_{oN})$	$2R$	$2I_{LPN}$

TABLE-2.1 (contd.)

SRC - SUMMARY OF EQUATIONS

Para-meter	DCM - 1 $0 < \omega_N \leq 1$ $V_{oN} = 1$ $0 < R \leq 2$	DCM - 2 $0 < \omega_N \leq 0.5$ $0 \leq V_{oN} < 1$	CCM $0.5 \leq \omega_N < 1$ $0 \leq V_{oN} < 1$ $1 + V_{oN} \leq R < \infty$	CCM $1 < \omega_N < \infty$ $0 \leq V_{oN} < 1$ $1 - V_{oN} \leq R < \infty$
I_{DAVN}	0	$\frac{(1 - V_{oN})\omega_N}{\pi}$	$\frac{V_{CPN} + V_{C0N}}{2(\alpha + \beta)}$	$\frac{V_{CPN} - V_{C0N}}{2(\alpha + \beta)}$
I_{QAVN}	$\frac{R\,\omega_N}{\pi}$	$\frac{(1 + V_{oN})\omega_N}{\pi}$	$\frac{V_{CPN} - V_{C0N}}{2(\alpha + \beta)}$	$\frac{V_{CPN} + V_{C0N}}{2(\alpha + \beta)}$
I_{LAVN}	$\frac{2R\,\omega_N}{\pi}$	$\frac{4\,\omega_N}{\pi}$	$\frac{2\,V_{CPN}}{\alpha + \beta}$	$\frac{2\,V_{CPN}}{\alpha + \beta}$
I_{DRN}	0	$\frac{(1 - V_{oN})}{2}\sqrt{\omega_N}$	$\frac{R - 2\,V_{oN}}{2} \times \sqrt{\frac{\alpha - (1/2)\sin 2\alpha}{\alpha + \beta}}$	$\frac{R + 2\,V_{oN}}{2} \times \sqrt{\frac{\alpha - (1/2)\sin 2\alpha}{\alpha + \beta}}$
I_{QRN}	$\frac{R\sqrt{\omega_N}}{2}$	$\frac{(1 + V_{oN})}{2}\sqrt{\omega_N}$	$\frac{R}{2} \times \sqrt{\frac{\beta - (1/2)\sin 2\beta}{\alpha + \beta}}$	$\frac{R}{2} \times \sqrt{\frac{\beta - (1/2)\sin 2\beta}{\alpha + \beta}}$
I_{LRN}	$\sqrt{2(I_{DRN}^2 + I_{QRN}^2)}$	$\sqrt{2(I_{DRN}^2 + I_{QRN}^2)}$	$\sqrt{2(I_{DRN}^2 + I_{QRN}^2)}$	$\sqrt{2(I_{DRN}^2 + I_{QRN}^2)}$

Equations for switching boundary S1 (Q1 turn-on):

$$\{(V_{C0N} + V_{oN})^2 - V_{oN}^2\}(1 - V_{oN})^2 - V_{oN}^2 I_{L0N}^2 = 0\,, \quad \omega_N < 1$$

$$(V_{C0N} + V_{oN} + V_{oN}^2)^2 - V_{oN}^2\,\{I_{L0N}^2 + (V_{C0N} + 1 + V_{oN})^2\} = 0\,, \quad \omega_N > 1$$

For switching boundary S2, substitute $-V_{C0N}$ and $-I_{L0N}$ for V_{C0N} and I_{L0N}, respectively.

tion in terms of ω_N instead of R and normalized load resistance $R_N = \frac{R_{LOAD}}{Z_0}$ instead of load voltage V_{oN}. However, such equations are more complex and often implicit in nature and, hence, difficult to derive and solve [20].

The equations in Table 2.1 covering the CCM operation modes below and above resonant frequency and the DCM-2 operation have been plotted in Appendix A. DCM-1 mode equations have not been used since this region occurs only at the limit $V_{oN} \rightarrow 1$ and is not of significance in the ideal analysis. The plots in Appendix A can be used by a designer to predict the ideal performance of the SRC and also to carry out a preliminary design of the converter. Some of the plots have been reproduced in Figs. 2.21, 2.22 and 2.23 corresponding to operation in type-2 DCM, CCM below resonance and CCM above resonance, respectively. As will be shown in Chapter 3, these curves are modified under certain operating conditions due to the presence of circuit losses. However, these ideal curves are still useful when used at operating frequencies away from resonant frequency and at output voltages away from the supply voltage. These aspects of SRC operation are further discussed in Chapter 3.

Figures. 2.24(a), (b) and (c) show dc characteristics of the SRC relating I_{oN} and V_{oN} for various ω_Ns under the different regions of operation. For operation in the CCM region, the following computational procedure is adopted for determining the value of I_{oN} for the given ω_N and V_{oN} . Table 2.1 shows the range of R under CCM conditions. Given R and V_{oN}, the equations of Table 2.1 can be used to compute the value of ω_N. By varying the value of R within its range, the magnitude of R which results in the required ω_N value can be iteratively determined. Thereafter, using this value of R and the given V_{oN}, other parameter values, including I_{oN} , can be determined using the equations of Table 2.1. The computer program for carrying this out is in Appendix A.

Figure 2.24(a) shows the characteristics predominantly in DCM-2. The SRC behaves very much like a current source for a given operating frequency in this region. Figure 2.24(b) shows the characteristics mostly in the CCM region below resonant frequency. Here, the performance deviates from that of a current source as the operating frequency is increased close to resonant frequency. Figure 2.24(c) shows the SRC characteristics when the operating frequency is above the resonant frequency. In this case, the behavior is that of a poor current source even at operating frequency away from the resonant frequency.

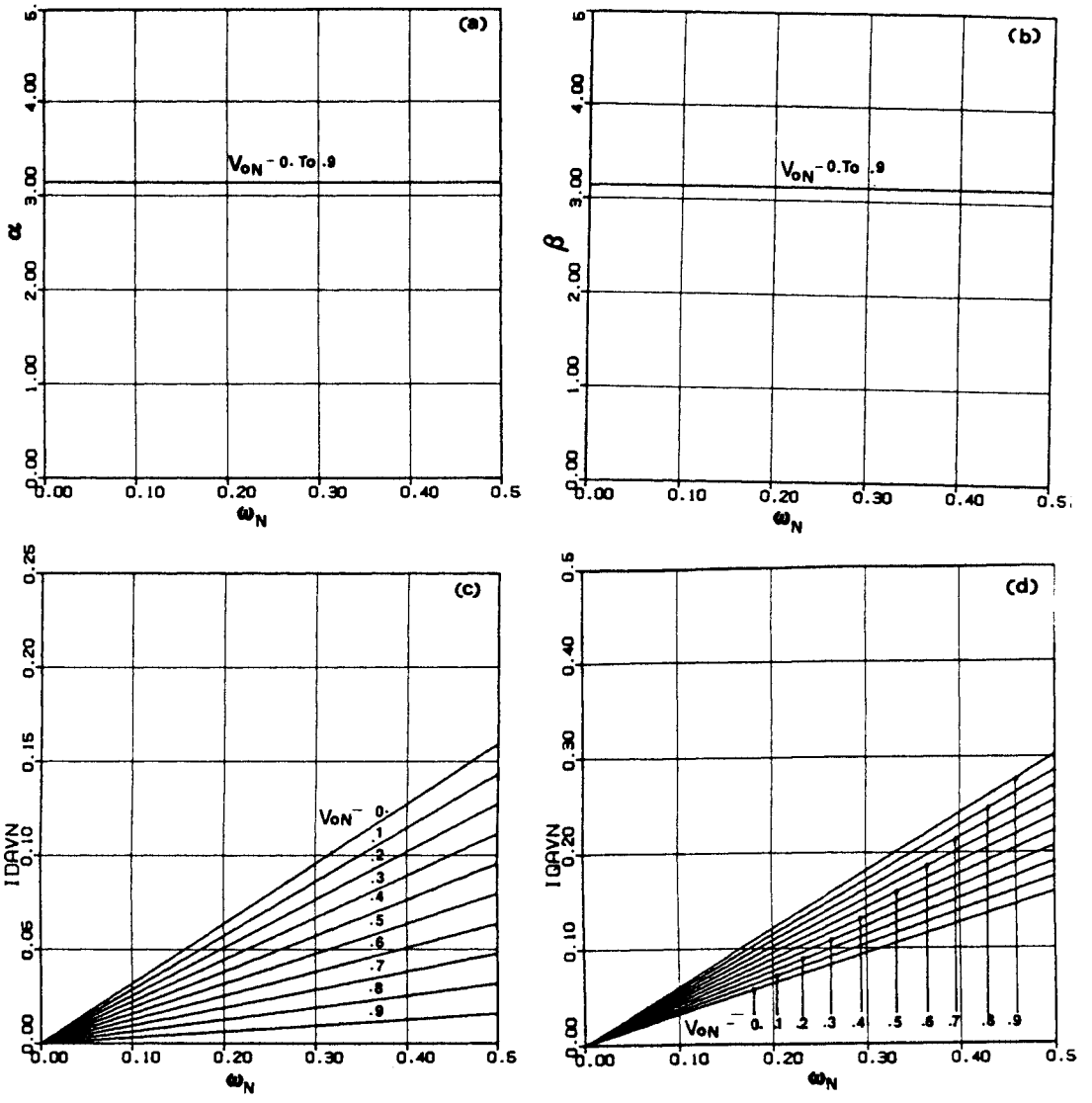

Figure 2.21. Ideal design curves for a SRC - $0 < \omega_N < 0.5$

a) Diode conduction angle
b) Transistor conduction angle
c) Normalized average diode current
d) Normalized average transistor current

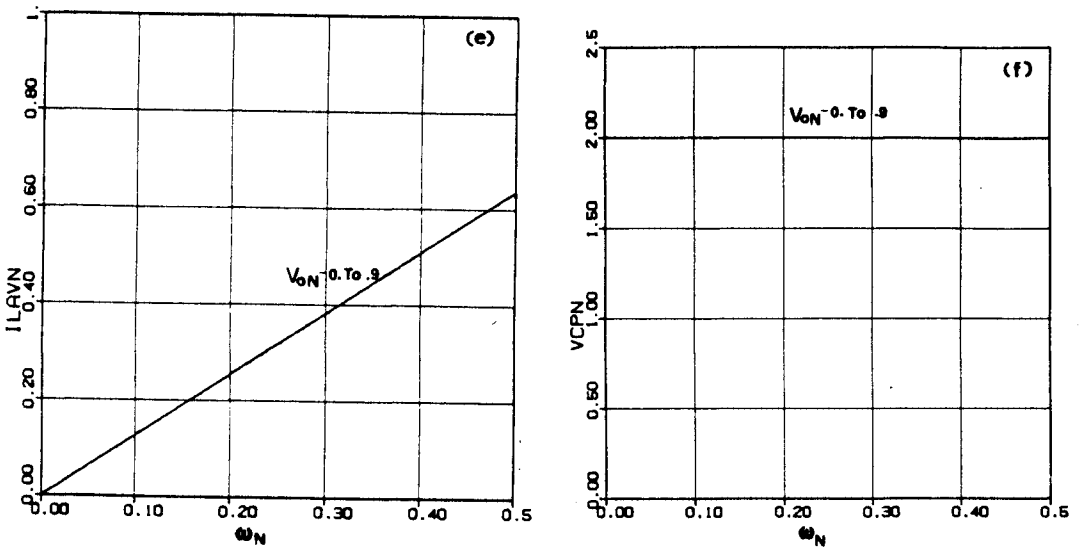

Figure 2.21 (contd.)
e) Normalized average inductor current/normalized output current
f) Normalized peak capacitor voltage

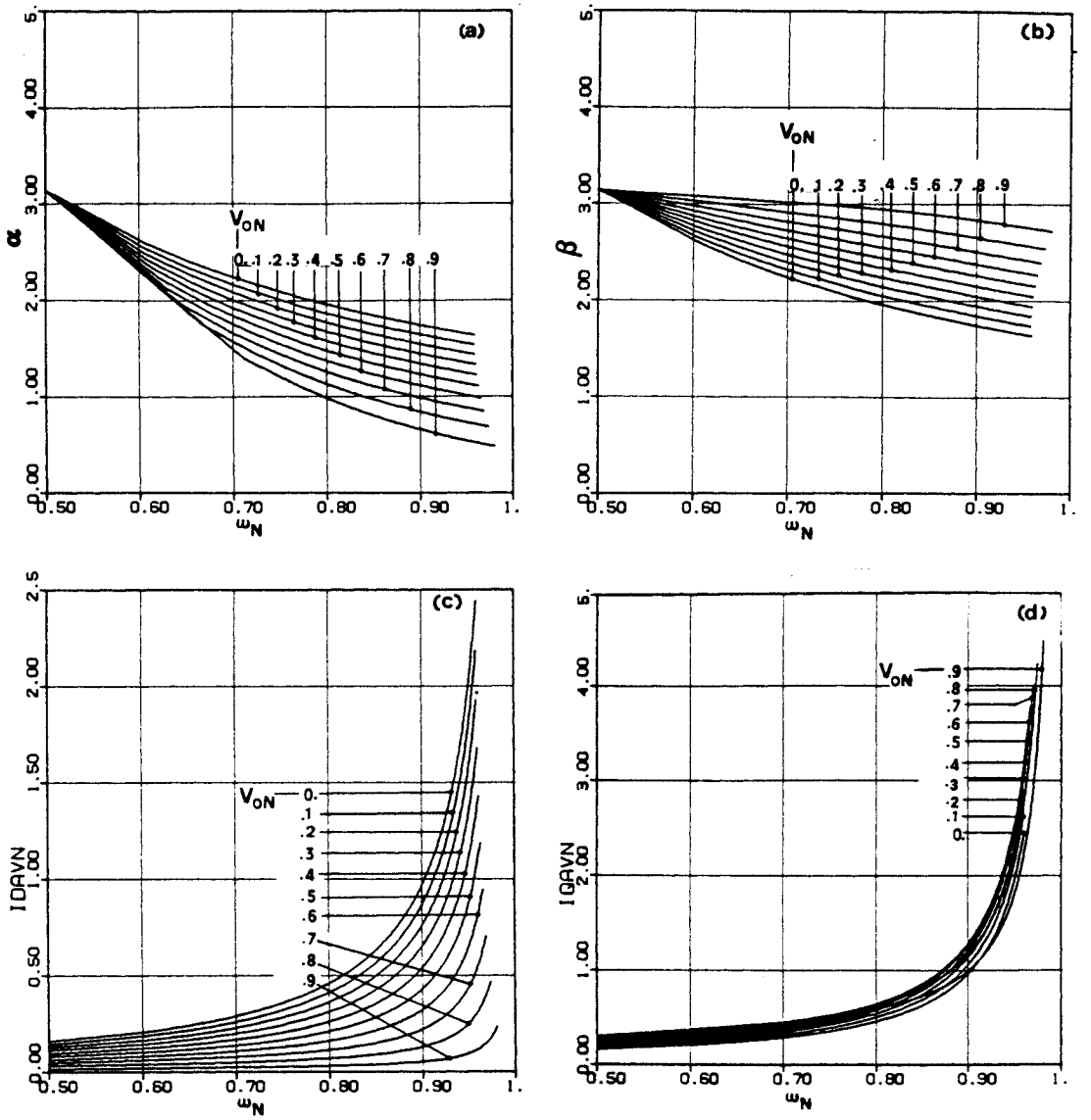

Figure 2.22. Ideal design curves for a SRC - $0.5 < \omega_N < 1.0$
a) Diode conduction angle
b) Transistor conduction angle
c) Normalized average diode current
d) Normalized average transistor current

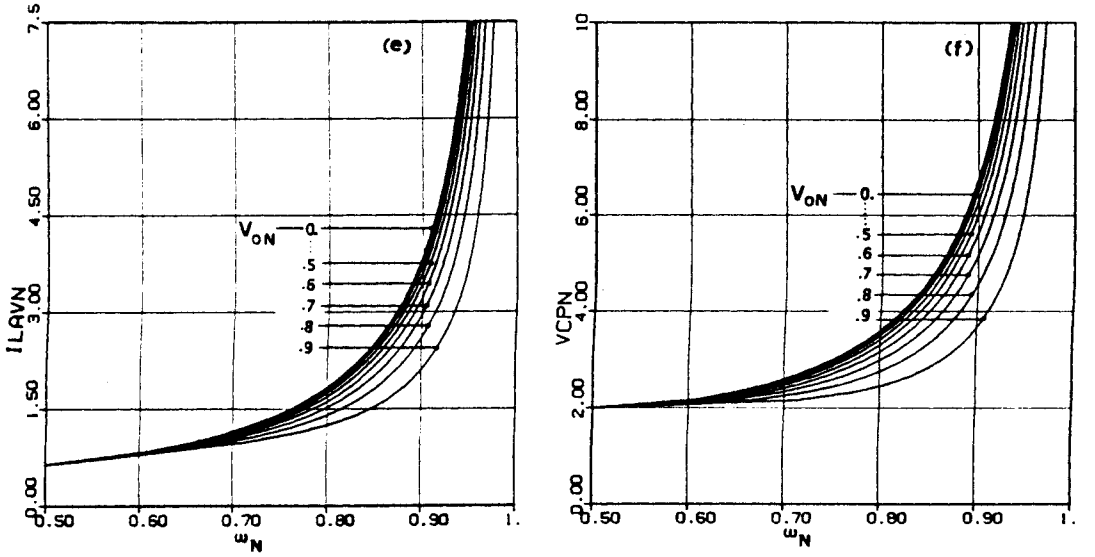

Figure 2.22 (contd.)
e) Normalized average inductor current/normalized output current
f) Normalized peak capacitor voltage

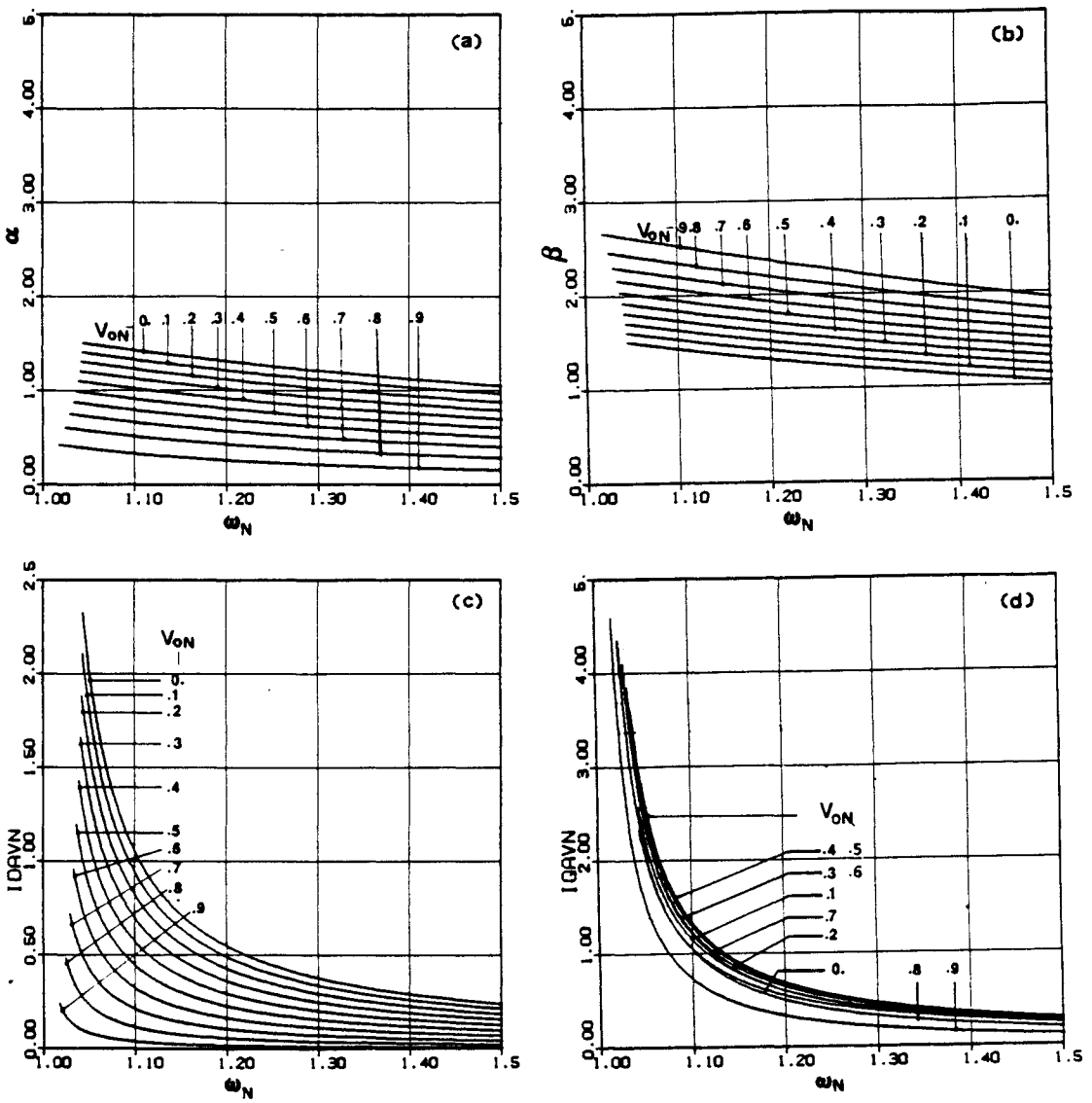

Figure 2.23. Ideal design curves for a SRC - $1.0 < \omega_N < 1.5$
a) Diode conduction angle
b) Transistor conduction angle
c) Normalized average diode current
d) Normalized average transistor current

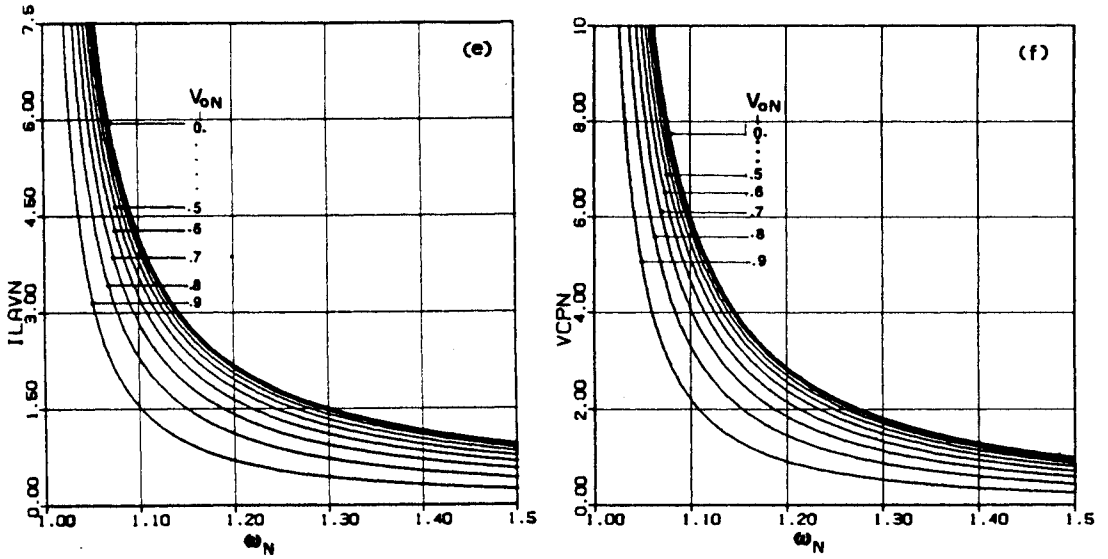

Figure 2.23 (contd.)
e) Normalized average inductor current/normalized output current
f) Normalized peak capacitor voltage

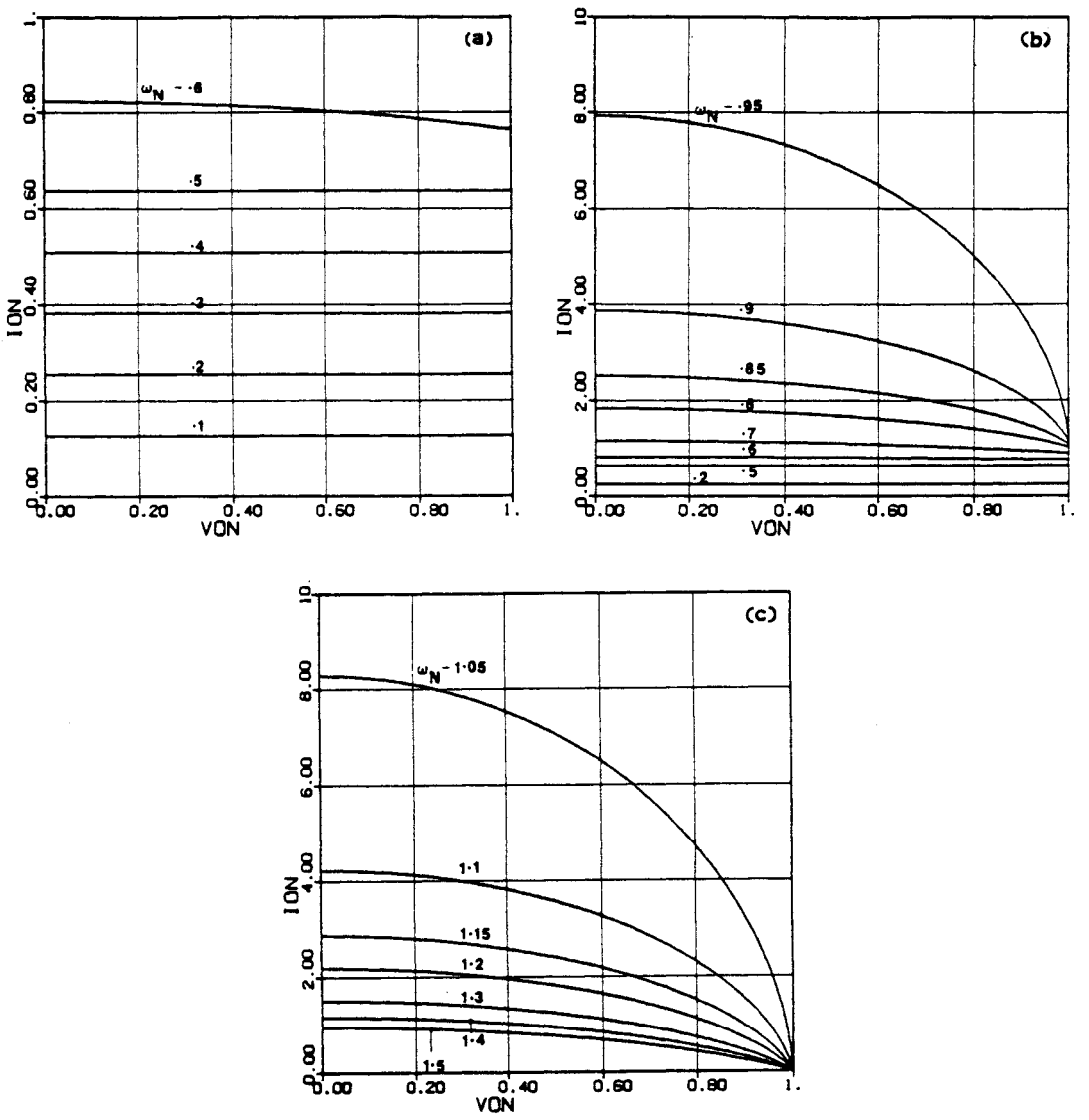

Figure 2.24. SRC ideal dc characteristics
a) Mainly DCM-2 b) Mainly CCM below resonance c) CCM above resonance

Since the basic characteristic of a SRC is that of a current source, to regulate the output voltage against load variations, generally a large operating frequency range is needed. Also, to regulate the output voltage under no load conditions, the SRC circuit requires the addition of a bleeder resistance, which would reduce converter efficiency. The SRC topology is desirable for use in applications, such as welding, in which good voltage regulation is not required but a near constant current has to be supplied to a widely varying load. SRCs can also be designed to be short-circuit proof which is an advantage in such applications.

2.4 Conclusions

The graphical state-plane technique was employed to study the operation of a series resonant converter. Using the inductor current and capacitor voltage of the tank circuit as the two coordinates, both large-signal dynamics and steady-state operation of a resonant converter can be graphically portrayed on the state plane. The state portrait of the converter, which includes all possible converter trajectories, reveals clearly the instantaneous resonant tank energy, output power, switching frequency and control. It serves as a natural vehicle to explore the properties of the system under both dynamic and steady-state conditions.

In this Chapter, the operation of a SRC was studied in detail using steady-state trajectory diagrams. The different modes of operation and their regions of occurrence were explained with these diagrams. Appendix A contains dc analyses including derivations of equations for various steady-state parameters based on a geometrical study of the state-plane diagrams. These analytical results were also discussed in this chapter.

Chapter 3

Effect Of Parasitic Losses On Series Resonant Converter

3.0 Symbols Of Variables

The symbols listed in Sec. 2.0 are used in this chapter and in Appendix B, except for the following changes.

α	-	Diode Trajectory Angle on $v_{CN} - i_{LN}$ Plane
β	-	Transistor Trajectory Angle on $v_{CN} - i_{LN}$ Plane
α_d	-	Diode Conduction Angle on $x_1 - x_2$ Plane
α_q	-	Transistor Conduction Angle on $x_1 - x_2$ Plane

Some of the additional symbols used in this chapter and in Appendix B are listed below.

μ, φ	-	Polar Coordinates on $x_1 - x_2$ Plane

μ_0, φ_0	-	Initial Values of μ and φ, respectively
ω_D	-	Damped Natural Frequency
ρ, θ	-	Polar Coordinates on $v'_{CN} - i_{LN}$ Plane
ρ_0, θ_0	-	Initial Values of ρ and θ, respectively
ζ	-	Damping Factor of Resonant Tank
k	-	A Factor Dependent on ζ
P_{oN}	-	Normalized Output Power
$\hat{P}_{oN}$	-	Normalized Maximum Output Power for a V_{oN}
$\hat{P}_{oNmax}$	-	Normalized Maximum Output Power for any V_{oN}
Q	-	Quality Factor of Resonant Tank
R_1, R_{10}, R_2 ...	-	Distances from a Topological Mode Center
$\hat{R}_1$, $\hat{R}_{10}$, $\hat{R}_2$ ...	-	Maximum Distances from a Topological Mode Center
v'_C	-	Modified Capacitor Voltage
v'_{CN}	-	Normalized Modified Capacitor Voltage
V'_{C0N}	-	Initial Value of v'_{CN}
x_1, x_2	-	Transformed State Variables
x_{10}, x_{20}	-	Initial Values of x_1 and x_2, respectively

3.1 Introduction

The dc analyses of resonant converters [18,19,20,21,22,23] largely ignore the parasitic losses occuring in them. However, it is found that in certain regions of operation, such as when the operating frequency is close to resonant frequency, the dc characteristics of these converters depend considerably on these loss factors. This is unlike the case with normal pulse-width modulated converters where the dc gain depends chiefly on the duty-cycle ratio and the parasitic losses can be ignored. Thus, there exists an imperative need to develop techniques for inclusion of losses in the analysis of resonant converters so that the circuits can be utilized optimally.

The series resonant converter topology(**SRC**) of Chapter 2 is chosen for carrying out the analysis with losses included. Since the SRC is more commonly used in its natural commutation region (operating frequency less than resonant frequency), the analysis is also limited to this region. The state-plane trajectories of Chapter 2 are modified to include the losses and then analyzed. Closed-form solutions are obtained wherever possible. In other cases, the results are obtained by following a numerical approach. The mathematical derivations and the computer algorithms are presented in Appendix B and the results are discussed in this chapter. Experimental verification of the analysis has also been provided.

3.2 State Plane Analysis

3.2.1 Modeling the Losses

The SRC circuit diagram is shown in Fig. 2.1. Figs 2.2, 2.3, 2.4 and 2.17 show the converter waveforms under different conditions of operation. The common equivalent circuit (Fig. 2.6) assumed in Chapter 2 under a resonant topological mode is reproduced in Fig. 3.1(a). Here, an ideal tank circuit driven by an equivalent dc voltage source has been assumed to represent the SRC during a given resonant interval.

In the present analysis, the various losses that occur at different parts of the circuit, such as the resonant inductor, devices Q1, D1, Q2, D2 and the output filter capacitor, are all lumped together to be represented by a single loss resistor in series with the resonant inductor. The voltage drops in the output rectifier bridge are, however, incorporated by increasing the output dc voltage appropriately. Figure 3.1(b) then replaces Fig. 3.1(a) as the common equivalent circuit for the four resonant topological modes of operation.

The analysis does not explicitly model any output transformer that may be present. However, it may be possible to include the leakage inductances of the transformer in the magnitude of the resonant inductor and the transformer losses in the lumped resistor in series with the tank circuit.

CONDUCTION	V_E
Q1	$V_S - V_O$
D1	$V_S + V_O$
Q2	$-V_S + V_O$
D2	$-V_S - V_O$

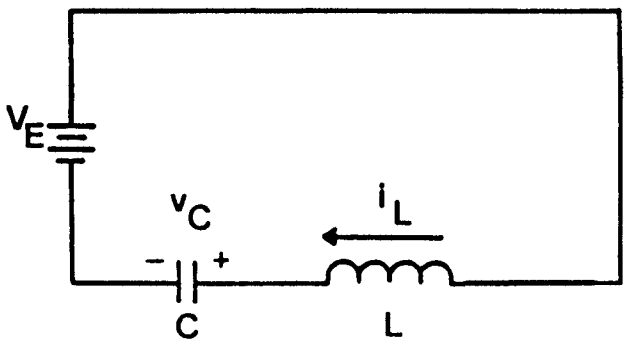

(a)

CONDUCTION	V_E
Q1	$V_S - V_O$
D1	$V_S + V_O$
Q2	$-V_S + V_O$
D2	$-V_S - V_O$

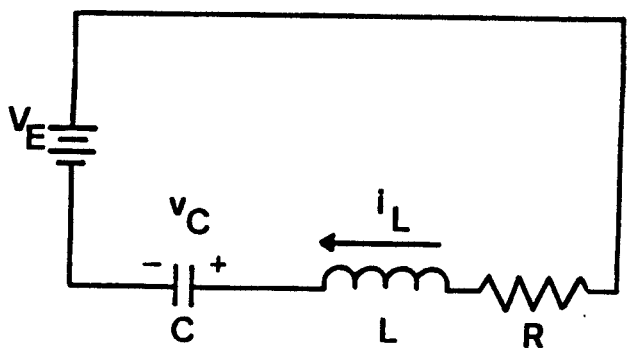

(b)

Figure 3.1. Common equivalent circuit for different resonant intervals
a) Losses neglected b) Losses included

3.2.2 Trajectory Equation With Loss

This section derives the state-trajectory equation for the circuit in Fig. 3.1(b) when losses are included. The state equations for the equivalent citcuit diagram in Fig. 3.1(b) are

$$\begin{bmatrix} \dot{v}_C \\ \dot{i}_L \end{bmatrix} = \begin{bmatrix} 0 & \frac{1}{C} \\ \frac{-1}{L} & \frac{-R}{L} \end{bmatrix} \begin{bmatrix} v_C \\ i_L \end{bmatrix} + \begin{bmatrix} 0 \\ \frac{1}{L} \end{bmatrix} V_E \tag{3.1}$$

with initial conditions $i_L/_{(t=t_0)} = I_{L0}$ and $v_C/_{(t=t_0)} = V_{C0}$. The derivation of the trajectory equations (3.33) and (3.34) from (3.1) is based on well-known techniques for obtaining the state- plane trajectory of a linear second-order system [40].

The first step in this process is to normalize and homogenize (3.1) into a general form. To do this let,

$$v'_C = v_C - V_E \tag{3.2}$$

Defining the following parameters,

$$Z_0 = \sqrt{\frac{L}{C}} = \text{characteristic impedance (ohms)} \tag{3.3}$$

$$\omega_0 = \frac{1}{\sqrt{LC}} = \text{resonant frequency (radians/sec)} \tag{3.4}$$

$$\zeta = \frac{R}{2}\sqrt{\frac{C}{L}} = \text{damping factor} \tag{3.5}$$

$$Q = \frac{\omega_0 L}{R} = \frac{1}{2\zeta} = \text{quality factor} \tag{3.6}$$

The voltage and current normalizing factors are

$$\begin{aligned} N_v &= \text{Voltage Normalizing Factor} \\ &= V_s \end{aligned} \tag{3.7}$$

$$N_i = \text{Current Normalizing Factor} = \frac{V_s}{Z_0} \tag{3.8}$$

Rewriting (3.1) using (3.2) through (3.6) and normalizing with (3.7) and (3.8),

$$\begin{bmatrix} \dot{v}'_{CN} \\ i_{LN} \end{bmatrix} = \begin{bmatrix} 0 & \omega_0 \\ -\omega_0 & -2\zeta\omega_0 \end{bmatrix} \begin{bmatrix} v'_{CN} \\ i_{LN} \end{bmatrix} = A \begin{bmatrix} v'_{CN} \\ i_{LN} \end{bmatrix} \tag{3.9}$$

with initial conditions,

$$V'_{CON.} = \frac{V_{C0} - V_E}{V_s} \quad \text{and} \quad I_{LON} = \frac{I_{L0} Z_0}{V_s} \tag{3.10}$$

Equation (3.9) is the desired normalized and homogenized form of the system equations. The subscript N in (3.9) and (3.10) refers to normalized variables.

As the second step, we will determine the eigenvalues and a set of eigenvectors for the system defined by (3.9).

The characteristic equation for (3.9) is ,

$$\det(\lambda I - A) = 0, \tag{3.11}$$

where I is a (2 × 2) identity matrix. Substituting A from (3.9) in (3.11), the characteristic equation is,

$$\lambda^2 + 2\zeta\omega_0\lambda + \omega_0^2 = 0 \tag{3.12}$$

Solving (3.12) for eigenvalues,

$$\lambda_1, \lambda_2 = -\zeta\omega_0 \pm j\omega_0\sqrt{1-\zeta^2} = -\sigma + j\omega_D , \tag{3.13}$$

$$\text{where } \omega_D = \omega_0\sqrt{1-\zeta^2} = \text{Damped natural frequency} \tag{3.14}$$

Eigen vector v is the solution of

$$A\,v = \lambda\,v \tag{3.15}$$

Vector v represents an infinite set of vectors and the one chosen here is of the form

$$v = \begin{bmatrix} 1 \\ \xi \end{bmatrix} \tag{3.16}$$

Substituting for A from (3.9) and v from (3.16) into (3.15) and manipulating

$$\begin{bmatrix} \lambda & -\omega_0 \\ \omega_0 & \lambda + 2\zeta\omega_0 \end{bmatrix} \begin{bmatrix} 1 \\ \xi \end{bmatrix} = 0 \tag{3.17}$$

Solving the homogeneous equations (3.17) for ξ and using (3.13),

$$\xi = -\zeta \pm j\sqrt{1-\zeta^2} \tag{3.18}$$

From (3.16) and (3.18) the eigenvectors are

$$v_1, v_2 = \begin{bmatrix} 1 \\ -\zeta \end{bmatrix} \pm j \begin{bmatrix} 0 \\ \sqrt{1-\zeta^2} \end{bmatrix} = a \pm jb \tag{3.19}$$

As the third step, we will transform (3.9) into a more convenient form by introducing new state variables x_1 and x_2 based on the eigenvectors. The trajectory equation is more easily obtained in this manner. Also in the $x_1 - x_2$ plane, the angle subtended by a segment of the state trajectory at the equilibrium point is proportional to the time elapsed. Hence, the trajectories are easily time scaled on the $x_1 - x_2$ plane.

Let us define the transformation matrix, T_m, by

$$T_m = [a \quad b] = \begin{bmatrix} 1 & 0 \\ -\zeta & \sqrt{1-\zeta^2} \end{bmatrix}, \quad \zeta \neq 1 \tag{3.20}$$

where a and b are the real and imaginary part of the eigenvectors in (3.19), respectively. The transformation is given by

$$\begin{bmatrix} v'_{CN} \\ i_{LN} \end{bmatrix} = T_m \begin{bmatrix} x_1 \\ x_2 \end{bmatrix} \tag{3.21}$$

$$\text{Also, } \begin{bmatrix} x_1 \\ x_2 \end{bmatrix} = T_m^{-1} \begin{bmatrix} v'_{CN} \\ i_{LN} \end{bmatrix} = \begin{bmatrix} 1 & 0 \\ \dfrac{\zeta}{\sqrt{1-\zeta^2}} & \dfrac{1}{\sqrt{1-\zeta^2}} \end{bmatrix} \begin{bmatrix} v'_{CN} \\ i_{LN} \end{bmatrix} \tag{3.22}$$

At $\zeta = 0$, of course, the $x_1 - x_2$ plane and the $v'_{CN} - i_{LN}$ plane are the same since T_m in (3.20) reduces to an identity matrix. Performing a similarity transformation on (3.9) using (3.21),

$$\begin{bmatrix} \dot{x}_1 \\ \dot{x}_2 \end{bmatrix} = T_m A T_m^{-1} \begin{bmatrix} x_1 \\ x_2 \end{bmatrix} = \Lambda_m \begin{bmatrix} x_1 \\ x_2 \end{bmatrix} \tag{3.23}$$

Substituting for T_m from (3.20) and A from (3.9) into (3.23),

$$\begin{bmatrix} \dot{x}_1 \\ \dot{x}_2 \end{bmatrix} = \Lambda_m \begin{bmatrix} x_1 \\ x_2 \end{bmatrix} = \begin{bmatrix} -\sigma & \omega_D \\ -\omega_D & -\sigma \end{bmatrix} \begin{bmatrix} x_1 \\ x_2 \end{bmatrix} \tag{3.24}$$

From (3.22), the initial conditions are

$$\begin{bmatrix} x_{10} \\ x_{20} \end{bmatrix} = \begin{bmatrix} 1 & 0 \\ \dfrac{\zeta}{\sqrt{1-\zeta^2}} & \dfrac{1}{\sqrt{1-\zeta^2}} \end{bmatrix} \begin{bmatrix} v'_{CON} \\ I_{LON} \end{bmatrix} \tag{3.25}$$

As the fourth step we will solve (3.24). The solution to (3.24) is given by

$$\begin{bmatrix} x_1 \\ x_2 \end{bmatrix} = e^{\Lambda_m t} \begin{bmatrix} x_{10} \\ x_{20} \end{bmatrix}, \quad \text{where} \tag{3.26}$$

$$e^{\Lambda_m t} = L^{-1} [SI - \Lambda_m]^{-1} \tag{3.27}$$

Substituting for Λ_m from (3.24) and solving (3.26) using (3.27),

$$\begin{bmatrix} x_1 \\ x_2 \end{bmatrix} = e^{-\sigma t} \begin{bmatrix} \cos \omega_D t & \sin \omega_D t \\ -\sin \omega_D t & \cos \omega_D t \end{bmatrix} \begin{bmatrix} x_{10} \\ x_{20} \end{bmatrix} \tag{3.28}$$

As the fifth step, we will obtain the trajectory equation on the $x_1 - x_2$ plane by eliminating the variable t from (3.28).

Defining the following polar coordinates for the $x_1 - x_2$ plane,

$$\mu = \sqrt{x_1^2 + x_2^2} \tag{3.29}$$

$$\mu_0 = \sqrt{x_{10}^2 + x_{20}^2} \tag{3.30}$$

$$\varphi = \tan^{-1}\left(\frac{-x_2}{x_1}\right) \quad \text{and} \tag{3.31}$$

$$\varphi_0 = \tan^{-1}\left(-\frac{x_{20}}{x_{10}}\right) \tag{3.32}$$

By eliminating t from (3.28) and using (3.29) through (3.32),

$$\mu = \mu_0 \exp\left[-\frac{\zeta}{\sqrt{1-\zeta^2}}(\varphi - \varphi_0)\right] \quad \text{and} \tag{3.33}$$

$$\varphi = \omega_D t + \varphi_0 \tag{3.34}$$

On the x_1-x_2 plane, (3.33) describes a logarithmic spiral. From (3.34), (3.31) and (3.32), angle φ subtended at the origin between two points on the spiral trajectory is proportional to the time elapsed. As time progresses, the value of μ progressively decreases as determined by (3.33). The value of the damping factor, ζ, determines the rate at which the spiral converges to origin. If ζ equals zero, then (3.33) reduces to a circular trajectory as assumed in Chapter 2.

Equations (3.33) and (3.34) represent a relatively simple geometrical curve and the $x_1 - x_2$ plane retains the property of the $v_{CN} - i_{LN}$ plane used in Chapter 2 in that the angles subtended by the trajectory segments are proportional to elapsed time. Thus, it would have been convenient if the closed steady-state trajectories could be drawn on a common plane similar to the $x_1 - x_2$ plane. However, the $x_1 - x_2$ planes do not remain the same for the four resonant topological modes. This is because the lateral translation performed by (3.2) depends on the value of V_E which varies with the topological mode. Hence, the construction and study of the steady-state trajectories in later sections of this chapter is done only on $v_{CN} - i_{LN}$ plane.

As the sixth step we will transform (3.33) and (3.34) back to the $(v'_{CN} - i_{LN})$ plane and obtain the desired trajectory equation in polar form. Between the $(v_{CN} - i_{LN})$ plane and the $(v'_{CN} - i_{LN})$ plane only a

translation along the x- axis as determined by (3.2) is involved and, hence, the trajectory equation will not be obtained in the $(v_{CN} - i_{LN})$ plane.

Defining the following polar coordinates for the $v'_{CN} - i_{LN}$ plane,

$$\rho = \sqrt{v'^2_{CN} + i^2_{LN}} \tag{3.35}$$

$$\rho_0 = \sqrt{V'^2_{C0N} + I^2_{L0N}} \tag{3.36}$$

$$\theta = \tan^{-1}\left(\frac{-i_{LN}}{v'_{CN}}\right) \text{ and} \tag{3.37}$$

$$\theta_0 = \tan^{-1}\left(\frac{-I_{L0N}}{V'_{C0N}}\right) \tag{3.38}$$

Before transforming the trajectory equation into the $v'_{CN} - i_{LN}$ plane, let us first determine the equations connecting the polar coordinate variables in the $x_1 - x_2$ plane and the $v'_{CN} - i_{LN}$ plane. Substituting (3.22) in (3.29) and utilizing (3.35),

$$\mu = \frac{\rho}{\sqrt{1-\zeta^2}}\sqrt{1 - \zeta \sin 2\theta} \tag{3.39}$$

Substituting (3.25) in (3.30) and utilizing (3.36),

$$\mu_0 = \frac{\rho_0}{\sqrt{1-\zeta^2}}\sqrt{1 - \zeta \sin 2\theta_0} \tag{3.40}$$

Substituting (3.22) in (3.31) and utilizing (3.37),

$$\varphi = \tan^{-1}\left[-\frac{\zeta}{\sqrt{1-\zeta^2}} + \frac{\tan\theta}{\sqrt{1-\zeta^2}}\right] \tag{3.41}$$

Substituting (3.25) in (3.32) and utilizing (3.38),

$$\varphi_0 = \tan^{-1}\left[-\frac{\zeta}{\sqrt{1-\zeta^2}} + \frac{\tan\theta_0}{\sqrt{1-\zeta^2}}\right] \tag{3.42}$$

Equations (3.39), (3.40), (3.41) and (3.42) allow us to determine the polar coordinates in the $x_1 - x_2$ plane given the polar coordinates in the $v'_{CN} - i_{LN}$ plane.

Substituting for μ from (3.39) and μ_0 from (3.40) into (3.33) and solving for ρ ,

$$\rho = \rho_0 \sqrt{\frac{1 - \zeta \sin 2\theta_0}{1 - \zeta \sin 2\theta}} \exp\left[\frac{-\zeta}{\sqrt{1-\zeta^2}}(\varphi - \varphi_0)\right] \tag{3.43}$$

Substituting for φ from (3.41) and φ_0 from (3.42) into (3.43),

$$\rho = \rho_0 \sqrt{\frac{1 - \zeta \sin 2\theta_0}{1 - \zeta \sin 2\theta}} \exp\left[\frac{-\zeta}{\sqrt{1-\zeta^2}}\left\{\tan^{-1}\left(\frac{-\zeta}{\sqrt{1-\zeta^2}} + \frac{\tan\theta}{\sqrt{1-\zeta^2}}\right) - \tan^{-1}\left(\frac{-\zeta}{\sqrt{1-\zeta^2}} + \frac{\tan\theta_0}{\sqrt{1-\zeta^2}}\right)\right\}\right] \tag{3.44}$$

Substituting for φ from (3.34) into (3.41) and solving for θ,

$$\theta = \tan^{-1}\left[\zeta + \sqrt{1-\zeta^2}\,\tan(\omega_D t + \varphi_0)\right] \tag{3.45}$$

The value of φ_0 in (3.45) is obtained from (3.25) and (3.32) given V'_{C0N} and I_{C0N}.

Equations (3.44) and (3.45) are the desired final trajectory equations in polar form on the $v'_{CN} - i_{LN}$ plane. As explained before, between the $v'_{CN} - i_{LN}$ plane and $v_{CN} - i_{LN}$ plane, only a translation along the x - axis as determined by (3.2) is involved. However, this is not carried out as it would involve cumbersome transformation into rectangular coordinates of the more compact polar form of (3.44) and (3.45).

The trajectories in the $v_{CN} - i_{LN}$ plane are again noncircular and spiral inward. In addition, the angle subtended on the $v_{CN} - i_{LN}$ plane at the center of the trajectory is no longer strictly proportional to the elapsed time. It will be so only in the $x_1 - x_2$ plane as explained earlier.

3.2.2.1 A Special Trajectory Segment

Let us consider a special case when the power switch conducts for half a resonant cycle. The trajectory segment shown in Fig.3.2 corresponds to this case. Steady-State trajectories composed of such trajectory segments occur in discontinuous conduction modes and under special conditions to be discussed in subsequent sections and in Appendix B. The equations derived in this section based on Fig.3.2 are utilized in such cases to derive certain useful closed-form results.

From Fig. 3.2,

$$\theta_0 = 0 \tag{3.46}$$

$$\theta = \pi \tag{3.47}$$

Substituting for θ_0 from (3.46) into (3.42) and θ from (3.47) into (3.41) and considering the appropriate quadrants for the angles,

$$\varphi_0 = \tan^{-1}\left(\frac{-\zeta}{\sqrt{1-\zeta^2}}\right) \quad - \quad 4^{th} \text{ Quadrant} \tag{3.48}$$

$$\varphi = \pi - \tan^{-1}\left(\frac{-\zeta}{\sqrt{1-\zeta^2}}\right) \quad - \quad 2^{nd} \text{ Quadrant} \tag{3.49}$$

Thus, in this special case, the change in angle as measured on the state plane $(\theta - \theta_0)$ and the change in conduction angle $(\varphi - \varphi_0)$ are both identical and equal to π.

Substituting for θ_0 from (3.46), θ from (3.47), φ_0 from (3.48) and φ from (3.49) into (3.43) and from Fig. 3.2,

$$\rho = \rho(t_1) = \rho_0 k, \quad \text{where} \tag{3.50}$$

$$k = \exp\left(\frac{-\zeta\pi}{\sqrt{1-\zeta^2}}\right) \tag{3.51}$$

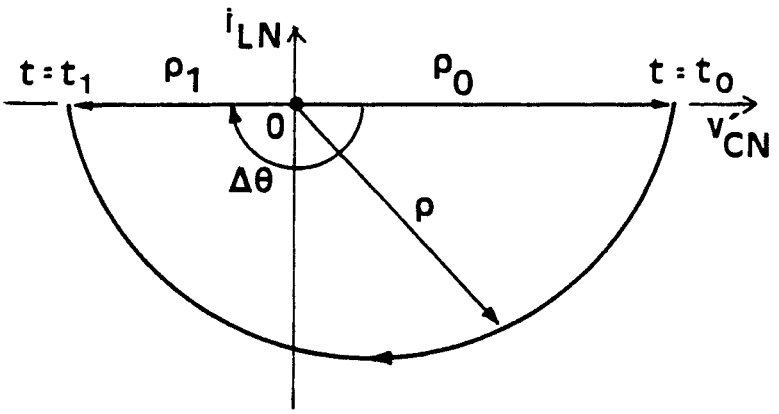

Figure 3.2. Trajectory for conduction angle π

3.2.3 Steady-State Trajectories

The composite state portrait of the SRC for an assumed damping factor $\zeta = \frac{1}{30}$ and $V_{oN} = 0.5$ is shown in Fig. 3.3. This figure is to be compared with Fig. 2.8. The individual trajectories in Fig. 3.3 have been plotted using (3.44). These trajectory segments, of course, spiral inward unlike in Fig. 2.8. The state portrait is no longer unique for a given output voltage, but depends on the circuit damping factor. From the perspective of the state-plane analysis, the behavior of the SRC in certain regions deviates from the ideal predictions of Chapter 2 due to the differences in the geometry of the state portrait. It will be shown in Sec. 3.4 that the regions of occurrences of CCM,DCM-1 and DCM-2 modes are altered from the ideal lossless case. These modes have been defined in Chapter 2. Figure 3.4 shows a set of CCM and type-2 DCM steady-state trajectories when losses are included for operation below resonance. These are to be compared with those in Fig. 2.11. In Fig. 3.4, the frequency normalizing factor is ω_D and not ω_0 as in Chapter 2.

$$\text{Thus,} \quad \omega_N = \frac{\omega}{\omega_D} = \text{Normalized operating frequency} \tag{3.52}$$

However, even for relatively large values of ζ, the difference between ω_0 and ω_D (3.14) is not practically significant.

In Fig. 3.4, the trajectory segments are no longer strictly proportional to the conduction angles of the devices. For any measured change in angle on the state plane, (3.41) and (3.42) are utilized to determine the change in the actual conduction angles. The switching boundaries in Fig. 3.4 marked S1 and S2 deviate considerably from the ideal boundaries marked S1′ and S2′ in the same figure. This also results in substantial reduction of diode conduction intervals particularly at higher frequencies. Another important point to be noted in Fig. 3.4 is that the maximum energy trajectory, T_{UB} which occurs when $\omega = \omega_D$, is no longer infinite in size but bounded. On T_{UB}, the transistors Q1 and Q2 conduct alternately without the antiparallel diodes ever conducting.

Discontinuous mode of operation (type-2 DCM) occurs once again when ω_N becomes less than 0.5. The innermost trajectory marked DCM-2 in Fig. 3.4 represents all the DCM trajectories for this output voltage and loss factor.

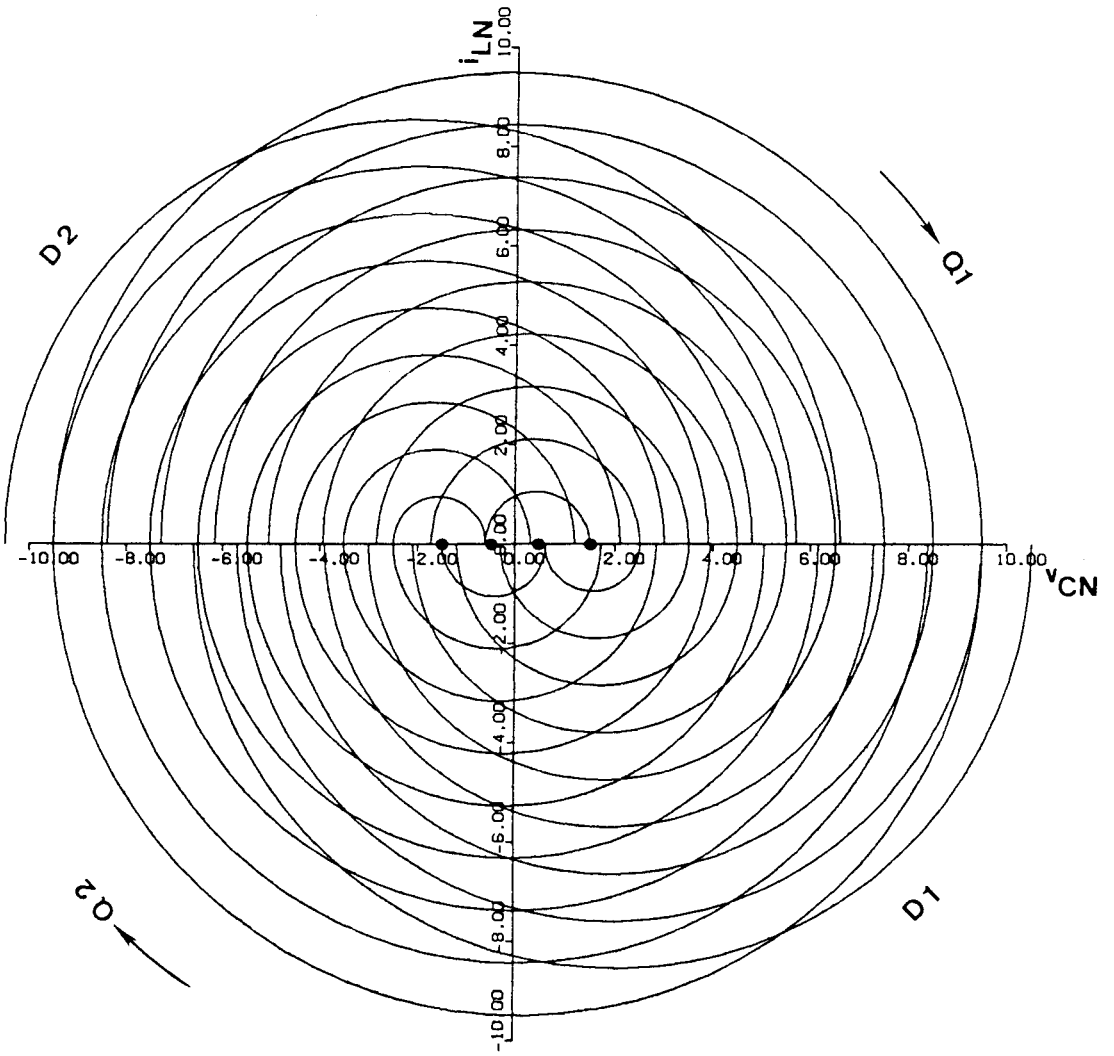

Figure 3.3. Composite state portrait with loss - ζ = 1/30 and V_{oN} = 0.5

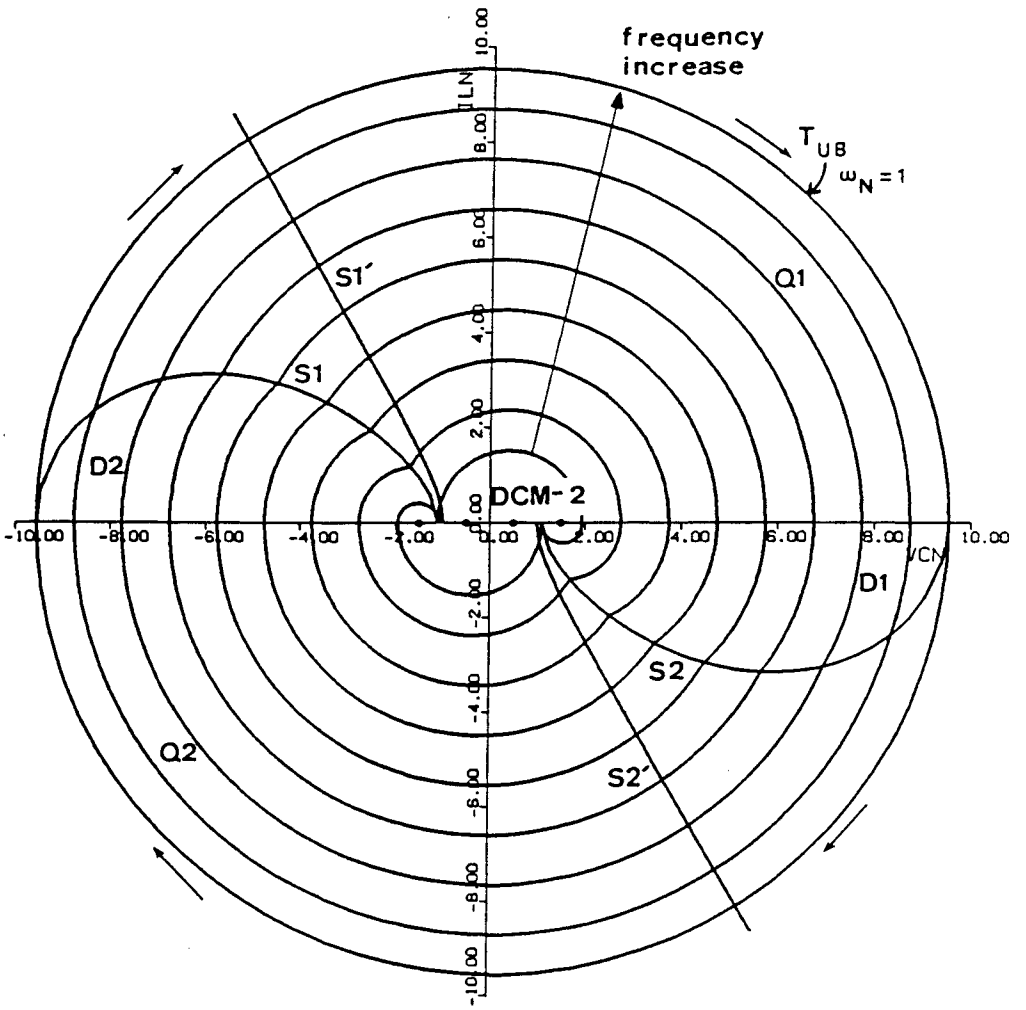

Figure 3.4. CCM/DCM-2 steady-state trajectories for $\omega_N < 1$, $V_{oN} = 0.5$, $\zeta = 1/30$

Type-1 DCM occurs when output voltage is close to supply voltage. As described in Sec. 2.2.5.3, after each transistor conduction, a discontinuous interval is introduced and the antiparallel diodes do not conduct at all in this mode of operation.

Fig. 3.5 shows typical steady-state trajectories with losses included in CCM, DCM-2 and DCM-1 operation. These are similar to the ideal trajectories for these modes in Chapter 2. The trajectory segments are damped spirals, as noted earlier. Owing to this , it becomes possible to construct DCM-1 trajectories even when V_{oN} is less than unity. Under the ideal conditions assumed in Chapter 2, however, DCM-1 occurs only when V_{oN} equals unity.

3.3 Upper Load Limit

Figure 3.6 shows the maximum tank energy trajectory, T_{UB}, of Fig. 3.4. As operating frequency is increased with constant output voltage, trajectoryT_{UB} is reached at $\omega = \omega_D$. Maximum current is delivered to the load when the converter is operated along this trajectory. Please refer to Fig. 3.6 for the meanings of $\hat{R}_1$, $\hat{R}_{10}$, $\hat{R}_2$ and $\hat{R}_{20}$ used in the following derivation.

First, we will show the maximum energy trajectory occurs at $\omega = \omega_D$. Reproducing (3.103) of Sec. 3.4.3, yet to be derived,

$$\omega_N = \frac{\pi}{\alpha_d + \alpha_q} \tag{3.53}$$

where α_d and α_q are the diode and transistor conduction angles, respectively. Since the diode does not conduct at all,

$$\alpha_d = 0 \tag{3.54}$$

Also, from the discussion following (3.49) in Sec. 3.2.2.1,

$$\alpha_q = \pi \tag{3.55}$$

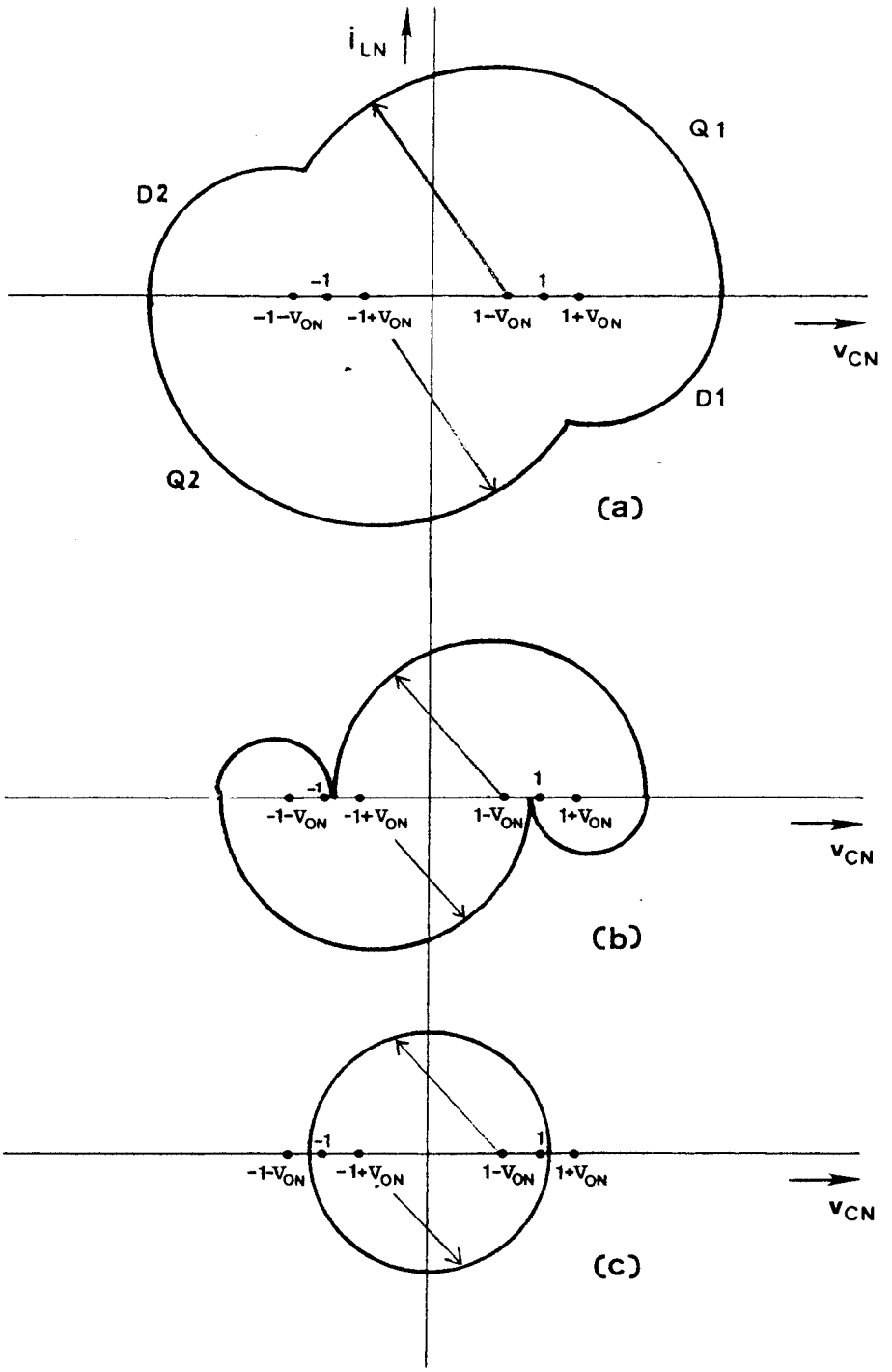

Figure 3.5. Typical steady-state trajeectories with loss
a) CCM b) DCM-2 c) DCM-1

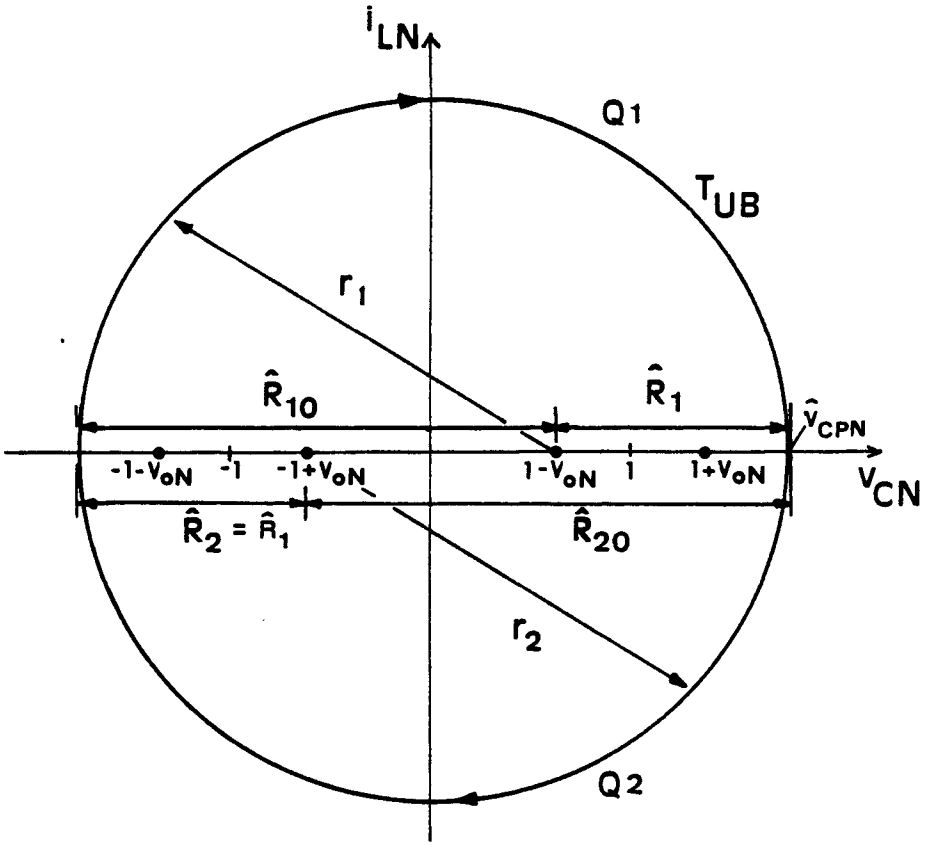

Figure 3.6. Maximum energy trajectory at $\omega = \omega_D$

Substituting these values of α_d and α_q in (3.53), the value of ω_N for the maximum energy trajectory is unity.

Next, we will establish the upper load limit for SRC operation based on Fig. 3.6.

From (3.50) and Fig. 3.6,

$$\begin{aligned}\hat{R}_2 &= \hat{R}_{20}\, k = \left\{\hat{R}_1 + 2\,(1 - V_{oN})\right\} k \\ &= \hat{R}_1, \quad \text{from symmetry}\end{aligned} \tag{3.56}$$

Solving for $\hat{R}_1$ in (3.56),

$$\hat{R}_1 = \frac{2\,k\,(1 - V_{oN})}{1 - k} \tag{3.57}$$

This equation effectively determines the dimensions of the maximum energy trajectory.

From Fig. 3.45 and (3.57),

$$V_{CPN} = 1 - V_{oN} + \hat{R}_1 = (1 - V_{oN})\,\frac{1 + k}{1 - k} \tag{3.58}$$

Reproducing (B.41) from Sec. B.3,

$$I_{oN} = I_{LAVN} = \frac{2V_{CPN}\sqrt{1 - \zeta^2}}{\alpha_d + \alpha_q} \tag{3.59}$$

Substituting for V_{CPN} from (3.58), α_d from (3.54) and α_q from (3.55) into (3.59),

$$\hat{I}_{oN} = \frac{2\,(1 - V_{oN})\,\sqrt{1 - \zeta^2}}{\pi}\,\frac{1 + k}{1 - k} = \text{Maximum normalized load current} \tag{3.60}$$

In (3.59) and (3.60), the factor $\sqrt{1 - \zeta^2}$ is generally very close to unity and may be dropped without any significant error. Equation (3.60) is an important equation that predicts the maximum normalized output current possible for a particular load voltage and factor "k", which depends on the damping factor. Figure 3.7 is a plot of $\hat{I}_{oN}$ as a function of V_{oN} for different ζ's based on (3.60) and (3.51). From Fig. 3.7, it may be observed that a converter with a given ζ cannot be operated in the region to the right of the line corresponding to that ζ. Thus, for a required maximum output current, the maximum voltage-conversion ratio, V_{oN}, is clearly limited to a value less than unity due to circuit losses. On the other hand, when the circuit is considered to be lossless (line-1 in Fig. 3.7), the maximum voltage-conversion

ratio is always unity at any load current. This limit on the output voltage is a critical factor to be considered by a designer.

3.3.1 Maximum Power Transfer

$$P_{oN} = V_{oN} I_{oN} = \text{Normalized output power} \tag{3.61}$$

Substituting for $\hat{I}_{oN}$ (3.60) in (3.61),

$$\hat{P}_{oN} = \frac{2 V_{oN} (1 - V_{oN}) \sqrt{1 - \zeta^2}}{\pi} \frac{1 + k}{1 - k} \tag{3.62}$$
$$= \text{Normalized maximum power transfer for given } V_{oN}$$

For maximum power transfer for any V_{oN} ,

$$\frac{d\hat{P}_{oN}}{dV_{oN}} = \frac{2 (1 - 2V_{oN}) \sqrt{1 - \zeta^2}}{\pi} \frac{1 + k}{1 - k} = 0 \tag{3.63}$$

$$\text{Thus,} \quad V_{oN} = 0.5 , \quad k \neq 1 \quad \text{or} \quad \zeta \neq 0 , \tag{3.64}$$

for maximum power transfer to the load. This result can be explained as follows.

From Fig. 3.7, it may be observed that at $\omega = \omega_D$, the SRC behaves as a source with a fixed linear internal resistance whose value is dependent on the damping factor. Thus, the maximum power transfer to the load will occur when the value of load resistance equals this internal resistance or, equivalently, when the output voltage V_o equals half the source voltage V_s .

Substituting (3.64) in (3.62), we obtain,

$$\hat{P}_{oNmax} = \frac{\sqrt{1 - \zeta^2}}{2\pi} \frac{1 + k}{1 - k} \tag{3.65}$$
$$= \text{Normalized maximum power transfer}$$

This maximum power transfer from SRC occurs at $\omega = \omega_D$ and $V_{oN} = 0.5$. In (3.65), once again the factor $\sqrt{1 - \zeta^2}$ is generally very close to unity and may be dropped without any significant error. Figure 3.8 shows the maximum normalized power that can be delivered to the load by the converter as a function

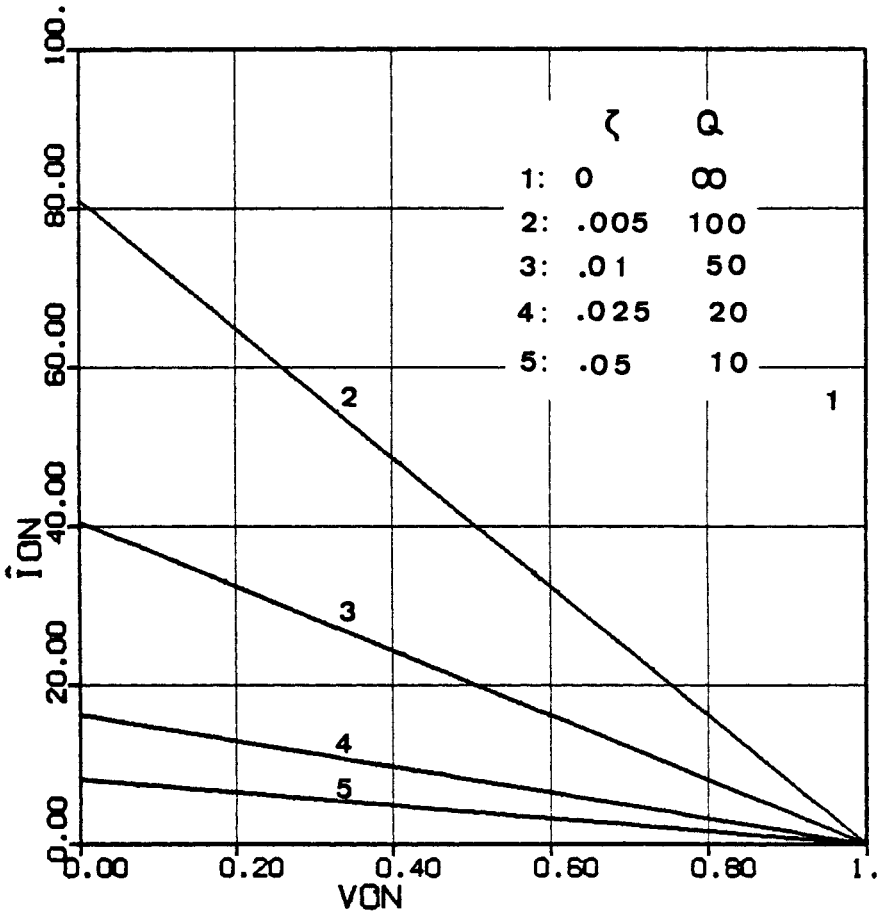

Figure 3.7. Effect of losses on maximum output current and output voltage

of the circuit damping factor ζ. This plot was generated using (3.65) and (3.51). Figure 3.8 shows that the maximum possible power transfer decreases rapidly with increasing ζ. As ζ approaches zero, however, the maximum possible power transfer approaches infinity, as may be expected.

3.4 Results Of DC Analysis

The state-plane diagrams of Fig. 3.5 have been analyzed quantitatively in Appendix B. Figure 3.9 shows the regions of converter operation below resonant frquency based on the results of Appendix B. The regions are determined by the switching frequency, output voltage and the factor "k" which depends on the damping factor as in (3.51). Figure 2.20 shows a similar figure for the lossless case. The difference between the two lies in the region of occurrence of type-1 DCM. Under the lossless case the type-1 DCM is seen to occur only as a limiting case as V_{oN} approaches unity. However, when losses are considered, type-1 DCM occurs over a range of V_{oN} values from $V_{oN} = k$ to $V_{oN} = 1$.

In the case of DCM-1 and DCM-2, closed-form equations for the dc characteristics are dervied in Appendix B. For the CCM operation, however, it was not possible to derive such closed-form equations. Appendix B presents a computer algorithm based on the state-plane analysis for obtaining the steady-state solution in this case.

Figure 3.10 shows the plots of various design parameters as function of frequency and output voltage for operation in the CCM for $\zeta = 0.025$. These plots were generated using the computer analysis program for the CCM case in Appendix B. Similar plots can be generated for other values of ζ. Figure 2.22 shows similar plots for the lossless case. Comparing Fig. 3.10 with Fig. 2.22, the following observations can be made.

Figs. 3.10(c), (d), (e) and (f) clearly show the bound on the circuit variables due to losses even as ω_N approaches unity, whereas the corresponding variables in Fig. 2.22 approach infinity. This effect is seen to be even more pronounced as V_{oN} approaches unity. The diode current I_{DAVN} as shown in Fig. 3.10(c), infact, reaches zero, when ω_N equals unity, whereas the ideal analysis predicts that it will approach in-

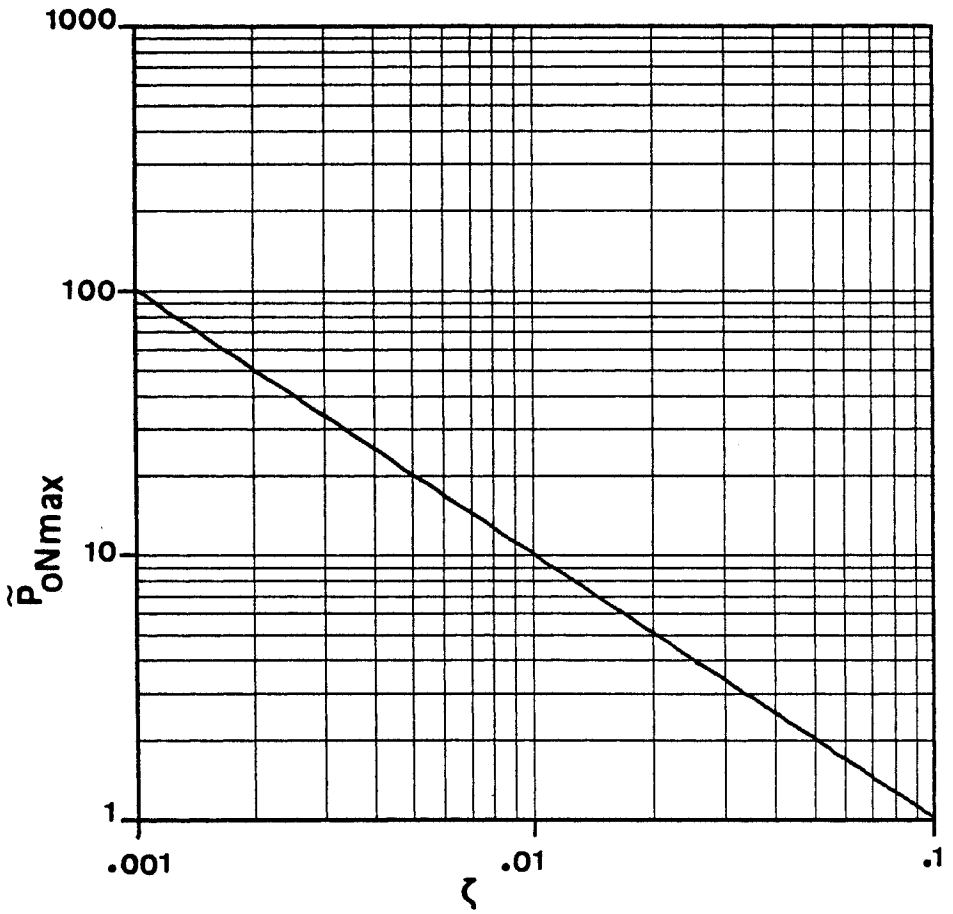

Figure 3.8. Maximum power output as function of damping factor

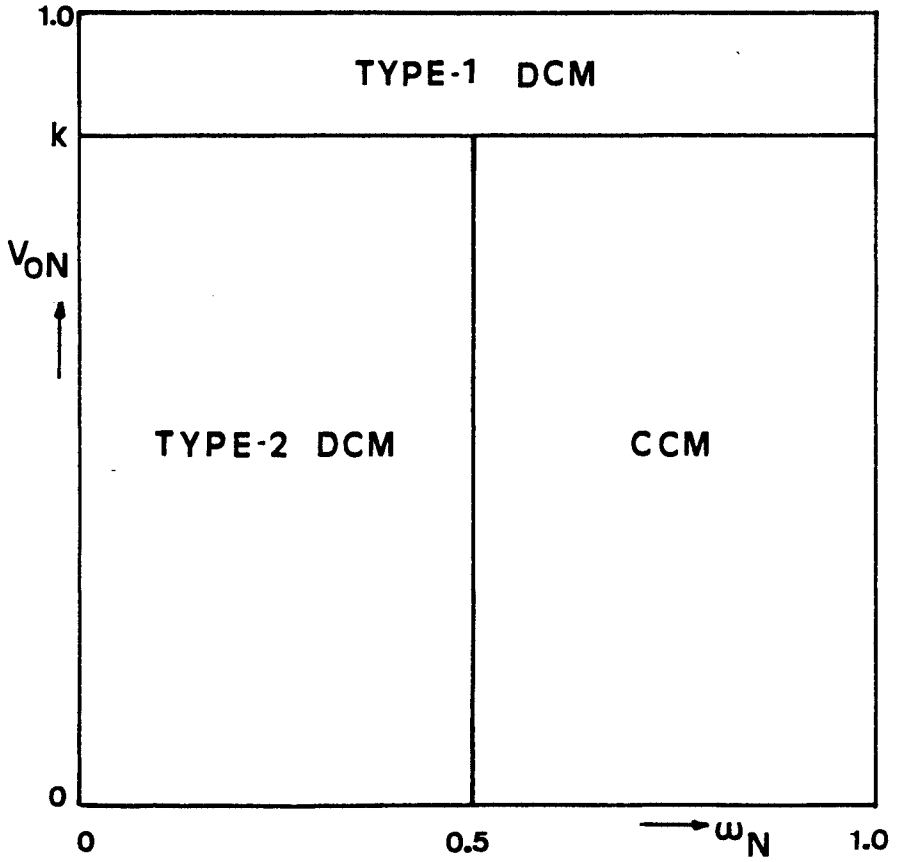

Figure 3.9. Regions of SRC operation below resonance - with loss

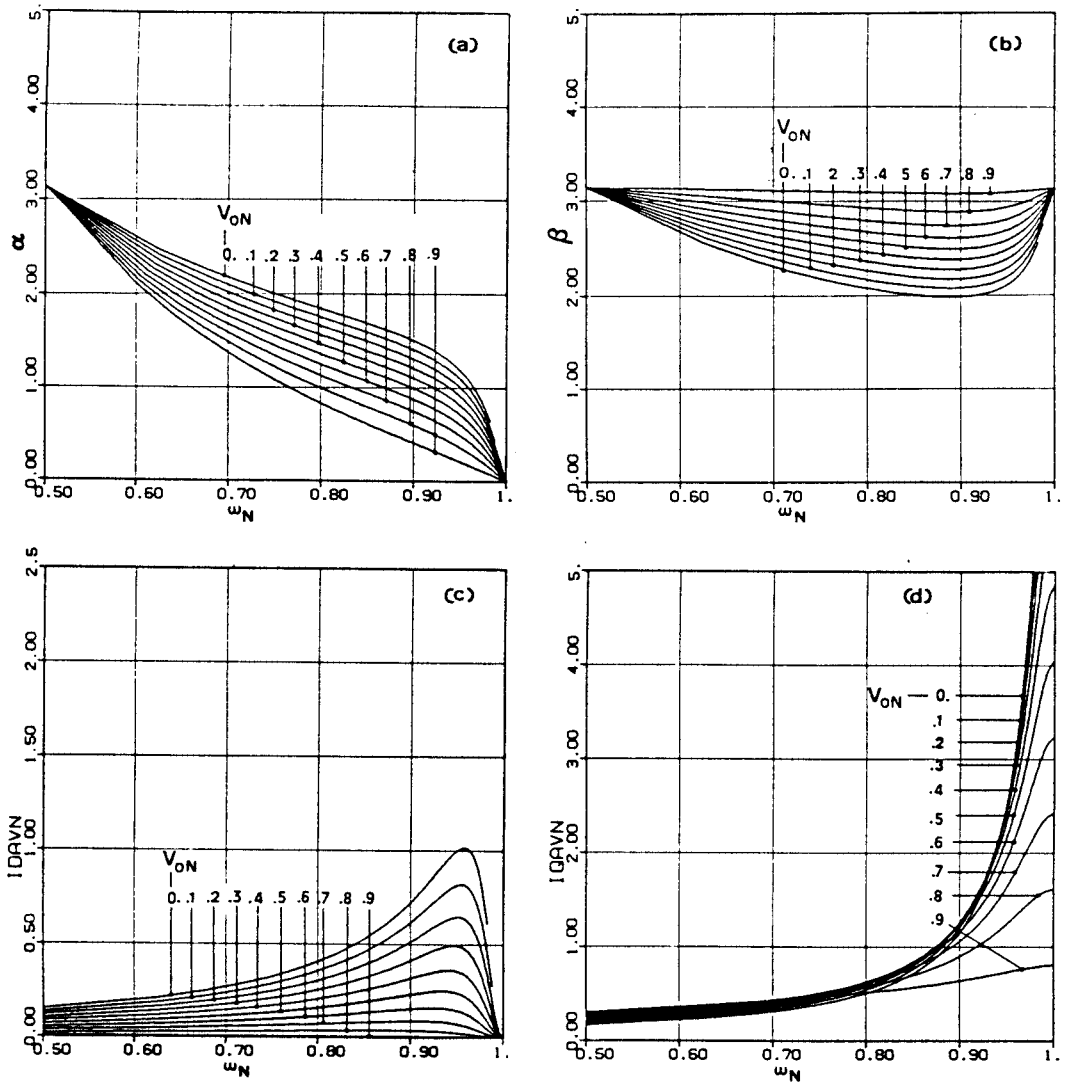

Figure 3.10. Design parameters vs normalized frequency - with loss; ζ = .025
a) Diode conduction angle
b) Transistor condcution angle
c)Normalized average diode current
d)Normalized average transistor current

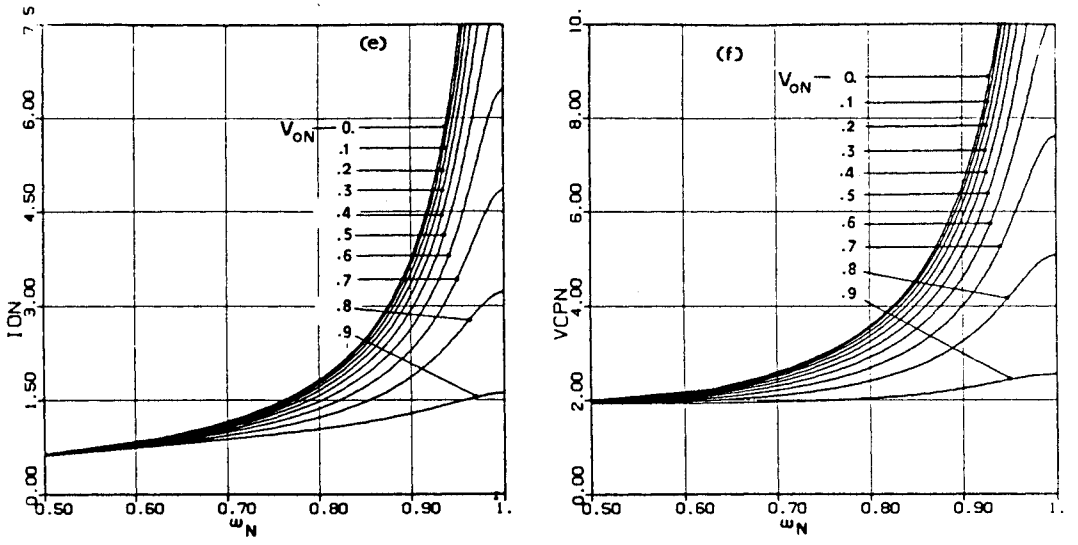

Figure 3.10 (contd.)
e) Normalized average inductor current/normalized output current
f) Normalized peak capacitor voltage

finity. Likewise the differences in the transistor and diode conduction angles can be observed from Figs. 3.10(a) and (b) and 2.22(a) and (b). For example, the ideal analysis predicts that the diode angle will approach a value of $\cos^{-1}V_{oN}$ as ω_N approaches unity (Table 2.1). However with loss, this angle approaches zero instead. These differences are significant and they point out the limitations and useful range of the loss-less analysis.

Based on the dc analysis of Appendix B, Figs. 3.11 and 3.12 show the plot of I_{oN} vs V_{oN} covering all three regions of operation with $\zeta = 0.025$ and $\zeta = 0$, respectively. Comparing these characteristics the following observations can be made.

1) The maximum output voltage, corresponding to $\omega_N = 1$, is drastically limited in Fig. 3.11; whereas in Fig. 3.12, the maximum output voltage ideally is always equal to the supply voltage, V_s. The region to the right of the curve for $\omega_N = 1.0$ in Fig. 3.11 is marked 'Inoperable Region'. It is not possible to operate the converter in this region due to the losses in the tank circuit as discussed earlier in Sec. 3.3.

2) Figure 3.11 predicts that, when V_{oN} is increased continuously, the output current, I_{oN} , will decrease sharply as the circuit enters type-1 DCM region. Eventually, the output current falls to zero as V_{oN} appoaches unity. As against this, Fig. 3.12 predicts that I_{oN} reaches a nonzero value as V_{oN} approaches unity.

3) In Fig. 3.12, at lower operating frequencies, $\omega_N < 0.7$, the output current remains essentially constant till $V_{oN} = 1$. Thus the SRC behaves like a constant dc current source at lower frequencies. The analysis with loss, however, indicates that this is no longer true at output voltages close to unity. Figure 3.11 shows that even at lower frequencies, the SRC enters type-1 DCM whenever V_{oN} is greater than k. In this region I_{oN} decreases rapidly with V_{oN} and the circuit no longer functions as a constant current source.

3.5 Experimental Results

The experimental power circuit is shown in Fig. 3.13. The drive circuits, which generate isolated gate drives for the power MOSFETs are shown in Fig. 3.14. The control circuit used was the frequency control

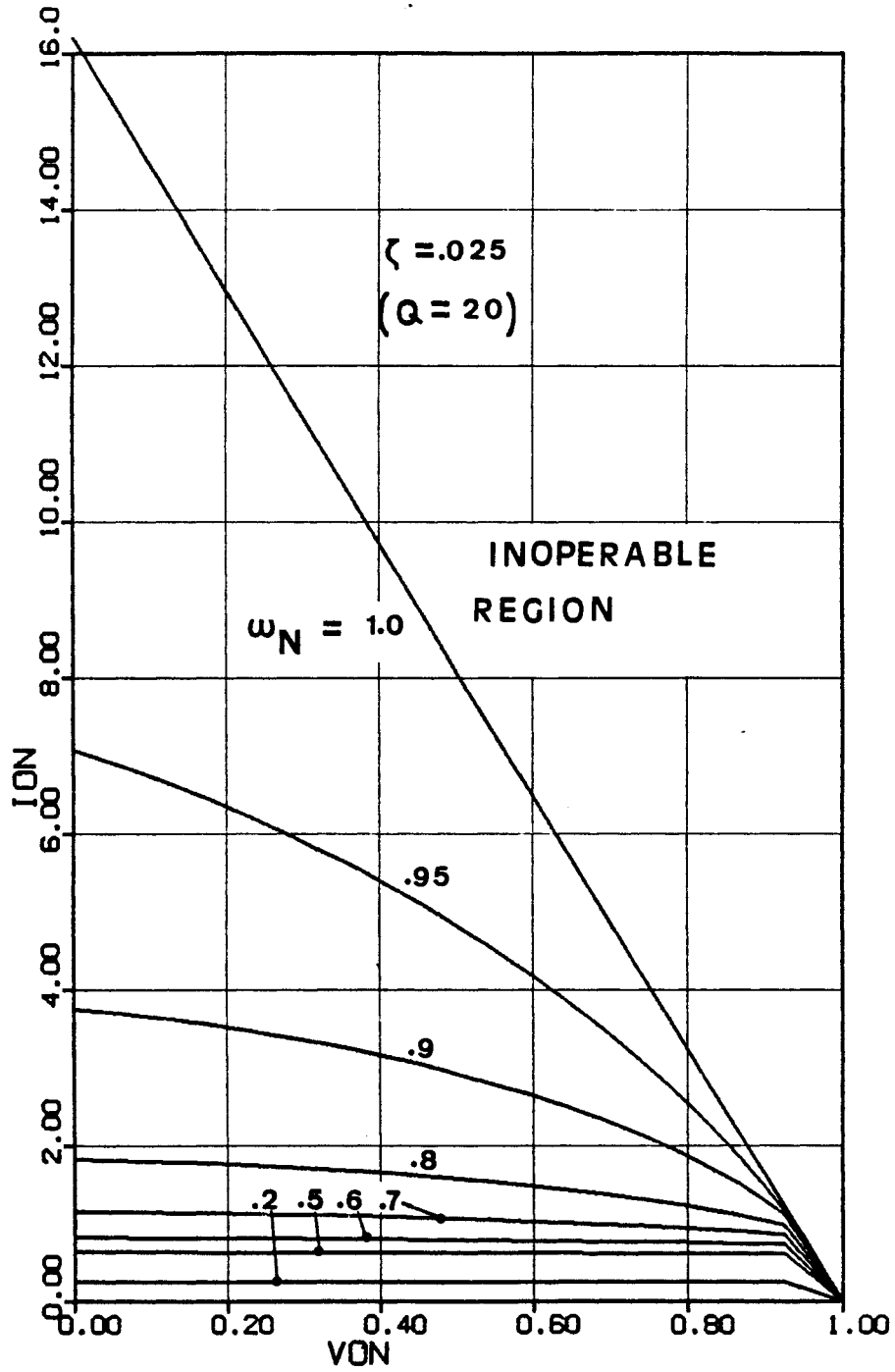

Figure 3.11. DC characteristics for $\omega_N < 1$ - with loss

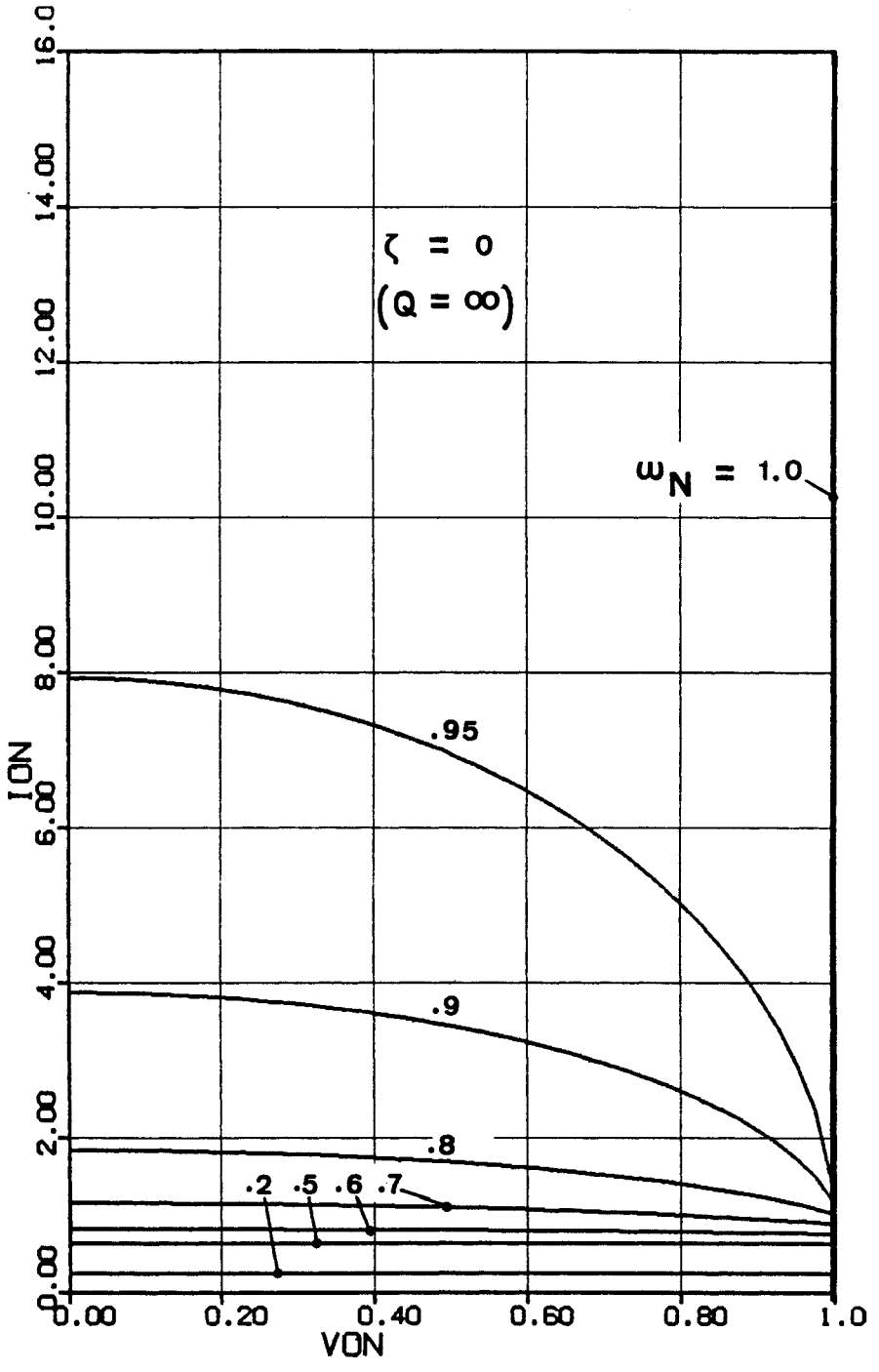

Figure 3.12. DC characteristics for $\omega_N < 1$ - without loss

circuit shown in Fig. 5.32. The base-drive strategy-2 in Fig. 5.32 is used. In this method, at low frequencies of operation, the transistor is not switched on again, once its antiparallel diode stops conducting. For a description of the operation of the control cicuit, please refer to Sec. 5.5. Diodes DQ1 and DQ2 in series with the power switches are included to block the slow, built-in antiparallel diode of the MOSFET. For this circuit, ω_D = 316,672.5 rad/sec and Z_0 = 25.904 Ω. Damped resonant frequency ω_D is established experimentally by measuring the frequency at which the largest state-plane trajectory occurs keeping the load on the converter as low as possible. The current and voltage normalizing factors for this experimental setup are 0.9651 A and 25.0 V, respectively.

In order to verify or use the analysis, it is necessary to establish a single damping constant for the tank circuit of the series resonant converter. One approach is to approximately compute the damping constant by theoretically determining the circuit losses under convenient operating conditions such as when $\omega = \omega_D$. If, however, the converter is already available, an alternative approach will be to determine the damping constant experimentally. The latter approach, described below, is followed in this work.

In this method, output dc voltage and current are measured at $\omega = \omega_D$ for a convenient value of the load resistor. By substituting for V_{oN} and I_{oN} obtained in this measurement into (3.60), the factor "k" can be determined. The factor $\sqrt{1 - \zeta^2}$ in (3.60) can be assumed to be unity in order to calculate factor "k". The damping factor ζ can then be calculated using (3.51). For the experimental circuit, the measured values of the output voltage and current are 17.3 V and 3.32 A, respectively. A voltage of 1.4 V (2 × 0.7 V) is then added to the output voltage to compensate for the output rectifier bridge. After normalizing, we get V_{oN} = 0.748 and I_{oN} = 3.4401. Substituting these in (3.60), we obtain k = .9109, which results in a ζ of .02970 (or a Q of 16.32).

Figure 3.15 shows the experimental verification of the dc characteristics. A voltage of 1.4 V was added to the output voltage in these measurements to compensate for the output bridge diode drops. Figure 3.15(a) compares the experimental data with the characteristics obtained with the lossless analysis. Figure 3.15(b) compares the same experimental data with the analysis including the loss. It is clear that the ideal analysis with loss neglected, fails to predict accurately the performance of the experimental converter, especially at operating frequencies near ω_D or at output voltages close to V_s. The simplified loss model assumed in the present analysis predicts the performance of the converter at different operating frequencies and output voltages in a reasonably accurate manner.

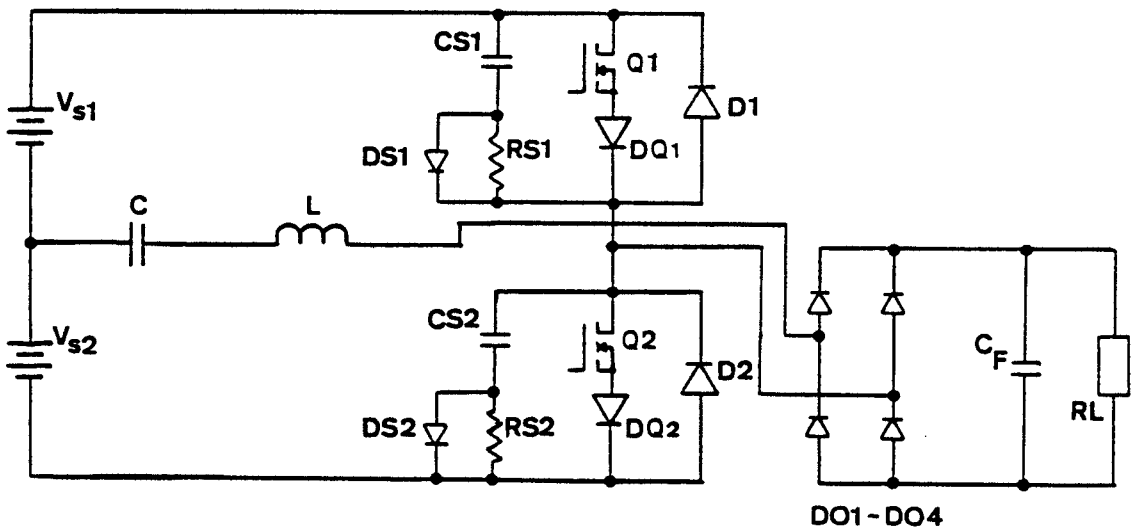

Vs1,Vs2: 25V, Q1,Q2: 2SK325, DQ1,DQ2: 20FQ045
D1,D2: 12FL60S02, DO1~DO4: 40HFL60S02
L: 81.8 μH, C: 0.125 μF, CF: 50.0 μF,
CS1,CS2: .047 μF, RS1,RS2: 18 Ω, DS1,DS2: A115E
f_0(measured) = 50.4 kHZ, Z_0 = 25.904 Ω
ζ (measured) = 0.0297

Figure 3.13. Experimental SRC circuit

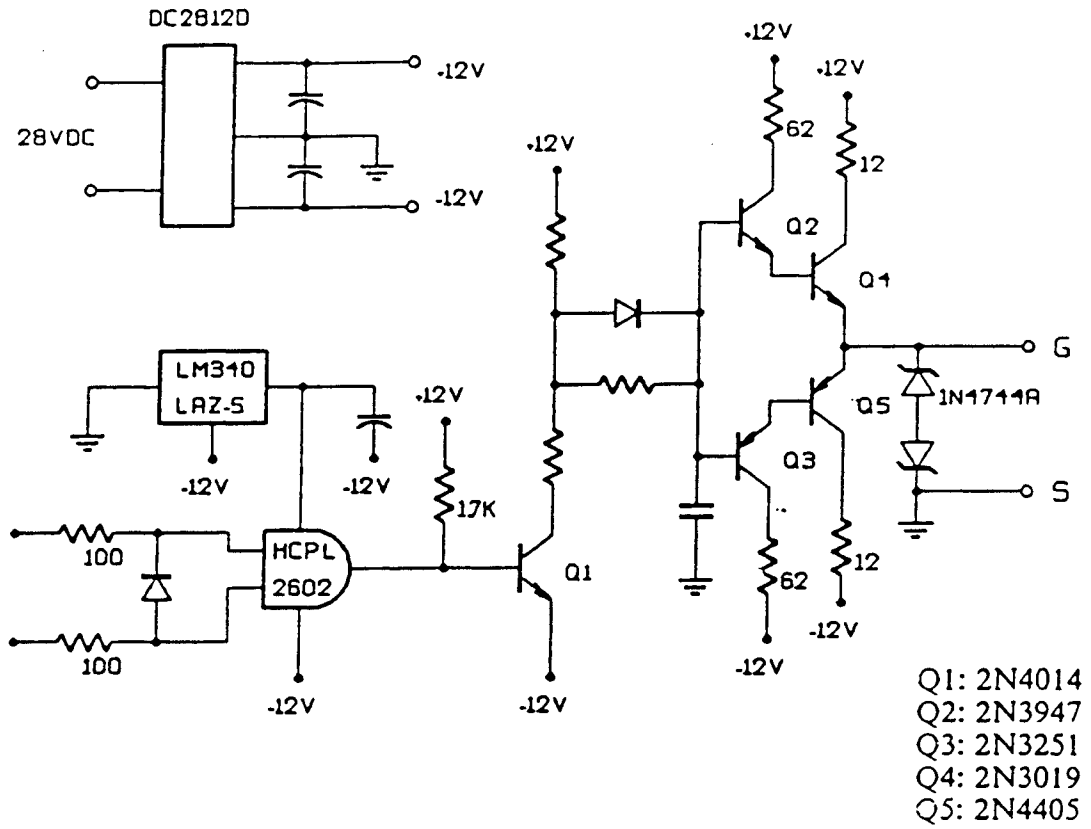

Figure 3.14. Drive circuit for the power MOSFET

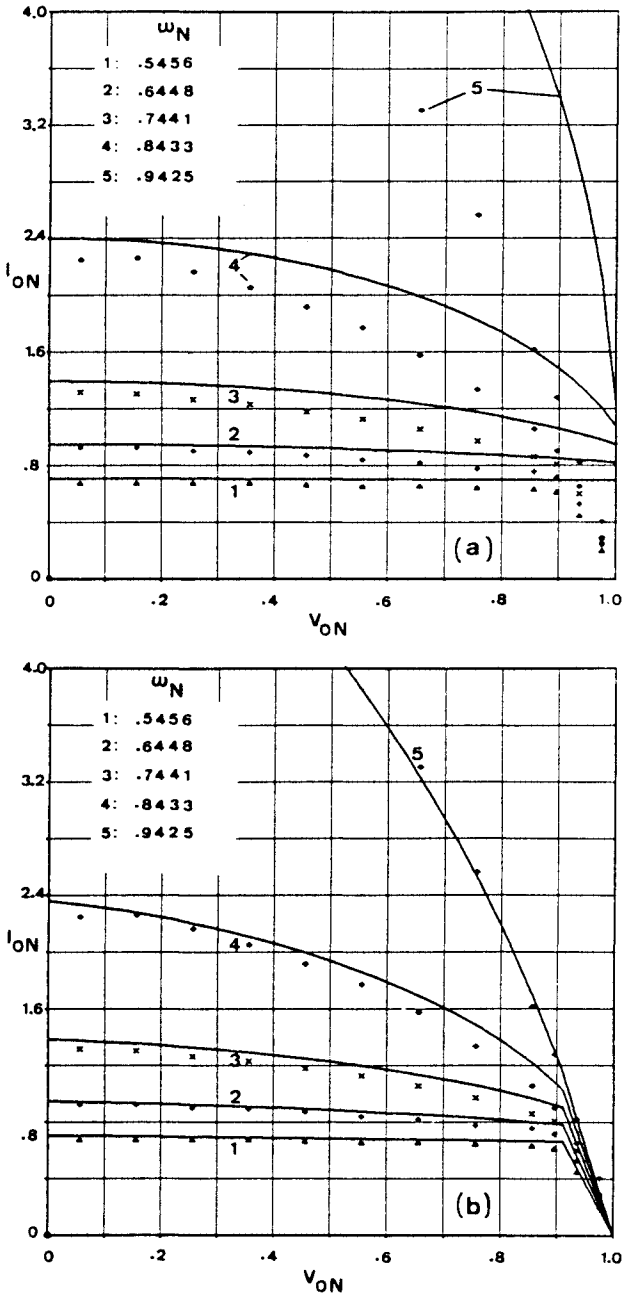

Figure 3.15. Experimental verification of analysis
Bold line: theoretical; Data points: experimental
a) Analysis with loss-less assumption b) Analysis with $\zeta = 0.0297$

Figure 3.16 shows experimental oscillograms of steady-state trajectories for the different operating modes. Fig. 3.16(a) shows a type-1 DCM trajectory as in Fig. 3.5(c). Fig. 3.16(b) shows a type-2 DCM trajectory as in Fig. 3.5(b). Fig. 3.16(c) is a CCM trajectory as in Fig. 3.5(a). Fig. 3.16(d) is a maximum size CCM trajectory corresponding to the T_{UB} trajectory of Fig. 3.6.

The experimental tank waveforms corresponding to the steady-state trajectories in Fig. 3.16 are shown in Fig. 3.17. In general, the waveforms are anticipated. However, the effect of parasitic inductances and capacitances which have been neglected in the analysis may be observed in the form of high frequency ringing on these waveforms.

3.6 Conclusions

Parasitic losses occur in resonant converters at various parts of the circuit, such as the power switch, the resonant inductor and resonant capacitor. These losses affect the steady-state performance of a resonant converter significantly as may be expected when dealing with any resonant phenomenon. However, the analyses of resonant converters published to date have neglected the losses. In this chapter, for the first time, a dc analysis of a series resonant converter including its losses was attempted for operating frequencies below resonant frequency.

The parasitic losses were modeled by a single resistor in the tank circuit. The resulting circuit damping factor was determined experimentally. Closed-form solutions for operation in the two types of discontinuous-conduction modes, type-1 DCM and type-2 DCM, were obtained using state-plane techniques. For the continuous-conduction mode (CCM) case, it is not possible to derive such closed-form solutions. The regions of occurrence of these modes have also been defined. The solution for this case was obtained numerically using a computer algorithm based on the state-plane analysis.

An upper limit on the maximum power delivered to the load is established. This limit depends on the load and decreases rapidly with an increase in the damping factor. Also, for the CCM case, useful design curves were generated, relating parameters such as output current, device currents and device con-

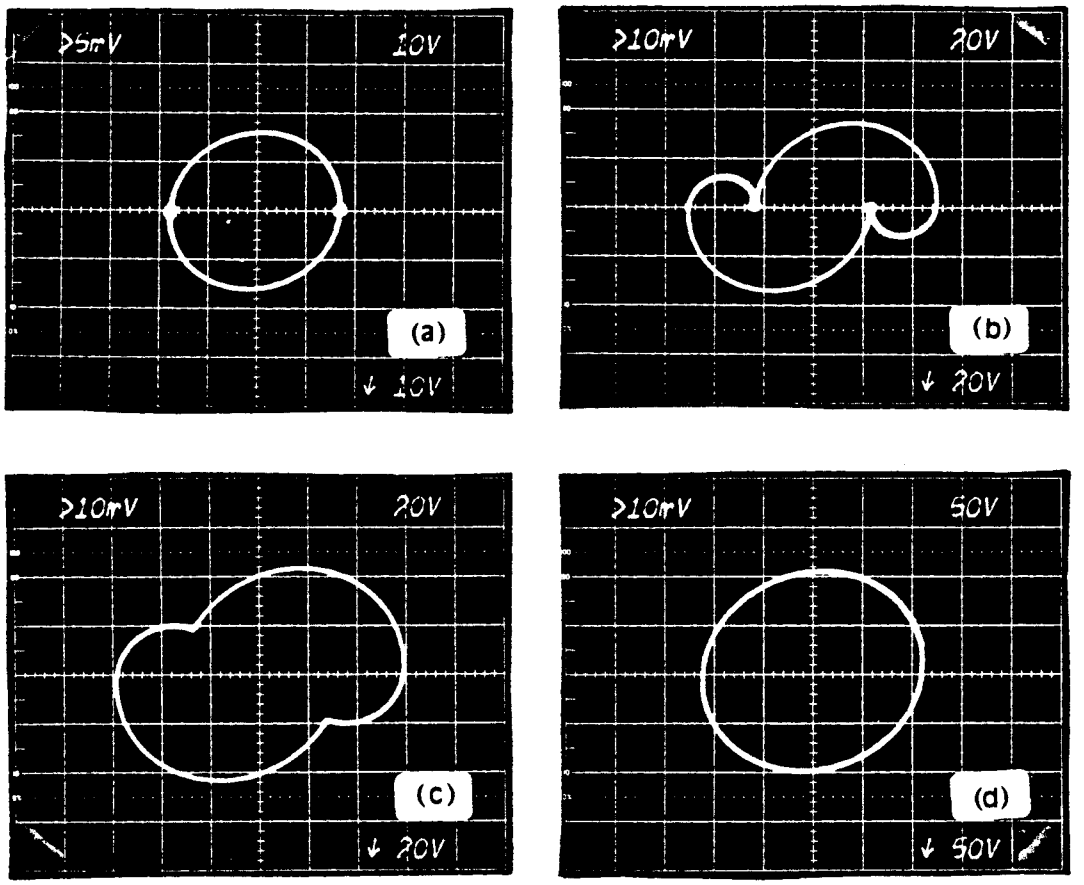

Figure 3.16. Experimental trajectories in different modes
a) Type-1 DCM (32.26 kHz, V_o = 23.4 V) c) CCM (33.62 kHz, V_o = 9.7 V)
b) Type-2 DCM (19.15 kHz, V_o = 9.7 V) d) CCM $\omega = \omega_D$(50.4kHz, V_o = 19.6 V)

To account for output bridge diode drops, a voltage of 2 x 0.7 V has been added to V_o.

Scale: a) Y - 0.387 A/div; X- 10 V/div d) Y - 1.935 A/div; X- 50 V/div
b) & c) Y - 0.774 A/div; X - 20 V/div

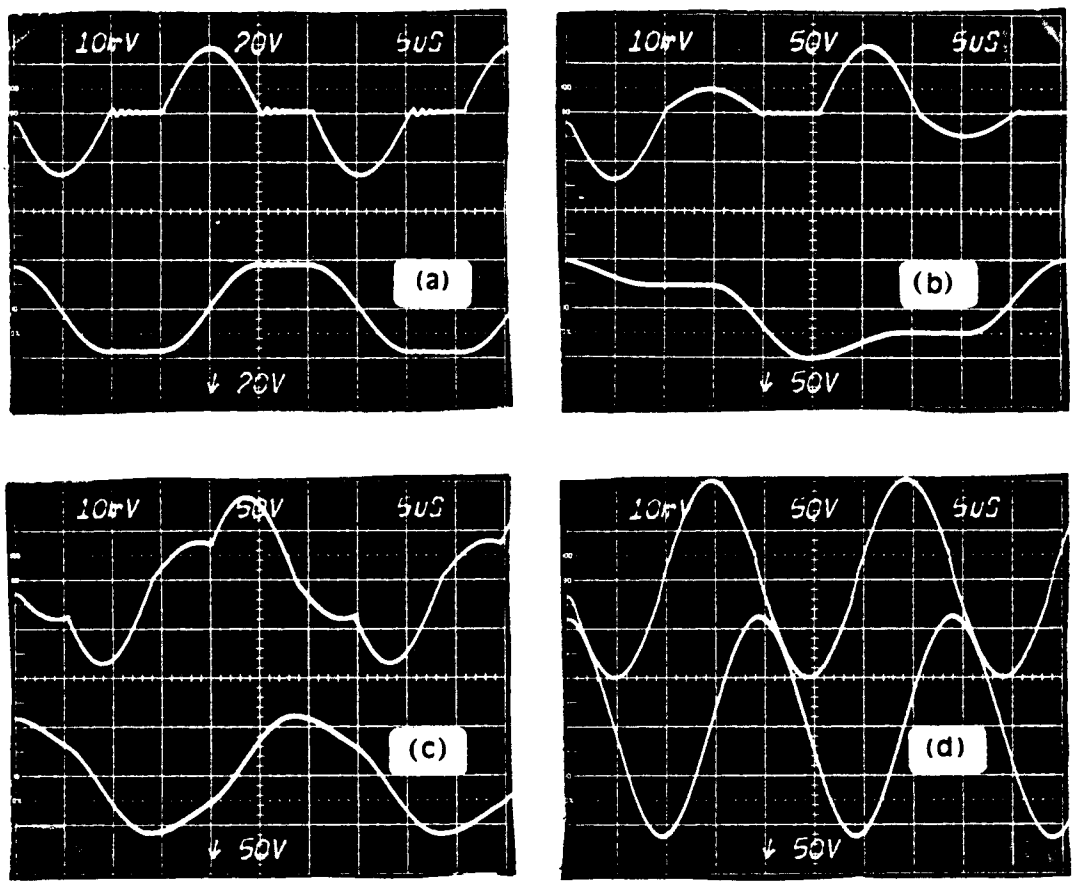

Figure 3.17. Experimental waveforms corresponding to Figure 3.16
Top trace (y1): Resonant inductor current
Bottom trace (y2): Resonant capacitor voltage

Scale: x - 5 μs/div
a) y1 - 0.5 A/div; y2 - 20 V/div
b) &c) y1 - 1 A/div; y2 - 50 V/div
d)y1 - 2 A/div; y2 - 50 V/div

duction angles with operating frequency. Differences existing between these curves and those obtained when losses were neglected were pointed out. Comparisons of the dc characteristics showed that, in general, the lossless case is not valid 1)whenever the switching frequency approaches resonant frequency or 2)whenever output voltage approaches supply voltage. Good correlation between the theoretical and experimental dc characteristics were obtained.

Chapter 4

Methods Of Control For Series Resonant Converter

4.0 Symbols Of Variables

The list of symbols in Sec. 2.0 is applicable for this chapter also. Some of the additional symbols used in this chapter are listed below.

ΔV_{CNDN}	-	Maximum Decrease in Normalized Peak Capacitor Voltage per Resonant Half-Period
ΔV_{CNUP}	-	Maximum Increase in Normalized Peak Capacitor Voltage per Resonant Half-Period
F	-	Logic Signal Dependent on i_L polarity
k, k'	-	Constants Of Proportionality
k_1, k_2, k_3, k_4	-	Scale Factors in Experimental Circuit
R_d	-	Distance of State from Transistor Mode Center
t_{dis}	-	Elapsed Time in Discontinuous Interval after Diode Conduction
t_E	-	Time Elapsed from Previous Switching Instant

V_{CONT} - Control Input Signal

v_r - Voltage at Input of Output Bridge Rectifier

4.1 Introduction

Switching converters with their large variety of circuit topologies and controls, in general, can be divided into two categories, pulse-width modulated (PWM) converters and resonant converters. In a PWM converter, the output energy-storage filter usually has a very large time constant, much larger than the switching period of the converter. The output is regulated by directly controlling the energy input to the slowly responding filter, as shown in Fig. 4.1(a). The duty-cycle control method adopted to vary the energy input is simple, straightforward and easy to implement in a feedback configuration. The dynamic properties of the converter are easily predictable and are dependent upon filter characteristics and duty-cycle control laws.

In resonant converters, on the other hand, two sets of energy storage elements are present, the output filter with slow time constants and the resonant circuit with fast time constants. The output is controlled indirectly through the control of the resonant tank energy as shown in the functional block diagram of Fig. 4.1(b). The tank possesses fast dynamics and exchanges large amounts of pulsating energy with the source and output filter in each half cycle of operation.

Due to the fast transient of the resonant tank, the control of resonant converters is considerably more complex than that of their PWM counterparts. The dynamics of the resonant converters, as will be illustrated in this chapter, often appears to be unpredictable, with an irregular sequence of conduction accompanied by large power surges in the tank circuit and excessive voltage and current stresses on the components. The lack of a method for understanding the control and for assessing various control properties is the primary obstacle that has impeded widespread use of resonant converters in power processing applications.

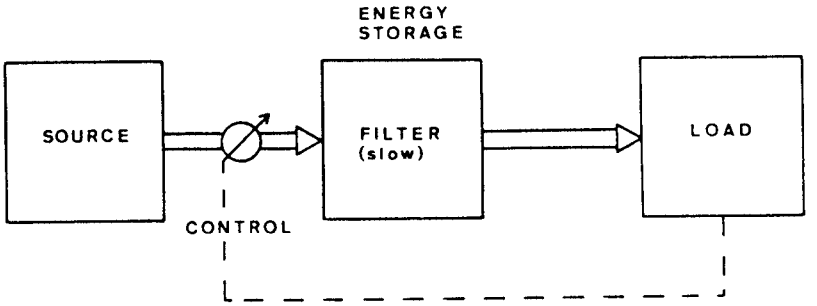

(a)

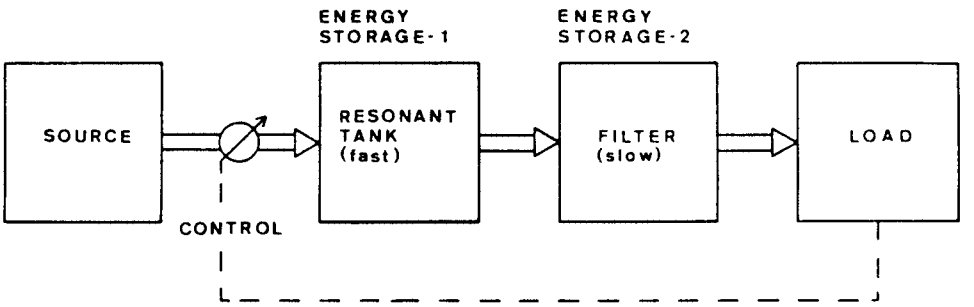

(b)

Figure 4.1. Functional Block Diagrams
a) Switching regulator b) Resonant converter

In Chapter 2 of this report, state-plane techniques were employed to characterize the steady state and transient behavior of a series resonant converter (SRC). The state portrait directly indicates the resonant tank energy level at which the system is operating. Hence, it provides a means to assess the effectiveness of a control in keeping the tank energy levels within bounds.

Graphical state-plane techniques have been used previously to analyze the control behavior of switching regulators [41,42,43]. In this chapter, the control properties of SRCs when operated below resonant frequency are analyzed with the use of the state plane. A number of new and existing control methods are identified and their relative performance evaluated. A promising new control technique, named "optimal trajectory control", is proposed based on the insight from the analysis. By utilizing the desired trajectory itself as the control law, this method attempts to achieve the lowest possible response times. In addition, since the control predetermines the trajectory of operation, the energy of the resonant tank, as measured by the trajectory size, is always kept within bounds unlike other methods of control. Experimental oscillograms comparing the performance of optimal trajectory control with the conventional frequency control are also provided.

4.2 Existing Methods Of Control

Some methods of control which have been applied to resonant converters are the following:

1. Analog-signal-to-discrete-interval converter (ASDTIC) control or average-current control [9]

2. Frequency control [27]

3. Capacitor-voltage control [6]

4. Diode-conduction-angle control [24]

Among these, methods 1 and 4 have been utilized to control SRCs, method 3 to control PRCs and method 2 to control both SRCs and PRCs. The operation of these four control techniques are explained

in the following subsections. Symbols $Q1$, $D1$, $Q2$ and $D2$ refer to the devices in the SRC circuit in Fig. 2.1. Variable i_L is the resonant inductor current, v_C is the resonant capacitor voltage and V_{CONT} is the control signal input. Furthermore, ω refers to the operating frequency, ω_0 ($= 1/\sqrt{LC}$) to the resonant frequency and ω_N to the normalized operating frequency given by ω/ω_0. For details of the circuit waveforms and a description of operation please refer to Chapter 2.

4.2.1 ASDTIC Control

Figure 4.2(a) shows the control waveforms applicable to ASDTIC control. In this control, the rectified inductor current $|i_L|$ is compared with control signal $k\,V_{CONT}$, where k is a proportionality constant. The error between the two is integrated to produce signal V'. The drive signals are generated at the zero-crossing instants of signal V' to turn on transistors $Q1$ and $Q2$ alternately.

Therefore, at time t_2 (Fig. 4.2(a)),

$$V' = 0 = \int_0^{t_2} (|i_L| - k\,V_{CONT})\,dt \tag{4.1}$$

For a constant value of control input,

$$k\,V_{CONT} = \frac{1}{t_2}\int_0^{t_2} |i_L|\,dt \tag{4.2}$$

According to (4.2), the average inductor current between instants 0 and t_2 is made equal to kV_{CONT}. Thus, ASDTIC control switches on the subsequent transistor when the average current from the previous switching instant equals the set value.

4.2.1.1. Simulation Of SRC With ASDTIC Control

ASDTIC control, originally proposed for the control of SRCs, attempts to maintain the average tank current in each half cycle of converter operation, so tank energy levels will be kept within bounds and the component stresses limited. As part of the present work, a SRC with ASDTIC control was simulated

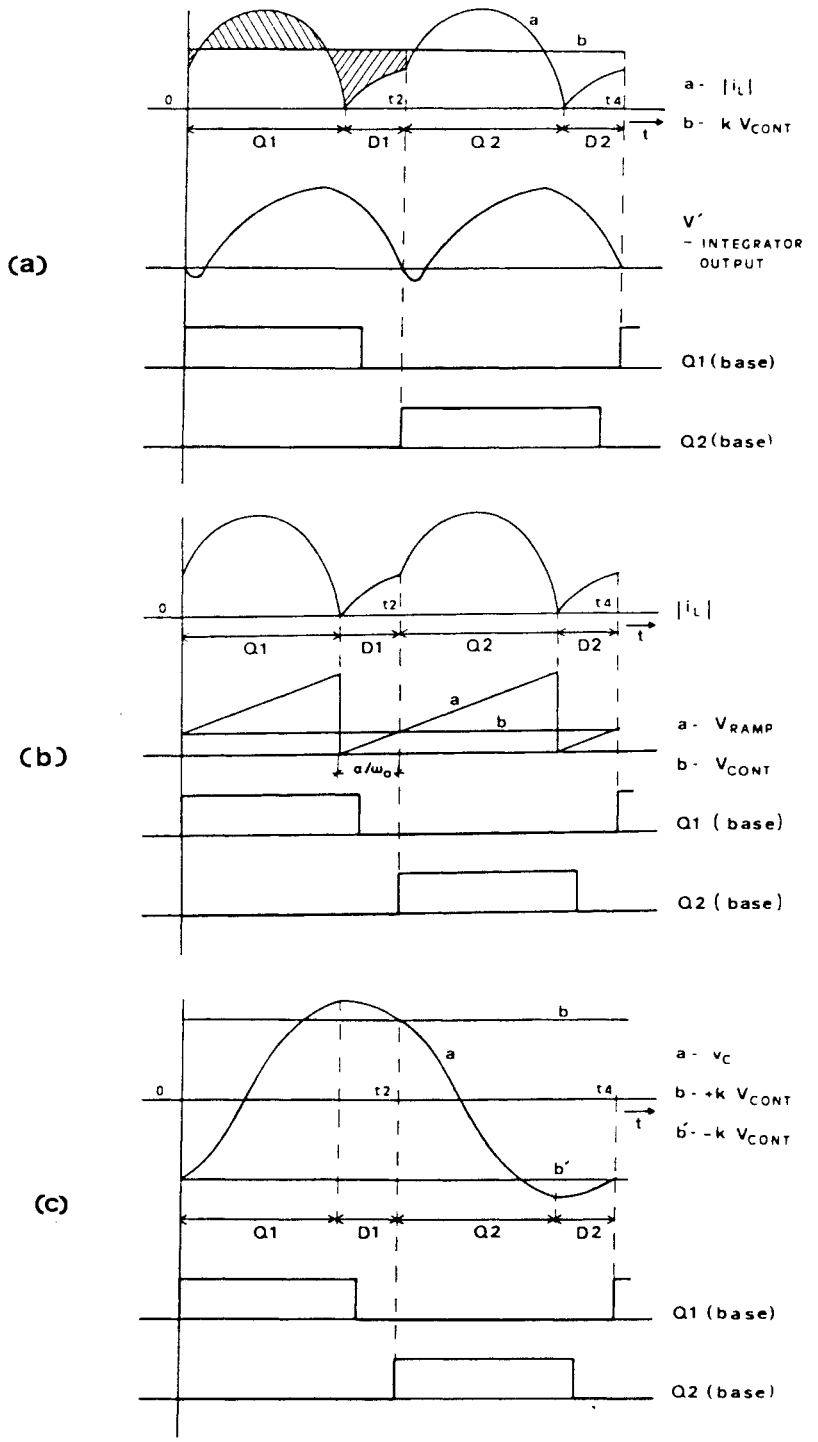

Figure 4.2. Control waveforms for SRC control
a) ASDTIC control b) Capacitor-voltage control c) Diode-conduction-angle control

using SPICE2 [48]. A listing of the simulation program is given in Appendix E. Two of the simulation results are presented below, and they illustrate the complexity of SRC operation.

A simulation result under a start-up condition is shown in Fig. 4.3(a). Although the average output current over a few cycles is maintained at the control value of 30 A, peak transient currents far in excess of this value occur causing instantaneous tank energy levels much greater than necessary. Furthermore, the simulation shows an irregular sequence of conduction Q1, Q2, *D*2, *D*1, discontinuous interval, Q1, Q2 and so on instead of the normal Q1, D1, Q2 and D2 sequence.

The second example, as shown in Fig. 4.3(b), concerns the operation of the SRC with ASDTIC control under steady-state conditions. The system is well behaved for the first few cycles and the waveforms are repetitive in nature. The circuit then slips into asymmetrical operation with high peak currents and large instantaneous tank energy levels. Such asymmetrical behavior can pose serious a problem by overstressing the circuit components.

4.2.2 Frequency Control

In this method of control, transistors Q1 and Q2 are driven alternately at a frequency determined by the control. Usually the relationship between control signal V_{CONT} and operating frequency ω is linear. In the continuous-conduction mode (CCM) of operation, the transistors are turned on alternately for a half-cycle duration each. In the type-2 discontinuous-conduction mode (DCM-2), which occurs when ω_N is less than 0.5, the duration for which the transistor is turned on is limited to a value less than a half-cycle duration. This is done in order to prevent the same transistor from turning on once more, after its antiparallel diode has already conducted. In this chapter, DCM refers to DCM-2 operation only.

4.2.3 Capacitor-Voltage Control

Figure 4.2(b) shows the control waveforms applicable to this method of control. Once antiparallel diode *D*1 (or *D*2) begins to conduct, the magnitude of resonant capacitor voltage v_C starts to fall. When v_C

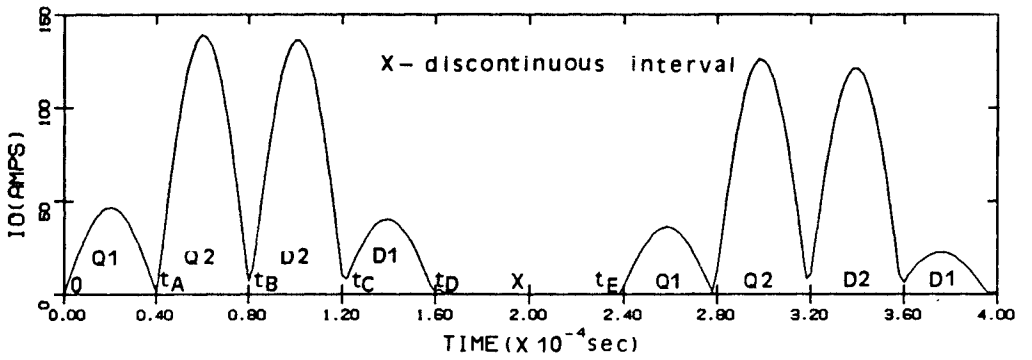

(a)

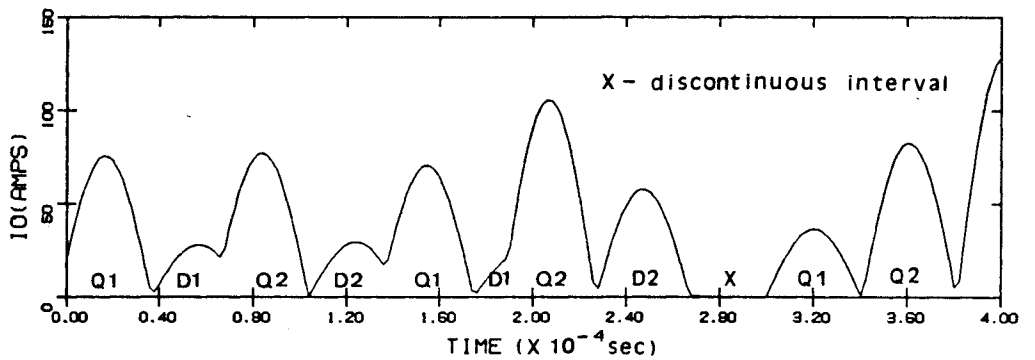

(b)

Figure 4.3. Simulation of SRC with ASDTIC control
a) Start-up (current ref = 30A) b) Near steady state (V_o = 150 V, current ref = 37.5 A)

reaches the magnitude set by control kV_{CONT} , device $Q2$ (or $Q1$) is switched on. Thus, this method controls the SRC by switching on the transistors at a set magnitude of the resonant capacitor voltage as determined by the control input.

4.2.4 Diode-Conduction-Angle Control

The control waveforms corresponding to this method are shown in Fig. 4.2(c). V_{RAMP} is a control waveform that monitors the time elapsed from the instant antiparallel diode $D1$ (or $D2$) starts to conduct. When this duration reaches the value set by control V_{CONT} , the drive to $Q2$ (or $Q1$) is generated. Thus, diode-conduction-angle control controls the SRC by switching on the transistors at a set magnitude of the diode-conduction-interval as determined by the control input.

4.3 State-Plane Analysis

In this section, the control of resonant converters is viewed on the two-dimensional state plane. By ignoring the large time constant of the output filter and considering only the dynamic effects of the tank, our attention is focused on the critical aspects of the control problem.

A steady-state trajectory under CCM is shown in Fig. 4.4. Having switched on transistor $Q2$ at instant t_A, the control determines instant t_B (and conduction angle α of diode $D2$) at which device $Q1$ must be switched on. This is carried out by a "control law" which is a function of the state of the system, elapsed time t_E from the previous instant t_A, and control input V_{CONT}. For transistor $Q1$, this control law can be stated generally as

$$g\ (i_L,\ v_C,\ t_E\ ,\ V_{CONT}) \geq 0 \qquad (4.3)$$

Provided $Q1$ is forward biased, transistor $Q1$ is switched on whenever inequality (4.3) is satisfied.

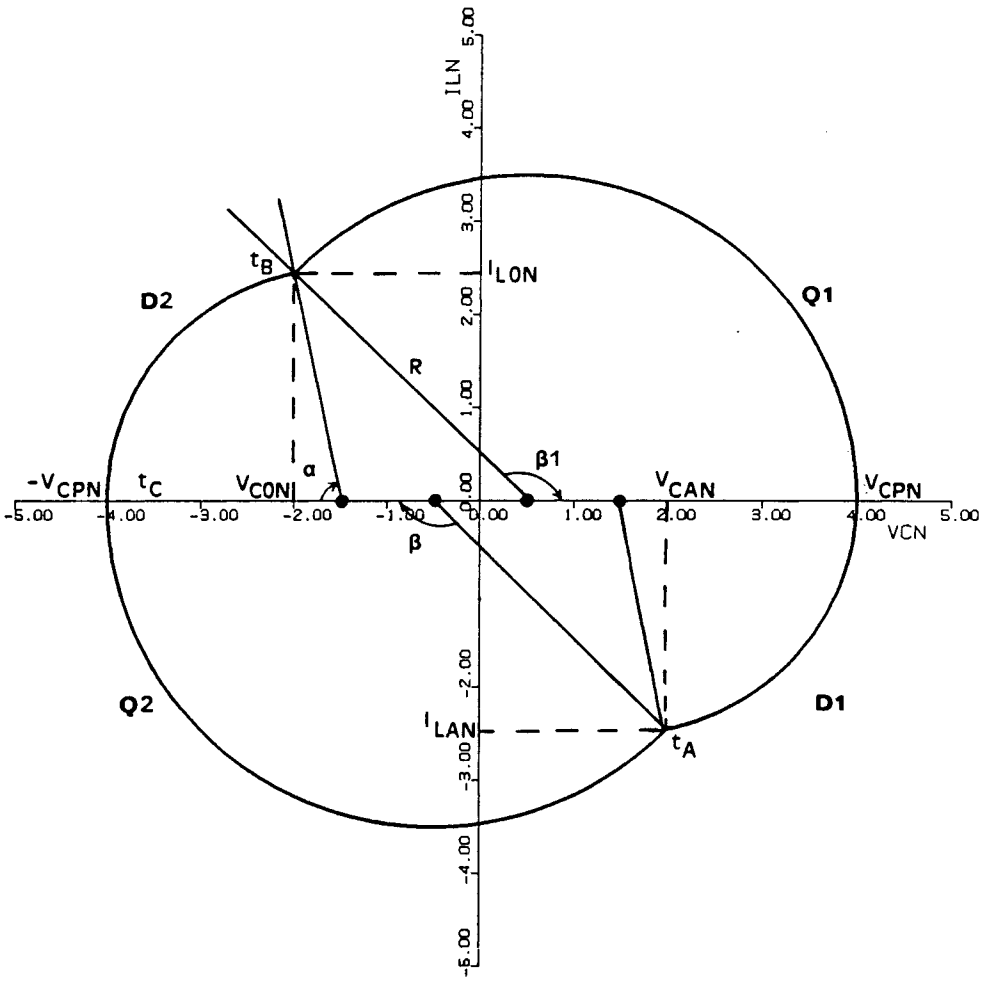

Figure 4.4. SRC steady-state trajectory under CCM V_{oN} = 0.5

The control law for Q2 is

$$g\ (-i_L,\ -v_C,\ t_E\ ,\ V_{CONT}) \geq 0\ , \tag{4.4}$$

where t_E is now the elapsed time from t_B, the previous Q1 turn-on instant. Usually, control variable V_{CONT} appears explicitly in the control law, so that inequality (4.3) for transistor Q1 can be written either as

$$V_{CONT} - f\,(i_L,\ v_C,\ t_E) \geq 0 \tag{4.5a}$$

or as

$$V_{CONT} - f\,(i_L,\ v_C,\ t_E) \leq 0 \tag{4.5b}$$

The control law for Q2 can be obtained by substituting $-i_L$ and $-v_C$ in place of i_L and v_C, respectively, in (4.5). At the instant of switching, the equality part of the control law must be satisfied. Thus, at switching instant t_B, for transistor Q1

$$V_{CONT} = f\ (i_L,\ v_C,\ t_E) \tag{4.6}$$

Figure 4.5(a) shows a simplified block diagram of a SRC with a control, which is applicable to all the control methods. In general, signal V_{CONT} is generated by an outer control loop, such as the current control loop shown in Fig. 4.5(b). In Fig. 4.5(a), the feedback element and the comparator implement the control law. When feedback signal $f\,(i_L,\ v_C,\ t_E)$ or $f\,(-i_L,\ -v_C,\ t_E)$ becomes equal to control input V_{CONT}, the control law is satisfied and corresponding transistor Q1 or Q2 is switched on. Note that, in Fig. 4.5(a), the output variable that directly responds to the control input has been considered to be the output dc current, I_o, and not the output dc voltage. This is because the behavior of the SRC is predominantly that of a current source, as pointed out in Chapter 2.

The many steady-state trajectories shown in Fig. 2.12 are the limit cycles of the nonlinear system of Fig. 4.5(a). Each of these limit cycles corresponds to a particular tank energy level, output current (or power) and switching frequency. The control law must enable the system to operate in a stable manner on a unique limit cycle for a paritcular V_{CONT} signal. By varying V_{CONT}, the system must be able to settle on any of the steady-state trajectories shown in Fig. 2.12.

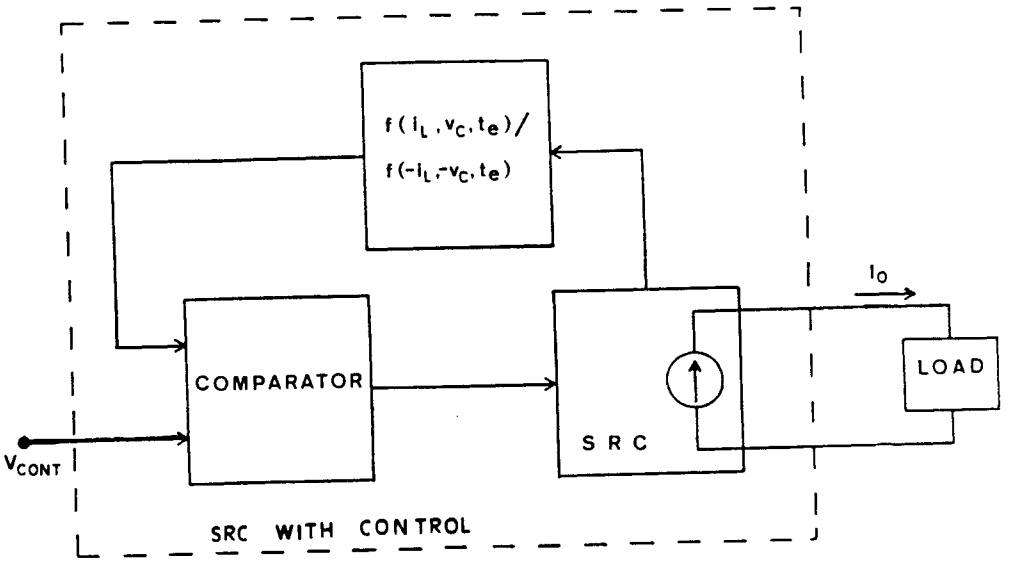

(a)

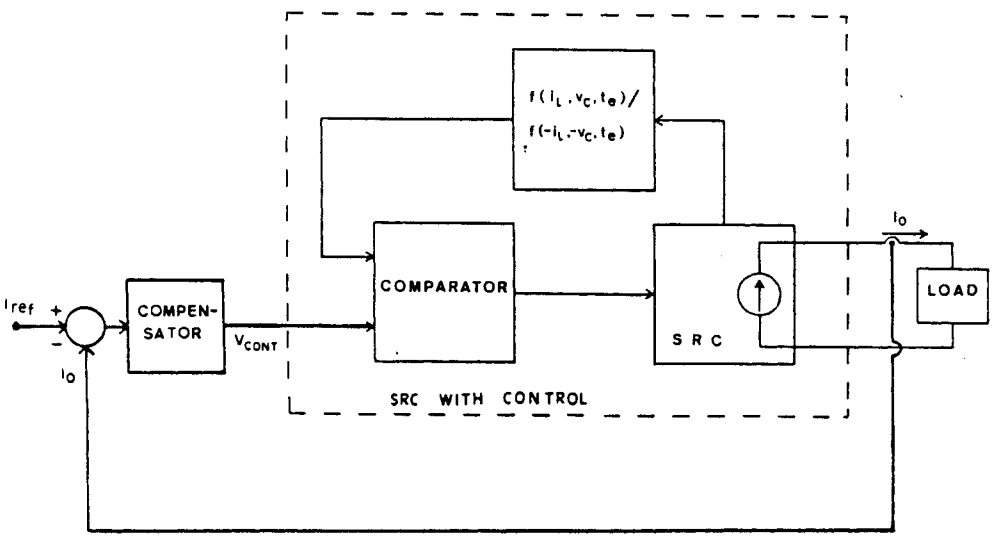

(b)

Figure 4.5. Control of SRC - Block diagrams
a) Inner control-loop b) Closed loop current regulation

If t_E does not appear in the control law, then the contol law is considered time invariant. The switching instants are then dependent on state-plane parameters i_L and v_C and control input V_{CONT} alone. This enables the control law to be depicted on the state plane, making the analysis simple and the behavior of the system easily predictable.

However, as can be observed from the trajectory marked DCM-2 in Fig. 2.11, i_L and v_C at the transistor switching points remain the same for all the steady-state trajectories under DCM. The trajectories are distinguished only by the different durations of their discontinuous intervals. A time-invariant control law, which does not monitor elapsed time t_E in some fashion, cannot distinguish between these different switching instants and, hence, cannot, in general, handle discontinuous currents.

4.3.1 Control Methods

A list of control methods along with their control laws are given below. The list is by no means complete. However, since the objective of this chapter is to present the basic approach to resonant converter control and to introduce optimal trajectory control, other possible control laws are not included. The control laws are given for transistor Q1 only. To obtain the control law for transistor Q2, replace i_L and v_C with $-i_L$ and $-v_C$, respectively. In the control law inequalities, factors k and k' are constants of proportionality.

4.3.1.1 Capacitor-Voltage Control

The control law can be defined as

$$V_{CONT} - \left(\frac{-v_C}{k}\right) \geq 0 \tag{4.7}$$

Normalizing with voltage normalizing factor V_s, the control law of (4.7) can be written as

$$k'V_{CONT} + v_{CN} \geq 0 \tag{4.8}$$

Fig. 4.6(a) marks the area on the state plane covered by the capacitor-voltage control law. The vertical line at $v_{CN} = -k'V_{CONT}$ (or at $v_{CN} = k'V_{CONT}$ for Q2) represents the control law as described by (4.8). Under transient conditions, however, there can be situations when the Q2 or D1 trajectory reaches the vertical axis to the right of the $v_{CN} = -k'V_{CONT}$ line for Q1 operation. In this case, the control law inequality of (4.8) has already been satisfied by the time Q1 is forward biased for conduction. Hence, the Q1 transistor will be switched on as soon as the trajectory reaches the horizontal axis. Thus the section on the v_{CN} axis between $-k'V_{CONT}$ and the Q1 transistor trajectory center $(1 - V_{oN})$ has also been included in the control law for Q1. The section on the v_{CN} axis between $k'V_{CONT}$ and the Q2 center $-(1 - V_{oN})$ has been included in the control law for Q2 transistor for similar reasons.

4.3.1.2 Frequency Control

The control law can be defined as

$$V_{CONT} - \frac{1}{k\,(2t_E)} \geq 0 \tag{4.9}$$

The control as indicated by (4.9) is time variant and so can not be marked explicitly on the state plane. Nomalizing the time interval, (4.9) can be rewritten as

$$V_{CONT} - \frac{1}{k'\,(2\omega_0 t_E)} \geq 0 \tag{4.10}$$

For CCM operation, the angular elapsed interval $\omega_0 t_E$ is defined on the state plane as per the folowing.

$$\omega_0\, t_E = \alpha + \beta\,, \tag{4.11}$$

where β is the transistor conduction angle.

A variation of the frequency control method is the elapsed-time control method with the following control law.

$$kV_{CONT} - 2\,t_E \leq 0 \tag{4.12}$$

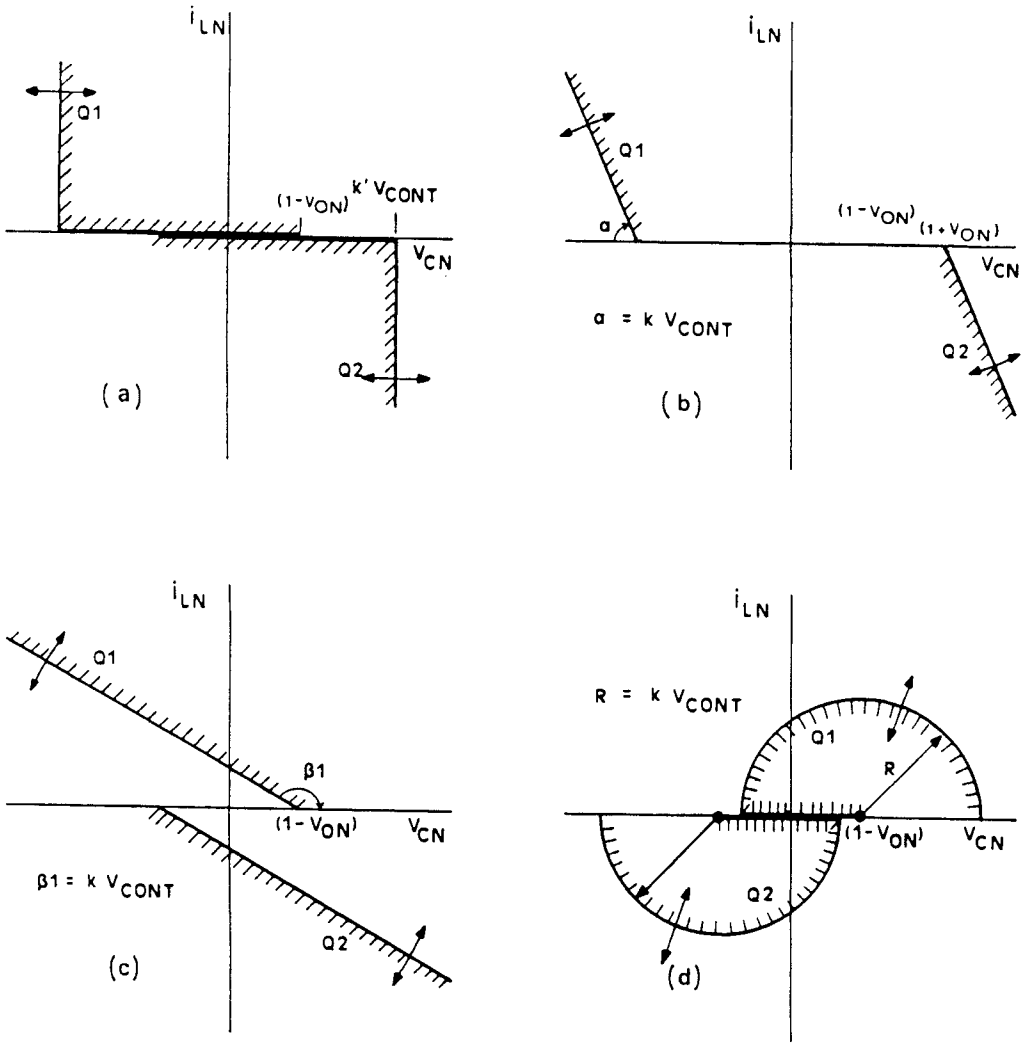

Figure 4.6. Control laws on state plane
a) Capacitor-voltage control
b) Diode-conduction angle control
c) Transistor-conduction-angle control
d) Optimal trajectory control

In this control method, Q1 is switched on when elapsed time t_E reaches a value set by the control. The state-plane analysis yields similar results for these two types of control.

4.3.1.3 ASDTIC Control

From (4.1), the control law is

$$kV_{CONT} - \frac{1}{t_E}\int_0^{t_E} |i_L|\, dt \geq 0 \tag{4.13}$$

Again elapsed time t_E is a parameter of the control law and the control law cannot be shown explicitly on the state plane. The integral can be found in terms of the state-plane parameters as follows.

Since $\int i_L\, dt = C\,\Delta v_C$,

$$\frac{1}{t_E}\int_0^{t_E} |i_L|\, dt = \frac{C}{t_E}\left[(V_{CP} + V_{CA}) + (-v_C + V_{CP})\right], \tag{4.14}$$

where V_{CP} is the peak capacitor voltage and V_{CA} is the capacitor voltage at instant t_A in Fig. 4.4. Normalizing (4.14),

$$\frac{1}{t_E}\int_0^{t_E} |i_L|\, dt = \frac{1}{\omega_0 t_E}\left[2V_{CPN} + V_{CAN} - v_{CN}\right]\frac{V_s}{Z_0}, \tag{4.15}$$

where the subscript N refers to the normalized parameters and $Z_0 = \sqrt{L/C}$ is the characteristic impedance.

Combining (4.13) and (4.15), the ASDTIC control law can be rewritten as

$$k'V_{CONT} - \frac{1}{\omega_0 t_E}\left[2V_{CPN} + V_{CAN} - v_{CN}\right] \geq 0 \tag{4.16}$$

For CCM, $\omega_0 t_E$ equals $(\alpha + \beta)$ on the state plane. Based on (4.16), the action of ASDTIC control law, both under CCM and DCM, can be followed on the state plane using parameters measured on the state plane itself.

4.3.1.4 Diode-Conduction-Angle Control

This control behaves as a time-invariant control under CCM and as a time-variant control under DCM. The control law for Q1 is

$$kV_{CONT} - t_d \leq 0 , \tag{4.17}$$

where t_d is the diode conduction interval, or strictly, the time elapsed after $Q2$ stopped conducting. Normalizing the time interval,

$$k'V_{CONT} - \omega_0 t_d \leq 0 \tag{4.18}$$

Under CCM, $\omega_0 t_d$ equals α, the diode conduction angle. Although α is obtained by the measurement of time, $k'V_{CONT} - \alpha = 0$ is a straight line on the state plane intersecting the v_{CN} axis at $\{ -(1 + V_{oN}), 0\}$. This is the reason this control method acts as a time-invariant control in CCM.

Under DCM, diode $D2$ conducts for a conduction angle of π and then ceases to conduct. Thus,

$$\omega_0 t_d = \pi + \omega_0 t_{dis}, \tag{4.19}$$

where t_{dis} is the elapsed-time in the discontinuous interval after $D2$ stops conducting. The control then behaves somewhat like the elapsed time control mentioned under frequency control (Sec. 4.3.1.2). The control law under the DCM cannot be marked on the state plane.

Figure 4.6(b) marks the area on the state plane covered by this control law under CCM. Under transient conditions, trajectory $Q2$ or $D1$ can reach the v_{CN} axis to the right of the diode center $\{ -(1 + V_{oN}) , 0\}$. As explained in Chapter 2, under these conditions, diode $D2$ is reverse biased and, hence, cannot conduct. The SRC then operates in the discontinuous interval and, hence, the control law under these conditions cannot be marked on the state plane.

4.3.1.5 Transistor-Conduction-Angle Control

The control law for this method is graphically shown in Fig. 4.6(c). This control law results in an unstable system as shown in Sec. 4.4. It is included to show that not all control methods considered on the state plane result in stable systems. The control law is given by

$$k'V_{CONT} - \beta_1 \geq 0 \tag{4.20}$$

Variable β_1, as shown in Fig. 4.4, refers to the predicted conduction period of device Q1 and, therefore, cannot be measured as time. Angle β_1 must be computed at every instant as the system moves along trajectory $D2$ from the measured values of i_L, v_C, V_o and V_s . The details of this computation are to be known for an actual implementation of this control method. However, as will be shown in Sec. 4.4, this control method results in an unstable system and, hence, these details are omitted here.

4.3.1.6 Optimal Trajectory Control

This new method of control utilizes the desired transistor trajectory itself as the control law. The parameter characterizing a particular transistor trajectory on the state plane is its radius R. Thus, in this control method, as diode $D2$ conducts under CCM, distance R_d of the state of the system from the center of trajectory $Q1$ located at $\{(1 - V_{oN}), 0\}$ is monitored. When this distance equals the desired radius value, as set by the control input, transistor $Q1$ is switched on. A similar procedure is followed to switch on transistor $Q2$.

Figure 4.6(d) shows the control law marked on the state plane and it is given by

$$kV_{CONT} - R_d \geq 0, \qquad \text{where} \tag{4.21}$$

$$\begin{aligned} R_d &= \text{Distance of the state from } Q1 \text{ center} \\ &= \sqrt{(1 - V_{oN} - v_{CN})^2 + i_{LN}^2} \end{aligned} \tag{4.22}$$

In Fig. 4.6(d), for $Q1$ conduction, the horizontal line segment on the v_{CN} axis between $\{(1 - V_{oN} - R)\ ,\ 0\}$ and $\{(1 - V_{oN})\ ,\ 0\}$ has also been included in the control law. The reasoning be-

hind this is similar to that given in Sec. 4.3.1.1 for capacitor-voltage control. If trajectory of $Q2$ or $D1$ reaches the v_{CN} axis within this line segment, the control law inequality (4.21) has been already satisfied and, hence, $Q1$ will be immediately switched on.

4.3.2 DC Gain Characteristics

Methods mentioned in Secs. 4.3.1.1, 4.3.1.2, 4.3.1.4 and 4.3.1.6 are identified as those usable in Sec. 4.4, wherein their relative performances are discussed. For these methods, dc gain curves relating normalized output current and normalized control input for various output voltages are shown in Figs. 4.7(a)-(d). These plots were generated based on the dc analysis of Appendix A.

The dc characteristics are useful in determining the control range for a required output dc current range. Another important consideration is whether, by limiting the control input to a maximum value, the output current will be limited for load voltage variations. However, the current limit thus obtained will still be sensitive to input supply-voltage fluctuations. Such a feature of the control method is of importance in determining the need for an additional overcurrent protection scheme. A study of Figs. 4.7(a)-(d) reveals that by limiting the control input an approximate current limiting action is obtained in the case of optimal trajectory control and to a lesser extent in the case of frequency control.

4.3.3 Limits On Dynamic Performance Of Resonant Converters

Maximum limits exist on the rates at which the tank energy of a resonant converter can increase or decrease. We shall examine these by considering the maximum rate at which the peak capacitor voltage can increase of decrease in a SRC.

The maximum energy build up occurs if no diode conduction takes place and transistor $Q1$ ($Q2$) is switched on immediately following the commutation of $Q2$ ($Q1$) with each transistor conducting for 180 degrees (Fig. 4.8(a)).

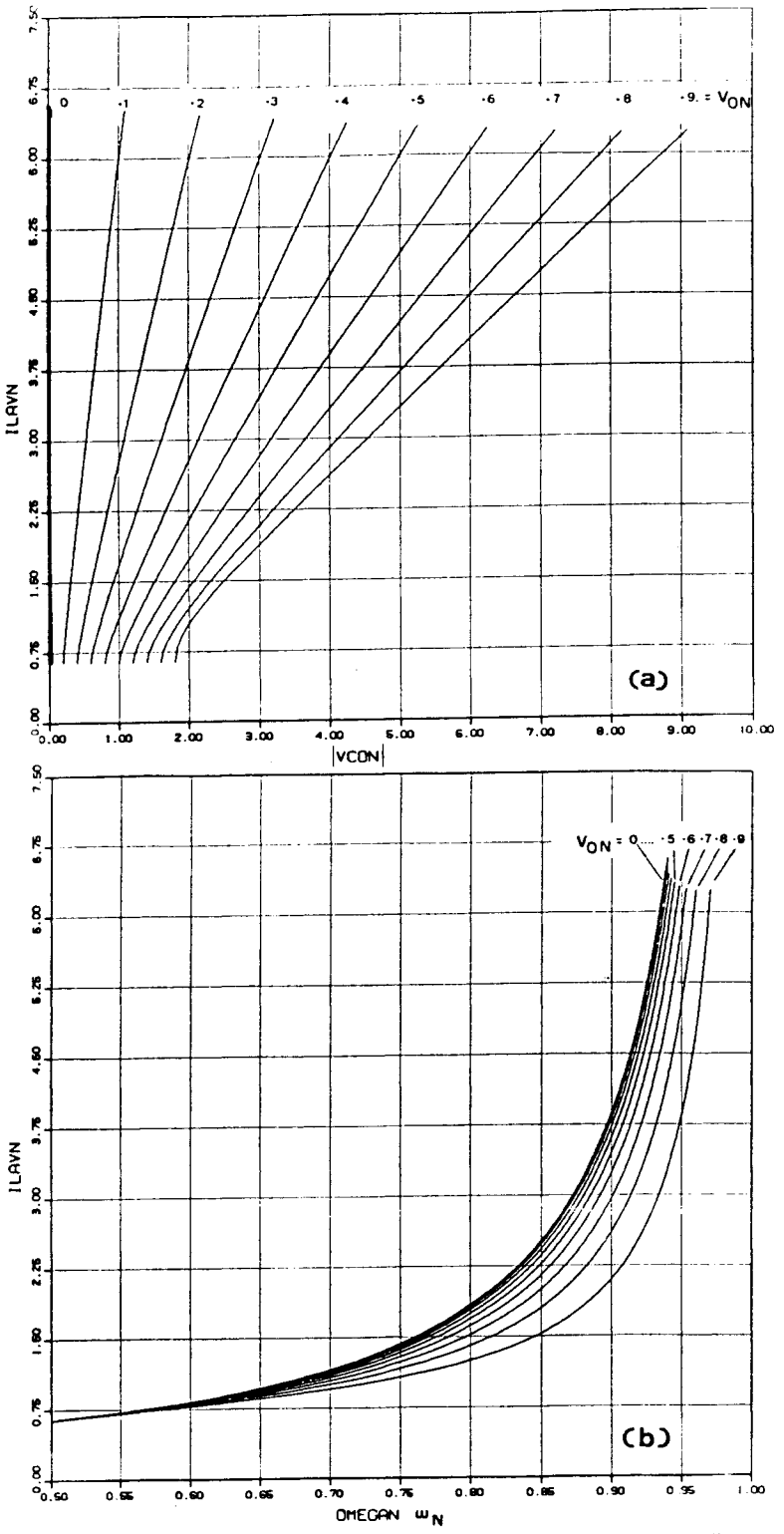

Figure 4.7. DC gain characteristics - Normalized output current versus normalized control input
a) Capacitor-voltage control b) Frequency control

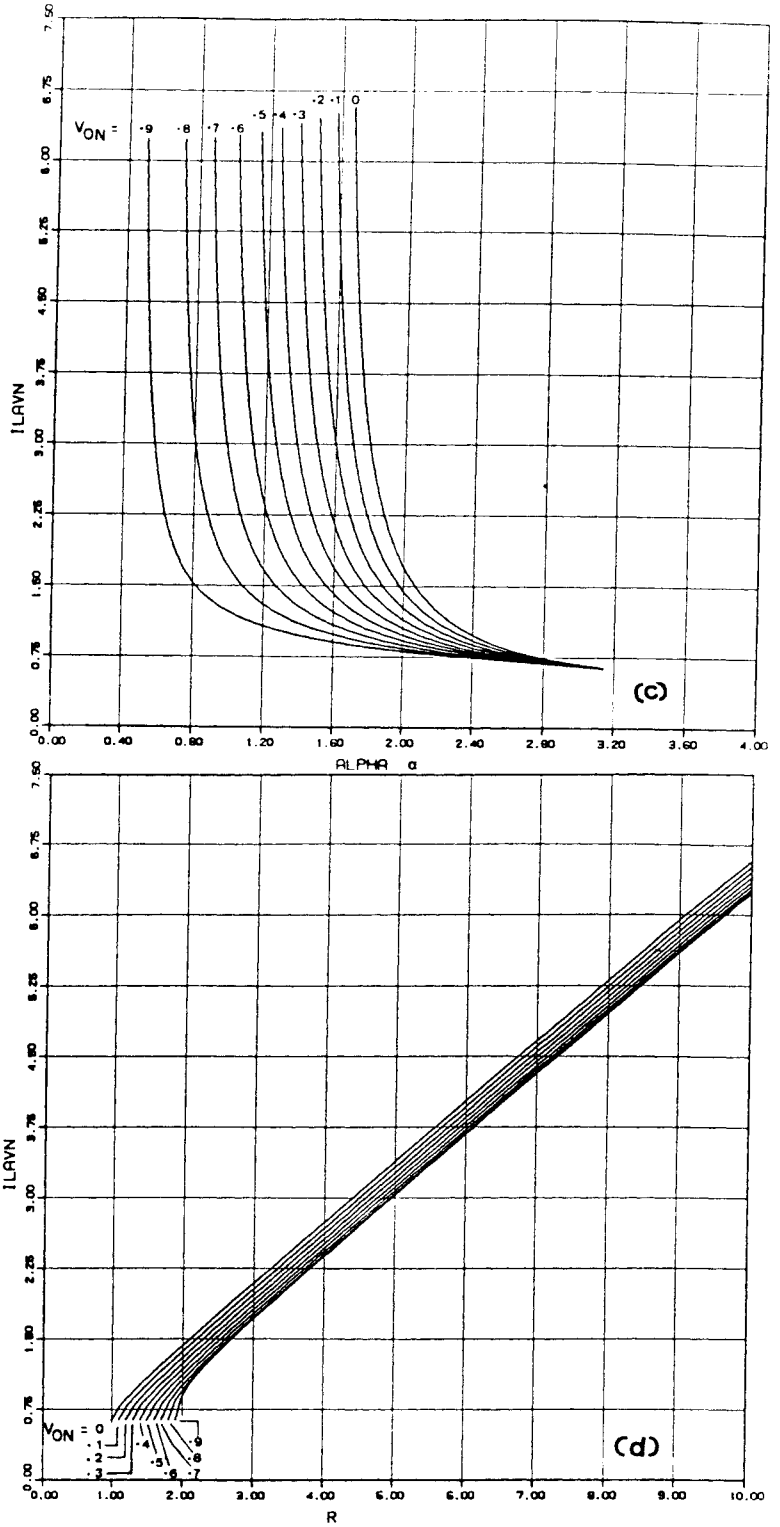

Figure 4.7. (contd.)
c) Diode-conduction-angle control d) Optimal trajectory control

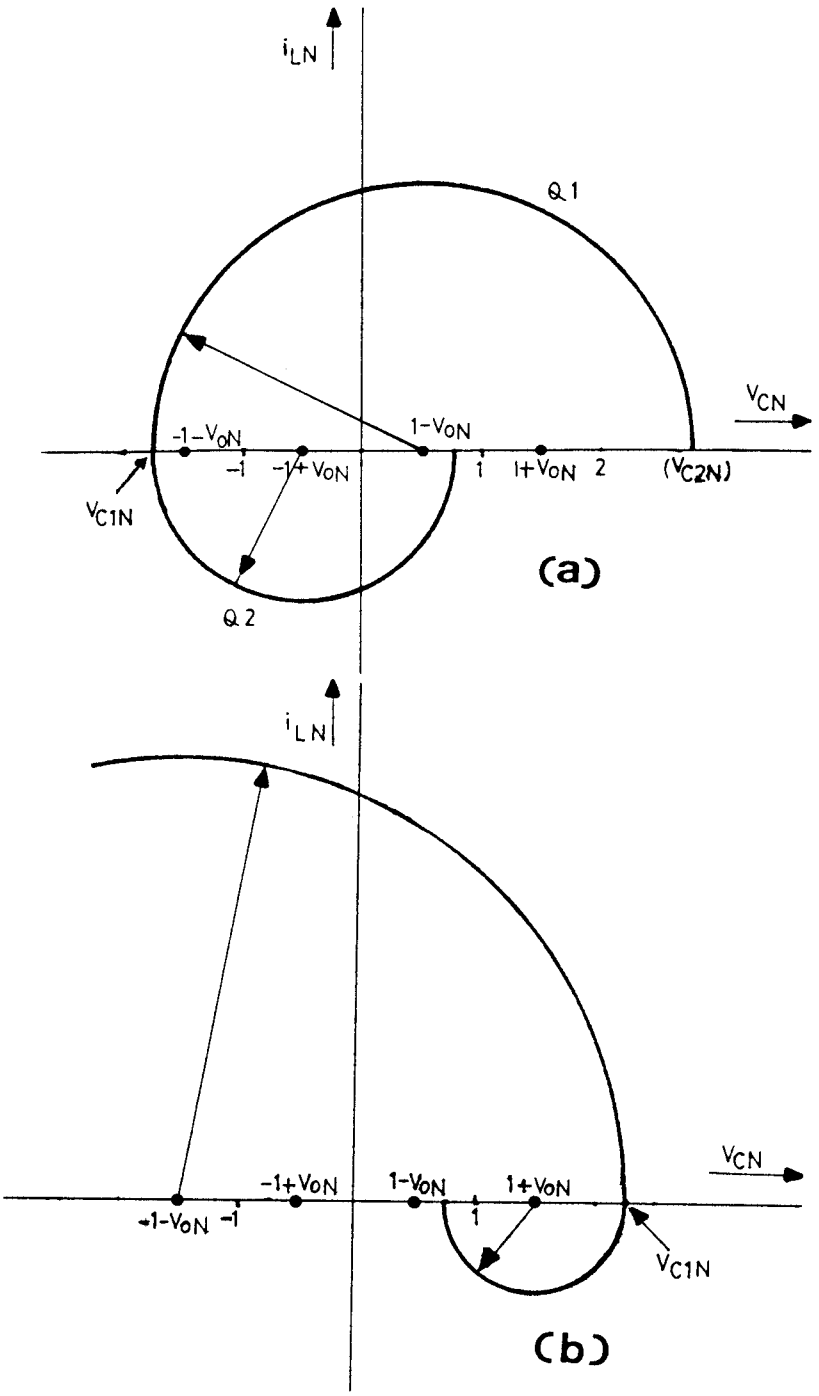

Figure 4.8. Limits on dynamic performance of SRC
a) Maximum energy increase b) Maximum energy decrease

Let the normalized peak capacitor voltage at the start of $Q1$ conduction be V_{C1N}. From Fig. 4.8(a), normalized peak capacitor voltage V_{C2N} , at the end of a resonant half period, is

$$V_{C2N} = V_{C1N} + 2(1 - V_{oN}) \tag{4.23}$$

So, maximum increase in the normalized peak capacitor voltage, ΔV_{CNUP} , per resonant half period, is limited and is given by

$$\Delta V_{CNUP} = V_{C2N} - V_{C1N} = 2(1 - V_{oN}) \tag{4.24}$$

The value of ΔV_{CNUP} tends to zero as V_{oN} approaches unity. Thus, at high output voltages, the maximum rate at which the tank energy can be increased is reduced.

Likewise, the maximum tank energy reduction in a half cycle occurs if the antiparallel diodes conduct successively without the transistors being switched on (Fig. 4.8(b)). Let V_{C1N} now be the normalized peak capacitor voltage at the start of $D1$ conduction. From Fig. 4.8(b), the normalized peak capacitor voltage at the end of a resonant half period is

$$V_{C2N} = V_{C1N} - 2(1 + V_{oN}) \tag{4.25}$$

So, the maximum decrease in normalized peak capacitor voltage ΔV_{CNDN} per resonant half period is limited and is given by

$$\Delta V_{CNDN} = V_{C1N} - V_{C2N} = 2(1 + V_{oN}) \tag{4.26}$$

The value of ΔV_{CNDN} never approaches zero and the tank energy can always be decreased at a fast rate. When V_{oN} equals unity, the tank capacitor voltage can be reduced twice as fast as compared to the case when V_{oN} equals zero.

These are inherent limitations imposed by the structure of the state portrait of the SRC and no method of control can change the tank energy faster than those dictated by (4.24) and (4.26).

4.4 Performance Of Control Methods

Based on the control law, the trajectory followed by a SRC under a control method can be generated on the state portrait. In the case of a time-invariant control such as capacitor-voltage control or optimal trajectory control, the control law itself can be marked on the state plane. Hence, the transistor switching point is determined directly on the state plane by locating the point where the trajectory intersects the control law. In the case of a time-variant control law, such as frequency control or ASDTIC control, the transistor's switching point data is first obtained from calculations based on the control law and the switching point is then located on the state plane.

The trajectories in this section were generated using a computer program (Appendix A) to calculate and plot the state trajectories with different methods of control. A partial computer flowchart applicable to all control methods, including both time-variant and time-invariant, is shown in Fig. 4.9. Assuming the state variables at one particular switching point are known, the flowchart shows how the state variables at the following switching point is computed using the control law. An explanation of the flowchart is given below.

Let $Q1$ switching point data $I_{LON}(n-1)$ and $V_{CON}(n-1)$ be known. The following equations are then obtained from simple geometrical considerations based on Fig. 4.4.

$$\begin{aligned} R(n-1) &= \text{Radius of the } Q1 \text{ trajectory} \\ &= \sqrt{\{1 - V_{oN} - V_{CON}(n-1)\}^2 + I_{LON}^2(n-1)} \end{aligned} \tag{4.27}$$

$$\begin{aligned} \beta(n-1) &= \text{Conduction angle of } Q1 \\ &= \pi - \cos^{-1}\frac{1 - V_{oN} - V_{CON}(n-1)}{R(n-1)} \end{aligned} \tag{4.28}$$

$$\begin{aligned} V_{CPN}(n-1) &= \text{Peak capacitor voltage at the end of } Q1 \text{ conduction} \\ &= 1 - V_{oN} + R(n-1) \end{aligned} \tag{4.29}$$

At the end of $Q1$ conduction the state variables are given by $\{V_{CPN}(n-1), 0\}$. Then, setting the angle $\omega_0 t_d$ to zero, the program checks whether the control inequality has been already satisfied. If it has, the new switching point state variables for transistor $Q2$ are given by

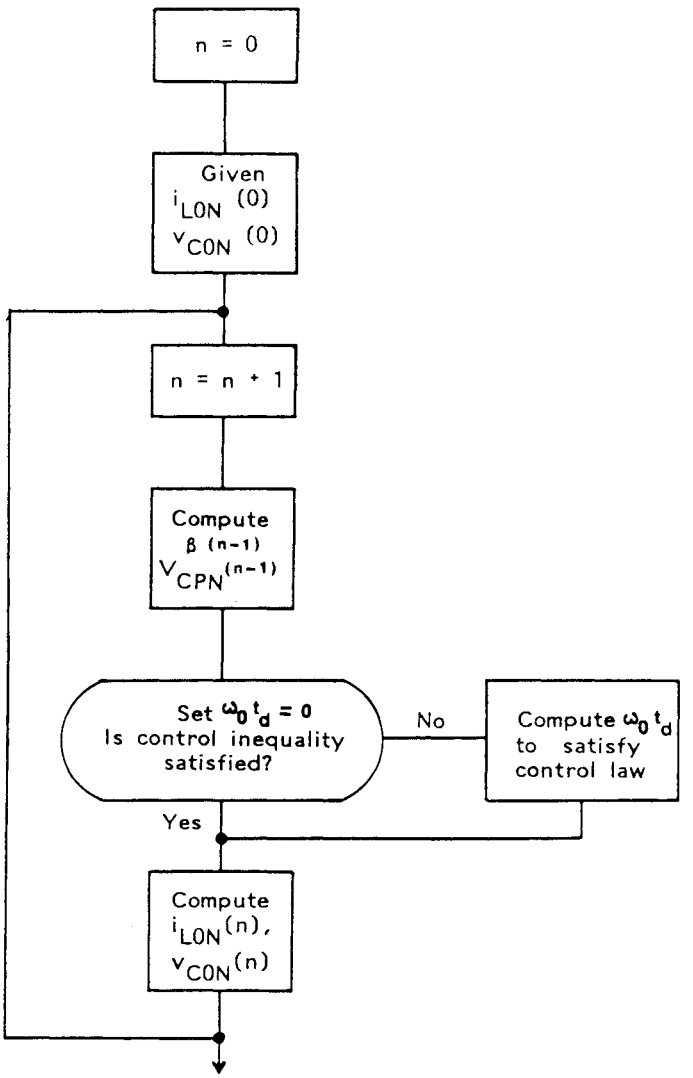

Figure 4.9. Partial computer flowchart for state-plane study of control methods

$$V_{CON}(n) = V_{CPN}(n-1)$$
$$I_{LON}(n) = 0 \tag{4.30}$$

If not, then the value of $\omega_0 t_d$ to satisfy the control law is determined. If $\omega_o t_d$ is less than π, then the new switching-point state variables for transistor Q2 are obtained from Fig. 4.4 as follows.

$$R'(n-1) = V_{CPN}(n-1) - (1 + V_{oN}) \tag{4.31}$$

$$V_{CON}(n) = R'(n-1)\cos(\omega_0 t_d) + 1 + V_{oN}$$
$$I_{LON}(n) = -R'(n-1)\sin(\omega_0 t_d) \tag{4.32}$$

There can be instances when the value of $\omega_0 t_d$, determined from the control law, exceeds π. A computer program to handle these cases will be complex and was not written. Whenever such situations arose, the trajectories were plotted by hand using the control law.

4.4.1 Performance Criteria

The large-signal and relatively, small-duration transient properties of the different control methods were evaluated on the state plane based on the following criteria:

1. Stability
2. Response to control change
3. Load increase/ short-circuit behavior
4. Control range

Brief descriptions of these criteria are given below.

4.4.1.1 Stability

This is the basic requirement to be fulfilled by any control method. Values of switching point state variables I_{LON} and V_{CON} for the steady-state steady-state trajectory were calculated first from the analysis of Appendix A and were then used as the starting values. If the control method does not result in a

stable system, then any perturbations, including numerical ones introduced by the computations, would move the system away from the steady-state trajectory.

4.4.1.2 Response To Control Change

The response to a step change in control was plotted on the state plane. The basic nature of the response of the system with a particular control is, thus, evaluated. Large changes in control input were made in order to render the transient behavior more clearly visible on the state-plane diagrams. Smaller changes in control also produced similar response trajectories.

4.4.1.3 Load Increase / Short-Circuit

As pointed out in Chapter 2, a SRC is suited for applications where a constant current output is required against dynamic load fluctuations. A sudden decrease in load resistance value would cause the output voltage to drop. The increase in the energy level of the tank and the speed of the transient generated, under this condition, can be studied by introducing a marginal decrease in the output voltage.

Effect of a dead short circuit on the system is studied by assuming that the output voltage drops to zero suddenly at some point in time. In practice, short circuits are rarely so severe and, hence, the study indicates worst-case possibilities.

The load increase or short circuit is assumed to occur just after a transistor is switched on so that the resulting transient will be most severe. Furthermore, the control signal is assumed to remain constant throughout. Any additional control mechanism, such as an overcurrent limiter which would reduce the output current under these conditions, is not considered.

A preliminary idea of the behavior of the system under load increase or short-circuit conditions can be obtained from the dc characteristics in Fig. 4.7(a)-(d) as suggested in [24]. However, state-plane analysis shows the actual dynamics of tank energy build up and, hence, is useful to the designer in determining the level and speed of additional protection, if any, needed.

4.4.1.4 Control Range

Limitations that may exist on the part of the control method in handling different conditions such as CCM and DCM are also investigated.

4.4.2 Performance Evaluation

4.4.2.1 ASDTIC Control

The problem of ASDTIC control start-up, referred to in Sec. 4.2.1.1, will now be studied on the state plane. It is assumed that output V_o remains at zero for the first few cycles of operation. The state portrait for the case $V_{oN} = 0$ is shown in Fig. 4.10(a). The following explanation is given with reference to both Fig. 4.3(a) and 4.10(a).

At $t = 0$, $Q1$ is switched on. Due to the low current level of resulting trajectory $T1$, ASDTIC control switches on $Q2$ at t_A. This, however, takes the tank circuit to a very high energy level through trajectory $T2$. Because of this high current transient, ASDTIC control delays the application of the turn-on signal to $Q1$ after t_B. Thus, diode $D2$ conducts at t_B after the natural commutation of $Q2$. However, diode conduction trajectory $T3$ is again a high-current trajectory. Consequently, $Q1$ is not turned on when $D2$ is conducting. Following the commutation of $D2$ at t_C, diode $D1$ is forward biased immediately. Thus, the system continues on trajectory $T4$ following $T3$. Transistor $Q2$, in principle, can be switched on any time after instant t_C. However, due to the heavy transient currents previously established in trajectory segments $T2$ and $T3$, the average rectified inductor current from $t = 0$ is still larger than the value set by the ASDTIC control. Hence, the control delays the turn-on signal for $Q2$ and allows the system to reach the origin at instant t_D. The system remains in discontinuous operation after instant t_D till, at instant t_E, the ASDTIC control law is satisfied. At t_E, either $Q1$ or $Q2$ will be switched on again depending on the control implementation.

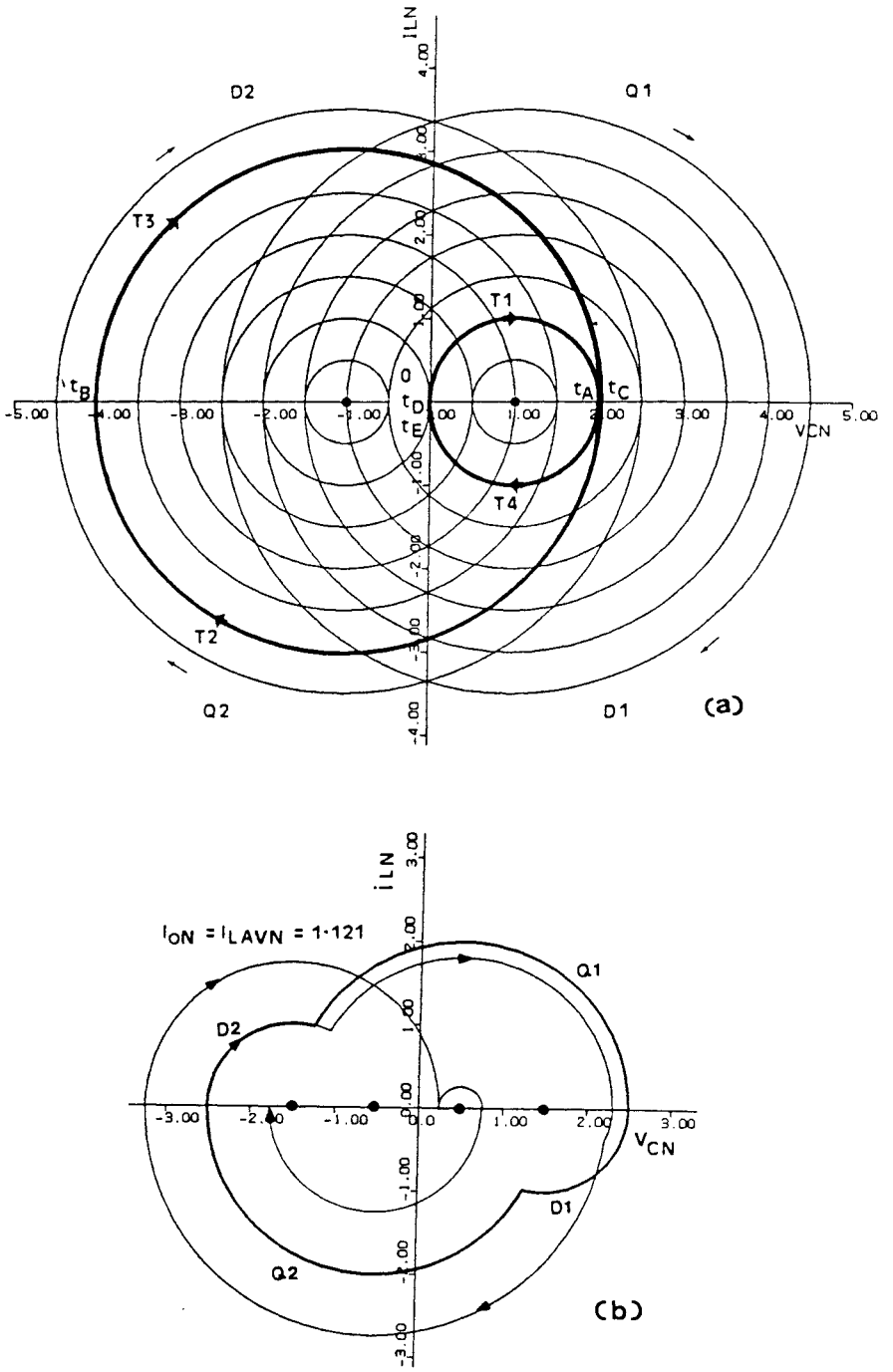

Figure 4.10. ASDTIC control problems viewed on state plane
a) Start-up b) Stability $V_{oN} = 0.5$

It is clear from Fig. 4.10(a) that the problem of high currents and irregularity of switching sequence could have been avoided had the control delayed the turn-on of $Q2$ beyond time t_A by allowing $D1$ to conduct for a while. In other words, the ASDTIC control noticed low-current trajectory $T1$ and promptly switched on $Q2$ at instant t_A. The control did not anticipate the resulting high current and high-energy trajectory $T2$, dictated by the structure of the state portrait.

Next we will study the operation of the ASDTIC control when started under steady-state conditions (Fig. 4.10(b)). The thick, closed curve in Fig. 4.10(b) shows the steady-state trajectory on which the system stays for a few cycles of operation. However, a small perturbation due to computational error is sufficient to move the system away from this steady-state trajectory into asymmetrical and abnormal sequences of conduction including discontinuous operation. The conduction sequence in Fig. 4.10(b) is $Q1$, $D1$, $Q2$, $D2$, $Q1$, $D1$, $Q2$, $D2$, discontinuous operation, $Q1$ and so on. This inability of ASDTIC control to retain the system on a steady-state trajectory is also confirmed by the result of the SPICE2 simulation as shown by the waveform in Fig. 4.3(b).

An additional problem was found when higher energy steady-state trajectories were dealt with. In these cases, the ASDTIC control law is satisfied at times other than the steady-state switching instant. Owing to this, the control was not able to keep the system on the steady-state trajectory even for one cycle.

In general, SRC waveforms under ASDTIC control are bounded but appear chaotic. It is concluded that ASDTIC control does not result in a stable system and it is not considered further.

4.4.2.2 Transistor-Conduction-Angle Control

The performance of this control for a step change in control input is shown in Fig. 4.11. The two conduction-angle inputs are $\beta1 = 2.366$ radians and $\beta2 = 2.636$ radians. The corresponding steady-state trajectories, $T1$ and $T2$, respectively, have been drawn with heavy lines in Fig. 4.11. The control laws corresponding to β_1 and β_2 have also been drawn on the state plane. The system is intially assumed to be on steady-state trajectory $T1$. Now, if a control input change is made from $\beta1$ to $\beta2$, it is seen that the tank energy, instead of decreasing, builds up demonstrating the instability of this control. This control method is also not considered further.

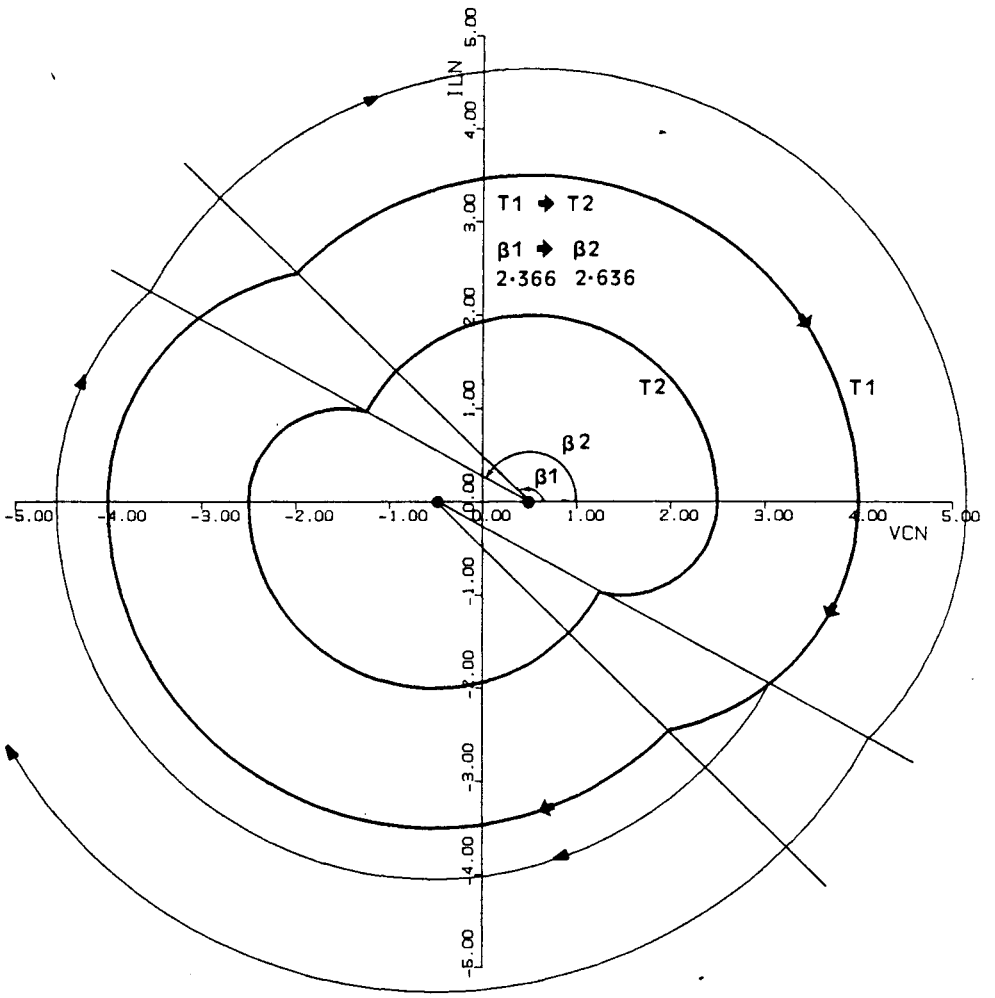

Figure 4.11. Unstable response of transistor-conduction-angle control $V_{oN} = 0.5$

4.4.2.3 Capacitor-Voltage Control

Figure 4.12(a) shows the response of a SRC for a step change in control input with this control method. Steady-State trajectories *T*1 and *T*2 correspond to control inputs V_{CON1} = 2.00 and V_{CON2} = 1.25, respectively. When the control input changes from 2.00 to 1.25, the resulting transient takes several cycles to settle down. The response is asymptotic and nonoscillatory.

The performance of the control is dependent on whether the output voltage is low or high. If lossless operation is assumed, then under the limiting case of V_{oN} = 0, all steady-state trajectories have the same capacitor voltage of value zero at the switching instants, as shown in Fig. 2.12(a). Due to this, the capacitor-voltage control method, ideally, will not function when the output voltage is zero. For low V_{oN} values the response of the system to control changes is extremely slow. The response improves considerably at higher voltages (say $V_{oN} \geq 0.3$). This phenomenon is illustrated in Figs. 4.14(a) and (b). The tank energy is reduced in both cases with V_{oN} = 0.1 in Fig. 4.14(a) and V_{oN} = 0.9 in Fig. 4.14(b). The system response is slow in Fig. 4.14(a), whereas in Fig. 4.14(b) the response is fast.

When a sudden load increase occurs, the output current can build up to a high magnitude at low values V_{oN} (Fig. 4.14(c)). The rate of increase of this current, however, is small. On the other hand, at large values of V_{oN} (Fig. 4.14(d)), the output current increases only by a small amount.

The response under a dead short circuit is shown in Fig. 4.13(a). The output current builds up at a high rate, theoretically, without any limit. Thus capacitor-voltage control, ideally, does not possess inherent short-circuit capability and requires external protection. The dc characteristics in Fig. 4.7(a) also confirm this. In this figure, when V_{oN} is made zero, the output current will increase without any limit. Also, since this control method is time invariant, it can only operate in the CCM region.

4.4.2.4 Frequency Control

This is probably the simplest method for the control of SRCs. In Fig. 4.12(b), steady-state trajectories *T*1 and *T*2 correspond to normalized control inputs ω_{1N} = 0.841 and ω_{2N} = 0.704 , respectively. When the control input changes from ω_{1N} to ω_{2N}, the response is asymptotic and oscillatory. Figure 4.15(a)

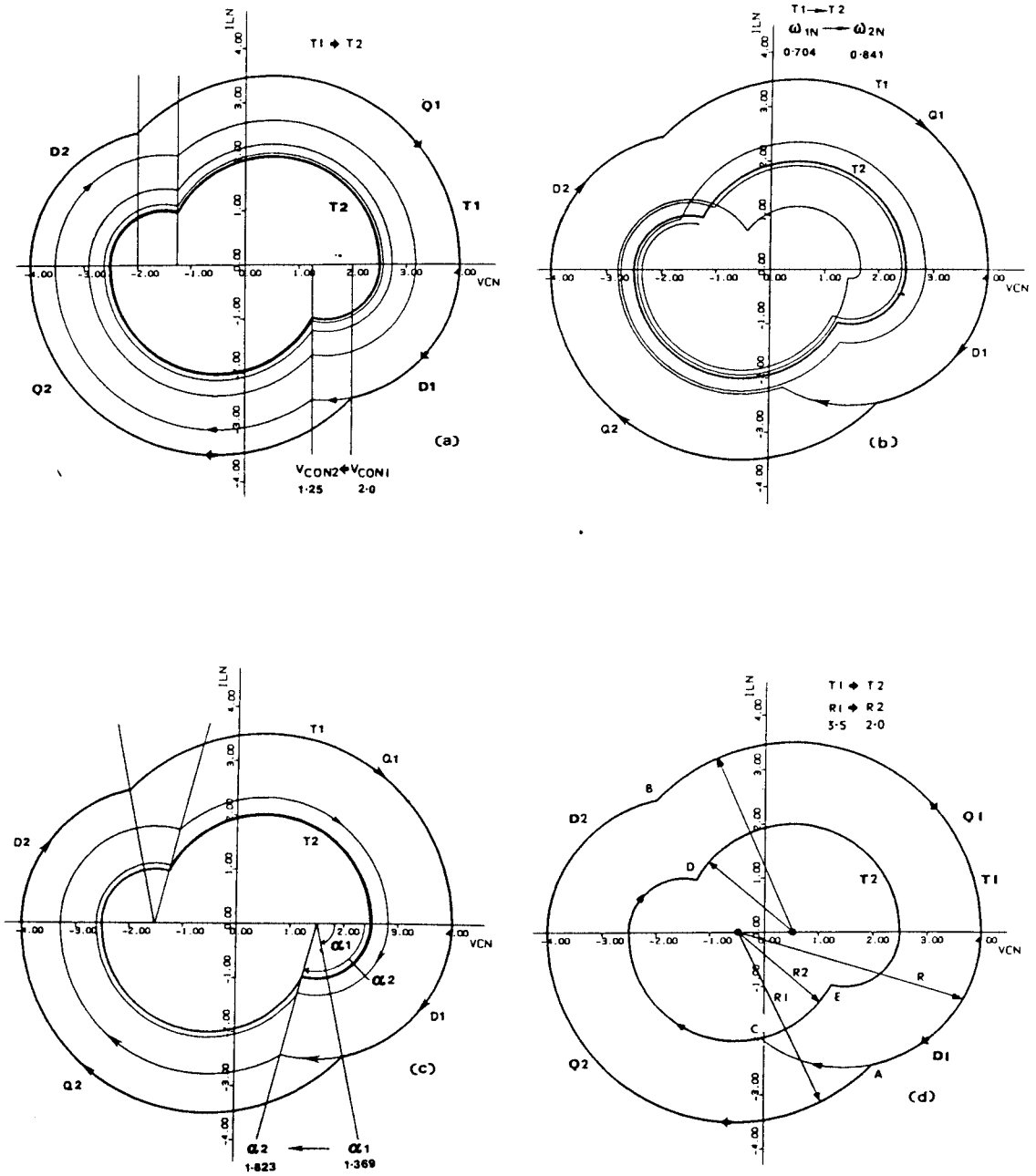

Figure 4.12. Response for step control change $V_{oN} = 0.5$
a) Capacitor-voltage control
b) Frequency control
c) Diode-conduction-angle control
d) Optimal trajectory control

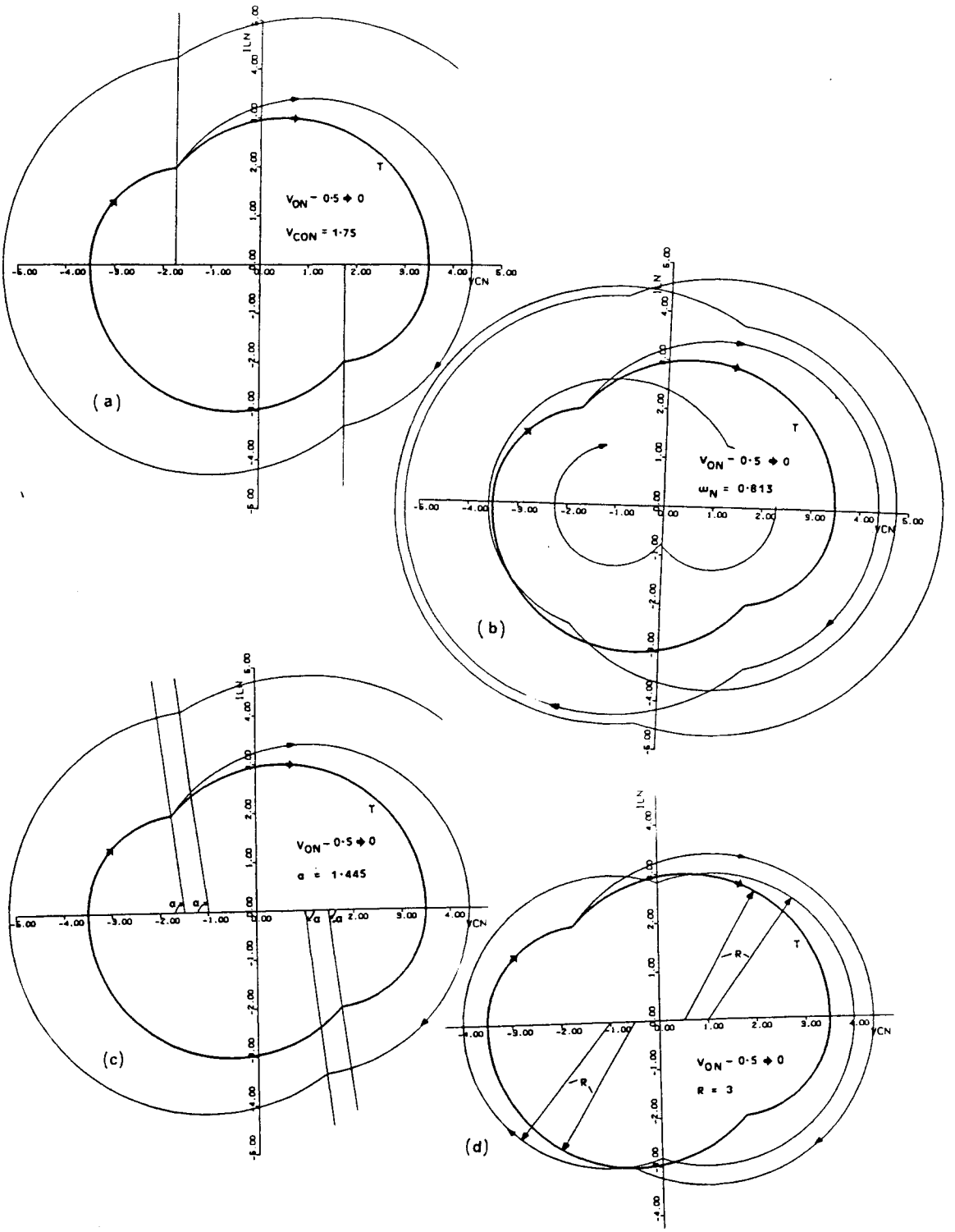

Figure 4.13. Transient under short circuit
a) Capacitor-voltage control
b) Frequency control
c) Diode-conduction-angle control
d) Optimal trajectory control

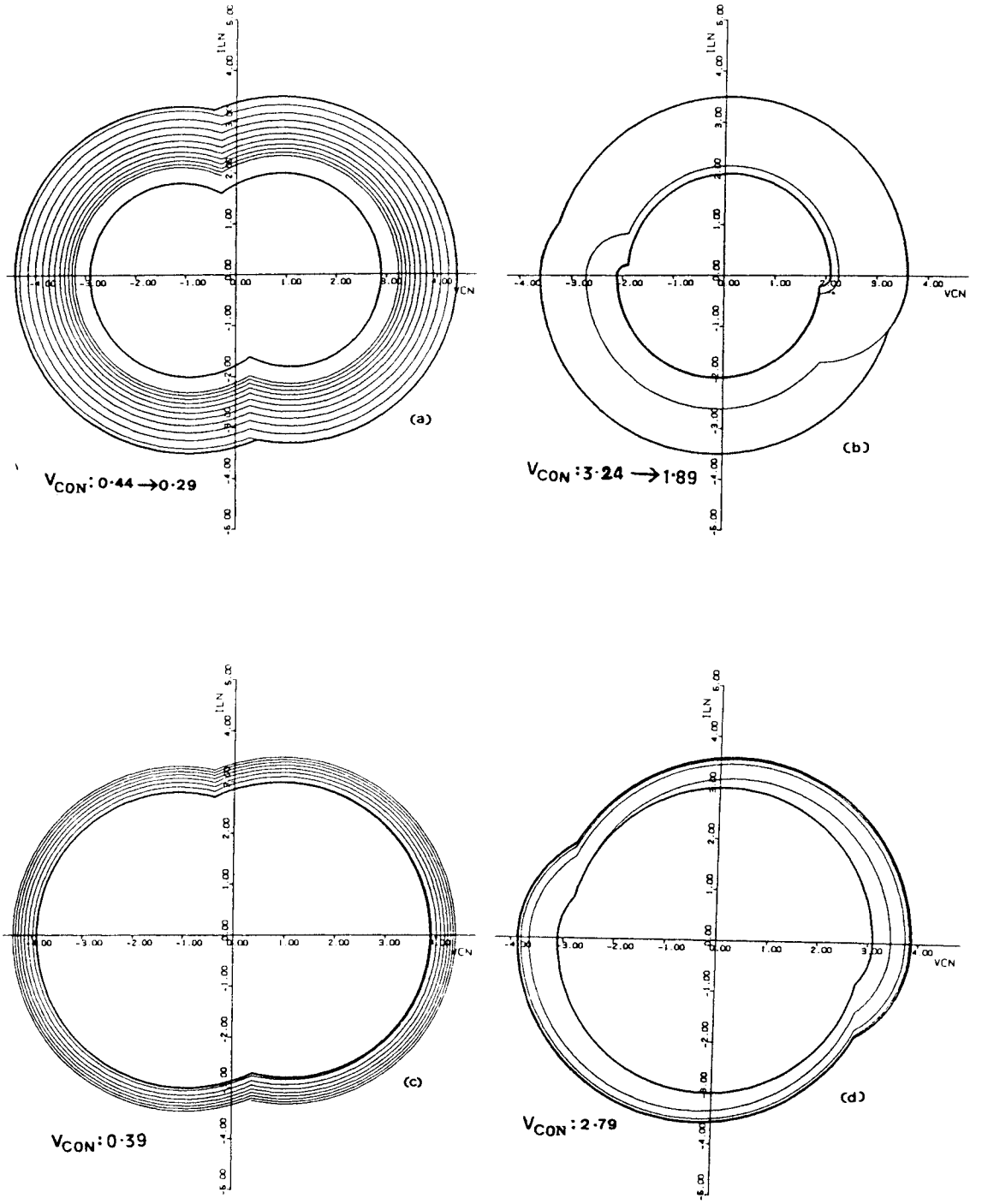

Figure 4.14. Capacitor-voltage control - Response trajectories
a) Energy decrease - V_{oN} = 0.1
b) Energy decrease - V_{oN} = 0.9
c) Step-load change - V_{oN} 0.1 to 0.08
d) Step-load change - V_{oN} 0.9 to 0.72

shows the response to a step change in control calling for an increase in the tank energy at low output voltages. The response is extremely oscillatory with high current and voltage overshoots which can stress the components of the circuit. Though the basic nature of response with frequency control is oscillatory, the response is nonoscillatory at high output voltages (Fig. 4.15(b)), since the rate at which the tank energy can be built up at these output voltages is limited (Sec. 4.3.3).

When sudden load increases occur, the output current, in general, is bounded (Figs 4.15(c) - (d)). However, at frequencies near resonant frequency, the output current for small decreases in output voltage can reach high values, though bounded. This may be observed from the dc characteristics given in Fig. 4.7(b). Under short-circuit conditions, the output is again bounded though extremely oscillatory, as shown in Fig. 4.13(b). However, since considerable overcurrents and overvoltages can occur under short circuit, additional protection circuitry may still be needed.

Since the frequency control method is time variant, as explained before, it can operate both in the CCM and DCM regions.

4.4.2.5 Diode-Conduction-Angle Control

Figure 4.12(c) shows the operation of this control method when a step change in control is made to reduce the tank energy at $V_{oN} = 0.5$. The response is asymptotic and nonoscillatory. During a preliminary investigation, this method appeared to be promising. However, further study indicated the existence of a limitation. The response to a control input change calling for an increase in tank energy is very slow at all output voltages. As shown in Sec. 4.3.3, at low output voltage, the state portrait of a SRC allows the tank energy to build up quickly. However, as Fig. 4.16(a) shows, at $V_{oN} = 0.1$, tank energy increases slowly when an input change is made. When the tank energy is decreased at $V_{oN} = 0.1$ (Fig. 4.16(b)), the response of the system is reasonably fast.

The slow build up of the tank energy was also observed when the output voltage was suddenly reduced due to load demand (Fig. 4.16(c) - (d)). The output current tends to increase to large values over a period of many cycles. A study of Fig. 4.7(c) also shows that for a given α, I_{oN} varies over a wide range for a small change of output voltage. Under short-circuit conditions, the control behaves similar to

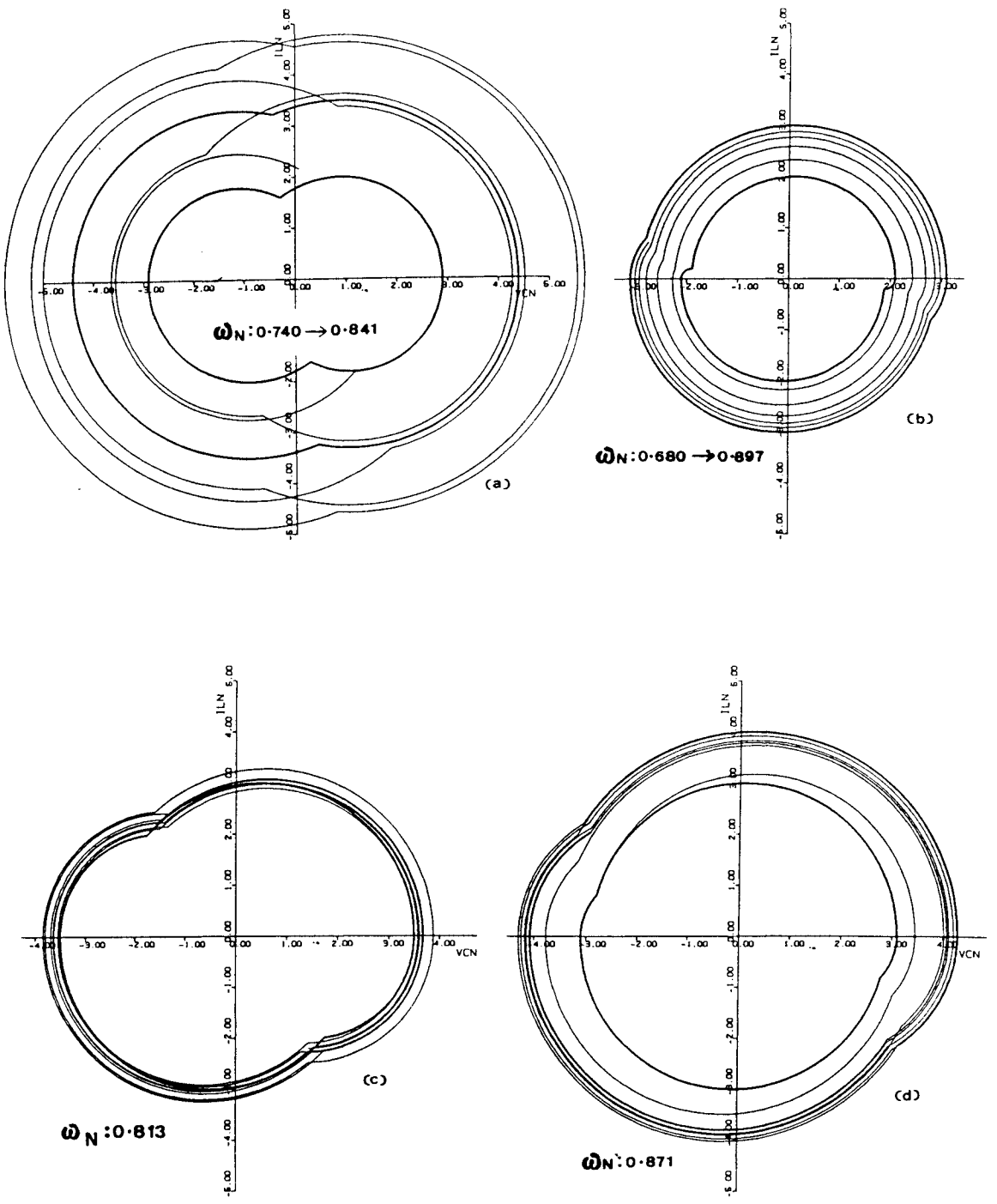

Figure 4.15. Frequency control - Response trajectories
a) Energy increase - V_{oN} = 0.1
b) Energy increase - V_{oN} = 0.9
c) Step-load change - V_{oN} 0.5 to 0.4
d) Step-load change - V_{oN} 0.9 to 0.72

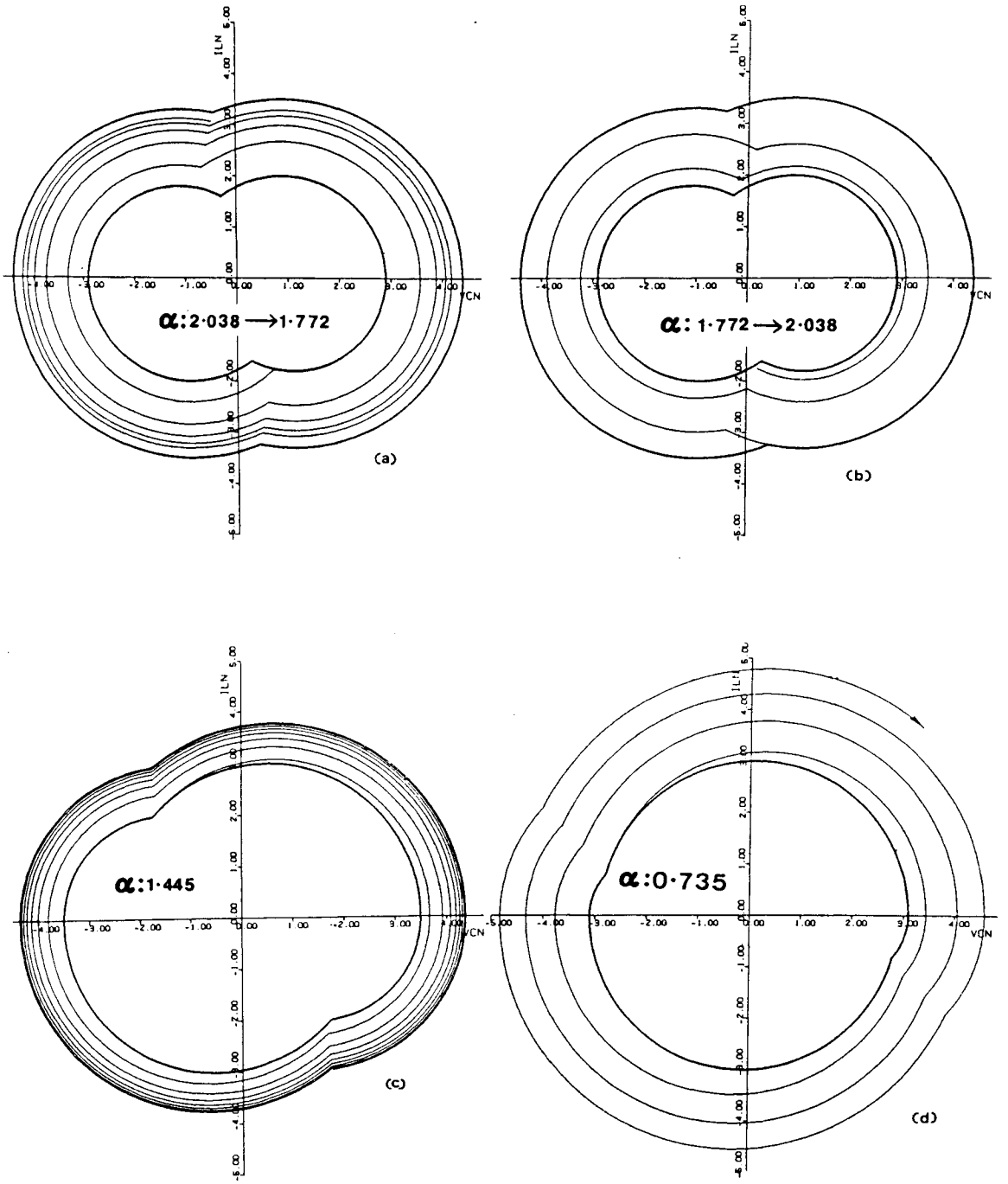

Figure 4.16. Diode-conduction-angle control - Response trajectories
a) Energy increase - V_{oN} = 0.1
b) Energy decrease - V_{oN} = 0.1
c) Step-load change - V_{oN} 0.5 to 0.4
d) Step-load change - V_{oN} 0.9 to 0.72

capacitor-voltage control. Figure 4.13(c) shows the tank energy continuing to rise in each half cycle. Unless the protection circuitry acts quickly, components in the circuit can be overstressed.

Since the diode-conduction-angle control acts as a time-variant control under DCM conditions, it can operate the converter in DCM also.

4.4.2.6 Optimal Trajectory Control

In this method, the desired trajectory during a transistor-conduction interval, is utilized as the control law as shown in Fig. 4.6(d). The operation of this control method is described below using Fig. 4.17.

In Fig. 4.17 the semicircular trajectory segment *HBF* is the control law for *Q*1 conduction. Likewise, segment *JAG* is the control law for *Q*2 conduction. As diode *D*1 conducts, the control circuit computes variable R_d from continuous measurements of i_L, v_C, V_0 and V_s . The distance, R_d, in this case, is measured from the center of trajectory of *Q*2. When R_d becomes equal to control input *R*1 at *A* , transistor *Q*2 is switched on. After *Q*2 naturally switches off at *G*, *D*2 starts to conduct. Distance R_d is once again monitored, this time, however, as measured from the *Q*1 trajectory center. At *B*, once again R_d equals *R*1 and transistor *Q*1 is switched on. Thus, the control law keeps the system on steady-state trajectory *T*1 corresponding to *R*1 by alternately switching on at *A* and *B*.

Figure 4.12(d) shows the response of the system for a step change in control input from *R*1 to *R*2. Initially, the control input is *R*1 and the system is on trajectory *T*1. Now, let the control input be changed to *R*2 somewhere between *B* and *A* on *T*1. When the system reaches *A*, R_d is no longer equal to the new control input *R*2. So, *Q*2 is not switched on and *D*1 continues to conduct till the state trajectory reaches point *C* where R_d equals *R*2. At *C*, *Q*2 is switched on. From now on the control keeps the system on trajectory *T*2 by alternately switching on the transistors at *D* and *E*. Thus, by utilizing the transistor trajectory itself as the control law, the new steady state is reached in an abrupt, time-optimal and nonasymptotic manner.

Figures 4.18(a)-(b) show once again the response with this control method for low output voltage (V_{oN} = 0.1) both when tank energy is decreased and when it is increased. The control method achieves excellent responses here also by utilizing the structure of the state portrait effectively.

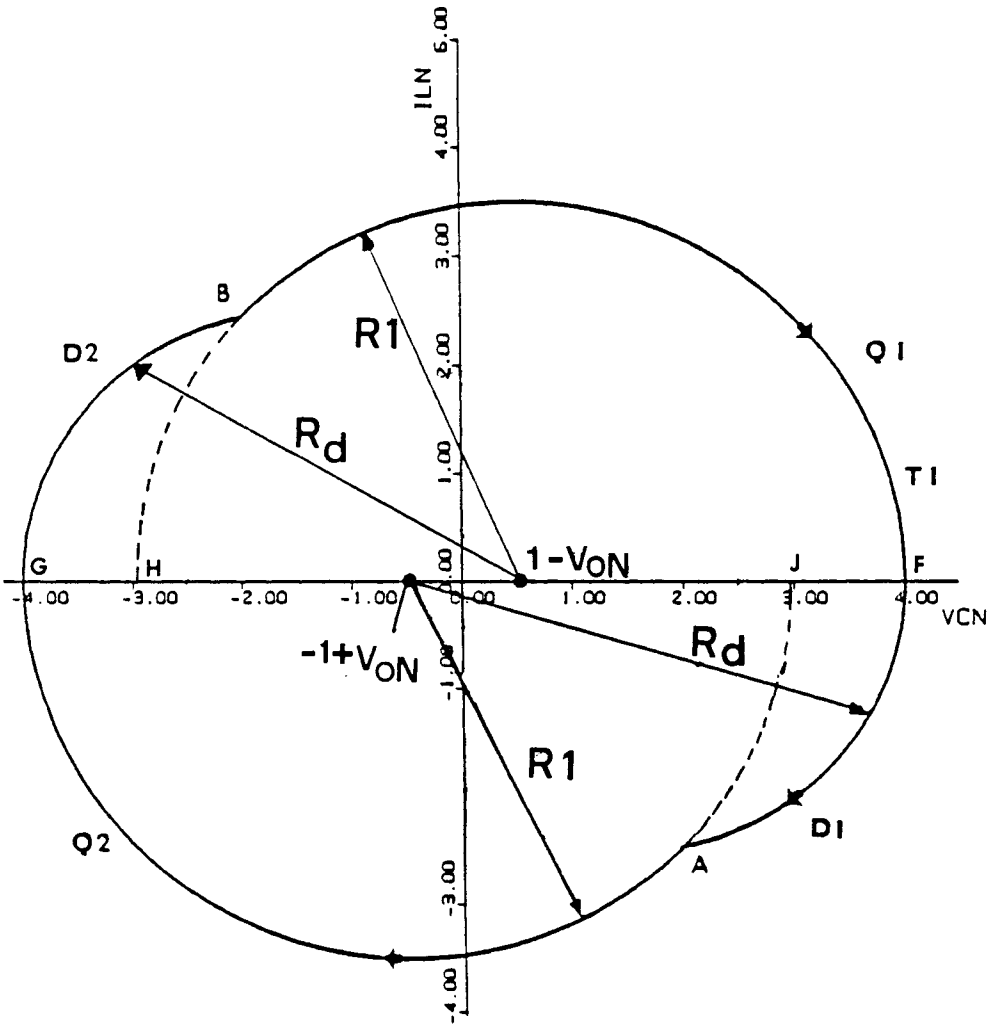

Figure 4.17. Explanatory diagram for operation of optimal trajectory control

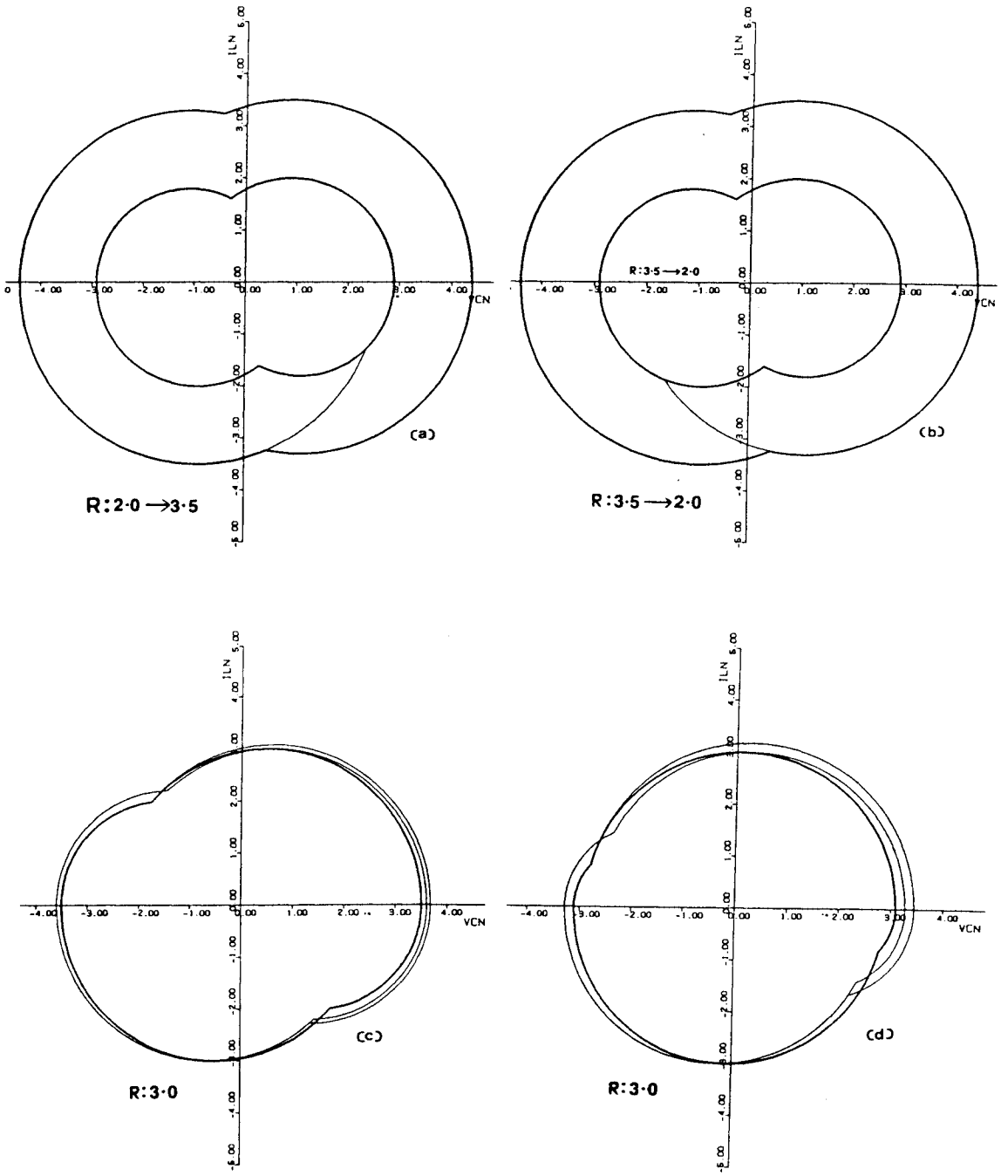

Figure 4.18. Optimal trajectory control - Response trajectories
a) Energy increase - $V_{oN} = 0.1$
b) Energy decrease - $V_{oN} = 0.1$
c) Step-load change - V_{oN} 0.5 to 0.4
d) Step-load change - V_{oN} 0.9 to 0.72

Figure 4.19 shows the operation of optimal trajectory control for large changes in control input. As noted previously, the maximum rate at which the tank energy can change in a half cycle is limited. Thus, the system takes more than a trajectory segment to reach the target steady-state trajectory. In Fig. 4.19(a), the tank energy is increased largely by a series of transistor conductions. Likewise, in Fig. 4.19(b), the tank energy is decreased by a series of diode conductions. In both cases, the system reaches the new steady-state trajectory in the minimum possible time limited only by the intrinsic properties of the SRC as determined by its state portrait.

When sudden load voltage changes occur, the system settles abruptly on a new trajectory close to the original one without much variation in the tank energy levels (Figs 4.18(c)-(d)). Figure 4.7(d) also shows that under this control method, the output current varies only a little for changes in output voltage for given control input R. The performance of this method under short circuit is also remarkable as shown in Fig. 4.13(d). Within a short time from the occurrence of the short circuit, the system abruptly reaches another steady-state trajectory at an energy level only slightly greater than the earlier one. Thus, optimal trajectory control fully exploits the potential of a SRC to respond quickly to the demands of control and load.

Since optimal trajectory control is time invariant, it can control the converter only in the CCM region. However, it is possible to modify this control method such that a time-invariant control takes over the operation in the DCM region.

4.4.3 Summary

The characteristics of the different usable methods of control described above are summarized in Table 4.1. From Table 4.1 and the discussions so far, the following key features of each method of control are summarized.

Capacitor-voltage control is a simple control method. It can be used when the SRC is not required to operate under low output voltages and when short-circuit ability and good dynamic performance are not essential.

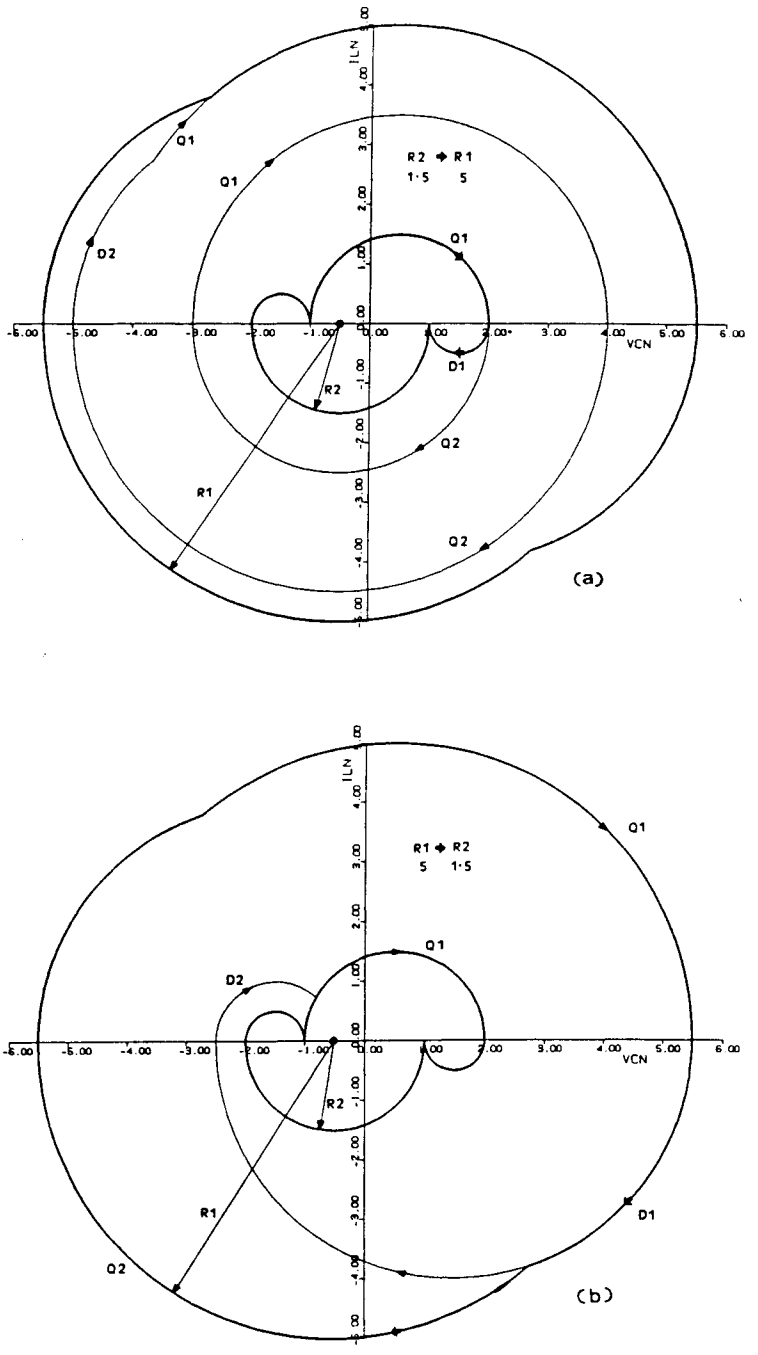

Figure 4.19. Response of optimal trajectory control for large control changes V_{ON} = 0.5
a) Control radius increased from 1.5 to 5.0 b) Control radius decreased from 5.0 to 1.5

TABLE-4.1

EVALUATION OF CONTROL METHODS

Control	Response Type	Response Up	Response Down	Step Load Change	Short Circuit Capability	Current Limiting	Dis-Continuous Current Capability	Complexity	Remarks
Capacitor Voltage	Asymptotic Non-Oscillatory				Poor	Poor	No	Simple	Control fails when $V_{ON} = 0$
Low V_{ON}		Very slow	Very slow	Poor					In general poor performance at low V_{ON}'s and under short circuit.
High V_{ON}		Medium fast	Fast	Good					
Frequency	Asymptotic Oscillatory			Fair	Fair	Fair	Yes	Very simple	Extremely oscillatory response esp. at low V_{ON}'s
Low V_{ON}		Very slow	Very slow						
High V_{ON}		Medium fast	Fast						
Diode Conduction Angle	Asymptotic Non-Oscillatory	Very slow	Fast	Poor	Poor	Poor	Yes	Simple	Builds up the tank energy slowly at all output voltages
Optimal Trajectory Control	Time Optimal Abrupt	Fastest Possible	Fastest Possible	Excellent	Excellent	Fair	No	Complex	Excellent performance but complex

The Frequency control method produces a slow, oscillatory response especially at low output voltages. It has, however, the virtues of simplicity and ability to handle discontinuous currents.

Diode-conduction-angle control is another simple method which produces a nonoscillatory response and can handle discontinuous currents. The response is slow at all output voltages whenever tank energy is increased while it is fast whenever tank energy is decreased.

Optimal trajectory control produces abrupt and time-optimal response exploiting the structure of the SRC state portrait to the fullest. It has excellent ability to handle overload and short-circuit currents. Thus, despite its apparent complexity and need for modification to handle discontinuous current conduction, optimal trajectory control appears to be the most promising control method.

4.5 Implementation Of Optimal Trajectory Control

In this section, an experimental implementation of optimal trajectory control will be presented. The experimental results are compared with those obtained with the frequency control method. The control circuit diagram of the frequency control scheme is shown in Fig. 5.32.

From (4.22), the instantaneous values i_L, v_C, V_o and V_s are to be known for monitoring R_d. If these four quantities are sensed independently and with electrical isolation, greater flexibility will be available in control implementation. However, the resulting sensor scheme will be complex. In Sec. 4.5.1, the equations for computing the feedback variable are manipulated such that the number of voltage sensors required is only two. Moreover, by proper arrangement of power circuit components, both voltage sensors can be used without isolation.

The computation of R_d requires the arithmetical manipulation of parameters such as i_L, v_C and V_s. It is necessary to follow a scaling procedure such that the different elements determining R_d are weighted appropriately. The details of the scaling procedure adopted in this work are discussed in Sec. 4.5.4.

Optimal trajectory control attempts to achieve time-optimal response in a resonant converter. However, experimental errors can be expected during sensing, scaling, etc., and these errors will cause deviations in the actual response. The problem is further compounded by the time delays involved in different parts of the circuit such as the computation elements and the driver circuit. Another important reason which can cause the operation of the actual circuit to deviate from time optimal response is given below.

The theoretical analysis, which motivated the invention of optimal trajectory control, assumed an ideal, lossless converter. Thus, the control law that was experimentally implemented is a circular trajectory segment. However, as shown in Chapter 3, the trajectory segments spiral toward the center when losses are considered. Hence, the actual transistor trajectory is not being used as the control law and this can cause, once again, deviations in the transient response.

Due to the above reasons, the performance of the experimental circuit cannot be strictly time-optimal. Hence, it is important to know the extent of the deviation that occurs in the actual dynamic performance of the system when compared with the theoretical predictions. The experimental transient responses presented in this section show that this deviation is not significant.

The time delay introduced by the control circuit must be small when compared to the period of operation. Thus, it is necessary to use op-amps with high slew rate, multipliers with large bandwidth, etc. In addition, the control scheme is arranged such that signal delays are minimized.

4.5.1 Computation Of Feedback Variable

From Fig. 4.17,

$$\begin{aligned} R_d &= \sqrt{(1 - V_{oN} - v_{CN})^2 + i_{LN}^2} \quad i_{LN} > 0, \quad \text{for } Q1 \\ &= \sqrt{(1 - V_{oN} + v_{CN})^2 + i_{LN}^2} \quad i_{LN} < 0, \quad \text{for } Q2 \end{aligned} \tag{4.33}$$

Multiplying (4.33) by V_s and squaring,

$$\begin{aligned} (R_d V_s)^2 &= (V_s - V_o - v_C)^2 + (i_L Z_0)^2 \quad i_L > 0 \\ &= (V_s - V_o + v_C)^2 + (i_L Z_0)^2 \quad i_L < 0 \end{aligned} \tag{4.34}$$

Combining the two equations in (4.34),

$$(R_d V_s)^2 = (v_C + FV_o - FV_s)^2 + (i_L Z_0)^2 \qquad (4.35)$$

$$\text{where} \qquad F = \text{sign } i_L \qquad (4.36)$$

From the measured values of i_L, v_C, V_0 and V_s , the value of $(R_d V_s)^2$ is computed using (4.35). If R_d is required, it may be obtained by taking the square root of $(R_d V_s)^2$ and then dividing by V_s . In the present work, $(R_d V_s)^2$ itself was used to implement the control law instead of R_d, thus, saving a square root operation and a division operation.

4.5.2 Power Circuit

The SRC power circuit shown in Fig. 3.13 was rearranged (Fig. 4.20) to implement the sensor scheme. In Fig. 4.20, the common point connecting the cathode of V_{s1} and the anode of V_{s2} is the ground terminal connected to the zero potential of the control circuit. Resonant frequency f_0 of the experimental set up is 50.4 kHZ and characteristic impedance Z_0 equals 25.9 Ω.

Current i_L is sensed by the current transformer (CT) and its burden ($R5$). Output voltage $k_1 i_L$ of the CT is proportional to i_L . The potential divider ($R1$, $R2$) across V_{s1} senses the dc input supply. It would be preferable to add a similar resistor network across V_{s2} also and then to use a differential input amplifier to obtain the signal proportional to supply voltage. Signal $k_3 V_s$ would then reflect changes in both V_{s1} and V_{s2} .

The voltages v_C and V_o are sensed together by the network ($R3$, $R4$). This method reduces the number of sensors by one and also avoids the need for an isolating dc voltage sensor for sensing V_o. Moreover, by including the diode drops of the output rectifier in the sensing process, the topological mode centers are determined more accurately. Another advantage is that this sensing method can be used without modification when the output bridge rectifier is connected to the tank circuit through a transformer.
The voltage at the input of the bridge rectifier is v_r and is given by

$$v_r = F V_o , \qquad (4.37)$$

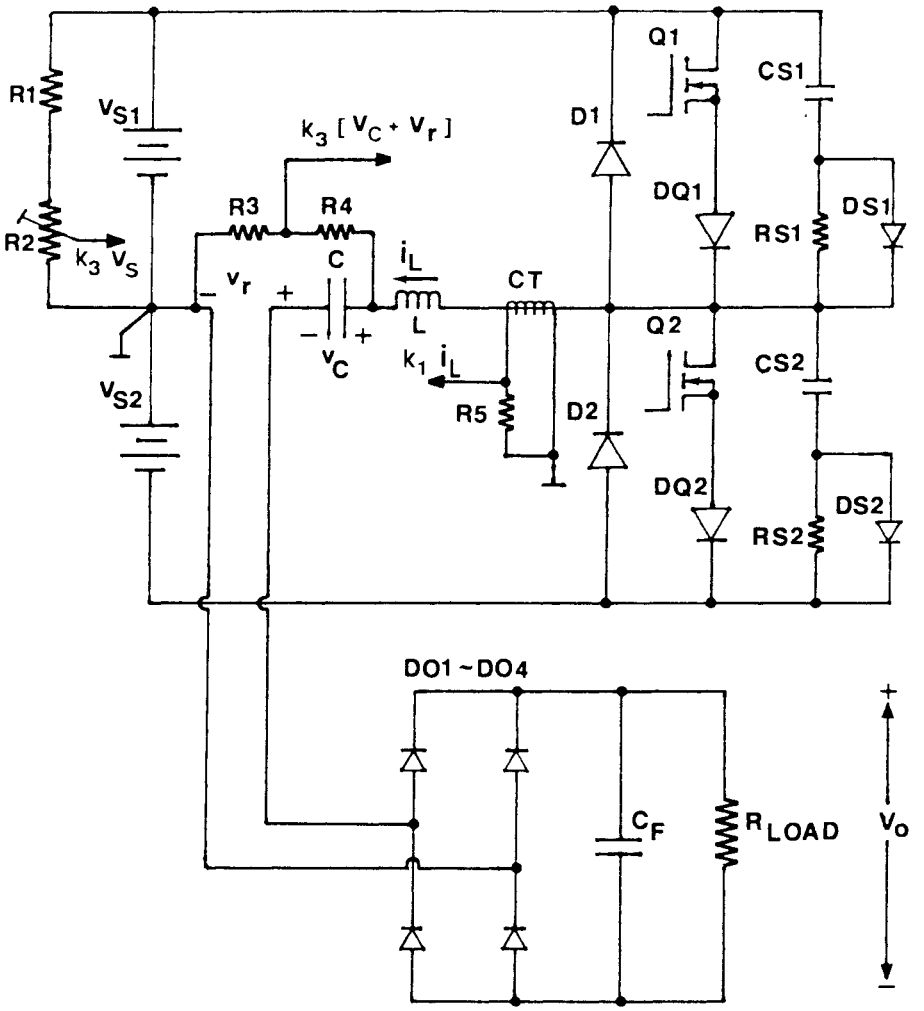

Vs1,Vs2: 25V, Q1,Q2: 2SK325, DQ1,DQ2: A115E
D1,D2: 12FL60S02, DO1~DO4: 40HFL60S02
L: 81.8 µH, C: 0.125 µF, CF: 50.0 µF,
CS1,CS2: .047 µF, RS1,RS2: 18 Ω, DS1,DS2: A115E
f_0(measured) = 50.4 kHZ, Z_0 = 25.904 Ω

Figure 4.20. Experimental power circuit diagram

where F is defined by (4.36).

$$\text{So,} \qquad v_C + v_r = v_C + F\,V_o \tag{4.38}$$

Thus, the potential divider ($R3$, $R4$) senses the term ($v_C + F\,V_o$) in (4.35) directly.

4.5.3 Control Circuit

The driver circuit for providing isolated base drives to the MOSFETS is shown in Fig. 3.15. The functional block diagram of the control circuit is shown in Fig. 4.21, while Fig. 4.22 shows the actual control circuit. The following explanation for the control circuit operation is given with respect to both these figures.

Control signal $k_1\,i_L$, from the current sensor in Fig. 4.20, is fed to comparator $D3$. The output of $D3$ is the logical signal, F, whose state ($+1$ or -1) is determined by the sign of i_L. Devices $D4$ and $D10$ are multipliers configured to perform squaring operation. Device $D4$ squares signal $k_1\,i_L$ to produce signal $k_2\,(i_L Z_0)^2$, where the characteristic impedence Z_0 is a constant.

Signal $k_3\,V_s$, from the supply voltage sensor in Fig. 4.20, is fed to unity gain buffer $D7$. The outputs from op-amps $D7$ and $D8$ are signals $+\,k_3\,V_s$ and $-\,k_3\,V_s$ respectively. Analog switch $D6/1$ selects one of these outputs depending on the state of F. Thus, the output of $D6/1$ is signal $F\,k_3\,V_s$.

As seen in Sec. 4.5.2, control signal $k_3\,(v_C + v_r)$ in Fig. 4.20 is equivalent to $k_3\,(v_C + F\,V_o)$. The difference between $F\,k_3\,V_s$ signal and $k_3\,(v_C + F\,V_o)$ signal is squared by $D10$ to generate the $k_2\,(v_C + F\,V_o - F\,V_s)^2$ signal.

Op-amp $D11$ sums the output of the two squaring units, $D4$ and $D10$, to generate $k_4\{(v_C + F\,V_o - F\,V_s)^2 + (i_L Z_0)^2\}$. From (4.35), the output of $D11$ is the control signal $k_4\,(R_d\,V_s)^2$. Scaling factor k_4 and signal $k_4(R_d V_s)^2$ are negative, since op-amp $D11$ inverts the polarity of its input signal. The control input signal V_{CONT} is compared with signal $k_4\,(R_d\,V_s)^2$ by comparator $D12$. The output of $D12$, V_{PULSE}, determines the instants for turning on the transistors $Q1$ and $Q2$. Flip-flop $D13$ in the steering circuit produces inputs for the transistor drivers at the trailing edges of the V_{PULSE} signal. Gating signal F to the flip-flop ensures that only the appropriate transistor is turned on. When diode $D2$, in Fig. 4.20,

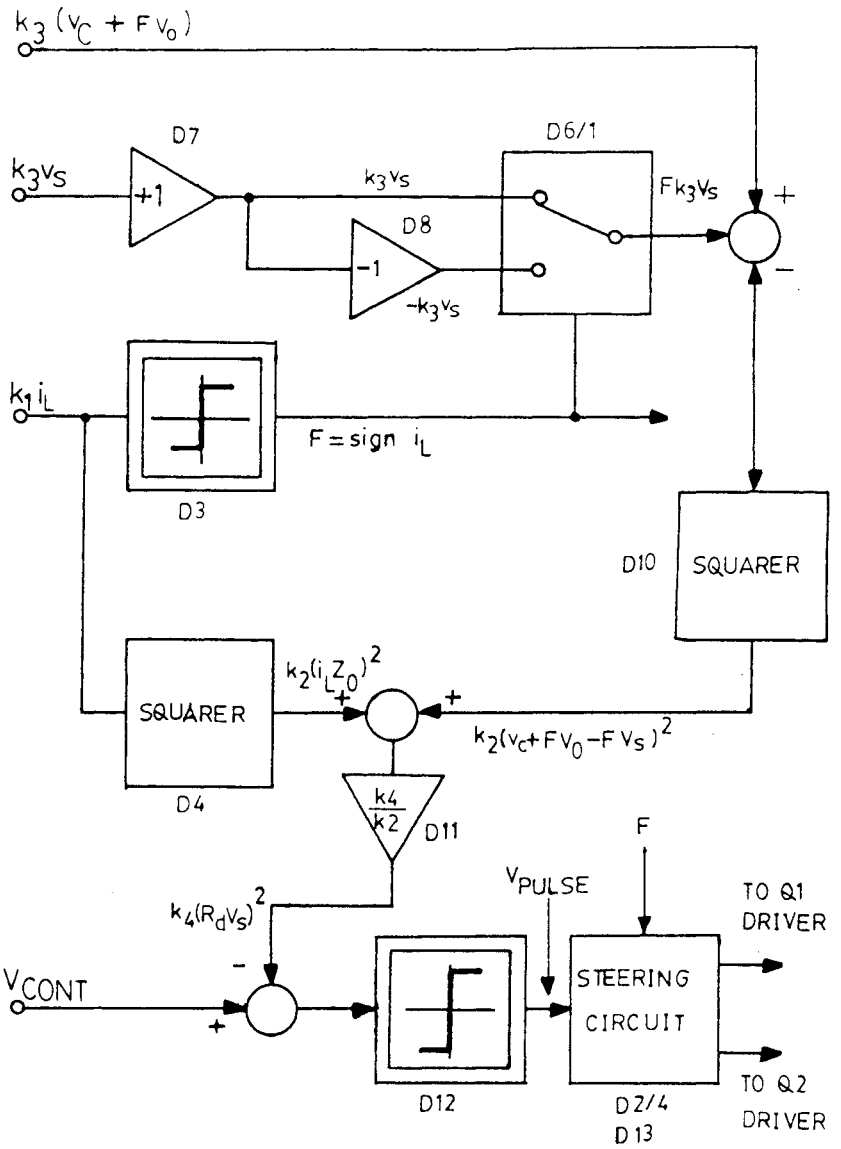

Figure 4.21. Functional block diagram of experimental control circuit

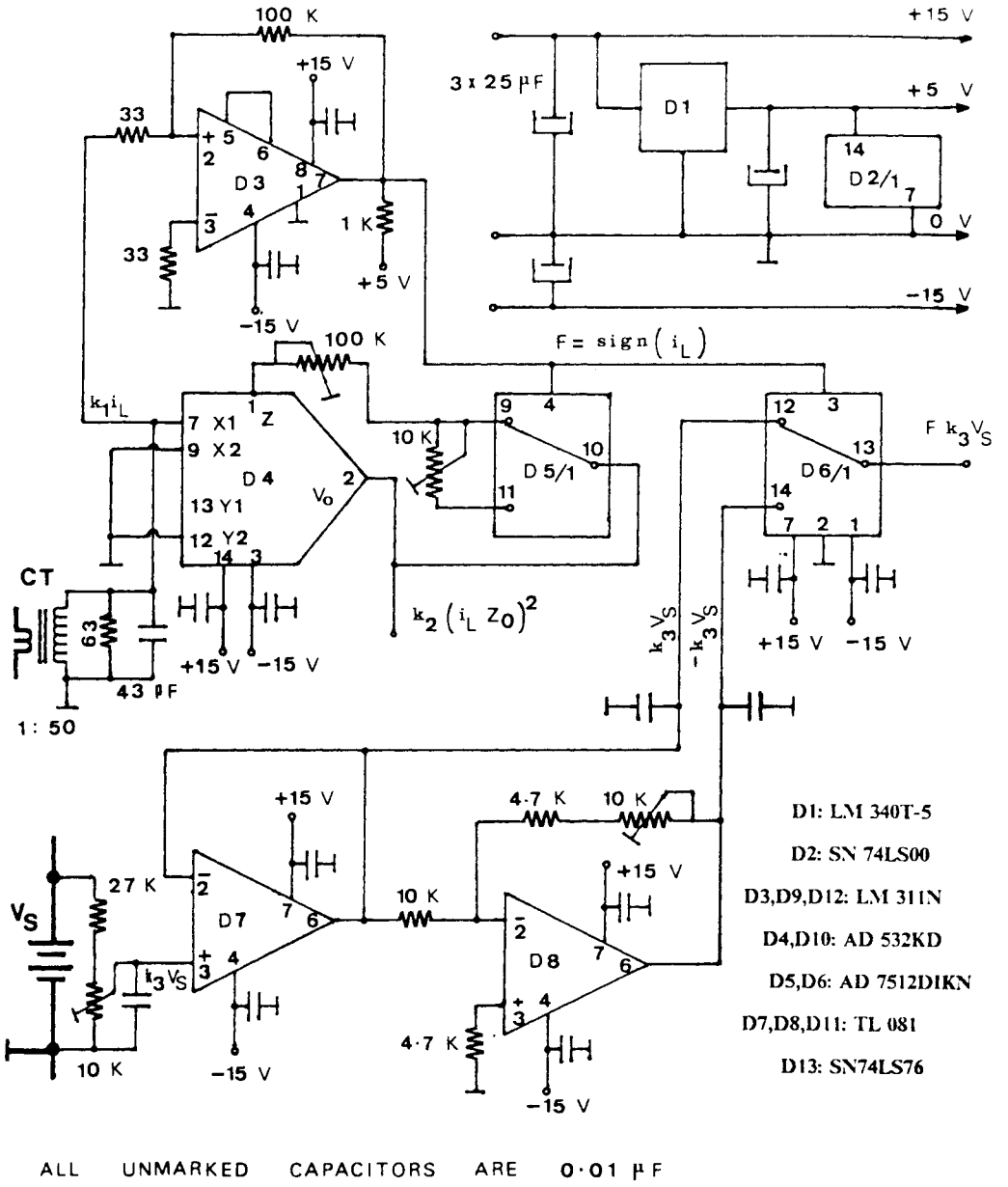

Figure 4.22. Optimal trajectory control circuit diagram

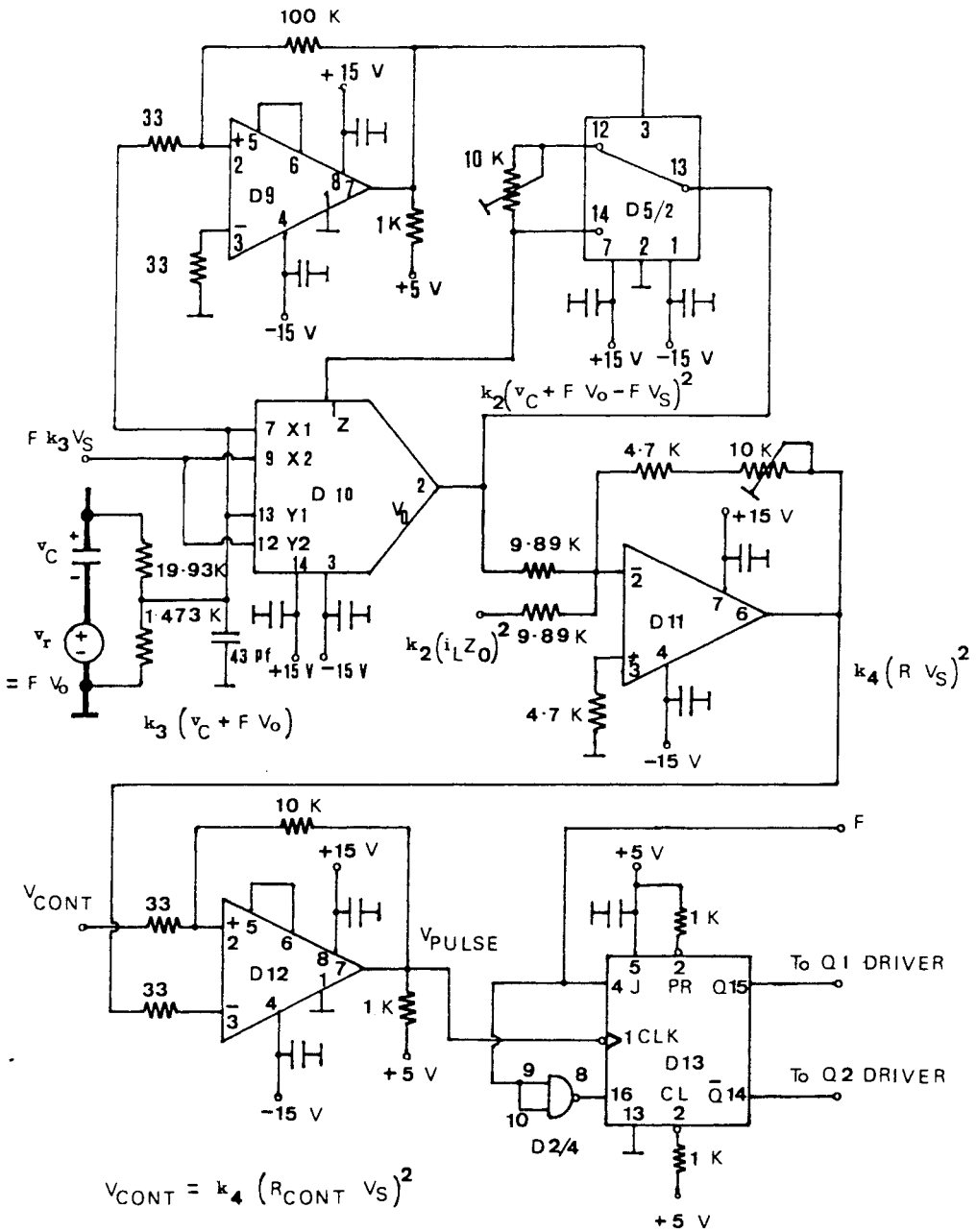

Figure 4.22. (contd.)

is conducting, i_L is positive and signal F enables transistor $Q1$ to be turned on next. Similarly, when diode $D1$ is conducting, i_L is negative and signal F now enables only $Q2$ to be turned on next.

In implementing the control scheme, it was found that the gain of the squarer ($D4$ or $D10$) varied slightly depending on the input polarity. Additional elements, $D5/1$, $D9$ and $D5/2$, are included in the circuit so that the squaring operation can be adjusted to be symmetrical.

Typical control waveforms from the experimental setup are shown in Fig. 4.23. The waveforms of v_C, v_r and $v_C + F\,V_o$, shown in an oscillogram of Fig. 4.23(c), are obtained from the power circuit and not from the control circuit. The oscillograms in Fig. 4.23 are self explanatory and have been arranged according to the computation sequence. They will assist in the understanding of the operation of the control circuit.

In Fig. 4.17, once the transistor is turned on by the control, distance R_d stays at a constant value equal to the control value ($R1$ in Fig. 4.17). In Fig. 4.23(f), the magnitude of signal $k_4\,(R_d\,V_s)^2$ decreases in a ramp-like fashion whenever a diode conducts. The transistor ($Q1$ or $Q2$) is switched on whenever the magnitude of $k_4\,(R_d\,V_s)^2$ falls below control input V_{CONT}. Once a transistor is switched on, the value of R_d must be constant. However, signal $k_4\,(R_d\,V_s)^2$ which depends on R_d, does not remain constant, as seen from Fig. 4.23(f). This is attributed to the inaccuracies involved in experimentally setting the scale factors k_1 , k_2 , etc.

4.5.4 Scaling The Variables

In this subsection, the scaling procedure followed is described. The various settings were mostly done based on visual oscilloscope measurements only. It would be preferable to carry out this scaling using more accurate measuring measurements.

The multipliers used have a nominal scale factor of ten. For device $D10$ connected as a squarer, the actual scale factor was first determined. The output of $D10$ was measured at 3.4 Volts for a differential input of 6 Volts.

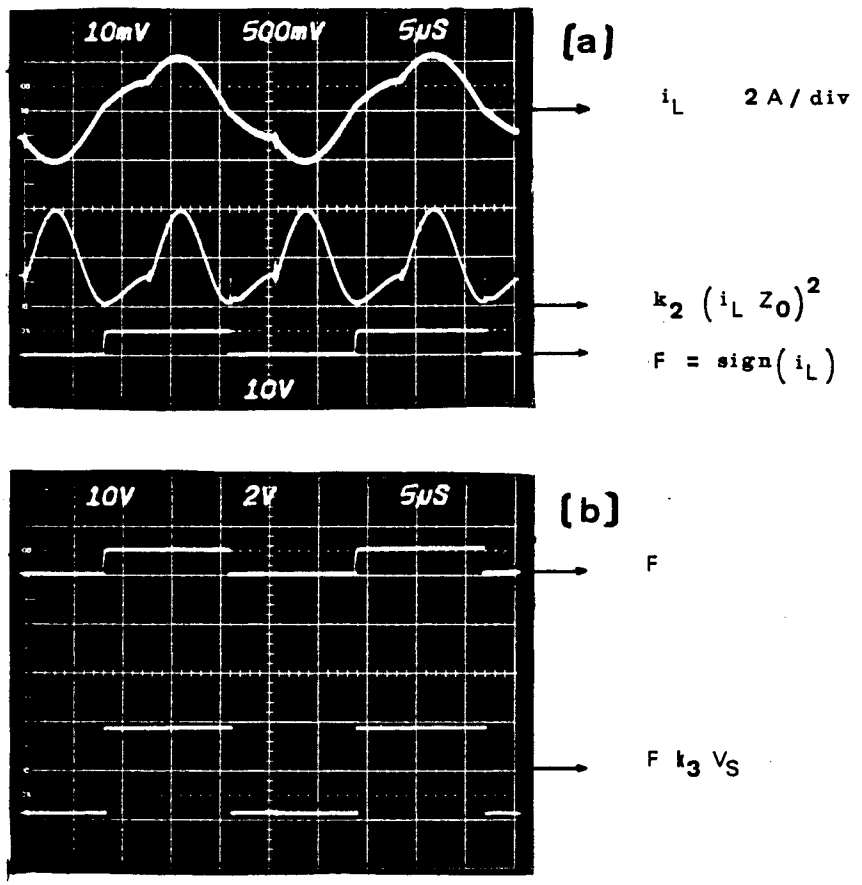

Figure 4.23. Typical control waveforms of optimal trajectory control V_o = 9 V, f = 37.50 kHZ

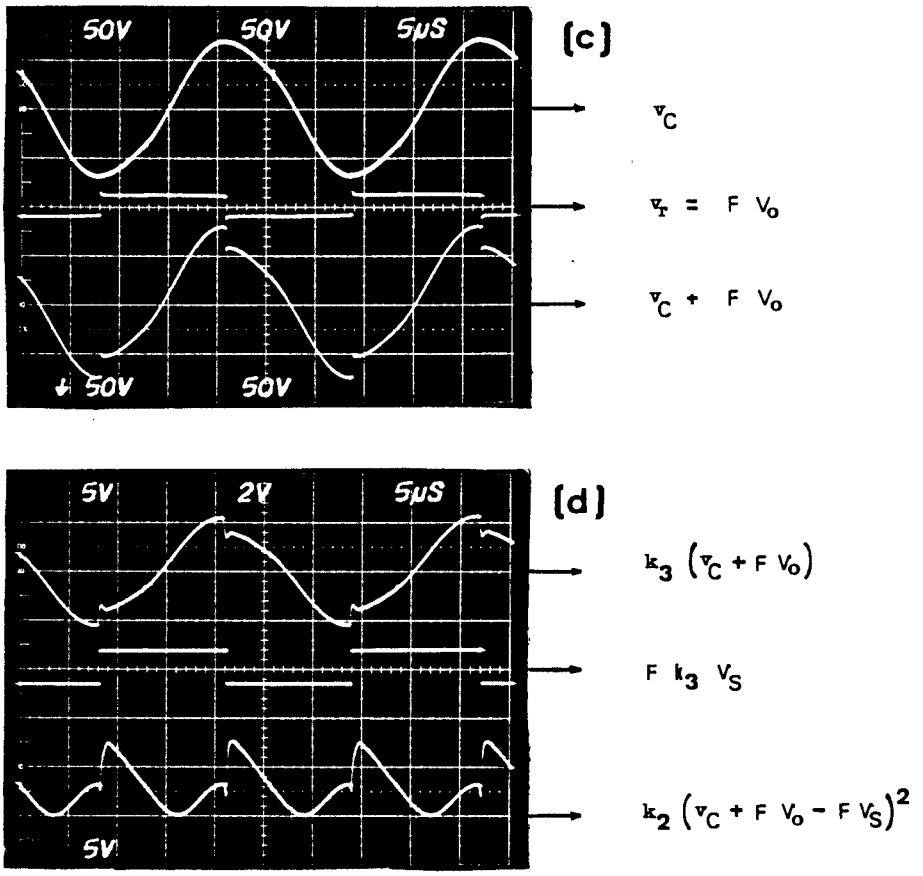

Figure 4.23. (contd.)

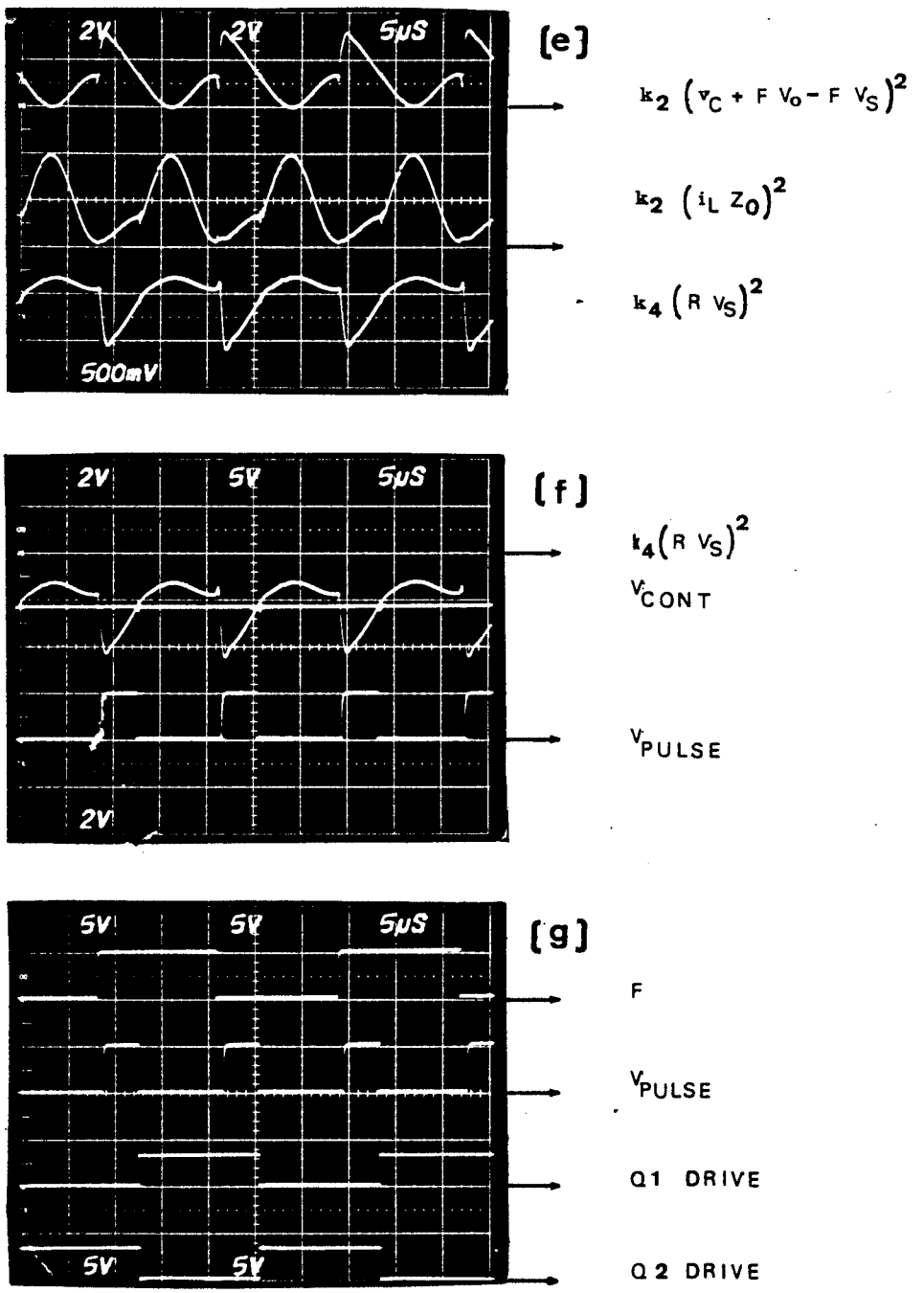

Figure 4.23. (contd.)

$$\text{Thus,} \quad g_M = \text{Scale factor of } D10$$
$$= \frac{6^2}{3.4} = 10.588$$

From Fig. 4.22, scale factor k_3 is determined by the voltage sensor across $(v_C + v_r)$.

$$\text{Therefore,} \quad k_3 = \frac{1.473\ \text{k}}{1.473\ \text{k} + 19.93\ \text{k}} = 0.06882$$

For proper scaling, scale factor k_3 in signal k_3V_s in Fig. 4.22 must also have the above value. Since V_s equals 25 Volts,

$$k_3V_s = 0.06882 \times 25 = 1.720$$

With V_s kept at 25 Volts, the 10 k potentiometer in the V_s sensing network is adjusted such that signal k_3V_s equals 1.720 Volts.

As the next step, scale factor k_2 is determined. For squarer $D10$,

$$k_2 (v_C + FV_o - FV_s)^2 = \frac{\{k_3 (v_C + FV_o - FV_s)\}^2}{g_M}$$

$$\text{Thus,} \quad k_2 = \frac{k_3^2}{g_M} = \frac{(0.06882)^2}{10.588} = 0.0004473$$

For proper scaling, k_2 in signal $k_2(i_LZ_0)^2$ in Fig. 4.22 must have the same value as above. The procedure for ensuring this is described below.

The CT turns ratio is 1:50 and its burden is 63Ω.

$$k_1 = \text{Gain of } CT$$
$$= \frac{63}{50} = 1.26\ \text{Volts/Amp}$$

The SRC was then operated in CCM under frequency control. The optimal trajectory control circuit was also connected. The inputs to the transistor drivers from the optimal trajectory control was, however, disconnected. Signal k_1i_L was displayed on the oscilloscope and its peak value was found to be

$$(k_1i_L)_{PEAK} = 1.9\ \text{Volt}$$

$$\text{Therefore,} \qquad (i_L)_{PEAK} = \frac{1.9}{1.26} = 1.508 \text{ Amp}$$

$$\text{Hence,} \qquad \{k_2 (i_L Z_0)^2\}_{PEAK} = 0.0004473 (1.508 \times 25.9)^2 = 0.682$$

From the above, the peak value of the output signal of squarer *D*4 must equal 0.682 Volt under these conditions. The 100 k potentiometer across *D*4 was varied to achieve this.

Lastly, the gain of *D*11 and, consequently, scaling factor k_4 were arbitrarily set to convenient values through the adjustment of the 10 k feedback potentiometer across *D*11.

4.5.5 Experimental Performance

The control was set as per the method and calculations in Sec. 4.5.4. No fine tuning was done to improve the resulting performance.

Figure 4.24 shows a circuit used to generate the V_{CONT} signal for obtaining the transient response of the system by introducing step changes in control input. If signal V_{ALT} equals +5V, then V_{CONT} equals V_{CONT1}. If V_{ALT} is connected to ground, then V_{CONT} equals V_{CONT2}. By generating V_{ALT} with a square-wave oscillator, V_{CONT} is switched between levels V_{CONT1} and V_{CONT2} at a frequency, f_{SW}, determined by the oscillator.

Figure 4.25 shows a set of oscillograms illustrating the excellent dynamic performance obtained from the experimental setup. In all three cases, (a), (b) and (c), shown in Fig. 4.25, output voltage V_o was set to the same value of 9 Volts by adjusting the load resistor magnitude. For each of the three cases, oscillograms of both the state trajectory and the tank waveforms are shown. In Fig. 4.25(a), V_{CONT}(= V_{CONT1}) was set for a small control radius. The resulting operating frequency, f_1, of the converter was 29.22 kHZ. In Fig. 4.25(b), V_{CONT}(= V_{CONT2}) was set for a large control radius. The corresponding operating frequency, f_2, was 37.50 kHZ. In Fig. 4.25(c), the control was switched back and forth between V_{CONT1} and V_{CONT2}. Thus, Fig. 4.25(c) shows the system transient performance both when the tank energy is increased and when it is decreased. The transient performances in both cases are as

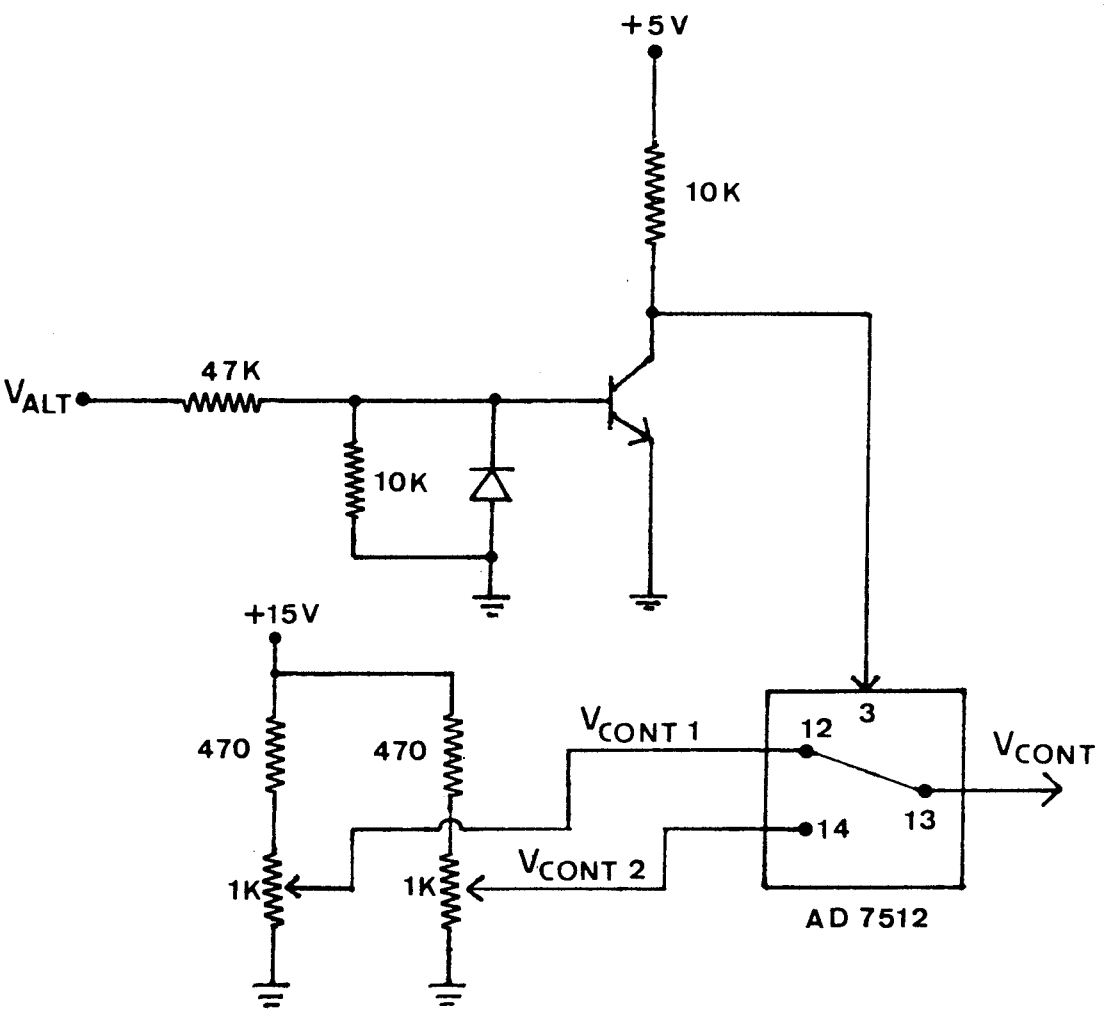

Figure 4.24. Circuit for introducing step-control change

predicted with the system reaching the desired steady state trajectory in minimum time. The tank waveforms in Fig. 4.25(c) also illustrate this phenomenon. Both the inductor current and the capacitor voltage waveforms show virtually abrupt transitions from one steady state to another without overshoot and any apparent transient.

The series of oscillograms in Fig. 4.26 illustrate the performance of the frequency control method under the same conditions. In this case also, the control was switched between the two steady-state conditions (f_1 and f_2) at a lower frequency, f_{SW}. Figure 4.26(a) shows the transient response of the system when the operating frequency is increased from f_1 to f_2. Likewise, Fig. 4.26(b) is for a reduction in operating frequency from f_2 to f_1. In the trajectory oscillogram in Fig. 4.26(a), the transient response from the larger trajectory to the smaller has been suppressed. Similarly, in Fig. 4.26(b), the transition from the smaller to the larger trajectory has been suppressed. These were done by feeding a suitably phase-shifted square-wave voltage at a frequency of f_{SW} to the Z (intensity) modulation terminal at the back of the oscilloscope.

The transient responses in Figs. 4.26(a)-(b) show the oscillatory nature of the response with the system taking several cycles to settle at the new steady-state trajectory. When contrasted with optimal trajectory control, the inferior dynamic performance of the frequency control method is clearly observed.

The good response of optimal trajectory control was obtained over a wide range of load and operating frequency. The minimum and maximum operating frequency limits, however, were dependent on the load. Operating frequencies as low as 25.5 kHz (ω_N = 0.51) and as high as 45.0 kHz (ω_N = 0.90) were reached in the experimental set up. The upper frequency limit can be increased by 1) fine tuning the experimental set-up and 2) reducing the time delays in the control circuit by using faster components.

Figure 4.27(a) shows the operation of the system for large control changes both for trajectory energy increase and for energy reduction. The tank waveforms under the dynamic conditions are also shown in Fig. 4.27(a). Greater deviation from the ideal performance may be observed in these oscillograms, though the response of the system is still very good. When the trajectory energy is increased in Fig. 4.27(a), the system takes more than a resonant half-cycle to reach the desired trajectory as anticipated in Fig. 4.19(a). The tank waveforms for frequency control under similar large control changes are shown in Figs. 4.27(b) and (c) for comparison. As anticipated, the response in this case is extremely oscillatory and slow.

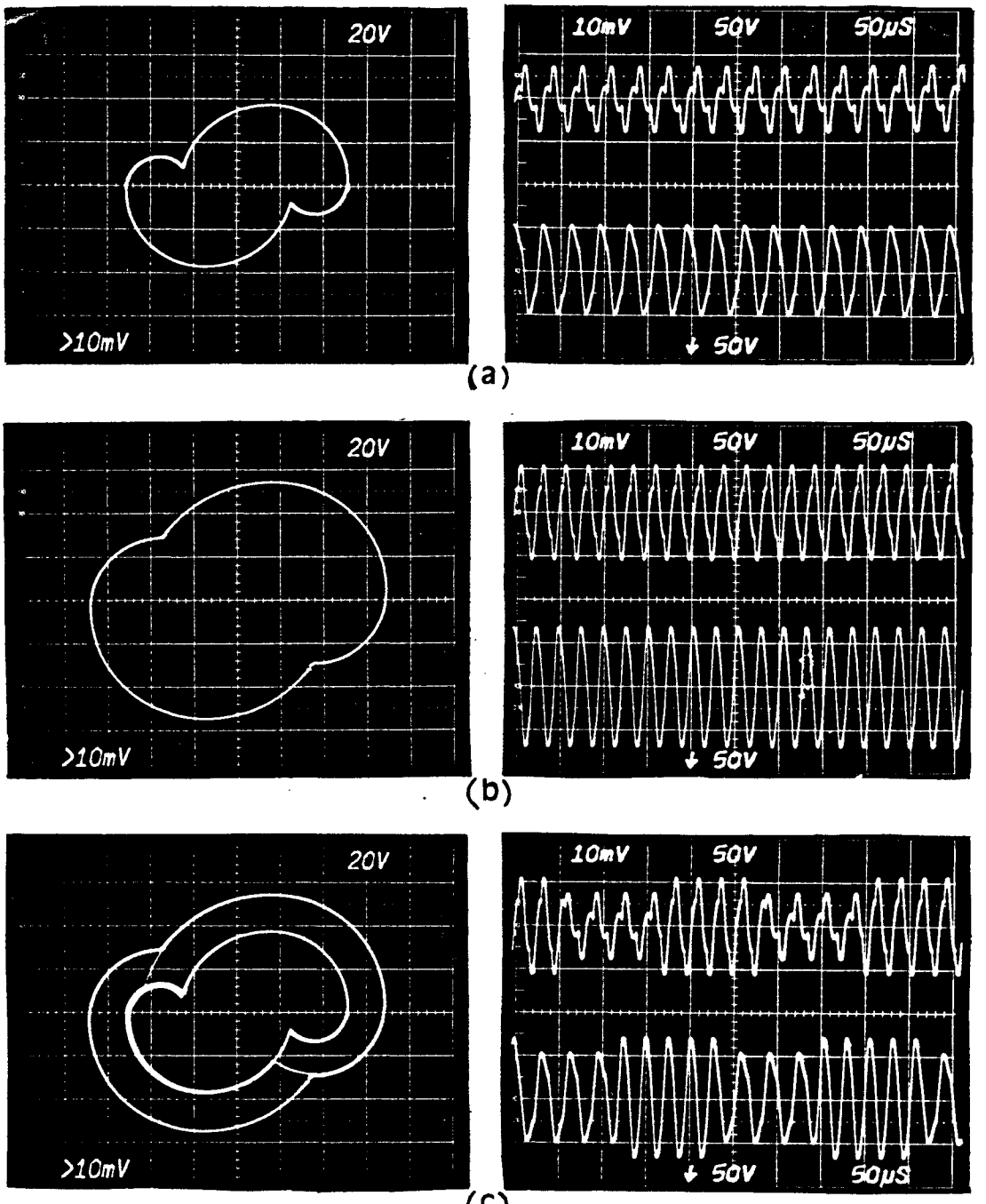

Figure 4.25. Transient response for step-change in control - Optimal trajectory control
a) f_1 b) f_2 c) f switches between f_1 and f_2; (V_o = 9 V f_1 = 29.22 kHZ f_2 = 37.50 kHZ)

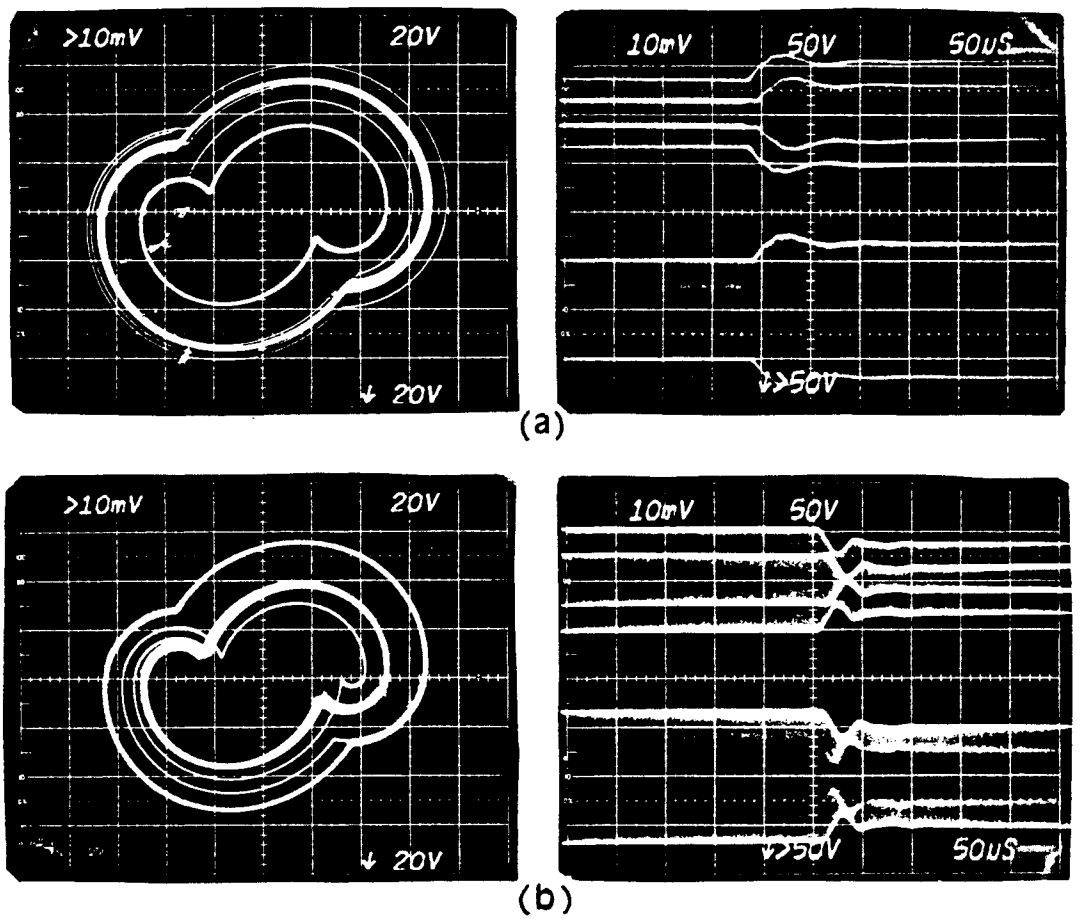

Figure 4.26. Transient response for step-control change - Frequency control
V_o = 9 V f_1 = 29.22 kHZ f_2 = 37.50 kHZ
a) f switched from f_1 to f_2 b) f switched from f_2 to f_1

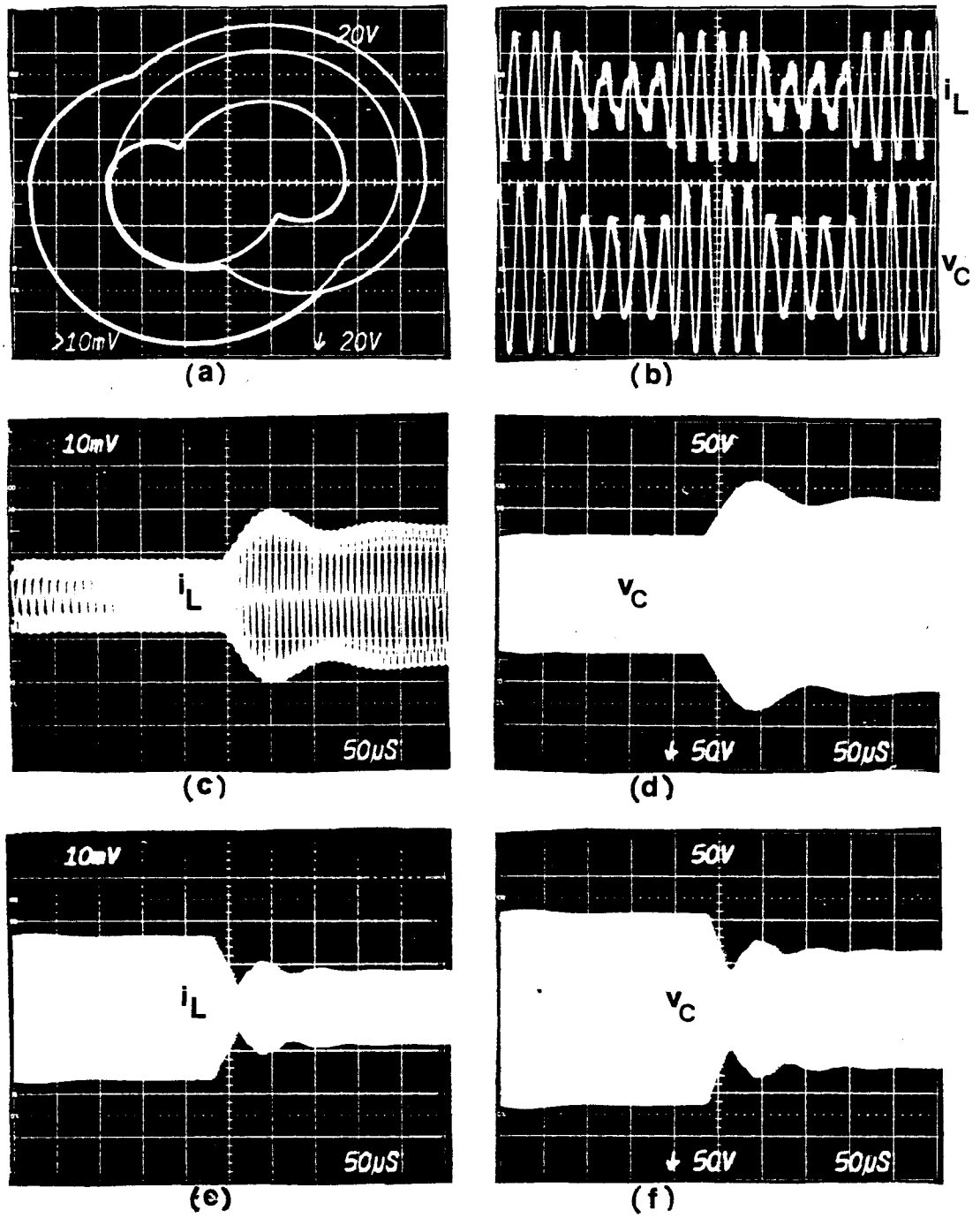

Figure 4.27. Transient performance for large tank energy changes
a) & b) Optimal trajectory control - f_1 = 32.0 kHz, f_2 = 41.67 kHz, V_o = 7.3 V
c), d), e) &f) Frequency control - f_1 = 34.07 kHz, f_2 = 41.76 kHz, V_o = 4.0 V

Scale:- For waveforms in b), through f) - x: 50 μs/div
a) x: 20 V/div, y: 0.774 A/div
b) c) & e) i_L : 2 A/div
b)i_L : 2 A/div, v_C : 50 V/div
d) & f) v_C : 50 V/div

4.6 Conclusions

The state-plane technique was shown to be a powerful tool in providing a basis for understanding the characteristics of resonant converter control. Using this analysis method, different control techniques for a SRC were identified. Among the existing control methods, ASDTIC control, previously suggested for resonant converters, was shown to result in an unstable system under certain conditions. Employing the state-plane analysis, three existing methods, capacitor-voltage control, frequency control, diode-conduction-angle control and a new method, named optimal trajectory control, were evaluated for properties, such as stability, response to control changes and performance under a short circuit.

Optimal trajectory control was proposed based on the insight gained from the state-plane analysis. By utilizing the required transistor trajectory itself as the control law, this control method attempts to reach its steady-state operation in a nonasymptotic and time-optimal manner. The control automatically selects the optimum sequence of device conduction under all dynamic conditions. Also, since the control predetermines its operating trajectory, the resonant tank is fully controlled with the tank energy, inductor current and capacitor voltage, all staying within bounds under all circumstances, including a short circuit across the output terminals of the converter.

An implementation scheme, for this new control method was presented. The scheme implemented in this chapter reduces the complexity of the control method by making efficient use of the control circuit elements. The scaling procedure followed to determine and set the scaling factors in the control scheme was also described. The transient performance of the experimental setup was excellent as predicted. Comparison with the frequency control method was made to confirm superior dynamic performance of the new optimal trajectory control.

Chapter 5

DC Analysis Of Parallel Resonant Converter

5.0 Symbols Of Variables

The symbols listed below include those used in Appendix C also. In alphabetical order,

α	-	Conduction Angle During M2 or M4 Topological Mode
α_d	-	Diode Conduction Angle
α_q	-	Transistor Conduction Angle
β	-	Conduction Angle During M1 or M3 Topological Mode
Δi_L	-	Change in Inductor Current
Δi_{LN}	-	Normalized Change in Inductor Current
Δt	-	Change in Time
Δv_C	-	Change in Capacitor Voltage
Δv_{CN}	-	Normalized Change in Capacitor Voltage
ρ	-	Radius of a State Trajectory
θ	-	Angular Interval on State Plane

θ_0	-	Initial Angle on State Plane
$\theta_1, \theta_2, ..$	-	Different Angular Intervals on State-Plane
θ_{XY}	-	Angular Interval between X and Y on State Plane
τ	-	Maximum Pulse Width of Base Drive in Strategy-2
ω	-	Operating Frequency
ω_0	-	Resonant Frequency of the *LC* Circuit
ω_{DISC}	-	Normalized DCM Boundary Frequency
ω_{HIGH}	-	Normalized Upper CCM Boundary Frequency
ω_{LIMIT}	-	Normalized Limit Mode Boundary Frequency
ω_{LOW}	-	Normalized Lower CCM Boundary Frequency
ω_{MAX}	-	Normalized Boundary Frequency Between Intersections-1 & 2
ω_{MUL}	-	Normalized Multiple Region Boundary Frequency
ω_N	-	Normalized Operating Frequency
ω_{TRAN}	-	Normalized Boundary Frequency Between TM1 And TM2
C	-	Value of Resonant Capacitor
d	-	Instantaneous Distance of State from Origin
I_{DAV}	-	Average Diode Current
I_{DAVN}	-	Normalized Average Diode Current
I_E	-	Equivalent Load Current
I_{EN}	-	Normalized Equivalent Load Current
I_{QAV}	-	Average Transistor Current
I_{QAVN}	-	Normalized Average Transistor Current
i_I	-	Instantaneous Current to Ouput Bridge Rectifier
i_L	-	Instantaneous Resonant Inductor Current
I_{LAV}	-	Half-Cycle Average Inductor Current
I_{LAVN}	-	Normalized Half-Cycle Average Inductor Current
i_{IN}	-	Normalized Instantaneous Current to Ouput Bridge Rectifier
i_{LN}	-	Normalized Instantaneous Inductor Current
I_{L0}	-	Initial Inductor Current
I_{L0N}	-	Normalized Initial Inductor Current
I_{L1}	-	i_L when M1 Trajectory Reaches Vertical Axis
I_{L1N}	-	Normalized Value of I_{L1}

I_{L2}	-	i_L when M1 and M2 trajectories intersect
I_{L2N}	-	Normalized Value of &*IL*2.
I_{LP}	-	Peak Inductor Current
I_{LPN}	-	Normalized Peak Inductor Current
I_o	-	Output DC Current
I_{oN}	-	Normalized Output DC Current
I_{XAV}	-	Average Current of Device X
I_{XAVN}	-	Normalized Average Current of Device X
L	-	Value of Resonant Inductor
N_i	-	Current Normalizing Factor
N_v	-	Voltage Normalizing Factor
R	-	Radius of M2 or M4 Trajectory
R'	-	Radius of M1 or M3 Trajectory
R_{max}	-	Maximum Value of R
R_{min}	-	Minimum Value of R
t	-	Time
T	-	Operating Period
$t_1, t_2, .. t_A, t_B, ..$	-	Particular Instants of Time
t_0	-	Initial Time
T_N	-	Angular Operating Period
t_{on}	-	ON Duration of Transistor Base Drive
t_{XY}	-	Time Interval Between Points X and Y on State-Plane
v_C	-	Instantaneous Resonant Capacitor Voltage
$V_{CA1.}$	-	Capacitor Voltage at $t = t_{A1}$
V_{CA1N}	-	Normalized Capacitor Voltage at $t = t_{A1}$
V_{CAV}	-	Half-Cycle Average Capacitor Voltage
V_{CAVN}	-	Normalized Half-Cycle Average Capacitor Voltage
V_{CB1}	-	Capacitor Voltage at $t = t_{B1}$
$V_{CB1N.}$	-	Normalized Capacitor Voltage at $t = t_{B1}$
v_{CN}	-	Normalized Instantaneous Capacitor Voltage
V_{C0}	-	Initial Capacitor Voltage
V_{C0N}	-	Normalized Initial Capacitor Voltage

V_{CP} - Peak Capacitor Voltage

V_{CPN} - Normalized Peak Capacitor Voltage

V_E - Equivalent Driving Voltage

V_{EN} - Normalized Equivalent Driving Voltage

v_L - Instantaneous Voltage Across Inductor

v_{LN} - Normalized Instantaneous Voltage Across Inductor

V_o - Output DC Voltage

V_{oN} - Normalized Output DC Voltage

V_s - Supply DC Voltage

(VS) - Volt-Seconds Across Inductor

$(VS)_N$ - Normalized Volt-Seconds Across Inductor

$(VS)_P$ - Peak Volt-Seconds Across Inductor

$(VS)_{PN}$ - Normalized Peak Volt-Seconds Across Inductor

Z_0 - Characteristic Impedance of Resonant Tank

5.1 Introduction

The parallel resonant converter (**PRC**) is another popular member of the resonant converter family. In a PRC, the load circuit is connected across the resonant capacitor (Fig. 5.1) instead of in series as in a series resonant converter. Strictly, the name parallel load-capacitor link resonant converter is more appropriate for this topology. However, the name parallel resonant converter has also been used in the literature and is more convenient and, hence, it is utilized in the present work.

We noted in Sec. 2.3 that the behavior of a SRC resembles that of a current source to a certain extent. In a similar fashion, the PRC functions somewhat like a voltage source. Thus, in voltage regulator applications, PRC may be expected to require much less operating frequency range than the SRC to compensate for load variations and is the superior configuration.

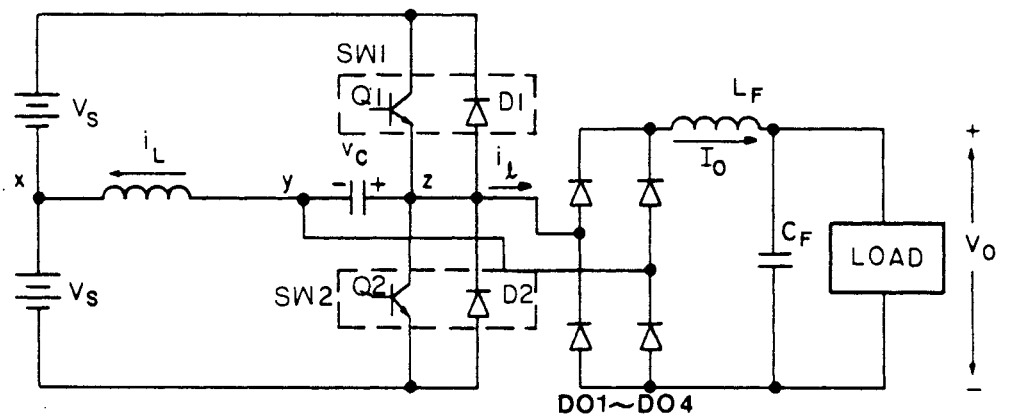

Figure 5.1. A half-bridge parallel resonant converter (PRC)

While the steady state and the dynamic properties of a SRC have been analyzed in recent literature, the analysis of PRC is scarce and has been limited to only continuous-conduction mode of operation [21]. The various modes of operation that occur when load current and operating frequency are changed have not been understood owing to the complexity of PRC operation and to the lack of an appropriate analytical tool to tackle the problem.

In this chapter, a detailed, graphical, state-plane analysis of a PRC is carried out. The analysis reveals, for the first time, the presence of a variety of modes of operation including some hitherto unknown and establishes the boundaries between them. Using the state-plane diagrams the operation of the converter in the different regions are fully explored.

A novel resonant converter circuit, named **resonant buck converter** is derived from the state-plane analysis of a PRC. This circuit may be viewed as a resonant analog of the buck-type converter. It possesses many desirable properties. For example, the voltage-transfer ratio varies almost linearly with the control frequency and is almost load-independent, unlike most resonant converters. Since both turn-on and turn-off losses are eliminated, the new converter circuit can operate at very high frequencies.

The resonant buck converter is, in fact, a member of a class of resonant converters termed **Quasi-Resonant Converters (QRC)** [61]. Chapter 6 carries out a generalized state-plane analysis of the basic QRCs and all their topological variations.

Certain symbols used in [60] have been altered in this chapter primarily to make them consistent with those in Chapter 2. Thus transistors T1 and T2 (Fig. 1 of [60]) have been renamed as Q1 and Q2, respectively. Also, the bidirectional switches Q1 and Q2 in [60] have been renamed as SW1 and SW2, respectively.

5.2 *Ideal State-Plane Analysis*

Fig. 5.1 shows the circuit diagram of a half-bridge version of a PRC. The state-plane analysis is simplified by assuming that 1) current of the output filter inductor, I_o , is constant and 2) circuit losses are negligible. The first assumption is justified since the operating frequency of the inverter is usually much higher than the corner frequency of the output filter. Thus, in one switching cycle, I_o is essentially constant. Since a tank circuit with a high quality factor is desirable in practical design, the second assumption also is generally reasonable. However, under certain operating conditions, such as when the operating frequency is close to the resonant frequency, the effect of parasitic losses tend to be more pronounced and the analysis will only be approximately correct.

5.2.1 Resonant Topological Modes

In this chapter, the term **mode**, when used alone, refers to the circuit mode of operation under steady state, such as continuous-conduction mode or discontinuous-conduction mode. The term **topological mode**, on the other hand, refers to a particular equivalent circuit assumed by the converter during a certain interval of operation.

The transistor, Q1, and its antiparallel diode, D1, (Fig. 5.1) together act as a bidirectional switch, termed SW1. Likewise, Q2 and D2 act as another bidirectional switch, SW2. Depending on whether SW1 or SW2 is on, the voltage across "zx" in the circuit is either $+ V_s$ or $- V_s$. Also, depending on the polarity of v_C, the link current, i_l , is either $+ I_o$ or $- I_o$.

The resulting four resonant topological modes (M1 through M4) are shown in Fig. 5.2. Figure 5.3 shows a common equivalent circuit for these four topological modes along with the values of the equivalent source voltage, V_E , and the equivalent load current, I_E. Figure 5.4 shows the circuit waveforms under continuous-conduction mode of operation (**CCM**) to illustrate the occurrence of these topological modes. In Fig. 5.4, during the interval (0 to t'_1) a single device Q1 conducts. However, two topological modes, M1 and M2, occur. On the contrary, interval (t_1 to t_2) is associated with a single topological mode, M2,

though two devices, Q1 and D1, conduct. Thus, in a PRC, the topological modes and the device conduction intervals do not uniquely correspond to each other, unlike in a SRC. These four resonant topological modes are adequate to describe the operation in CCM. Five additional, nonresonant, topological modes exist under other operating conditions and will be discussed in Sec. 5.2.5.

5.2.2 State Portrait Development

The development of the state portrait in this section follows the lines established in Sec. 2.2.4. The network equations for the circuit in Fig. 5.3 are

$$\begin{bmatrix} \dot{v}_C \\ \dot{i}_L \end{bmatrix} = \begin{bmatrix} 0 & \frac{1}{C} \\ \frac{-1}{L} & 0 \end{bmatrix} \begin{bmatrix} v_C \\ i_L \end{bmatrix} - \begin{bmatrix} 0 & \frac{1}{C} \\ \frac{-1}{L} & 0 \end{bmatrix} \begin{bmatrix} V_E \\ I_E \end{bmatrix} \tag{5.1}$$

with initial conditions $i_L/_{(t=t_0)} = I_{L0}$ and $v_C/_{(t=t_0)} = V_{C0}$.

The single equilibrium point (center) of the system described by (5.1) is at $v_C = V_E$ and $i_L = I_E$. Let,

$$Z_0 = \sqrt{\frac{L}{C}} = \text{characteristic impedance (ohms)} \tag{5.2}$$

$$\omega_0 = \frac{1}{\sqrt{LC}} = \text{resonant frequency (radians/sec)} \tag{5.3}$$

and

$$\theta = \omega_0 (t - t_0) = \text{angular interval (radians)} \tag{5.4}$$

Solving (5.1) and utilizing (5.2), (5.3) and (5.4),

$$\begin{aligned} v_C - V_E &= (I_{L0} - I_E) Z_0 \sin\theta + (V_{C0} - V_E) \cos\theta \\ i_L - I_E &= (I_{L0} - I_E) \cos\theta - \frac{(V_{C0} - V_E)}{Z_0} \sin\theta \end{aligned} \tag{5.5}$$

The voltage and current normalizing factors are

$$\begin{aligned} N_v &= \text{Voltage Normalizing Factor} \\ &= V_s \end{aligned} \tag{5.6}$$

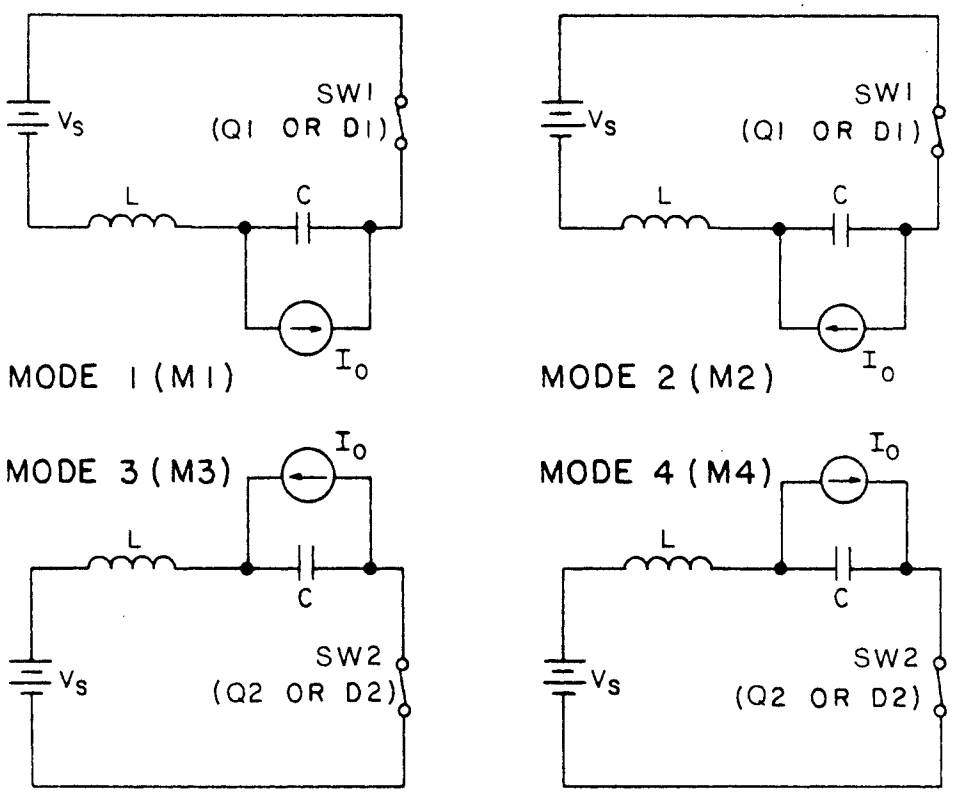

Figure 5.2. Resonant topological modes of a PRC

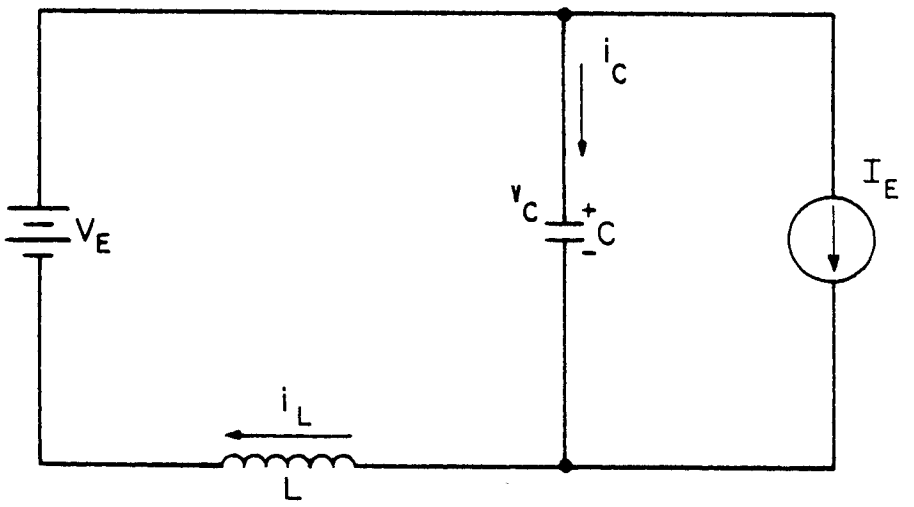

TOPOLOGICAL MODE	UNDER CONDITIONS	V_E	I_E
M1	SW1'ON' & v_c–ve	V_s	$-I_o$
M2	SW1'ON' & v_c+ve	V_s	$+I_o$
M3	SW2'ON' & v_c+ve	$-V_s$	$+I_o$
M4	SW2'ON' & v_c–ve	$-V_s$	$-I_o$

Figure 5.3. Common equivalent circuit for different resonant intervals

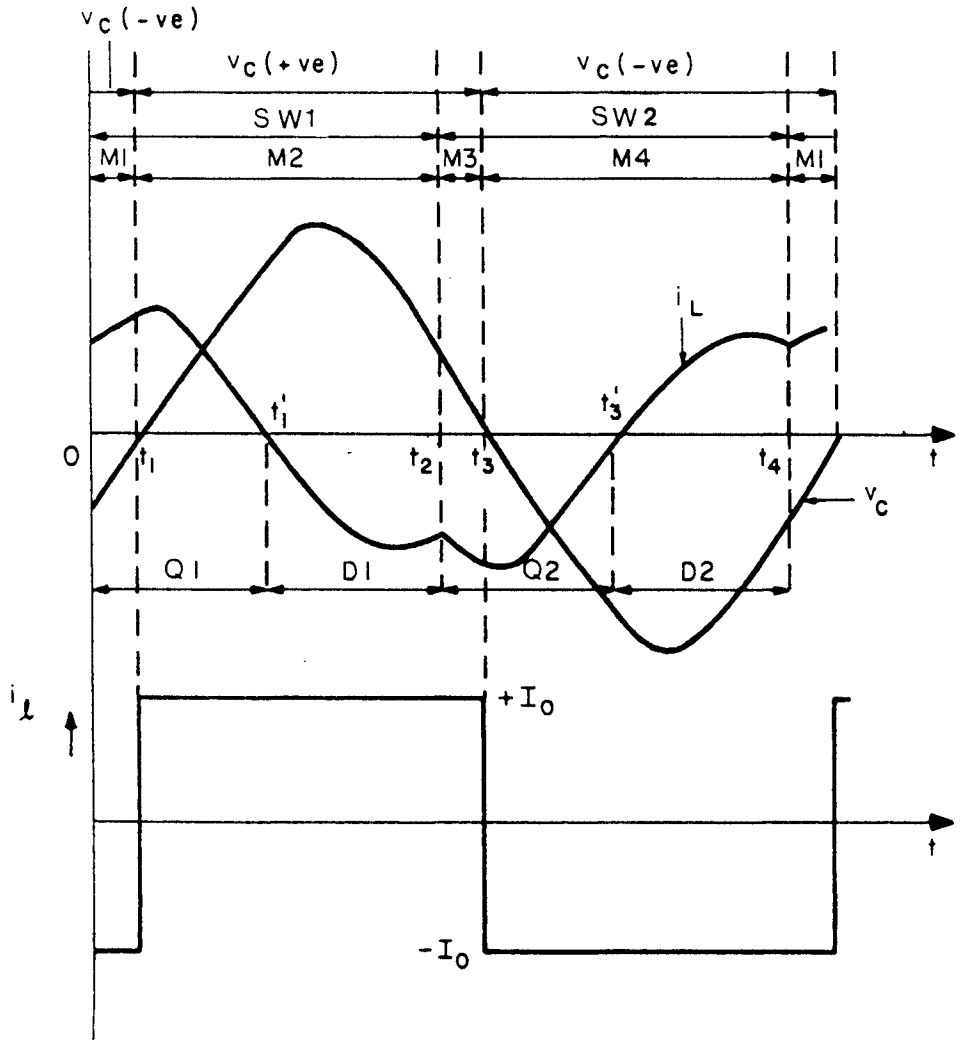

Figure 5.4. Continuous-conduction mode (CCM) waveforms - $I_{oN} < 1$, $\omega_N < 1$

$$N_i = \text{Current Normalizing Factor} = \frac{V_s}{Z_0} \tag{5.7}$$

Normalizing all currents and all voltages with these factors, (5.5) can be written as

$$\begin{aligned} v_{CN} - V_{EN} &= (I_{LON} - I_{EN}) \sin\theta + (V_{CON} - V_{EN}) \cos\theta \\ i_{LN} - I_{EN} &= (I_{LON} - I_{EN}) \cos\theta - (V_{CON} - V_{EN}) \sin\theta \end{aligned} \tag{5.8}$$

The subscript N in (5.8) refers to normalized circuit variables.

By eliminating θ in (5.8) the equation for the state trajectory is

$$(i_{LN} - I_{EN})^2 + (v_{CN} - V_{EN})^2 = (I_{LON} - I_{EN})^2 + (V_{CON} - V_{EN})^2 = \rho^2 \tag{5.9}$$

$$\text{Also,} \qquad \theta = \tan^{-1}\left\{ -\frac{(i_{LN} - I_{EN})}{v_{CN} - V_{EN}} \right\} - \theta_0, \qquad \text{where} \tag{5.10}$$

$$\theta_0 = \tan^{-1}\left\{ -\frac{(I_{LON} - I_{EN})}{V_{CON} - V_{EN}} \right\} \tag{5.11}$$

The state trajectories are circles with radius ρ , which depends on the initial conditions, and with their center located at (V_{EN} , I_{EN}). The time elapsed between two points on the circular trajectory is proportional to the angle subtended at its center.

Based on (5.9), four sets of state trajectories, one for each of the four topological modes, are shown in Figs. 5.5(a)-(d), along with their corresponding mode centers. The symbols M1, M2, M3 and M4 are used to denote voth the topological modes and the centers of the trajectories on the state plane corresponding to these topological modes. Since each topological mode corresponds to only one polarity of v_C , the corresponding set of trajectories extends to only one half of the $v_{CN} - i_{LN}$ plane. By combining these sets of trajectories, a composite state portrait, which completely characterizes the PRC at a given load current, can be constructed as in Fig. 5.6. As shown in Sec. 2.2.4, the instantaneous energy of the resonant tank is proportional to d^2, where "d" is the distance between the current state of the tank and the origin. Thus, the size of the trajectory directly indicates the tank energy level. An interesting feature

of the PRC state portrait is that the tank energy does not always increase uniformly when a transistor (Q1 in M2 or Q2 in M4) conducts. This is unlike the case with the state portrait of SRC.

5.2.3 Steady-State Trajectories

The normalized operating frequency is given by,

$$\omega_N = \frac{\omega}{\omega_0}, \tag{5.12}$$

where ω is the operating frequency.

$$\text{Also,} \qquad I_{oN} = \text{Normalized load current} = \frac{I_o Z_0}{V_s} \tag{5.13}$$

For a given ω and I_{oN}, a closed steady-state trajectory curve that corresponds to the steady-state waveforms can be drawn on the state plane. Figures 5.7(a) and 5.7(b) are examples of steady-state trajectories in the CCM when $I_{oN} = 0.5$. Figure 5.7(a) is applicable when $\omega_N < 1$ and Fig. 5.7(b) when $\omega_N > 1$. Waveforms corresponding to Fig. 5.7(a) and Fig. 5.7(b) are shown in Fig. 5.4 and Fig. 5.8, respectively.

The topological mode sequence in Fig. 5.7(a) and Fig. 5.7(b), in fact for all CCM operations, is M1, M2, M3 and M4. However, the device sequence is Q1, D1, Q2 and D2 in Fig. 5.7(a) while it is Q1, D2, Q2 and D1 in Fig 5.7(b). In Fig. 5.7(a), the transistors are naturally commutated and the diodes are force commutated. In Fig. 5.7(b), it is the diodes which are self-commutated and the transistors are force commutated. In general, the larger trajectories correspond to higher tank energy levels and larger output voltages. In Fig. 5.7(a), the trajectory size increases with frequency, whereas in Fig. 5.7(b) the trajectory size decreases with frequency. In both diagrams, the trajectory size ideally approaches infinite proportions when the operating frequency approaches the resonant frequency.

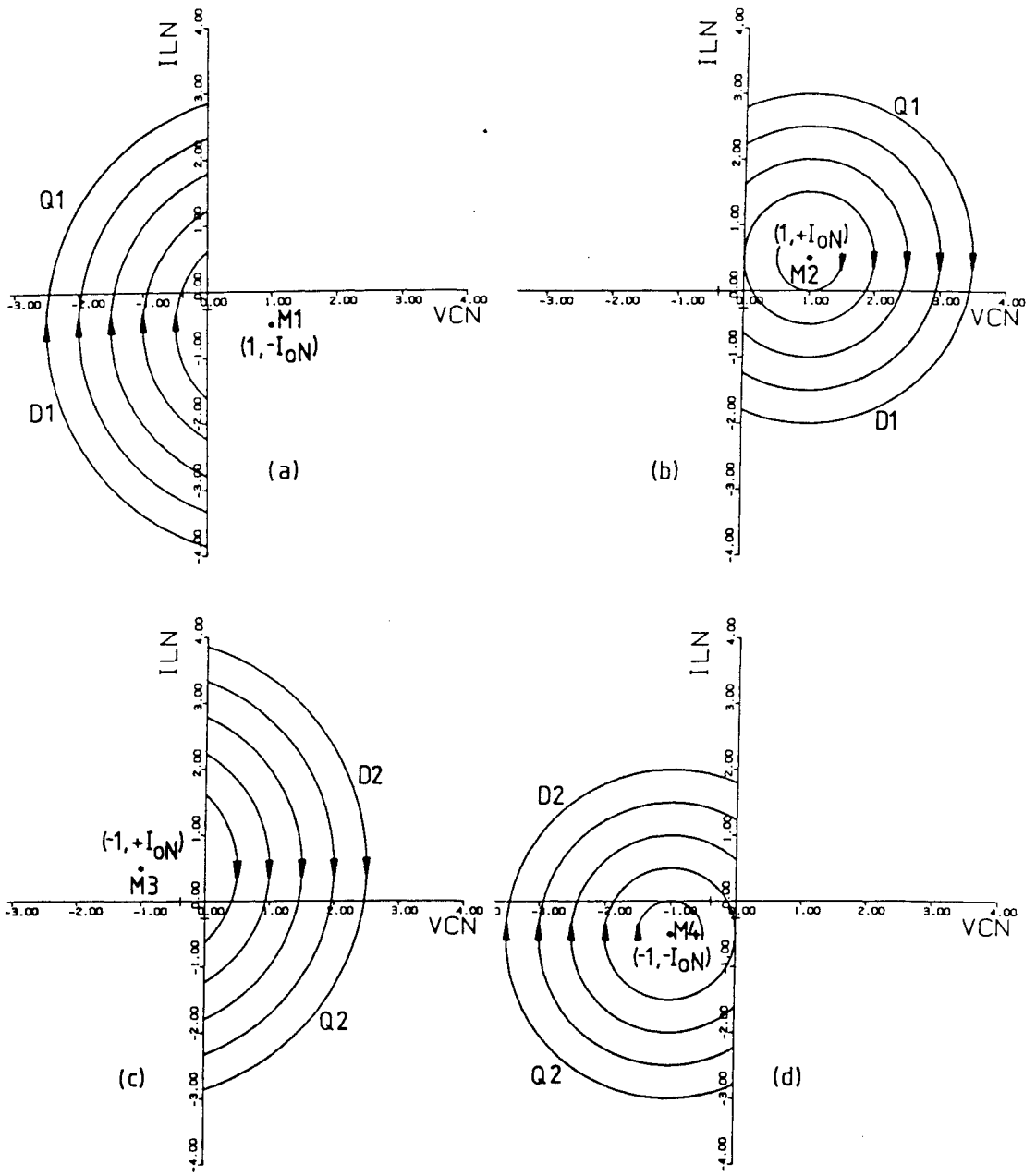

Figure 5.5. State trajectories under different resonant topological modes (I_{oN} = 0.5)
a) M1 Trajectories
b) M2 Trajectories
c) M3 Trajectories
d) M4 Trajectories

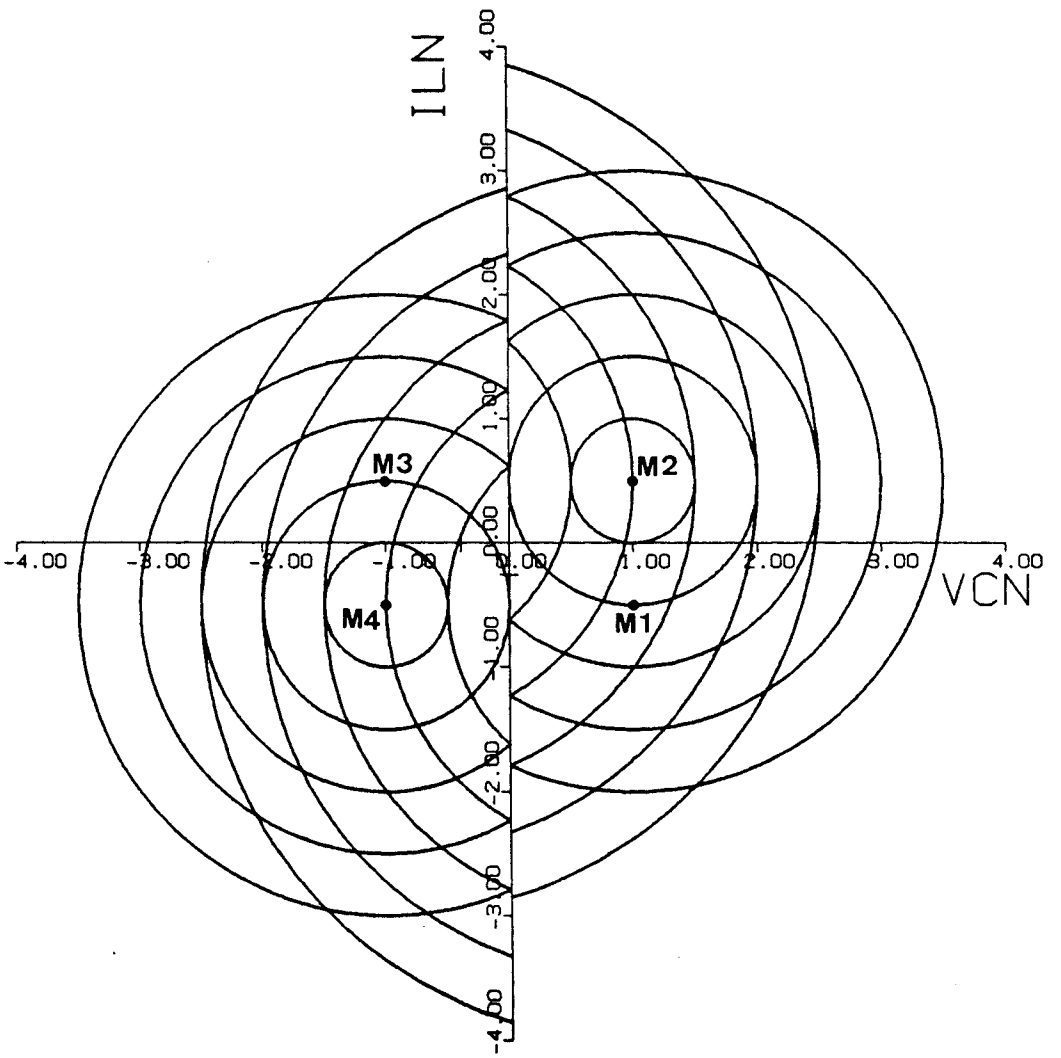

Figure 5.6. Composite state portrait of a PRC (I_{oN} = 0.5)

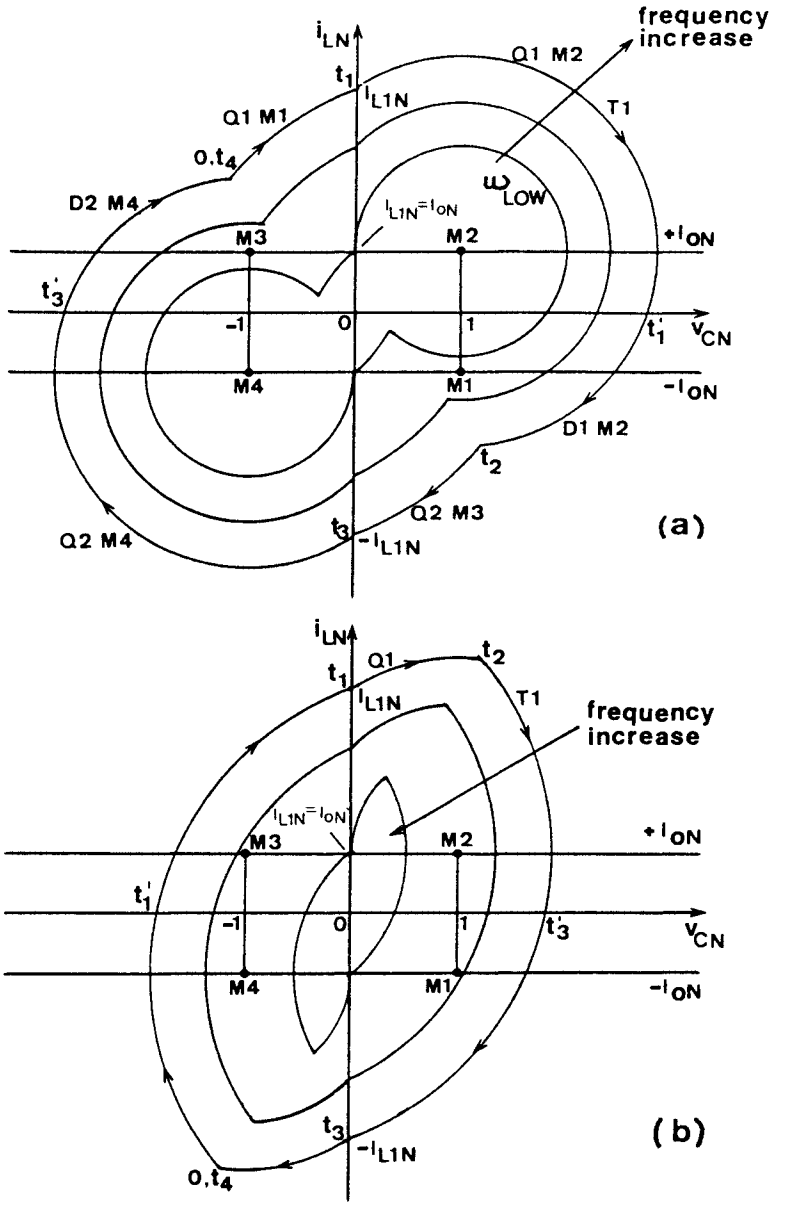

Figure 5.7. CCM steady-state trajectories - $I_{oN} < 1$

a) Below resonant frequency b) Above resonant frequency

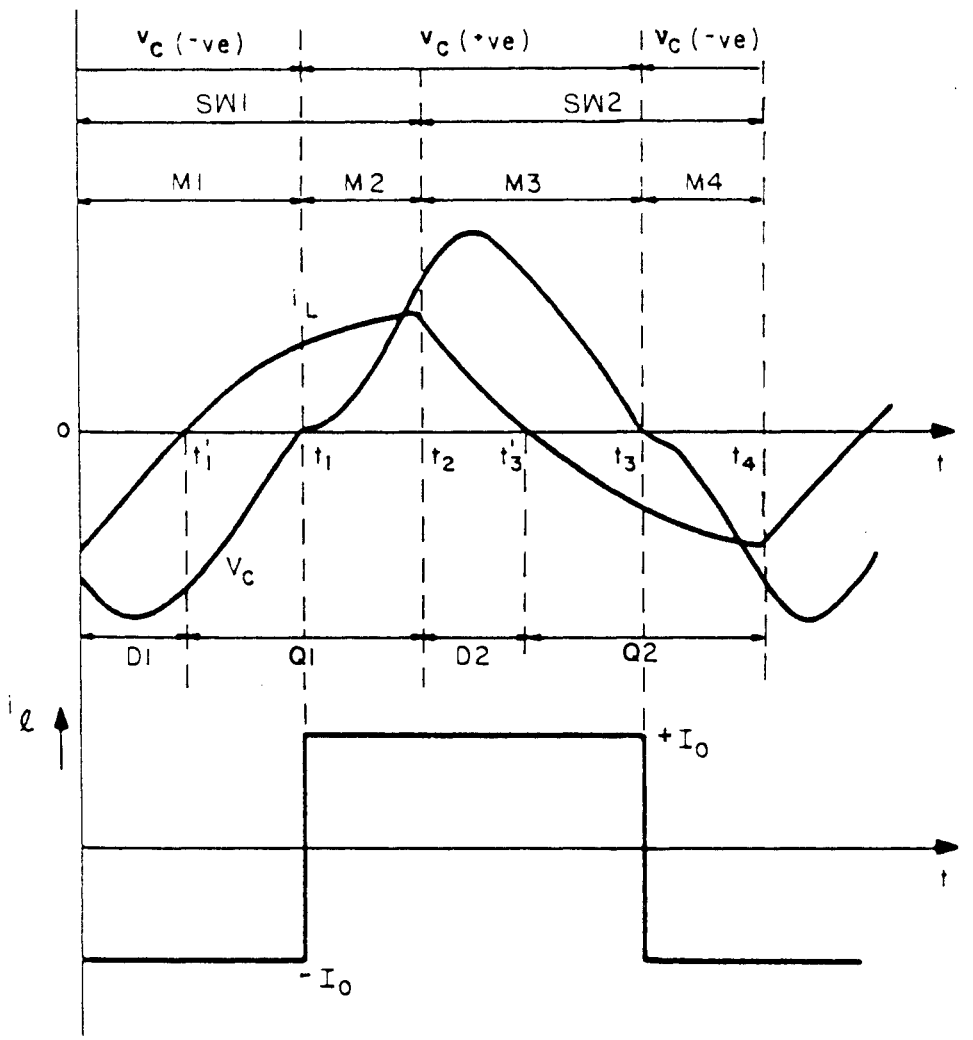

Figure 5.8. CCM waveforms for Fig. 5.7 (b) - $I_{oN} < 1$, $\omega_N > 1$

5.2.4 Forced Commutation Trap Zones

Figure 5.9 shows a set of steady-state trajectories similar to that in Fig. 5.7(a), in which the power switch is naturally commutated. The circular areas (radius = I_{oN}), marked around centers M2 and M4, are named the **forced commutation trap zones.** As illustrated by the transient trajectory, "S", in Fig. 5.9, if under transient conditions Q1 is switched on while in 'TRAP1' zone , it will no longer be naturally commutated. This is because the dc offset in current I_{oN} is more than the oscillatory peak current amplitude. If the converter is designed for natural commutation only, switching in the trap zones should be avoided.

5.2.5 Nonresonant Topological Modes

In addition to the four resonant topological modes discussed earlier, five nonresonant topolgical modes occur in a PRC, which are described in the following subsections.

5.2.5.1 *Inductor Charging Intervals:*

In Figs. 5.7(a) and 5.7(b), I_{L1N} ($-I_{L1N}$) is the normalized inductor current at instant $t_1(t_3)$ when the M1(M3) trajectory reaches the vertical axis. If I_{L1N} ($-I_{L1N}$) happens to be between $-I_{oN}$ and $+I_{oN}$, a careful examination of the state portrait in Fig. 5.6 reveals that there is no available resonant trajectory on which the system could proceed further. Following are two possible explanations of further circuit operation for the case when SW1 (Q1 or D1) is kept "on", once the system reaches the vertical axis between $-I_{oN}$ and $+I_{oN}$. Similar explanations can be offered for the case when SW2 (Q2 or D2) is kept "on", after the system reaches vertical axis. The first explanation is as follows.

Assume that v_C is slightly positive. The link current, i_l, which forms the excess current = ($I_o - I_{L1}$), will be positive . The resonant capacitor will be charged in the the opposite polarity by i_l. This would then make v_C slightly negative and, as a consequence, i_l will also become negative. Again, i_l will charge the

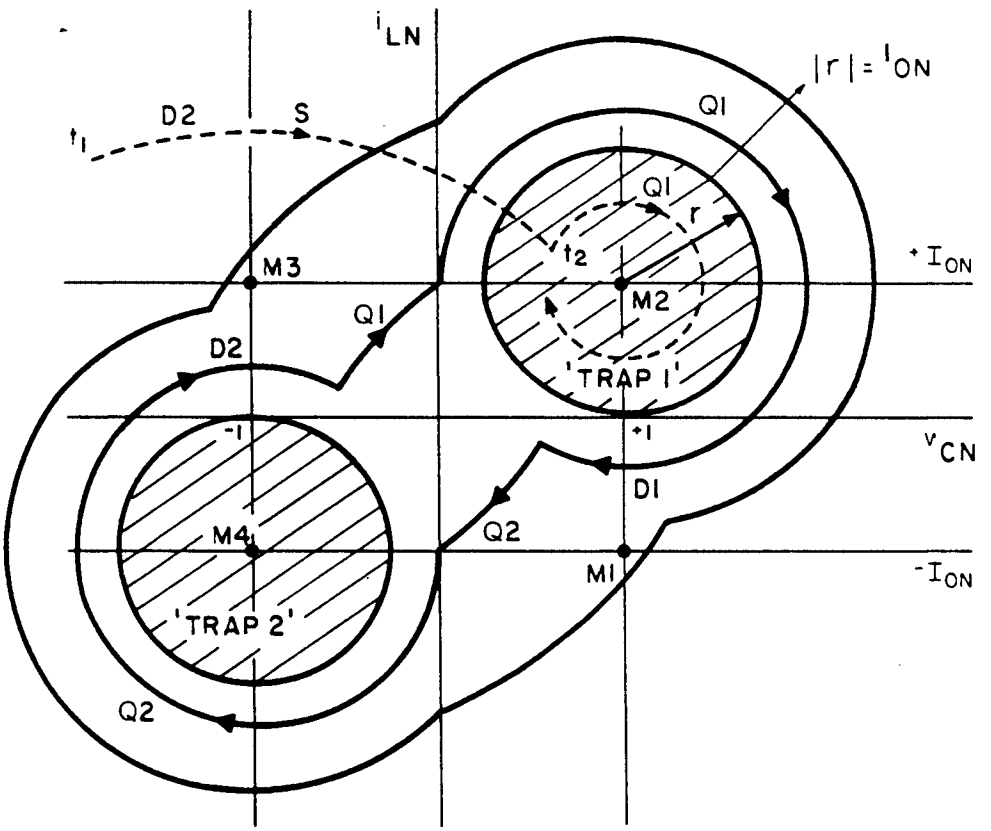

Figure 5.9. Forced commutation trap zones

resonant capacitor - this time to a slightly positive value. Thus, the resonant capacitor is effectively clamped and v_C will chatter around zero value during this operation. Since SW1 is closed during this period, a voltage V_s is impressed across the inductor thereby linearly charging the inductor to a current of I_o. On the state plane this will be represented by a vertical 'sliding line' (with chatter around it) from I_{L1N} to I_{oN}. Once the inductor current reaches I_o value, the clamp on the capacitor is released and the circuit operates in M2.

The second alternative explanation is now given. The excess load current over the resonant inductor current freewheels through the diodes of the output bridge as shown in Fig. 5.10. This would clamp the resonant capacitor voltage to zero during this interval. Q1 (or D1, if the instantaneous i_L is negative) conducts and the inductor is linearly charged to load current. Once i_L reaches I_o value, the clamp on the resonant capacitor is released, and the circuit operates in M2. Thus, in this explanation the circuit is assumed to function in a new nonresonant topological mode.

In both the cases, the inductor is linearly charged by the voltage V_s and the state trajectory lies on the vertical axis. The overall circuit operation remains unaltered in both cases. Though there may be situations when the circuit operation is as per the first explanation, the experimental PRC built as a part of this work followed the explanation.

Topological modes M5 and M6 correspond to this interval of operation when SW1 and SW2, respectively, are "on". The equivalent circuit diagrams for these two modes are shown in Figs. 5.11(a) and 5.11(b), respectively, while Figs. 5.12(a) and 5.12(b) show the corresponding state-plane trajectories.

5.2.5.2 Capacitor Discharge Intervals:

A study of Figs. 5.5(a) and 5.5(b) shows that at the end of D1 conduction, the trajectory can reach the horizontal axis. If at this instant v_{CN} is between -1 and $+1$ and if Q1 is not reswitched on, once again none of the four resonant topological modes can follow. During this interval both the bidirectional switches SW1 and SW2 are 'off' and the residual, resonant-capacitor voltage is linearly discharged by the circulating load current. The equivalent circuit diagrams for the resulting topological modes M7 (for

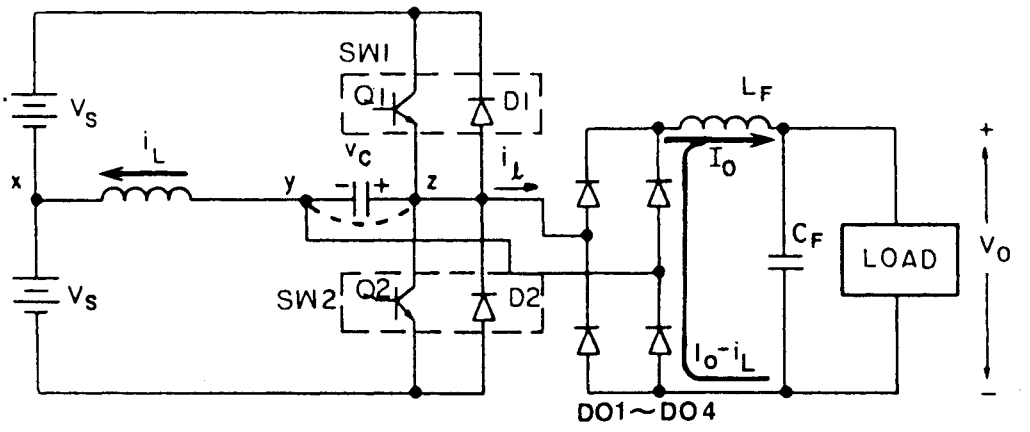

Figure 5.10. Explanatory diagram for inductor charging/discharging interval

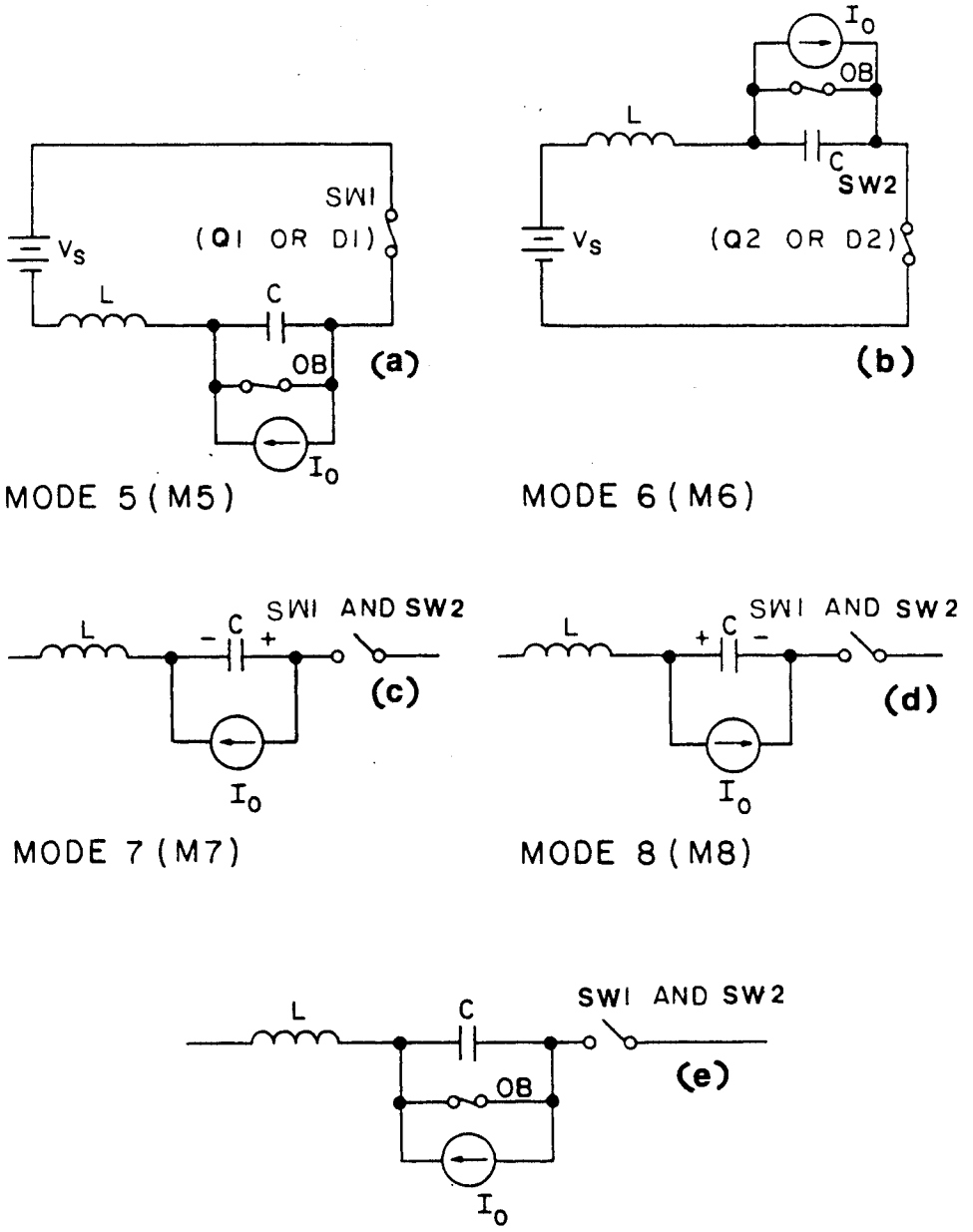

Figure 5.11. Nonresonant topological modes - equivalent circuit diagrams

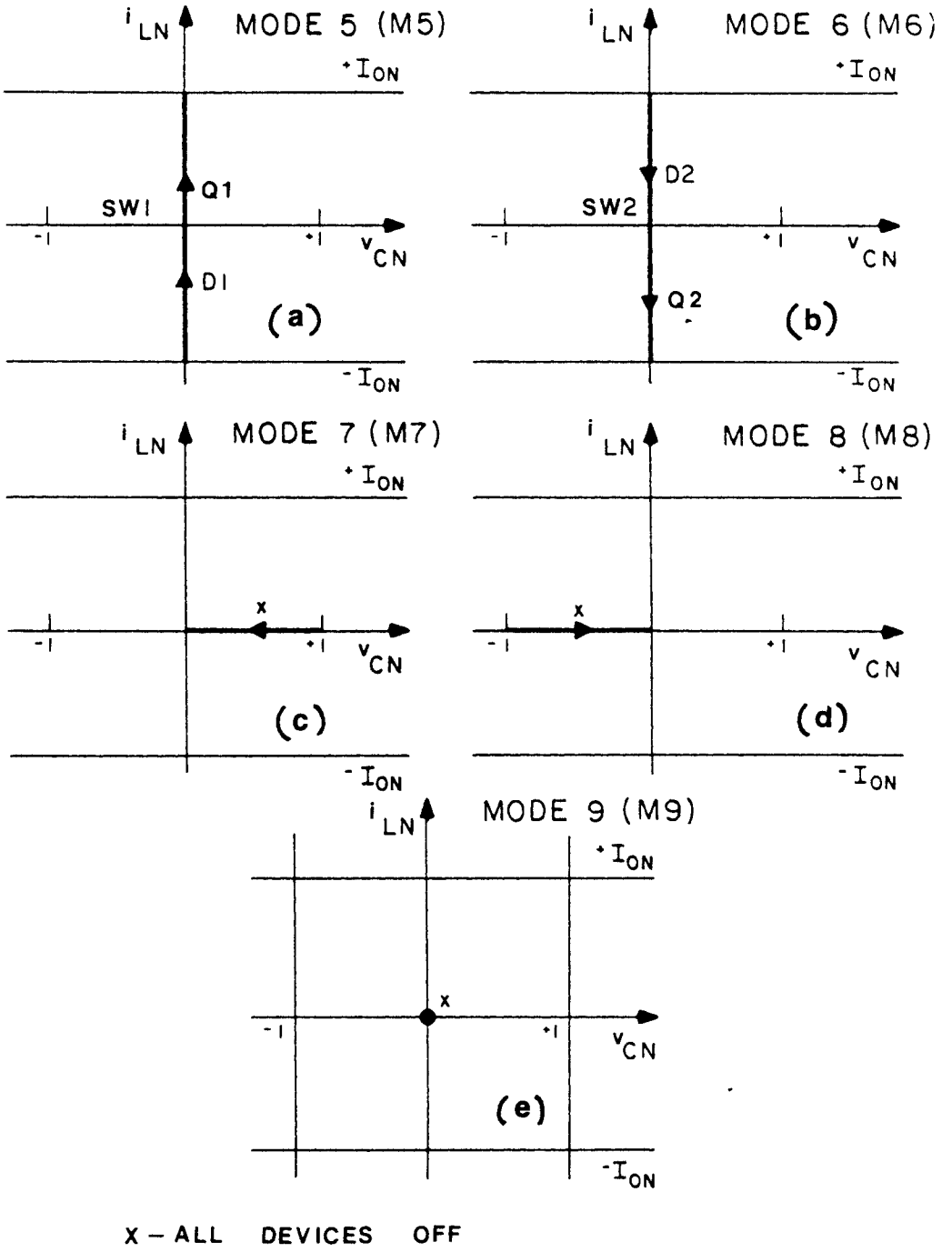

Figure 5.12. Nonresonant topological modes - state-plane trajectories

positive v_C) and M8 (for negative v_C) are shown in Figs. 5.11(c) and 5.11(d), respectively. Figures 5.12(c) and 5.12(d) show the corresponding state-plane trajectories.

5.2.5.3 Discontinuous Operation Interval:

If inductor current and capacitor voltage are both zero and if Q1 and Q2 are both "off", the system can remain at the origin for an indefinite interval with the load current freewheeling through the output rectifier. Figure 5.11(e) shows the circuit diagram and Fig 5.12(e) the state trajectory (just a point) corresponding to this topological mode, called M9.

5.3 Complete Mode Analysis

In this section the different modes exhibited by the PRC are investigated by using the state-plane diagrams. These diagrams can also be used to derive the equations for the mode boundaries and dc characteristics for operation in a given mode. These derivations are presented in Appendix C.

5.3.1 Construction Of CCM Steady-State Trajectories

Given the load current, the construction of steady-state, CCM steady-state trajectories is illustrated in Fig. 5.13. The steps are as follows:

1. Locate the mode centers M1, M2, M3 and M4.
2. With centers at M2 and M4, draw arcs ABCD and EFGH, respectively, with radius R.
3. With M1 as center, draw arc AHIF of radius R' (= M1 A). This intersects arc EFGH at H and F.
4. Do likewise with M3 as center. The intersection points are D and B.
5. ABCDEFGH is one steady-state trajectory due to one set of intersection points, called **intersection-1**.
6. ABJDEFIH is another steady-state trajectory due to the other set of intersection points, called

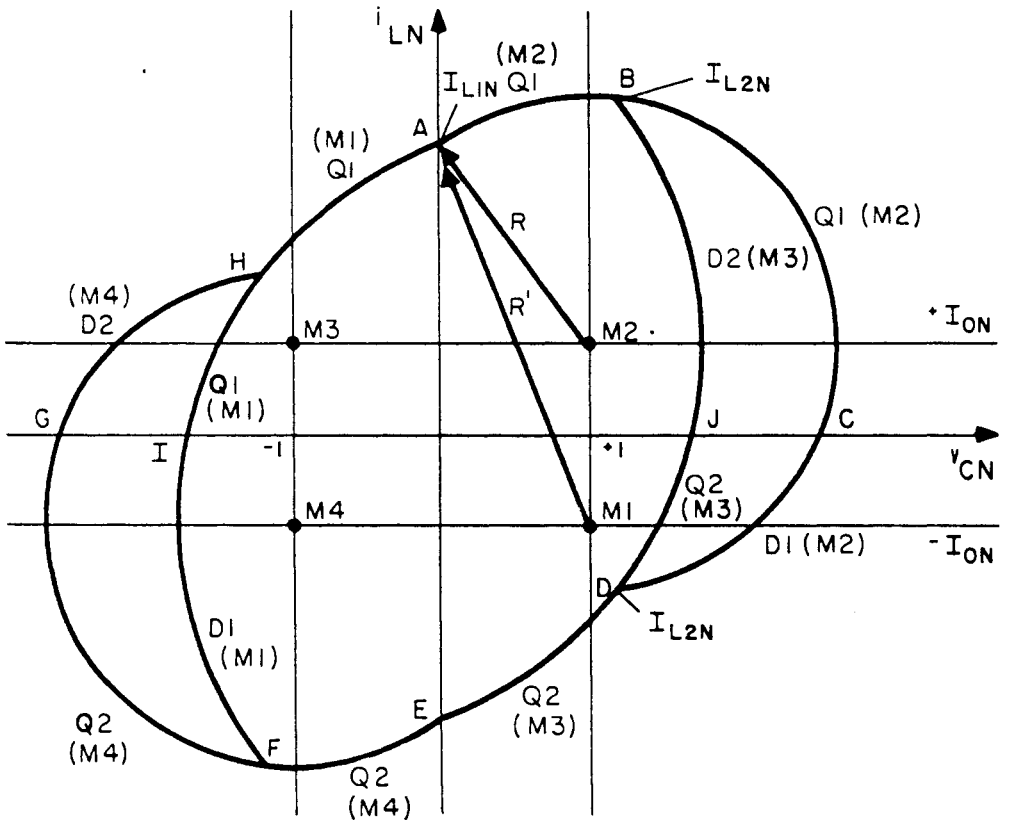

Figure 5.13. State-plane construction of CCM trajectories

intersection-2.

A study of the angles subtended by the trajectories shows that an intersection-1 trajectory with greater radius R corresponds to a higher operating frequency than the one with smaller R. Thus, as the operating frequency is increased, intersection-1 trajectory increases in size (see Fig. 5.7(a)), while intersection-2 trajectory decreases in size (see Fig. 5.7(b)). In general, as the frequency is increased the circuit follows initially intersection-1 trajectories and the tank energy and the output voltage increases. At a certain boundary frequency ($\omega_N = \omega_{MAX}$), the trajectory reaches a maximum size. Beyond ω_{MAX}, the circuit follows intersection-2 trajectories and the tank energy and output voltage decreases.

Figure 5.13 is also used to define two values of the inductor current, I_{L1N} and I_{L2N}, which are used in other sections. I_{L1N} is the current at point A for both intersection-1 and -2 trajectories. I_{L2N} is the current at point D for intersection-1 trajectory and is the current at point B for intersection-2 trajectory.

5.3.2 Method Of Mode Analysis

For an assumed load current, steady-state trajectories of intersections-1 and -2 are established. The operating frequency is then assumed to be varied in order to establish the different modes occurring in a PRC and the boundaries between them. The above process is repeated for different load current ranges. In this manner, the operation of a PRC is studied for the entire useful range of frequency and load current.

The different load current ranges utilized in this analysis are

1. Range A $0 \leq I_{oN} \leq 1$
2. Range B $1 \leq I_{oN} \leq \sqrt{2}$
3. Range C $\sqrt{2} \leq I_{oN} < \infty$

5.3.3 Mode Definitions

1. CCM(Continuous-Conduction Mode) - Neither v_C nor i_L stays constant for any interval.

2. DCM(Discontinuous-Conduction Mode) - v_C and i_L stay constant for some duration together.

3. TM1(Transition Mode 1) - v_C alone stays constant for some interval. This mode may also be called the Discontinuous Capacitor-Voltage Mode.

4. TM2(Transition Mode 2) - v_C and i_L stay constant for some interval but not together.

5. LIMIT(Current Limit Mode) - v_C is always constant.

6. MULTIPLE(Multiple Conduction-Cycle Modes) - Modes in which a resonant topological mode (M1 thru M4) occurs for more than a resonant period in a switching cycle. Many modes of operation are actually included in this definition.

5.3.4 PRC Base-Drive Strategies

Two base-drive schemes for the power transistors are possible. The converter operation depends on the type of base-drive strategy adopted under certain operating frequencies and load currents. In such cases, the analysis is separately carried out for the two base-drive strategies.

In the first method, called **strategy-1**, the transistors are always switched on alternately for a half-cycle duration each, as shown in Fig. 5.14(a). In the second method called **strategy-2**, the transistors are switched on, as shown in Fig. 5.14(b), for an interval $t_{ON} = \tau < T/2$ where T is the period of one switching cycle. The time duration τ is set in such a way that the same transistor is not reswitched on after its antiparallel diode conducts. When $T/2$ is less than τ, then t_{ON} is set equal to $T/2$ and strategies -1 and -2 are identical. In strategy-2, τ represents the maximum pulse width of the base drive.

5.3.5 Load Current Equals Zero

In this limiting case, the centers M1 and M2 coincide at (1,0) and M3 and M4 at (-1,0). Intersection-1 steady-state trajectories, when $\omega_N < \omega_{MAX}$ (= 1) , are shown in Fig. 5.15(a). As ω is increased, the trajectory size increases and is ideally infinite in size at ω_{MAX}. As ω is increased beyond ω_{MAX}, the trajectory size begins to decrease following intersection-2 trajectories (Fig. 5.15(b)) and will shrink, ideally, to the origin as the frequency approaches infinity. In Fig. 5.15(a) the transistors are naturally commutated whereas in Fig. 5.15(b) they must be force commutated.

In Fig. 5.15(a), when the frequency is decreased the trajectory marked DCM, which is the lower limit of CCM, is reached. Each of the two transistors and two diodes conduct for half of a resonant period. This boundary occurs when the operating frequency equals half the resonant frequency. Let us assume that strategy-2 is adopted for the base drive at a switching frequency below this boundary frequency. This implies that after Q1 and D1 conduct, Q1 is not reswitched on. Instead, the system remains at the origin till Q2 is switched on. Thus, the trajectory marked DCM in Fig. 5.15(a) represents not only the boundary between CCM and DCM but also all the DCM trajectories. The different DCM trajectories are characterized by different dwell times at the origin.

5.3.6 Load Current In Range A

The converter behavior in the range $0 \leq I_{oN} \leq 1$ is studied in this section.

Figure 5.7(a) shows CCM steady-state trajectories corresponding to intersection-1. As frequency is increased, at $\omega_N = \omega_{MAX}$(= 1) the trajectory reaches, ideally, infinite proportions. Beyond ω_{MAX}, the trajectory reduces in size, following intersection-2 trajectories shown in Fig. 5.7(b). The conduction sequence in Fig. 5.7(a) is Q1, D1, Q2 and D2, with the transistors being naturally commutated and the diodes force commutated. The conduction sequence in Fig. 5.7(b) is Q1, D2, Q2 and D1 with the diodes being naturally commutated and the transistors force commutated. The topological mode sequence in both cases is M1, M2, M3 and M4.

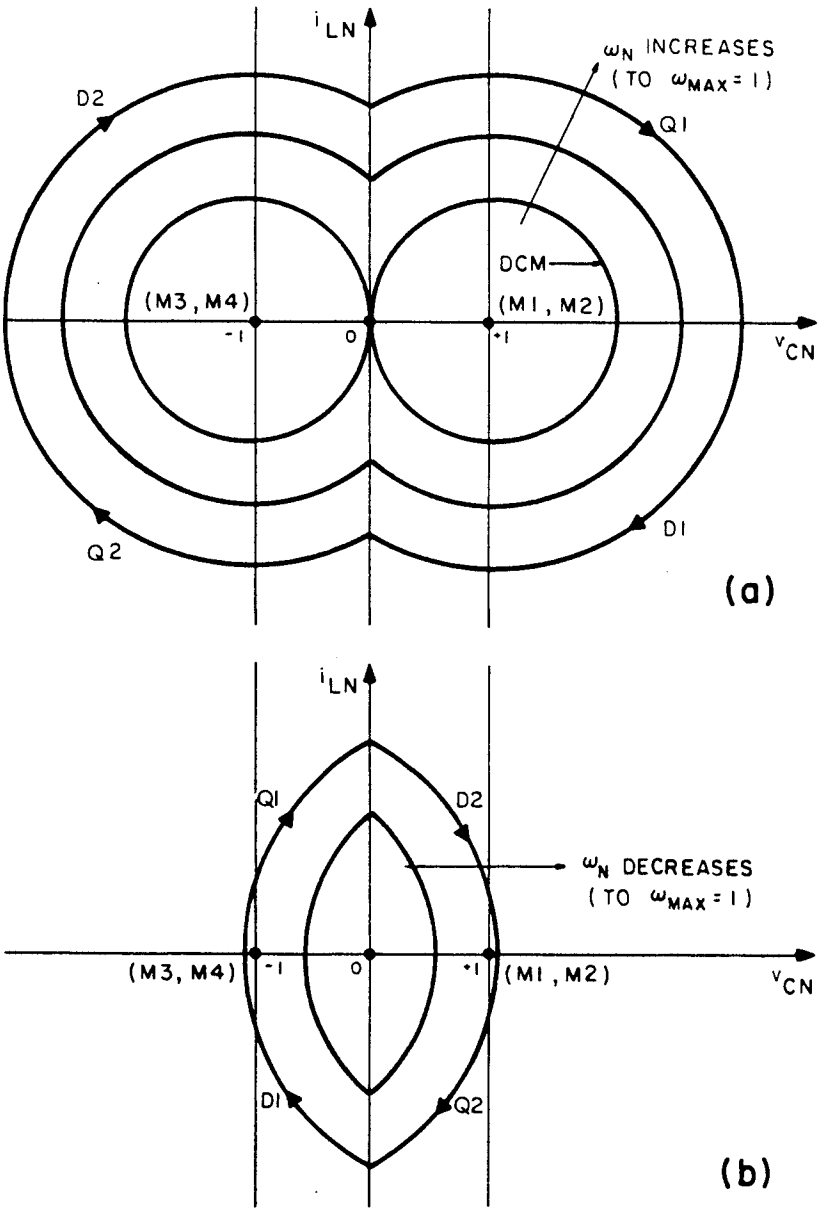

Figure 5.15. Steady-State trajectories for $I_{oN} = 0$

In the next two subsections, we shall consider the nonCCM operation of the circuit for this load range.

5.3.6.1 NonCCM Trajectories With Intersection-1

In Fig. 5.7(a), when switching frequency is reduced I_{L1N} (defined in Sec. 5.3.1) progressively decreases until it equals I_{oN} at $\omega_N = \omega_{LOW}$, which is the lower limit of CCM operation. In SRC operation, the ideal lower limit of CCM operation occurs always when the switching frequency equals half the resonant frequency. A study of the ω_{LOW} trajectory in Fig. 5.7(a) shows this to be not true for PRC operation, except when I_{oN} equals zero.

When ω is less than ω_{LOW} the operation of the circuit depends on the type of base drive adopted, and this is discussed here.

a) Operation Under Base-Drive Strategy-1: Figure 5.16 shows the sequence of state-plane diagrams when ω_N is progressively decreased below ω_{LOW} under strategy-1. Figure 5.16(a) shows the trajectory corresponding to ω_{LOW}. In Fig. 5.16(b) the operating frequency is less than ω_{LOW}. Here the triggering of Q1 is delayed and this results in $I_{L1N} < I_{oN}$ at the end of M1 interval. The resonant inductor, then, linearly charges to I_o (M5) and M2 follows, with Q1 first conducting followed by D1. At the end of the half cycle, Q2 is triggered and the second half cycle proceeds in a similar way. This mode of operation is named **transition mode 1 (TM1)** and the topological mode sequence for this is M1, M5, M2, M3, M6 and M4. This mode may also be appropriately called the **discontinuous capacitor-voltage mode**.

Figure 5.16(c) shows the operation of the converter when ω is further reduced. The converter is still in TM1 since the topological mode sequence is unaltered. However, the device conduction sequence, Q1, D1, Q1, D2, Q2, D2, Q2 and D1, is quite different from that in Fig. 5.16(b). Also, the transistors are no longer naturally commutated, which can be considered a disadvantage of using the base-drive strategy-1.

In Fig. 5.16(d), ω is reduced still further such that M2 (and likewise M4) occurs exactly for one resonant cycle - as represented by the circles on the trajectory. The frequency corresponding to this boundary is called ω_{MUL}. At even lower operating frequencies, multiple resonant cycles occur, as illustrated in Fig.

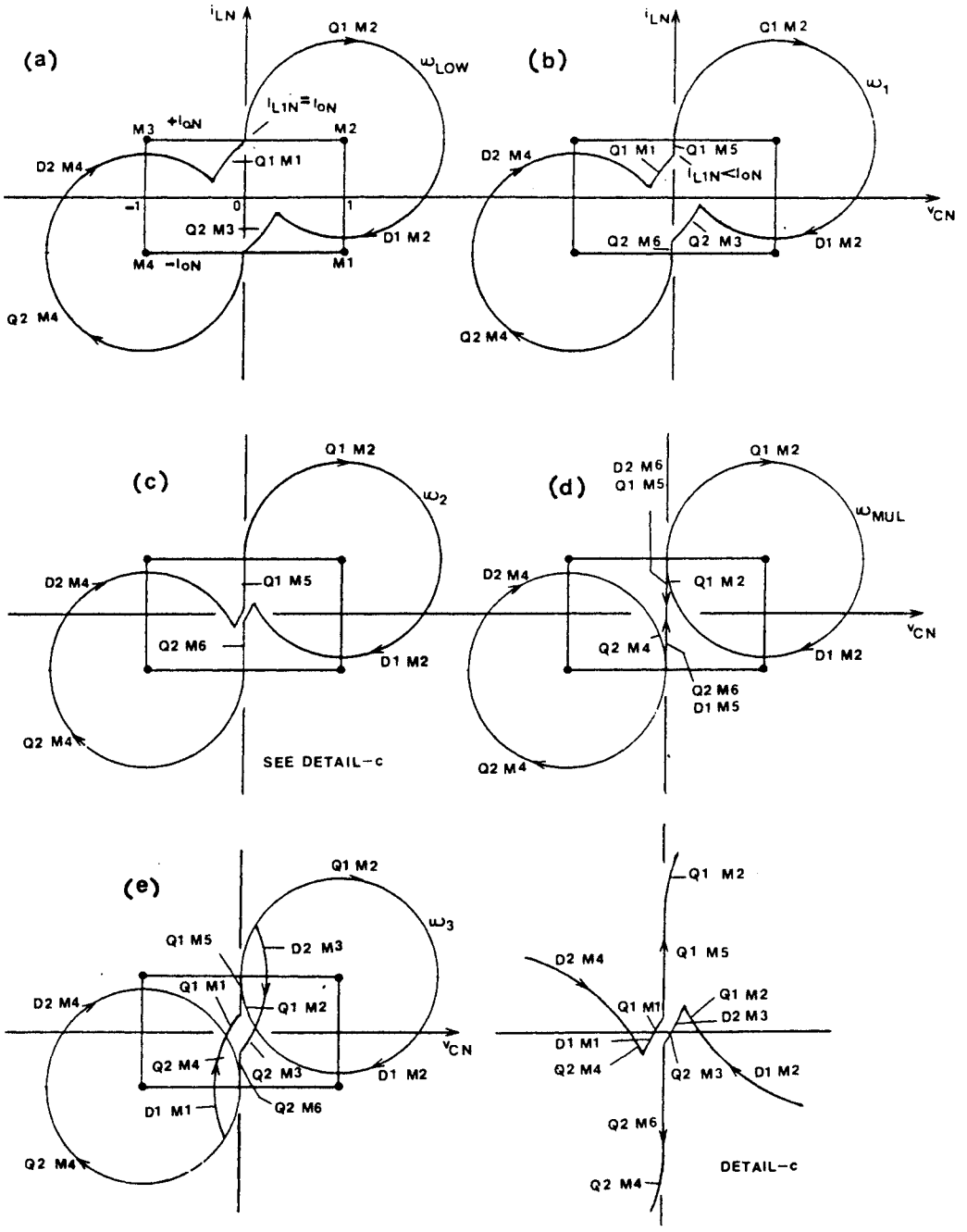

Figure 5.16. NonCCM operation for $I_{oN} < 1$ below ω_{LOW} - strategy - 1

a) ω_{LOW}: CCM/TM1 Boundary

b) & c) TM1 operation

d) ω_{MUL}: TM1/MULTIPLE Boundary

e) MULTIPLE region

5.16(e). Figure 5.16(e) shows only one of the many possible operating modes in this region, named the **MULTIPLE** modes region. The many operating modes in the MULTIPLE region are similar in nature to those referred to in Sec. 2.2.5.2 for series resonant converters. This region occurs under strategy-1 for all load current ranges. The main disadvantage of operating the converter in this region is as follows.

In Fig. 5.7(a) and Figs. 5.16(a) to 5.16(d), as operating frequency is decreased, the trajectory size progressively decreases. A study of the dc characteristics shows that the output voltage also continuously decreases with frequency (see Fig. 5.30, yet to be introduced). This no longer holds true once MULTIPLE modes region is entered. The circuit exhibits many resonant peaks in this region. This would make the control extremely difficult and impractical. Due to this reason, the present paper does not carry out a detailed analysis of the converter operation in this region.

b) Operation Under Base-Drive Strategy-2: Figure 5.17 shows the corresponding sequence of state-plane diagrams. Figures 5.17(a) and 5.17(b) are identical to Figs. 5.16(a) and 5.16(b). As ω is further reduced below that of Fig. 5.17(b), the lower boundary for TM1 is reached when $\omega_N = \omega_{TRAN}$ (Fig. 5.17(c)), below which the circuit operates in another mode named **transition mode 2 (TM2)**. When $\omega_N < \omega_{TRAN}$, as shown in Fig. 5.17(d), the diodes also are naturally commutated. Here, after Q1 and D1 conduct, Q1 cannot conduct again under this base-drive strategy. The residual capacitor voltage at the end of diode conduction is discharged linearly (M7) till Q2 is switched on again. Q2 conducts now in M3 till the trajectory reaches the vertical axis. Then, Q2 linearly charges the inductor (M6) till the current reaches the load current magnitude, I_o. At this instant the clamp on the output capacitor is released and Q2 conducts in M4 topological mode. The operation of the circuit in the second half of the cycle follows in a similar fashion. This is the mode of operation named Transition Mode 2 (TM2). The topological mode sequence for TM2 is M1, M5, M2, M7, M3, M6, M4 and M8.

When ω is further reduced, the discharge interval of the capacitor progressively increases until at a boundary frequency, ω_{DISC} , the capacitor fully discharges to zero before Q2 (or Q1) is switched on (Fig. 5.17(e)). As ω is reduced below ω_{DISC}, the trajectory remains the same with only the dwell time at the origin increasing. The topological mode sequence under DCM is M9, M5, M2, M7, M9, M6, M4 and M8. The resonant tank waveforms under DCM operation are shown in Fig. 5.18 with the time instants corresponding to those in Fig. 5.17(e).

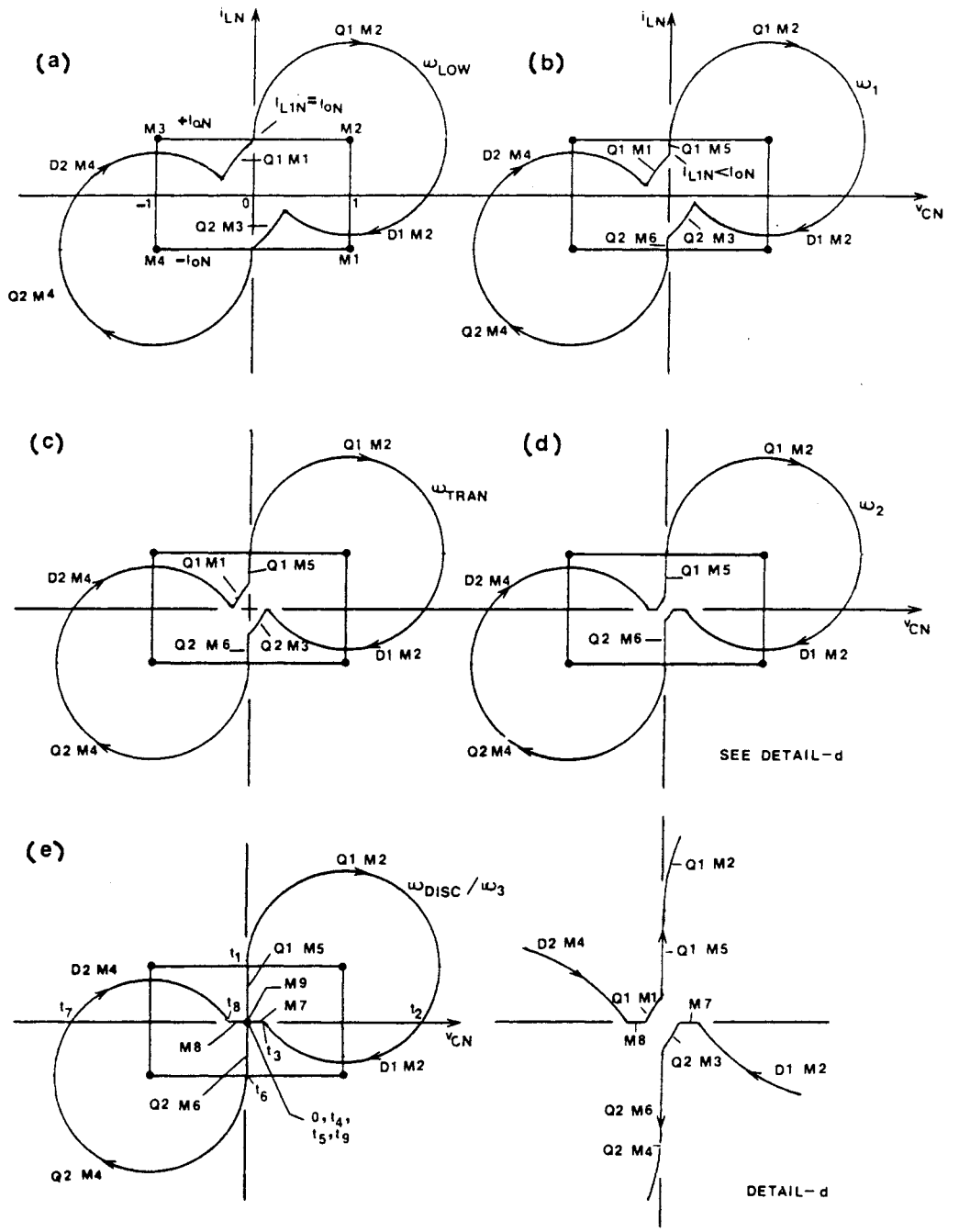

Figure 5.17. NonCCM operation for I_{oN} < 1 below ω_{LOW} - strategy - 2

a) ω_{LOW}: CCM/TM1 Boundary

b) TM1 operation

c) ω_{TRAN}: TM1/TM2 Boundary

d) TM2 operation

e) ω_{DISC}: TM2/DCM Boundary

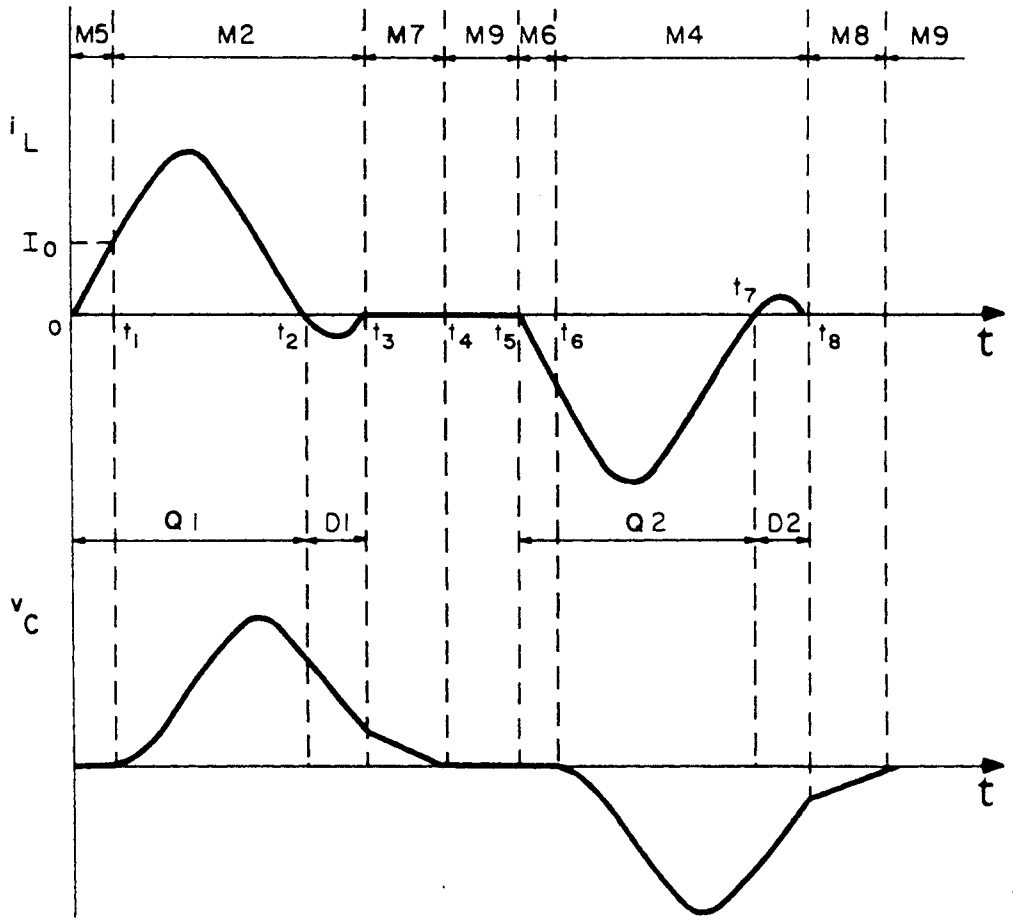

Figure 5.18. Discontinuous-conduction mode (DCM) waveforms for Fig. 5.17(e)

In all the trajectories of Fig. 5.17, the transistors are naturally commutated due to the base-drive strategy. The undesirable MULTIPLE region encountered with strategy-1 is also avoided. It may also be noted that unlike SRC operation, the change between CCM and DCM occurs in a PRC in a gradual fashion through two transition modes, TM1 and TM2.

5.3.6.2 NonCCM Trajectories With Intersection-2

In Fig. 5.7(b), as ω is increased, a boundary is reached at ω_{HIGH}, at which once again $I_{L1N} = I_{oN}$. The circuit cannot operate in CCM beyond this frequency. Figure 5.19 shows a series of diagrams for the case when $\omega_N > \omega_{HIGH}$. Figure 5.19(a) shows the trajectory for the boundary, ω_{HIGH}. When ω is increased beyond ω_{HIGH} (Fig. 5.19(b)), current I_{L1N} becomes less than I_{oN}. Hence, following conduction in M1 topological mode, Q1 will continue to conduct in M5, linearly charging the inductor. When the inductor current reaches I_o, the circuit switches to M2. The rest of the operation is self-explanatory. The resulting mode of operation is the Transition Mode 1 introduced earlier.

Figure 5.19(c) shows the operation of the circuit at a still higher frequency. The circuit operating mode and the device conduction sequence are unaltered. However, the tank circuit waveforms are shared by the power devices differently. For example, in Fig. 5.19(b), Q1 alone charges the inductor in M5 interval, whereas in Fig. 5.19(c) D1 followed by Q1 carry out this function.

As ω is increased, a further limit is reached at $\omega_N = \omega_{LIMIT}$ in Fig. 5.19(d). Here, the durations of topological modes M1,M2,M3 and M4 in TM1 have decreased to zero. The resonant inductor is merely charged and discharged linearly with the resonant capacitor clamped at zero voltage permanently. Thus, the output voltage will be zero. As ω is further increased the trajectory stays on the vertical axis. This mode of operation is named the **LIMIT** mode and would occur, ideally, when the output is short-circuited. The topological mode sequence under LIMIT mode is M5 and M6. It is interesting to note that although the PRC acts as a voltage-fed converter normally, it has the current limiting capability under short circuit conditions due to the series inductor of the tank circuit. The output power delivered by the circuit is zero, since the output voltage is zero and the output current is finite. Due to this, under short circuit conditions, the input voltage source, V_s, supplies only the parasitic losses. Hence, the dc average current and average power drawn from the source would be quite small, ideally zero. However, when

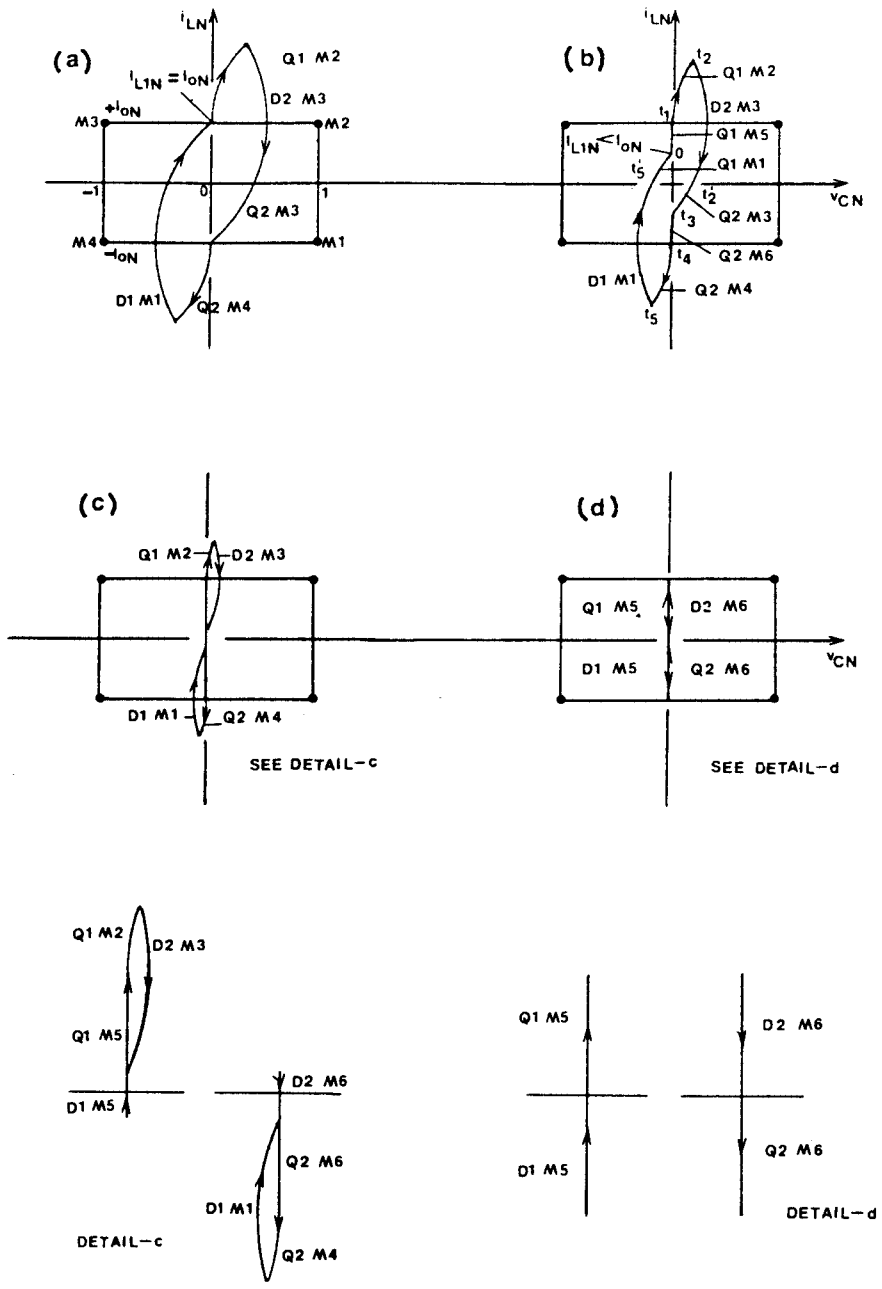

Figure 5.19. NonCCM operation for $I_{oN} < 1$ above ω_{HIGH}

a) ω_{HIGH}: CCM/TM1 Boundary

b) and c) TM1 operation

d) ω_{LIMIT}: TM1/LIMIT Boundary

output is shorted at a low ω, the peak source current (and the load current) can still be considerably large and could be a limiting factor.

The devices are force commutated in all the cases shown in Fig. 5.19. Figure 5.20 shows the tank waveforms corresponding to the transition mode, TM1, in Fig. 5.19(b). The time instants of the waveforms in Fig. 5.20 have also been marked on Fig. 5.19(b).

5.3.7 Load Current In Range B

The converter behavior in the range $1 \leq I_{oN} \leq \sqrt{2}$ is studied in this section.

Figure 5.21 shows the CCM steady-state trajectories for this range of load current. Figure 5.21(a) corresponds to intersection-1 ($\omega_N \leq \omega_{MAX}$) and Fig. 5.21(b) to intersection-2 ($\omega_N \geq \omega_{MAX}$). In Fig. 5.21(a), as frequency is decreased, a lower bound, ω_{LOW} , is reached, when I_{L1N} equals I_{oN}. As frequency is increased, intersection-1 and -2 trajectories merge at $\omega_N = \omega_{MAX}$. A study of the angles subtended at the topological mode centers, shows that ω_{MAX} in this case is less than unity. Thus, when I_{oN} is more than 1, the maximum trajectory size occurs at an operating frequency less than the resonant frequency. I_{L2N} has been previously defined in Sec. 5.3.1. The trajectory corresponding to ω_{MAX} occurs when I_{L2N} equals I_{oN}. Also, ω_{MAX} trajectory has finite dimensions, unlike the earlier case when I_{oN} was less than unity (Fig. 5.7). This implies that, if I_{oN} is greater than 1, the output voltage is bounded even if losses are neglected. As ω is increased above ω_{MAX}, intersection-2 trajectories in Fig. 5.21(b) follow till the upper CCM boundary, ω_{HIGH} , is reached when $I_{L1N} = I_{oN}$.

Another major difference in this load current range is that the transistors are no longer naturally commutated, even when $\omega_N < \omega_{MAX}$, as shown in Fig. 5.21(a). This can be explained in the following manner. When Q1 conducts in M2, even though the tank current, i_L, varies in a resonant manner, the dc offset in i_L, I_o, is so large that i_L does not reverse its polarity. Hence, if natural commutation of transistors is desired, the normalized load current, I_{oN}, must be kept less than unity.

As frequency is decreased below ω_{LOW}, the series of trajectories in Fig. 5.22 apply. Since the transistor does not naturally commutate at all, base-drive strategy-2 can no longer be used and only strategy-1 is

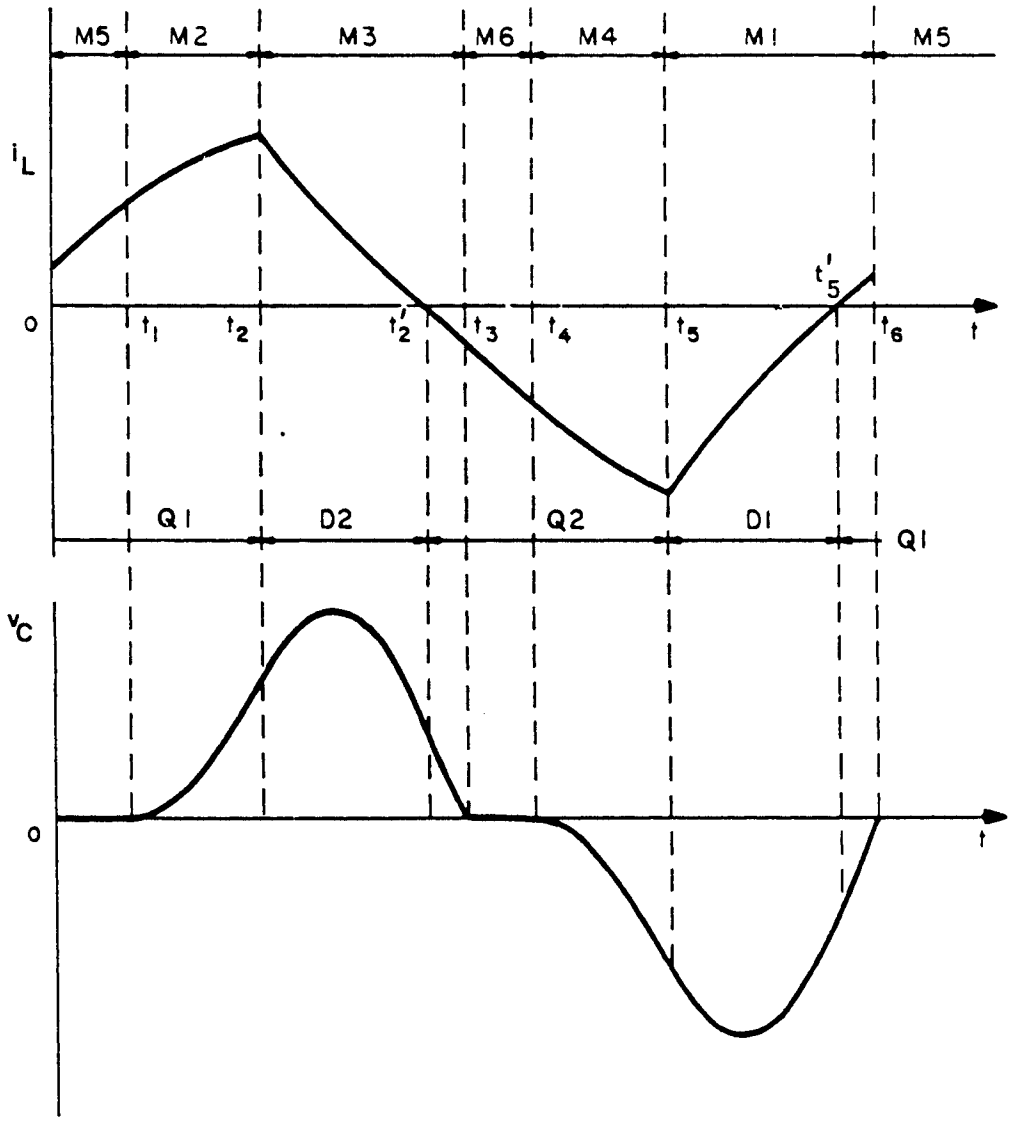

Figure 5.20. TM1 waveforms for Fig. 5.19 (b)

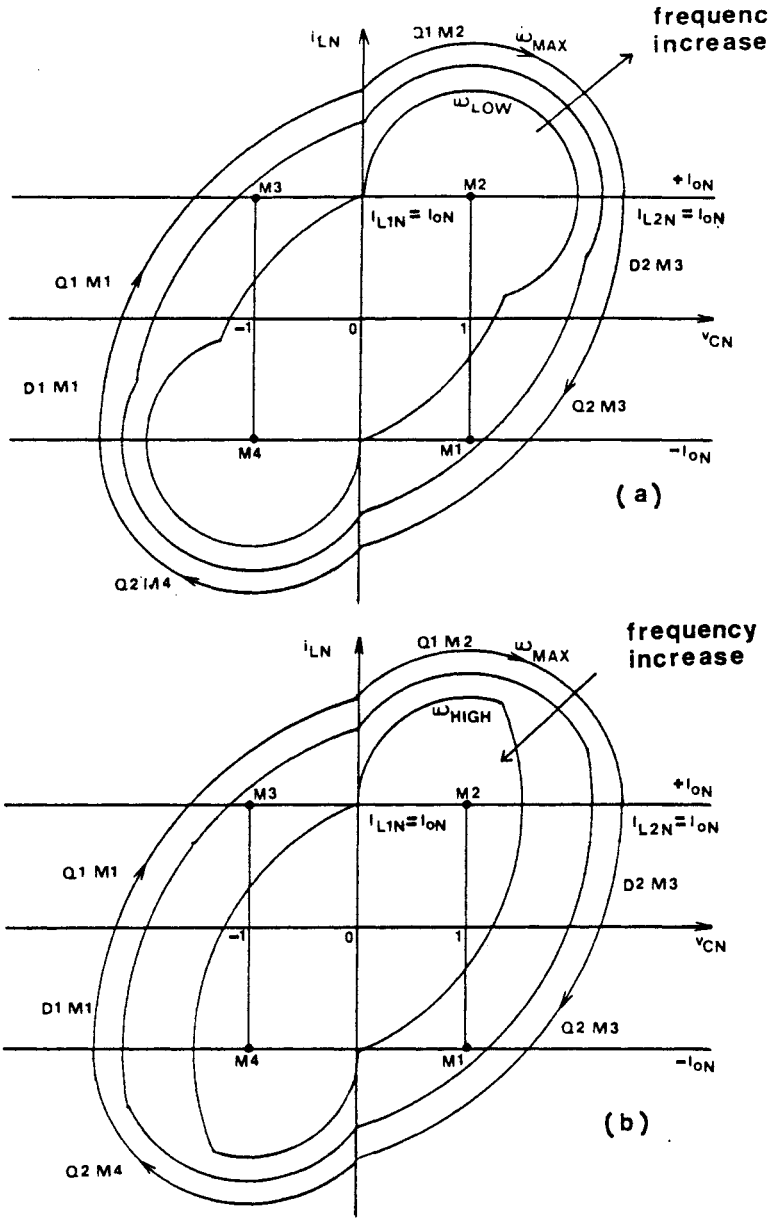

Figure 5.21. CCM steady-state trajectories - $0 < I_{oN} < \sqrt{2}$

a) $\omega_{LOW} < \omega_N < \omega_{MAX}$
b) $\omega_{MAX} < \omega_N < \omega_{HIGH}$

applicable. Though Fig. 5.22 is similar to Fig. 5.16, the device sequences in these load ranges are not identical. Figure 5.22(a) corresponds to ω_{LOW}, the boundary between CCM and TM1. Figure 5.22(b) shows a trajectory in TM1 operation. Figure 5.22(c) shows the boundary, ω_{MUL}, below which multiple-cycle conduction occurs. Figure 5.22(d) shows one possible trajectory in MULTIPLE region.

The resulting sequence of trajectories, when ω is increased beyond ω_{HIGH}, is shown in Fig. 5.23. These can be understood based on the previous discussions and, hence, are not explained here.

5.3.8 Load Current In Range C

The converter behavior in the range $I_{oN} \geq \sqrt{2}$ is studied in this section. Figures 5.24 and 5.25 show the steady-state trajectories for this load range. Here, it is not possible to construct CCM intersection-1 and -2 trajectories. The maximum trajectory size, at $\omega_N = \omega_{MAX}$, again occurs when I_{L2N} (see Sec. 5.3.1 for definition) equals I_{oN}. In this range, however, this happens while the circuit is in TM1. A study of the state-plane diagrams shows that for load currents above $I_{oN} = \sqrt{2}$, CCM operation is not possible.

Figure 5.24 shows a sequence of trajectories for operation below ω_{MAX} and Fig. 5.25 corresponds to operation above ω_{MAX}. These can be understood based on the previous discussions and, hence, are not explained here.

5.3.9. Results Of Mode Analysis

Table 5.1 summarizes the different possible converter modes along with their unique topological mode sequences. The multiple resonant cycle region, MULTIPLE, actually contains many converter modes of operation. For the reason explained in subsection (a) of Sec. 5.3.6.1, a detailed analysis of these modes is omitted in this report.

In Appendix C, the equations for the boundary frequencies, such as ω_{MAX} and ω_{LOW}, are derived directly from those state-plane diagrams which correspond to the boundary operation. These equations have

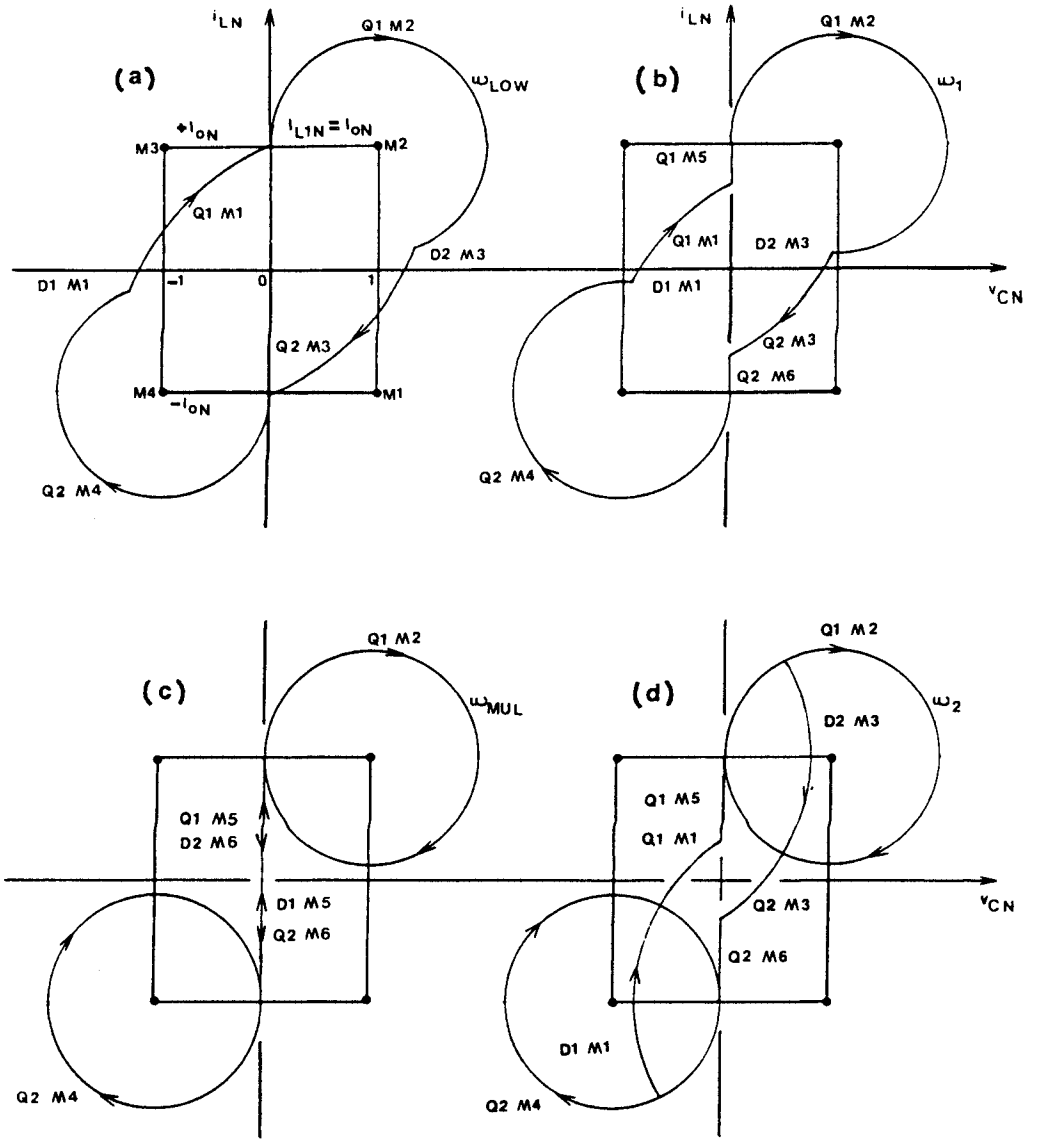

Figure 5.22. NonCCM operation for $1 < I_{oN} < \sqrt{2}$ below ω_{LOW}

a) ω_{LOW}: CCM/TM1 Boundary

b) TM1 operation

c) ω_{MUL}: TM1/MULTIPLE Boundary

d) MULTIPLE region

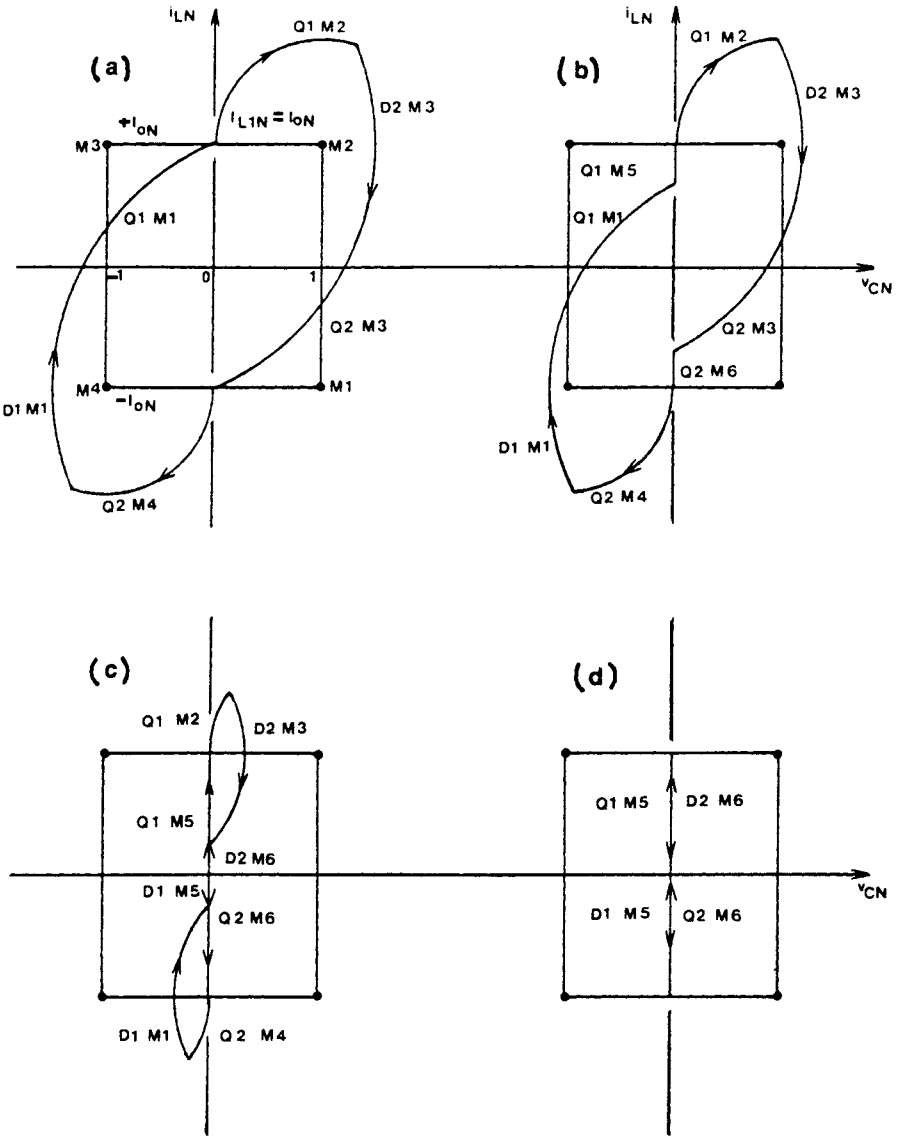

Figure 5.23. NonCCM operation for $1 < I_{oN} < \sqrt{2}$ above ω_{HIGH}

a) ω_{HIGH}: CCM/TM1 Boundary

b) and c) TM1 operation

d) ω_{LIMIT}: TM1/LIMIT Boundary

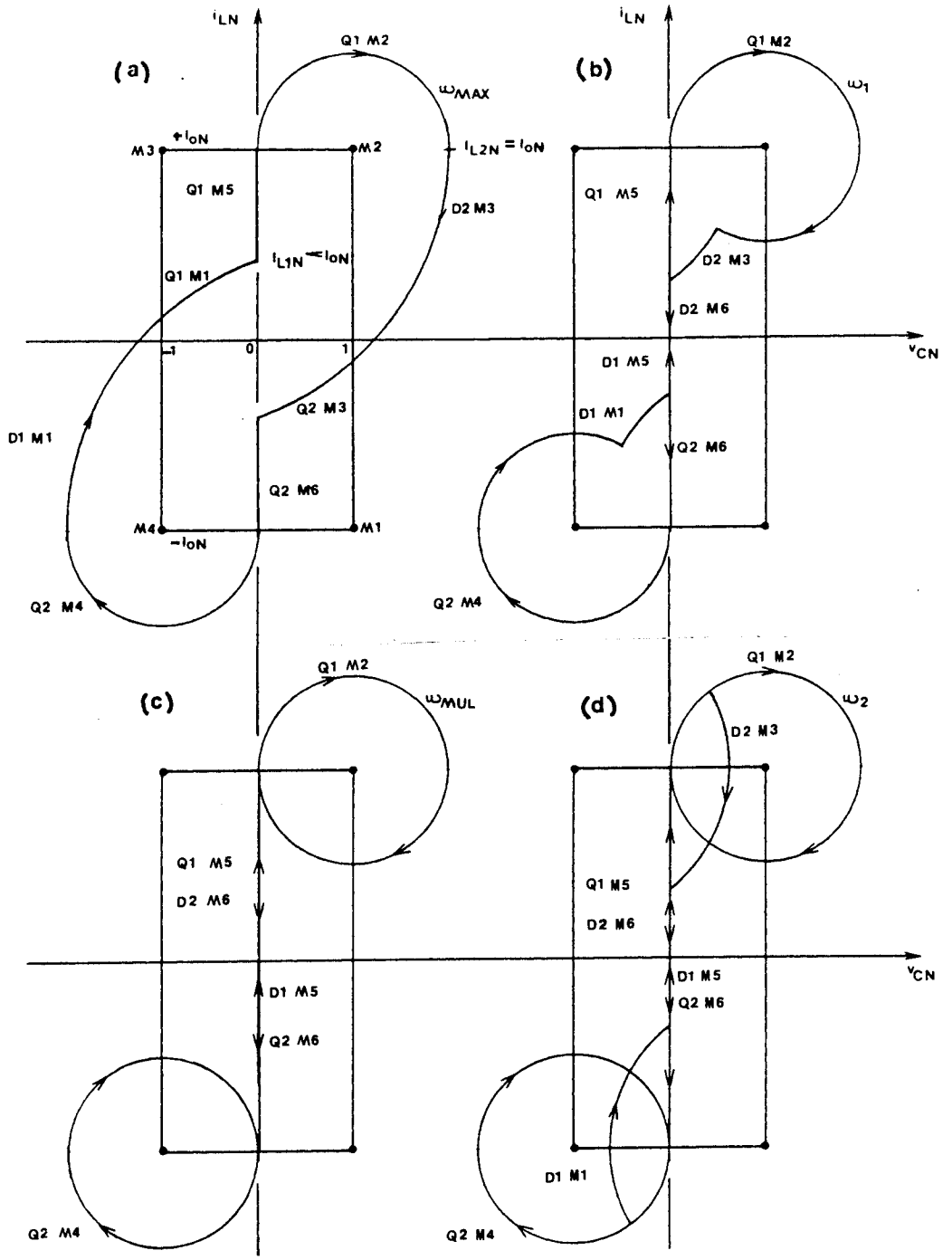

Figure 5.24. Steady-State trajectories for $I_{oN} > \sqrt{2}$ below ω_{MAX}

a) ω_{MAX}: TM1 operation

b) TM1 operation

c) ω_{MUL}: TM1/MULTIPLE Boundary

d) MULTIPLE Region

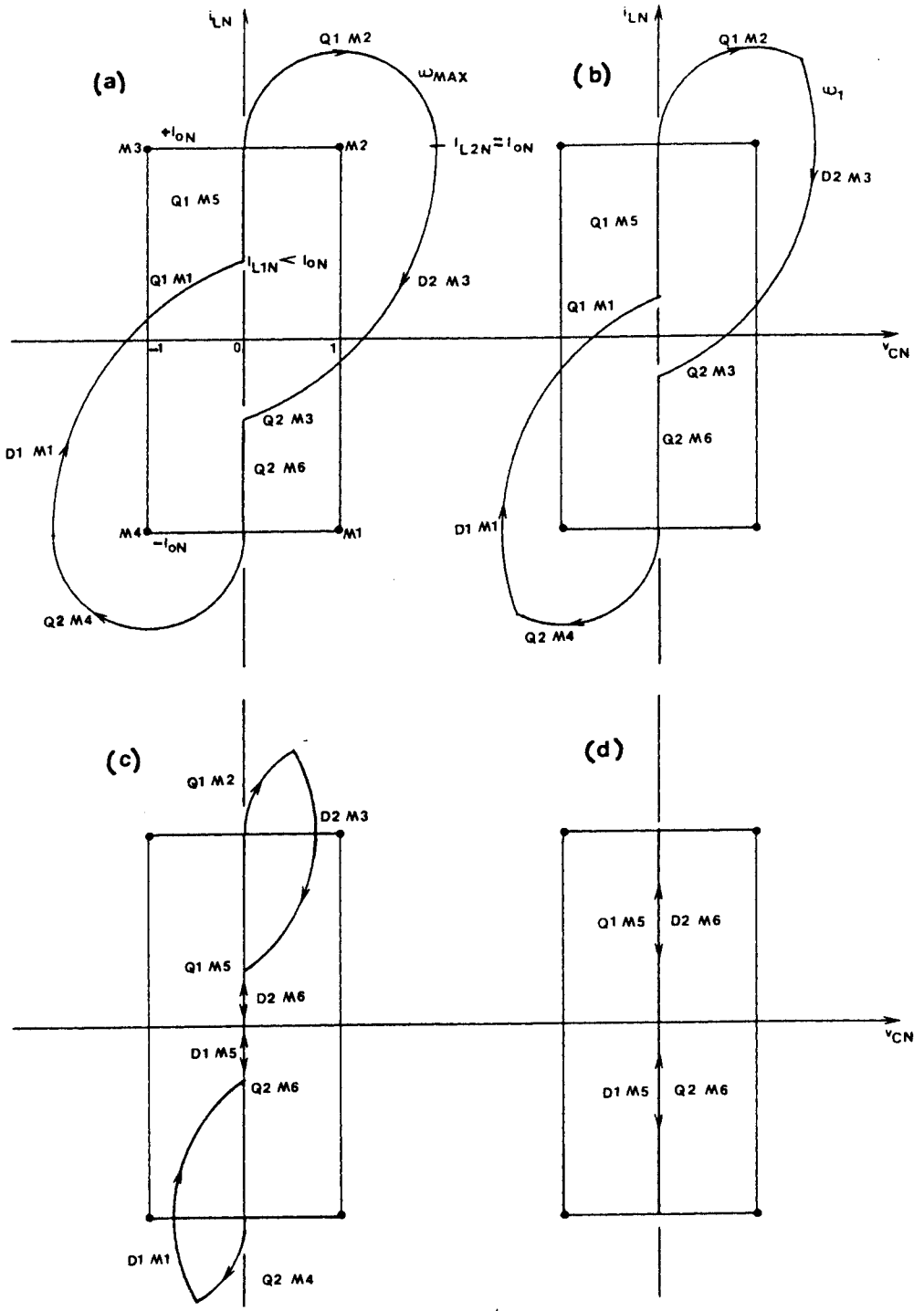

Figure 5.25. Steady-State trajectories for $I_{oN} > \sqrt{2}$ above ω_{MAX}

a) ω_{MAX}: TM1 operation

b) & c) TM1 operation

d) ω_{LIMIT}: TM1/LIMIT Boundary

TABLE - 5.1

PRC - OPERATING MODES

CONVERTER MODE	TOPOLOGOCAL MODE SEQUENCE
DCM	M9, M5, M2, M7, M9, M6, M4 and M8
MULTIPLE	MANY POSSIBLE SEQUENCES
LIMIT	M5 and M6
TM1	M1, M5, M2, M3, M6 and M4
TM2	M1, M5, M2, M7, M3, M6, M4 and M8
CCM	M1, M2, M3 and M4

been plotted in Fig. 5.26. Figure 5.26(a) shows the boundaries between the regions, whereas Fig. 5.26(b) shows the same diagram with the different regions marked. Given load current and operating frequency, one can determine the PRC region of operation from Fig. 5.26(b). Table 5.2 gives a listing of the different PRC regions of operation together with their ranges of occurrence and other features.

Figure 5.27 is used to highlight certain features of Fig. 5.26. The three major regions of a PRC are shown in Fig. 5.27(a). The area under the bell-shaped curve defines the CCM region. Operation in the (current) LIMIT mode is not possible in practice as it implies an ideal short circuit. For a particular ω_N, the value of I_{oN} as given by boundary b7 in Fig. 5.26(a) can be considered as the ideal short-circuit current. The area marked "Multiple Modes" in Fig. 5.27(a) indicates the MULTIPLE region of operation under strategy-1. As explained earlier, operation in this region can pose control problems and, hence, ω_{MUL} (boundary b1 in Fig. 5.26(a)) can be treated as the lower limit on the operating frequency under strategy-1. However, when I_{oN} is less than unity, by adopting base-drive strategy-2, the MULTIPLE region can be avoided altogether. As operating frequency is continuously reduced below ω_{MAX}, the nonCCM sequence (Fig. 5.26(b)) would then be TM1 (Region 5A), TM2 (Region 4) and DCM (Region 1).

Figure 5.27(b) divides the $I_{oN} - \omega_N$ plane as per the nature of commutation of the power switches. By restricting the operation to $I_{oN} < 1$ and $\omega_N < 1$ and using base-drive strategy-2, the PRC can be operated entirely with natural commutation.

5.4 Results Of DC Analysis

Using the state-plane diagrams of Sec. 5.3, the steady-state characteristics of the converter can be obtained for each mode of operation. These derivations have been carried out in Appendix C. Since the converter is more commonly used in its CCM operating regions, the equations for the design parameters, such as the transistor and diode currents, have been derived only for these regions. For all other regions, only the dc gain equations for determining normalized output voltage V_{oN} have been obtained. If required, the equations for the other design parameters in these regions also may be derived in a similar manner from the state-plane diagrams.

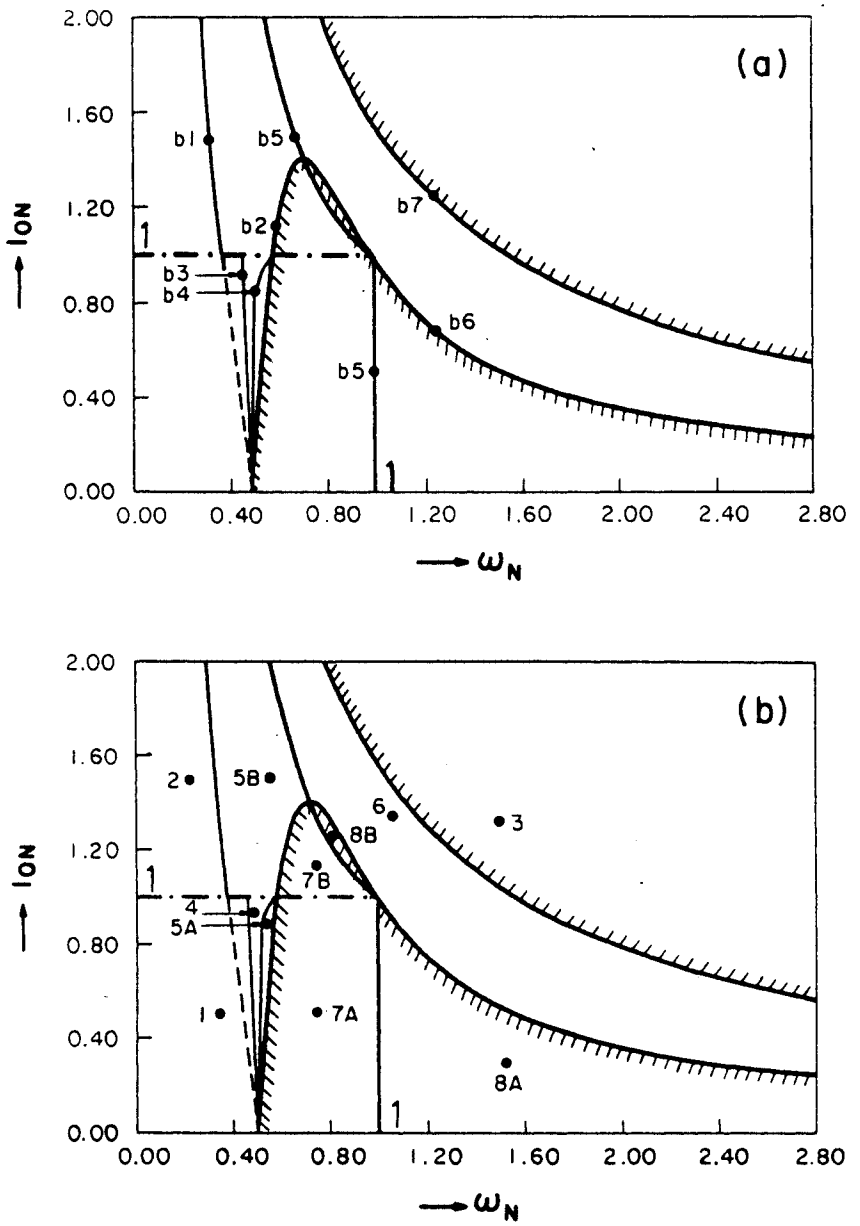

Figure 5.26. Operating regions of a PRC

a) Boundaries - b1: ω_{MUL}; b2: ω_{LOW}; b3: ω&cDISC; b4: ω_{TRAN}; b5: ω_{MAX}; b6: ω_{HIGH}; b7: ω_{LIMIT}

b) Regions - 1: DCM; 2: MULTIPLE; 3:LIMIT; 4: TM2; 5A,5B&6: TM1; 7A,7B,8A&8B: CCM

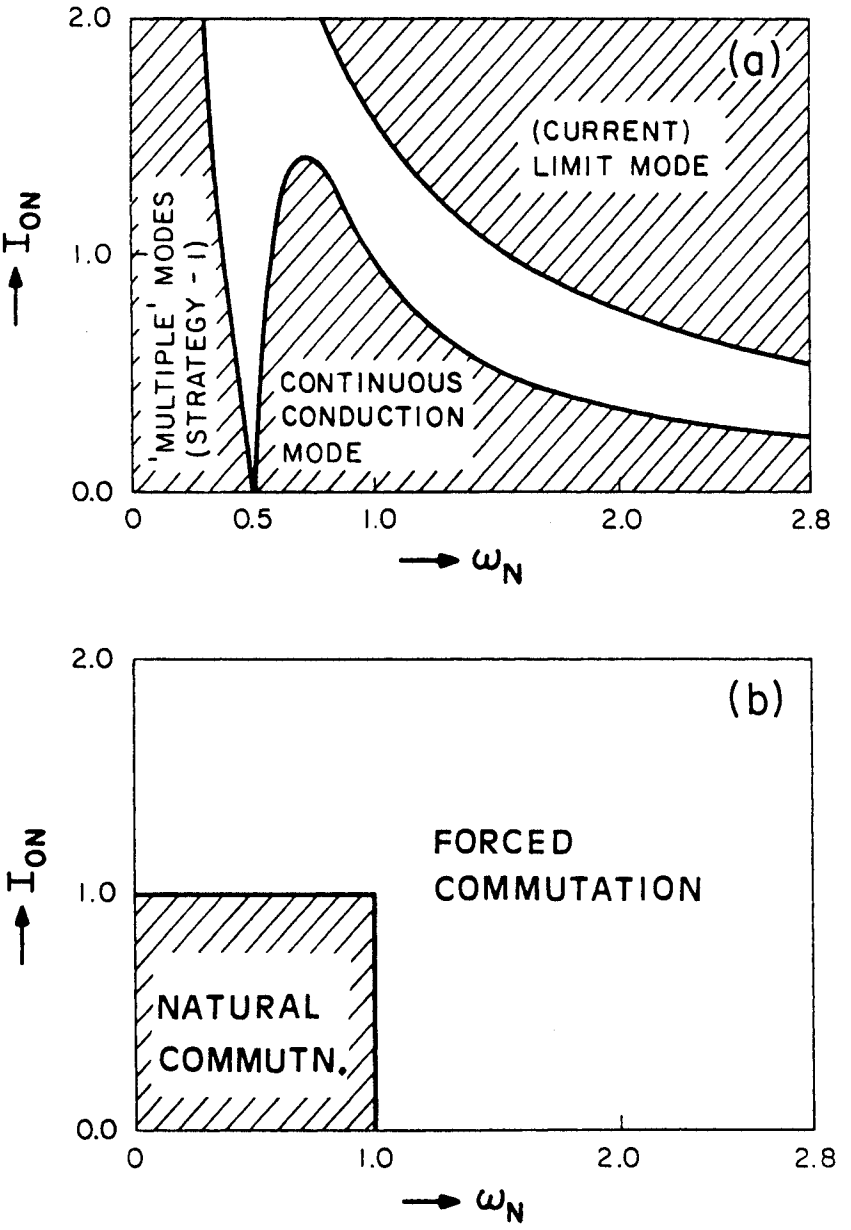

Figure 5.27. Features of PRC operating regions

TABLE - 5.2

PRC - REGIONS

Region	I_{oN} Range	ω_N Range	Mode	Commutation	T	B
1	$0 \le I_{oN} \le 1$	$0 < \omega_N \le \omega_{DISC}$	DCM	Natural	1	2
2	$0 \le I_{oN} < \infty$	$0 < \omega_N \le \omega_{MUL}$	MULTIPLE	Natural/Forced	1	1
3	$0 \le I_{oN} < \infty$	$\omega_{LIMIT} \le \omega_N < \infty$	LIMIT	Forced	2	1 or 2
4	$0 \le I_{oN} \le 1$	$\omega_{DISC} \le \omega_N \le \omega_{TRAN}$	TM2	Natural	1	2
5A	$0 \le I_{oN} \le 1$	$\omega_{TRAN} \le \omega_N \le \omega_{LOW}$	TM1	Natural	1	2
	$0 \le I_{oN} \le 1$	$\omega_{MUL} \le \omega_N \le \omega_{LOW}$		Natural/Forced	1	1
5B	$1 \le I_{oN} \le \sqrt{2}$	$\omega_{MUL} \le \omega_N \le \omega_{LOW}$		Forced	1	1
	$\sqrt{2} \le I_{oN} < \infty$	$\omega_{MUL} \le \omega_N \le \omega_{MAX}$				
6	$0 \le I_{oN} \le \sqrt{2}$	$\omega_{HIGH} \le \omega_N \le \omega_{LIMIT}$		Forced	2	1 or 2
	$\sqrt{2} \le I_{oN} < \infty$	$\omega_{MAX} \le \omega_N \le \omega_{LIMIT}$				
7A	$0 \le I_{oN} \le 1$	$\omega_{LOW} \le \omega_N \le \omega_{MAX}$	CCM	Natural	1	1 or 2
7B	$1 \le I_{oN} \le \sqrt{2}$	$\omega_{LOW} \le \omega_N \le \omega_{MAX}$		Forced	1	1 or 2
8A	$0 \le I_{oN} \le 1$	$\omega_{MAX} \le \omega_N \le \omega_{HIGH}$		Forced	2	1 or 2
8B	$1 \le I_{oN} \le \sqrt{2}$	$\omega_{MAX} \le \omega_N \le \omega_{HIGH}$		Forced	2	1 or 2

T - Intersection trajectory number B - Base-drive strategy number

The design equations for CCM operation mentioned above have been plotted in Appendix C. These plots can be used to predict the ideal performance of the PRC in the CCM regions and also to carry out a preliminary design of the converter. These curves will be modified under certain operating conditions due to the presence of the circuit losses. However, the ideal analysis is still useful at low load currents and at operating frequencies away from the resonant frequency. Also, the ideal analysis represents the first stage in the analysis and allows the incorporation of the losses at a later stage.

Figures 5.28 and 5.29 show the dc characteristics of the PRC converter, based on the equations of Appendix C, for the cases when the operating frequency is below the resonant frequency and when the operating frequency is above the resonant frequency, respectively. All the different regions of converter operation, except the MULTIPLE regions, have been included in these diagrams. At lower frequencies, base-drive strategy-2 is assumed to have been adopted. At low frequencies in Fig. 5.28, ($\omega_N \leq 0.7$), V_{oN} is virtually constant except at high, load currents. In this region the PRC acts as a good voltage source. At high I_{oN} values, due to the current limiting action of the PRC (LIMIT region), the output voltage falls rapidly to zero. At frequencies close to resonant frequency in Fig. 5.28, the inherent regulation of a PRC is poor even at low loads.

Figure 5.29 shows the performance of PRC as a voltage source is even poorer at operating frequencies above resonant frequency. Also, the load capability of the converter is low, since the output voltage falls rapidly to zero in Fig. 5.29 even at moderate loads. In fact, for $I_{oN} > 1$ virtually no output voltage can be obtained for operation above resonance. Thus, the load current capability of a PRC is lower for operation above resonance.

Figure 5.30 shows the complete ideal dc characteristics of the PRC for all regions of operation excepting the MULTIPLE region on the $\omega_N - V_{oN}$ plane. This diagram shows all the features of the PRC discussed so far with respect to Figs. 5.28 and 5.29. In addition, for the range $0 \leq I_{oN} \leq 1$, the ideal maximum value of V_{oN} is infinity and occurs at a normalized frequency of unity. However, for $I_{oN} > 1$, as can be observed from Fig. 5.30, the ideal maximum value of V_{oN} is finite and actually occurs at an operating frequency less than resonant frequency ($\omega_N < 1$). Also, at ω_N less than approximately 0.5, the $V_{oN} - \omega_N$ characteristics are linear and almost independent of the load current. Thus, in the DCM operation, the dc characteristics are load independent and linear with respect to operating frequency.

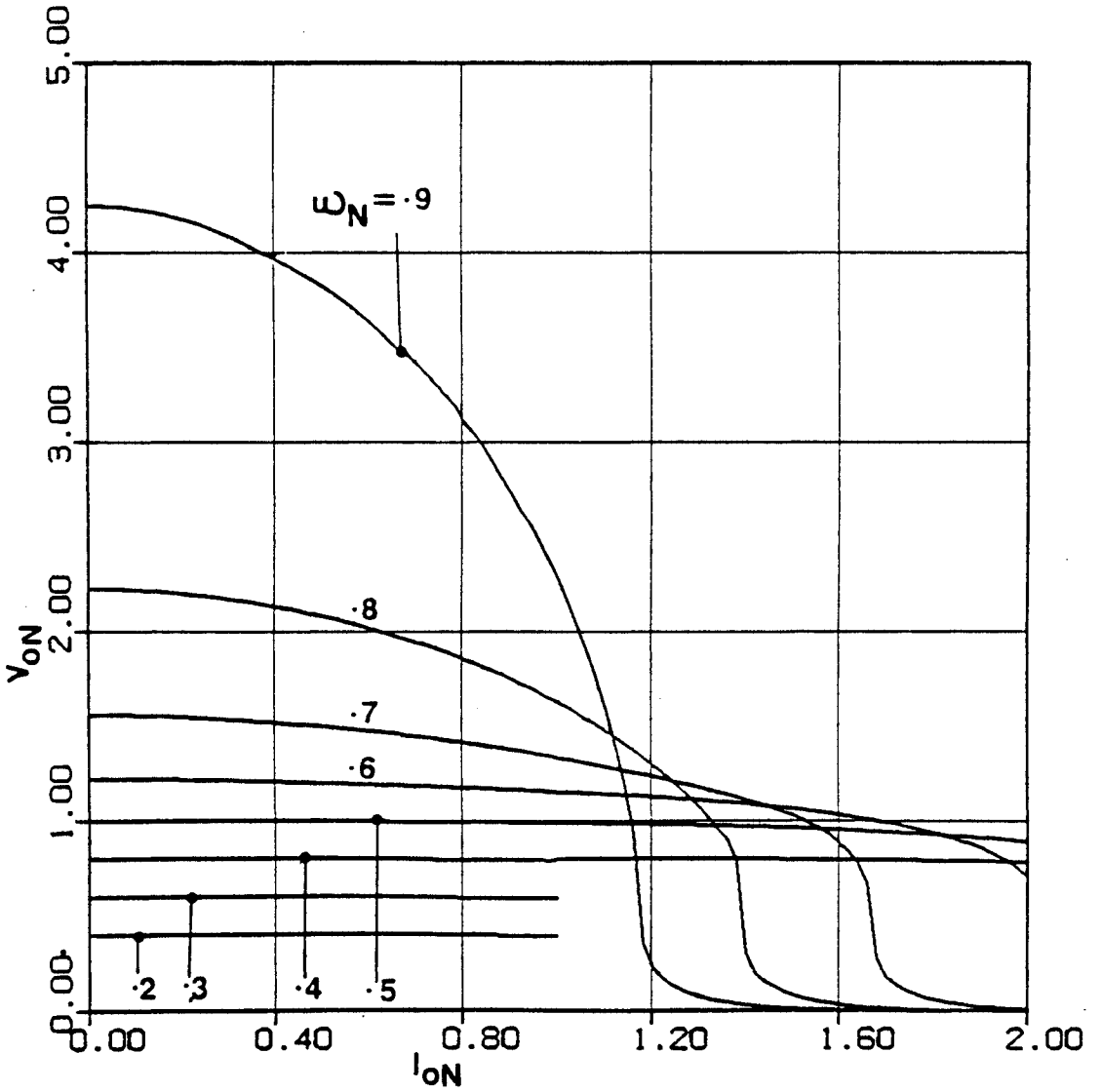

Figure 5.28. Ideal DC characteristics of a PRC - Below resonant frequency

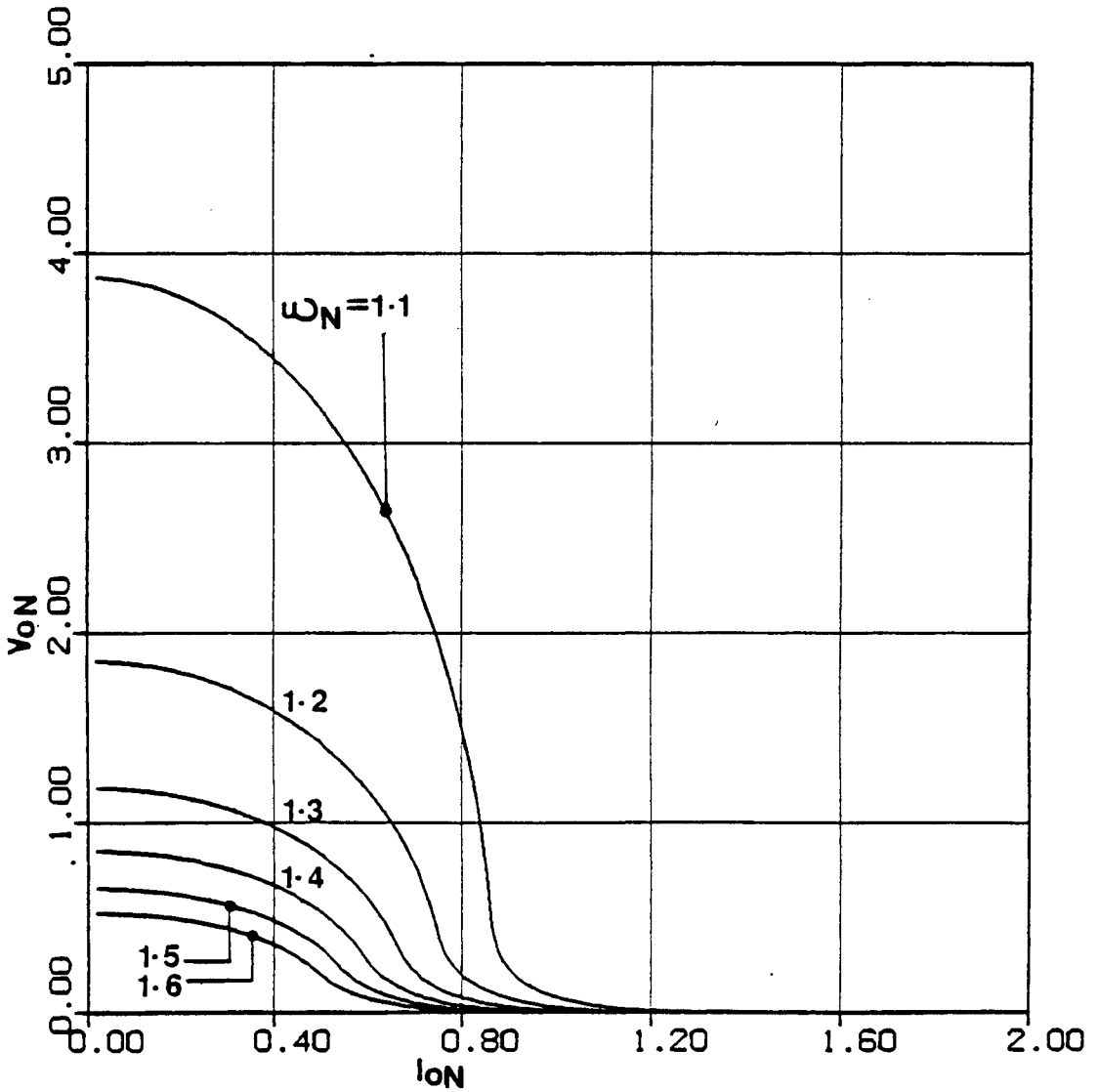

Figure 5.29. Ideal DC characteristics of a PRC - Above resonant frequency

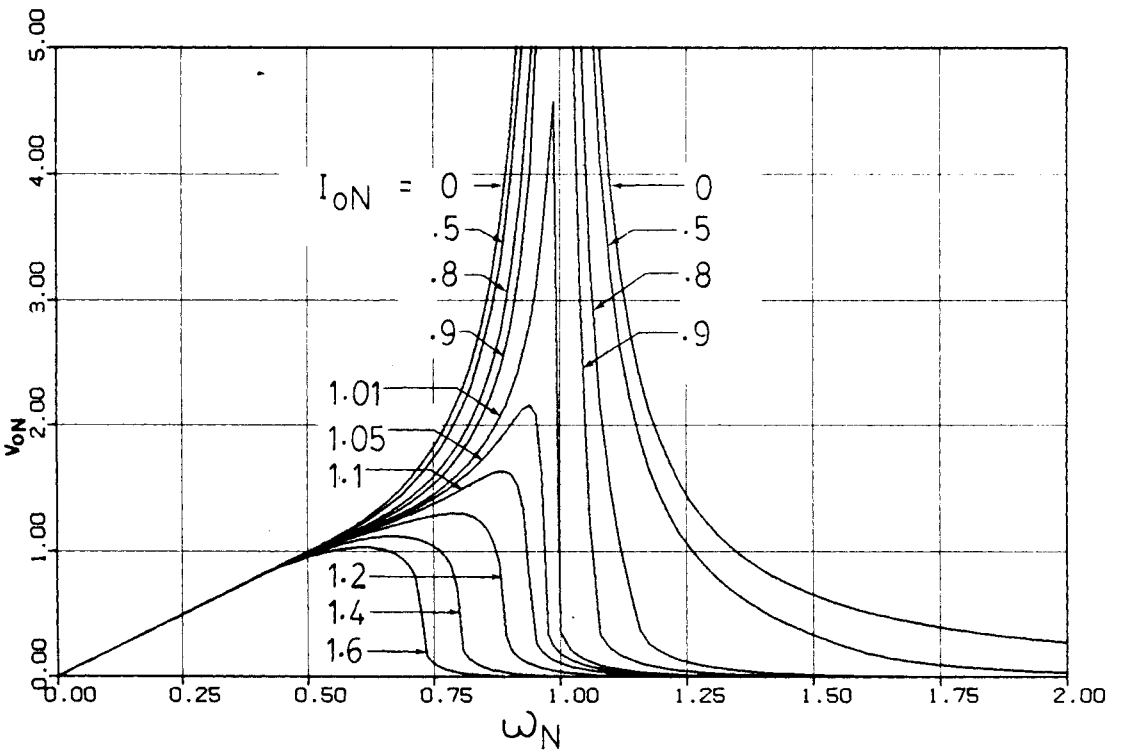

Figure 5.30. Complete Ideal DC characteristics of a PRC

5.5 Experimental Results

The power circuit diagram of the experimental parallel resonant converter is shown in Fig. 5.31. Diodes DQ1 and DQ2 have been included in order to block the resonant current from flowing through the slow, built-in antiparallel diode of the MOSFET. A small snubber circuit across the power switch is found desirable due to the presence of the source lead inductances. The resonant frequency for the tank circuit was measured experimentally to be 315,887 radians/second (50.275 kHZ). The characteristic impedance, Z_0, was equal to 25.847 Ω and the voltage and current normalizing factors were 25 Volts and 0.9672 Amps, respectively.

The gate-drive circuit diagram is given in Fig. 3.14. The control circuit is shown in Fig. 5.32. Here, the output from a variable-frequency oscillator (signal f1) forms the input to the control circuit. The frequency of this input signal is set to be twice the desired operating frequency of the converter. The 7474 flip-flop (D1/1) divides the frequency by two. When operation with base-drive strategy-1 is required, the outputs Q and $\overline{Q}$ of the flip-flop are fed directly to the drivers of the two power MOSFETs. For base-drive strategy-2, the outputs from the flip-flop are further fed to two monostables. The outputs from the monostables are then fed to the two gate drivers. The pulse widths of the monostables are adjusted by means of the 10K potentiometers provided for that purpose such that retriggering of the MOSFETs are avoided as explained in Sec. 5.3.4. At high frequencies, when the input pulse width at pin B of the monostable is less than the monostable pulse width, the CLR pin of the monostable is utilized to clear the output. Thus, at high frequencies the monostable outputs simply follow their inputs and strategy-1 and strategy-2 generate identical base-drive signals.

5.5.1 Existence Of The Modes

Three sets of oscillograms are presented to demonstrate the variety of modes that exist in a PRC. Figure 5.33 is the diagram of the PRC operating regions previously shown in Fig. 5.26. If the frequency ω_N is continuously increased keeping I_{oN} constant at a value less than unity (line a of Fig. 5.33), then the successive circuit operating modes under base-drive strategy-2 will be DCM, TM2, TM1, CCM ($\omega_N < 1$),

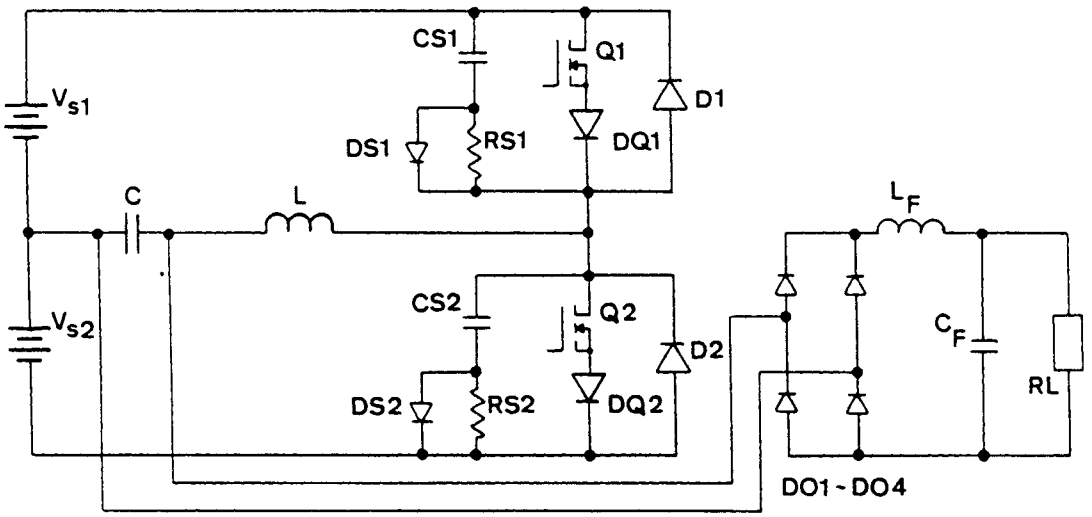

Vs1, Vs2: 25 V	T1, T2: 2SK325	DQ1, DQ2: A115E
D1, D2: 12FL60S02	DO1 ¬ DO4: 40HFL60S02	
L: 81.8 μH	C: 0.125 μF	
CF: 18.5 μF	LF: 85.66 mH	
CS1, CS2: 1.0 nF	RS1, RS2: 470 Ω	DS1, DS2: A115E
f_0 (measured): 50.275 kHz	Z_0: 25.847 Ω	

Figure 5.31. Experimental PRC circuit - power circuit

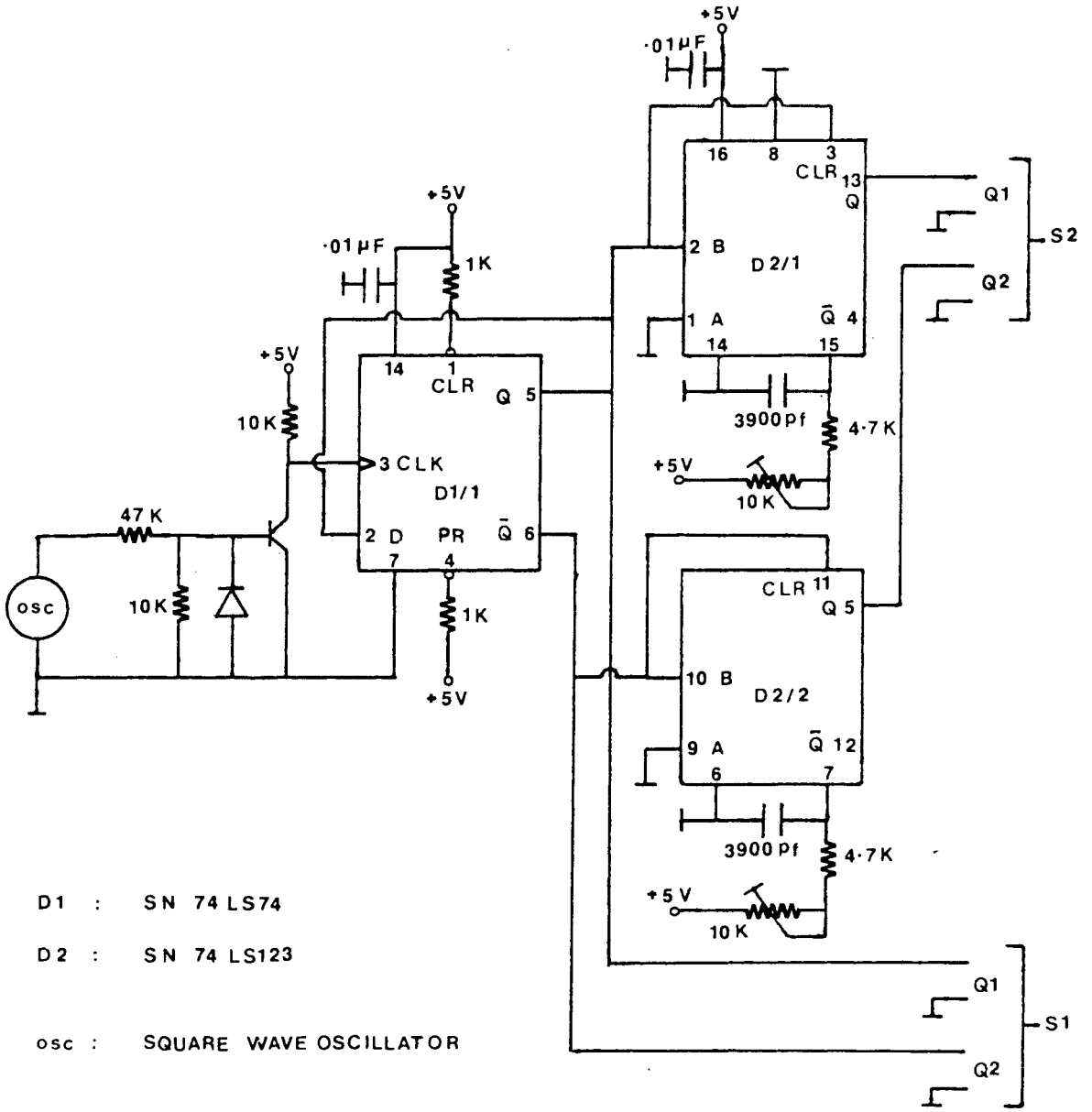

Figure 5.32. Controller circuit diagram

CCM ($\omega_N > 1$), TM1 and LIMIT. The observed sequence of trajectories for $I_o = 0.5A$ ($I_{oN} = 0.517$) , is shown in Fig. 5.34, which follow the predictions quite well. It was, however, difficult to clearly identify TM1 occurring between CCM and TM2 (Fig. 5.17(b)) due to the effect of parasitics on the waveforms and the trajectories. The resonant tank waveforms corresponding to the trajectories in Fig. 5.34 are shown in Fig. 5.35.

The effect of parasitics due to the circuit layout and nonideal components are clearly observable in these oscillograms. The trajectory segments are not strictly circular but somewhat spiral inwards, due to the effect of circuit damping. In DCM and TM2 (Figs. 5.34(a), 5.34(b), 5.35(a) and 5.35(b)), during the capacitor-discharging period, the resonant inductor current oscillates instead of remaining at zero. This is probably due to the interaction of the device junction capacitances, snubber capacitances and the tank inductances in the circuit. In addition, since an ideal short circuit is not realizable in practice, the trajectory in Fig. 5.34(h) does not quite stay on the vertical axis, as predicted in Fig. 5.19(d).

The horizontal line b of Fig. 5.33 represents the case when I_{oN} is between 1 and $\sqrt{2}$. Only base-drive strategy-1 is possible in this load range. The order of modes for increasing operating frequency will then be MULTIPLE, TM1, CCM ($\omega_N < \omega_{MAX}$), CCM ($\omega_N > \omega_{MAX}$), TM1 and LIMIT. Figure 5.36 shows the experimental trajectories for $I_o = 1.0A$ ($I_{oN} = 1.034$) which confirms the sequence of trajectories predicted. The corresponding experimental waveforms are shown in Fig. 5.37. The effect of parasitics is again responsible for the trajectory to cross the vertical axis prior to mode change (see Figs. 5.36(c) and 5.36(d)), whereas this mode change occurs exactly at the vertical axis under ideal conditions.

Line c in Fig. 5.33 is for the case when $I_{oN} > \sqrt{2}$ under ideal lossless conditions. Again the order of mode occurrence when operating frequency is continuously increased is MULTIPLE, TM1 ($\omega_N < \omega_{MAX}$), TM1 ($\omega_N > \omega_{MAX}$) and LIMIT. In this case, as noted earlier, CCM does not occur at all. The trajectory figures in Fig. 5.38 for $I_o = 1.5A$ ($I_{oN} = 1.551$) confirm this phenomenon clearly. In Fig. 5.38, the trajectory corresponding to ω_{MAX} (Fig. 5.38(d)) occurs in TM1 (and not in CCM) at an operating frequency less than the resonant frequency. In the case of the MULTIPLE region operation (Fig. 5.38(a)), the trajectory during the resonant interval differs from that in Fig. 5.24(a) because the output dc current was not strictly constant during the entire operating period. This causes a gradual shift in the topological mode centers M2 and M4 during the resonant intervals. The waveforms corresponding to the trajectories of Fig. 5.38 are shown in Fig. 5.39.

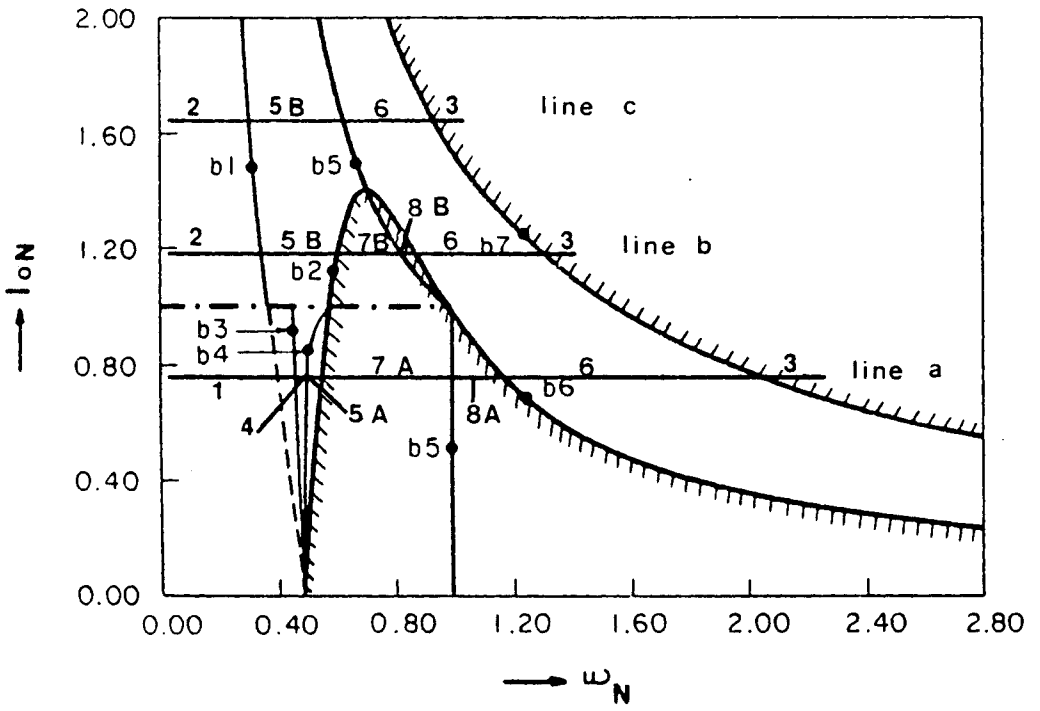

Figure 5.33. Explanatory diagram for the experimental verification of PRC modes

5.34

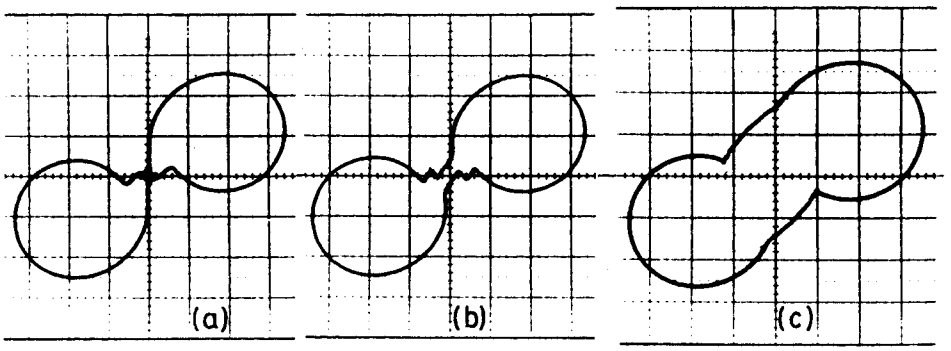

5.34

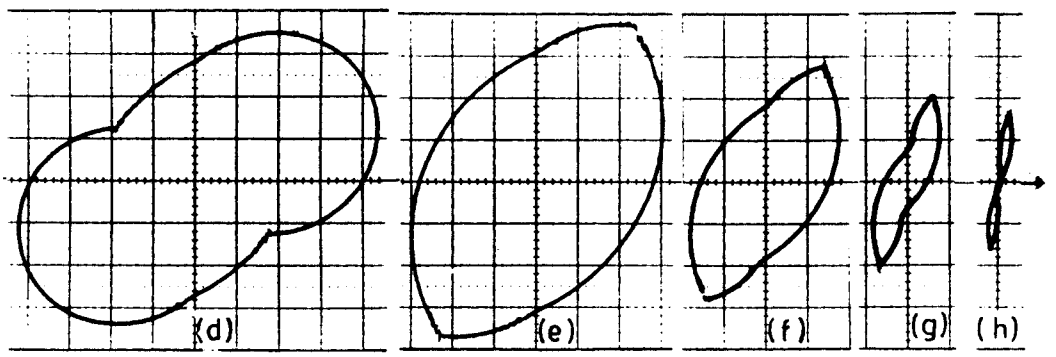

Figure 5.34. Oscillograms of experimental trajectories under Strategy-2 with I_o = 0.5 A (I_{oN} = 0.517) - line 'a' of Fig. 5.33

Scale:- x: 12.925 V/div y: 0.5 A/div

a) 15.05 kHz; DCM
b) 24.63 kHz; TM2
c) 30.73 kHz; CCM (ω_N < 1)
d) 36.78 kHz; CCM (ω_N < 1)
e) 63.06 kHz; CCM (ω_N > 1)
f) 68.59 kHz; CCM (ω_N > 1)
g) 78.70 kHz; TM1
h) 90.60 kHz; near LIMIT

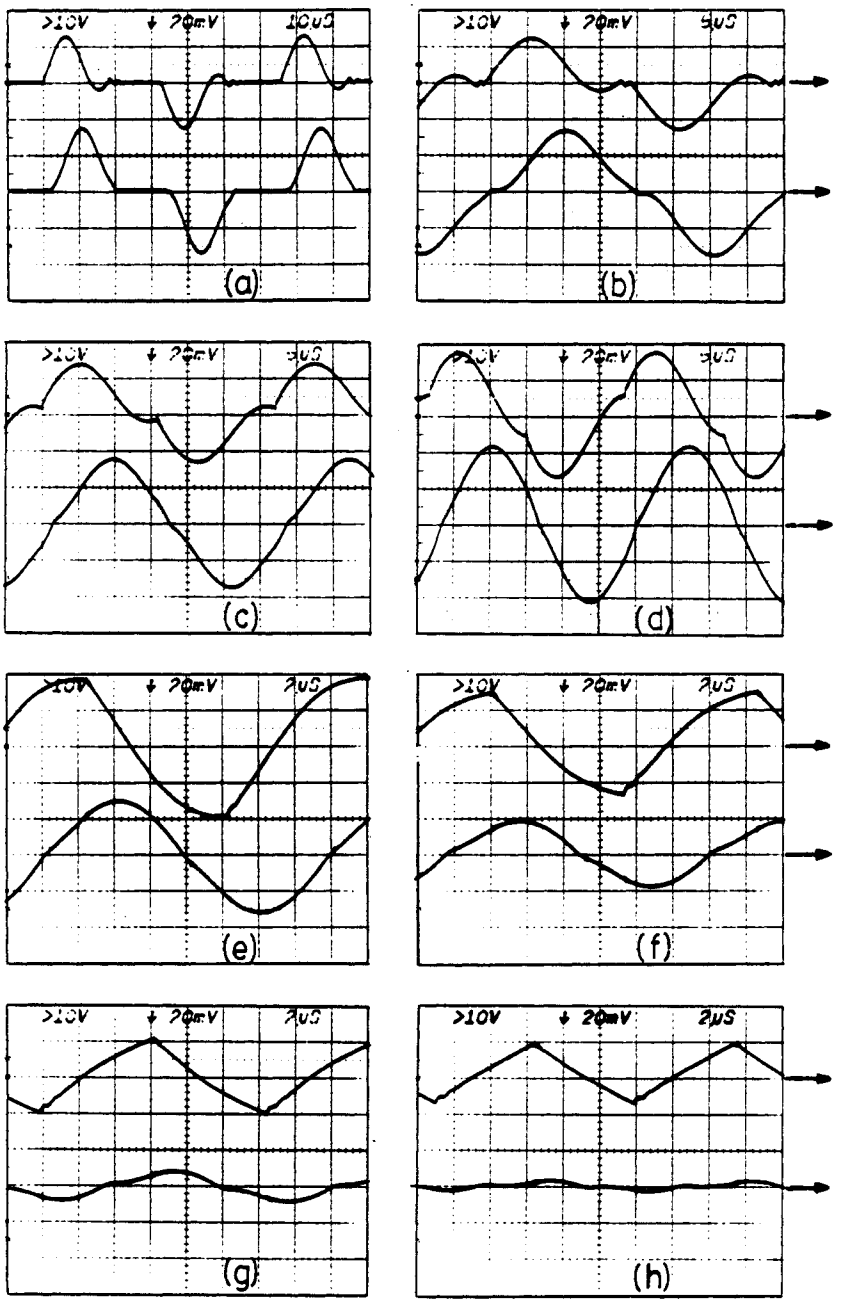

Figure 5.35. Waveforms corresponding to Fig. 5.34

Scale:- x: a) 10 μs/div; b) to d) 5 μs/div; e) to h) 2 μs/div
y: top trace i_L 1 A/div; bottom trace v_C 25.85 V/div

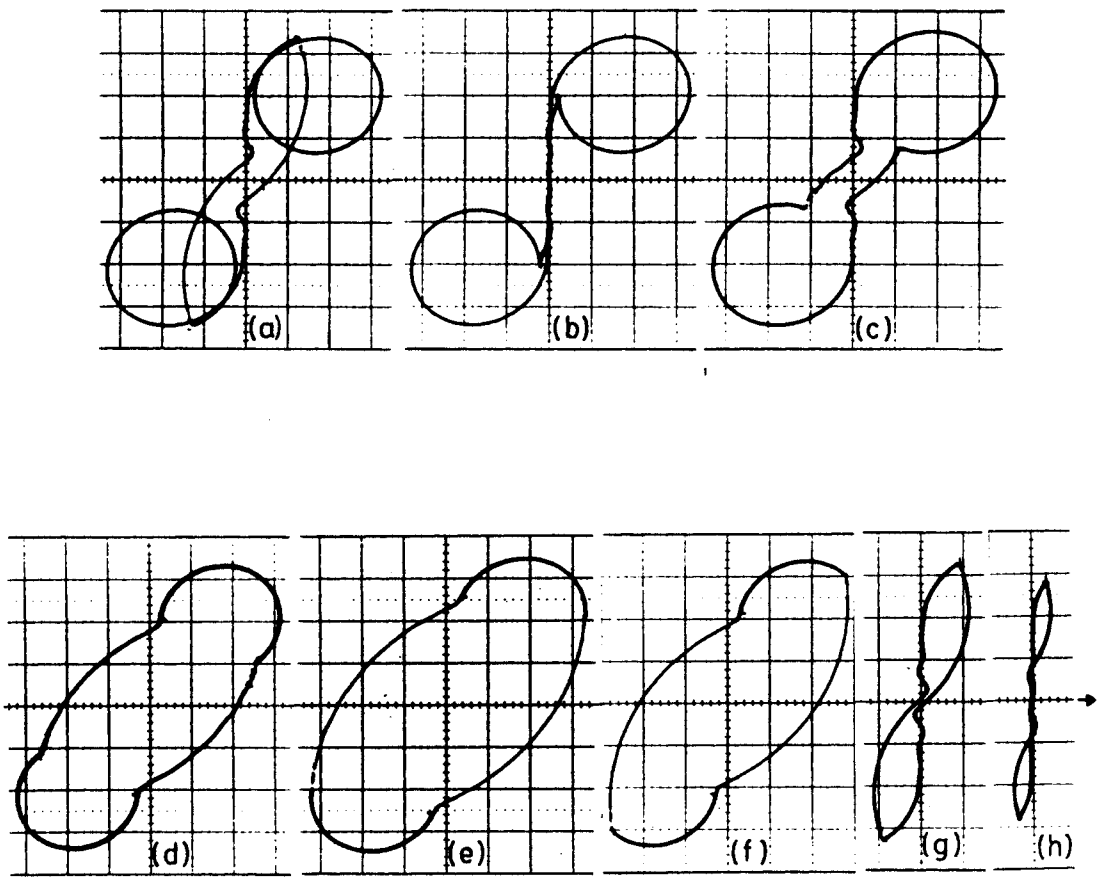

Figure 5.36. Oscillograms of experimental trajectories under Strategy-1 with $I_o = 1.0$ A ($I_{oN} = 1.034$) - line 'b' of Fig. 5.33

Scale:- x: 12.925 V/div y: 0.5 A/div

a) 17.32 kHz; MULTIPLE
b) 19.92 kHz; MULTIPLE/TM1 boundary
c) 26.00 kHz; TM1
d) 33.62 kHz; CCM ($\omega_N < \omega_{MAX}$)
e) 40.92 kHz; CCM ($\omega_N = \omega_{MAX}$)
f) 44.48 kHz; CCM ($\omega_N > \omega_{MAX}$)
g) 48.00 kHz; TM1
h) 52.27 kHz; near LIMIT

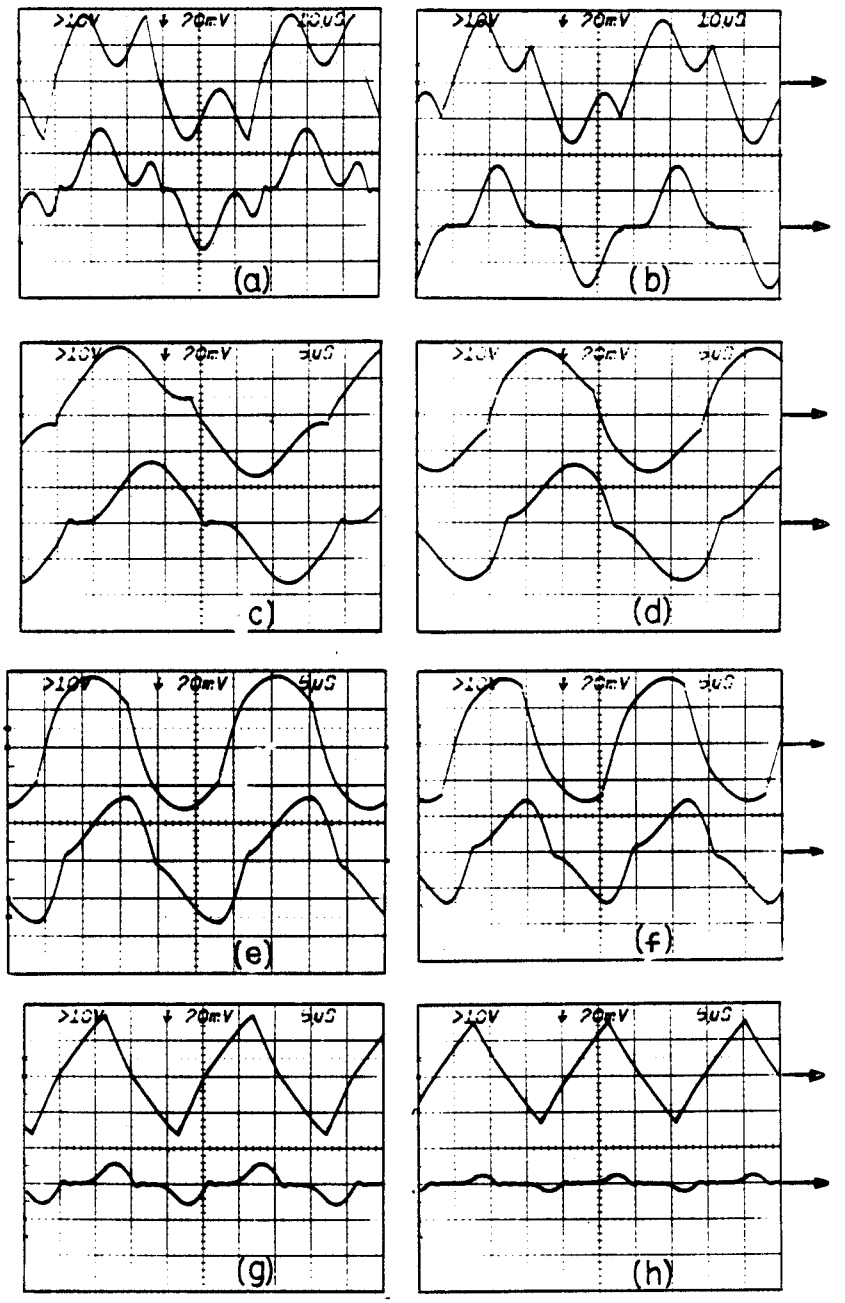

Figure 5.37. Waveforms corresponding to Fig. 5.36

Scale:- x: a) & b) 10 µs/div; c) to h) 5 µs/div
y: top trace i_L 1 A/div; bottom trace v_C 25.85 V/div

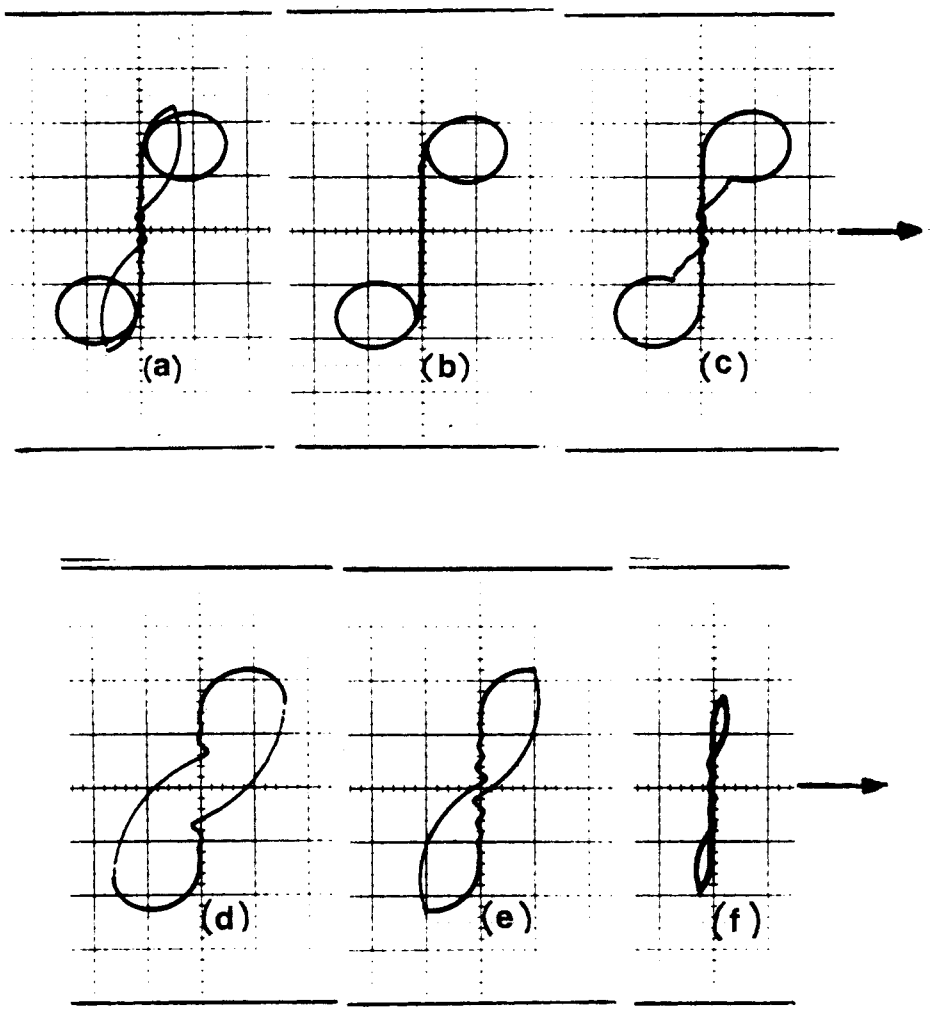

Figure 5.38. Oscillograms of experimental trajectories under Strategy-1 with I_o = 1.5 A (I_{oN} = 1.551) - line 'c' of Fig. 5.33

Scale:- x: 25.85 V/div y: 1.0 A/div
a) 15.66 kHz; MULTIPLE d) 31.80 kHz; TM1 ($\omega_N = \omega_{MAX}$)
b) 17.50 kHz; MULTIPLE/TM1 boundary e) 34.57 kHz; TM1 ($\omega_N > \omega_{MAX}$)
c) 22.23 kHz; TM1 ($\omega_N < \omega_{MAX}$) f) 40.88 kHz; near LIMIT

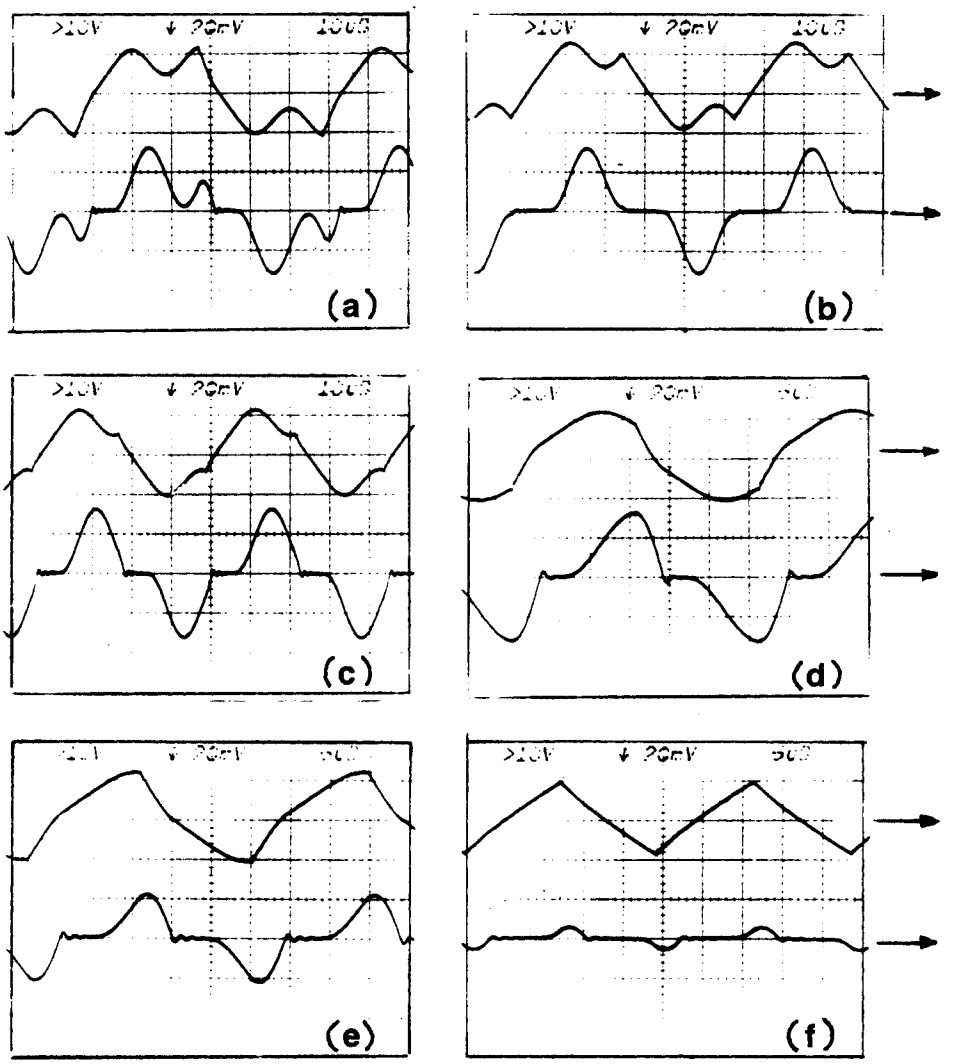

Figure 5.39. Waveforms corresponding to Fig. 5.38

Scale:- x: a), b) &c) 10 μs/div; d), e) & f) 5 μs/div
y: top trace i_L a) & b) 2 A/div c) to f) 1 A/div; bottom trace v_C 25.85 V/div

5.5.2 Mode Boundaries

The mode boundaries of the PRC were experimentally determined and compared with the theoretical boundaries. These results are given in Figs. 5.40, 5.41 and 5.42. The boundary data points were determined based on visual observations of oscilloscope trajectories. Since in many cases the change of modes appears to occur gradually, the measurements of the mode boundaries are somewhat approximate.

The experimental boundaries in Figs. 5.40, 5.41 and 5.42 follow the pattern of the theoretical predictions. However, deviations are observed between the theoretical and experimental boundaries. These are, most probably, due to the effects of the parasitic losses present in an actual circuit. Qualitative explanations of how this can occur are provided with respect to two of the boundaries in this section.

Figure 5.40 shows the theoretical and experimental CCM boundary (ω_{LOW} and ω_{HIGH} together). The nature of the experimental curve is similar to that of the theoretical curve. However, under heavy loads, deviations are observed between the theoretical and the experimental results.

Figure 5.41 shows three more boundaries of interest. They are ω_{MUL},ω_{MAX} and ω_{LIMIT}. The results for the ω_{MUL} boundary clearly follows the theoretical results. In the case of the ω_{MAX} boundary, ω_{MAX} equals unity at low values of I_{oN} as per prediction whereas, deviations are observed at large load current values. The ω_{LIMIT} experimental curve again clearly follows the shape of the theoretical curve. Of course, under short-circuit conditions, the circuit parasitics can be expected to play a dominant part. Thus, the actual short-circuit current is much less than even the theoretical values. This feature is actually an advantage when using this circuit.

Figure 5.42 shows two boundaries under base-drive strategy-2. The boundary ω_{TRAN} was not experimentally determined since it was difficult to determine from oscilloscope observations the exact transition points between TM1 and TM2. In Fig. 5.42, the actual natural commutation region is seen to be smaller than the theoretical predictions. The main deviation is in the lowering of the maximum I_{oN} value for natural commutation from unity to lesser values. A qualitative explanation of this phenomenon based on the effect of circuit losses is provided below.

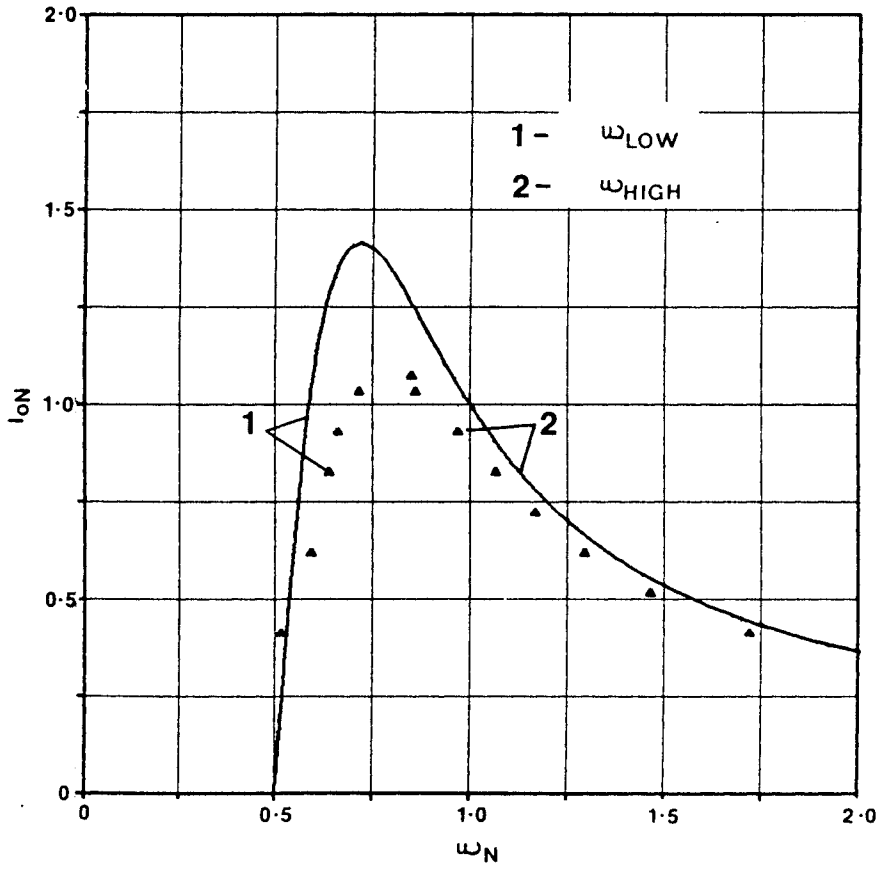

Figure 5.40. Experimental mode boundaries - ω_{LOW} and ω_{HIGH}

Bold line - theoretical; Data points - experimental

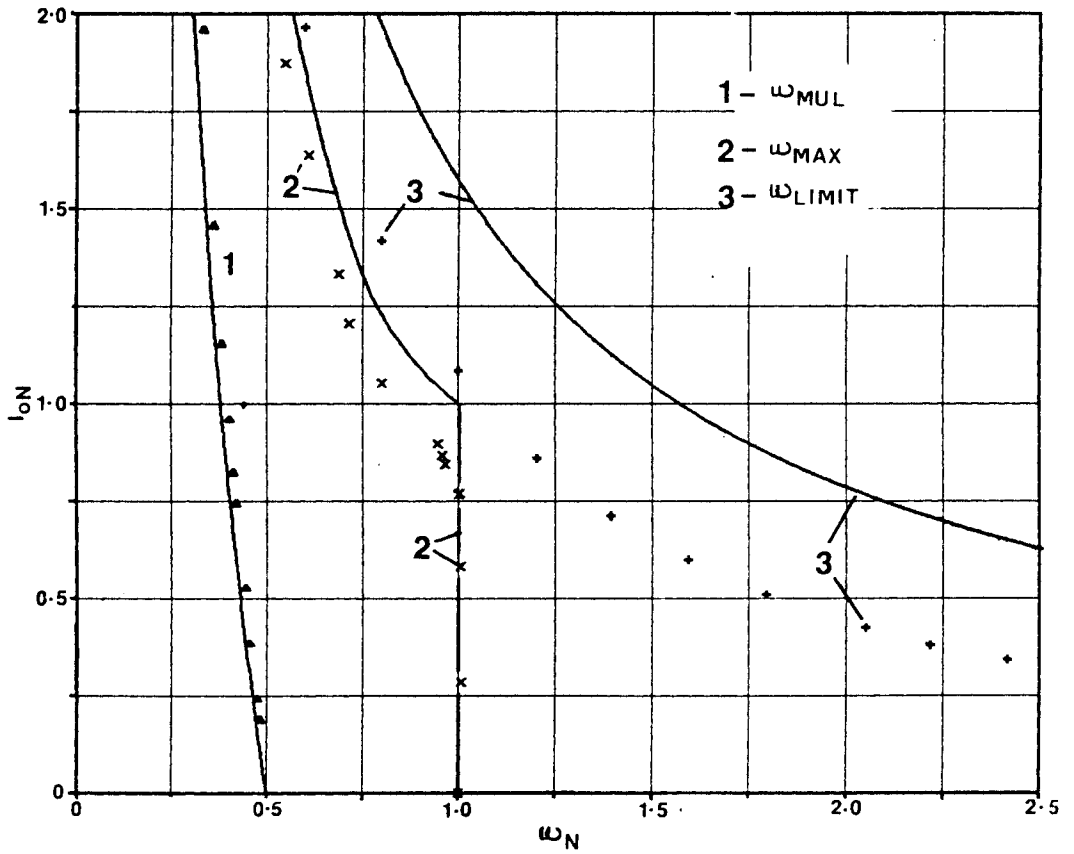

Figure 5.41. Experimental boundaries - ω_{MUL}, ω_{MAX} and ω_{LIMIT}

Bold line - theoretical; Data points - experimental

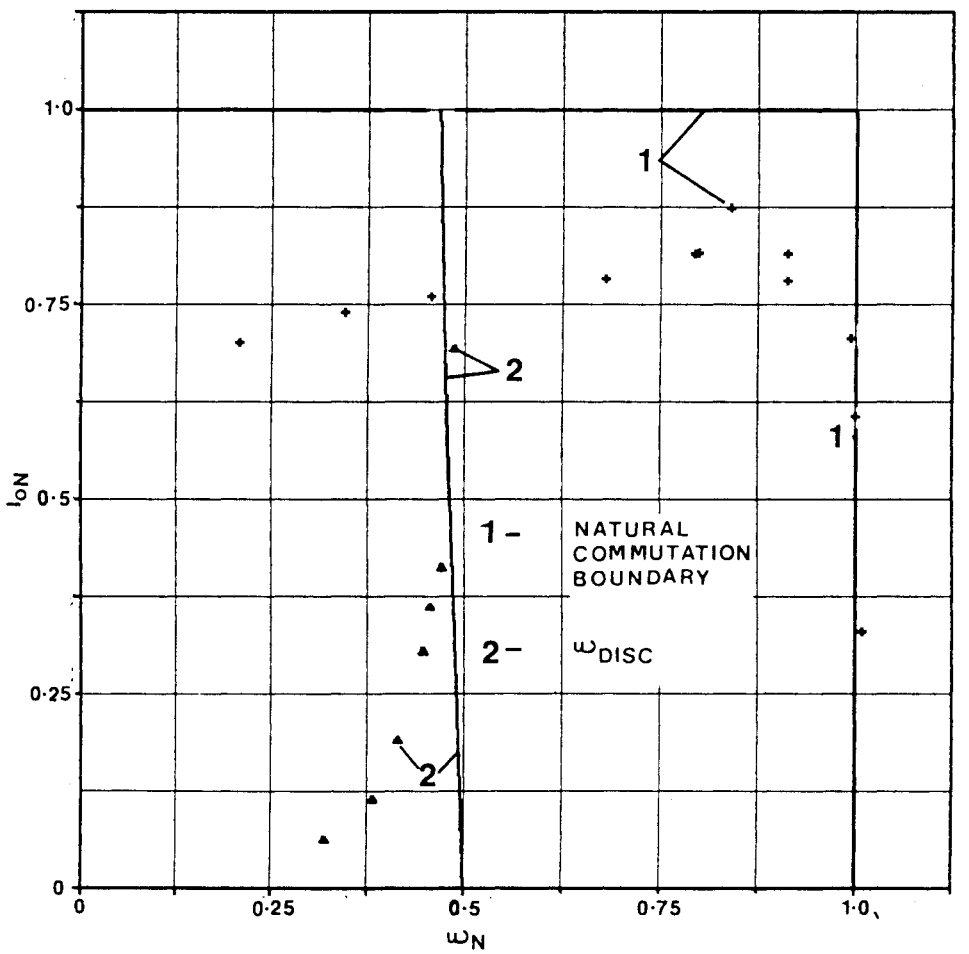

Figure 5.42. Experimental boundaries - Natural commutation region and ω_{DISC}

Bold line - theoretical; Data points - experimental

Figure 5.43 shows a series of diagrams used to explain this phenomenon. Figure 5.43(a) is the trajectory diagram for operation below ω_{DISC} when I_{oN} equals unity. This diagram is similar to Fig. 5.17(e) when $I_{oN} = 1$. In Fig. 5.43(a) if I_{oN} is greater than unity, the transistors will not be naturally commutated, since the antiparallel diodes fail to conduct. In this diagram, during the resonant period, the starting radius (M2A) equals unity. Since no losses have been assumed, the radius at the end of the resonant cycle (M2D) is also unity. If, however, losses are included, then the radius of the trajectory can be expected to gradually reduce, in a spiral fashion, as was shown for a series resonant converter in Chapter 3. Thus, M2D will no longer be unity but a value less than unity. This situation is illustrated in Fig. 5.43(b). This figure clearly shows how circuit parasitic losses cause loss of commutation when I_{oN} is unity. Figure 5.43(c) shows the operation with the new boundary value of I_{oN} for the natural commutation region. Thus, the existence of the parasitic losses tend to reduce the maximum load possible with natural commutation operation.

Figure 5.42 also shows the experimental and theoretical ω_{DISC} boundary. Once again discrepancies are observed between these two results. Particularly as $I_{oN} \rightarrow 0$, the theoretical value of ω_{DISC} , approaches 0.5 whereas the experimental value tends to zero. These deviations may be explained qualitatively with the help of Fig. 5.44 as follows.

Figure 5.44(a) is similar to Fig. 5.17(e) and represents the operation at the boundary frequency ω_{DISC}. Reproducing (C.52), the angular time period $\omega_0 T$ corresponding to this boundary frequency is given by

$$\omega_0 T = 2\,(2\pi - \theta_2 + \frac{OH}{I_{oN}} + I_{oN}) \tag{5.14}$$

In the above equation, the term OH/I_{oN} is the contribution of the capacitor discharging interval, to the total operating period. Since no losses are assumed in the ideal analysis, the radius M2A ($=1$) stays constant throughout the resonant interval. Thus M2A = M2D = R = 1 in Fig. 5.44(a). When losses are included the radius progressively reduces with time during the resonant interval as shown in Fig. 5.44(b). Thus, the distance OH in Fig. 5.44(b) will be more than that in Fig. 5.44(a). This has the effect of making angular period $\omega_0 T$ at the DCM boundary longer when losses are considered than when losses are neglected. In other words, for the same load current, the value of ω_{DISC} when losses are considered will be less than the ideal case, as confirmed by Fig. 5.42.

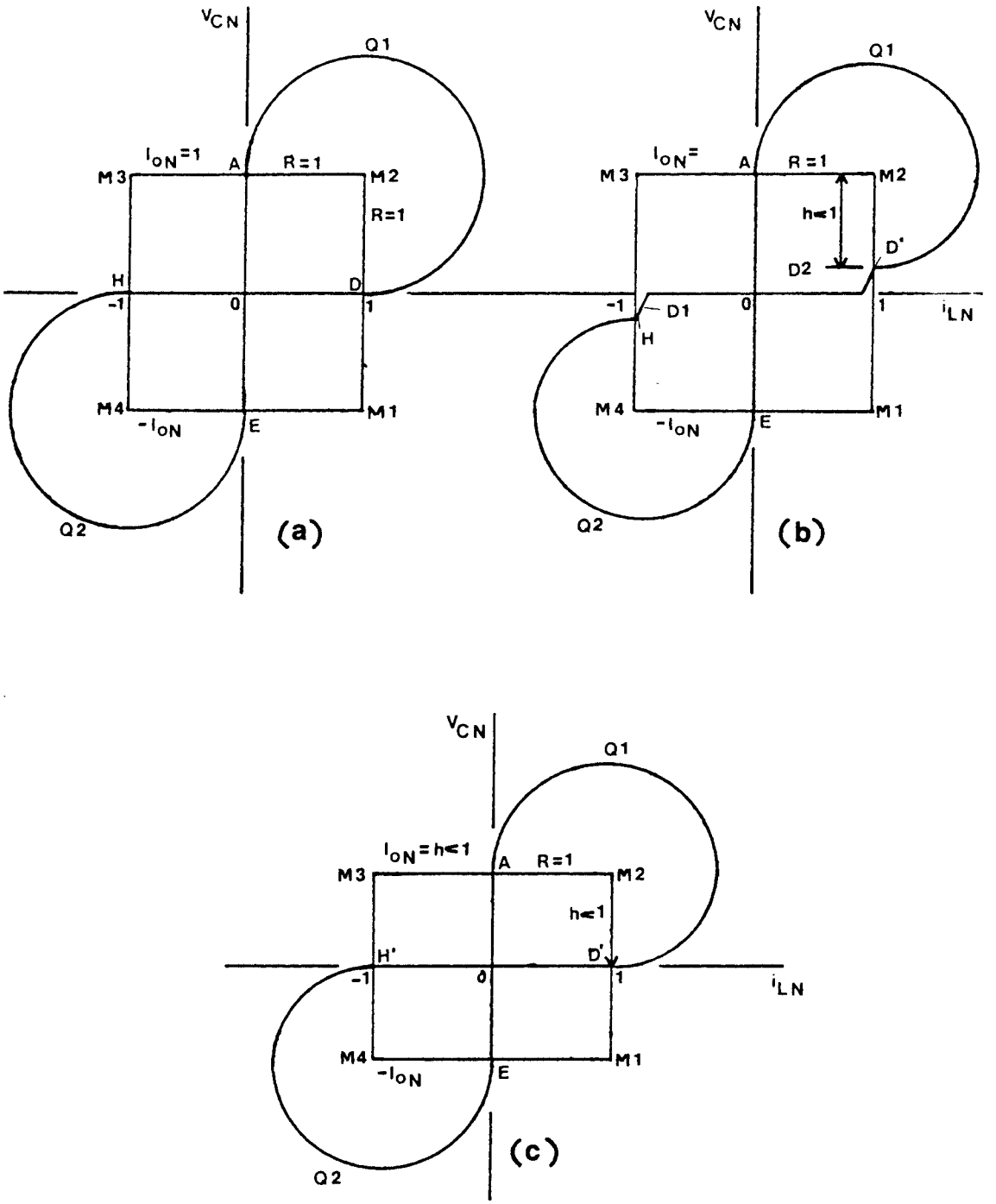

Figure 5.43. Explanatory diagrams for reduction in natural commutation region

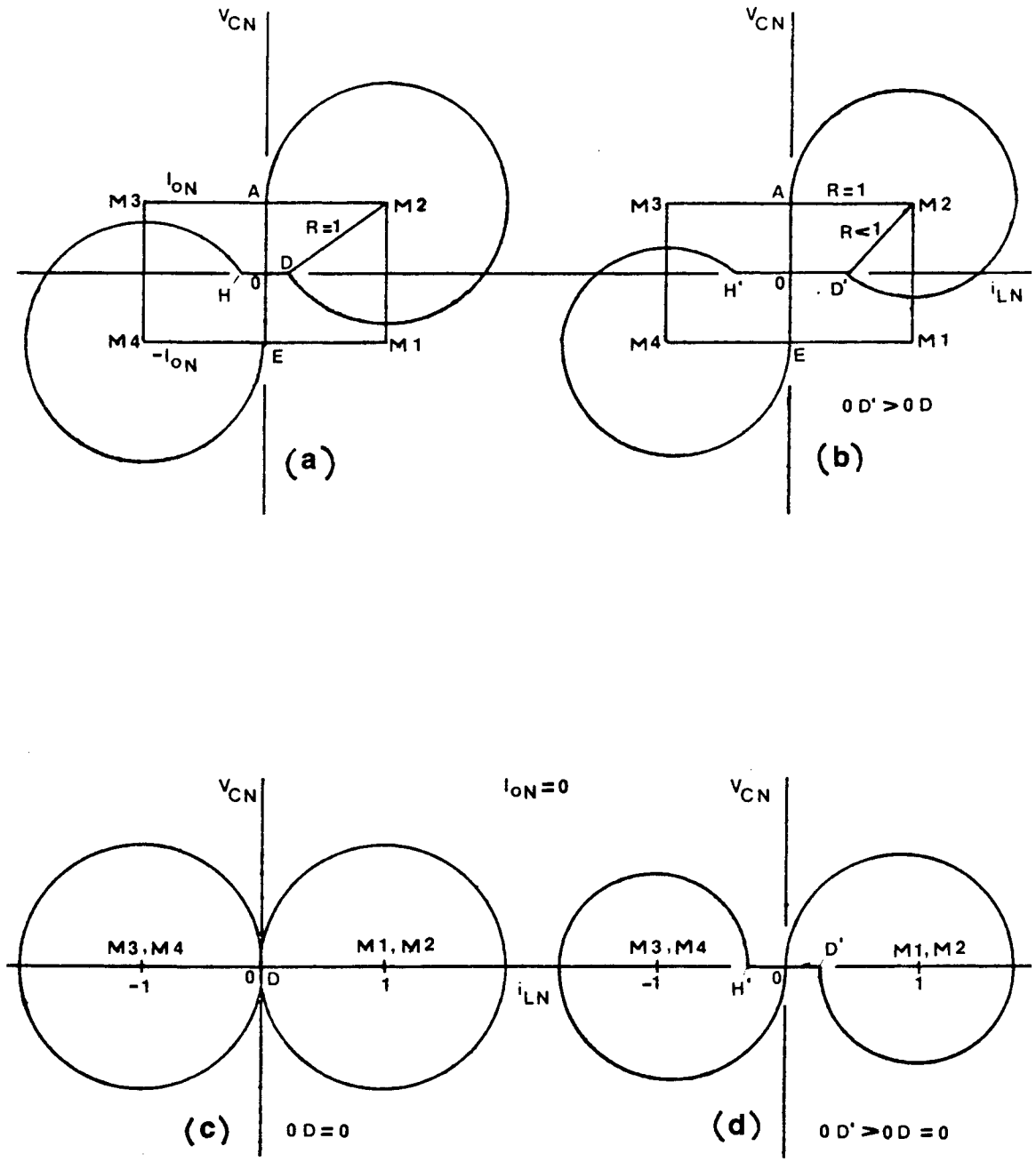

Figure 5.44. Explanatory diagrams for deviation observed in ω_{DISC} boundary

Figures 5.44(c) and 5.44(d) are used to explain the reason for ω_{DISC} boundary to tend towards the origin as I_{oN} approaches zero in Fig. 5.42. Figure 5.44(c) shows the ideal steady-state trajectory when the load current equals zero. However, when losses are included, based on previous explanations, the situation in Fig. 5.44(d) can be anticipated. Such experimental trajectories were, in fact, observed for operation close to no load conditions. In Fig. 5.44(d), the distance OH is no longer zero. Since I_{oN} is zero, the contribution of the capacitor-discharge-interval term, OH/I_{oN}, to the operating period in (5.14) tends to infinity. This, of course, has the effect of reducing the ω_{DISC} boundary frequency to zero as no load conditions are approached. The experimental measurements, as shown in Fig. 5.42, confirm this.

5.5.3 DC Characteristics

The results of the experimental verification of the dc characteristics are shown in Figs. 5.45 and 5.46. Figure 5.45 is applicable for operating frequencies below resonant frequency and Fig. 5.46 for operating frequencies above resonant frequency. In making these measurements, an additional voltage of 1.4 volts has been added to the measured output voltage to account for the voltage drops in the output rectifier bridge (2 X 0.7 volts).

In Figs. 5.45 and 5.46, at operating frequencies away from resonant frequency and at low loads, the PRC behaves somewhat like a good dc voltage source as mentioned earlier. At frequencies close to resonant frequency, the operation deviates from that of the voltage source. The experimental results confirm the above. The experimental data also confirm the ability of the PRC circuit to limit the current under short-circuit conditions.

At operating frequencies close to resonant frequency and at large magnitudes of the load current, the observed data and the predicted curves differ significantly. This is particularly true for operation below resonant frequency. In Chapter 3, it was shown that the experimental data from a series resonant converter also exhibits a similar pattern and that by inclusion of the losses in the analysis, the deviations that occur in practice are predicted more accurately. In the case of the PRC also, the inclusion of losses in the analysis will, most probably, result in better matching between the theoretical characteristics and the experimental results.

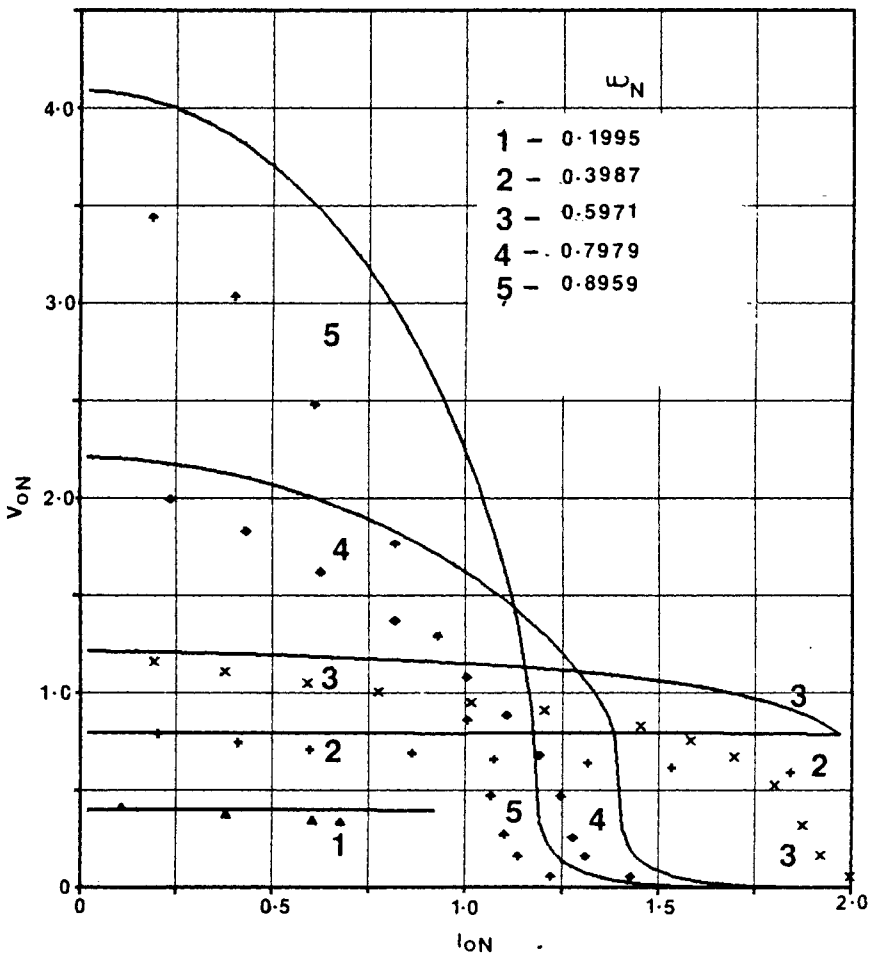

Figure 5.45. Experimental DC characteristics - Below resonant frequency

Bold line - theoretical; Data points - experimental

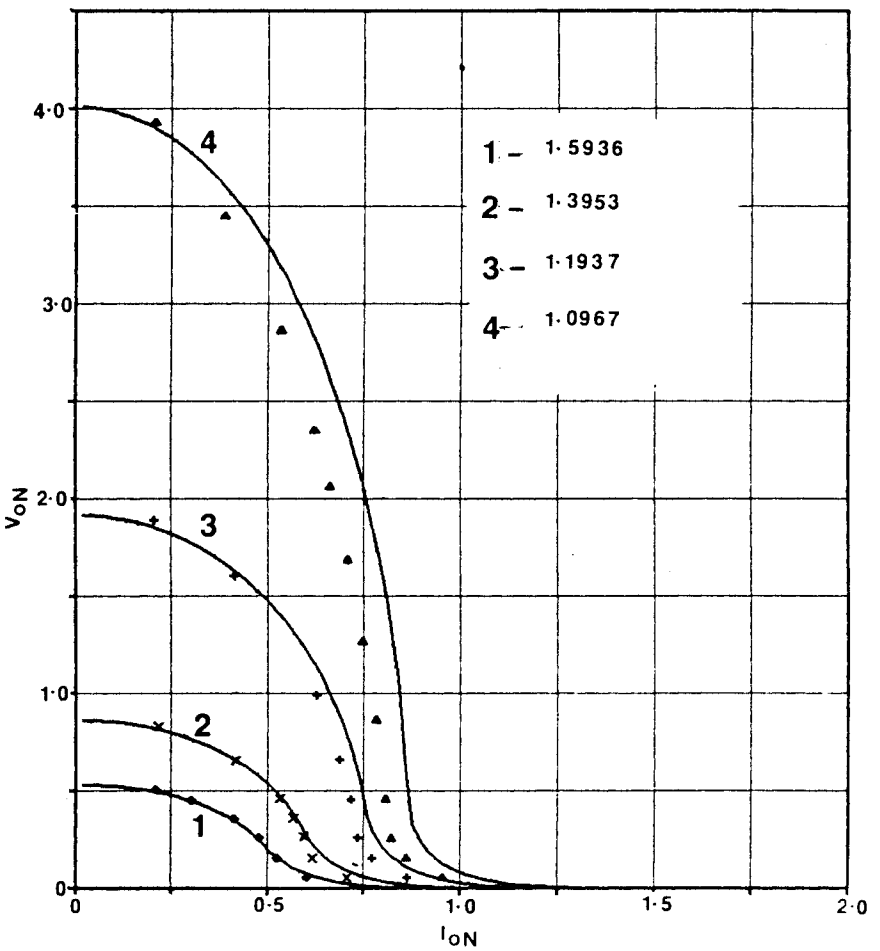

Figure 5.46. Experimental DC characteristics - Above resonant frequency

Bold line - theoretical; Data points - experimental

5.6 Novel Resonant Buck Converter

5.6.1 Circuit Derivation

In Fig. 5.30, when ω_N is less than 0.5, the dc conversion ratio is almost a linear function of ω_N and is almost independent of load. Figure 5.47(a) shows the state-plane diagram, similar to Fig. 5.17(e), of the PRC operating in DCM. In this mode, after Q1 and D1 conduct and after the discharge period of the resonant capacitor, the circuit comes to rest at the origin. Instead of triggering Q2 as in normal PRC operation, Q1 can be again switched on, thus repeating the previous half-cycle. The resulting steady-state trajectory is shown in Fig. 5.47(b). In Fig. 5.47(b), Q1 is triggered at $t = 0$. The inductor current is linearly charged (topological mode M5) till it equals I_o. At t_1, the clamp on the resonant capacitor is released and the circuit continues in M2 with Q1 conducting. At t_2, Q1 naturally commutates and D1 starts to conduct with the topological mode still remaining at M2. At t_3, D1 commutates naturally leaving a residual capacitor voltage. The resonant capacitor now discharges through the load linearly (M7) and the system reaches origin at t_4. The circuit stays at origin (M9) till t_5, when Q1 is switched on again. Figure 5.48 shows the corresponding tank waveforms.

Figure 5.49 shows a circuit realization of such an operation. In Fig. 5.49(b), devices Q2 and D2 of the PRC in Fig. 5.49(a) have been removed. From Fig. 5.47(b), we note that the resonant capacitor voltage does not reach negative values. Hence, the output bridge rectifier no longer performs any rectifying function. It is needed only to provide a freewheeling path for the load current during the discontinuous-conduction interval ($t_4 - t_5$) and during the inductor-charging interval ($t_5 - t_6$). Due to this, the output circuit can be further simplified with a freewheel diode (Fig. 5.49(c)). The derivation is now complete and Fig. 5.49(c) shows the circuit diagram of the proposed **resonant buck converter**. This converter is one member of a class of resonant converters, named **quasi-resonant converters**, and a complete state-plane analysis including determination of modes and mode boundaries and the dc characteristics applicable to all the members of the quasi-resonant converters is performed in Chapter 6.

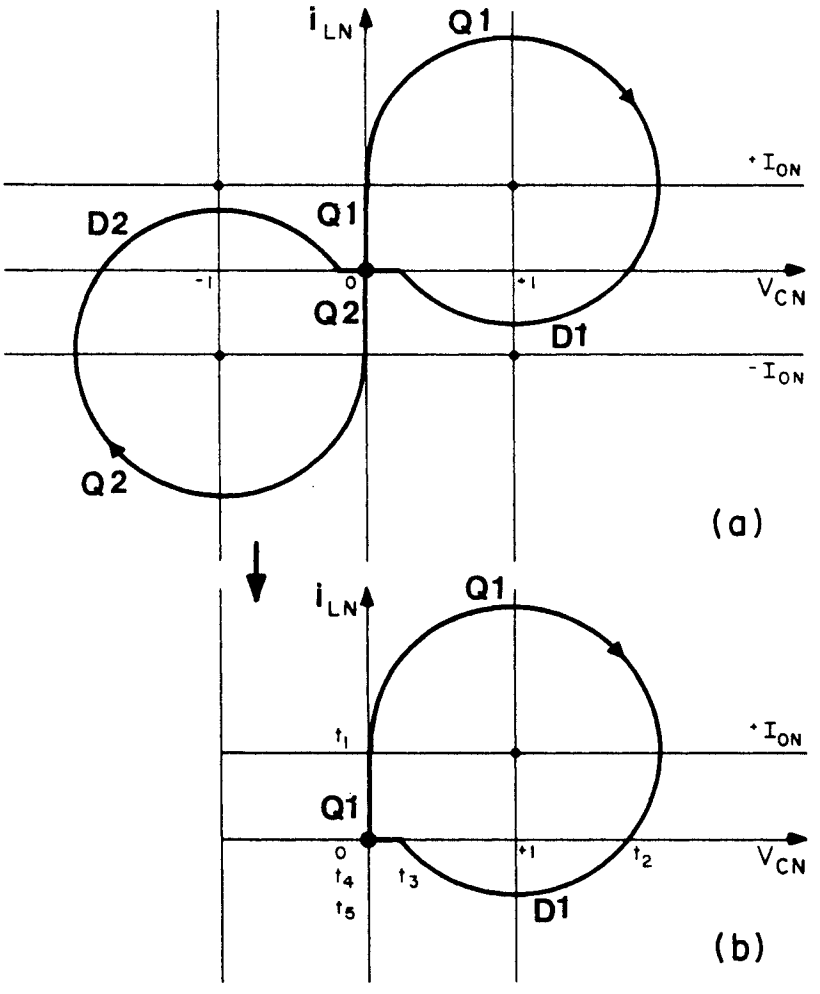

Figure 5.47. State-plane derivation of the resonant buck converter

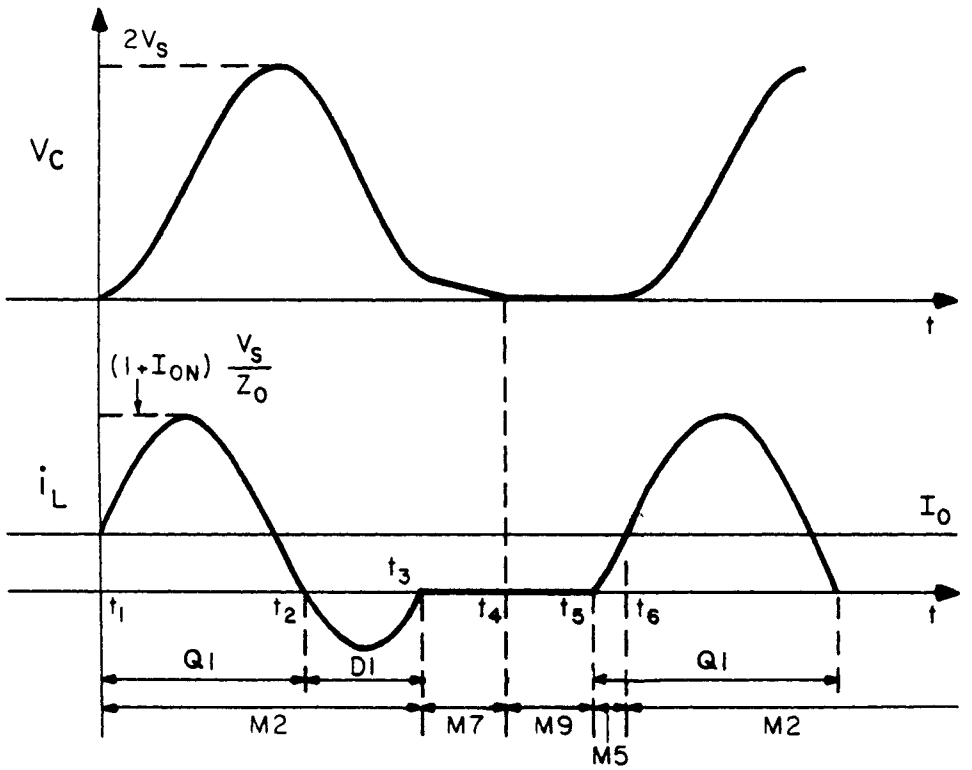

Figure 5.48. Tank waveforms for Fig. 5.47 (b)

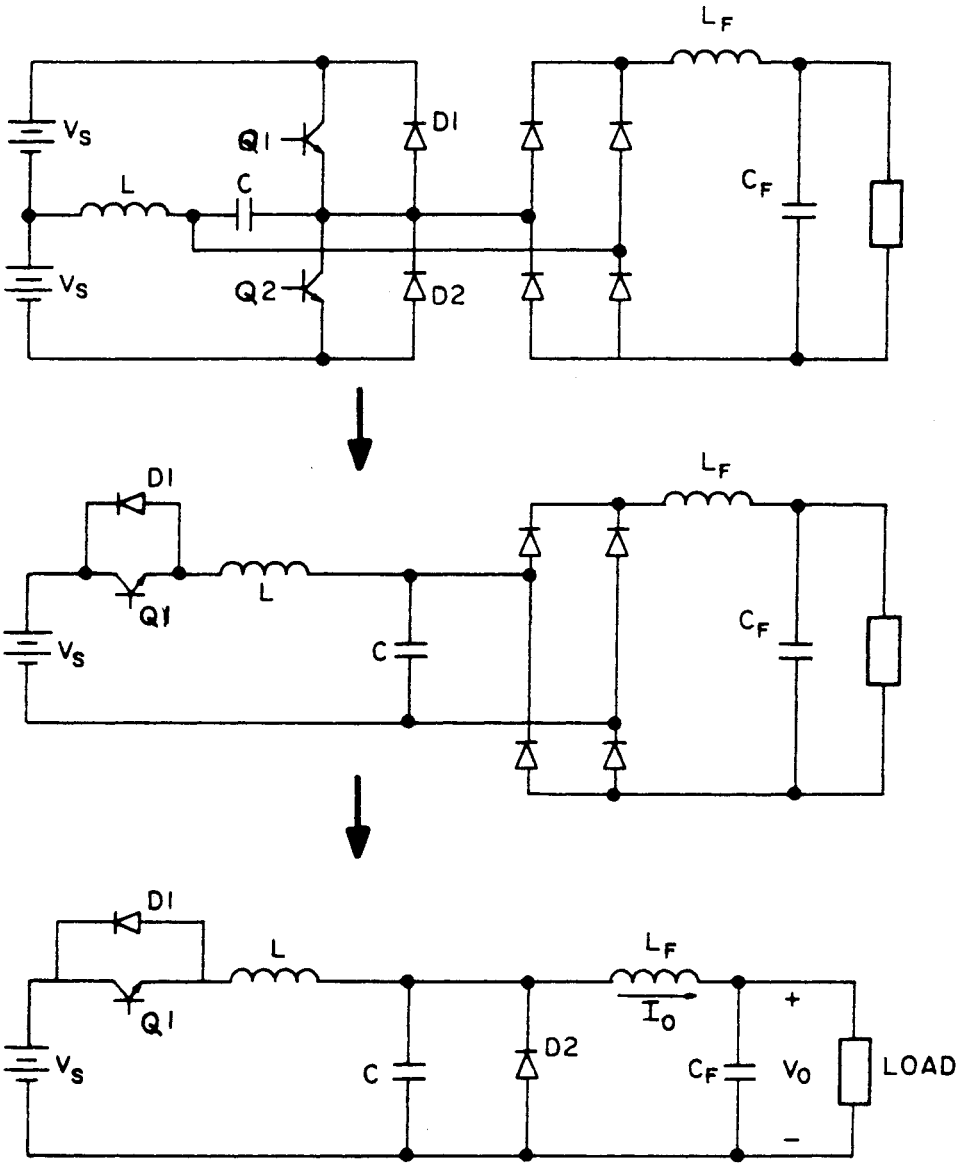

Figure 5.49. Circuit derivation of the novel resonant buck converter

Fig. 5.50 shows the dc characteristics of this resonant buck converter. Since the operation of this converter is similar to DCM operation of a PRC, the output voltage is almost independent of load current. For the same reason, the output voltage varies almost linearly with frequency.

5.6.2 Features Of Resonant Buck Converter

The proposed circuit has certain attractive features which are stated below.

Firstly, the circuit requires only one power switch to implement the resonant converter concept. Secondly, both the transistor and the diode are naturally commutated, thus, virtually eliminating all switching losses. Due to this, the circuit shows potential for very high frequency applications [61]. Thirdly, the output voltage is almost independent of load current, unlike most resonant converters . This is an important feature since the switching frequency can be maintained essentially constant for a varying load.

On the negative side, the circuit requires more components than a normal buck converter. The device rms currents will be somewhat higher. Since the no-load tank current is high, larger idling losses will be present and this may be undesirable in certain applications.

On the whole, however, it is felt that this circuit is an important addition to the family of power processing circuits. Based on this circuit idea and the concept of "resonant switch" developed in [59], a host of new resonant power processing circuits has been introduced [61].

5.7 Conclusions

This chapter presented a graphical state-plane technique for analyzing the complex operating modes of a parallel resonant converter. The analysis uncovers, for the first time, the presence of many modes of operation, besides continuous-conduction mode (CCM) and discontinuous-conduction mode (DCM).

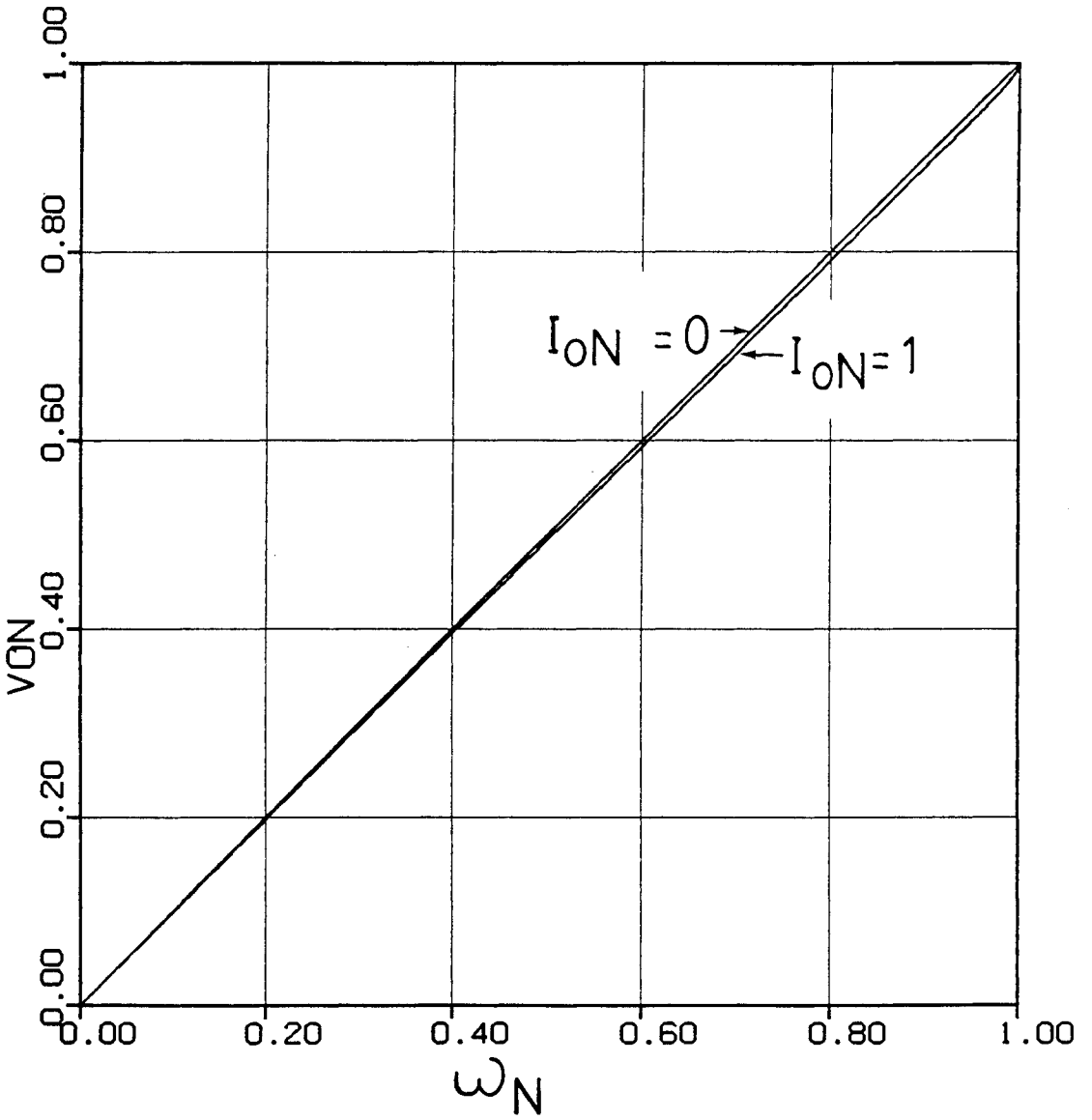

Figure 5.50. Theoretical DC characteristics of the novel resonant buck converter

These different modes of operation are easily predicted as well as portrayed on the state plane by means of closed steady-state trajectory diagrams. Employing such state portrayals, the different regions of operation, such as the CCM regions, transition regions, DCM region, natural commutation region, short-circuit current limit region and multiple cycle conduction region are clearly defined. As part of the analysis, two base-drive strategies for the power switches were also identified and their relative merits discussed.

Appendix C presents a detailed quantitative analysis of the mode boundaries and dc characteristics using the state-plane diagrams developed in this chapter. The results of this ideal analysis, in the form of mode boundary curves and dc characteristic curves, were included in this chapter. These and the remaining design curves given in Appendix C define the operating limits and make a preliminary design of a PRC possible.

The experimental results clearly confirm the existence of the various circuit modes. Also, the mode boundaries and the dc characteristics follow, generally, the pattern established by the ideal analysis. However, deviations were observed between the ideal analytical curves and the experimental ones which are attributed to the effect of circuit parasitic losses. Chapter 3 described a method for predicting the effect of these losses on the performance of a series resonant converter. Similar work may be done for a PRC also, to account for the observed deviations.

The insight gained form the analysis has led to the proposal of a novel resonant buck converter, possessing the combined properties of a PRC operated in DCM and a conventional buck converter. A desirable feature of this converter is that the voltage-conversion ratio is almost independent of load. Since the control does not have to compensate for load variations, the converter's operating frequency range can be smaller, which is an advantage. Furthermore, since the power switch and its antiparallel diode are both naturally commutated, all switching losses and stresses are virtually eliminated. This enables this converter to operate at very high frequencies. This circuit is a member of a family of resonant conveters called "quasi-resonant converters". Chapter 6 carries out a detailed state-plane analysis of these converters.

Chapter 6

State-Plane Analysis Of Quasi-Resonant Converters

6.0 Symbols Of Variables

The symbols listed below include those used in Appendix d also. In alphabetical order,

Δi_L	-	Change in Inductor Current
Δi_{LN}	-	Normalized Change in Inductor Current
Δt	-	Change in Time
Δv_C	-	Change in Capacitor Voltage
Δv_{CN}	-	Normalized Change in Capacitor Voltage
φ	-	Conduction Angle during Resonant Interval
ρ	-	Radius of a State Trajectory
θ	-	Angular Interval on State Plane
θ_0	-	Initial Angle on State Plane
$\theta_1, \theta_2, ..$	-	Different Angular Intervals on State Plane
ω	-	Operating Frequency

ω_0	-	Resonant Frequency of the *LC* Circuit
ω_N	-	Normalized Operating Frequency
ω_{MAX}	-	Normalized Upper Limit Frequency
ω_{ND}	-	Normalized Boundary Frequency between Modes 1 & 2
ω_{NU}	-	Normalized Boundary Frequency between Modes 2 & 3
C	-	Value of Resonant Capacitor
C_i	-	Value of Energy Transfer Capacitor
I_2	-	DC Current in Transfer Inductor
I_E	-	An Equivalent DC Current
I_{EN}	-	Normalized Equivalent DC Current
I_i	-	DC Input Current
i_{LN}	-	Normalized Instantaneous Inductor Current
I_{L0}	-	Initial Inductor Current
I_{L0N}	-	Normalized Initial Inductor Current
I_o	-	Output DC Current
I'_{oN}	-	Modified Normalized Output DC Current
L	-	Value of Resonant Inductor
N_i	-	Current Normalizing Factor
N_v	-	Voltage Normalizing Factor
R, R'	-	Radius of Trajectory during Resonant Interval
t	-	Time
T	-	Operating Period
$t_1, t_2, .. t_A, t_B, ..$	-	Particular Instants of Time
t_0	-	Initial Time
$T_I, T_{II}, ..$	-	Durations of Interval I, Interval II, etc.
T_N	-	Angular Operating Period
v_C	-	Instantaneous Resonant Capacitor Voltage
V_{CAV}	-	Average Capacitor Voltage
V_{CAVN}	-	Normalized Average Capacitor Voltage
v_{CN}	-	Normalized Instantaneous Capacitor Voltage
V_{C0}	-	Initial Capacitor Voltage
V_{C0N}	-	Normalized Initial Capacitor Voltage

V_{EN}	-	Normalized Equivalent Driving Voltage
V_I	-	DC Voltage across Transfer Capacitor
v_L	-	Instantaneous Voltage Across Inductor
v_{LN}	-	Normalized Instantaneous Voltage Across Inductor
V_o	-	Output DC Voltage
V'_{oN}	-	Modified Normalized Output DC Voltage
V_s	-	Supply DC Voltage
Z_0	-	Characteristic Impedance of Resonant Tank

6.1 Introduction

The conventional switch of a pulse-width modulated converter (PWM) may be replaced in many cases by a resonant switch [61,62], which is a combination of a switch and an LC resonant network. The addition of the LC network modifies the current and voltage waveforms of the switch such that the turn-on and turn-off losses are minimized. The family of converters thus realized are called quasi-resonant converters (QRC). In a period of steady-state operation, a QRC circuit undergoes, besides the resonant operating interval, other nonresonant intervals also. Thus, the name quasi-resonant converter is appropriate.

The novel, resonant-buck-converter circuit, which was derived in Chapter-5 from the parallel resonant converter (PRC), is a member of the QRC family. Several different quasi-resonant converter topologies exist and the task of analyzing and understanding them can be laborious. The present work aims to perform dc analysis applicable to all members of the QRC family. To do this, sixteen QRC topologies, each one corresponding to one type of QRC circuit, are identified for convenience as the "basic quasi-resonant converters". Among these, certain groups of converters have identical state-plane diagrams and, hence, can be analyzed together. This reduces the number of independent analyses needed to only four. Detailed dc analyses including determination of mode boundaries and dc characteristics are performed for each of these four cases and these analyses are then extended to all QRC topologies.

Two circuit rules, named the 'inductor shift rule' and the 'capacitor shift rule', are introduced. Using these rules many topological variations, including new ones, are derived from the basic QRC circuits. The dc analyses performed on the basic QRCs are shown to be unaltered by these transformations. Thus, the analysis in this chapter is general and valid for all the different QRC circuits. However, certain specific waveforms and component ratings vary among these different QRC topologies and can be determined from the shift rules. A few examples are provided in which the QRC variations are compared based on their relative component stresses. On the basis of such comparisons, sixteen QRC topologies, each corresponding to one type of QRC circuit, are identified as having low component stresses.

6.2 Basic Quasi-Resonant Converters

Resonant switches are classified into zero-current resonant switches (ZCS) [61] and zero-voltage resonant switches (ZVS) [62] which are electrically the dual of one another. Each of these can be either a half-wave type or a full-wave type. Thus, the four types of resonant switches (see Fig. 6.1) are:

1. Half-wave ZCS
2. Full-wave ZCS
3. Half-wave ZVS
4. Full-wave ZVS

Each of the switches in Fig. 6.1 has only two terminals. This makes it possible to replace a (two terminal) normal switch in a PWM converter with a resonant switch.

The combination of the switch and the LC elements in the novel resonant buck converter (Fig. 5.49) can be recognized as the full-wave ZCS (Fig. 6.1(b)). The derivation of the resonant buck converter presented in Sec. 5.6 led to the identification of the full-wave ZCS and its superior load handling ability [60,61].

In the ZCS (Figs. 6.1(a) and 6.1(b)), device current i_{S1} is zero at both switch-on and switch-off, thereby minimizing loss. In the ZVS (Figs. 6.1(c) and 6.1(d)), device voltage v_{S1} is likewise zero at both switch-on

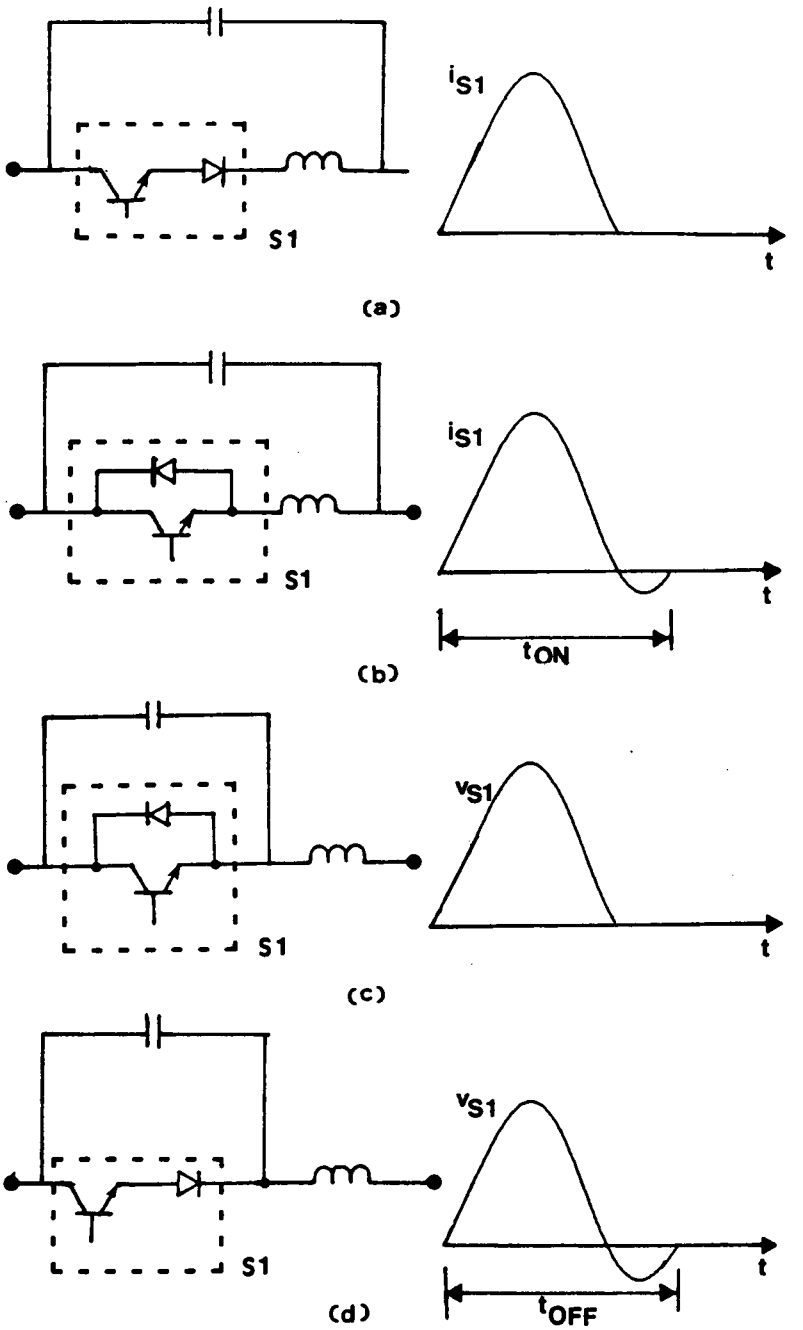

Figure 6.1. Resonant switches
a) Half-wave zero current switch
b) Full-wave zero current switch
c) Half-wave zero voltage switch
d) Full-wave zero voltage switch

and switch-off, thus, once again minimizing loss. The resonant circuit is completed in the ZCS when switch S1 is closed, whereas in the ZVS, the resonant circuit is completed when switch S1 is opened.

The four PWM converter topologies used for obtaining QRCs are buck, boost, buck-boost and Cuk (boost-buck). By substituting each of the four resonant switches of Fig. 6.1 for the normal switch in each of the four PWM converter topologies, a group of sixteen converters, called "basic quasi-resonant converters" (Fig. 6.2), is obtained. The number of QRCs in Fig. 6.2 is actually sixteen since either a half-wave resonant switch or a full-wave resonant switch may be used in these circuits.

6.3 *Intervals Of Operation*

The different intervals of operation (or topological modes) that occur in ZCS and ZVS QRCs are shown in Table-6.1. These intervals are similar to the topological modes M1 through M9 exhibited by the PRC which were discussed in Chapter 5. Figure 6.3 shows the equivalent circuits applicable to the different intervals of operation for both ZCS QRCs and ZVS QRCs. Brief descriptions of these intervals are given below.

During the inductor charging/discharging interval (Fig. 6.3(a) & (e)), the resonant inductor has a dc voltage across it. The current in the inductor either increases or decreases in a linear manner. The state trajectory during this interval lies on a vertical line parallel to the i_{LN} axis.

The resonant interval (Fig. 6.3(b) & (f)) will be studied in detail in Sec. 6.3.1. Switch S1 is closed for a ZCS QRC and open for a ZVS QRC. The resonant capacitor voltage and the resonant inductor current are not clamped to any value so that the resonant circuit is free to resonate. The state trajectory is circular.

During the capacitor charging/discharging interval (Fig. 6.3(c) & (g)), a dc current charges/discharges the resonant capacitor. The voltage across the capacitor rises or falls in a linear manner.

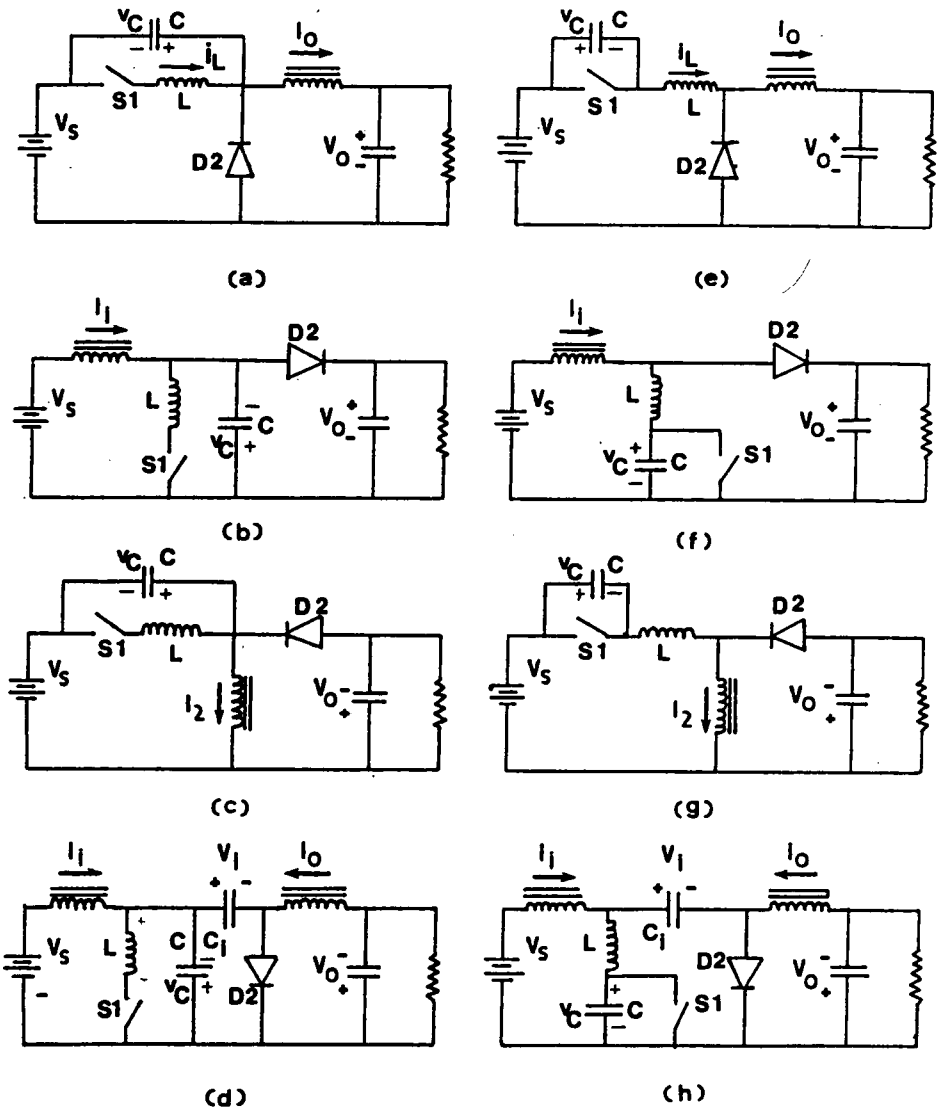

Figure 6.2. Basic quasi-resonant converters
a) Buck with ZCS
b) Boost with ZCS
c) Buck-boost with ZCS
d) Boost-buck with ZCS
e) Buck with ZVS
f) Boost with ZVS
g) Buck-boost with ZVS
h) Boost-buck with ZVS

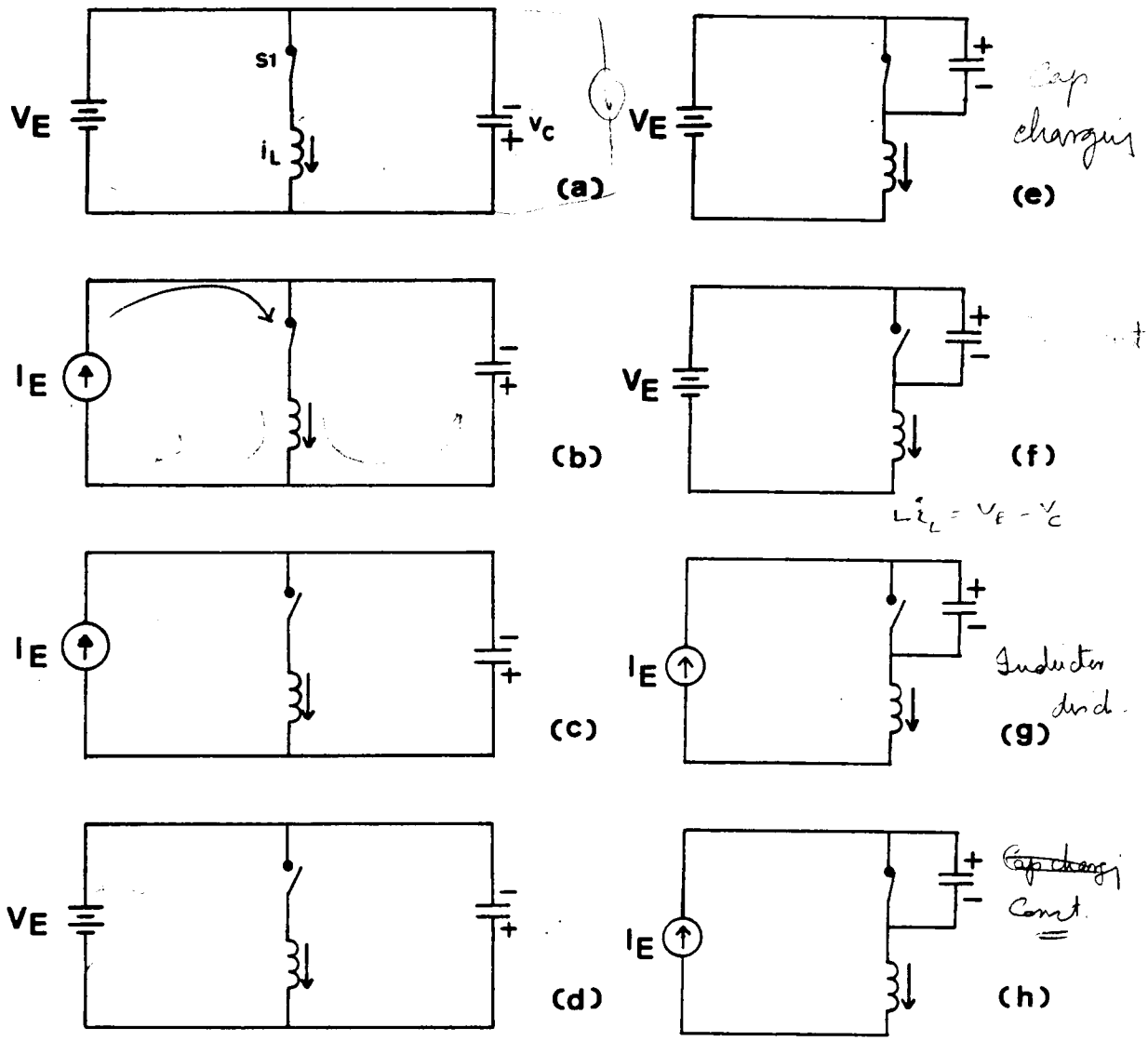

Figure 6.3. Equivalent circuits during different intervals of operation
a) Inductor charging/discharging interval : ZCS
b) Resonant interval : ZCS
c) Capacitor charging/discharging interval : ZCS
d) Constant state interval : ZCS
e) Same as (a) but with ZVS
f) Same as (b) but with ZVS
g) Same as (c) but with ZVS
h) Same as (d) but with ZVS

TABLE-6.1

QRC - INTERVALS OF OPERATION

Interval Number		Interval Name
ZCS	ZVS	
I	III	Inductor charging/discharging interval
II	II	Resonant interval
III	I	Capacitor charging/discharging interval
IV	IV	Constant state interval

The resonant inductor current and the resonant capacitor voltage are both held at constant values during the constant state interval (Fig. 6.3(d) & (h)). The state trajectory on the state plane is a point.

6.3.1 Resonant Interval Analysis

The state trajectory equation for both ZCS and ZVS-based basic QRCs will be derived in this section. The two assumptions made are that the 1)parasitic losses are neglected and 2)the filter inductors and capacitors are sufficiently large such that current and voltage ripple can be neglected. Certain parameters are now defined to make analysis common to the different converter topologies. Let,

$$\omega_0 = \frac{1}{\sqrt{L\,C}} = \text{Tank resonant frequency (rad/sec)} \tag{6.1}$$

$$Z_0 = \sqrt{\frac{L}{C}} = \text{Characteristic impedance (ohm)} \tag{6.2}$$

$$\theta = \omega_0 (t - t_0) = \text{Angular interval on state plane} \tag{6.3}$$

Define equivalent voltage V_E as per the following.

$$V_E = V_s \quad \text{(Buck)} \tag{6.4}$$

$$V_E = V_o \quad \text{(Boost)} \tag{6.5}$$

$$V_E = V_s + V_o \quad \text{(Buck-Boost)} \tag{6.6}$$

$$V_E = V_i \quad \text{(Boost-Buck)} \tag{6.7}$$

In (6.4) through (6.7), V_o is the output voltage, V_s , the supply voltage and V_i is the transfer capacitor voltage associated with capacitor C_i (Fig. 6.2) in the case of boost-buck converters.

Define likewise the equivalent current I_E.

$$I_E = I_o \quad \text{(Buck)} \tag{6.8}$$

$$I_E = I_i \quad \text{(Boost)} \tag{6.9}$$

$$I_E = I_2 \qquad \text{(Buck-Boost)} \tag{6.10}$$

$$I_E = I_i + I_o \qquad \text{(Boost-Buck)} \tag{6.11}$$

In (6.8) through (6.11), I_o is the output filter current, I_i is the input filter current and I_2 is the current of the transfer filter inductor in the case of the buck-boost converter.

The normalizing factors used in the analysis are as follows:

$$N_v = V_E = \text{ Voltage normalizing factor} \tag{6.12}$$

$$N_i = \frac{V_E}{Z_o} = \text{ Current normalizing factor} \tag{6.13}$$

6.3.1.1 Basic ZCS QRCs

During the resonant interval, the equivalent circuit in Fig. 6.3(b) is common to the different basic ZCS converters. The circuit equation for Fig. 6.3(b) is,

$$\begin{bmatrix} \dot{v}_C \\ \dot{i}_L \end{bmatrix} = \begin{bmatrix} 0 & \frac{1}{C} \\ \frac{-1}{L} & 0 \end{bmatrix} \begin{bmatrix} v_C \\ i_L \end{bmatrix} - \begin{bmatrix} \frac{1}{C} \\ 0 \end{bmatrix} I_E \tag{6.14}$$

with initial conditions $i_L/_{(t=t_0)} = I_{L0}$ and $v_C/_{(t=t_0)} = V_{C0}$.

Solving (6.14),

$$\begin{aligned} v_C &= (I_{L0} - I_E) Z_0 \sin \omega_0 (t - t_0) + V_{C0} \cos \omega_0 (t - t_0) \\ i_L - I_E &= (I_{L0} - I_E) \cos \omega_0 (t - t_0) - \frac{V_{C0}}{Z_0} \sin \omega_0 (t - t_0) \end{aligned} \tag{6.15}$$

Normalizing all voltages with N_v and all currents with N_i, and using (6.3), (6.15) can be written as

$$\begin{aligned} v_{CN} &= (I_{L0N} - I_{EN}) \sin \theta + V_{C0N} \cos \theta \\ i_{LN} - I_{EN} &= (I_{L0N} - I_{EN}) \cos \theta + V_{C0N} \sin \theta \end{aligned} \tag{6.16}$$

The subscript N in (6.16) refers to normalized circuit variables. By eliminating θ in (6.16), the equations for the state trajectory are

$$(i_{LN} - I_{EN})^2 + v_{CN}^2 = (I_{LON} - I_{EN})^2 + V_{CON}^2 = \rho^2 \tag{6.17}$$

$$\text{Also,} \quad \theta = \tan^{-1}\left\{\frac{-(i_{LN} - I_{EN})}{v_{CN}}\right\} - \theta_0, \quad \text{where} \tag{6.18}$$

$$\theta_0 = \tan^{-1}\left\{\frac{-(I_{LON} - I_{EN})}{V_{CON}}\right\} \tag{6.19}$$

The center of the circular state trajectory is located at $(0, I_{EN})$ on the state plane. The angle subtended by the trajectory segment is proportional to time elapsed as indicated by (6.3), (6.18) and (6.19).

6.3.1.2 Basic ZVS QRCs

In this case, during the resonant interval, the equivalent circuit in Fig. 6.3(f) is applicable. The circuit equation for Fig. 6.3(f) is,

$$\begin{bmatrix} \dot{v}_C \\ \dot{i}_L \end{bmatrix} = \begin{bmatrix} 0 & \frac{1}{C} \\ \frac{-1}{L} & 0 \end{bmatrix} \begin{bmatrix} v_C \\ i_L \end{bmatrix} + \begin{bmatrix} 0 \\ \frac{1}{L} \end{bmatrix} V_E \tag{6.20}$$

with initial conditions $i_L/_{(t=t_0)} = I_{L0}$ and $v_C/_{(t=t_0)} = V_{C0}$.

Solving (6.20) and normalizing with (6.12) and (6.13) and using (6.3),

$$\begin{aligned} v_{CN} - V_{EN} &= I_{LON} \sin\theta + (V_{CON} - V_{EN}) \cos\theta \\ i_{LN} &= I_{LON} \cos\theta - (V_{CON} - V_{EN}) \sin\theta, \end{aligned} \tag{6.21}$$

where the subscript N again refers to normalized circuit variables.

By eliminating θ in (6.19), the following equation for the state trajectory is obtained.

$$i_{LN}^2 + (v_{CN} - 1)^2 = I_{LON}^2 + (V_{CON} - 1)^2 = \rho \tag{6.22}$$

$$\text{Also,} \quad \theta = \tan^{-1}\left\{\frac{-i_{LN}}{v_{CN} - 1}\right\} - \theta_0, \quad \text{where} \tag{6.23}$$

$$\theta_0 = \tan^{-1}\left\{\frac{-I_{LON}}{V_{CON}-1}\right\} - \theta_0 \qquad (6.24)$$

The center of the circular trajectory is located for these converters at (1, 0) on the state plane. The angle subtended by the trajectory segment is proportional to the elapsed time for this case also.

6.4 Normal Mode (Mode-1) Steady-State Trajectories

Normal mode or mode-1 operation refers to the predominant mode of operation of a QRC. Figure 6.4 shows the steady-state trajectories of the basic QRCs for this mode with the four types of resonant switches. The state-plane diagrams depend only on the type of resonant switch. They are found to be identical for different converter topologies such as buck and buck-boost, if the resonant switch used is the same. The numerals I, II, III and IV on these diagrams refer to the different intervals of circuit operation.

Figures. 6.5, 6.6, 6.7 and 6.8 show the common waveforms corresponding to the four different switches. These waveforms vary according to the type of resonant switch and are common to the different converter topologies, such as buck and boost. In these figures, i_{S1} and v_{S1} refer to the current and voltage, respectively, of switch S1. Variables i_{rs} and v_{rs} refer to the current and voltage, respectively, of the resonant switch combination. Variables i_{D2} and v_{D2} correspond to the current and voltage of diode $D2$.

The circuit waveforms other than those shown in Figs. 6.5 through 6.8, can differ among the different topologies as will be illustrated now. For a ZCS buck converter (Fig. 6.2(a)), input supply current i_1 equals resonant switch current i_{rs}. Thus, for this converter, the i_{rs} waveform of Figs. 6.5 or 6.6 corresponds to the input supply current. However, for a ZCS boost converter input supply current i_1 equals input filter inductor current I_l. From (6.9), I_l is the equivalent current I_E for the boost converter. Thus, for this converter, the I_E waveform of Figs. 6.5 or 6.6 is the current waveform of the input supply.

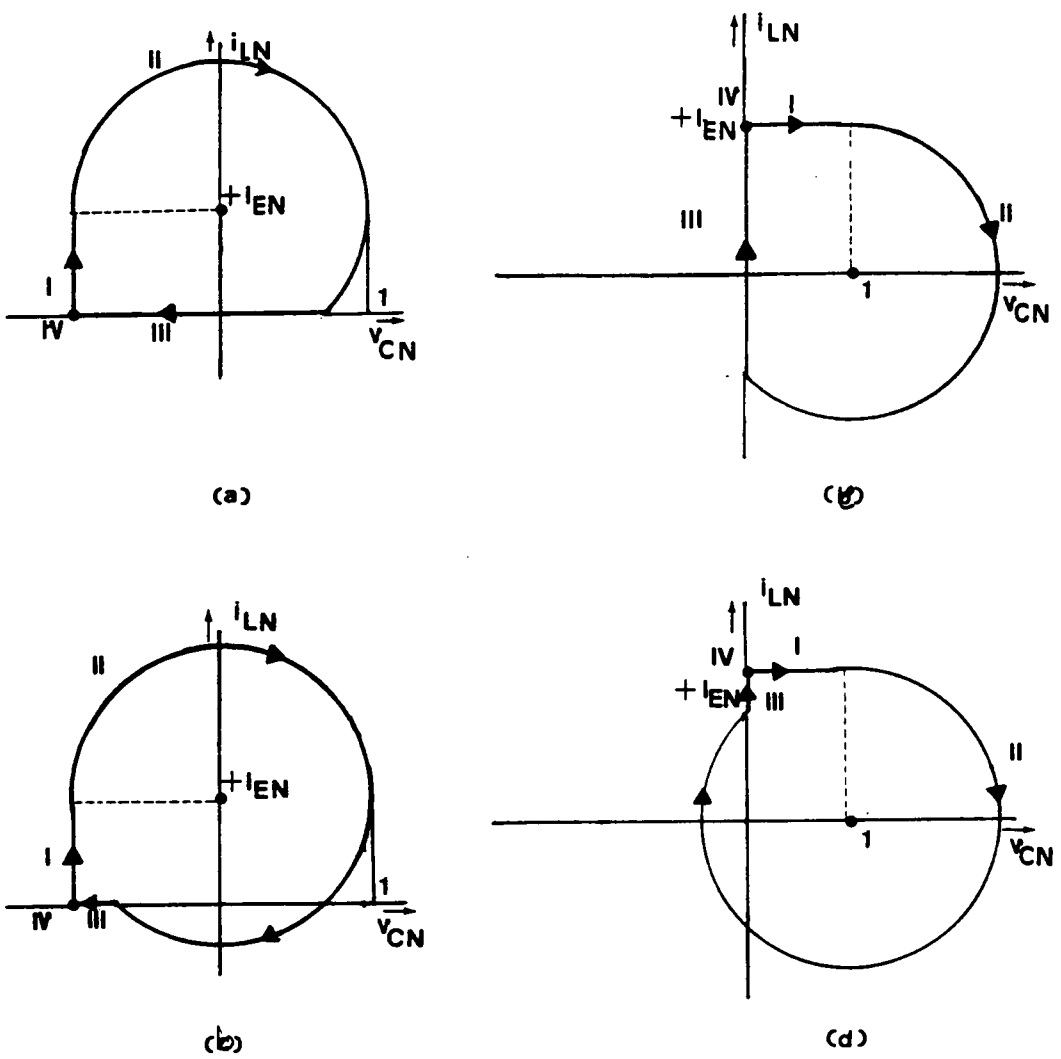

Figure 6.4. Common steady-state trajectories in mode-1
a) Half-wave ZCS
b) Full-wave ZCS
c) Half-wave ZVS
d) Full-wave ZVS

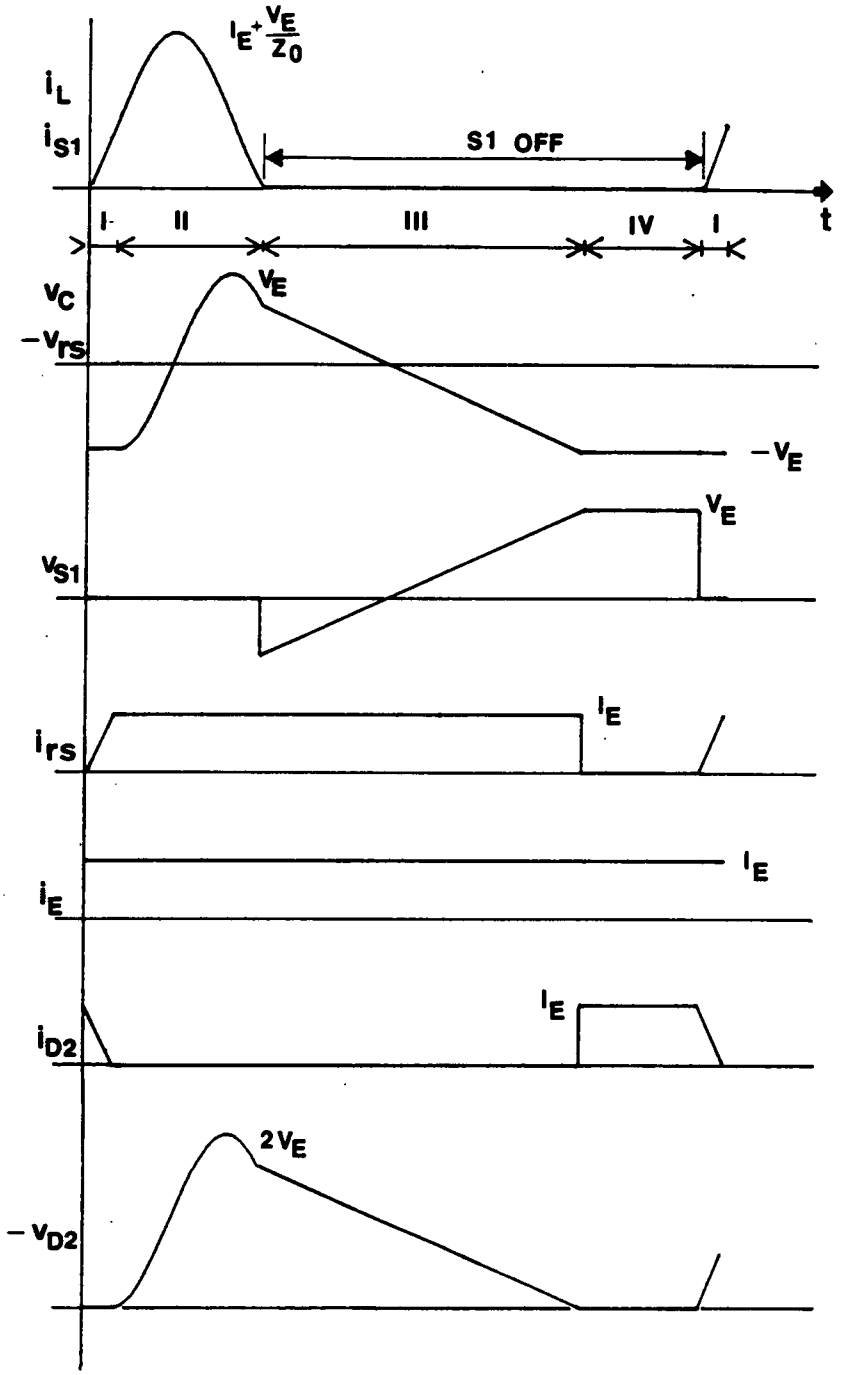

Figure 6.5. Common waveforms for QRCs with half-wave ZCS

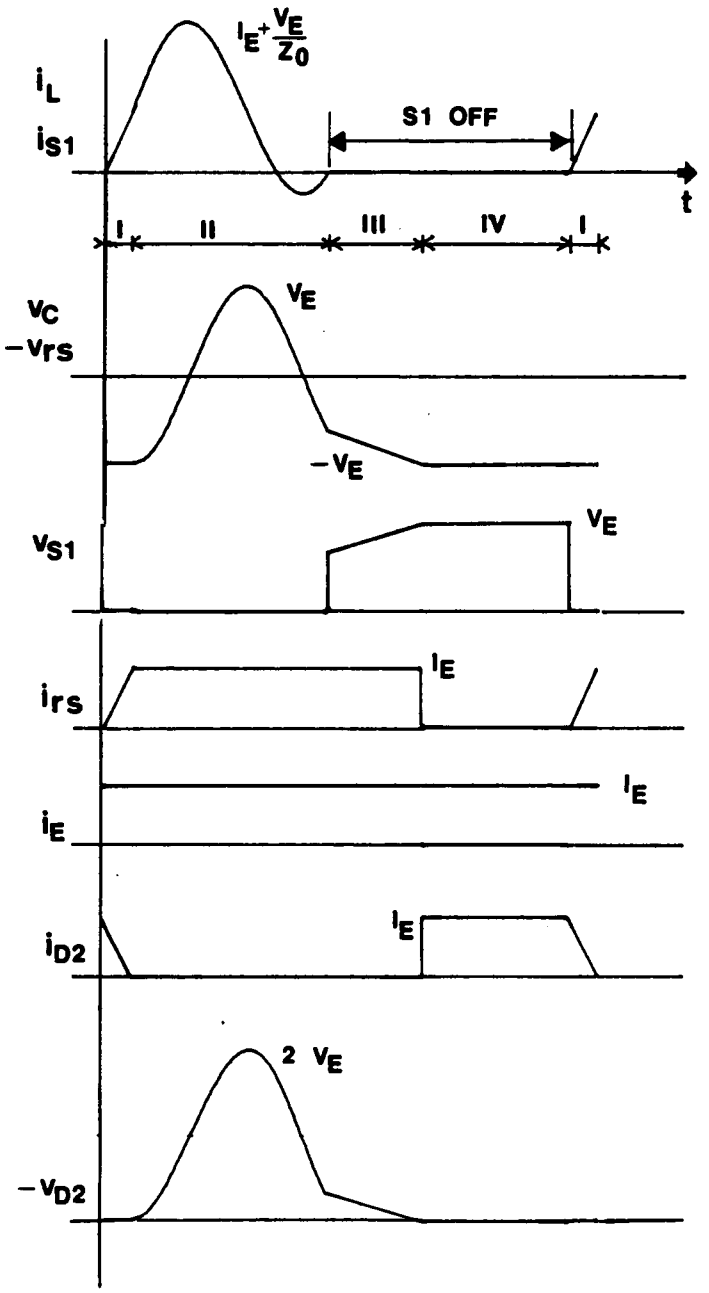

Figure 6.6. Common waveforms for QRCs with full-wave ZCS

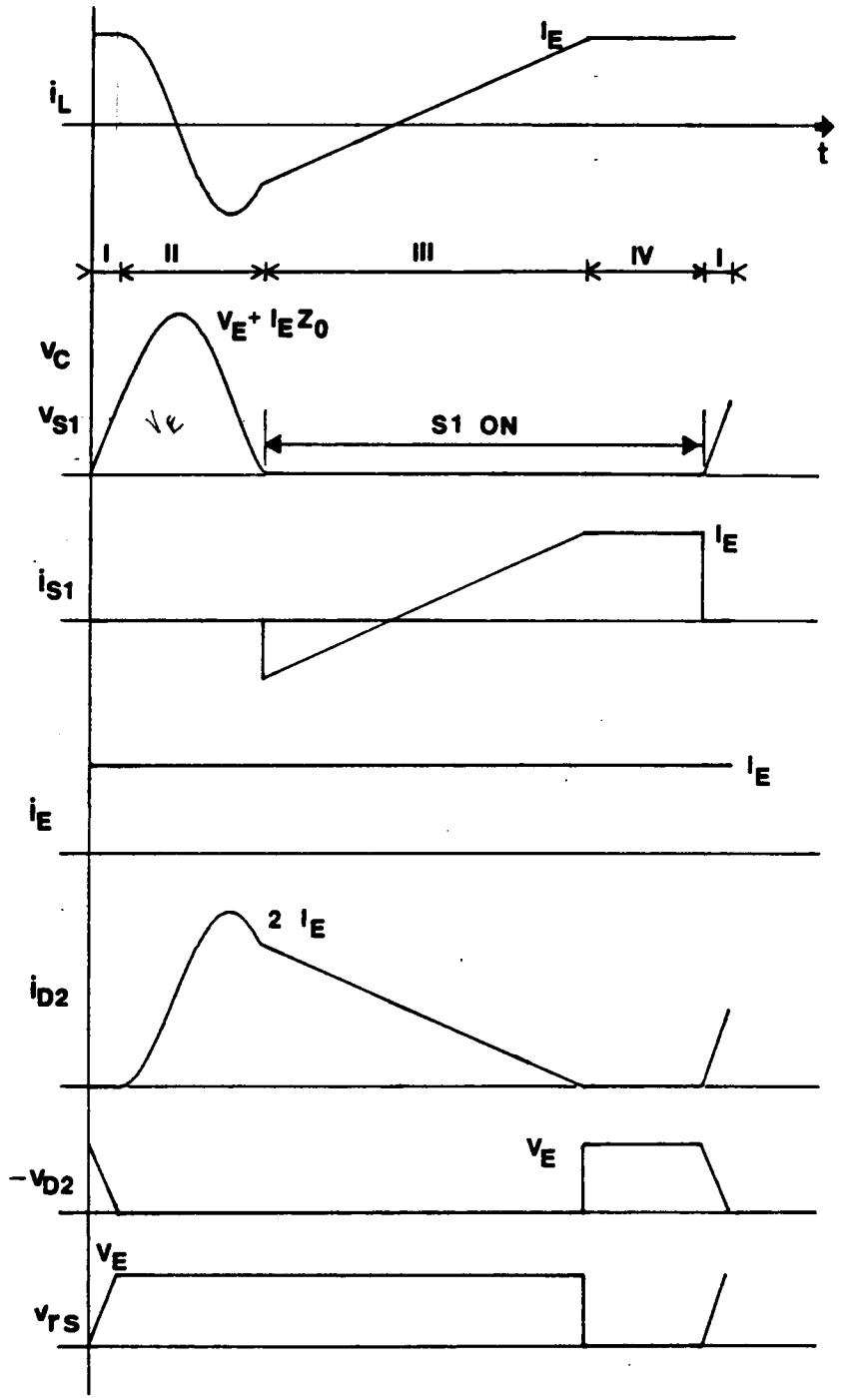

Figure 6.7 Common waveforms for QRCs with half-wave ZVS

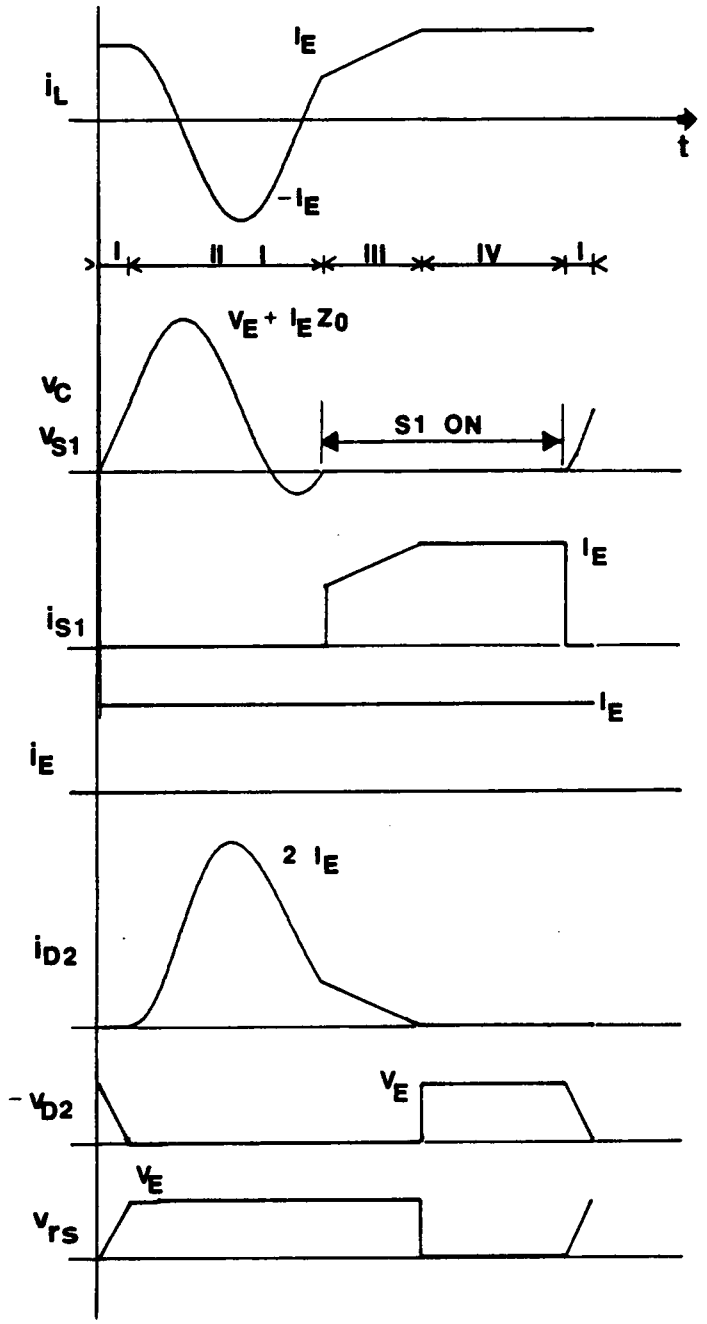

Figure 6.8 Common waveforms for QRCs with full-wave ZVS

6.4.1 Mode-1 Operation In ZCS QRCs

Following is a description of the mode-1 operation, applicable to all half-wave and full-wave ZCS basic QRCs. In the following discussion, please refer to Figs. 6.2 (a) through (d) for the circuit diagrams, to Figs. 6.4 (a) and (b) for the trajectories, and Figs. 6.5 and 6.6 for the waveforms.

Prior to $t = 0$, S1 is off. Current i_L equals zero and D2 carries freewheeling current I_E. Thus, the voltage across D2 is zero imposing a dc voltage of $-V_E$ on the capacitor, C.

At $t = 0$, S1 is closed. Diode D2 is still forward biased. Resonant inductor is linearly charged by voltage V_E. This is the inductor charging/discharging interval (interval-I). During this interval, D2 carries the excess current of I_E over linearly rising current i_L. The capacitor voltage stays at $-V_E$ ($v_{CN} = -1$) due to clamping action of conducting diode D2.

At $t = t_1$, the value of i_L reaches that of I_E. The current through D2 drops to zero and the diode stops conducting. The tank circuit is now free to resonate and is fed by current I_E . This is the resonant interval (interval-II). The center for the resonant trajectory is located at $(0, I_{EN})$ on the state plane and the radius equals unity.

The termination of the resonant interval depends on the type of ZCS used. For the half-wave ZCS (Fig. 6.1(a)), current i_L , which is the same as the current of switch S1, attempts to reverse at $t = t_2$. Since S1 has no antiparallel diode across the transistor, it cannot conduct in the reverse direction. So, it switches off at $t = t_2$. In the case of a full-wave ZCS (Fig. 6.1(b)), current i_L is allowed to reverse once due to the antiparallel diode across the transistor. However, the base drive for the power transistor is removed when this antiparallel diode is conducting. Thus at $t = t_2$, when current i_L attempts to reverse polarity once more, switch S1 blocks the current. Hence, in both half-wave and full-wave ZCS converters, S1 is switched off with the switch current ($= i_L$) at zero. At the end of the resonant interval the capacitor voltage is left at some residual value greater than $-V_E$. The capacitor is now discharged by current I_E. This is the capacitor charging/discharging interval (interval-III) during which D2 remains off.

When v_C is charged to $-V_E$, $D2$ is forward biased and conducts again carrying current I_E. The resonant inductor current stays at zero and the resonant capacitor voltage at $-V_E$. This is the constant state interval (interval-IV) with which we started our explanation of the operation.

6.4.2 Mode-1 Operation in ZVS Converters

In this section, the description of the mode-1 operation for all half-wave and full-wave ZVS basic QRCs is given. Since a ZVS is the dual of a ZCS, the following description will be similar in many respects to that in Sec. 6.4.1. In the following discussions, please refer to Figs. 6.2 (e) through (h) for the circuit diagrams, Figs. 6.4 (c) and (d) for the trajectories, and Figs. 6.7 and 6.8 for the waveforms.

Prior to $t = 0$, $S1$ is ON. The resonant inductor carries dc current I_E. Due to this, $D2$ is reverse biased with voltage V_E. The voltage across the capacitor, v_C, remains at zero.

At $t = 0$, S1 is opened. Diode $D2$ is still reverse biased. Resonant capacitor, C, is linearly charged by current I_E. This is the capacitor charging/discharging interval (interval-I). The excess voltage of V_E over linearly rising voltage v_C is impressed across $D2$ keeping it reverse biased. Since $D2$ is open, all of I_E flows through L and, thus, the value of i_L stays at I_E during this interval.

At $t = t_1$, v_C equals V_E . The voltage across $D2$ drops to zero enabling it to conduct. The tank circuit is now free to resonate and is fed by voltage V_E . This is the resonant interval (interval-II). The center for the resonant trajectory is located at (1,0) on the state plane and the radius equals I_{EN}.

The termination of the resonant interval depends on the type of ZVS used. The resonant capacitor voltage, v_C , which is the same as the voltage across switch $S1$, attempts to reverse in polarity. In the case of the half-wave ZVS, the antiparallel diode across the transistor conducts at $t = t_2$ and, thus, $S1$ closes at this point. In the case of the full-wave ZVS, the diode in series with the transistor ensures that $S1$ remains open while v_C reverses polarity. The transistor base drive is applied sometime during the interval when the v_C polarity is negative. Thus, in this case, when v_C attempts to change polarity once more at $t = t_2$, switch S1 finally turns on. Hence, in both half-wave and full-wave ZVS converters, switch $S1$ is switched on when the switch voltage ($= v_C$) is zero. At the end of the resonant interval, the

resonant inductor current is left at some intermediate value less than I_E. Since $S1$ is closed, L is charged by the voltage, V_E, across it. Diode $D2$ stays on during this interval carrying the excess current of I_E over i_L. This is the inductor charging/discharging interval (interval-III).

At $t = t_3$, i_L equals I_E . The current in $D2$ drops to zero and the diode starts to block. Thus, a constant current I_E flows through L. Voltage v_C stays at zero due to the closure of $S1$. This is the constant state interval (interval-IV) with which we started our description of the operation.

6.5 Load Ranges of Quasi-Resonant Converters

From Figs. 6.4(a) and (b), normalized current I_{EN} must be less than unity for normal operation of ZCS converters. For $I_{EN} > 1$, the switch current ($= i_L$) does not reach zero at all. Thus, when $S1$ is switched off at t_2, the switch is forced to interrupt the resonant inductor current which can be catastrophic. Hence, for ZCS converters,

$$I_{EN} < 1 , \qquad \text{where} \tag{6.25}$$

$$I_{EN} = \frac{I_E Z_0}{V_E} \tag{6.26}$$

In the case of ZVS converters, based on Figs. 6.4 (c) and (d), I_{EN} must be greater than unity for circuit operation. For $I_{EN} < 1$, the switch voltage ($= v_C$) does not reach zero at all. Thus, when $S1$ is closed at t_2, the switch carries the discharge current of the resonant capacitor and this can increase the losses considerably. Hence, for ZVS converters,

$$I_{EN} > 1 \tag{6.27}$$

Equations (6.25) and (6.27) together define the operating limit for all QRCs. However, I_{EN} and V_{EN} are not known parameters, in general. In the remainder of this section, the operating limit on converters will be obtained in terms of known variables.

In the following, symbols I_o and I_i refer to the average current into the load and from the source respectively, for all topologies. Define a modified, normalized, load current parameter, I'_{oN}, common for all topologies, as follows.

$$I'_{oN} = \text{Modified normalized load current} = \frac{I_o Z_0}{V_s} \tag{6.28}$$

The input power equals output power under lossless conditions for all converters. Thus,

$$V_s I_i = V_o I_o \tag{6.29}$$

Next, we will evaluate I_{EN} in terms of I'_{oN} for each of the converter topologies.

6.5.1 Buck Converter

Substituting for V_E from (6.4) and I_E from (6.8) into (6.26) and using (6.28),

$$I_{EN} = \frac{I_o Z_0}{V_s} = I'_{oN} \tag{6.30}$$

6.5.2 Boost Converter

Substituting for V_E from (6.5) and I_E from (6.9) into (6.26),

$$I_{EN} = \frac{I_i Z_0}{V_o} \tag{6.31}$$

Substituting for I_i from (6.29) into (6.31) and using (6.28),

$$I_{EN} = \frac{I_o Z_0}{V_s} = I'_{oN} \tag{6.32}$$

6.5.3 Buck-Boost Converter

The average current over a period through a node under steady state must be zero. Considering the node in Figs. 6.2(c) and (g) which connects the resonant switch, the filter inductor and $D2$,

$$I_l + I_o - I_2 = 0 \tag{6.33}$$

Substituting for V_E from (6.6) and I_E from (6.10) into (6.26),

$$I_{EN} = \frac{I_2 Z_0}{V_s + V_o} \tag{6.34}$$

Substituting for I_2 from (6.33) and V_o from (6.29) into (6.34) and using (6.28),

$$I_{EN} = \frac{I_o Z_0}{V_s} = I'_{oN} \tag{6.35}$$

6.5.4 Boost-Buck Converter

The average voltage over a period around a loop must be zero under steady state. Also, the average voltage across an inductor under steady state must be zero. Considering the loop consisting of the two filter inductors, transfer capacitor C_l, input supply V_s and load V_o, in Figs. 6.2(d) and (h),

$$V_s + V_o = V_l \tag{6.36}$$

Substituting for V_E from (6.7) and I_E from (6.11) into (6.26),

$$I_{EN} = \frac{(I_l + I_o) Z_0}{V_l} \tag{6.37}$$

Substituting for I_l from (6.29) and V_l from (6.36) into (6.37) and using (6.28),

$$I_{EN} = \frac{I_o Z_0}{V_s} = I'_{oN} \tag{6.38}$$

6.5.5 Discussion

From (6.30), (6.32), (6.35) and (6.38), under lossless conditions, for all converters topologies,

$$I_{EN} = \frac{I_E Z_0}{V_E} = \frac{I_o Z_0}{V_s} = I'_{oN} \tag{6.39}$$

Thus, I_{EN} equals I'_{oN}, ideally for all converters. Combining (6.39) with (6.25), the ideal limit on load for all ZCS converters is

$$I'_{oN} = \frac{I_o Z_0}{V_s} < 1 \tag{6.40}$$

Likewise, combining (6.39) with (6.27), the ideal limit on load for all ZVS converters is

$$I'_{oN} = \frac{I_o Z_0}{V_s} > 1 \tag{6.41}$$

Equations (6.40) and (6.41) define the load limit in terms of I_o, Z_0 and V_s , which are considered known variables.

6.6 *Effect Of Frequency Variation*

The effect of varying the frequency on the steady-state operation will now be studied using the method developed in Chapter 5 for a PRC. Due to the duality between the ZCS and the ZVS, the behavior of ZCS-based converters and ZVS-based converters under varying operating frequencies will be similar.

6.6.1 Half-Wave ZCS Converters

Figure 6.9 shows a series of diagrams for the basic QRCs with a half-wave ZCS, when the operating frequency is increased continuously. Figure 6.9(a) shows the mode-1 operation, discussed earlier in Sec. 6.4.1. The sequence of the intervals of operation in mode-1 is I, II, III and IV. As ω_N is increased, the duration of interval-IV reduces to zero (Fig.6.9(b)) at $\omega_N = \omega_{ND}$, the upper boundary for mode-1 operation.

When $\omega_N > \omega_{ND}$, a transition mode, mode-2 (Fig.6.9(c)), occurs. In this mode, *S*1 is switched on during interval-III before the capacitor is fully charged to $-V_E$ (or v_{CN} reaches -1). Thus, the circuit operates in interval-II following interval-III till v_{CN} reaches minus one. The circuit then continues in interval-I operation. The sequence of intervals for mode-2 operation is II, I, II and III.

As ω_N is increased further, another boundary ($\omega_N = \omega_{NU}$) is reached when interval-I in mode-2 reduces to zero (Fig. 6.9(d)). When $\omega_N > \omega_{NU}$, a second transition mode, mode-3 (Fig. 6.9(e)), occurs. In this mode, *S*1 is switched on such that interval-I does not occur at all. The sequence of operating intervals in mode-3 is II and III. As frequency is increased further, an upper limit is reached at $\omega_N = \omega_{MAX}$ when interval-III is also reduced to zero (Fig. 6.9(f)). At ω_{MAX}, the sequence of conduction is simply II and the converter has reached its upper operating frequency.

6.6.2 Full-Wave ZCS Converters

Figure 6.10 shows a series of state-plane diagrams for the basic QRCs using a full-wave ZCS, when the operating frequency is increased continuously. Figure 6.10(a) shows the mode-1 operation, discussed earlier in Sec. 6.4.1 The sequence of operating intervals for mode-1 is I, II, III and IV. As ω_N is increased, the dwell time in interval-IV progressively decreases till, at boundary frequency $\omega_N = \omega_{ND}$, the duration of interval-IV reaches zero (Fig. 6.10(b)).

When $\omega_N > \omega_{ND}$, a transition mode, mode-2 (Fig. 6.10(c)), occurs. In this case, *S*1 is closed before the capacitor fully charges to $-V_E$ (or v_{CN} reaches -1). The resulting sequence of operating intervals for

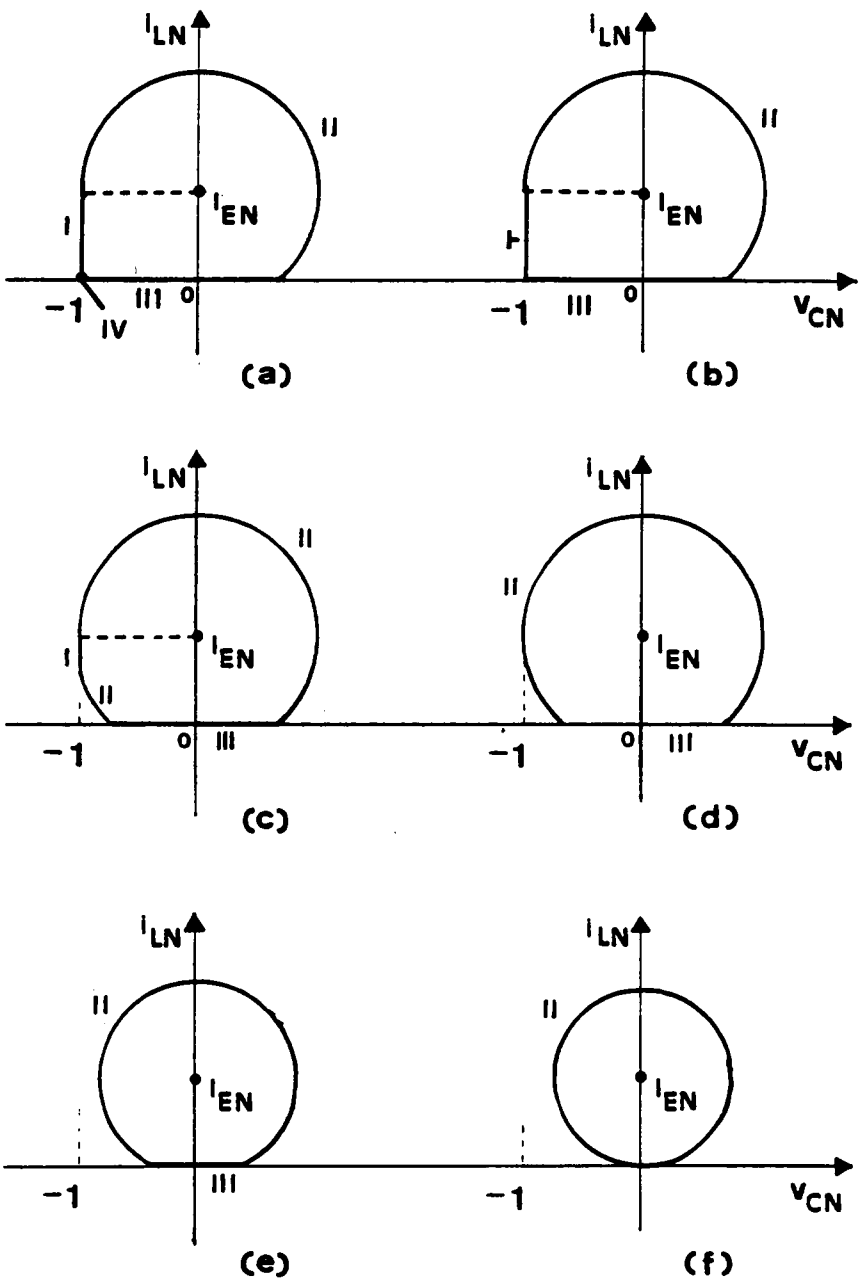

Figure 6.9. Effect of frequency variation - QRCs with half-wave ZCS
a) Mode-1
b) Mode-1/mode-2 boundary
c) Mode-2
d) Mode-2/mode-3 boundary
e) Mode-3
f) Upper boundary

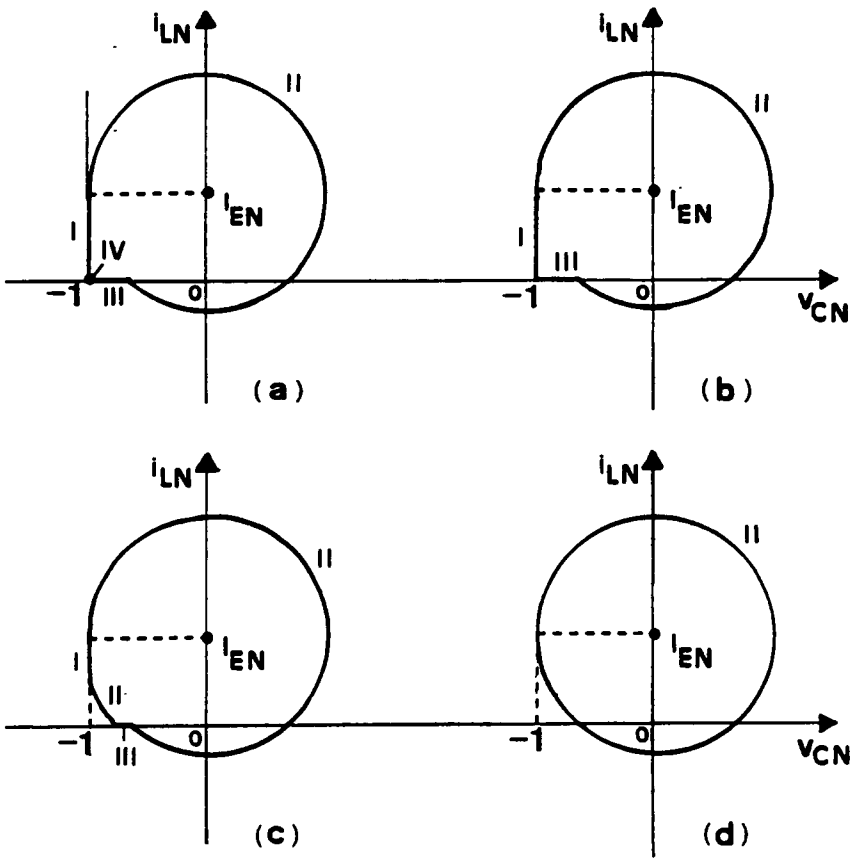

Figure 6.10. Effect of frequency variation - QRCs with full-wave ZCS
a) Mode-1
b) Mode-1/mode-2 boundary
c) Mode-2
d) Upper boundary

mode-2 is II, I, II and III. As frequency is increased still further, an upper limit to the converter operation is reached ($\omega_N = \omega_{MAX}$), when, ideally, intervals III and I are together reduced to zero. At ω_{MAX}, under lossless conditions, the conduction sequence is simply II (Fig. 6.10(d)) and the converter has reached its upper operating frequency.

6.6.3 Half-Wave ZVS Converters

The sequence of state-plane diagrams for the basic QRCs with a half-wave ZVS when ω_N is continuously increased is shown in Fig. 6.11. The sequence of conduction intervals in mode-1 (Fig. 6.11(a)) is I, II, III and IV. As frequency is increased, at $\omega_N = \omega_{ND}$, the duration of interval-IV reaches zero (Fig. 6.11(b)). When $\omega_N > \omega_{ND}$, the transition mode, mode-2 (Fig. 6.11(c)), occurs. Here, S1 is switched off before i_L reaches I_E (i_{LN} reaches I_{EN}). The circuit operates in interval-II following interval-III till i_{LN} equals I_{EN}. The circuit then operates in interval-I. Thus, the sequence of operation in mode-2 is II, I, II and III.

Boundary frequency ω_{NU} is reached in Fig. 6.11(d) when interval-I in mode-2 reduces to zero. At $\omega_N > \omega_{NU}$, operation in mode-3 (Fig.6.11(e) occurs. The sequence of operation in this mode is II and III. As frequency is increased further at the upper boundary ω_{MAX} , interval-III also vanishes to zero (Fig. 6.11(f)). The trajectory is circular and the sequence of conduction is simply II.

6.6.4 Full-Wave ZVS Converters

Figure 6.12 shows the sequence of state-plane diagrams for this case. The operating sequence for mode-1 (Fig. 6.12(a)) is I, II, III and IV. At $\omega_N = \omega_{ND}$, the boundary between mode-1 and mode-2 (Fig. 6.12(b)) is reached when interval-IV is reduced to zero. When $\omega_N > \omega_{ND}$ (Fig. 6.12(b)), switch S1 is switched on during interval-III itself before the i_{LN} value equals I_{EN} (mode-2). The sequence of operating intervals in mode-2 is II, I, II and III. As frequency is increased further, the upper operating boundary is reached at ω_{MAX} (Fig. 6.12(d)). Here, ideally, both intervals-III and -I are reduced to zero. The trajectory is circular with the sequence of conduction being only interval-II.

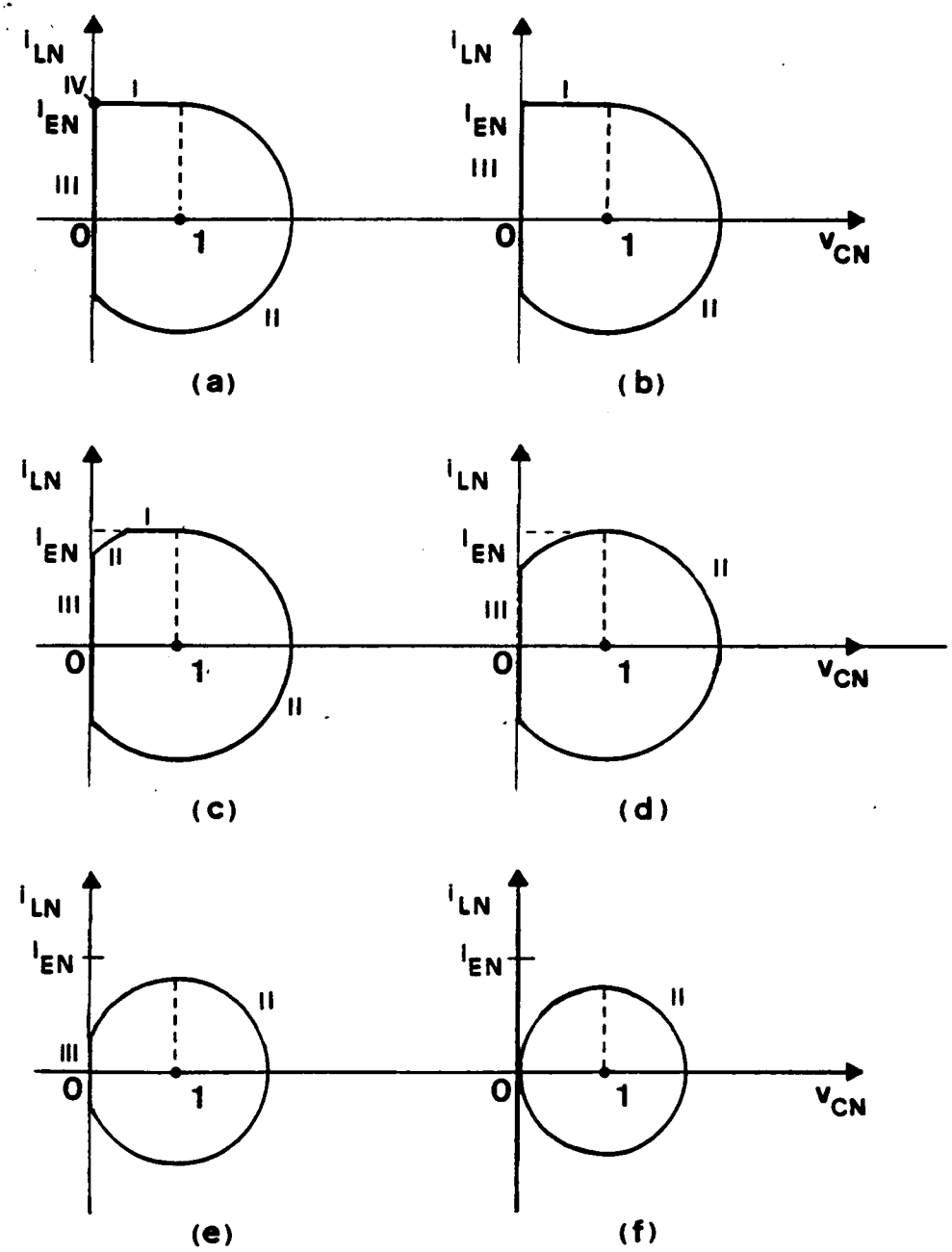

Figure 6.11. Effect of frequency variation - QRCs with half-wave ZVS
a) Mode-1
b) Mode-1/mode-2 boundary
c) Mode-2
d) Mode-2/mode-3 boundary
e) Mode-3
f) Upper boundary

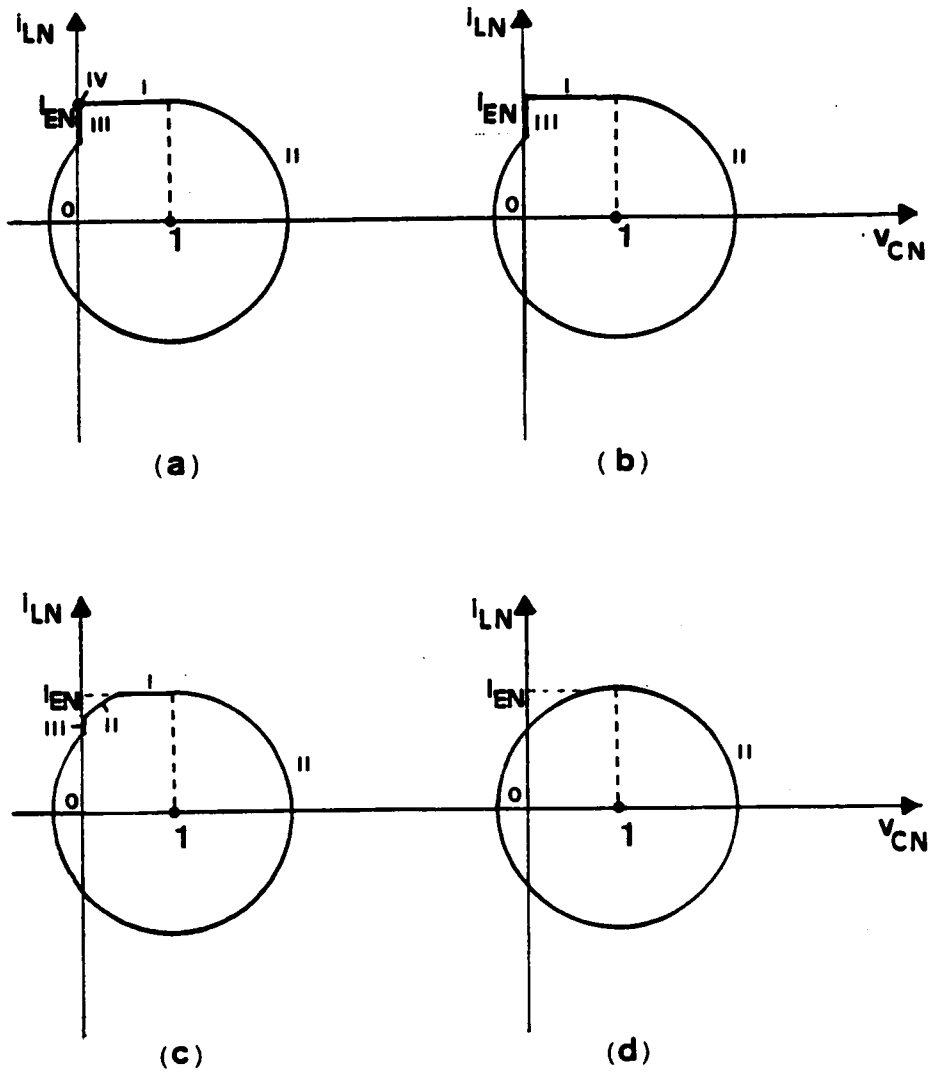

Figure 6.12. Effect of frequency variation - QRCs with full-wave ZVS
a) Mode-1
b) Mode-1/mode-2 boundary
c) Mode-2
d) Upper boundary

6.7 Results Of DC Analysis

6.7.1 Mode Boundaries

Figures 6.9, 6.10, 6.11 and 6.12 include state-plane diagrams, which correspond to operation at the boundary frequencies such as ω_{ND} and ω_{MAX}. Using these diagrams, the equations for the boundary frequencies are derived in Appendix D. The mode boundary equations are valid for all QRCs with a particular type of resonant switch and have been plotted in Fig. 6.13. The symmetry between ZCS converters and ZVS converters can be observed in these figures. The boundaries for the ZCS when plotted on the (ω_N, I'_{oN}) plane and the boundaries for the ZVS when plotted on the (ω_N, $1/I'_{oN}$) plane, are identical in form.

It is shown in Appendix D that for a QRC using a half-wave switch the converter output voltage is saturated in mode-3. Thus, for both half-wave and full-wave switches, only mode-1 and mode-2 are the useful operating regions. As seen in Fig. 6.13, the mode-2 region is relatively small and, thus, the predominant operating mode of any QRC is mode-1.

6.7.2 DC Characteristics

Figures 6.9, 6.10, 6.11 and 6.12 include state-plane diagrams which correspond to operation in the different modes, such as mode-1 and mode-2. Using these diagrams, the complete dc analysis of the basic QRCs have been performed in Appendix D. The results of this analysis can be used to compute the normalized average voltage across diode $D2$, V_{D2AVN}, given ω_N and I'_{oN}.

The desired output from a converter, however, is not V_{D2AVN} but the dc gain defined by

$$V'_{oN} = \text{DC gain} = \frac{V_o}{V_s} \tag{6.42}$$

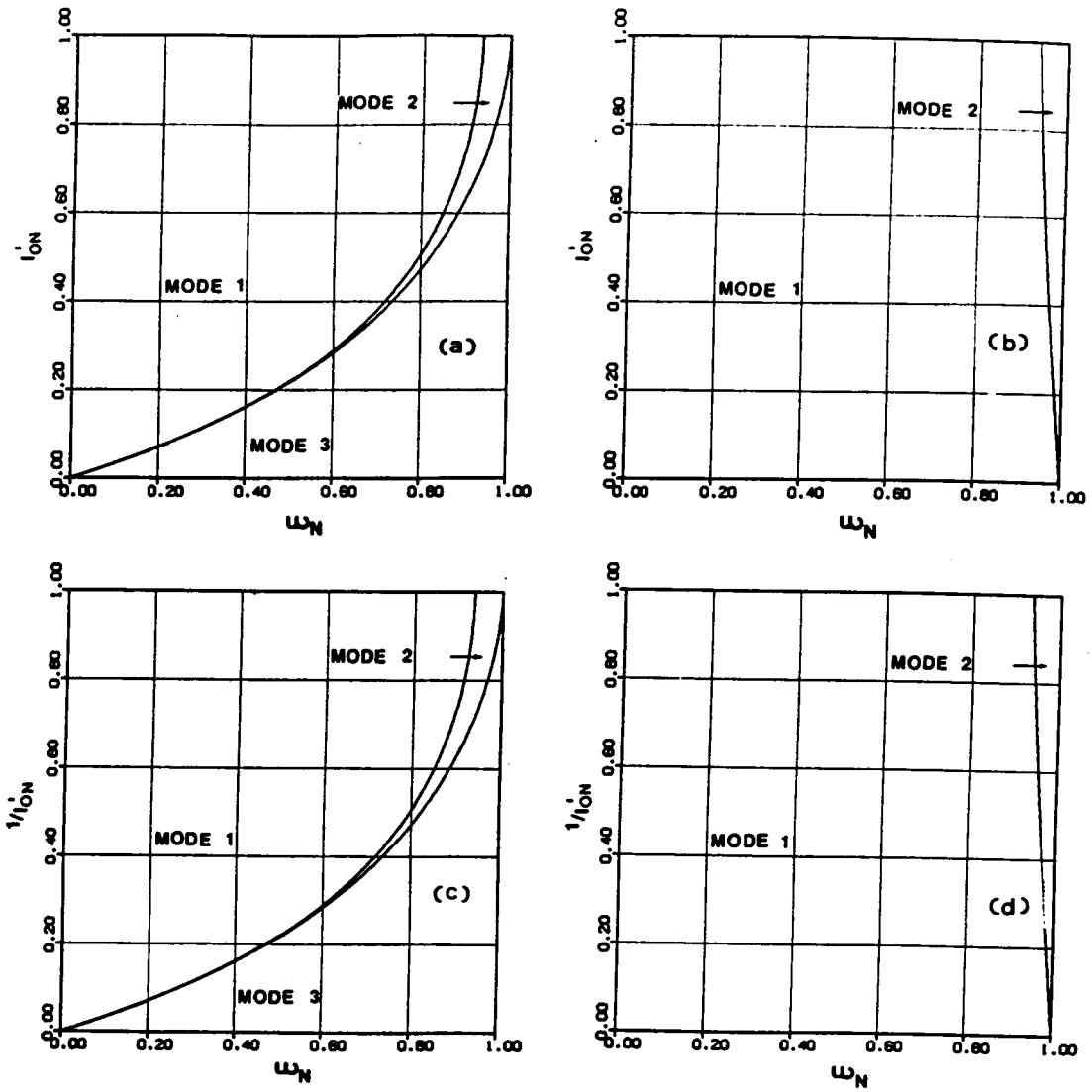

Figure 6.13. Operating regions of QRCs
a) Half-wave ZCS
b) Full-wave ZCS
c) Half-wave ZVS
d) Full-wave ZVS

TABLE-6.2

DC GAINS OF QUASI-RESONANT CONVERTERS

DC Gain $V'_{oN} = \frac{V_o}{V_s}$	BUCK	BOOST	BUCK-BOOST	BOOST-BUCK
All converters	$-V_{D2AVN}$	$\frac{1}{V_{D2AVN}+1}$	$-\frac{V_{D2AVN}}{V_{D2AVN}+1}$	$-\frac{V_{D2AVN}}{V_{D2AVN}+1}$
Full Wave ZCS (approximate)	ω_N	$\frac{1}{1-\omega_N}$	$\frac{\omega_N}{1-\omega_N}$	$\frac{\omega_N}{1-\omega_N}$
Full Wave ZVS (approximate)	$1-\omega_N$	$\frac{1}{\omega_N}$	$\frac{1-\omega_N}{\omega_N}$	$\frac{1-\omega_N}{\omega_N}$

Appendix D derives equations relating V'_{oN} and V_{D2AVN} according to the type of converter and these have been reproduced in the first row of Table 6.2. Note, in Table 6.2, the dc gain for a buck-boost QRC and a boost-buck QRC are the same.

It is shown in Appendix D that for full-wave switches the equations for V_{D2AVN} are almost independent of load and can be approximated as follows.

$$V_{D2AVN} \cong -\omega_N \qquad \text{Full-wave ZCS} \tag{6.43}$$

$$V_{D2AVN} \cong -(1-\omega_N) \qquad \text{Full-wave ZVS} \tag{6.44}$$

Substituting (6.43) and (6.44) for V_{D2AVN} in the equations given in Table 6.2, the approximate equations for V'_{oN} shown in the second and third rows of the same table are obtained. The approximate gain equation for a QRC with a full-wave ZCS is identical to that of the corresponding PWM converter with constant t_{ON} and variable operating frequency. Similarly, for a QRC with a full-wave ZVS, the approximate gain equation is the same as that of the corresponding PWM converter with constant t_{OFF} and variable operating frequency.

Figures 6.14(a)-(d) shows the V_{D2AVN} characteristics according to the type of resonant switch. The dc gain curves have been plotted as functions of ω_N and I'_{oN} for all types of QRCs in Figs. 6.15 and 6.16. For converters with half-wave switches (Figs. 6.15(a)-(c) and 6.16(a)-(c)), ω_N must be varied over a wide range to regulate the output voltage against load variations. This is generally undesirable and is overcome by the use of full-wave resonant switches (Figs. 6.15(d)-(f) and 6.16(d)-(f)).

6.8 QRC - Topological Variations

The aims of this section are threefold. First is the establishment of the rules for the generation of new QRC topologies. Using these rules, many topological variations, including new ones, are derived from the basic QRCs. Secondly, it will be shown that the dc analyses presented in the earlier sections remain unaffected when these variations are considered. Thus, the previous analyses of the basic QRCs are,

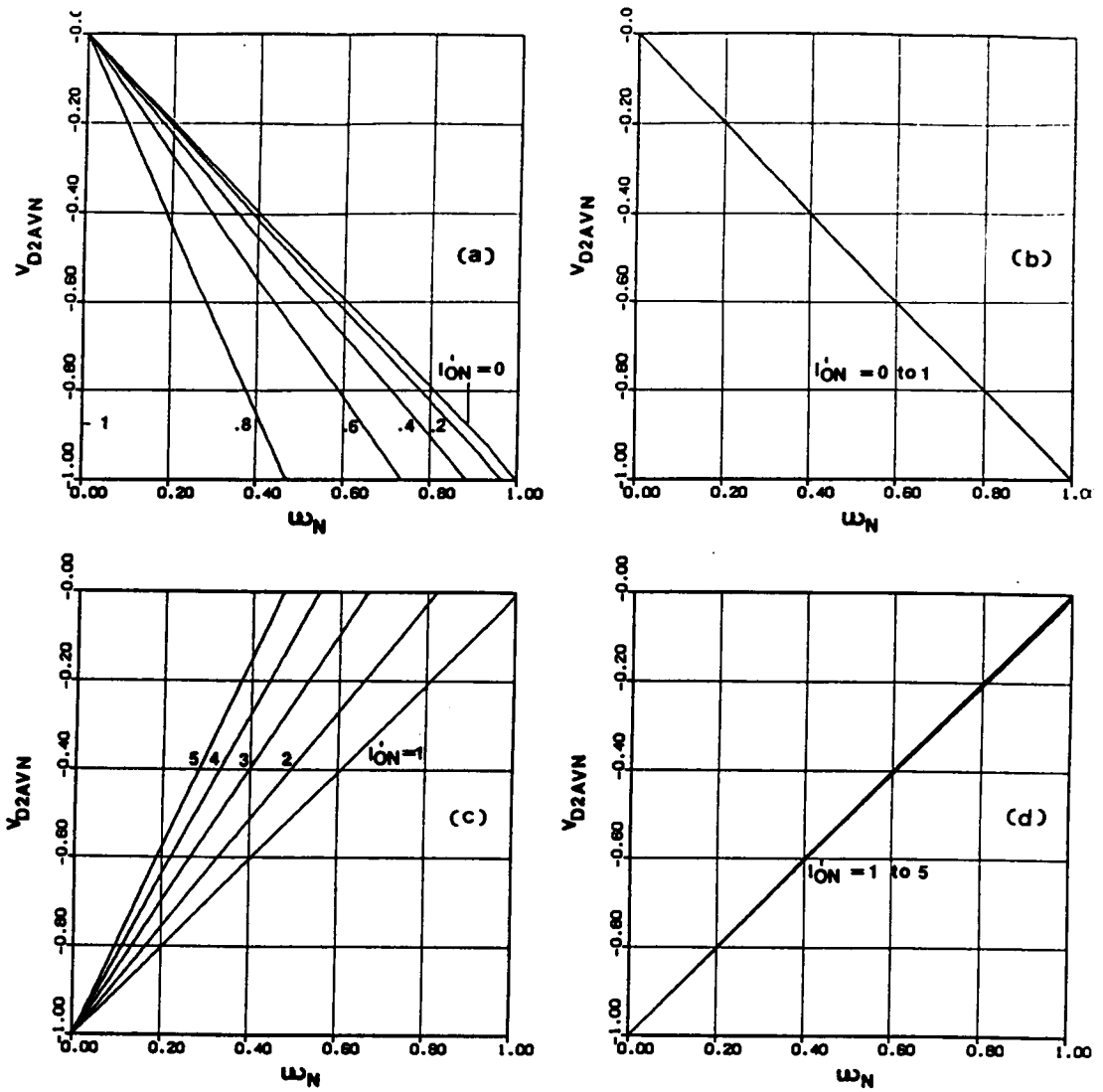

Figure 6.14. Diode voltage characteristics of QRCs
a) Half-wave ZCS
b) Full-wave ZCS
c) Half-wave ZVS
d) Full-wave ZVS

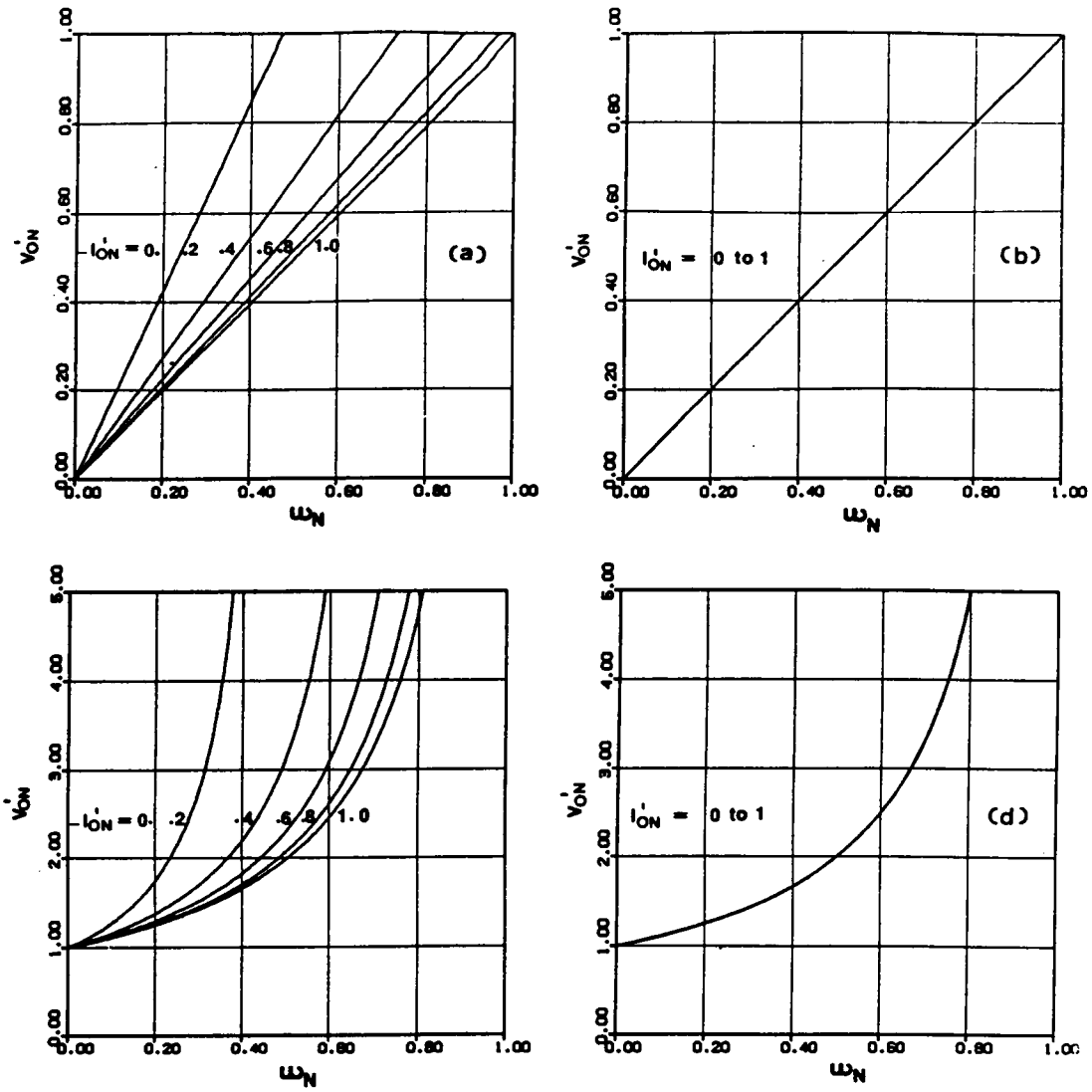

Figure 6.15. DC gain characteristics of QRCs with ZCS
a) Buck (half-wave)
b) Buck (full-wave)
c) Boost (half-wave)
d) Boost (full-wave)

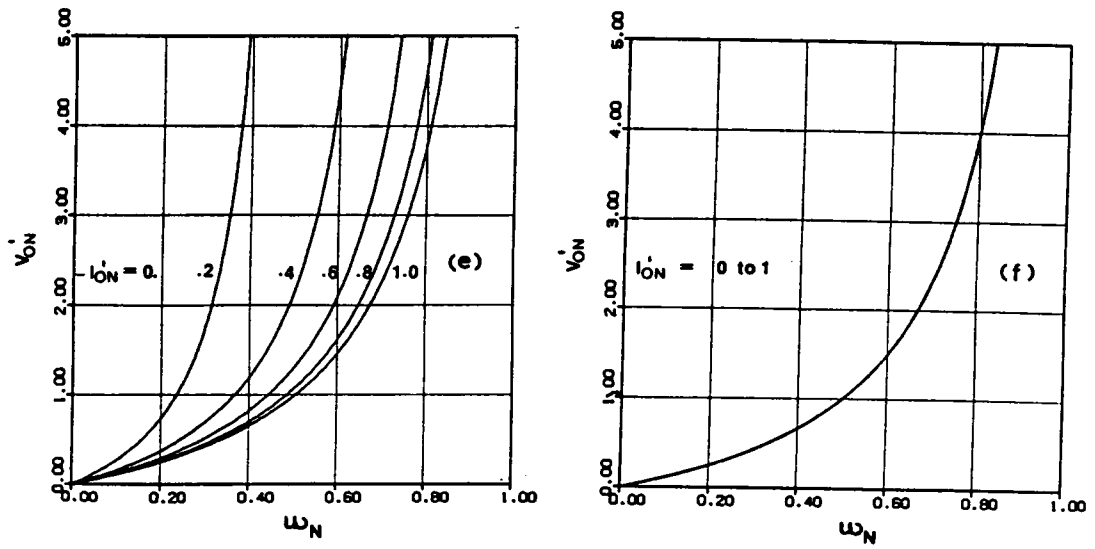

Figure 6.15. (contd.)
e) Buck-boost and boost-buck (half-wave)
f) Buck-boost and boost-buck (full-wave)

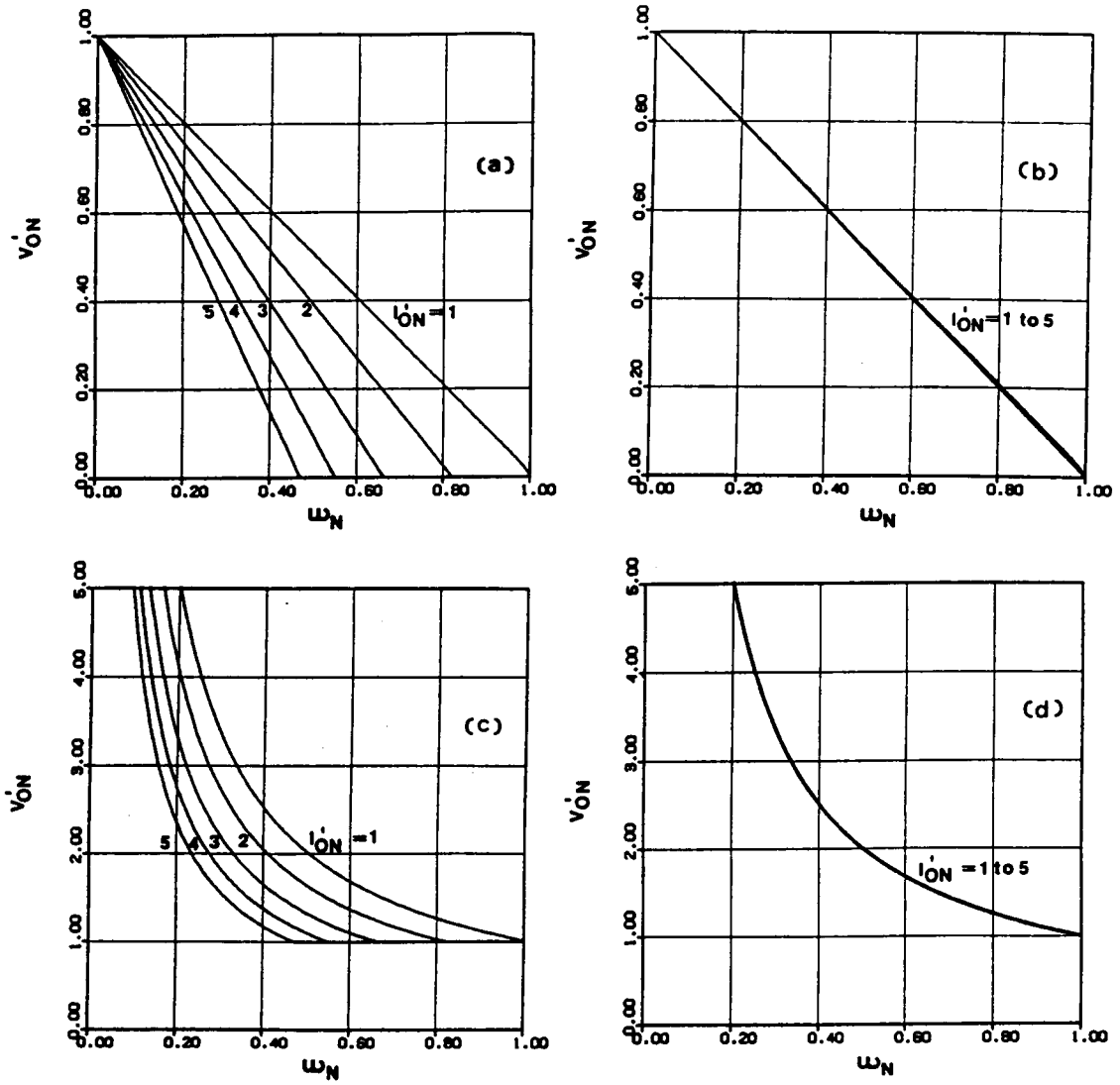

Figure 6.16. DC gain characteristics of QRCs with ZVS
a) Buck (half-wave)
b) Buck (full-wave)
c) Boost (half-wave)
d) Boost (full-wave)

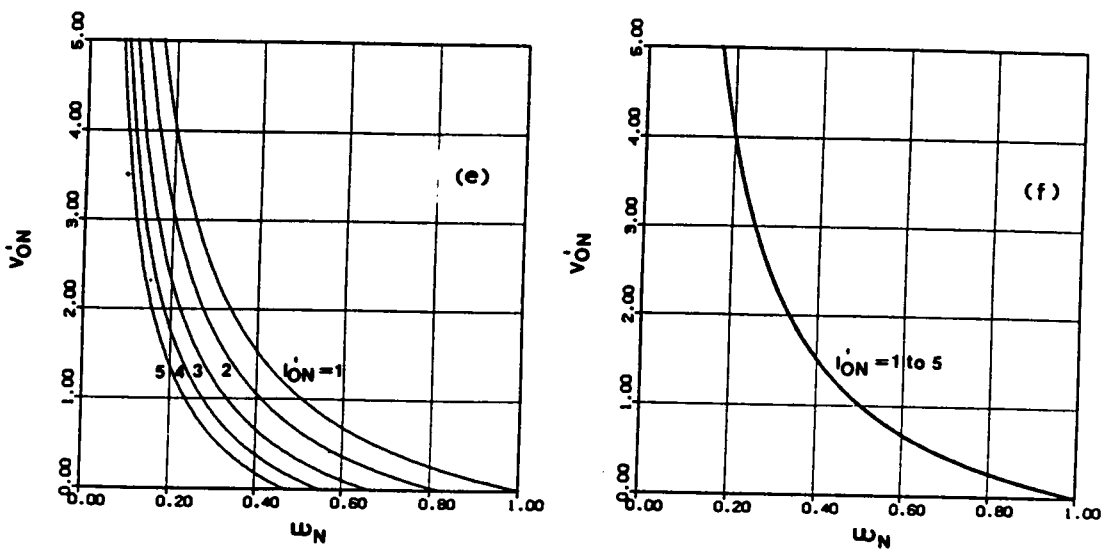

Figure 6.16. (contd.)
e) Buck-boost and boost-buck (half-wave)
f) Buck-boost and boost-buck (full-wave)

in fact, general in scope and the results are applicable to all QRCs. Thirdly, the differences among the many circuit toplogies will be established. A single QRC topology called will be recommended for each converter type based on the relative stresses on the components.

6.8.1 The Shift Rules

These are the rules used to generate a variety of QRC circuit topologies from the basic converters. These are general rules and are applicable to other circuits besides resonant converters.

6.8.1.1 Inductor Shift Rule

Figures 6.17 (a)-(b) show this rule as applied to the node of a circuit. The inductor shift rule may be stated as follows.

Let subcircuit-A (Fig. 6.17(a)) occur as a part of any circuit, C_G , in which there is no circuit elements whose value is dependent on the inductor current, i_L, or voltage v_I across the dc current source. Then C_G can be transformed by substituting subcircuit-B in place of subcircuit-A without affecting the operation of C_G outside the subcircuit. The variables whose values are altered are within the subcircuit itself. The value of i_L is altered by the magnitude of the dc current source, I, and the value of v_I is altered by that of the voltage across the inductor, L.

In power electronic circuits, the dc current source, I, is usually realized by means of a large filter inductor. Next, we will prove the inductor shift rule.

Divide circuit C_G into two subcircuits (Fig. 6.17(c)) 1)subcircuit-A or -B and 2)subcircuit-P containing the rest of the circuit. The unknown circuit variables in subcircuit-A or -B are v_{12}, v_{23}, v_{31}, i_1, i_2 and i_3 . The circuit equations can be written as

$$\vec{F}\,(\vec{P},\, v_{12},\, v_{23},\, i_1,\, i_3) = 0 \tag{6.45}$$

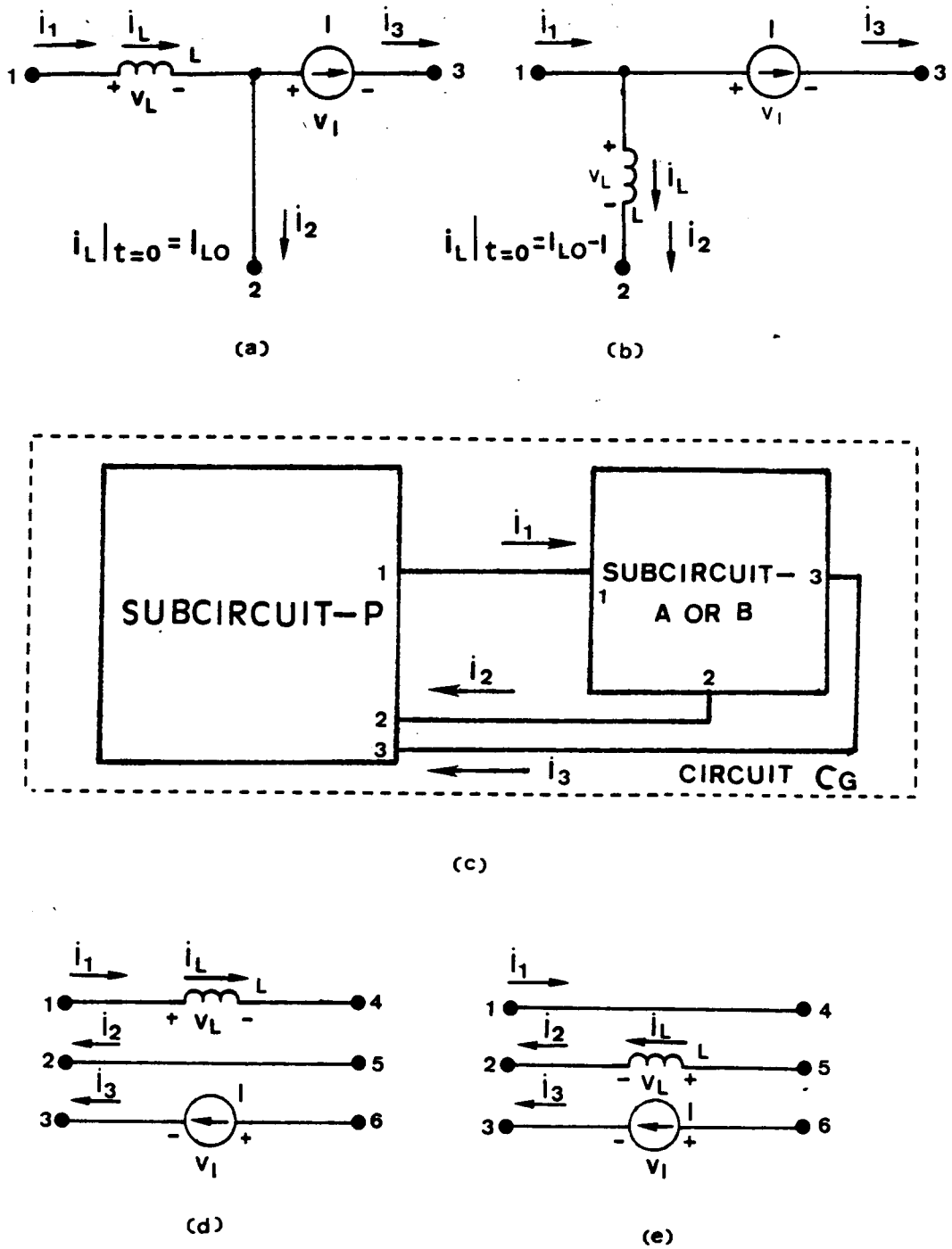

Figure 6.17. Inductor shift rule
a) Subcircuit-A for node version
b) Subcircuit-B for node version
c) Explanatory diagram
d) Subcircuit-A for cutset version
e) Subcircuit-B for cutset version

$$\bar{f}\,(v_{12},\, v_{23},\, v_{31},\, i_1,\, i_2,\, i_3) = 0 \tag{6.46}$$

Equation (6.45) is a set of equations for the subcircuit-P. The vector $\bar{P}$ in (6.45) is the set of unknown variables to be solved for in subcircuit-P. Equation (6.46) is the set of equations for subcircuit-A or -B. In order to obtain the solution to circuit C_G, (6.45) and (6.46) have to be solved together with appropriate initial conditions.

The equations for subcircuit-A are

$$\frac{di_1}{dt} = \frac{v_{12}}{L} \tag{6.47}$$

$$v_{31} = -v_{23} - v_{12} \tag{6.48}$$

$$i_2 = i_1 - I \tag{6.49}$$

$$i_3 = I \tag{6.50}$$

$$\text{The initial condition is} \quad i_L/_{t=0} = I_{L0} = i_1/_{t=0} \tag{6.51}$$

Similarly, the equations for subcircuit-B are

$$\frac{di_2}{dt} = \frac{v_{12}}{L} \tag{6.52}$$

$$v_{31} = -v_{23} - v_{12} \tag{6.53}$$

$$i_2 = i_1 - I \tag{6.54}$$

$$i_3 = I \tag{6.55}$$

$$\text{The initial condition is} \quad i_L/_{t=0} = I_{L0} - I = i_2/_{t=0} \tag{6.56}$$

From (6.54) and (6.56),

$$i_1/_{t=0} = I_{L0} \tag{6.57}$$

Thus, the initial condition, $i_1/_{t=0}$, is the same in both subcircuit-A and -B.

From (6.54),

$$\frac{di_1}{dt} = \frac{di_2}{dt} \tag{6.58}$$

Substituting for $\frac{di_2}{dt}$ from (6.58) into (6.52), the equations governing subcircuit-A and sub-circuit-B are identical. Thus, in both cases the set of equations contributed by (6.46) together with intial conditions are the same.

Let $\bar{p}$ be the set of variables (such as i_L) within subcircuit-A or -B, whose values are altered by the substitution. Assume that subcircuit-P does not contain any circuit element dependent on any variable from $\bar{p}$. Since subcircuit-P itself has not been altered and since no circuit element in subcircuit-P is dependent on any member from the set $\bar{p}$, the equations in (6.45) are unaltered by the subcircuit substitution. Thus, the governing equations for C_G ((6.45) and (6.46) together) and the inital conditions remain unchanged by the transformation and, hence, the rule.

Lastly, let us determine variables $\bar{p}$ within the subcircuit which change. Variables v_{12}, v_{23}, v_{31}, i_1, i_2 and i_3 have been included in circuit equations ((6.45) and (6.46)) and, hence, are not altered, as shown earlier. The other variables are 1) i_L, 2) v_L, voltage across the inductor, 3) I and 4) v_I, the voltage across the current source. Of these, current I equals i_3 in both the subcircuits and remains unaltered. Also, v_L equals v_{12} in both the cases and, thus, is unchanged by the transformation. Next, let us consider the inductor current, i_L. Defining i_{LA} as the inductor current variable in subcircuit-A,

$$i_{LA} = i_1 \tag{6.59}$$

Similarly defining i_{LB} as the inductor current variable in subcircuit-B,

$$i_{LB} = i_2 = i_1 - I = i_{LA} - I \tag{6.60}$$

Thus, the inductor current waveform in subcircuit-B is shifted downward by the magnitude of the dc current source involved in the inductor shift. The current stresses seen by the inductors in the two cases, as well as their energy storage requirements, are different.

Next, let us consider voltage v_I across the current source. Defining v_{IA} as voltage v_I in subcircuit-A,

$$v_{IA} = v_{23} \tag{6.61}$$

Similarly defining v_{IB} as voltage v_I in subcircuit-B,

$$v_{IB} = v_{13} = v_{23} + v_{12} = v_{IA} + v_L \tag{6.62}$$

Thus, the voltage across the current source is altered by the value of the voltage across the inductor involved in the inductor shift. This will affect the volt-seconds seen be the filter inductor acting as the dc current source in the two cases. The size of the filter inductor can significantly depend on the application of the inductor shift rule.

The inductor shift rule can be shown to be valid for a circuit cut-set also, in a similar manner. The subcircuit in Fig. 6.17(e) can replace that in Fig. 6.17(d) wihout affecting the operation of overall circuit C_G, provided there are no elements in C_G dependent on i_L or v_I. The parameters affected within the subcircuit are once again i_L and v_I.

6.8.1.2 Capacitor Shift Rule

This is the dual of the previous rule with a capacitor and a voltage source replacing the inductor and current source, respectively, of the inductor shift rule.. The statement of the rule and its proof follow closely those of the previous rule. In power electronic circuits, the dc voltage source required for this rule may either be a true dc source or a large capacitor. The capacitor shift rule may be stated as follows.

Let subcircuit-A (Fig. 6.18(a)) occur as a part of any circuit, C_G , in which there is no circuit element whose value is dependent on the capacitor voltage, v_C, or current i_E through the dc voltage source. Then C_G can be transformed by substituting subcircuit-B in place of subcircuit-A without affecting the operation of C_G outside the subcircuit. The variables whose values are altered are within the subcircuit itself. The value of v_C is altered by the magnitude of the dc voltage source, E, and the value of i_E is altered by that of the current through the capacitor, C.

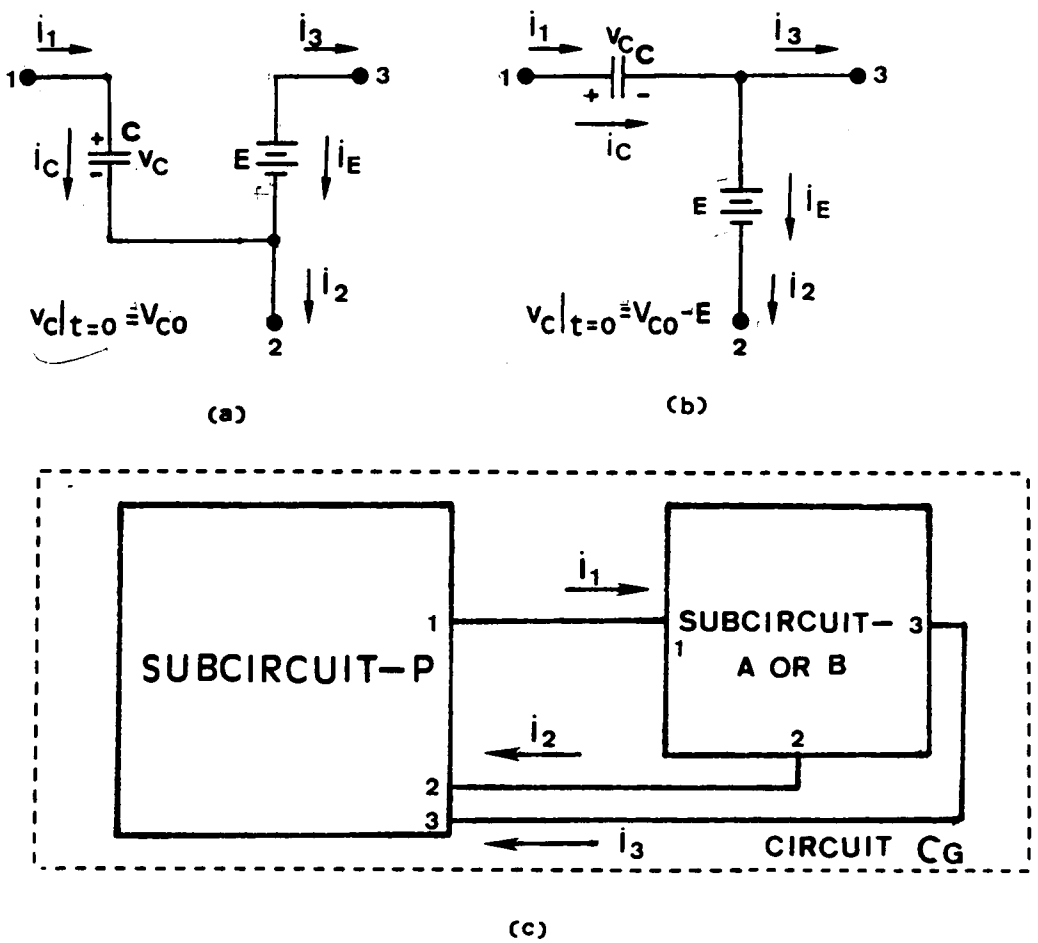

Figure 6.18. Capacitor shift rule
a) Subcircuit-A
b) Subcircuit-B
c) Explanatory diagram

To prove this rule, once again, divide circuit C_G into two subcircuits (Fig. 6.18(c)) 1)subcircuit-A or -B and 2)subcircuit-P containing the rest of the circuit. The unknown circuit variables in subcircuit-A or -B are v_{12}, v_{23}, v_{31}, i_1, i_2 and i_3. The circuit equations can be written as

$$\bar{F}\,(\bar{P},\, v_{12},\, v_{23},\, i_1,\, i_3) = 0 \tag{6.63}$$

$$\bar{f}\,(v_{12},\, v_{23},\, v_{31},\, i_1,\, i_2,\, i_3) = 0 \tag{6.64}$$

Equation (6.63) is a set of equations for subcircuit-P. Vector $\bar{P}$ in (6.63) is the set of unknown variables to be solved for in subcircuit-P. Equation (6.64) is the set of equations for subcircuit-A or -B. In order to obtain the solution to circuit C_G, (6.60) and (6.61) have to be solved together with appropriate initial conditions.

The equations for subcircuit-A are

$$\frac{dv_{12}}{dt} = \frac{i_1}{C} \tag{6.65}$$

$$i_2 = i_1 - i_3 \tag{6.66}$$

$$v_{23} = -E \tag{6.67}$$

$$v_{31} = E - v_{12} \tag{6.68}$$

$$\text{The initial condition is} \quad v_C/_{t=0} = V_{C0} = v_{12}/_{t=0} \tag{6.69}$$

Similarly, the equations for subcircuit-B are

$$\frac{dv_{31}}{dt} = -\frac{i_1}{C} \tag{6.70}$$

$$i_2 = i_1 - i_3 \tag{6.71}$$

$$v_{23} = -E \tag{6.72}$$

$$v_{31} = E - v_{12} \tag{6.73}$$

$$\text{The initial condition is} \quad v_C/_{t=0} = V_{C0} - E = -v_{31}/_{t=0} \tag{6.74}$$

From (6.74) and (6.73),

$$v_{12}/_{t=0} = V_{C0} \tag{6.75}$$

Thus, the initial condition, $v_{12}/_{t=0}$, is the same in both subcircuit-A and -B.

From (6.73),

$$\frac{dv_{31}}{dt} = -\frac{dv_{12}}{dt} \tag{6.76}$$

Substituting for $\frac{dv_{31}}{dt}$ from (6.76) into (6.65), the equations governing subcircuit-A and sub-circuit-B are identical. Thus, in both cases the set of equations contributed by (6.64) and the inital conditions are the same.

Once again, let $\bar{p}$ be the set of variables (such as v_C) within subcircuit-A or -B, whose values are altered by the substitution. Let it be assumed that subcircuit-P does not contain any circuit element dependent on any variable from $\bar{p}$. Since subcircuit-P itself has not been altered and since no circuit element in subcircuit-P is dependent on any member from set $\bar{p}$, the equations in (6.63) are unaltered by the sub-circuit substitution. Thus, the governing equations for C_G ((6.63) and (6.64) together) and the inital conditions remain unchanged by the transformation and, hence, the rule.

Lastly, let us determine variables $\bar{p}$ within the subcircuit which change. Variables v_{12}, v_{23}, v_{31}, i_1, i_2 and i_3 have been included in the circuit equations ((6.63) and (6.64)) and, hence, are not altered, as shown earlier. The other variables are 1) v_C, 2) i_C, current through the capacitor 3) E and 4) i_E, the current through the voltage source. Of these, voltage E equals ($-v_{23}$) in both subcircuits and remains unaltered. Also, i_C equals i_1 in both cases and, thus, is unchanged by the transformation. Next, let us consider the capacitor voltage, v_C. Defining v_{CA} as the capacitor voltage variable in subcircuit-A,

$$v_{CA} = v_{12} \tag{6.77}$$

Similarly defining v_{CB} as the capacitor voltage variable in subcircuit-B,

$$v_{CB} = -v_{31} = v_{12} - E \tag{6.78}$$

Thus, the capacitor voltage waveform in subcircuit-B is shifted downward by the magnitude of the dc voltage source involved in the capacitor shift. The voltage stresses seen by the capacitors in the two cases, as well as their energy storage requirements, are different.

Next, let us consider current, i_E through the voltage source. Defining i_{EA} as current i_E in subcircuit-A,

$$i_{EA} = -i_3 \tag{6.79}$$

Similarly defining i_{EB} as current i_E in subcircuit-B,

$$i_{EB} = i_2 = -i_3 + i_1 = -i_3 + i_C \tag{6.80}$$

Thus, the current through the voltage source is altered by the value of the current through the capacitor involved in the capacitor shift. This will affect the ripple current through the filter capacitor/dc voltage source. The size of the filtering needed can significantly depend on the application of the capacitor shift rule.

6.8.2 QRC Topological Variations

A power converter, typically, exhibits piecewise linear or piecewise nonlinear operation. The operating period of the converter can be divided into several intervals. Thus, in a power converter, the equations for subcircuit-P (see Sec. 6.8.1.1) are different in each of these intervals. However, since the shift rules are valid for each of the intervals, it can be easily established that the shift rules can be applied directly to a power converter.

By using the shift rules, the basic QRCs shown in Fig. 6.2 were manipulated to obtain many more quasi-resonant converter topologies. While using the inductor shift rule, the cut-set version of the rule was used in a few instances in place of the node version of the rule. Figures 6.19, 6.20, 6.21 and 6.22 show many QRC topological variations obtained in this manner. It may be possible to obtain even more topological variations by further application of the shift rules. To obtain the topological variations shown

in Figs. 6.19 through 6.22, the resonant inductor and the resonant capacitor have been shifted to various locations using input power supply, output and transfer filter capacitors and filter inductors as dc source elements. In certain cases, the sequence of components was changed before the application of the shift rules. The number of topological variations available with boost-buck QRC is rather large (Fig. 6.22). This is due to the greater number of filter elements present in the boost-buck circuit, each of which can be considered as a dc current or a dc voltage source for the application of the shift rules.

In obtaining the different circuits, variations based on mere reordering of components or on the symmetry of the topologies have been omitted. Also, a few circuit variations have the same state plane diagrams and component stresses, even though the circuits are topologically different.

When applying the inductor shift rule, the current through the resonant inductor is altered by the dc current source magnitude, which implies that all corresponding state-plane diagrams are shifted along the i_{LN} axis by the dc current source magnitude. In a similar manner, when applying the capacitor shift rule, the voltage across the resonant capacitor is altered by the dc voltage source magnitude, which has the effect of shifting all corresponding state-plane diagrams along the v_{CN} axis by the dc voltage source magnitude. Thus, all the state-plane diagrams in Sec. 6.6, including those corresponding to operation at the different boundary frequencies remain the same as before, being merely shifted to a new location on the state plane. Hence, the equations for the boundary frequencies derived in Appendix D and plotted in Fig. 6.13 are applicable for all QRC circuits. Furthermore, according to the shift rules, the only parameters that change among the circuit variations are the voltages across the filter inductors, currents through voltage sources and filter capacitors, currents through the resonant inductor and the voltages across the resonant capacitor. Since the diode voltage and the output voltage are not among these parameters, the dc gain characteristics obtained in Appendix D and plotted in Figs. 6.14, 6.15 and 6.16 are valid for all QRC topological variations of the current section also.

Thus, the analysis for mode boundaries and dc gain characteristics previously presented are general in scope and applicable to both the basic QRC circuits and their topological variations.

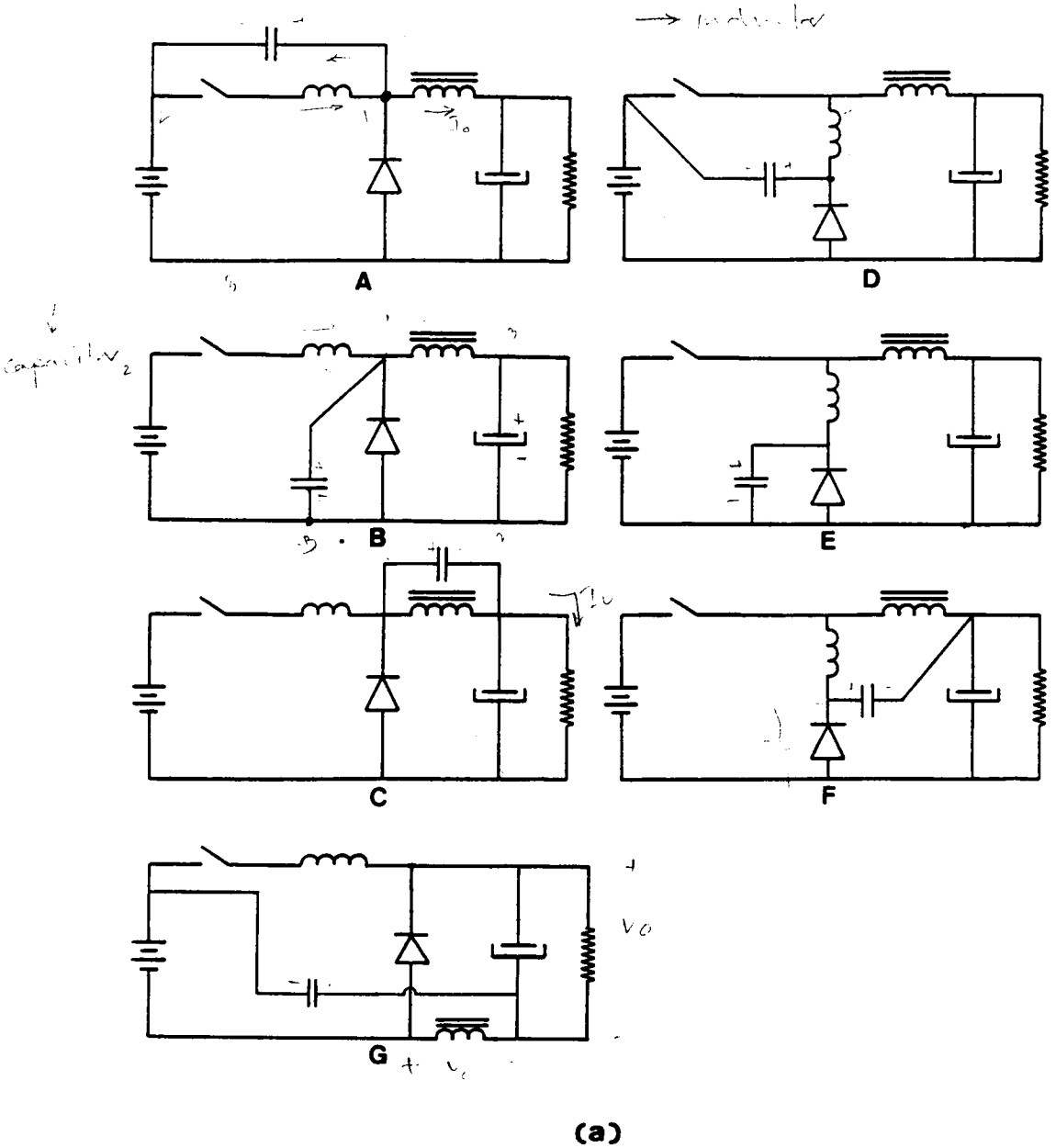

Figure 6.19. Resonant buck converter variations
a) Zero current switch

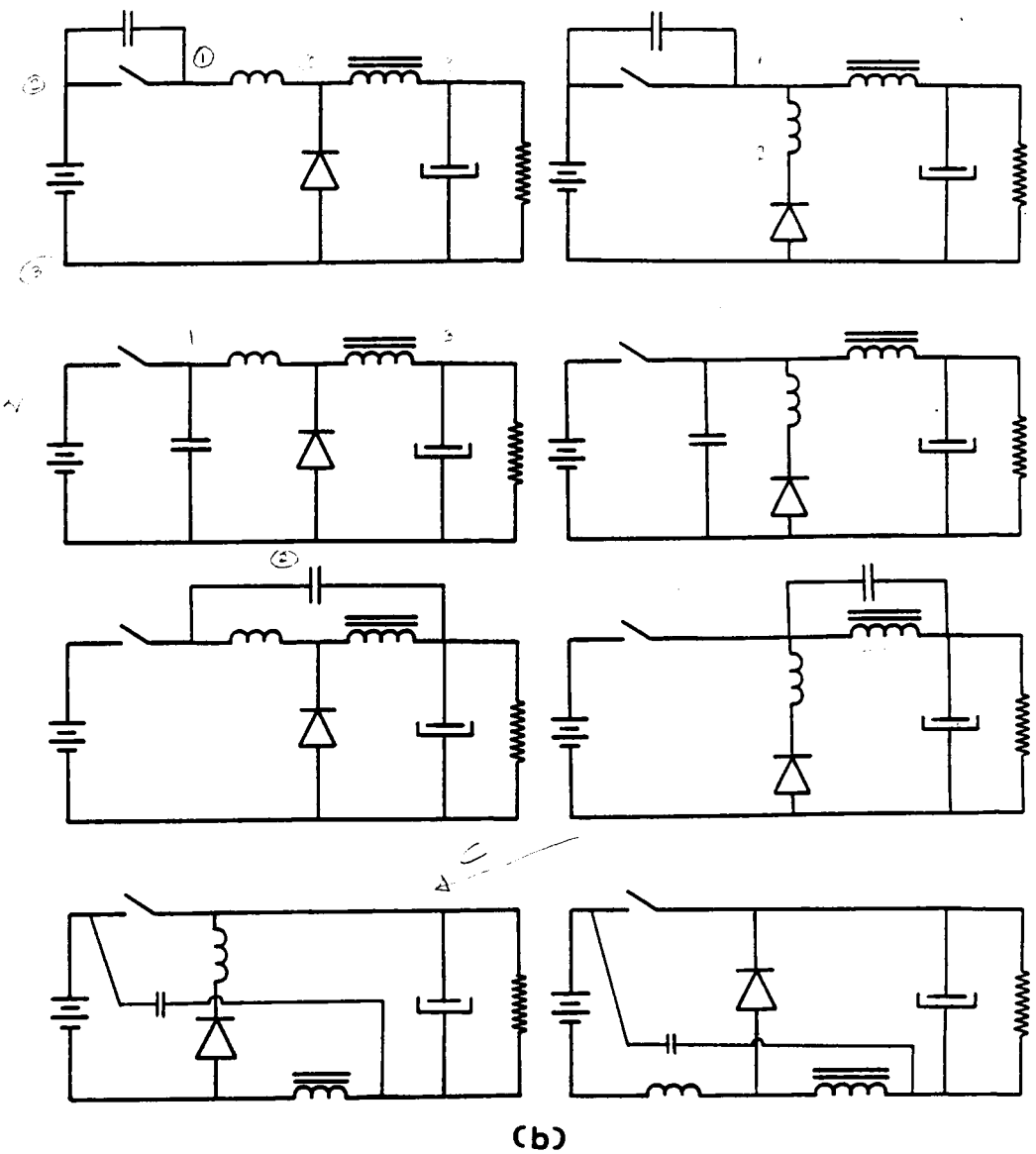

Figure 6.19. (contd.)
b) Zero voltage switch

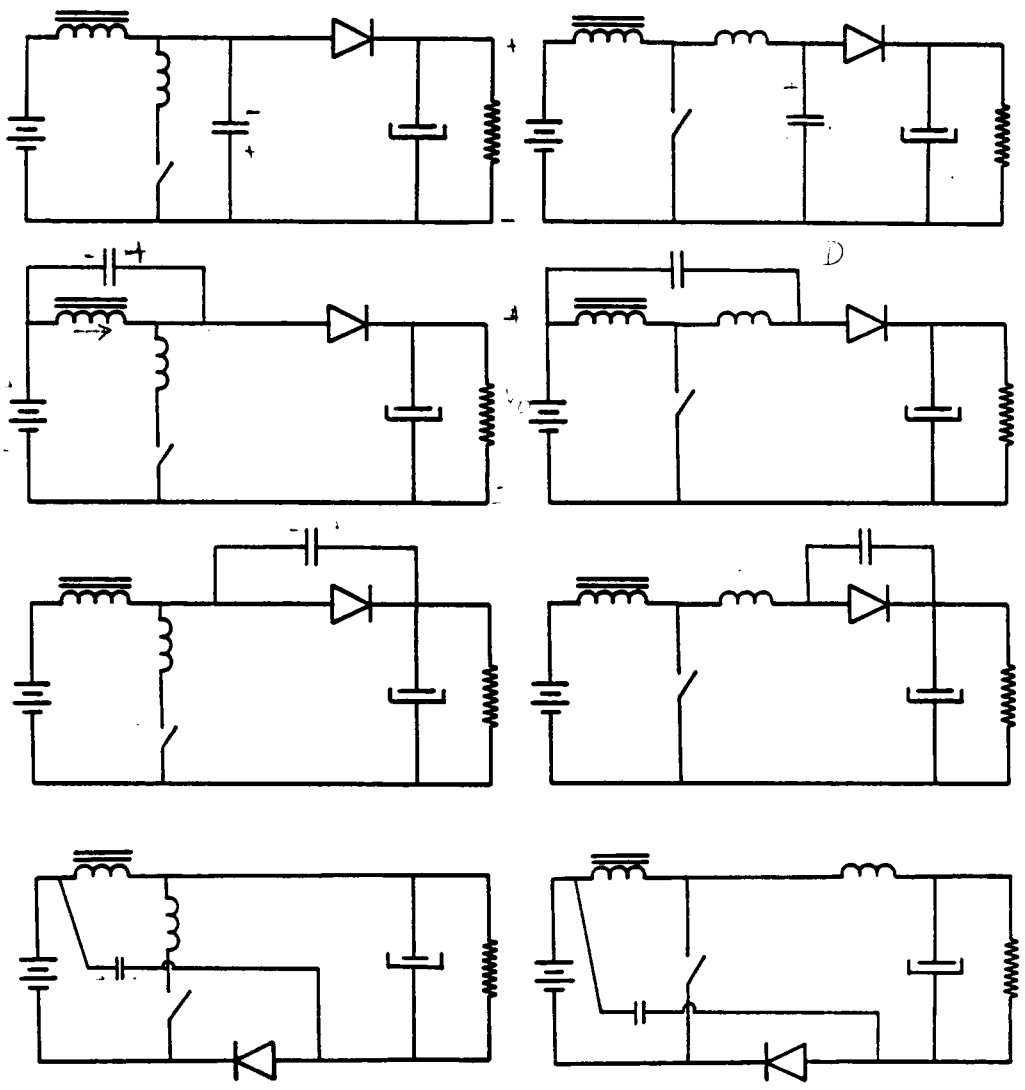

(a)

Figure 6.20. Resonant boost converter variations
a) Zero current switch

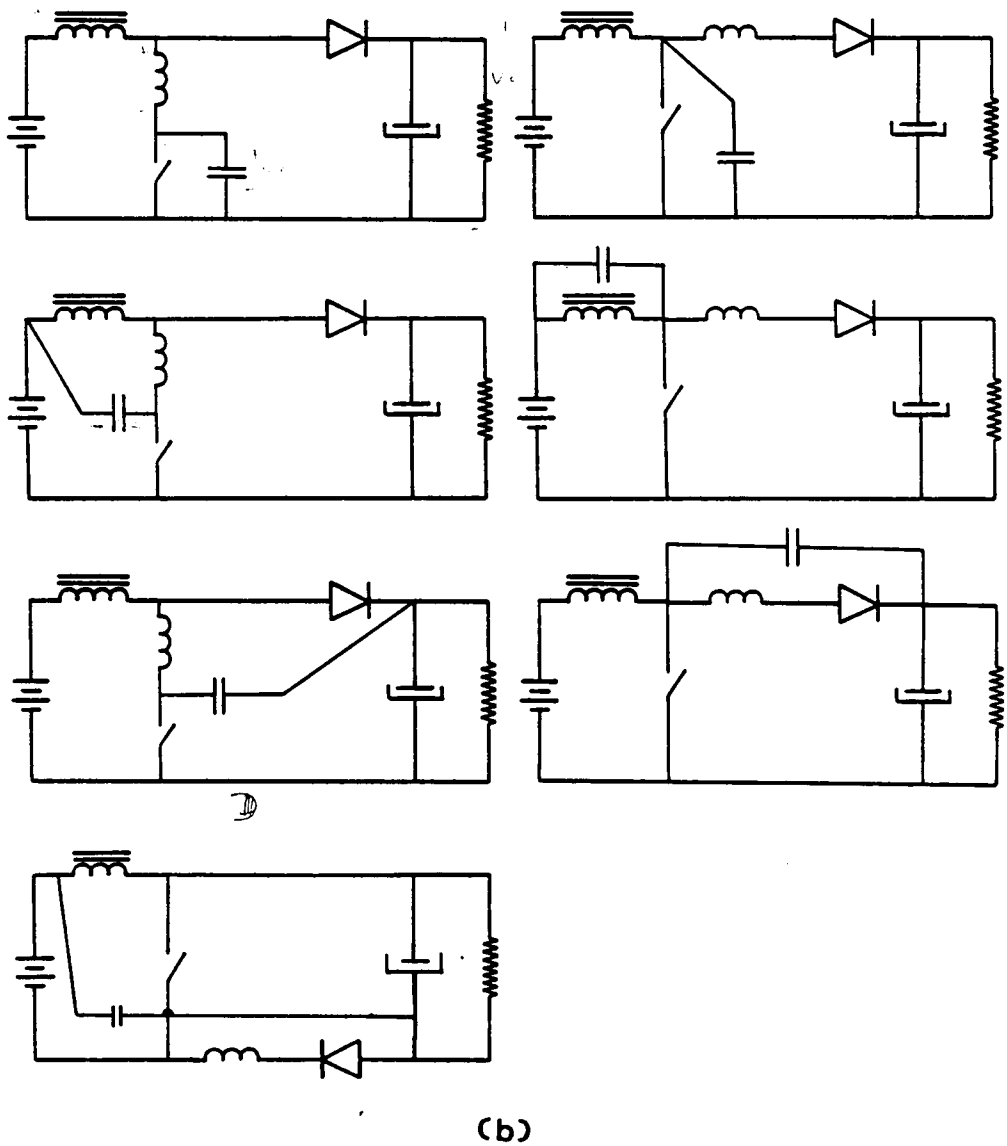

Figure 6.20. (contd.)
b) Zero voltage switch

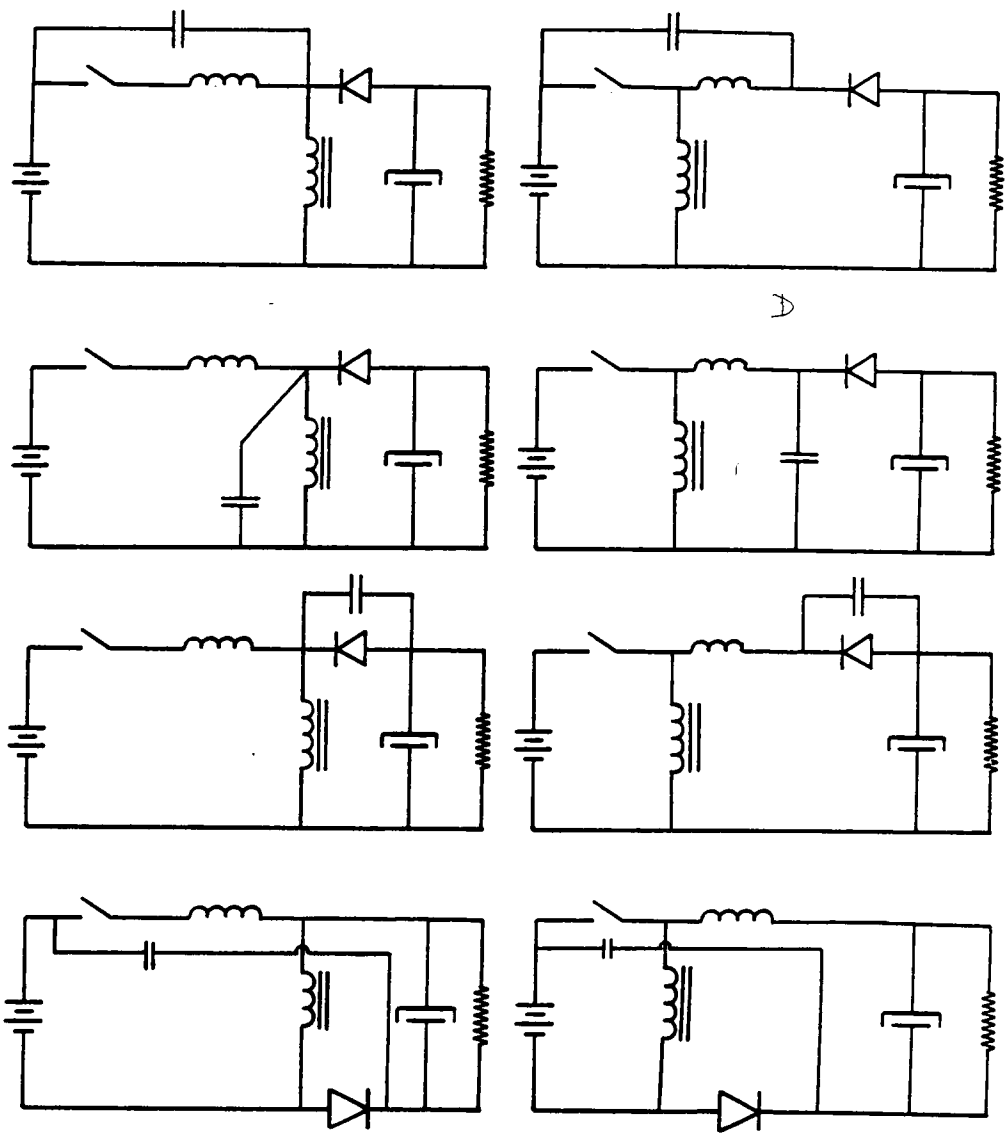

Figure 6.21. Resonant buck-boost converter variations
a) Zero current switch

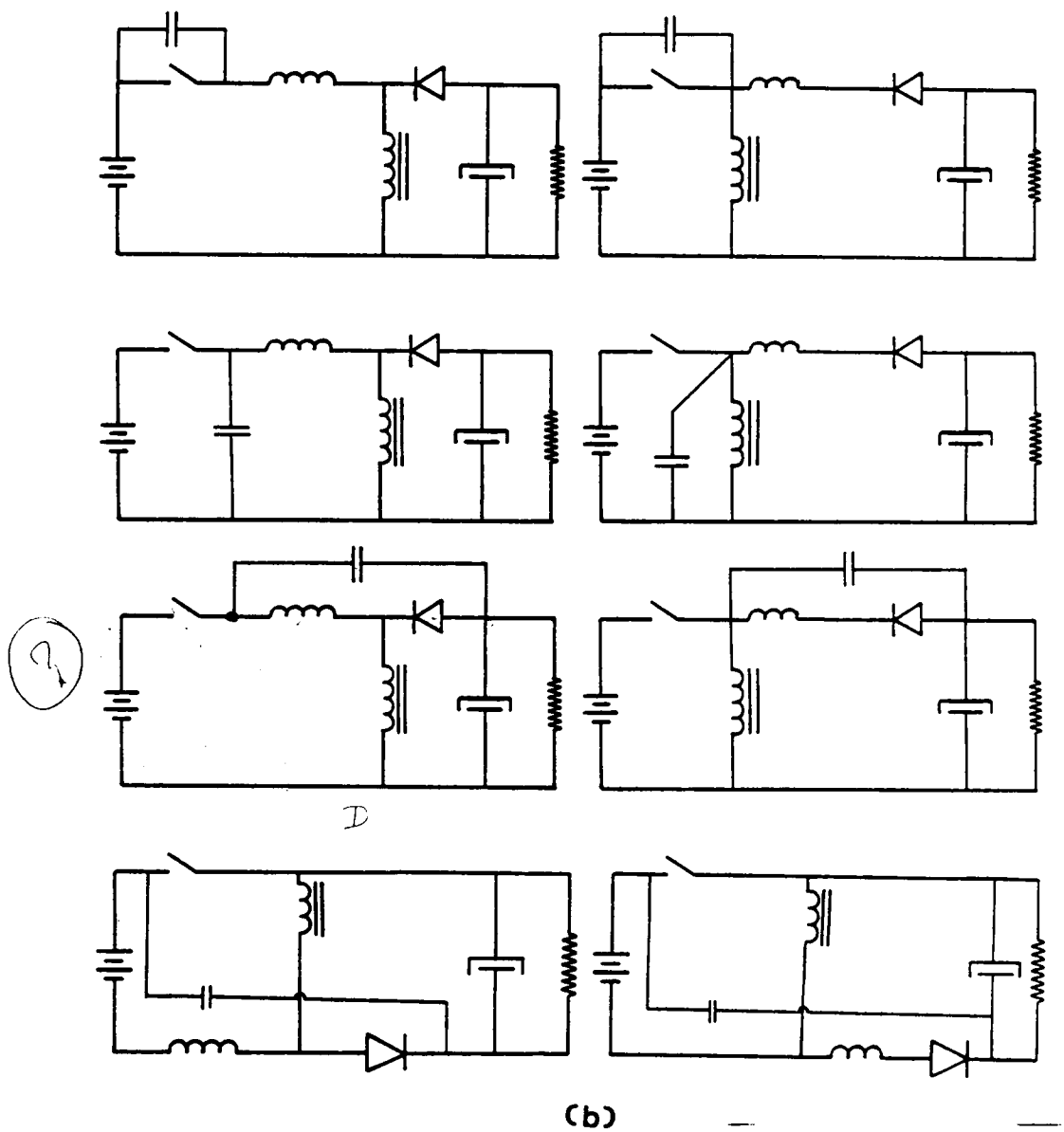

Figure 6.21. (contd.)
b) Zero voltage switch

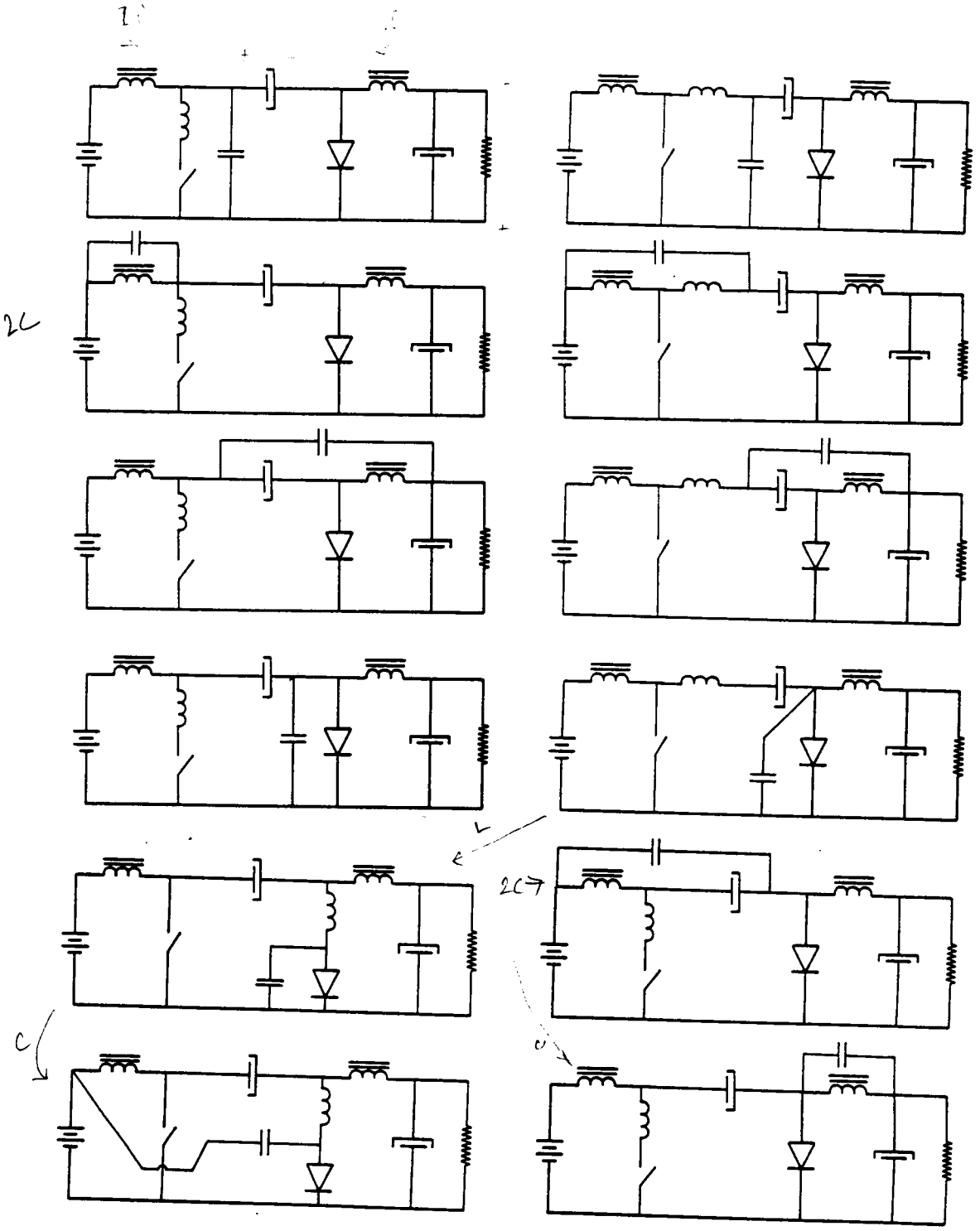

(a)

Figure 6.22 Resonant boost-buck converter variations
a) Zero current switch

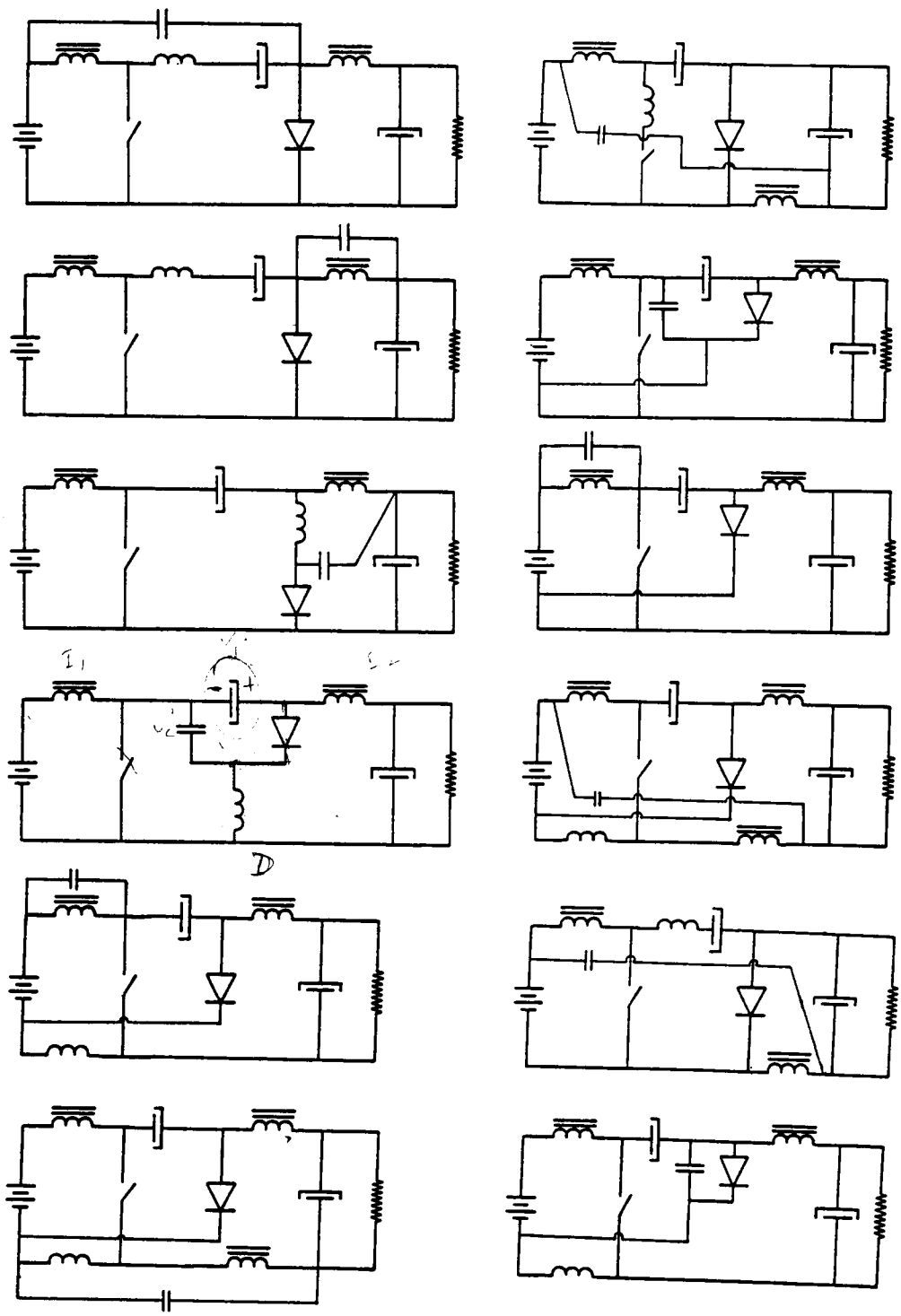

Figure 6.22. (contd.)

(a) (contd.)

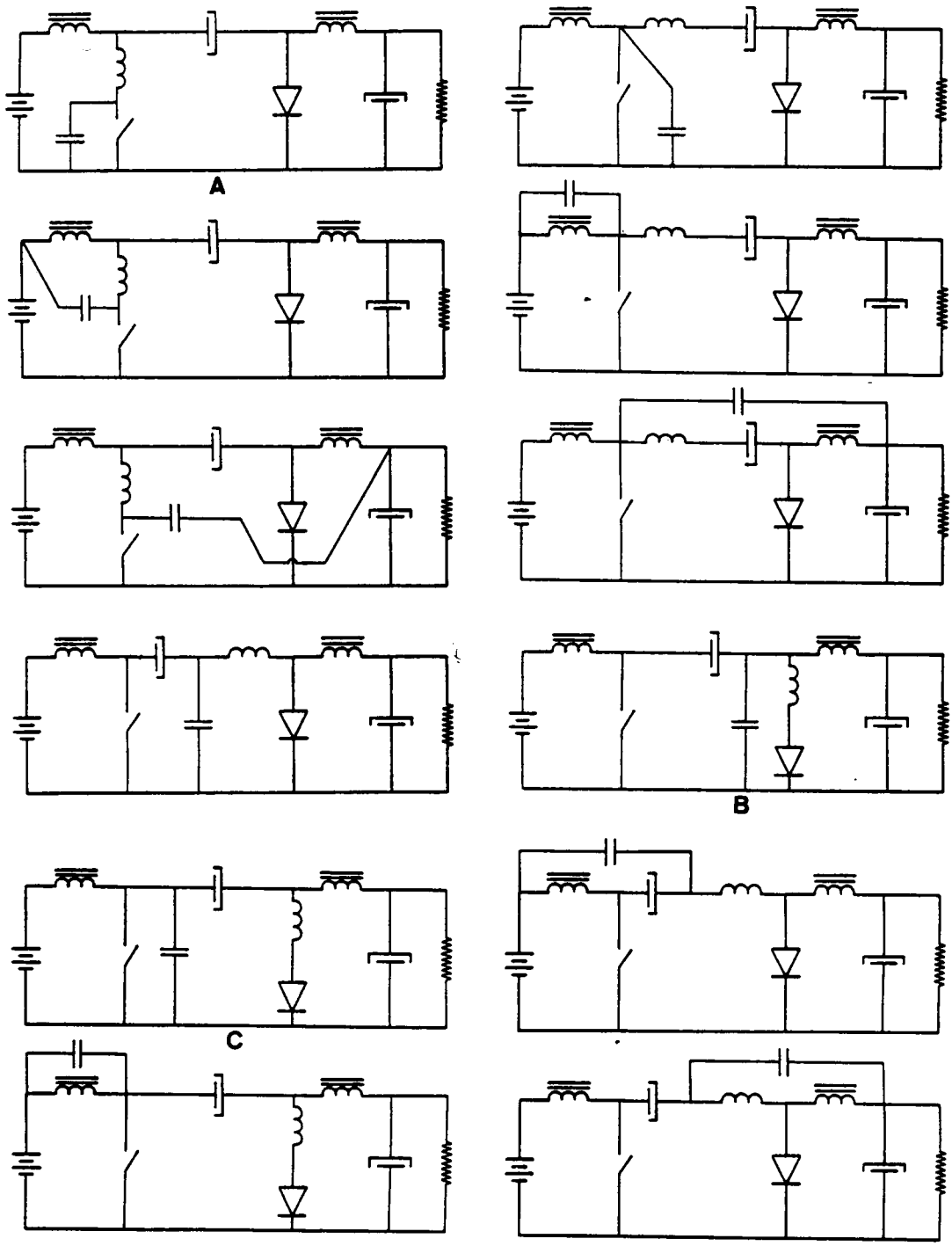

Figure 6.22 (contd.)
b) Zero voltage switch

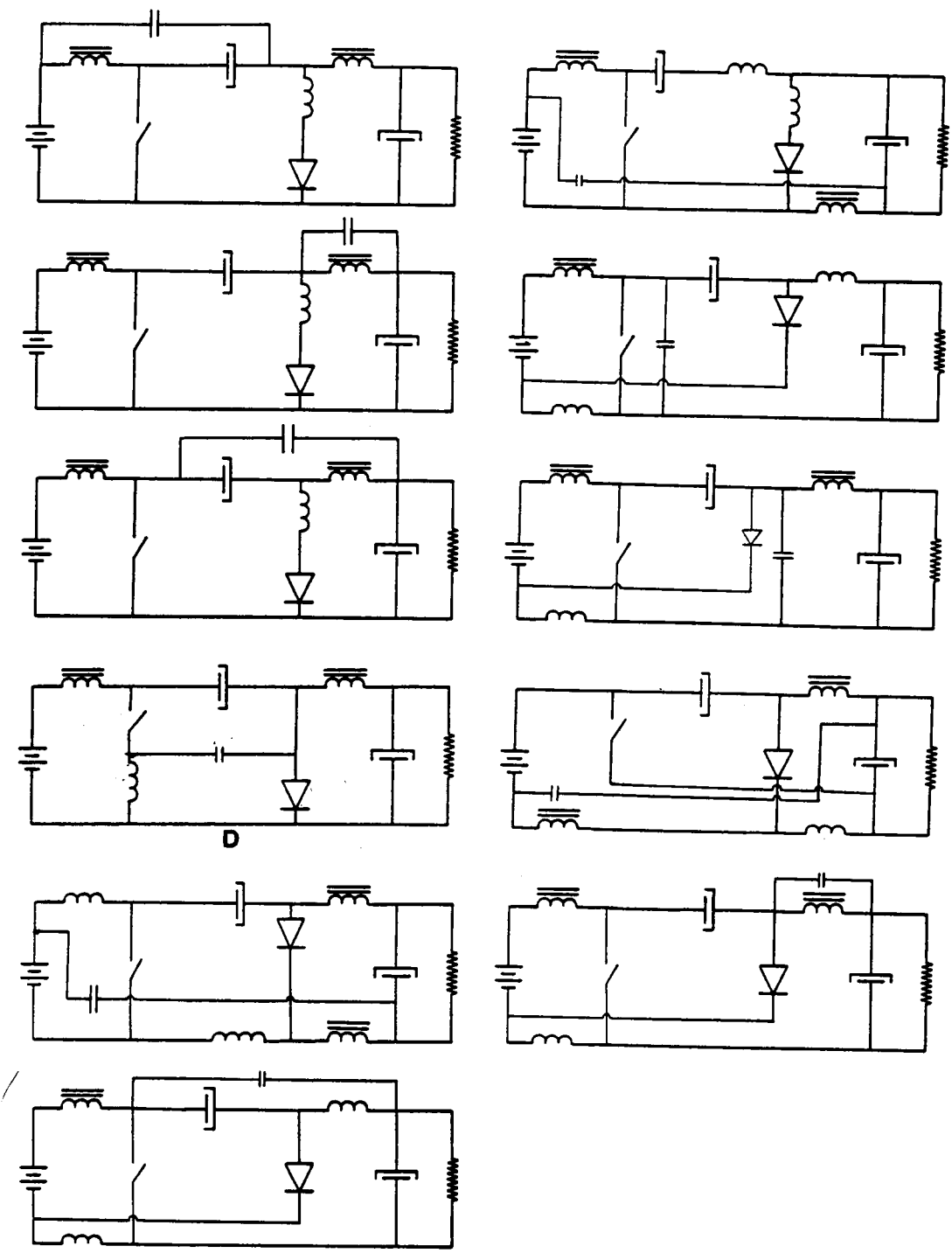

(b) (contd.)

Figure 6.22. (contd.)

6.8.3 Evaluation Of QRC Variations

Even though the different QRC variations have the same performance characteristics, individual component stresses can vary among them and can influence the choice of a suitable topology. The shift rules of Sec. 6.8.1 permit us to identify and estimate these differences in component stresses. In this section, examples of evaluations of a few QRC variations base on their relative component stresses are presented. Based on such evaluations, sixteen QRC topologies are recommended from the point of view of low component stresses. It must be remembered that factors such as parasitic elements including circuit losses may affect the performance of these variations differently. Also, other considerations such as ease of implementation and reduction of critical parasitics may play important roles in determining the desired topology.

6.8.3.1 ZCS Resonant Buck Converters

Figure 6.19 shows the circuit variations of the resonant buck converter. Figure 6.23 shows the mode-1, state-plane diagrams for both the half-wave and the full-wave ZCS resonant buck converters of Fig. 6.19. As mentioned in Sec. 6.8.2, the state-plane diagrams are merely shifted on the state plane by the magnitudes of the dc sources involved in the application of the shift rules. The differences in the waveforms of the resonant components can be deduced from these figures. In Fig. 6.23, variation D has the state-plane origin itself as the trajectory center during the resonant interval. From Fig. 6.24, it may be observed that this variation has the lowest capacitor-voltage stress ($v_{CN} = 1$ or $v_C = V_s$) and lowest inductor-current stress ($i_{LN} = 1$ or $i_L = \frac{V_s}{Z_0}$) among all the full-wave, ZCS, resonant-buck-converter variations.

Figure 6.24 contains those circuit waveforms which differ among these converters when full-wave ZCS is used. Figure 6.24(a) shows the resonant inductor current waveform as affected by the inductor shift process. The peak current in variations A, B, C and G equals $I_o + \frac{V_s}{Z_0}$, whereas it is $\frac{V_s}{Z_0}$ in variations D, E and F. Thus, the resonant inductor-current stress is lower in variations D, E and F. Figure 6.24(b) shows the voltage across the filter inductor (the dc current source) as affected by the resonant inductor shift. Once again variations D, E and F have lower volt-seconds impressed on their filter inductors than

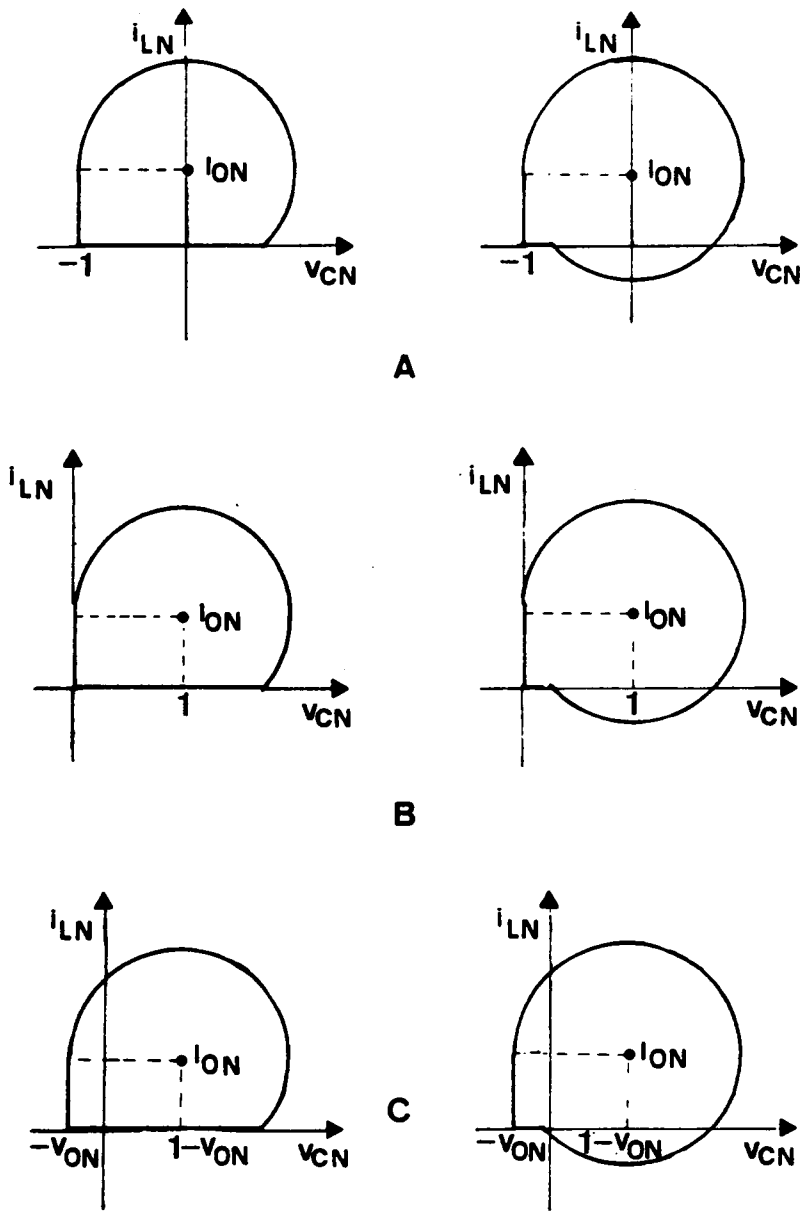

Figure 6.23. Mode-1 state plane diagrams of resonant buck converters with ZCS

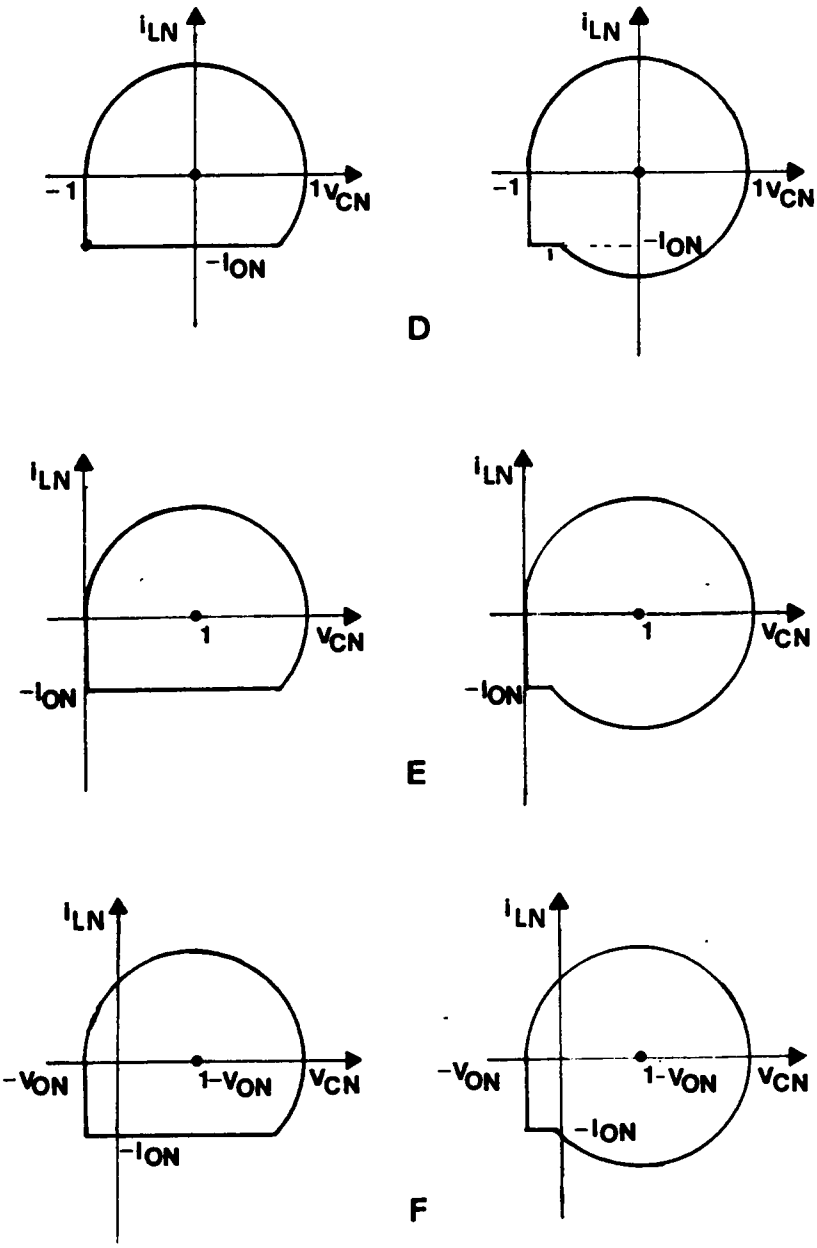

Figure 6.23. (contd.)

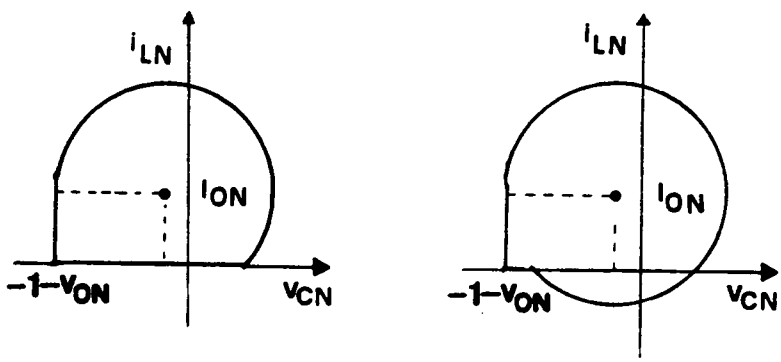

G

Figure 6.23. (contd.)

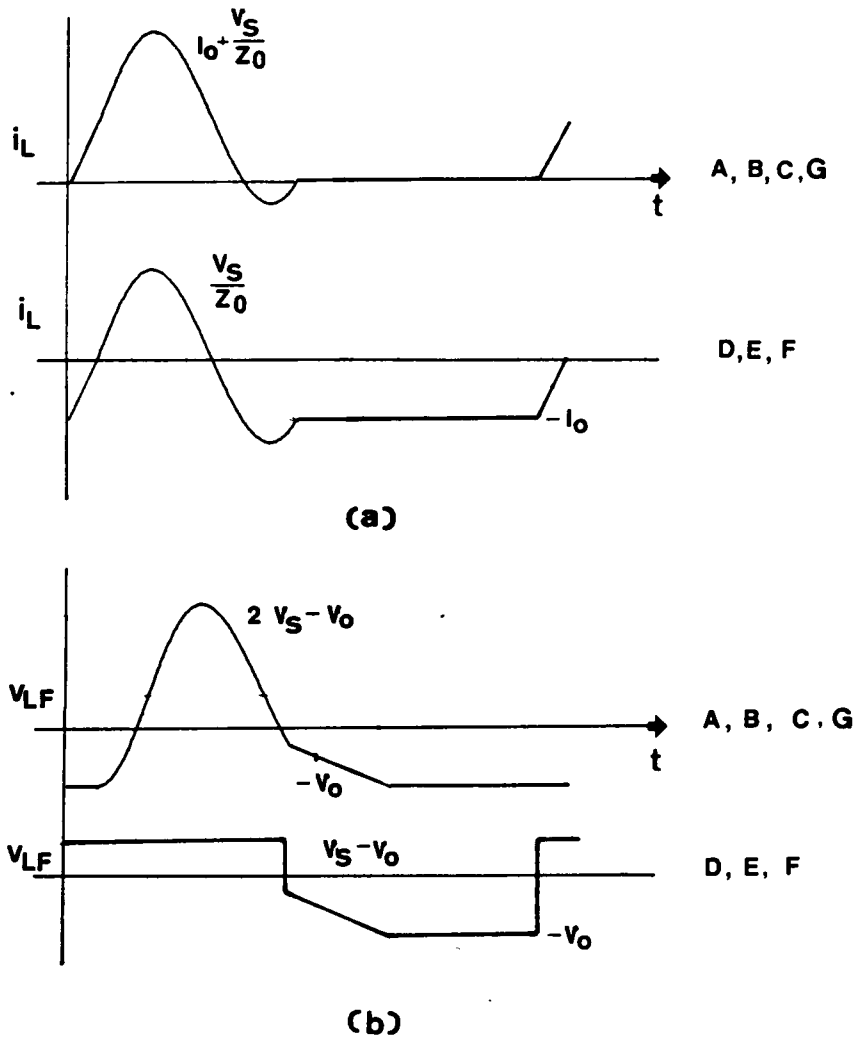

Figure 6.24. Comparison of full-wave ZCS resonant buck converters

a) Resonant inductor current, i_L
b) Output filter voltage, v_{LF}

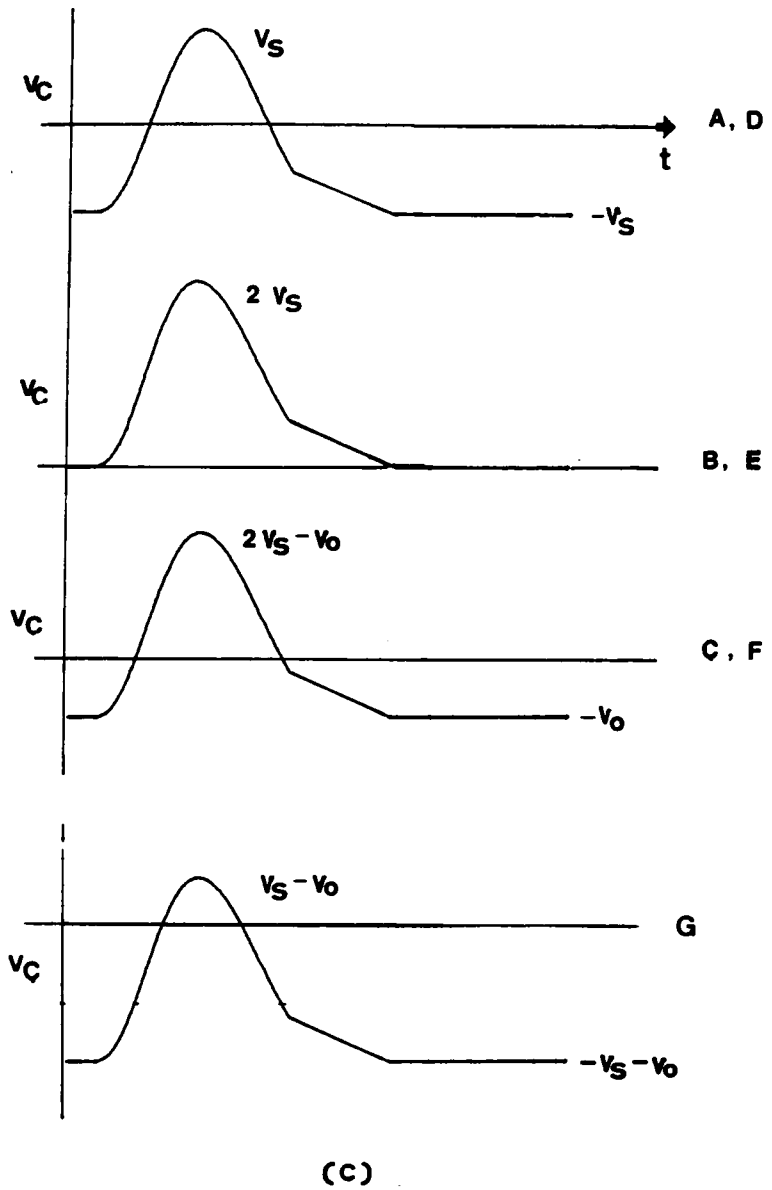

Figure 6.24. (contd.)
c) Resonant capacitor voltage, v_C

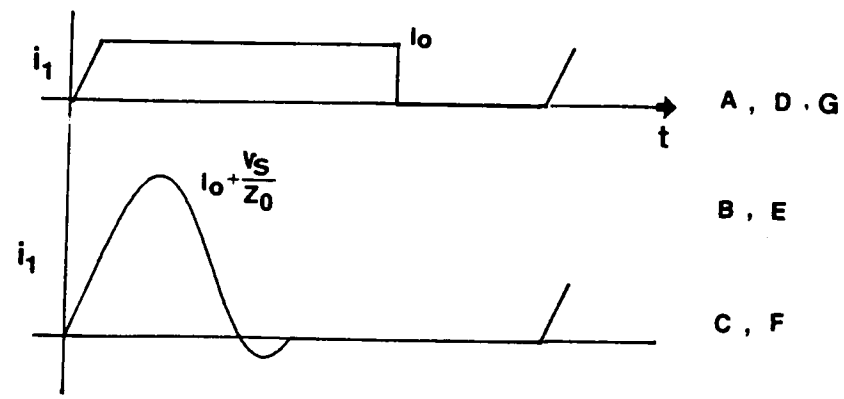

(d)

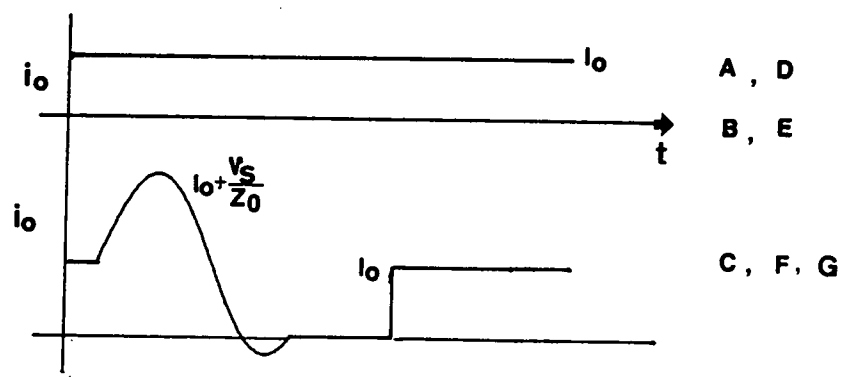

(e)

Figure 6.24. (contd.)
d) Input source current, i_1 e) Output load current, i_o

variations A, B, C and G. This implies, of course, that the filter inductor used in variations D, E and F can be of smaller dimensions.

Figure 6.24(c) shows the resonant capacitor voltage waveform affected by the capacitor shift process. The peak capacitor voltage in variations A and D is V_s, in B and E is 2 V_s, in C and F is 2 V_s − V_o and in G is V_s + V_o. Thus, variations A and D have lower voltage stress on the resonant capacitor than the others.

Figures 6.24(d) and 6.24(e) show the current waveforms through the input power supply and the output filter capacitor, respectively. Topologies A, D and G have lower input current ripple and topologies A and D have lower output current ripple.

Table 6.3 summarizes the discussions so far regarding the component stresses. We note from this table that variation D of Fig. 6.19 offers superior features with lower 1) peak resonant-inductor current, 2) volt-seconds across the filter inductor, 3) peak resonant-capacitor voltage, 4) ripple current of the input supply and 5) ripple current of the output filter capacitor, as compared to the other variations.

6.8.3.2 A Few ZVS Resonant Boost-Buck Variations

Figure 6.25 shows the state-plane diagrams in mode-1 operation of a few ZVS resonant boost-buck converters selected from among those in Fig. 6.22. These converters have been marked as A, B, C and D in Fig. 6.22(b). In Fig. 6.25, variation D has the state-plane origin itself as the trajectory center during the resonant interval. As may be observed from Fig. 6.25, this variation has the lowest capacitor-voltage stress ($v_{CN} = I_{EN}$ or $v_C = (I_l + I_o)Z_0$) and the lowest inductor current stress ($i_{LN} = I_{EN}$ or $i_L = (I_l + I_o)$) among these four ZVS resonant buck converter variations.

Figure 6.26 shows the circuit waveforms that differ among these selected converters due to the application of the shift rules. Figure 6.26(a) shows the resonant inductor current waveform. The peak resonant inductor current in circuits A and D is $I_o(1 + \frac{V_o}{V_s})$, whereas in circuits B and C the peak resonant inductor current is twice that value. Thus, circuits A and D have lower resonant inductor current stress.

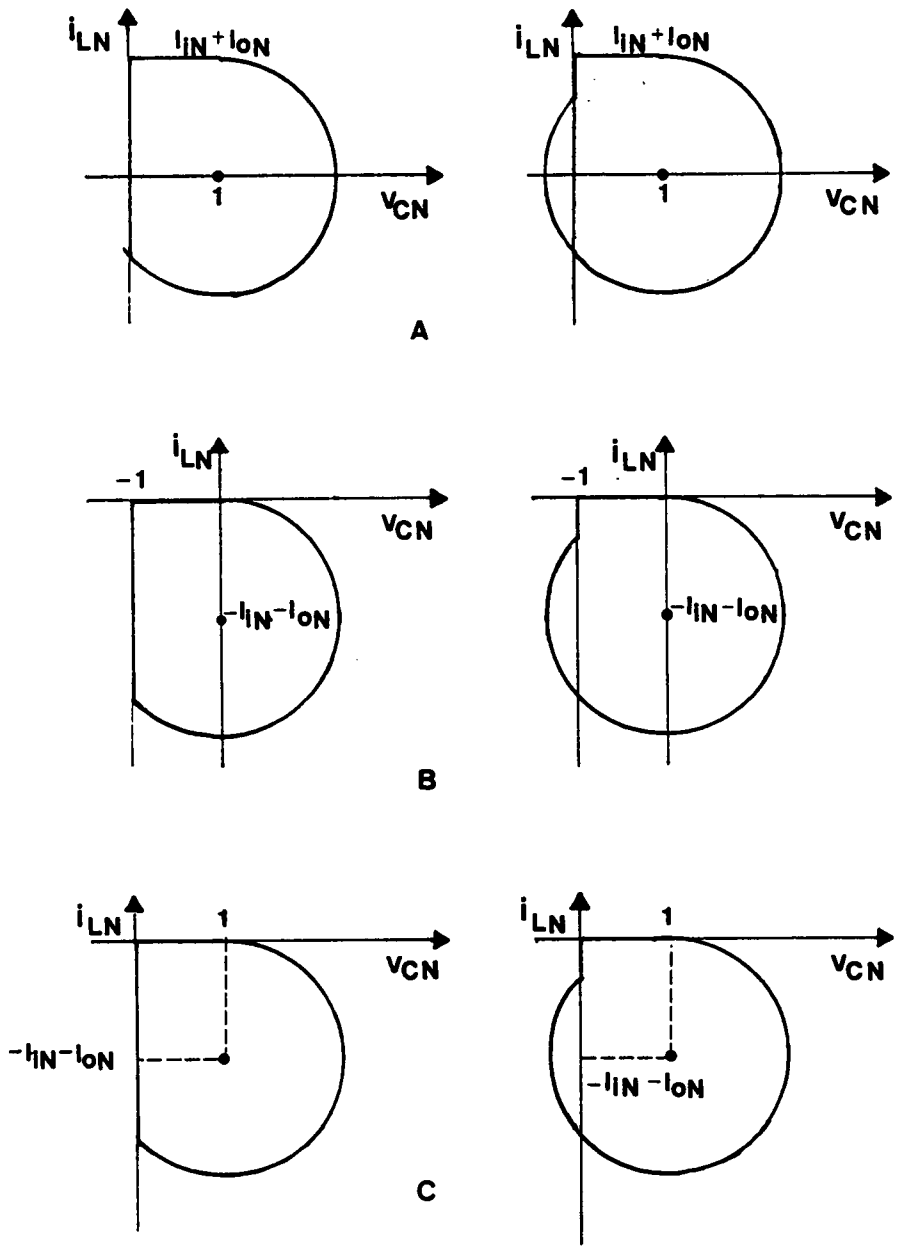

Figure 6.25. Mode-1 state plane diagrams of a few resonant boost-buck converters with ZVS

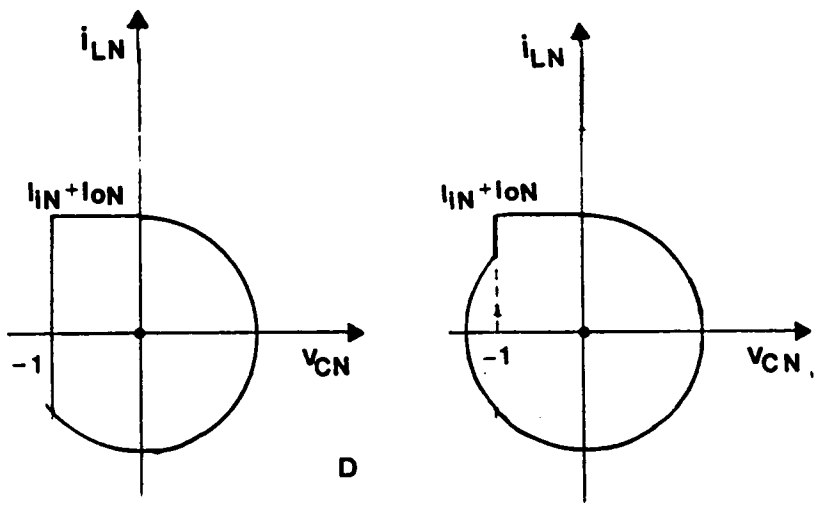

Figure 6.25. (contd.)

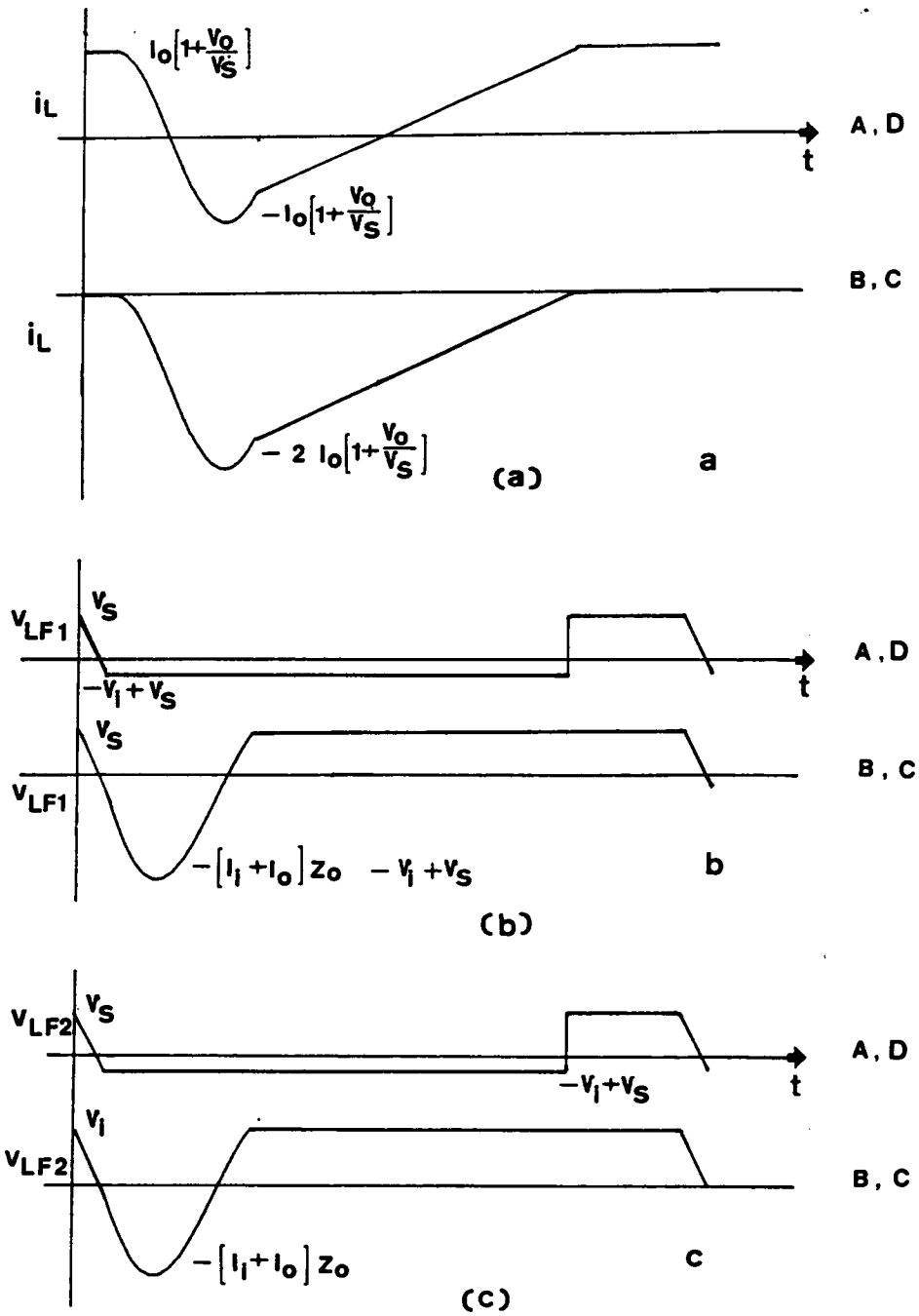

Figure 6.26. Comparison of half-wave ZVS resonant boost-buck converters

a) Resonant inductor current, i_L
b) Input filter inductor voltage, v_{LF1}
c) Output filter inductor voltage, v_{LF2}

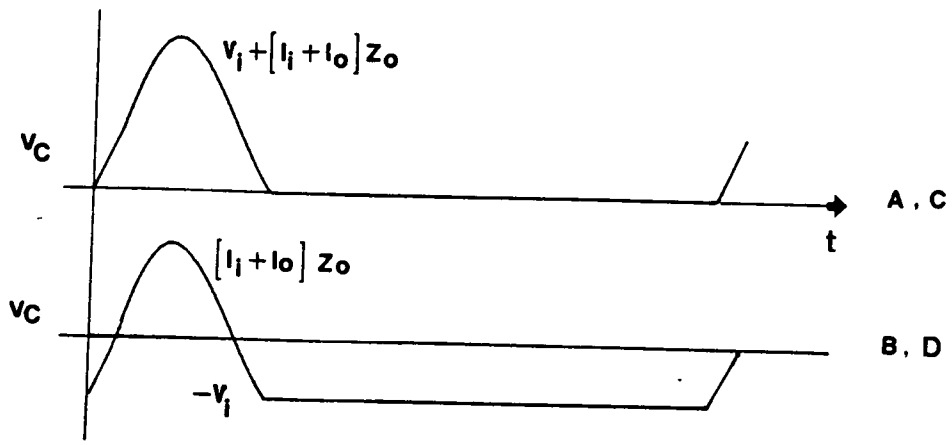

(d)

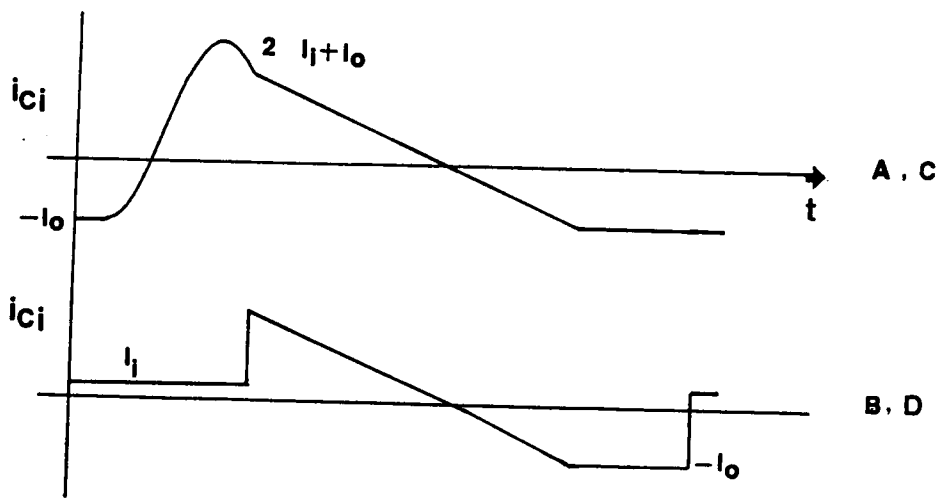

(e)

Figure 6.26. (contd.)

d) Resonant capacitor voltage, v_C e) Energy transfer capacitor current, i_{Ci}

TABLE-6.3

COMPARISON OF FULL-WAVE ZCS RESONANT BUCK CONVERTERS

	A	B	C	D	E	F	G
Resonant-inductor current				Lowest	Lowest	Lowest	
Volt-secs across filter ind.				Lowest	Lowest	Lowest	
Resonant-capacitor voltage	Lowest			Lowest			
Input supply ripple	Lowest			Lowest			Lowest
Output filter ripple	Lowest			Lowest			

Considering the voltage waveform across the input filter inductor (Fig. 6.26(b)) and across the output filter inductor (Fig. 6.26(c)), once again, circuit variations A and D have lower volt-seconds applied to these filter inductors. Figure 6.26(d) shows that variations B and D have a lower peak voltage applied to the resonant capacitor compared to the other two variations. Lastly, Fig. 6.26(e) shows that the ripple current to be handled by the transfer capacitor, C_f, is lower in circuit variations B and D than in A and C. The currents through the input dc supply ($= I_i$) and through the output filter capacitor ($= I_o$) are the same for all three variations and, hence, are not shown in Fig. 6.26.

Table 6.4 summarizes the discussion, thus far, regarding these four ZVS boost-buck converters. From this table, variation D of Fig. 6.26 has the lowest 1) peak resonant-inductor current, 2) volt-seconds across input filter inductor, 3) volt-seconds across output filter inductor, 4) peak resonant-capacitor voltage, 5) ripple current of the transfer capacitor filter, 6) ripple current of the input power supply and 7) ripple current of the output filter capacitor.

6.8.3.3 QRC Topologies With Low Component Stresses

The mode-1 state-plane diagrams, when the trajectory center during the resonant interval is at the state-plane origin, are shown in Fig. 6.27. It is found that in the case of QRCs with full-wave switches, the QRC circuit operating on the trajectory shown has lower stresses on its components than its topological variations. For QRCs with half-wave switches, other topologies which do not operate along the shown trajectory may have lower inductor current stress or capacitor voltage stress under certain operating conditions. However, QRCs with half-wave switches which operate on the trajectory shown represent a good compromise when the stresses on the components are considered.

Figure 6.28 shows the QRCs, one for each type of converter, which operate along the preferred steady-state trajectory. In Fig. 6.28, both half-wave and full-wave versions of the resonant switches may be used. These circuits form the best choices among the different QRC topologies from the point of view of component stress. It is interesting to note that the two terminal resonant switches introduced in Sec. 6.2 do not retain their original structure in any of the topologies of Fig. 6.28.

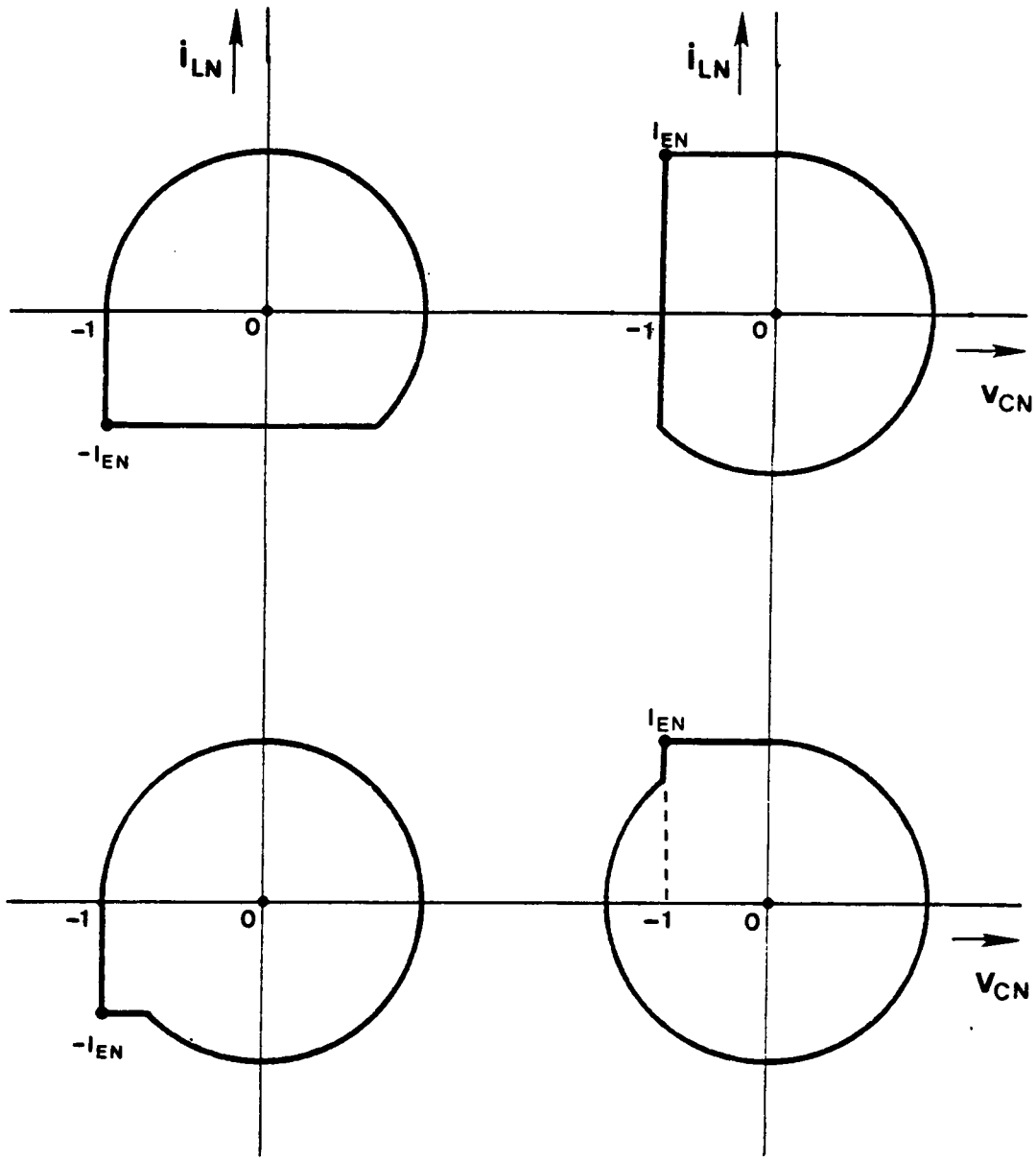

Figure 6.27. Mode-1 steady-state trajectories for QRCs with low component stress
a) Half-wave ZCS
b) Full-wave ZCS
c) Half-wave ZVS
d) Full-wave ZVS

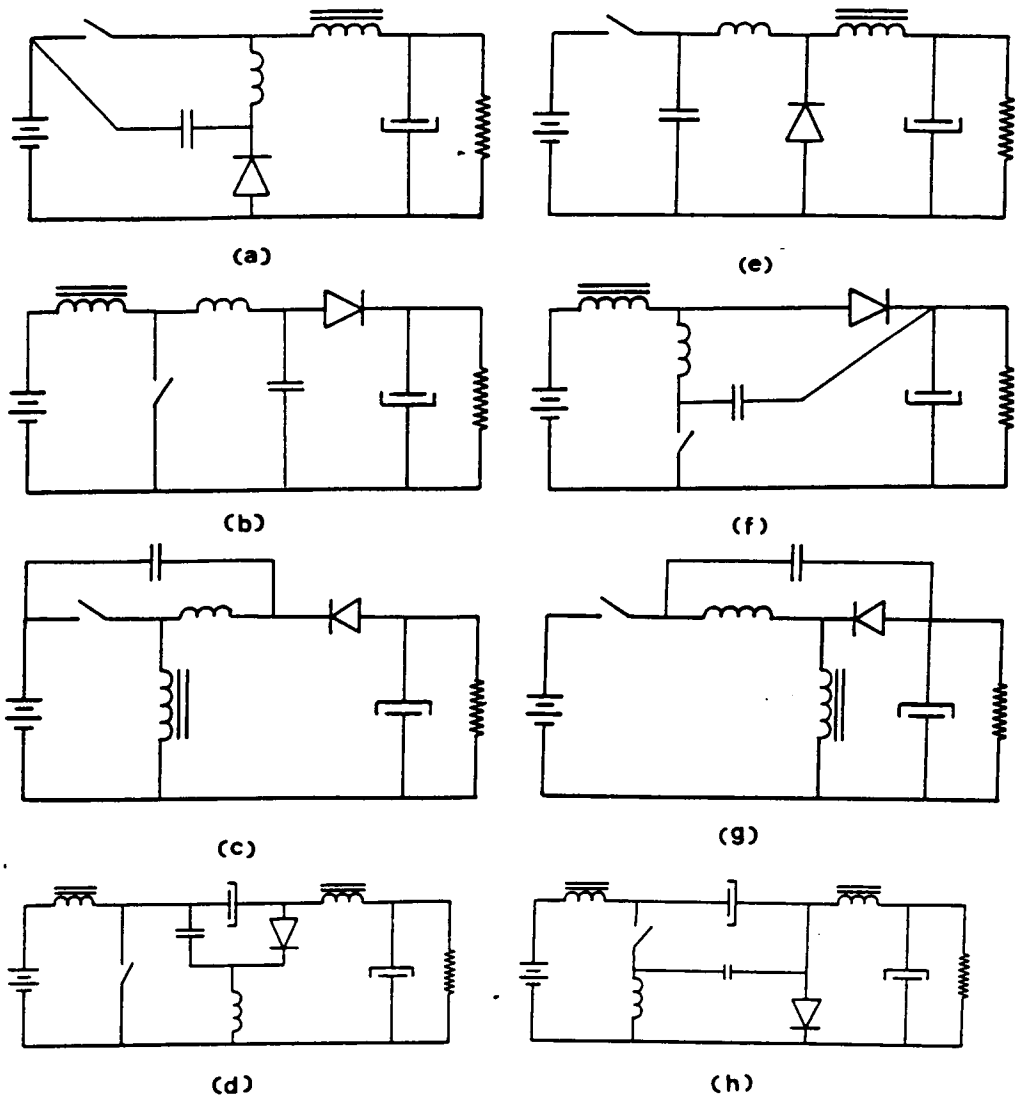

Figure 6.28. Quasi-resonant converters with low component stress
a) Buck with ZCS
b) Boost with ZCS
c) Buck-boost with ZCS
d) Boost-buck with ZCS
e) Buck with ZVS
f) Boost with ZVS
g) Buck-boost with ZVS
h) Boost-buck with ZVS

TABLE-6.4

COMPARISON OF A FEW HALF-WAVE ZVS RESONANT BOOST-BUCK CONVERTERS

	A	B	C	D
Resonant-inductor current	Lowest			Lowest
Volt-seconds across input filter inductor	Lowest			Lowest
Volt-seconds across output filter inductor	Lowest			Lowest
Resonant-capacitor voltage		Lowest		Lowest
Transfer capacitor ripple		Lowest		Lowest
Input supply ripple	Lowest	Lowest	Lowest	Lowest
Output filter ripple	Lowest	Lowest	Lowest	Lowest

6.9 Summary And Conclusion

State-plane analysis and two circuit rules have been utilized to unify and analyze the various QRC topologies. Sixteen converter topologies were identified as the basic QRCs. These were obtained from the 1) buck, 2) boost, 3) buck-boost and 4) Cuk or boost-buck topologies as modified by the inclusion of a)half-wave ZCS, b)full-wave ZCS, c)half-wave ZVS and d)full-wave ZVS. Complete dc analyses including determination of mode boundaries and dc gain characteristics for all QRCs were performed using state-plane diagrams. The analyses were simplified because a single set of state-plane diagrams was found applicable to all four basic QRCs with a particular type of resonant switch.

An inductor shift rule and capacitor shift rule were introduced which together give a method of deriving circuit variations from the basic quasi-resonant converters. These shift rules also show that the detailed dc analyses performed on the basic QRCs are applicable to their topological variations too. Furthermore, using the shift rules the variations of a QRC can be compared based on their relative component stresses. Sixteen converter circuits, one for each type of QRC, were selected base on such comparisons. These sixteen circuits represent the best choices among the different QRC topologies from the point of view of component stress.

Chapter 7

Conclusions And Future Work

The work presented in this report demonstrated the effectiveness of graphical state-plane methods in understanding and analyzing resonant power converters under both steady-state and transient conditions. Using closed steady-state trajectories on the state plane, the operation of resonant converters under varying switching frequency and load were studied and complex operating modes predicted. The equations governing the ideal performance were derived by geometrically analyzing the trajectory diagrams. The mode boundaries, which determine the regions of converter operation, and the characteristics in the different modes were determined by such analyses. Thus, the identification of modes and their quantitative analyses follow from the application of the same analytical technique. Furthermore, the report showed that the state-plane analysis can be modified to include parasitic losses and then analyzed, by carrying out such an analysis of a series resonant converter (SRC). It was also shown that the state-plane analysis was useful in understanding and evaluation of control methods, again by utilizing a SRC. Since the energy stored in the resonant tank depends on the trajectory size, the ability of a control method in keeping the tank energy within bounds, without high-energy transients, was clearly seen on the state plane.

The operation of a SRC under different modes, type-2 discontinuous conduction mode (type-2 DCM), CCM and type-1 discontinuous conduction mode (type-1 DCM), was discussed using state plane diagrams. The complete dc analysis of a SRC was performed and theoretical design curves covering dif-

ferent regions were also generated. DC analysis of a SRC with losses included was carried out for operating frequencies below resonant frequency by modifying the ideal state-plane analysis. Comparison of the regions of operation showed that the type-1 DCM region is significantly altered due to the losses. An upper limit on the maximum power to the load was shown to exist. This limit depends on the circuit losses. Comparisons of the dc characteristics showed that, in general, the lossless analysis is not valid 1)whenever the switching frequency approaches resonant frequency or 2)whenever output voltage approaches supply voltage. Good correlation between the theoretical and experimental dc characteristics were obtained.

The future work that needs to be done in this area includes 1)analysis of a SRC above resonant frequency with losses and 2)modification of analysis to include output transformer.

The different control techniques for a SRC were identified and evaluated, for properties, such as stability, response to control changes and performance under a short circuit. Among the existing methods, Analog-Signal-To-Discrete-Time-Interval-Converter (ASDTIC) control was shown to result in an unstable system under certain conditions. A new method, "optimal trajectory control", was proposed based on the analysis. By utilizing the required transistor trajectory itself as the control law, this control method attempts to reach its steady-state operation in a nonasymptotic and time-optimal manner. The control automatically selects the optimum sequence of device conduction under all dynamic conditions. Also, since the control predetermines its operating trajectory, the resonant tank is fully controlled with the tank energy, inductor current and capacitor voltage, all staying within bounds under all circumstances, including a short circuit across the output terminals of the converter. The report also described in detail an implementation scheme for this control method. The transient performance of the experimental setup was excellent as predicted. This method, though somewhat complex, shows good potential for use in high performance, low and medium frequency ($\cong$300 *kHz*) bridge type of resonant converters.

Future work in this area includes 1)small signal modeling of the different control methods, 2)extension of optimal trajectory control operation to DCM region, 3)determination of sensitivity of performance to parameter variations and 4)evaluation of control methods when an outer loop, such as a current loop or a voltage loop, is present.

Analysis of a parallel resonant converter (PRC), uncovering, for the first time, the presence of many modes besides CCM and DCM, was carried out. Employing state plane diagrams, the different regions

of operation, such as the CCM regions, transition regions, DCM region, natural commutation region, short-circuit current limit region and multiple cycle conduction region were defined. The detailed quantitative analysis of the operation of the PRC, including determination of the mode boundaries and dc characteristics, were also presented. Theoretical design curves based on analysis results were also generated. Experimental results confirmed the existence of the variety of modes and and also showed that the characteristics of a PRC followed, generally, the pattern established by the ideal analysis. However, deviations attributable to parasitic losses were observed between the theoretical and experimental curves.

Future work in this topic includes 1)inclusion of losses in analysis, as was done for a SRC, to account for deviations between theoretical and experimental characteristics 2)modification of analysis to include output transformer.

The insight gained form the analysis led to the proposal of a "novel resonant buck converter", with a voltage conversion ratio almost independent of load. Due to this feature, the converter's operating frequency range in many applications can be smaller, which is desirable. The converter has potential to operate at very high frequencies. The proposal of this converter helped to identify the bidirectional or full-wave Zero Current Switch, which is one of the resonant switches used in the family of "quasi-resonant converters (QRCs)".

State-plane analysis and two circuit rules were utilized to unify and analyze the various QRC topologies. Sixteen topologies derived from the four pulse-width modulated (PWM) converters, buck, boost, buck-boost and Cuk (or boost-buck), as modified by the inclusion of the four types of resonant switches were identified as "basic" QRCs. Complete dc analyses including determination of mode boundaries and dc gain characteristics for all QRCs were performed for all the basic QRCs.

An inductor shift rule and a capacitor shift rule were introduced, using which many circuit variations including new ones, were derived. Using these shift rules, it was also shown that the dc analyses performed on the basic QRCs are applicable to their topological variations too and thus the dc analyses presented in this chapter is general in scope. Sixteen circuits, one for each type of QRC, were selected as the best choices from among the numerous QRC topologies based on assessment of relative component stresses.

Future work in this area include 1)study of effect of losses on mode boundaries and dc characteristics 2)verification of operation of some of the variations and 3)verification of low component stresses predicted for the selected topologies and 4)assessment of these selected topologies from other considerations such as ease of implementation and efficiency.

References

1. B. D. Bedford and R. G. Hoft, "Principles of Inverter Circuits". New York: Wiley, 1964, pp. 128-148.

2. B. R. Pelly, "Latest Developments in Static High Frequency Power Sources for Induction Heating". *IEEE Transactions of Industrial Electronics and Control instrumentation*, IECI-7, No.4, June 1970.

3. N. Mapham, "An SCR Inverter with Good Regulation and Sinewave Output". *IEEE Transactions on Industry and General Applications*, IGA-3, No.2, Mar/Apr 1967, pp. 176-187.

4. R. Myers and R. D. Peck, "200 kHZ Power FET Technology in New Modulator Supplies". *Hewlett-Packard Journal*, Aug 1981, pp. 3-10.

5. S. R. Babu, "A Practical resonant converter using high speed Power Darlington Transistors". *Proceedings of PCI/Motorcon*, 1982, pp. 122-141.

6. V. T. Ranganathan, P. D. Ziogas and V. R. Stefanovic, " A Regulated DC-DC Voltage Source Converter Using a High Frequency Link". *IEEE Transactions on Industry Applications*, Vol. IA-18, No.3, pp.279-287, May/June 1982.

7. R. L. Steigerwald, "High-Frequency Resonant Transistor DC-DC Converters". *IEEE Transactions on Industrial Electronics*, Vol. IE-31, No. 2, pp. 181-191, May 1984.

8. F. C. Schwarz, "A Method of Resonant Current Pulse Modulation for Power Converters". *IEEE Transactions of Industrial Electronics and Control instrumentation*, IECI-17, No.3, May 1970, pp. 209-221.

9. F. C. Schwarz, "An Improved Method of Resonant Current Pulse Modulation for Power Converters". *IEEE Power Electronics Specialists Conference, Record*, 1975, pp. 194-204.

10. J. G. Kassakian, "A New Current Mode Sine Wave Inverter". *IEEE Transactions on Industry Applications*, IA-18, No.3, May/June 1982, pp. 273-278.

11. J. G. Kassakian, A. F. Goldberg and D. R. Moretti, "A Comparative Evaluation of Series amd Parallel Structure for High Frequency Transistor Inverters". *IEEE Power Electronics Specialists Conference, Record*, 1982, pp. 20-26.

12. F. C. Schwarz and J. B. Klassens, " A Controllable Secondary Multi-Kilowatt DC Current Source with Constant Maximum Power Factor in its three phase Supply line". *IEEE Transactions of Industrial Electronics and Control instrumentation*, IECI-23, No.2, May 1976, pp. 142-150.

13. F. C. Schwarz, "A Doublesided Cyclo-Converter". *IEEE Power Electronics Specialists Conference, Record*, 1979, pp. 437-447.

14. J. B. Klassens, "DC to AC Series Resonant Converter System with High Internal Frequency Generating Synthesized Waveforms for Multikilowatt Power Levels". *IEEE Power Electronics Specialists Conference, Record*, 1984, pp. 99-110.

15. F. C. Schwarz and W. L. Motze de Chateleux, "A Multi-Kilowatt ployphase AC/DC converter with Reversible Power Flow and without Passive Low Frequency filters". *IEEE Power Electronics Specialists Conference, Record*, 1979, pp. 448-458.

16. S. Muroyama and K. Sakakibara, "Characteristics of a New Series Resonant Converter". *IEEE INTELEC Conference, Record*, 1982, pp. 111-116.

17. J. Chen and R. Bonert, "Load Independent AC/DC Power Supply for Higher Frequencies with Sine-Wave Output". *IEEE Transactions on Industry Applications*, IA-19, No.2, March/April 1983, pp. 223-227.

18. R. J. King and T. A. Stuart, "A Normalized Model for the Half-Bridge Series Resonant Converter". *IEEE Transactions on Aerospace and Electronic Systems*, AES-17, No.2, Mar 1981, pp 190-198.

19. R. J. King and T. A. Stuart, "Modeling the Full Bridge Series Resonant Converter". *IEEE Transactions on Aerospace and Electronic Systems*, AES-18, No.4, July 1982, pp. 449-459

20. V. Vorperian and S. Cuk, "A Complete DC Analysis of the Series Resonant Converter". *IEEE Power Electronics Specialists Conference, Record*, 1982, pp. 85-100.

21. V. Vorperian and S. Cuk, "Small Signal Analysis of Resonant Converters". *IEEE Power Electronics Specialists Conference, Record*, 1983, pp. 269-282.

22. A. F. Witulski and R. W. Erickson, "Steady-State Analysis of the Series Resonant Converter". *IEEE Transactions on Aerospace and Electronic Systems*, AES-21, No.6, Nov 1985.

23. S. D. Johnson and R. W. Erickson, "Steady-State Analysis and Design of the Parallel Resonant Converter". *IEEE Power Electronics Specialists Conference, Record*, 1986.

24. R. J. King and T. A. Stuart, "Inherent Overload Protection for the Series Resonant Converters". *IEEE Transactions on Aerospace and Electronic Systems*, AES-19, No. 6, Nov 1983, pp. 820-830.

25. S. W. H. DeHaan, "A New Integral Pulse Module for the Series Resonant Converter". *IEEE Transactions on Industrial Electronics*, IE-31, No.3, Aug 1984, pp. 255-262.

26. S. W. H. DeHaan and H. Huisman, "Novel Operation and Control Methods for Series-Resonant Converters". *IEEE Transactions on Industrial Electronics*, IE-32, No. 2, May 1985, pp. 150-157.

27. R. R. Robson and D. J. Hancock, "A 10 KW Series Resonant Converter Design, Transistor Characterization, and Base Drive Optimization". *IEEE Power Electronics Specialists Conference, Record*, 1982, pp. 33-44.

28. R. Oruganti and F. C. Lee, "Resonant Power Processors: Part I - State Plane Analysis". *IEEE-IAS-1984 Annual Meeting, Conference Record*, 1984, pp.860-867. Also in *IEEE Transactions on Industry Applications*, IA-21, No.6, Nov/Dec 1985.

29. R. Oruganti and F.C.Lee, "Resonant Power Processors: Part II - Methods of Control". *IEEE-IAS-1984 Annual Meeting, Conference Record*, 1984, pp. 868-878. Also in *IEEE Transactions on Industry Applications*, IA-21, No.6, Nov/Dec 1985.

30. V. T. Ranganathan, P. D. Ziogas, V. Stefanovic, "Performance Characteristics of High Frequency Links under Forward and Regenerative Power Flow Conditions". *IEEE-IAS-1983 Annual Meeting, Conference Record*, 1983, pp. 831-839.

31. F. S. Tsai, R. Oruganti, F. C. Lee, " A Novel Control for Bidirectional Flow of a Parallel Resonant Converter". *IEEE-IAS-1985 Annual Meeting, Conference Record*, 1985, pp. 1124-1129.

32. V. T. Ranganathan, P. D. Ziogas and V. R. Stefanovic, "A DC-AC Power Conversion Technique using Twin Resonant High Frequency Links". *IEEE Transactions on Industry Applications*, IA-19, No.3, May/June 1983, pp. 393-400.

33. K. Harada and C. Chen, "A Resonant Type Constant Current Converter with Feedback"., *IEEE INTELEC Conference, Record*, 1983, pp. 601-606.

34. I. J. Pitel, "Phase-Modulated, Resonant Power Conversion Techniques for High-Frequency Link Invereters". *IEEE-IAS-1985 Annual Meeting, Conference Record*, 1985, pp. 1163-1172.

35. F. G. Turnbull and R. E. Tompkins, "Design of a Pulse-Width Modulated Resonant Converter for a High Output Voltage Power Supply". *IEEE-IAS-1985 Annual Meeting, Conference Record*, 1985, pp. 1145-1150.

36. V. Vorperian, "High-Q Approximations in the Small-Signal Analysis of Resonant Converters". *IEEE Power Electronics Specialists Conference, Record*, 1985, pp. 707-715.

37. G. C. Verghese, M. E. Elbuluk and J. G. Kassakian, "A General Approach to Sampled-Data Modeling for Power Electronics Circuits". *IEEE Power Electronics Specialists Conference, Record*, 1984, pp. 316-328.

38. R. J. King and T. A. Stuart, "A Large Signal Dynamic Simulation for the Series Resonant Converter". *IEEE Transactions on Aerospace and Electronic Systems*, AES-19, No.6, nov 1983, pp. 859-870.

39. R. J. King and T. A. Stuart, "Transformer Induced Instability of the Series Resonant Converter". *IEEE Transactions on Aerospace and Electronic Systems*, AES-19, No.3, May 1983, pp.474-482.

40. D. P. Atherton, "Nonlinear Control Engineering". Van Nostrand Reinhold Company, London, 1982, Chapter 2.

41. F. C. Lee and T. G. Wilson, "Modeling and Analysis of Several Classes of Self-Oscillating Inverters: Part I - State Plane Representations". *IEEE Transactions on Circuits and Systems*,CAS-29, No.6, pp.355-365, June 1982.

42. F. C. Lee and T. G. Wilson, "Modeling and Analysis of Several Classes of Self-Oscillating Inverters: Part II - Model Extension, Classification and Duality Relationship". *IEEE Transactions on Circuits and Systems* CAS-29, No.6, pp.366-374, June 1982.

43. W. W. Burns III and T. G. Wilson, "State-Plane Trajectories Used to Observe and Control the Behavior of a Voltage Step-Up DC-to-DC Converter". *IEEE Power Electronics Specialists Conference, Record*, 1976, pp.212-222.

44. R. Kasturi, "An Analysis of Series Inverter Circuits". *IEEE Transactions of Industrial Electronics and Control instrumentation*, IECI-22, No.4, Nov 1975, pp. 515-519.

45. M. P. Dougherty, "A Series Resonant Inverter Simulation using Super-Sceptre". *IEEE National Aerospace and Electronics Conference, Record*, May 1979, pp. 517-524.

46. J. G. Kassakian, "Simulating Power Electronic Systems - A New Approach". *Proceedings of IEEE* Vol-67, No.10, Oct 1979, pp. 1428-1439.

47. R. L. Avant and F. C. Lee, "The J3 SCR Model Applied to Resonant Converter Simulation". *IEEE INTELEC Conference, Record*,1983, pp. 541-548.

48. L. W. Nagel, "SPICE2: A Computer Program to Simulate Semiconductor circuits". *Memorandum No. ERL-M520*, May 9, 1975, Electronics Research Laboratory, College of Engineering, University of California, Berkeley.

49. D. L. Cronin, "2800 Watt Series Inverter DC Power Supply". *IEEE Power Electronics Specialists Conference, Record*, 1971, pp. 117-123.

50. J. Biess, L. Inouye and J. H. Shank, "High Voltage Series Resonant Inverter Ion Engine Screen Supply". *IEEE Power Electronics Specialists Conference, Record*, 1974, pp. 97-105.

51. R. C. Cole, "A Gated Resonant Inverter Power Processor for Pulsed Loads". *IEEE Power Electronics Specialists Conference, Record*, 1981, pp. 312-326.

52. D. Chambers, "Designing High Power SCR Resonant Converters for Very High Frequency Operation". *Proceedings of Powercon-9*, 1982, session F, paper 2.

53. R. R. Robson, "Advances in Series Resonant Inverter Technology and its Effect on Spacecraft Employing Electric Propoulsion". *AIAA/JSASS/DGLR, 16th International Electric Propulsion Conference*, Nov. 1982, pp. 1-4.

54. R. R. Robson, "Designing a 25 Kilowatt High Frequency Series Resonant DC/DC Converter". *Proceedings of Powercon-11*, 1984, session H1, paper 3.

55. E. E. Buchanan, Jr., and E. J. Miller, "Resonant Switching Power Conversion Technique". *IEEE Power Electronics Specialists Conference, Record*, 1975, pp. 188-193.

56. E. J. Miller, "Resonant Switching Power Conversions". *IEEE Power Electronics Specialists Conference, Record*, 1976, pp. 206-211.

57. N. O. Sokal and A. D. Sokal, "Class E - A New Class of High-Efficiency Tuned Single-Ended Switching Power Amplifiers". *IEEE Journal of Solid-State Circuits*, SC-10, no. 3, June 1975, pp. 168-176.

58. R. Redl, B. Molnar and N. O. Sokal, "Class-E Resonant Regulated DC/DC Power Converters: Analysis of Operation, and Experimental Results at 1.5 MHZ". *IEEE Power Electronics Specialists Conference, Record*, 1983, pp. 50-60.

59. K. H. Liu and F. C. Lee, "Resonant Switches - A Unified Approach to Improve Performances of Switching Converters". *IEEE INTELEC Conference, Record*, 1984, pp. 344-351.

60. R. Oruganti and F. C. Lee, "State-Plane Analysis of Parallel Resonant Converters". *IEEE Power Electronics Specialists Conference, Record*, 1985, pp. 56-73.

61. K.H.Liu, R. Oruganti and F. C. Lee, "Resonant Switches - Topologies and Characteristics". *IEEE Power Electronics Specialists Conference, Record*, 1985, pp. 860-867.

62. K. H. Liu and F. C . Lee, "Zero-Voltage Switching Technique in DC/DC Converters". *IEEE Power Electronics Specialists Conference, Record*, 1986, pp. 58-70.

63. T. Zeng, D. Y. Chen and F. C. Lee, "Variations of Quasi-Resonant Converter Topologies". *IEEE Power Electronics Specialists Conference, Record*, 1986.

64. R. Oruganti and F. C. Lee, "Resonant Converters, Analysis and Control". *Continually Updated Lecture Notes*, First presentation at Sundstrand Corporation at Rockford, IL, July 1984.

65. R. Oruganti and F. C. Lee, "Effects of Parasitic Losses on the Performance of Series Resonant Converters". *IEEE-IAS-1985 Annual Meeting, Conference Record*, 1985, pp. 1233-1243.

66. M. M. Jovanovic, K. H. Liu, R. Oruganti and F. C. Lee, "State-Plane Analysis of Quasi-Resonant Converters". *IEEE Transactions on Power Electronics*, PE-2, No.5, Jan 1987.

67. Vorperian, Tymerski, Liu and Lee, "Generalized Resonant Switches Part 1: Topologies". *Power Electonics Seminar sponsored by VPEC Center*, Dept. of Elec. Eng., Virginia Poly. Inst. & St. Univ., Blacksburg, Va.

68. Vorperian, Tymerski, Liu and Lee, "Generalized Resonant Switches Part 2: Analysis and Circuit Models". *Power Electonics Seminar sponsored by VPEC Center*, Dept. of Elec. Eng., Virginia Poly. Inst. & St. Univ., Blacksburg, Va.

Appendix A

Ideal Analysis Of SRC

In Secs. A.1 to A.4 of this appendix, quantitative analyses of the state-plane diagrams in Chapter 2 are carried out. Certain results of the analyses, including mode boundaries and dc characteristics have been presented in Secs. 2.2.6 & 2.3. Section A.5 contains design curves obtained from the analysis. Section A.6 presents examples of SRC design to demonstrate use of the curves and to highlight certain features of SRC operation. Section A.7 presents computer programs based on the analytical results, including those used to generate SRC state portrait and steady-state trajectories. The computer programs for plotting the transient trajectories under different control methods (Chapter 4) are also included in Sec. A.7. Refer to Sec. 2.0 for definitions of symbols used in this appendix.

A.1 CCM Analysis Below Resonance

Fig. A.1 shows a single CCM steady-state trajectory below resonant frequency. The equations in this section are derived from analysis of this diagram.

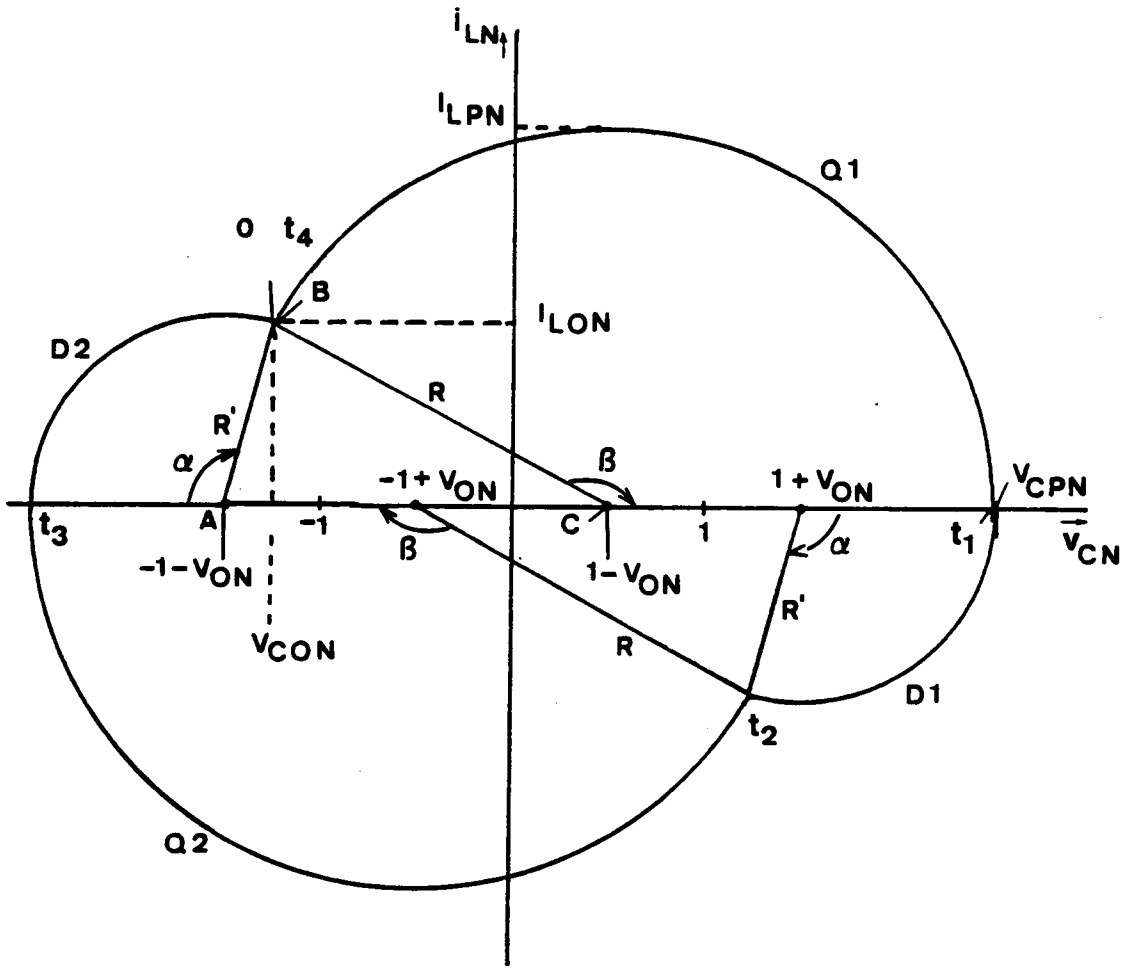

Figure A.1 Ideal CCM operation below resonance - Analysis diagram

A.1.1 Switching Boundary

Based on (2.9), the trajectory equation when device Q1 is conducting (interval 0 to t_1) is

$$\begin{aligned} i_{LN}^2 + (v_{CN} - 1 + V_{oN})^2 &= R^2 \\ &= I_{LON}^2 + (V_{CON} - 1 + V_{oN})^2 \end{aligned} \tag{A.1}$$

At $t = t_1$, $i_{LN} = 0$ and $v_{CN} = V_{CPN}$. Thus,

$$(V_{CPN} - 1 + V_{oN})^2 = I_{LON}^2 + (V_{CON} - 1 + V_{oN})^2 \tag{A.2}$$

Similarly, the trajectory equation when D2 is conducting is

$$\begin{aligned} i_{LN}^2 + (v_{CN} + 1 + V_{oN})^2 &= R'^2 \\ &= (V_{CPN} - 1 - V_{oN})^2 \end{aligned} \tag{A.3}$$

At $t = t_4$, $i_{LN} = I_{LON}$ and $v_{CN} = V_{CON}$. Thus,

$$I_{LON}^2 + (V_{CON} + 1 + V_{oN})^2 = (V_{CPN} - 1 - V_{oN})^2 \tag{A.4}$$

Substituting for V_{CPN} from (A.4) into (A.2) and rearranging,

$$(V_{CON} + V_{oN}) + V_{oN}^2 = - V_{oN} \sqrt{I_{LON}^2 + (V_{CON} + 1 + V_{oN})^2} \tag{A.5}$$

Squaring and rearranging the terms further,

$$\{(V_{CON} + V_{oN})^2 - V_{oN}^2\}(1 - V_{oN})^2 - V_{oN}^2 I_{LON}^2 = 0 \tag{A.6}$$

Equation (A.6) is the switching boundary S1 relating the state-variables at the instant of switching-on (I_{LON}, V_{CON}) of transistor Q1, for a given normalized load voltage, V_{oN}. Due to the symmetry of the steady-state trajectory, the equation for the switching boundary S2, can be obtained by substitution of $- V_{CON}$ and $- I_{LON}$ in place of V_{CON} and I_{LON} , respectively, in (A.6).

A.1.2 Analysis Of A Steady-State Trajectory

In this section, the different circuit parameters related to steady-state operation are derived from analysis Fig. A.1. The transistor trajectory radius R and the normalized load voltage V_{oN} are assumed to be the known variables. In some of the following cases, the equation for the desired circuit parameter has been expressed directly in terms of R and V_{oN} , as in (A.9) which shows the equation for computing α. In other cases, in order to avoid cumbersome equations, the desired equation is written in terms of other parameters. These parameters, in turn, have been expressed as functions of R and V_{oN}, earlier. An example is (A.35) which expresses normalized average diode current, I_{DAVN}, in terms of normalized peak capacitor voltage, V_{CPN}, normalized switching point voltage, V_{C0N}, diode conduction angle, α and transistor conduction angle, β. Equations (A.23), (A.18), (A.9) and (A.11) are the equations for V_{CPN}, V_{C0N}, α and β , respectively. By substitution of these into (A.35), the equation for I_{DAVN} can be written solely in terms of R and V_{oN}, if so required.

Diode Conduction Radius: From Fig. A.1,

$$\begin{aligned} R' &= \text{Radius of Diode Trajectory} \\ &= R - 2V_{oN} \end{aligned} \tag{A.7}$$

Diode Conduction Angle: Considering Δ ABC in Fig. A.1, it can be shown

$$\alpha = \pi - \cos^{-1}\left\{\frac{R'^2 + 4 - R^2}{4R'}\right\} \tag{A.8}$$

Substituting for R' from (A.7) into (A.8),

$$\alpha = \pi - \cos^{-1}\left\{\frac{V_{oN}^2 - RV_{oN} + 1}{R - 2V_{oN}}\right\} \tag{A.9}$$

Transistor Conduction Angle: Considering Δ ABC of Fig. A.1, it can be shown

$$\beta = \pi - \cos^{-1}\left\{\frac{R^2 + 4 - R'^2}{4R}\right\} \tag{A.10}$$

Substituting for R' from (A.7) into (A.10)

$$\beta = \pi - \cos^{-1}\left\{\frac{-V_{oN}^2 + RV_{oN} + 1}{R}\right\} \tag{A.11}$$

Period of Operation

$$\begin{aligned} T_N &= \text{Angular Operating Period} \\ &= \omega_0 T, \qquad \text{where} \end{aligned} \tag{A.12}$$

$$\begin{aligned} T &= \text{Operating Period} \\ &= 2t_d + 2t_q \end{aligned} \tag{A.13}$$

From (2.17), (2.18), (A.12) and (A.13),

$$T_N = 2\ (\alpha + \beta) \tag{A.14}$$

Equations (A.13) and (A.14) are valid for CCM operation both below and above resonant frequency.

Frequency of Operation

$$\omega_N = \frac{\omega}{\omega_0} = \frac{2\pi}{T} \times \frac{1}{\omega_0} = \frac{2\pi}{T_N} \tag{A.15}$$

$$\text{Thus,} \qquad \omega_N = \frac{\pi}{\alpha + \beta} \tag{A.16}$$

Equations (A.15) and (A.16) are valid for CCM operation both below and above resonant frequency.

Switching Point Voltage: From Fig. A.1,

$$V_{CON} = 1 - V_{oN} + R\cos\beta \tag{A.17}$$

Substituting for β from (A.11) into (A.17) and simplifying,

$$V_{CON} = -V_{oN}(R + 1 - V_{oN}) \tag{A.18}$$

Using (A.23), an equation to be derived, an alternative form for (A.18) is

$$V_{CON} = -V_{oN}\, V_{CPN} \tag{A.19}$$

Switching Point Current: From Fig. A.1,

$$I_{LON} = R \sin \beta \tag{A.20}$$

Substituting for β from (A.11) into (A.20) and simplifying,

$$I_{LON} = \sqrt{R^2 - (-V_{oN}^2 + RV_{oN} + 1)^2} \tag{A.21}$$

Peak Capacitor Voltage: From Fig. A.1,

$$V_{CPN} = R' + 1 + V_{oN} \tag{A.22}$$

Substituting for R' from (A.7) into (A.22),

$$V_{CPN} = R + 1 - V_{oN} \tag{A.23}$$

Peak Inductor Current: From Fig. A.1,

$$I_{LPN} = R \tag{A.24}$$

Peak Inductor Volt-Seconds: The peak inductor volt-seconds is a useful parameter in designing resonant inductor. Define

(VS) = Volt-Seconds across Inductor

$(VS)_P$ = Peak Volt-Seconds across Inductor

$(VS)_N$ = Normalized Volt-Seconds across Inductor

$(VS)_{PN}$ = Normalized Peak Volt-Seconds across Inductor

The normalizing factor for volt-seconds is $\frac{V_s}{\omega_0}$ and hence,

$$(VS)_{PN} = \frac{(VS)_P \times \omega_0}{V_s} \tag{A.25}$$

$$(VS) = \int v_L \, dt = L \, \Delta i_L \tag{A.26}$$

Normalizing (A.26),

$$(VS)_N = \Delta i_{LN} \tag{A.27}$$

Equation (A.27) is a general equation valid in all cases. From Fig. A.1, the maximum change in inductor current equals twice I_{LPN}. Thus,

$$(VS)_{PN} = 2\, I_{LPN} \tag{A.28}$$

Substituting for I_{LPN} from (A.24) into (A.28),

$$(VS)_{PN} = 2\, R \tag{A.29}$$

Average Diode Current: From Fig. 2.1, if t_A is the start and t_B is the end of conduction of a device X, then,

$$C\,(V_{CB} - V_{CA}) = \int_{t_A}^{t_B} i_L \, dt, \qquad \text{where} \tag{A.30}$$

$$V_{CA} = v_C/_{(t=\,t_A)} \qquad \text{and} \qquad V_{CB} = v_C/_{(t=\,t_B)} \tag{A.31}$$

The average device current I_{XAV} is

$$I_{XAV} = \frac{1}{T} \int_{t_A}^{t_B} i_L \, dt = \frac{C\,(V_{CB} - V_{CA})}{T} \tag{A.32}$$

$$\text{Thus,} \quad I_{XAVN} = \text{Normalized Average Device Current} = \frac{I_{XAV}\, Z_0}{V_s} = \frac{V_{CBN} - V_{CAN}}{T_N}, \tag{A.33}$$

where V_{CAN} and V_{CBN} are normalized values of voltages V_{CA} and V_{CB}, respectively. Equation (A.33) is valid for all cases of SRC operation.

For the antiparallel diode (considering D2), from Fig. A.1,

$$V_{CAN} = -\,V_{CPN}; \qquad V_{CBN} = V_{C0N} \tag{A.34}$$

From (A.34), (A.33) and (A.14),

$$I_{DAVN} = \text{Normalized Average Diode Current} = \frac{V_{CPN} + V_{C0N}}{2\ (\alpha + \beta)} \tag{A.35}$$

Average Transistor Current: For the transistor (considering Q1), from Fig. A.1,

$$V_{CAN} = V_{C0N}\,; \qquad V_{CBN} = V_{CPN} \tag{A.36}$$

From (A.36), (A.33) and (A.14),

$$I_{QAVN} = \text{Normalized Average transistor Current} = \frac{V_{CPN} - V_{C0N}}{2\ (\alpha + \beta)} \tag{A.37}$$

Output DC Current: From Fig. A.1,

$$\begin{aligned} I_o &= \text{Output DC Current} \\ &= I_{LAV} = \text{Half-Cycle Average of Inductor Current} \\ &= \frac{2}{T}\left[\int_{t_3}^{t_4} i_L\ dt + \int_0^{t_1} i_L\ dt\right] = 2\ (I_{DAV} + I_{QAV}) \end{aligned} \tag{A.38}$$

$$\begin{aligned} I_{oN} &= \frac{I_o\ Z_0}{V_s} = \text{Normalized Output DC Current} \\ &= I_{LAVN} = \frac{I_{LAV}\ Z_0}{V_s} = \text{Normalized Half-Cycle Average of Inductor Current} \\ &= 2\ (I_{DAVN} + I_{QAVN}) \end{aligned} \tag{A.39}$$

Equation (A.39) is valid for all the modes of SRC operation under consideration. Substituting for I_{DAVN} from (A.35) and I_{QAVN} from (A.37) into (A.39),

$$I_{oN} = I_{LAVN} = \frac{2\ V_{CPN}}{\alpha + \beta} \tag{A.40}$$

RMS Diode Current: From Fig. A.1,

$$I_{DR} = \text{RMS Diode Current} = \sqrt{\frac{1}{T}\int_{t_3}^{t_4} i_L^2\ dt} \tag{A.41}$$

From *D2* trajectory in Fig. A.1, i_L when D2 is conducting is

$$i_L = \frac{R'\ V_s}{Z_0} \sin\theta, \quad \text{where} \tag{A.42}$$

$$\theta = \omega_0 (t - t_3) \tag{A.43}$$

Substituting for i_L from (A.42) in (A.41), integrating (now between limits 0 and α) and normalizing,

$$I_{DRN} = \frac{I_{DR}\ Z_0}{V_s} = \text{Normalized RMS Diode Current}$$
$$= \sqrt{\frac{1}{T_N}\ \frac{R'^2}{2}\ (\alpha - \frac{1}{2}\sin 2\alpha)} \tag{A.44}$$

Equation (A.44) is applicable whenever current is zero either at turn-on or at turn-off of the diode. Since this condition is always satisfied, (A.44) is valid for all the modes under consideration. Substituting for T_N from (A.14) and R' from (A.7) into (A.44),

$$I_{DRN} = \frac{R - 2V_{oN}}{2} \sqrt{\frac{\alpha - \frac{1}{2}\sin 2\alpha}{\alpha + \beta}} \tag{A.45}$$

RMS Transistor Current: From Fig. A.1,

$$I_{QR} = \text{RMS Transistor Current}$$
$$= \sqrt{\frac{1}{T}\ \int_0^{t_1} i_L^2\ dt} \tag{A.46}$$

From *Q2* trajectory in Fig. A.1, i_L when Q2 is conducting is

$$i_L = \frac{R\ V_s}{Z_0} \sin\ (\theta + \pi - \beta), \quad \text{where} \tag{A.47}$$

$$\theta = \omega_0\ t \tag{A.48}$$

Subsituting for i_L from (A.47) in (A.46), integrating (now between limits $(\pi - \beta)$ and π) and normalizing,

$$I_{QRN} = \frac{I_{QR}\, Z_0}{V_s} = \text{Normalized RMS Transistor Current}$$
$$= \sqrt{\frac{1}{T_N}\frac{R^2}{2}\left(\beta - \frac{1}{2}\sin 2\beta\right)} \qquad (A.49)$$

As was the case with (A.44), (A.49) is also valid for all cases of normal SRC operation. Substituting for T_N from (A.14) into (A.49),

$$I_{QRN} = \frac{R}{2}\sqrt{\frac{\beta - \frac{1}{2}\sin 2\beta}{\alpha + \beta}} \qquad (A.50)$$

RMS Inductor Current: From Fig. A.1,

$$I_{LR} = \text{RMS Inductor Current}$$
$$= \sqrt{\frac{2}{T}\left[\int_{t_3}^{t_4} i_L^2\, dt + \int_0^{t_1} i_L^2\, dt\right]} \qquad (A.51)$$

From (A.41), (A.46) and (A.51),

$$I_{LR} = \sqrt{2\,(I_{DR}^2 + I_{QR}^2)} \qquad (A.52)$$

Hence,
$$I_{LRN} = \frac{I_{LR}\, Z_0}{V_s} = \text{Normalized RMS Inductor Current}$$
$$= \sqrt{2\,(I_{DRN}^2 + I_{QRN}^2)} \qquad (A.53)$$

Equation (A.53) is valid for all cases of SRC operation under consideration. Substituting for I_{DRN} from (A.45) and I_{QRN} from (A.50) into (A.53),

$$I_{LRN} = \sqrt{\frac{1}{2(\alpha + \beta)}\left\{(R - 2V_{oN})^2\left(\alpha - \frac{1}{2}\sin 2\alpha\right) + R^2\left(\beta - \frac{1}{2}\sin 2\beta\right)\right\}} \qquad (A.54)$$

A.1.3 Parameter Values Under Limiting Conditions

In this section, we will compute the range of values of parameters studied in Sec. A.1.2, when the trajectory radius, R, is varied between its limits. In order to carry this out, the minimum and maximum values of R must first be determined.

Maximum Radius: Ideally, in creating the trajectory in Fig. A.1, radius R can be increased indefinitely. It is possible to construct a CCM steady-state trajectory with as large a radius as desired. Thus,

$$R_{max} = \infty \tag{A.55}$$

Minimum Radius: As R is reduced in Fig. A.1, a boundary is reached, as shown in Fig. A.2. This figure is valid for all DCM-2 trajectories including DCM-2/CCM boundary. At this boundary, the dwell times at points A and B of DCM-2 operation in Fig. A.2 are reduced to zero. The structure of the state-portrait does not allow the construction of a symmetrical steady-state trajectory with a smaller radius. From Fig. A.2,

$$R - R' = 2\ V_{oN} \tag{A.56}$$

$$R + R' = 2 \tag{A.57}$$

From (A.56) and (A.57),

$$R = R_{min} = 1 + V_{oN} \tag{A.58}$$

Range of Circuit Parameters: The limits reached by the equations of Sec. A.1.2 as R approaches R_{min} and R_{max} are tabulated in Table A.1. The following discussion substantiates the statement made in Sec. 2.2.5.1 regarding the effect of frequency variation on the circuit parameters.

From Table A.1, it is observed that the frequency ω_N reaches a low of 0.5 at R_{min} and reaches a maximum value of 1 at R_{max}. Thus, when the frequency is increased from 0.5 to 1, the trajectory size as indicated by the radius, R, increases from $1 + V_{oN}$ to infinity. Likewise, the normalized output current, I_{oN}, increases from $2/\pi$ to infinity as ω_N is raised from 0.5 to unity.

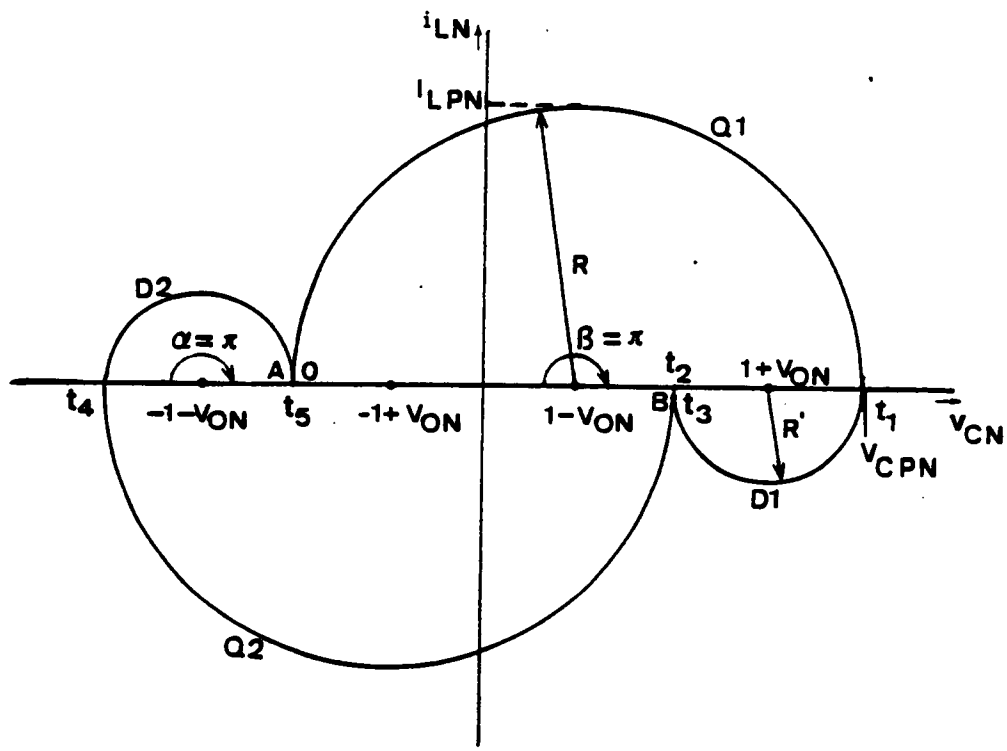

Figure A.2 Ideal type-2 DCM operation - Analysis diagram

TABLE A.1

PARAMETERS UNDER LIMITING CONDITIONS

Para-	CCM Below Resonance		CCM Above Resonance	
meter	$R \to R_{min}$	$R \to R_{max}$	$R \to R_{min}$	$R \to R_{max}$
R	$R_{min} = 1 + V_{oN}$	$R_{max} = \infty$	$R_{min} = 1 - V_{oN}$	$R_{max} = \infty$
R'	$1 - V_{oN}$	R_{max}	$1 + V_{oN}$	R_{max}
α	π	$\cos^{-1}V_{oN}$	0	$\cos^{-1}V_{oN}$
β	π	$\pi - \cos^{-1}V_{oN}$	0	$\pi - \cos^{-1}V_{oN}$
T_N	4π	2π	0	2π
ω_N	1/2	1	∞	1
V_{C0N}	$-2V_{oN}$	$R_{max}V_{oN}$	0	$R_{max}V_{oN}$
I_{L0N}	0	$R_{max}\sqrt{1 - V_{oN}^2}$	0	$R_{max}\sqrt{1 - V_{oN}^2}$
V_{CPN}	2	R_{max}	0	R_{max}
I_{LPN}	$1 + V_{oN}$	R_{max}	0	R_{max}
$(VS)_{PN}$	$2(1 + V_{oN})$	$2R_{max}$	0	$2R_{max}$
I_{DAVN}	$\frac{1 - V_{oN}}{2\pi}$	$\frac{R_{max}(1 - V_{oN})}{2\pi}$	0	$\frac{R_{max}(1 - V_{oN})}{2\pi}$
I_{QAVN}	$\frac{1 + V_{oN}}{2\pi}$	$\frac{R_{max}(1 + V_{oN})}{2\pi}$	0	$\frac{R_{max}(1 + V_{oN})}{2\pi}$
$I_{oN} = I_{LAVN}$	$\frac{2}{\pi}$	$\frac{2R_{max}}{\pi}$	0	$\frac{2R_{max}}{\pi}$

Reproducing (A.59), the normalized tank energy at any instant is

$$e_{TN} = (v_{CN}^2 + i_{LN}^2) / 2 = d^2 / 2 \qquad (A.59)$$

The maximum distance d of the trajectory from the origin occurs when the capacitor voltage is at its maximum. Thus, the peak normalized tank energy is

$$E_{TPN} = V_{CPN}^2 / 2 \qquad (A.60)$$

As ω_N is increased from 0.5 to 1, V_{CPN} increases from 2 to infinity, which causes the value of E_{TPN} also to increase from to 2 to infinity.

Thus, in this operating region, the tank energy, output current and trajectory size increase as operating frequency is increased.

A.2 Type-2 DCM Analysis

Refer to Fig. A.2 for the derivation of equations in this section. As observed before, the trajectory size and shape remains the same in this mode of operation for a given output voltage. In the following derivations, ω_N and V_{oN} are assumed to be the known variables.

Transistor and Diode Conduction Radii: Equations (A.56) and (A.57) have been derived from Fig. A.2 and, hence, are valid for DCM-2 operation. From (A.56) and (A.57),

$$R = 1 + V_{oN} \qquad (A.61)$$

$$R' = 1 - V_{oN} \qquad (A.62)$$

Conduction Angles and Period of Operation: From Fig. A.2,

$$\alpha = \pi \qquad (A.63)$$

$$\beta = \pi \tag{A.64}$$

Given ω_N, the angular period of operation T_N is obtained from (A.15).

$$T_N = \frac{2\ \pi}{\omega_N} \tag{A.65}$$

Switching Point State-Variables: From Fig. A.2,

$$I_{LON} = 0 \tag{A.66}$$

$$V_{CON} = -1 - V_{oN} + R' = -2\,V_{oN} \tag{A.67}$$

Peak State-Variables: From Fig. A.2,

$$I_{LPN} = R = 1 + V_{oN} \tag{A.68}$$

$$V_{CPN} = R' + 1 + V_{oN} = 2 \tag{A.69}$$

Peak Inductor Volt-Seconds: From Fig. A.2, the maximum change in inductor current equals twice I_{LPN}. Thus, from (A.27),

$$(VS)_{PN} = 2\,I_{LPN} \tag{A.70}$$

Substituting for I_{LPN} from (A.68) into (A.70),

$$(VS)_{PN} = 2\,(1 + I_{oN}) \tag{A.71}$$

Average Currents: For the antiparallel diode (considering D2), from Fig. A.2,

$$V_{CAN} = -V_{CPN}; \qquad V_{CBN} = V_{CON} \tag{A.72}$$

From (A.72) and (A.33),

$$I_{DAVN} = \frac{V_{CPN} + V_{CON}}{T_N} \tag{A.73}$$

Substituting for V_{CPN} from (A.69), V_{C0N} from (A.67) and T_N from (A.65) into (A.73),

$$I_{DAVN} = \frac{(1 - V_{oN})\ \omega_N}{\pi} \tag{A.74}$$

For the transistor (considering Q1), from Fig. A.2,

$$V_{CAN} = V_{C0N}; \qquad V_{CBN} = V_{CPN} \tag{A.75}$$

From (A.75) and (A.33),

$$I_{QAVN} = \frac{V_{CPN} - V_{C0N}}{T_N} \tag{A.76}$$

Substituting for V_{CPN} from (A.69), V_{C0N} from (A.67) and T_N from (A.65) into (A.76),

$$I_{QAVN} = \frac{(1 + V_{oN})\ \omega_N}{\pi} \tag{A.77}$$

Substituting for I_{DAVN} from (A.74) and I_{QAVN} (A.77) into (A.39),

$$I_{oN} = I_{LAVN} = \frac{4\ \omega_N}{\pi} \tag{A.78}$$

RMS Currents: Substituting for T_N from (A.65), R' from (A.62) and α (A.63) into (A.44),

$$I_{DRN} = \frac{1 - V_{oN}}{2} \sqrt{\omega_N} \tag{A.79}$$

Substituting for T_N from (A.65), R from (A.61) and β from (A.64) into (A.49),

$$I_{QRN} = \frac{1 + V_{oN}}{2} \sqrt{\omega_N} \tag{A.80}$$

Substituting for I_{DRN} from (A.79) and I_{QRN} from (A.80) into (A.53),

$$I_{LRN} = \sqrt{(1 + V_{oN}^2)\ \omega_N} \tag{A.81}$$

A.3 CCM Analysis above Resonance

Refer to Fig. A.3, which shows a steady-state trajectory above resonant frequency, for the derivation of equations in this section.

A.3.1 Switching Boundary

Based on (2.9), the trajectory equation when device Q1 is conducting (interval 0 to t_1) is

$$\begin{aligned} i_{LN}^2 + (v_{CN} - 1 + V_{oN})^2 &= R^2 \\ &= (V_{CPN} + 1 - V_{oN})^2 \end{aligned} \tag{A.82}$$

At $t = t_1$, $i_{LN} = I_{LON}$ and $v_{CN} = V_{CON}$. Thus,

$$I_{LON}^2 + (V_{CON} - 1 + V_{oN})^2 = (V_{CPN} + 1 - V_{oN})^2 \tag{A.83}$$

Similarly, the trajectory equation when D2 is conducting is given by

$$\begin{aligned} i_{LN}^2 + (v_{CN} + 1 + V_{oN})^2 &= R'^2 \\ &= I_{LON}^2 + (V_{CON} + 1 + V_{oN})^2 \end{aligned} \tag{A.84}$$

At $t = t_2$, $i_{LN} = 0$ and $v_{CN} = V_{CPN}$. Thus,

$$(V_{CPN} + 1 + V_{oN})^2 = I_{LON}^2 + (V_{CON} + 1 + V_{oN})^2 \tag{A.85}$$

Substituting for V_{CPN} from (A.85) into (A.83)

$$(\sqrt{I_{LON}^2 + (V_{CON} + 1 + V_{oN})^2} - 2V_{oN})^2 = I_{LON}^2 + (V_{CON} - 1 + V_{oN})^2 \tag{A.86}$$

Expanding and rearranging (A.86),

$$(V_{CON} + V_{oN} + V_{oN}^2)^2 - V_{oN}^2 \{I_{LON}^2 + (V_{CON} + 1 + V_{oN})^2\} = 0 \tag{A.87}$$

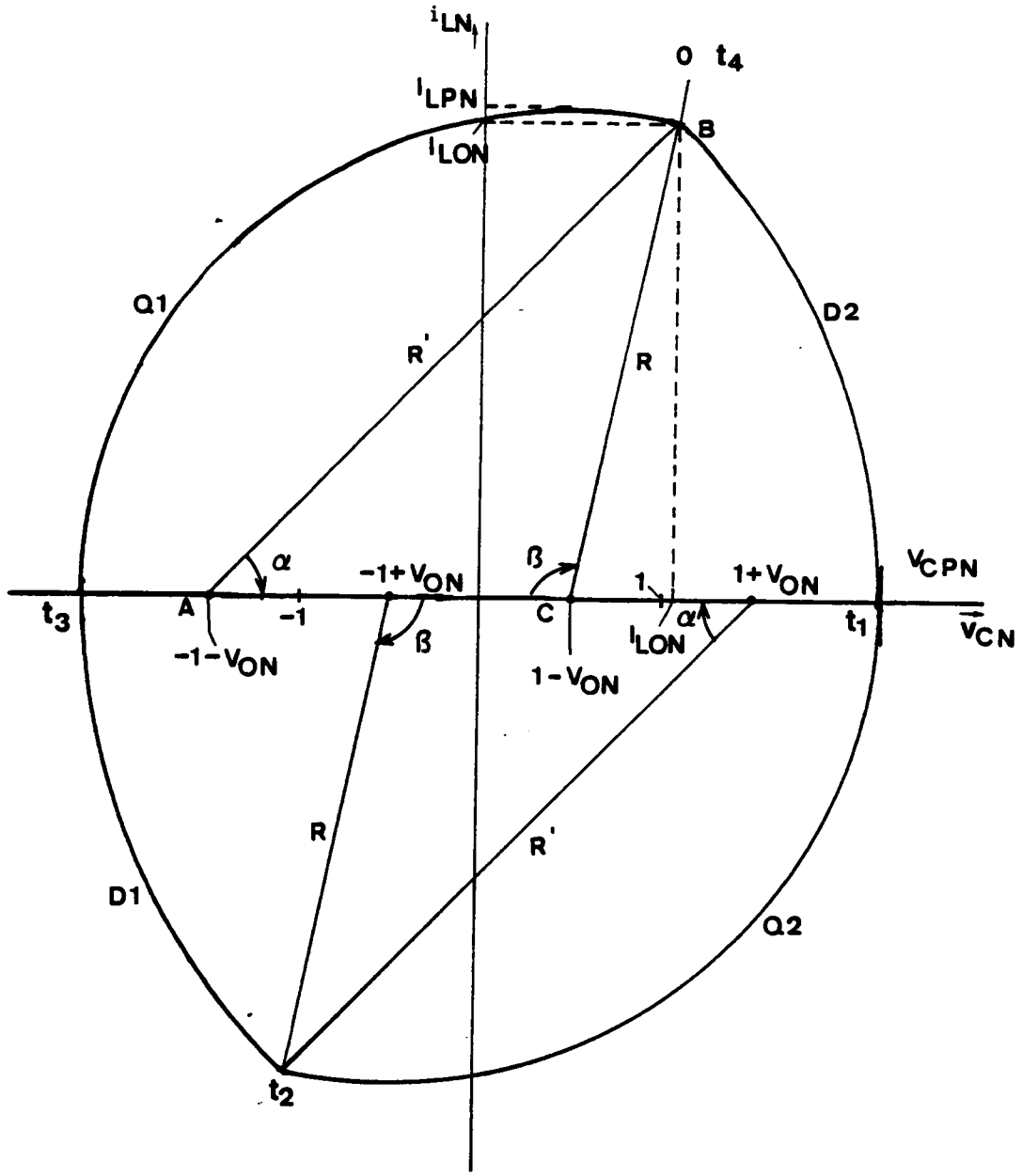

Figure A.3 Ideal CCM operation above resonance - Analysis diagram

Equation (A.87) is for switching boundary S1 and relates the state-variables at the instant of switching-off (I_{LON}, V_{CON}) of the transistor Q1, for a given V_{oN}. Due to the symmetry of the steady-state trajectory, the equation for switching boundary S2, can be obtained by substitution of $-V_{CON}$ and $-I_{LON}$ in place of V_{CON} and I_{LON}, respectively, in (A.87).

A.3.2 Analysis Of A Steady-State Trajectory

In this section, the different circuit parameters related to the steady-state operation are derived from analysis Fig. A.3. As in Sec. A.1.2, it is assumed that R and V_{oN} are known. Many of the steps in the following derivations are similar to those in Sec. A.1.2. For a discussion of the choice of R and V_{oN} as the known variables, please see the first paragraph of Sec. A.1.2.

Diode Conduction Radius: From Fig. A.3,

$$R' = R + 2V_{oN} \tag{A.88}$$

Diode Conduction Angle: Considering Δ ABC in Fig. A.3, it can be shown

$$\alpha = \cos^{-1}\left\{\frac{R'^2 + 4 - R^2}{4R'}\right\} \tag{A.89}$$

Substituting for R' from (A.88) into (A.89),

$$\alpha = \cos^{-1}\left\{\frac{V_{oN}^2 + RV_{oN} + 1}{R + 2V_{oN}}\right\} \tag{A.90}$$

Transistor Conduction Angle: Considering Δ ABC of Fig. A.3, it can be shown

$$\beta = \cos^{-1}\left\{\frac{R^2 + 4 - R'^2}{4R}\right\} \tag{A.91}$$

Substituting for R' from (A.88) into (A.91),

$$\beta = \cos^{-1}\left\{\frac{-V_{oN}^2 - RV_{oN} + 1}{R}\right\} \tag{A.92}$$

Period of Operation: Reproducing (A.14),

$$T_N = 2\ (\alpha + \beta) \tag{A.14}$$

Frequency of Operation: Reproducing (A.16)

$$\omega_N = \frac{\pi}{\alpha + \beta} \tag{A.16}$$

Switching Point Voltage: From Fig. A.3,

$$V_{CON} = 1 - V_{oN} - R\cos\beta \tag{A.93}$$

Substituting for β from (A.92) into (A.93) and simplifying,

$$V_{CON} = V_{oN}(R - 1 + V_{oN}) \tag{A.94}$$

Using (A.98), an equation to be derived, an alternative form for (A.94) is

$$V_{CON} = V_{oN}\ V_{CPN} \tag{A.95}$$

Switching Point Current: From Fig. A.3,

$$I_{LON} = R\sin\beta \tag{A.96}$$

Substituting for β from (A.92) into (A.96) and simplifying,

$$I_{LON} = \sqrt{R^2 - (-V_{oN}^2 - RV_{oN} + 1)^2} \tag{A.97}$$

Peak Capacitor Voltage: From Fig. A.3,

$$V_{CPN} = R - 1 + V_{oN} \tag{A.98}$$

Peak Inductor Current From Fig. A.3,

$$\begin{aligned} I_{LPN} &= R\,, \qquad \beta \geq \pi/2 \\ &= I_{L0N}\,, \qquad \beta \leq \pi/2 \end{aligned} \tag{A.99}$$

Peak Inductor Volt-Seconds: From Fig. A.3, the maximum change in inductor current equals twice I_{LPN}. Thus, from (A.27),

$$(VS)_{PN} = 2\, I_{LPN} \tag{A.100}$$

Substituting for I_{LPN} from (A.99) into (A.100),

$$\begin{aligned} (VS)_{PN} &= 2\, R\,, \qquad \beta \geq \pi/2 \\ &= 2\, I_{L0N}\,, \qquad \beta \leq \pi/2 \end{aligned} \tag{A.101}$$

Average Diode Current: For the antiparallel diode (considering D2), from Fig. A.3,

$$V_{CAN} = V_{C0N}\,; \qquad V_{CBN} = V_{CPN} \tag{A.102}$$

From (A.102), (A.33) and (A.14),

$$I_{DAVN} = \frac{V_{CPN} - V_{C0N}}{2\ (\alpha + \beta)} \tag{A.103}$$

Average Transistor Current: For the transistor (considering Q1), from Fig. A.3,

$$V_{CAN} = -\,V_{CPN}\,; \qquad V_{CBN} = V_{C0N} \tag{A.104}$$

From (A.104), (A.33) and (A.14),

$$I_{QAVN} = \frac{V_{CPN} + V_{C0N}}{2\ (\alpha + \beta)} \tag{A.105}$$

Output DC Current: Substituting for I_{DAVN} from (A.103) and I_{QAVN} from (A.105) into (A.39),

$$I_{oN} = I_{LAVN} = \frac{2\ V_{CPN}}{\alpha + \beta} \tag{A.106}$$

RMS Diode Current: Substituting for T_N from (A.14) and R' from (A.88) into (A.44),

$$I_{DRN} = \frac{R + 2V_{oN}}{2} \sqrt{\frac{\alpha - \frac{1}{2}\sin 2\alpha}{\alpha + \beta}} \tag{A.107}$$

RMS Transistor Current: Substituting for T_N from (A.14) into (A.49),

$$I_{QRN} = \frac{R}{2} \sqrt{\frac{\beta - \frac{1}{2}\sin 2\beta}{\alpha + \beta}} \tag{A.108}$$

RMS Inductor Current: Substituting for I_{DRN} from (A.107) and I_{QRN} from (A.108) into (A.53),

$$I_{LRN} = \sqrt{\frac{1}{2(\alpha + \beta)}\left\{(R + 2V_{oN})^2\left(\alpha - \frac{1}{2}\sin 2\alpha\right) + R^2\left(\beta - \frac{1}{2}\sin 2\beta\right)\right\}} \tag{A.109}$$

A.3.3 Parameter Values Under Limiting Conditions

In this section, we will compute the range of values of parameters studied in Sec. A.3.2, when R is varied between its limits, for the case of CCM operation above resonant frequency.

Maximum Radius: Ideally, it is possible to construct a CCM steady-state trajectory in this range with as large as a radius as we desire. Thus,

$$R_{max} = \infty \tag{A.110}$$

Minimum Radius: A study of Fig. A.3 reveals that the minimum R is reached when the steady-state trajectory shrinks to origin.. For such a case, the minimum R is given by,

$$R_{min} = 1 - V_{oN} \tag{A.111}$$

Range of Circuit Parameters: The limits reached by the equations of Sec. A.3.2 as R approaches R_{min} and R_{max} are tabulated in Table A.1. As may be expected, in Table A.1, the limits reached when R is increased to infinity from below resonant frequency and from above resonant frequency are the same.

The following discussion substantiates the statement made in Sec. 2.2.5.4 regarding the effect of frequency variation on circuit parameters.

From Table A.1, when R approaches a low of $(1 - V_{oN})$, ω_N approaches infinity. Thus, when ω_N is increased above unity, the trajectory size as indicated by V_{CPN} diminishes to zero. Since tank energy is dependent on the size of trajectory, it also decreases (to zero) as frequency approaches infinity. Also, from Table A.1, the normalized output current I_{oN} decreases to zero, as ω_N approaches infinity.

Thus, the tank energy, output current and trajectory size decrease as the operating frequency is increased in this region.

A.4 Type-1 DCM Analysis

The trajectory diagram in Fig. A.4 is used for the derivations in the following sections. Ideally, type-1 DCM occurs under the limiting case when the ouput voltage equals supply voltage. Depending on the magnitude of the load current, for the same ω_N and V_{oN} (= 1), different steady-state trajectories are possible. This behavior is unlike the other three modes of operation.

In the following discussion, the variables R and ω_N are assumed to be known. As $V_{oN} \rightarrow 1$, DCM-1 occurs as the limit of CCM whenever $0.5 < \omega_N < 1$ and as the limit of DCM-2 whenever $0 < \omega_N < 0.5$.

Diode Conduction Radius: From Fig. A.4,

$$R' = 0 \tag{A.112}$$

Conduction Angles and Period of Operation: From Fig. A.4,

$$\alpha = 0 \tag{A.113}$$

$$\beta = \pi \tag{A.114}$$

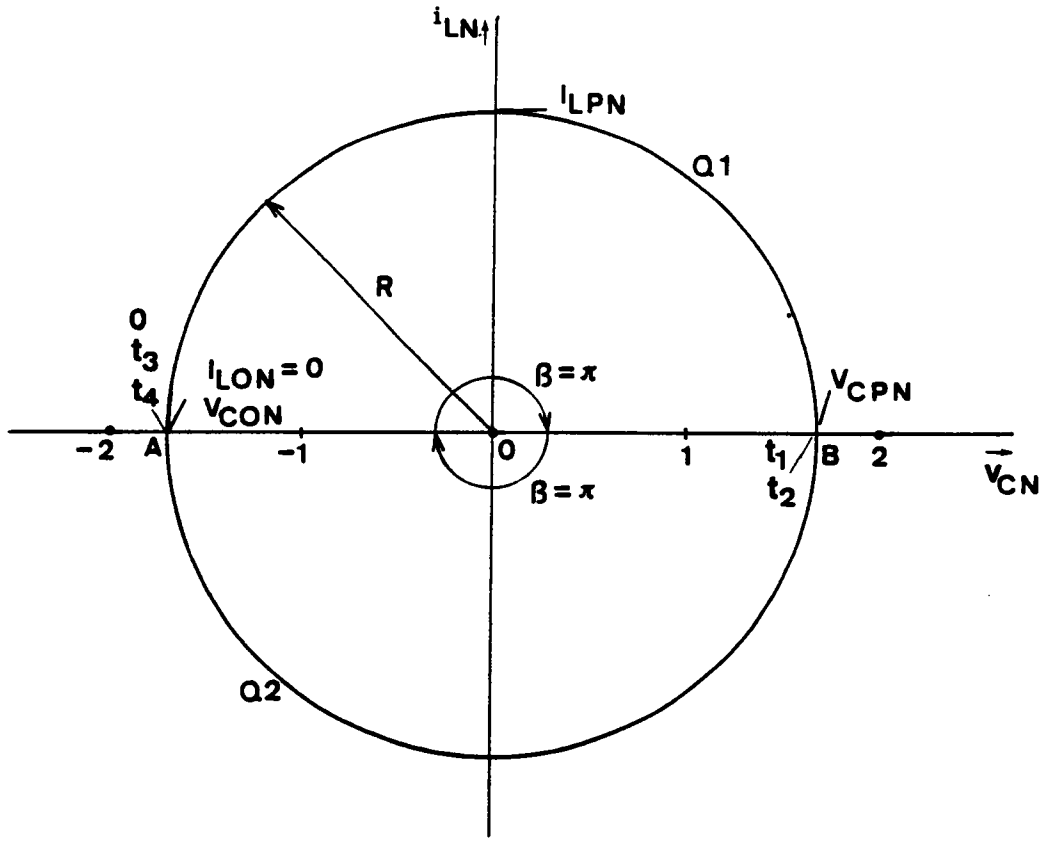

Figure A.4 Ideal type-1 DCM operation - Analysis diagram

Given ω_N, T_N is obtained from (A.65).

$$T_N = \frac{2\ \pi}{\omega_N} \tag{A.65}$$

Switching Point State-Variables: From Fig. A.4,

$$I_{L0N} = 0 \tag{A.115}$$

$$V_{C0N} = -R \tag{A.116}$$

Peak State-Variables: From Fig. A.4,

$$I_{LPN} = R \tag{A.117}$$

$$V_{CPN} = R \tag{A.118}$$

Peak Inductor Volt-Seconds: From Fig. A.4, the maximum change in inductor current equals twice I_{LPN}. Thus, from (A.27),

$$(VS)_{PN} = 2\, I_{LPN} \tag{A.119}$$

Substituting for I_{LPN} from (A.117) into (A.119),

$$(VS)_{PN} = 2R \tag{A.120}$$

Average Currents: Since the diodes do not conduct,

$$I_{DAVN} = 0 \tag{A.121}$$

For the transistor (considering Q1), from Fig. A.4,

$$V_{CAN} = -R\ ; \qquad V_{CBN} = +R \tag{A.122}$$

From (A.122), (A.65) and (A.33),

$$I_{QAVN} = \frac{R\ \omega_N}{\pi} \tag{A.123}$$

Substituting for I_{DAVN} from (A.121) and I_{QAVN} from (A.123) into (A.39),

$$I_{oN} = I_{LAVN} = \frac{2\,R\,\omega_N}{\pi} \tag{A.124}$$

RMS Currents: Since the diodes do not conduct,

$$I_{DRN} = 0 \tag{A.125}$$

Substituting for T_N from (A.65) and β from (A.114) into (A.49),

$$I_{QRN} = \frac{R}{2}\sqrt{\omega_N} \tag{A.126}$$

Substituting for I_{DRN} from (A.125) and I_{QRN} from (A.126) into (A.53),

$$I_{LRN} = R\sqrt{\frac{\omega_N}{2}} \tag{A.127}$$

A.5 SRC Design Curves

Computer programs based on equations in Secs. A.1 to A.4 are in Sec. A.7. Figures A.5, A.6 and A.7 show a set of design curves for DCM-2, CCM below resonance and CCM above resonance, respectively, generated using these programs. Since DCM-1 is only a limiting case under ideal conditions, curves for this mode have not been plotted.

The output characteristics of the converter (I_{oN} versus V_{oN} for different ω_Ns) are shown in Fig. A.8. Using the output characteristics and the load characteristics, the operating point of the converter can be determined. The curves shown in Figs. A.5 through A.8 are useful in carrying out a preliminary design of SRC.

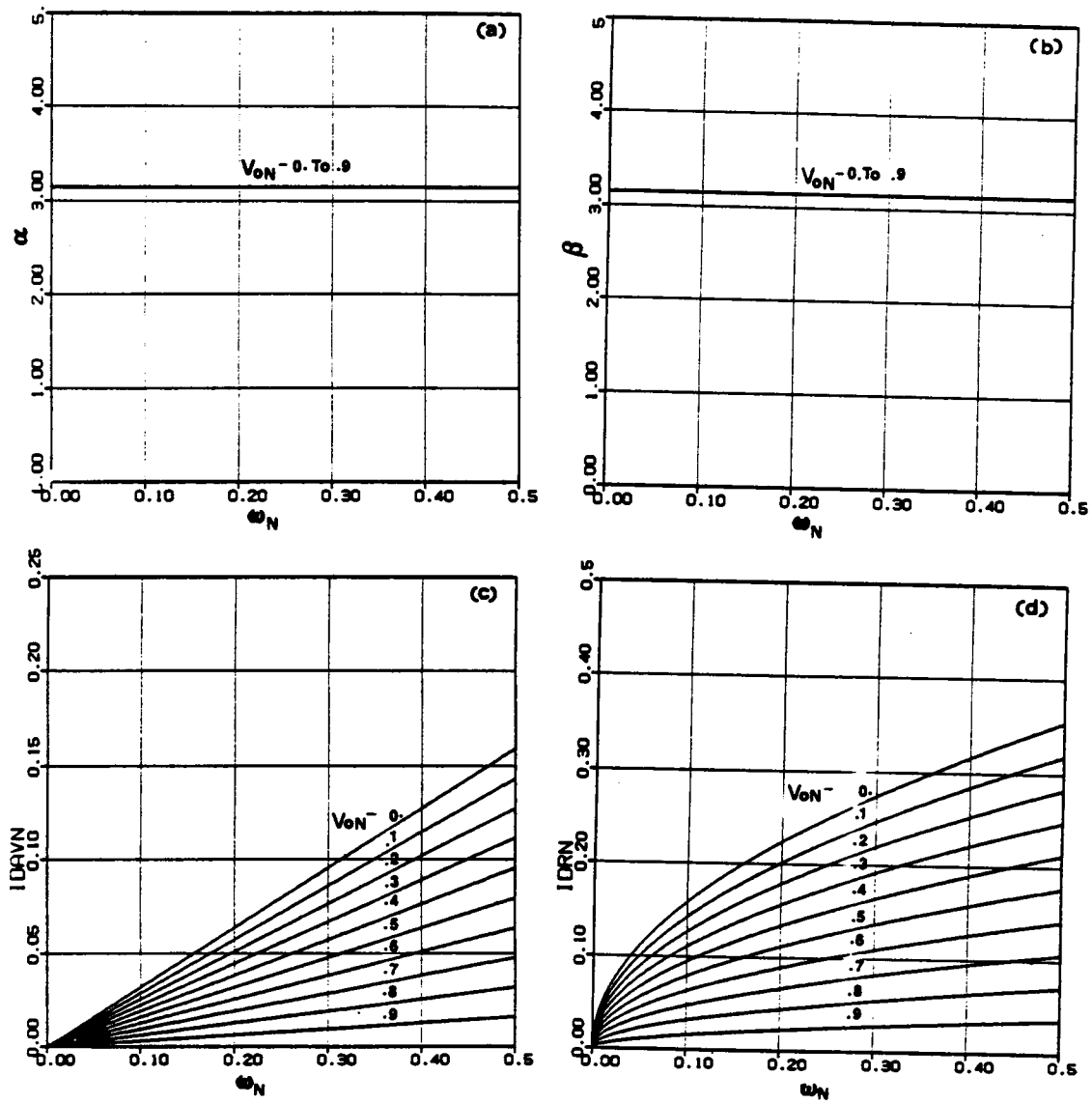

Figure A.5 Ideal design curves for a SRC - $0 < \omega_N < 0.5$

a) Diode conduction angle
b) Transistor conduction angle
c) Normalized average diode current
d) Normalized RMS diode current

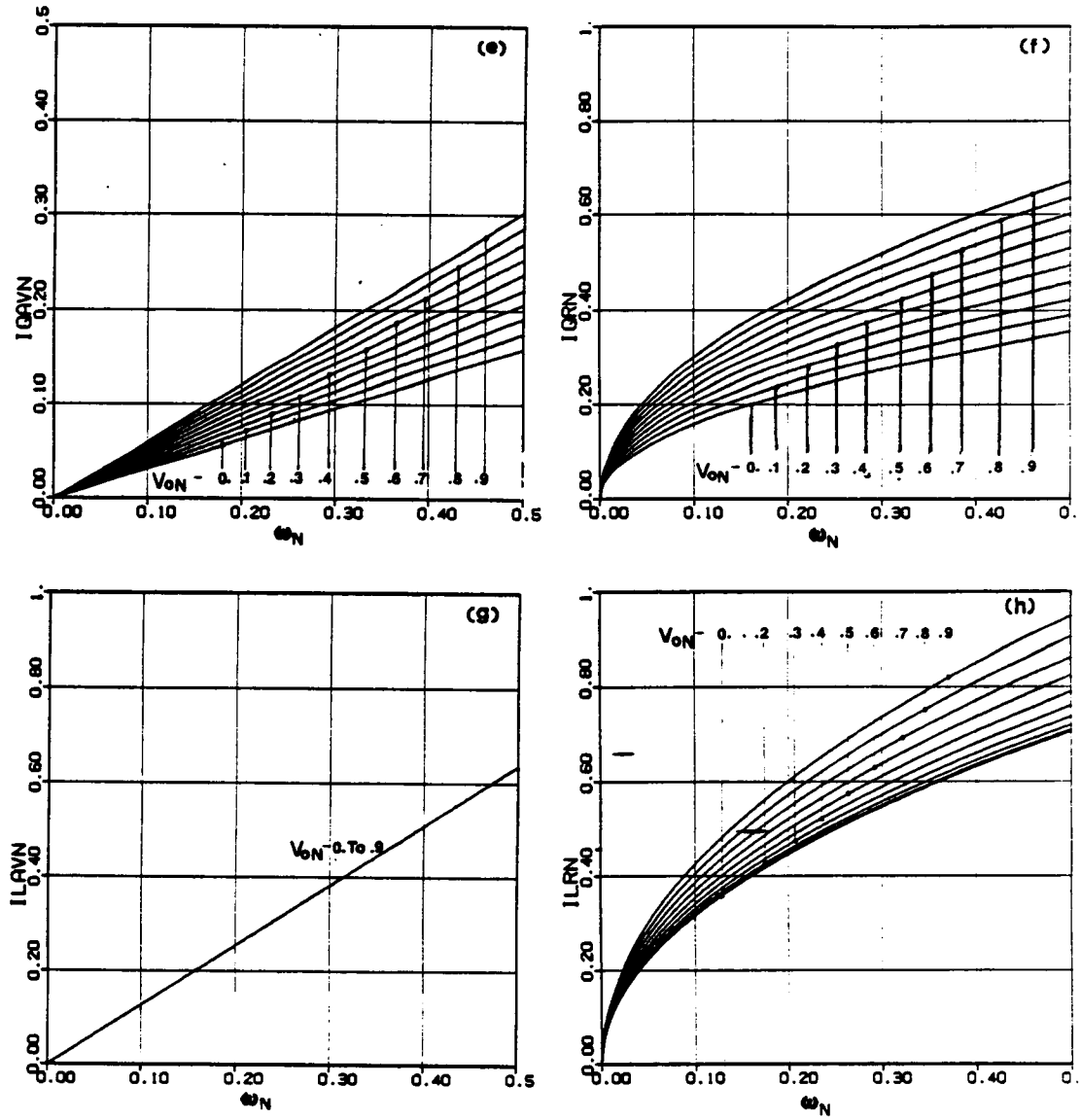

Figure A.5 (contd.)
e) Normalized average transistor current
f) Normalized RMS transistor current
g) Normalized average induct current/normalized output current
h) Normalized RMS inductor current

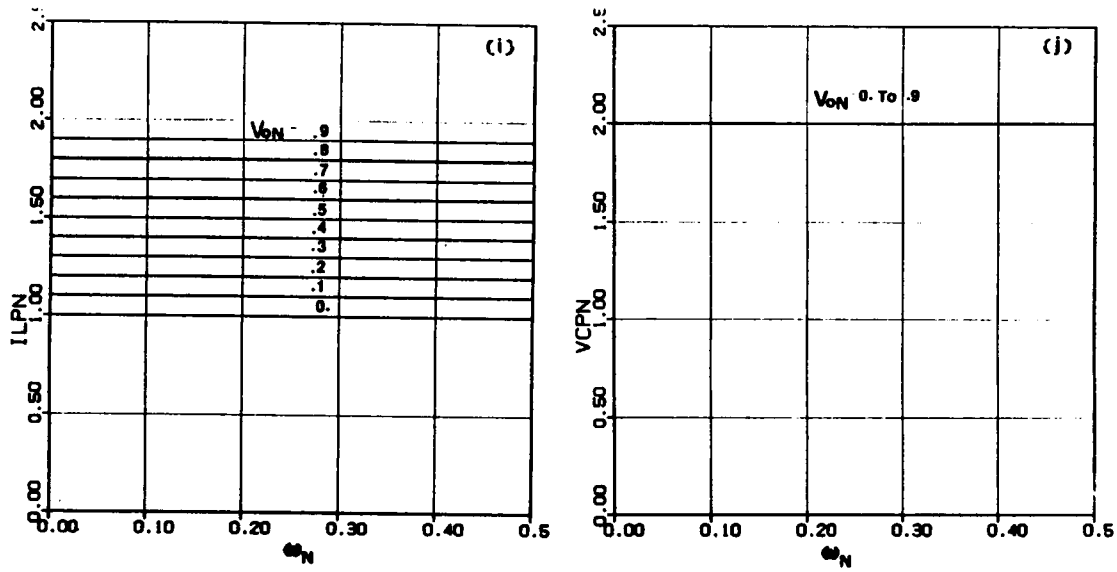

Figure A.5 (contd.)
i) Normalized peak inductor current
j) Normalized peak capacitor voltage

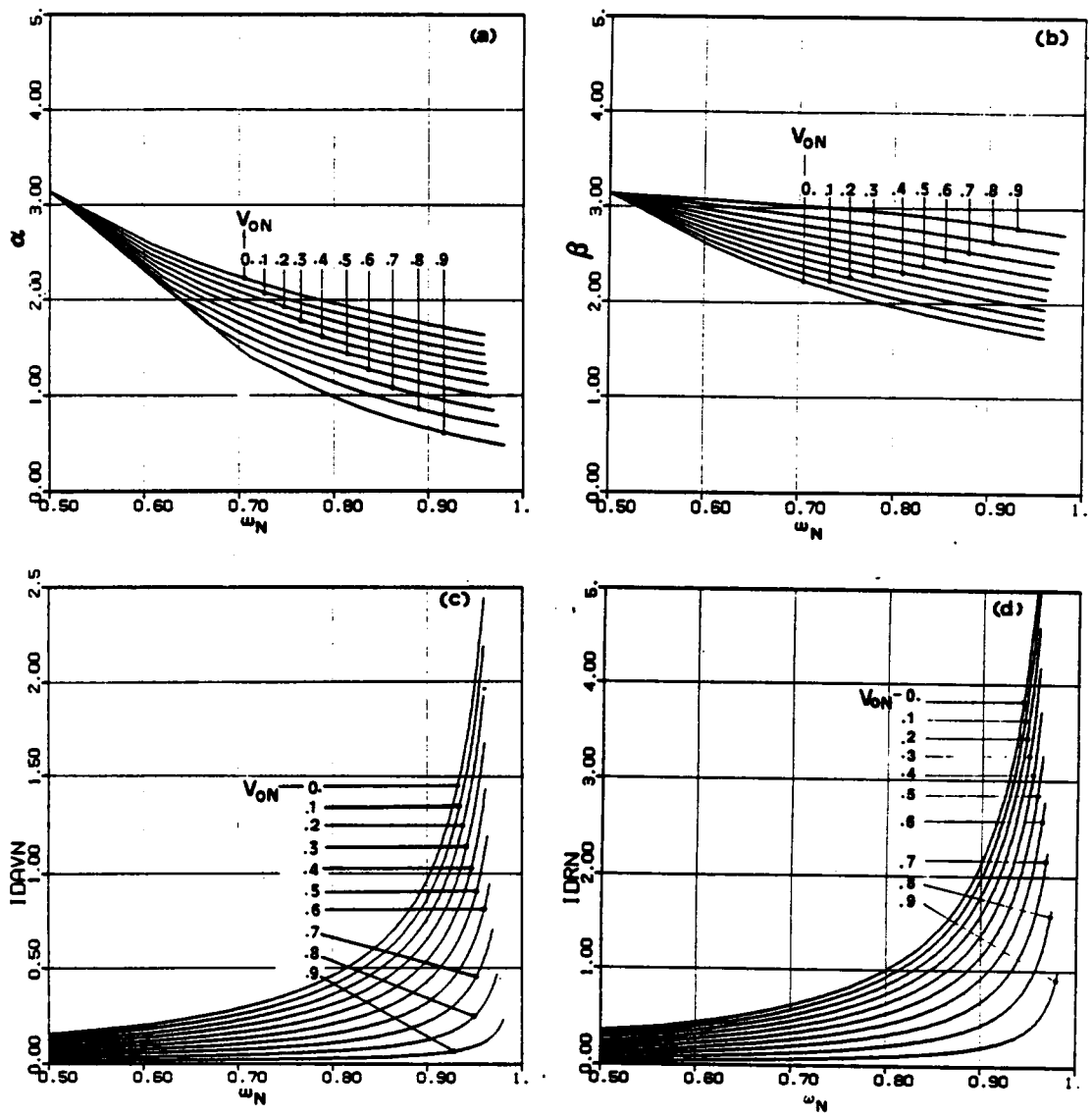

Figure A.6 Ideal design curves for a SRC - $0.5 < \omega_N < 1.0$

a) Diode conduction angle
b) Transistor conduction angle
c) Normalized average diode current
d) Normalized RMS diode current

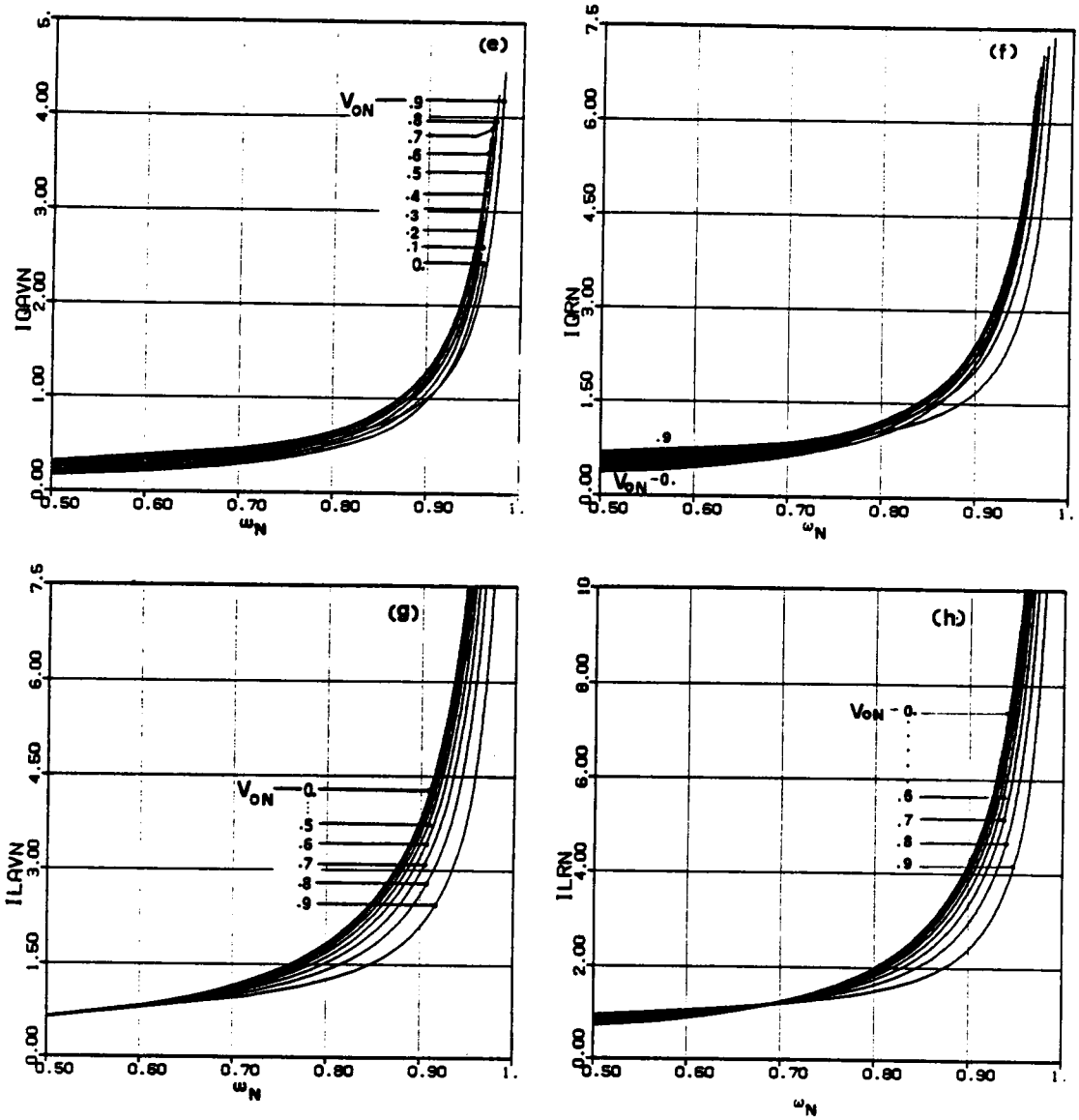

Figure A.6 (contd.)
e) Normalized average transistor current
f) Normalized RMS transistor current
g) Normalized average induct current/normalized output current
h) Normalized RMS inductor current

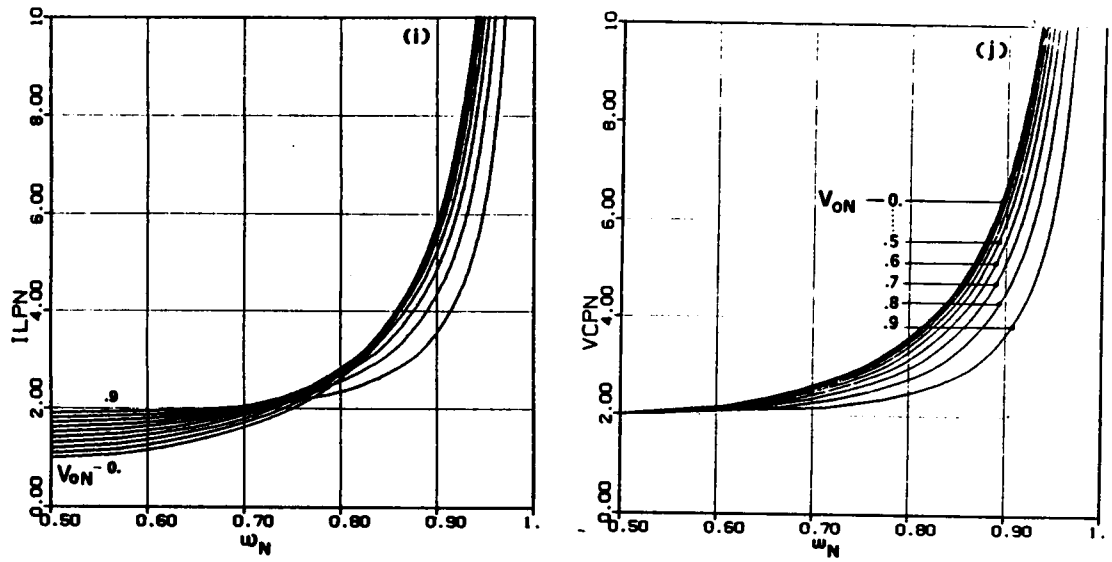

Figure A.6 (contd.)
i) Normalized peak inductor current
j) Normalized peak capacitor voltage

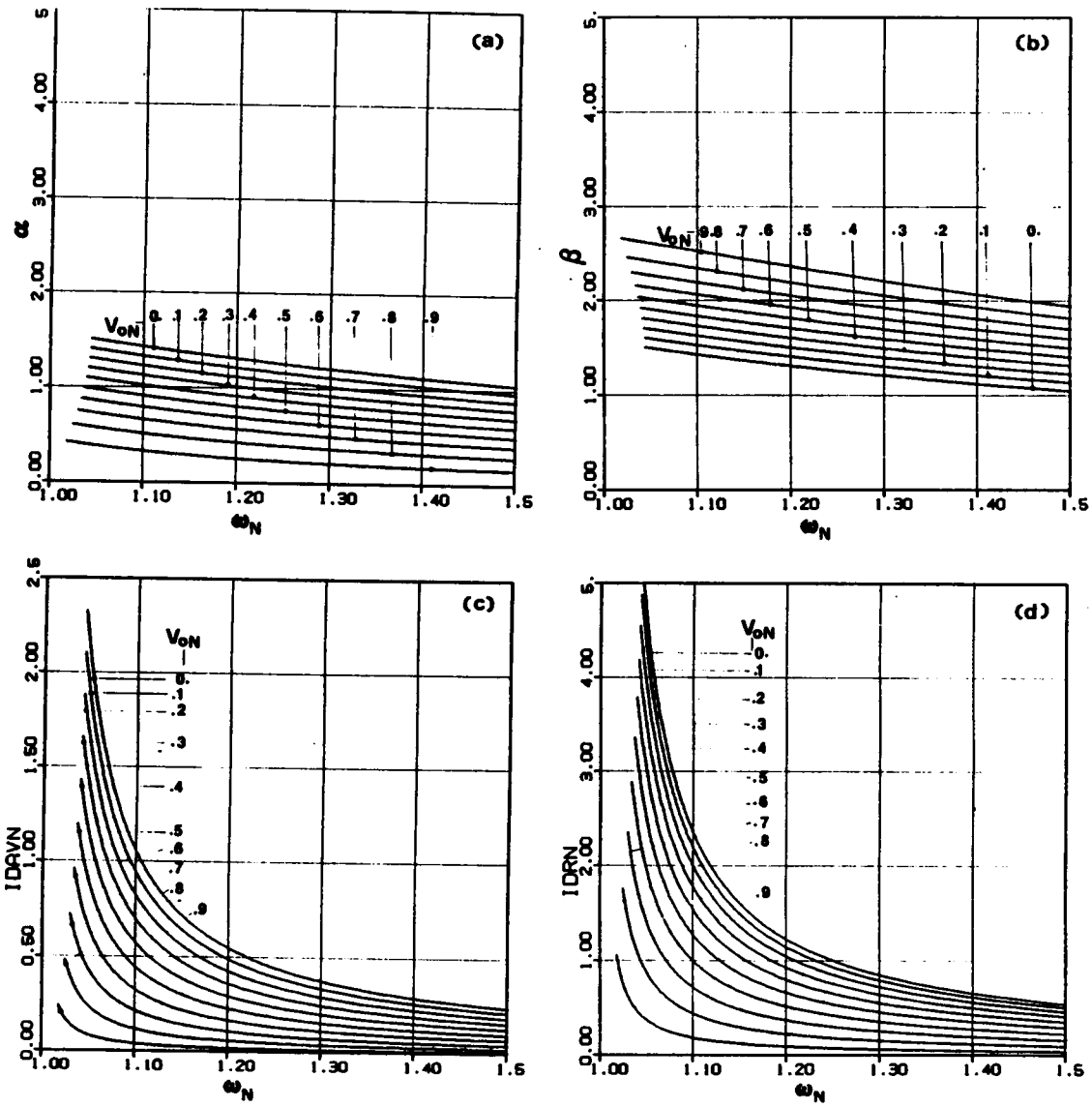

Figure A.7 Ideal design curves for a SRC - $1.0 < \omega_N < 1.5$

a) Diode conduction angle
b) Transistor conduction angle
c) Normalized average diode current
d) Normalized RMS diode current

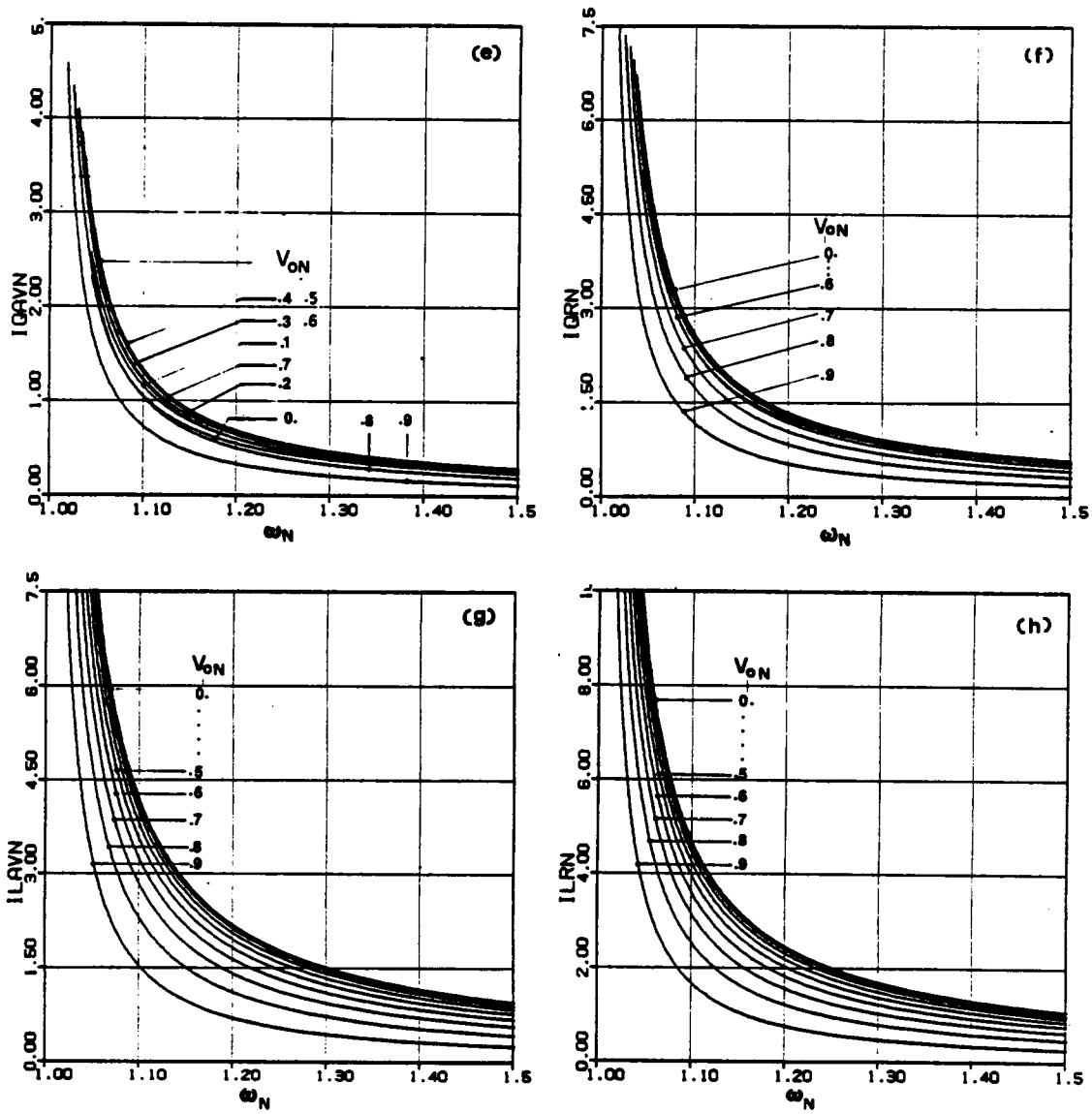

Figure A.7 (contd.)
e) Normalized average transistor current
f) Normalized RMS transistor current
g) Normalized average induct current/normalized output current
h) Normalized RMS inductor current

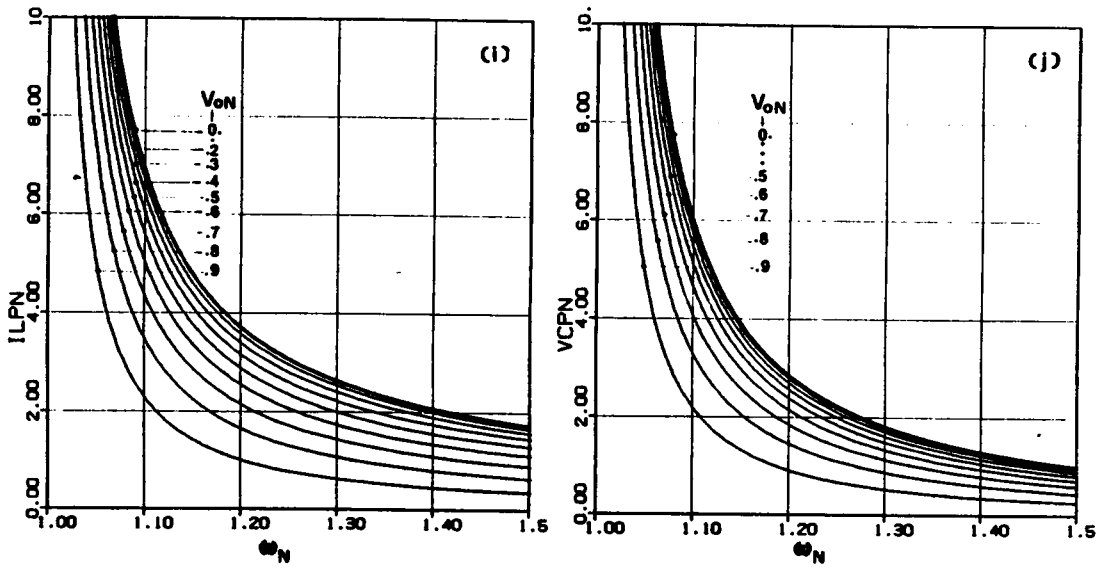

Figure A.7 (contd.)
i) Normalized peak inductor current
j) Normalized peak capacitor voltage

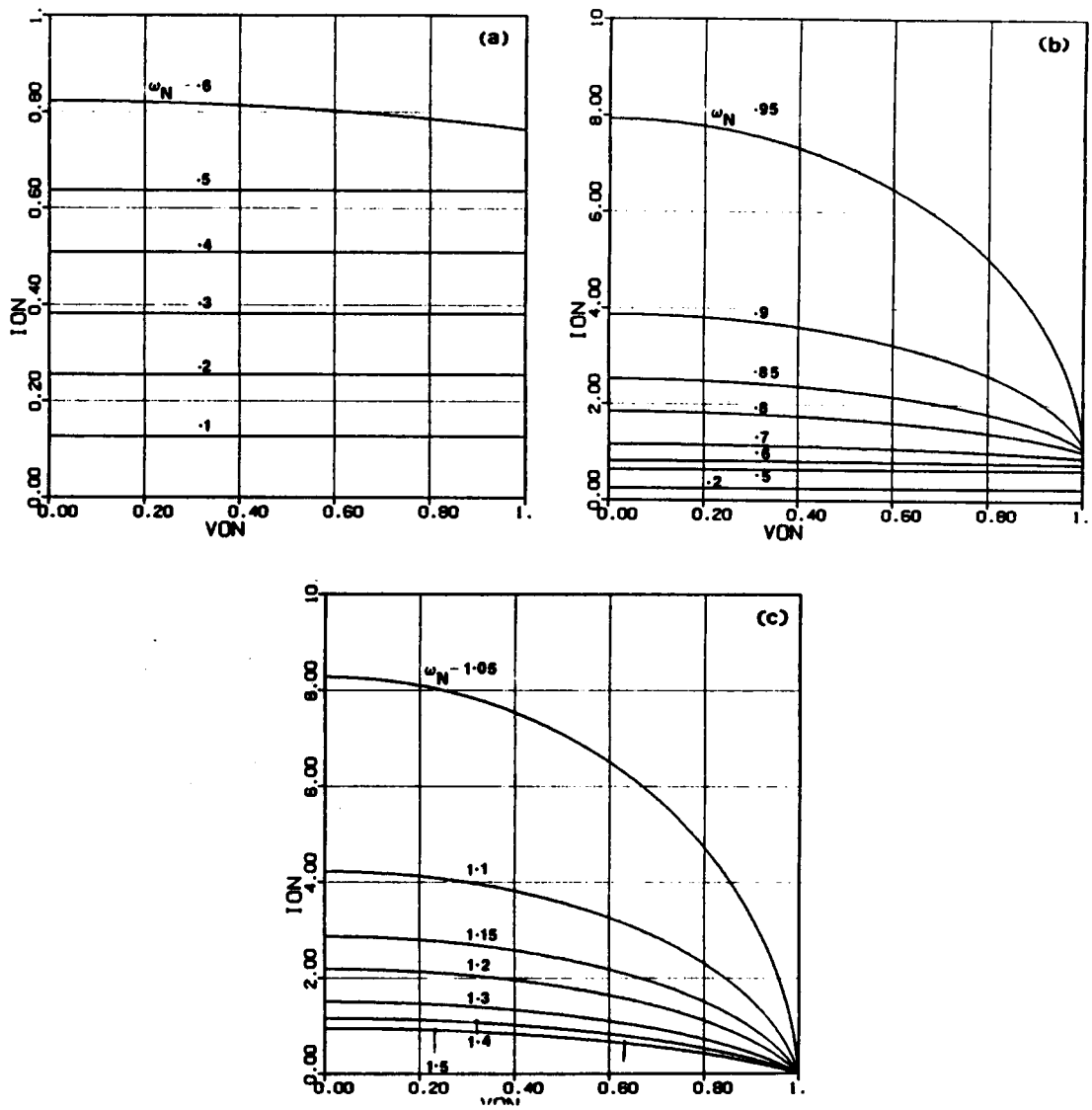

Figure A.8 SRC ideal DC characteristics
a) Mainly DCM-2
b) Mainly CCM below resonance
c) CCM above resonance

A.6 Numerical Examples

In the following two subsections, numerical problems illustrating the use of SRC design curves will be presented. The aims of these examples are to highlight certain aspects of SRC operation. In Sec. A.6.1, the problem faced by a SRC in handling light loads will be dealt with. Sec. A.6.2 presents an approach that can be followed in designing a SRC. This subsection presents two designs each meeting the given specifications and compares them. In the first design, the operation is restricted to CCM below resonance. In the second design, however, the circuit operates both in CCM below resonance and in DCM-2. In both the examples, ideal, lossless operation of the SRC has been assumed.

A.6.1 Example 1

Let $V_s = 50V$, $V_o = 30V$, $I_{oMAX} = 3A$, $I_{oMIN} = 2A$

$L = 47.75\ \mu H$, $C = 0.053\ \mu F$

We will now determine the operating frequency range for maintaining the output at 30 V. From the data given,

$$Z_0 = \sqrt{\frac{L}{C}} = \sqrt{\frac{47.75 \times 10^{-6}}{0.053 \times 10^{-6}}} = 30\ \Omega$$

$$\omega_0 = \frac{1}{\sqrt{LC}} = \frac{1}{\sqrt{47.75 \times 10^{-6} \times 0.053 \times 10^{-6}}} = 628601\ \textit{radians/second.}$$

$$f_0 = \frac{\omega_0}{2\pi} = \frac{628601}{2\pi} \cong 100\ kHz$$

$$I_{oNMAX} = \frac{I_{oMAX}}{V_s/Z_0} = \frac{3}{50/30} = 1.8$$

$$I_{oNMIN} = \frac{I_{oMIN}}{V_s/Z_0} = \frac{2}{50/30} = 1.2$$

$$V_{oN} = \frac{V_o}{V_s} = \frac{30}{50} = 0.6$$

Fig. A.8(b) shows the dc characteristics of SRC for operation below resonance. From Fig. A.8(b),

$$\text{at} \quad I_{oN} = 1.8 \text{ and } V_{oN} = 0.6, \quad \omega_N = \omega_{NMAX} = 0.82 \text{ and}$$

$$\text{at} \quad I_{oN} = 1.2 \text{ and } V_{oN} = 0.6, \ \omega_N = \omega_{NMIN} = 0.73$$

Since $f_0 = 100\ kHz$, the frequency variation is between 73 kHz and 82 kHz.

Now, let I_{oMIN} be reduced to 0.5 A with the other requirements remaining the same.

$$I_{oNMIN} = \frac{I_{oMIN}}{V_s/Z_0} = \frac{0.5}{50/30} = 0.3$$

The maximum operating frequency remains unaltered at 82 kHz. From Fig. A.8(a),

$$\text{at} \quad I_{oN} = 0.3, \ \omega_N = \omega_{NMIN} = 0.23$$

Thus the new frequency range is 23 kHz to 82 kHz.

Hence, the operating frequency of a SRC must be reduced to a low value in order to handle light load condition. In fact, at no load, the SRC frequency must theoretically be reduced to zero.

A.6.2 Example 2

We will design a SRC to meet the following specifications. The design is limited to operation below resonant frequency.

Input Voltage $= V_s = 40$ to $60\ V$

Output Voltage $= V'_o = 100\ V$ (Regulated)

Output Current $= I'_o = 2$ to $6\ A$

Minimum Operating Frequency $= f_{MIN} = 50\ kHz$

Note On Choice Of Transformer Ratio: Since the output voltage is more than the input dc voltage, a transformer is needed in this design. It is assumed that a transformer with turns ratio of n : 1 is located across the input terminals of the output bridge rectifier of the SRC (across points "z" and "y" in Fig. 2.1). The choice of n determines the normalized load voltage V_{oN} as seen from the primary side. If n is such that V_{oN} is low then the following holds true.

Since the transformer primary voltage is low, to handle the same power, the transformer primary current must be large. Thus, currents in the inductor, capacitor and switches will be large. Since a large ac current flows through the capacitor, its voltage stress also will be higher. Thus, larger components than necessary will be required with such a design.

Hence, the value of n should be chosen such that V_{oN} is as close to unity as possible. However, as shown in Sec. 3.3, it may not be possible to attain large V_{oN} values at heavy loads due to parasitic circuit losses. In addition, it is shown in Sec. 4.3.3 that the maximum rate at which the tank energy can be increased is severely curtailed as V_{oN} approaches unity.

In this particular example, since $V_{sMIN} = 40V$,

$$V_o \leq V_{sMIN} = 40V$$

$$\text{Thus,} \qquad n \leq \frac{V_o}{V'_o} = \frac{40}{100} = 0.4$$

A value of 0.3 is chosen for n. Hence,

$$V_o = n\,V'_o = 0.3 \times 100 = 30V$$

$$V_{oNMAX} = \frac{V_o}{V_{sMIN}} = \frac{30}{40} = 0.75$$

$$V_{oNMIN} = \frac{V_o}{V_{sMAX}} = \frac{30}{60} = 0.50$$

$$I_{oNMIN} = \frac{\frac{I'_{oMIN}}{n} Z_0}{V_{sMAX}} = \frac{\frac{2}{0.3} Z_0}{60} = 0.1111 Z_0$$

$$I_{oNMAX} = \frac{\frac{I'_{oMAX}}{n} Z_0}{V_{sMIN}} = \frac{\frac{6}{0.3} Z_0}{40} = 0.50 Z_0$$

A.6.2.1 Design 1

Let resonant frequency, $f_0 = 100\ kHz$. So,

$$\omega_{NMIN} = \frac{f_{MIN}}{f_0} = \frac{50 \times 10^3}{100 \times 10^3} = 0.5$$

From Fig. A.8(b),

$$\text{at} \quad \omega_N = 0.5 \text{ and } V_{oN} = 0.5, \quad I_{oN} = I_{oNMIN} = 0.635 = 0.1111 Z_0$$

$$\text{So,} \qquad Z_0 = \frac{0.635}{0.1111} = 5.715\ \Omega$$

$$I_{oNMAX} = 0.5 \times Z_0 = 0.5 \times 5.715 = 2.858$$

From Fig. A.8(b),

$$\text{at} \quad I_{oN} = 2.858 \text{ and } V_{oN} = 0.75, \quad \omega_N = \omega_{NMAX} = 0.905$$

$$f_{MAX} = \omega_{NMAX} \ f_0 = 0.905 \times 100 = 90.5\ kHz$$

Thus, in this design,

$$0.5 \leq \omega_N \leq 0.905$$

$$50.0\ kHz \leq f \leq 90.5\ kHz$$

Let us now calculate the value of the tank components.

$$\omega_0 = 2\pi f_0 = 2\pi \times 100 \times 10^3 = 628318.5\ \textit{radians/second}$$

Since $\omega_0 = \frac{1}{\sqrt{LC}}$ and $Z_0 = \sqrt{\frac{L}{C}}$,

$$L = \frac{Z_0}{\omega_0} = \frac{5.715}{628318.5} = 9.1\ \mu H$$

$$C = \frac{1}{Z_0\,\omega_0} = \frac{1}{5.715 \times 628318.5} = 0.28\ \mu F$$

A.6.2.2 Design 2

Let resonant frequency, $f_0 = 250\ kHz$. So,

$$\omega_{NMIN} = \frac{f_{MIN}}{f_0} = \frac{50 \times 10^3}{250 \times 10^3} = 0.2$$

From Fig. A.8(a),

$$\text{at} \quad \omega_N = 0.2 \text{ and } V_{oN} = 0.5, \quad I_{oN} = I_{oNMIN} = 0.255 = 0.1111 Z_0$$

$$\text{So,} \qquad Z_0 = \frac{0.255}{0.1111} = 2.295\ \Omega$$

$$I_{oNMAX} = 0.5 \times Z_0 = 0.5 \times 2.295 = 1.15$$

From Fig. A.8(b),

$$\text{at} \quad I_{oN} = 1.15 \text{ and } V_{oN} = 0.75, \quad \omega_N = \omega_{NMAX} = 0.73$$

$$f_{MAX} = \omega_{NMAX} f_0 = 0.73 \times 250 = 182.5\ kHz$$

Thus, in this design,

$$0.2 \le \omega_N \le 0.73$$

$$50.0\ kHz \le f \le 182.5\ kHz$$

Let us now calculate the value of the tank components.

$$\omega_0 = 2\pi f_0 = 2\pi \times 250 \times 10^3 = 1570796.3\ \textit{radians/second}$$

$$L = \frac{Z_0}{\omega_0} = \frac{2.295}{1570796.3} = 1.46\ \mu H$$

$$C = \frac{1}{Z_0\,\omega_0} = \frac{1}{2.295 \times 1570796.3} = 0.277\ \mu F$$

A.6.2.3 Comparison Of Design 1 and Design 2

The frequency range used in design 2 is approximately twice that in design 1. This increased frequency range can be justified only if significant reductions in component ratings are achieved with design 2 over design 1.

The component ratings may be determined by use of curves in Figs. A.5, A.6. By use of V_{CPN} plots in Figs. A.5(j) and A.6(j), it can be shown that the peak capacitor voltage in design 1 ($\cong$200 *V*) is higher than in design 2 ($\cong$120 *V*).

Since transformer ratio is the same, the average tank current magnitudes in the two cases are also same. Thus, in both design 1 and design 2,

$$I_{LAV}(\text{MAX}) = \text{Maximum half-cycle average tank current}$$
$$= \frac{I'_{oMAX}}{n} = \frac{6}{0.3} = 20\ A$$

Thus, it can be anticipated that the average current levels in the resonant components and the switches will be nearly the same in the two cases. This can be verified by computing the current stresses using the appropriate curves in Figs. A.5 and and A.6.

Since significant reduction in component stressess have not been realized with design 2, it is concluded that design 1 is the preferred design.

A.7 Program Listings

Please note that the symbols used for the various parameters in the programs may differ from those in the equations of the previous sections of this appendix.

A.7.1 DC Analysis - CCM Below Resonance

```
C  DC  ANALYSIS OF LOSSLESS SERIES RESONANT CONVERTER - PROGRAM 1A
C
C  GENERATES DESIGN CURVES OF VARIOUS CIRCUIT PARAMETERS, SUCH AS
C  OUTPUT CURRENT, ILAVN, DIODE CONDUCTION ANGLE, ALPHA, ETC.
C  AS A FUNCTION OF FREQUENCY, WN, FOR THE CCM MODE OF OPERATION
C  FOR WN LESS THAN 1.
C  THE PARAMETER R (RADIUS) IS VARIED OVER A WIDE RANGE AND THE
C  SUBROUTINE SER1A COMPUTES THE CORRESPONDING  CIRCUIT PARAMETER
C  VALUES, INCLUDING WN, WHICH ARE THEN OUPUTTED.
C  THE PROGRAM MAY ALSO BE USED TO PLOT THE PARAMETERS WHEN OTHER
C  CONTROL METHODS SUCH AS OPTIMAL TRAJECTORY CONTROL ARE USED.
C  USES SER1A SUBROUTINE.
C
C  BY RAMESH ORUGANTI
C
      IMPLICIT REAL*8(A-H,I,O-Z)
      RMAX     =  15.0
      DO 10 J  =  1,5
      VON      =  DFLOAT(J-1) * 0.1
      RMIN     =  1.0 + VON
      STEP1    =  (RMAX - RMIN)/200.
      DO 10 K  =  1,201
      R        =  RMIN + DFLOAT(K-1) * STEP1
      CALL SER1A (R,VON,VCON,ILON,ILPN,VCPN,ALPHA,BETA,WN,
     *              IDAVN,IDRN,IQAVN,IQRN,ILRN,ILAVN)
      WRITE(6,9010) WN,ILPN
 9010 FORMAT (2E14.5)
   10 CONTINUE
      STOP
      END
```

A.7.2 DC Analysis - Type-2 DCM

```
C  DC  ANALYSIS OF LOSSLESS SERIES RESONANT CONVERTER - PROGRAM 1B
C
C  GENERATES DESIGN CURVES OF VARIOUS CIRCUIT PARAMETERS, SUCH AS
C  OUTPUT CURRENT, ILAVN, DIODE CONDUCTION ANGLE, ALPHA, ETC.
C  AS A FUNCTION OF FREQUENCY, WN, FOR THE DCM MODE OF OPERATION
C  FOR WN LESS THAN 0.5
C  THE PARAMETER WN, FREQUENCY, IS VARIED OVER THE RANGE AND THE
C  SUBROUTINE SER1B COMPUTES THE CORRESPONDING  CIRCUIT PARAMETER
C  VALUES, WHICH ARE THEN OUPUTTED.
C  USES SER1B SUBROUTINE.
C
C  BY RAMESH ORUGANTI
C
      IMPLICIT REAL*8(A-H,I,O-Z)
      WNMAX    =  0.5
      WNMIN    =  1.0E-06
      STEP1    =  (WNMAX-WNMIN)/200.
      DO 10 J  =  1,10
      VON      =  DFLOAT(J-1) * 0.1
      DO 10 K  =  1,201
      WN       =  WNMIN + DFLOAT(K-1) * STEP1
      CALL SER1B (R,VON,VCON,ILON,ILPN,VCPN,ALPHA,BETA,WN,
     *              IDAVN,IDRN,IQAVN,IQRN,ILRN,ILAVN)
      WRITE(6,9010) WN,BETA
 9010 FORMAT (2E14.5)
   10 CONTINUE
      STOP
      END
```

A.7.3 DC Analysis - CCM Above Resonance

```
C  DC  ANALYSIS OF LOSSLESS SERIES RESONANT CONVERTER - PROGRAM 1C
C
C  GENERATES DESIGN CURVES OF VARIOUS CIRCUIT PARAMETERS, SUCH AS
C  OUTPUT CURRENT, ILAVN, DIODE CONDUCTION ANGLE, ALPHA, ETC.
C  AS A FUNCTION OF FREQUENCY, WN, FOR THE CCM MODE OF OPERATION
C  FOR WN GREATER THAN 1.
C  THE PARAMETER R (RADIUS) IS VARIED OVER A WIDE RANGE AND THE
C  SUBROUTINE SER1C COMPUTES THE CORRESPONDING  CIRCUIT PARAMETER
C  VALUES, INCLUDING WN, WHICH ARE THEN OUPUTTED.
C  USES SER1C SUBROUTINE.
C
C  BY RAMESH ORUGANTI
C
      IMPLICIT REAL*8(A-H,I,O-Z)
      RMAX     =  15.0
      DO 10 J  =  1,5
      VON      =  DFLOAT(J-1) * 0.1
      RMIN     =  1.0 - VON + 1.0E-06
      STEP1    =  (RMAX-RMIN)/200.
      DO 10 K  =  1,201
      R        =  RMIN + DFLOAT(K-1) * STEP1
      CALL SER1C (R,VON,VCON,ILON,ILPN,VCPN,ALPHA,BETA,WN,
     *            IDAVN,IDRN,IQAVN,IQRN,ILRN,ILAVN)
      IF(WN.GT.1.55) WN = 1.55
      WRITE(6,9010) WN,IQAVN
 9010 FORMAT (2E14.5)
   10 CONTINUE
      STOP
      END
```

A.7.4 DC Analysis Given Operating Frequency

```
C  DC ANALYSIS OF LOSSLESS SERIES RESONANT CONVERTER - PROGRAM 2A
C
C  TO COMPUTE IDEAL DC CHARACTERISTICS, ION VS VON FOR DIFFERENT
C  FREQUENCIES OF SERIES RESONANT CONVERTER WITH NO DAMPING
C  ASSUMED. THE SUBPROGRAMS SER1A, SER1B AND SER1C ARE BASED ON
C  THEORETICAL ANALYSIS OF THE LOSSLESS CASE DIRECTLY.
C  COVERS CCM ABOVE AND BELOW RESONANCE AND DCM MODES OF OPERATION.
C  USES SER1A, SER1B, SER1C AND AGAIN1 SUBROUTINES.
C
C     PROGRAMMED BY RAMESH ORUGANTI
      IMPLICIT REAL*8(A-H,I,O-Z)
          PI      =  4.*ATAN(1.0)
          VONMIN  =  1.0E-03
          VONMAX  =  1.0 - 1.0E-03
          STEP2   =  (VONMAX - VONMIN)/200.
C
      DO 500 K1   =  1, 6
      WNR     =  DFLOAT(K1-1) * 0.1 + 1.1
C
C  FOR A GIVEN VON, TRY DIFFERENT R'S SUCH THAT THE SPECIFIED WNR
C  IS REACHED. THE ION VALUE CORRESPONDING TO THAT R IS THE ONE
C  REQUIRED.
C
      DO  500  K2 =  1, 201
          VON     =  VONMIN + DFLOAT(K2-1) * STEP2
C
C  DETERMINE IF WNR LESS THAN 0.5, OR BETWEEN 0.5 AND 1.0 OR ABOVE 1.0.
C
          IF(WNR.GT.1.0) GO TO 100
          IF(WNR.LE.0.5) GO TO 200
C
          RMIN    =  1. + VON + 1.0E-06
          RMAX    =  1000.0
          R       =  RMIN
          STEP3   =  (RMAX - RMIN)/2.
C
      DO  20   K3 =  1,500
          CALL SER1A(R,VON,VCON,ILON,ILPN,VCPN,ALPHA,BETA,WN,
     *               IDAVN,IDRN,IQAVN,IQRN,ILRN,ILAVN)
          ERROR   =  WNR - WN
          IF (DABS(ERROR).LT.1.E-05) GO TO 400
          CALL AGAIN1(ERROR,RMIN,RMAX,R,STEP3)
   20 CONTINUE
C
```

```
  100     RMIN    =  1. - VON +1.0E-06
          RMAX    =  1000.0
          R       =  RMIN
          STEP4   =  (RMAX-RMIN)/2.
       DO 120   K4 =  1,500
          CALL SER1C(R,VON,VCON,ILON,ILPN,VCPN,ALPHA,BETA,WN,
     *               IDAVN,IDRN,IQAVN,IQRN,ILRN,ILAVN)
          ERROR   =  WN - WNR
          IF (DABS(ERROR).LT.1.E-05) GO TO 400
          CALL AGAIN1(ERROR,RMIN,RMAX,R,STEP4)
  120 CONTINUE
C
  200     CALL SER1B(R,VON,VCON,ILON,ILPN,VCPN,ALPHA,BETA,WNR,
     *               IDAVN,IDRN,IQAVN,IQRN,ILRN,ILAVN)
  400     WRITE(6,9010) VON, ILAVN
 9010 FORMAT(2E14.5)
  500 CONTINUE
C
      STOP
      END
```

A.7.5 Trajectory Plots - Steady-State

```
C  SRC - LOSSLESS STEADY-STATE TRAJECTORIES
C
C  MAIN PROGRAM TO PLOT 1)STATE-PORTRAIT  2)STEADY-STATE TRAJECTORIES
C  3)DEVICE SWITCHING BOUNDARIES AND 4)ASYMMETRICAL DCM STEADY-STATE
C  TRAJECTORIES FOR A GIVEN NORMALIZED OUTPUT VOLTAGE, VON.
C  IF ANY PARTICULAR PLOT, SUCH AS STATE-PORTRAIT, IS NOT REQUIRED
C  IT MAY BE COMMENTED OUT.
C  THE PROGRAM USES THE PLOTTING SUBROUTINES AVAILABLE TO ACCESS
C  VERSATEC AND CALCOMP PLOTTERS AND THE PLOT 10 PREVIEW PACKAGE
C  AND ALSO THE CIRCLE SUBROUTINE AVAILABLE AT VPI.
C  ADDITIONALLY THE PROGRAM USES FAMIL1 AND EQUIL1 SUBPROGRAMS.
C
C  BY RAMESH ORUGANTI
C
      DIMENSION X(500),Y(500)
C
C  NORMALIZED OUTPUT VOLTAGE VALUE
C
      VON  =  0.5
      CALL PLOTS(0,0,50)
C
C  DECIDE SCALING FACTOR
C
      CALL FACTOR(.75)
C
      CALL PLOT(1.,1.,-3)
C
C  CHOOSE PEN THICKNESS FOR THE AXIS
C
      CALL NEWPEN(2)
C
C  PLOT AXIS
C
      CALL AXIS(0.,5.,68H
     *                  VCN,-68,10.,0.,-5.0,1.)
      CALL AXIS(5.,0.,68H
     *                  ILN,+68,10.,90.,-5.0,1.)
C
C  CHOOSE PEN THICKNESS FOR THE STATE-PORTRAIT
C
      CALL NEWPEN(3)
C
      CALL PLOT(5.,5.,-3)
C
C  DRAW STATE PORTRAIT
C
C  STEP1: DETERMINE A TOPOLOGICAL MODE CENTER
C
      YC   =  0.
      XC   =  -1. - VON
C
C  STEP2: MARK THE CENTER (NOTE: THIS IS A VPI SUBROUTINE)
C
      CALL CIRCLE(XC,YC,.05)
C
C  STEP3: DRAW POSSIBLE TRAJECTORIES CORRESPONDING TO THIS TOPOLOGICAL
```

```
C         MODE
C
      CALL FAMIL1(XC,YC,1)
C
C  REPEAT STEPS 1,2 AND 3 FOR OTHER TOPOLOGICAL MODES

      XC    =  -1. + VON
      CALL CIRCLE(XC,YC,0.05)
      CALL FAMIL1(XC,YC,2)
C
      XC    =   1. - VON
      CALL CIRCLE(XC,YC,.05)
      CALL FAMIL1(XC,YC,1)
C
      XC    =   1. + VON
      CALL CIRCLE(XC,YC,.05)
      CALL FAMIL1(XC,YC,2)
C
C  CHOOSE PEN THICKNESS FOR STEADY-STATE TRAJECTORIES
C
      CALL NEWPEN(5)
C
C  PLOT A FAMILY OF STEADY-STATE TRAJECTORIES USING SUBROUTINE EQUIL
C  AND DIFFERENT RADII, R. THE VALUES OF RMAX AND RSTEP1 MAY BE CHANGED
C  AS REQUIRED.
C
      RMIN  =   1. + VON
      RMAX  =   3.5
      RSTEP1=   0.5
      DO 10 I = 1,100
      R     =   RMIN + FLOAT(I-1) * RSTEP1
      IF (R.GT.(RMAX+.01)) GO TO 20
      CALL EQUIL1(R,VON)
   10 CONTINUE
C
C  CHOOSE PEN THICKNESS FOR PLOTTING THE SWITCHING BOUNDARIES
C
   20 CALL NEWPEN(2)
C
C  COMPUTE AND PLOT THE SWITCHING BOUNDARY IN THE UPPER HALF OF THE
C  STATE-PLANE.
C
      RSTEP2 = 0.05
      DO 30 I = 1,100
      R       =   RMIN +FLOAT(I-1) * RSTEP
      IF (R.GT.(RMAX+.01)) GO TO 40
      X(I)    =  -VON * (R+1.-VON)
      Y(I)    =  SQRT((1.-VON**2) * ((R-VON)**2 - 1.))
      IF (I.EQ.1)  CALL PLOT(X(1),Y(1),3)
      CALL PLOT (X(I),Y(I),2)
   30 CONTINUE
C
C  PLOT SWITCHING BOUNDARY IN THE LOWER HALF OF THE STATE-PLANE
C
   40 DO 50 I = 1,100
      R     =  RMIN + FLOAT(I-1) * RSTEP
      IF (R.GT.(RMAX+.01)) GO TO 60
      X(I) = -X(I)
      Y(I) = -Y(I)
      IF (I.EQ.1) CALL PLOT(X(1),Y(1),3)
      CALL PLOT (X(I),Y(I),2)
   50 CONTINUE
C
C  CHOOSE PEN THICKNESS FOR ASYMMETRICAL DCM STEADY-STATE TRAJECTORIES.
C
   60 CALL NEWPEN(1)
C
C  PLOT THE ASYMMETRICAL TRAJECTORY USING THE RELEVANT RADIUS DATA.
C
      PI    =  4.*ATAN(1.)
      CALL ARC1(1.5,0.,.16666667,2,0.,PI)
      CALL ARC1(-.5,0.,1.833333,2,0.,PI)
      CALL ARC1(-1.5,0.,.8333333,1,0.,PI)
      CALL ARC1(.5,0.,1.16666667,1,0.,PI)
C
      CALL PLOT(12.,0.,999)
      STOP
      END
```

A.7.6 Trajectory Plots - Control Analysis

```
C  CONTROL ANALYSIS OF SERIES RESONANT CONVERTER
C
C  PROGRAM TO PLOT THE TRANSIENT TRAJECTORIES IN SRC UNDER SIX
C  METHODS OF CONTROL (MCON)
C
C  MCON = 1  FREQUENCY CONTROL (ELAPSED INTERVAL)
C  MCON = 2  ASDTIC CONTROL
C  MCON = 3  OPTIMAL TRAJECTORY CONTROL
C  MCON = 4  DIODE ANGLE CONTROL
C  MCON = 5  CAPACITOR VOLTAGE CONTROL
C  MCON = 6  TRANSISTOR ANGLE CONTROL
C
C  THE STEADY-STATE OPERATING TRAJECTORIES ARE DEFINED BY THEIR
C  CORRESPONDING RADIUS VALUES.
C  FOR EACH METHOD OF CONTROL THE PROGRAM PLOTS 1)THE STEADY-STATE
C  TRAJECTORY FOR A GIVEN R  2)THE TRANSIENT WHEN R IS CHANGED TO
C  ANOTHER VALUE AND 3)THE TRANSIENT WHEN VON GOES TO ZERO(SHORT-CKT).
C  IPLOT VALUE TO BE ASSIGNED 1, 2 OR 3 ACCORDINGLY.
C  THE PROGRAM USES THE PLOTTING SUBROUTINES AVAILABLE TO ACCESS
C  VERSATEC AND CALCOMP PLOTTERS AND THE PLOT 10 PREVIEW PACKAGE
C  AND ALSO THE CIRCLE SUBROUTINE AVAILABLE ART VPI.
C  ADDITIONALLY THE PROGRAM USES EQUIL1 AND LOCUS1 SUBPROGRAMS.
C
C  BY RAMESH ORUGANTI
C
C  GIVE VALUES TO IPLOT, MCON AND VON
C
      IPLOT  =  3
      MCON   =  4
      VON    =  0.5
C
C  ISCR = 1 IF DEVICE1 IS TO BE CONDUCTING INITIALLY, ELSE ISCR = 2.
C
      ISCR   =  2
      CALL PLOTS(0,0,50)
C
C  CHOOSE SCALE FACTOR
C
      CALL FACTOR(.75)
      CALL PLOT(1.,1.,-3)
C
C  CHOOSE PEN THICKNESS FOR THE AXIS
C
      CALL NEWPEN(2)
C
C  PLOT THE AXES
C
      CALL AXIS(0.,5.,68H
     *                  VCN,-68,10.,0.,-5.0,1.)
      CALL AXIS(5.,0.,68H
     *                  ILN,+68,10.,90.,-5.0,1.)
C
      CALL PLOT(5.,5.,-3)
C
C  IF IPLOT=1 THEN ASSIGN VALUE TO STEADY-STATE R.
C  IF IPLOT=2 THEN ASSIGN VALUE TO DESIRED R AND INITIAL R1.
C  IF IPLOT=3 THEN ASSIGN VALUE TO INITIAL R.
C
      IF(IPLOT.NE.1) GO TO 10
      R    =  2.0
   10 IF(IPLOT.NE.2) GO TO 20
      R1   =  2.
      R    =  3.5
   20 IF(IPLOT.NE.3) GO TO 30
      R    =  2.0
C
C  CHOOSE PEN THICKNESS FOR THE STEADY-STATE TRAJECTORIES
C
   30 CALL NEWPEN(5)
      CALL EQUIL1 (R,VON)
C
C  DETERMINE CONTROL VALUE, VALCON, DEPENDING ON THE CONTROL METHOD
C  AND DESIRED RADIUS, R.
C
      ALPHA0=  ARCOS(-(1.-VON*R+VON**2)/(R-2.*VON))
      BETA0 =  ARCOS(-(1.+VON*R-VON**2)/R)
      VCON0 =  VON*(R+1.-VON)
C
      IF(MCON.EQ.1) VALCON=  ALPHA0 + BETA0
```

```
      IF(MCON.EQ.2) VALCON=  2.*(R+1.-VON)/(ALPHA0+BETA0)
      IF(MCON.EQ.3) VALCON=  R
      IF(MCON.EQ.4) VALCON=  ALPHA0
      IF(MCON.EQ.5) VALCON=  VCON0
      IF(MCON.EQ.6) VALCON=  BETA0
C
C  IPLOT = 1  PLOT STEADY STATE PERFORMANCE
C
      IF(IPLOT.NE.1) GO TO 60
C
C  CHOOSE PEN THICKNESS FOR STEADY STATE PERFORMANCE
C
      CALL NEWPEN(2)
C
C  COMPUTE FIRST SET OF SWITCHING CONDITIONS
C
      AILON =  SQRT((1.-VON**2)*((R-VON)**2-1.))
      VCON  =  -VON*(R+1.-VON)
      IF(ISCR.NE.2) GO TO 40
      AILON =  - AILON
      VCON  =  - VCON
C
C  PLOT THE TRANSIENT TRAJECTORY
C
 40   DO 50 I = 1,6
      CALL LOCUS1(VON,VCON,AILON,MCON,VALCON,ISCR,
     *                     VC2N,AIL2N,R,BETA,ALPHA,IFLAG)
      IF (IFLAG.EQ.1) STOP
      ITEMP =  ISCR
      IF(ITEMP.EQ.1)  ISCR=2
      IF(ITEMP.EQ.2)  ISCR=1
      VCON  =  VC2N
      AILON =  AIL2N
 50   CONTINUE
C
C  IPLOT = 2  PLOT RESPONSE TO CONTROL CHANGE
C
 60   IF(IPLOT.NE.2) GO TO 90
C
C  PLOT THE INITIAL STEADY-STATE TRAJECTORY
C
      CALL EQUIL1(R1,VON)
C
C  CHOOSE PEN THICKNESS FOR THE TRANSIENT TRAJECTORY
C
      CALL NEWPEN(2)
C
C  COMPUTE FIRST SET OF SWITCHING CONDITIONS
C
      AILON =  SQRT((1.-VON**2)*((R1-VON)**2-1.))
      VCON  =  -VON*(R1+1.-VON)
      IF(ISCR.NE.2) GO TO 70
      AILON =  - AILON
      VCON  =  - VCON
C
C  PLOT THE TRANSIENT TRAJECTORY
C
 70   DO 80 I = 1,6
      CALL LOCUS1(VON,VCON,AILON,MCON,VALCON,ISCR,
     *                     VC2N,AIL2N,R,BETA,ALPHA,IFLAG)
      IF (IFLAG.EQ.1) STOP
      ITEMP =  ISCR
      IF(ITEMP.EQ.1)  ISCR=2
      IF(ITEMP.EQ.2)  ISCR=1
      VCON  =  VC2N
      AILON =  AIL2N
 80   CONTINUE
C
C  IPLOT = 3  PLOT RESPONSE TO SHORT CIRCUIT
C
 90   IF(IPLOT.NE.3) GO TO 120
C
C  CHOOSE PEN THICKNESS FOR THE TRANSIENT TRAJECTORY
C
      CALL NEWPEN(2)
C
C  COMPUTE FIRST SET OF SWITCHING CONDITIONS
C
      AILON =  SQRT((1.-VON**2)*((R-VON)**2-1.))
      VCON  =  -VON*(R+1.-VON)
      IF(ISCR.NE.2) GO TO 100
      AILON =  - AILON
      VCON  =  - VCON
C
```

```
C  SET OUTPUT VOLTAGE CLOSE TO ZERO FOR SHORT-CIRCUIT
C
 100  VON   =  0.01
C
C  PLOT THE TRANSIENT TRAJECTORY
C
      DO 110 I = 1,6
      CALL LOCUS1(VON,VCON,AILON,MCON,VALCON,ISCR,
     *                        VC2N,AIL2N,R,BETA,ALPHA,IFLAG)
      IF (IFLAG.EQ.1) STOP
      ITEMP =  ISCR
      IF(ITEMP.EQ.1)  ISCR=2
      IF(ITEMP.EQ.2)  ISCR=1
      VCON  =  VC2N
      AILON =  AIL2N
  110 CONTINUE
C
  120 CALL PLOT(12.,0.,999)
      STOP
      END
```

A.7.7 Subroutines

```
      SUBROUTINE SER1A(R,VON,VCON,ILON,ILPN,VCPN,ALPHA,BETA,WN,
     *                        IDAVN,IDRN,IQAVN,IQRN,ILRN,ILAVN)
C  FOR AN IDEAL LOSSLESS SRC, CALCULATES THE CIRCUIT PARAMETERS
C  GIVEN AN STEADY-STATE TRAJECTORY(R AND VON) FOR CC M OPERTATION
C  BELOW RESONANT FREQUENCY.
C  THE PARAMETERS ARE
C
C  VCON, ILON  - SWITCHING POINT STATE VARIABLES
C  VCPN, ILPN  - PEAK CAP VOLTAGE AND PEK IND CURRENT
C  ALPHA, BETA - DIODE AND TRANSISTOR CONDUCTION ANGLES
C  WN          - OPERATING FREQUENCY
C  IDAVN, IDRN - DIODE AVERAGE AND RMS CURRENTS
C  IQAVN, IQRN - TRANSISTOR AVERAGE AND RMS CURRENTS
C  ILAVN, ILRN - INDUCTOR (HALF-CYCLE) AVERAGE AND RMS CURRENT
C
C  ALL PARAMETERS ARE EXPLICITLY COMPUTED.
C
C  BY RAMESH ORUGANTI
C
      IMPLICIT REAL*8(A-H,I,O-Z)
C
      PI        =  4.*ATAN(1.)
C
      RPR       =  R - 2.0* VON
      ALPHA     =  PI - DARCOS( (RPR**2+4.-R**2) / (4.*RPR) )
      BETA      =  PI - DARCOS( (R**2+4.-RPR**2) / (4.*R) )
      WN        =  PI/(ALPHA + BETA)
      TN        =  2.*(ALPHA + BETA)
      VCPN      =  R + 1. - VON
      ILPN      =  R
      VCON      =  - VON * VCPN
      ILON      =  R * DSIN(BETA)
      ILAVN     =  2.*VCPN/(ALPHA+BETA)
      IQAVN     =  (VCPN + DABS(VCON))/TN
      IDAVN     =  (VCPN - DABS(VCON))/TN
      IQRN      =  (R/2.) *
     *             DSQRT( (BETA-DSIN(2.*BETA) / 2.) / (ALPHA+BETA) )
      IDRN      =  (RPR/2.) *
     *             DSQRT( (ALPHA-DSIN(2.*ALPHA) / 2.) / (ALPHA+BETA) )
      ILRN      =  DSQRT(2.*(IDRN**2 + IQRN**2))
      RETURN
      END
C
      SUBROUTINE SER1B(R,VON,VCON,ILON,ILPN,VCPN,ALPHA,BETA,WN,
     *                        IDAVN,IDRN,IQAVN,IQRN,ILRN,ILAVN)
C  FOR AN IDEAL LOSSLESS SRC, CALCULATES THE CIRCUIT PARAMETERS
C  GIVEN AN STEADY-STATE TRAJECTORY(WN AND VON) FOR DCM OPERTATION
C  BELOW RESONANT FREQUENCY.
C  THE PARAMETERS ARE
C
C  VCON, ILON  - SWITCHING POINT STATE VARIABLES
C  VCPN, ILPN  - PEAK CAP VOLTAGE AND PEK IND CURRENT
C  ALPHA, BETA - DIODE AND TRANSISTOR CONDUCTION ANGLES
C  R           - RADIUS OF TRANSISOR CONDUCTION
C  IDAVN, IDRN - DIODE AVERAGE AND RMS CURRENTS
C  IQAVN, IQRN - TRANSISTOR AVERAGE AND RMS CURRENTS
C  ILAVN, ILRN - INDUCTOR (HALF-CYCLE) AVERAGE AND RMS CURRENT
```

```
C
C  ALL PARAMETERS ARE EXPLICITLY COMPUTED.
C
C  BY RAMESH ORUGANTI
C
      IMPLICIT REAL*8(A-H,I,O-Z)
C
      PI        =  4.*ATAN(1.)
C
      R         =  1. + VON
      RPR       =  1. - VON
      ALPHA     =  PI
      BETA      =  PI
      TN        =  2.*PI/WN
      VCPN      =  2.
      ILPN      =  R
      VCON      =  - 2.*VON
      ILON      =  0.
      ILAVN     =  (4.*WN)/PI
      IQAVN     =  (1.+VON)*WN/PI
      IDAVN     =  (1.-VON)*WN/PI
      IQRN      =  ((1.+VON)/2.)*DSQRT(WN)
      IDRN      =  ((1.-VON)/2.)*DSQRT(WN)
      ILRN      =  DSQRT(2.*(IDRN**2 + IQRN**2))
      RETURN
      END
C
      SUBROUTINE SER1C(R,VON,VCON,ILON,ILPN,VCPN,ALPHA,BETA,WN,
     *                      IDAVN,IDRN,IQAVN,IQRN,ILRN,ILAVN)
C  FOR AN IDEAL LOSSLESS SRC, CALCULATES THE CIRCUIT PARAMETERS
C  GIVEN AN STEADY-STATE TRAJECTORY(R AND VON) FOR OPERATING FREQUENCIES
C  ABOVE RESONANT FREQUENCY.
C  THE PARAMETERS ARE
C
C  VCON, ILON  - SWITCHING POINT STATE VARIABLES
C  VCPN, ILPN  - PEAK CAP VOLTAGE AND PEK IND CURRENT
C  ALPHA, BETA - DIODE AND TRANSISTOR CONDUCTION ANGLES
C  WN          - OPERATING FREQUENCY
C  IDAVN, IDRN - DIODE AVERAGE AND RMS CURRENTS
C  IQAVN, IQRN - TRANSISTOR AVERAGE AND RMS CURRENTS
C  ILAVN, ILRN - INDUCTOR (HALF-CYCLE) AVERAGE AND RMS CURRENT
C
C  ALL PARAMETERS ARE EXPLICITLY COMPUTED.
C
C  BY RAMESH ORUGANTI
C
      IMPLICIT REAL*8(A-H,I,O-Z)
      PI        =  4.*ATAN(1.)
      RTANGL    =  PI/2.
C
      RPR       =  R + 2.0* VON
      ALPHA     =  DARCOS( (RPR**2+4.-R**2) / (4.*RPR) )
      BETA      =  DARCOS( (R**2+4.-RPR**2) / (4.*R) )
      WN        =  PI/(ALPHA + BETA)
      TN        =  2.*(ALPHA + BETA)
      VCPN      =  R - 1. + VON
      VCON      =  VON * VCPN
      ILON      =  R * DSIN(BETA)
      ILPN      =  R
      IF(BETA.LT.RTANGL) ILPN = ILON
      ILAVN     =  2.*VCPN/(ALPHA+BETA)
      IQAVN     =  (VCPN + DABS(VCON))/TN
      IDAVN     =  (VCPN - DABS(VCON))/TN
      IQRN      =  (R/2.) *
     *               DSQRT( (BETA-DSIN(2.*BETA) / 2.) / (ALPHA+BETA) )
      IDRN      =  (RPR/2.) *
     *               DSQRT( (ALPHA-DSIN(2.*ALPHA) / 2.) / (ALPHA+BETA) )
      ILRN      =  DSQRT(2.*(IDRN**2 + IQRN**2))
      RETURN
      END
C
      SUBROUTINE AGAIN1(E,AMIN,AMAX,A,STEP)
C
C  THIS SUBROUTINE COMPUTES THE NEW VALUE OF THE INDEPENDENT
C  VARIABLE, A, SO THAT THE CONVERGENCE OF DEPENDENT VARIABLE, W,
C  TO THE DESIRED VALUE, WN, IS ACHIEVED IN THE MAIN PROGRAM.
C  GIVEN AMIN, AMAX THE MINIMUM AND MAXIMUM VALUES OF A, THE
C  PREVIOUS ERROR E, AND THE ABSOLUTE MAXIMUM ALLOWABLE STEP IN A,
C  STEP, AND THE CURRENT VALUE OF A, A, THE PROGRAM RETURNS THE
C  NEW VALUE OF A, A, USING SIMPLE 'HALVING' TECHNIQUE.THIS SUBROUTINE
C  IS FOUND TO TAKE MORE ITERATIONS THAN AGAIN2.
C
C  BY RAMESH ORUGANTI
```

```
      IF(E.LT.0.) GO TO 50
C
      H       =  (AMAX-A)/2.
      IF(H.GT.STEP)  H = STEP
      AMIN    =  A
      A       =  A + H
      GO TO 100
C
   50 H       =  (A-AMIN)/2.
      IF(H.GT.STEP) H = STEP
      AMAX    =  A
      A       =  A - H
  100 CONTINUE
      RETURN
      END
C
      SUBROUTINE FAMIL1(XC,YC,IHALF)
C  PLOTS A FAMILY OF SEMI-CIRCULAR TRAJECTORIES CORRESPONDING TO
C  A DEVICE CONDUCTION IN SERIES RESONANT CONVERTER UNDER LOSS-LESS
C  CONDITIONS GIVEN THE CORRESPONDING MODE CENTER (XC, YC) AND
C  THE HALF-PLANE IN WHICH IT OCCURS. THE MINIMUM, MAXIMUM AND THE
C  STEP OF THE RADIUS CAN BE ALTERED IN THE SUB-PROGRAM AS REQUIRED.
C  USES SUB-ROUTINE ARC1.
C
C  BY RAMESH ORUGANTI
C
      RMIN =  0.5
      RMAX =  3.5
      RSTEP=  0.5
      DO 10 I = 1,100
      R    =  RMIN + FLOAT(I-1) * RSTEP
      IF (R.GT.(RMAX+.1)) GO TO 20
      PI   =  4.0*ATAN(1.)
      CALL ARC1(XC,YC,R,IHALF,0.,PI)
   10 CONTINUE
   20 RETURN
      END
C
      SUBROUTINE EQUIL1(R,VON)
C  PLOTS AN STEADY-STATE TRAJECTORY OF SERIES RESONANT CONVERTER UNDER
C  LOSSLESS CONDITIONS GIVEN THE RADIUS, R, AND THE NORMALIZED
C  OUTPUT VOLTAGE, VON.  THE PROGRAM USES SUBROUTINE ARC1 FOR PLOTTING
C  THE SEGMENTS.
C
C  BY RAMESH ORUGANTI
C
      PI    =  4.0*ATAN(1.)
      RPRIM =  R - 2.*VON
      ALPHA0=  ACOS(-(1.-VON*R+VON**2)/(R-2.*VON))
      BETA0 =  ACOS(-(1.+VON*R-VON**2)/R)
      GAMMA =  PI - ALPHA0
      YC    =  0.
      XC    =  -1. - VON
      CALL ARC1(XC,YC,RPRIM,1,GAMMA,PI)
      XC    =   1. + VON
      CALL ARC1(XC,YC,RPRIM,2,GAMMA,PI)
      XC    =  -1. + VON
      CALL ARC1(XC,YC,R,2,0.,BETA0)
      XC    =   1. - VON
      CALL ARC1(XC,YC,R,1,0.,BETA0)
      RETURN
      END
C
      SUBROUTINE ARC1(XC,YC,R,IHALF,ALPHA1,ALPHA2)
C  THE PROGRAM PLOTS AN ARC GIVEN THE CENTER (XC, YC), RADIUS (R),
C  BEGINNING AND END ANGLES IN RADIANS (ALPHA1, ALPHA2) AND
C  THE HALF-PLANE IN WHICH TO BE PLOTTED (IHALF)
C
C  BY RAMESH ORUGANTI
C
      DIMENSION X(43),Y(43)
      X(43)=  1.0
      Y(43)=  1.0
      H    =  (ALPHA2-ALPHA1)/40.
      DO 40 I = 1,41
      ALPHA=  H*FLOAT(I-1) + ALPHA1
      IF(IHALF.EQ.2) GO TO 10
      X(I) =  R*COS(ALPHA) + XC
      Y(I) =  R*SIN(ALPHA) + YC
      GO TO 20
   10 X(I) = -R*COS(ALPHA) + XC
      Y(I) = -R*SIN(ALPHA) + YC
   20 CONTINUE
      IF(I.GT.1)  GO TO 30
```

```
      CALL PLOT (X(1),Y(1),3)
      GO TO 40
   30 CALL PLOT (X(I),Y(I),2)
   40 CONTINUE
      RETURN
C
      SUBROUTINE LOCUS1(VON,VCON,AILON,MCON,VALCON,ISCR,
     *                          VC2N,AIL2N,R,BETA,ALPHA,IFLAG)
C
C  PLOTS THE TRANSIENT TRAJECTORY IN SRC FOR ONE
C  TRANSISITOR CONDUCTION (BETA) AND THE SUBSEQUENT DIODE CONDUCTION
C  (ALPHA) BASED ON SIX METHODS OF CONTROL (MCON).
C
C  MCON = 1  FREQUENCY CONTROL (ELAPSED INTERVAL)
C  MCON = 2  ASDTIC CONTROL
C  MCON = 3  OPTIMAL TRAJECTORY CONTROL
C  MCON = 4  DIODE ANGLE CONTROL
C  MCON = 5  CAPACITOR VOLTAGE CONTROL
C  MCON = 6  TRANSISTOR ANGLE CONTROL
C
C  VALCON IS THE REFERENCE VALUE FOR THE SRC CONTROL.
C  IN ADDITION TO MCON AND VALCON THE PROGRAM ALSO REQUIRES, OUTPUT
C  VOLTAGE, VON, INITIAL CONDITIONS, VCON AND AILON, AND THE # OF THE
C  DEVICE IN CONDUCTION, ISCR,(1 OR 2).
C  THE PROGRAM RETURNS THE NEXT SWITCHING POINT STATE VARIABLES,
C  VC2N AND AIL2N, RADIUS, R, TRANSISTOR AND DIODE CONDUCTION ANGLES,
C  BETA AND ALPHA.
C  IF AN ALPHA OF MORE THAN PI IS PREDICTED IN FREQUENCY CONTROL THEN
C  IFLAG IS SET TO 1, OR ELSE TO 0.
C
C  BY RAMESH ORUGANTI
C
      IFLAG = 0
      PI    =  4.*ATAN(1.)
C
C  CHANGE THE POLARITY OF INITIAL CONDITIONS IF ISCR IS 2.
C
      IF(ISCR.NE.2)  GO TO 10
      AILONX= -AILON
      VCONX = -VCON
   10 IF(ISCR.NE.1)  GO TO 15
      AILONX=  AILON
      VCONX =  VCON
   15 CONTINUE
C
C  FOR THE TRANSISTOR CONDUCTION PERIOD CALCULATE R, PEAK CAPACITOR
C  VOLTAGE(VC1N) AND BETA.
C
      R     =  SQRT(AILONX**2 + (1.-VON-VCONX)**2)
      VC1N  =  R+1.-VON
      BETA  =  ATAN(AILONX/(VCONX-1.+VON))
      IF(BETA.LE.0.)  BETA=PI+BETA
C
C  CALCULATE THE SUBSEQUENT DIODE CONDUCTION ANGLE, ALPHA, BASED ON THE
C  CONTROL METHOD
C
C  MCON = 1  FREQUENCY CONTROL (ELAPSED INTERVAL)
C
      IF(MCON.NE.1)  GO TO 20
      ALPHA =  VALCON - BETA
      IF (ALPHA.GE.PI) GO TO 100
   20 CONTINUE
C
C  MCON = 2  ASDTIC CONTROL
C
      IF(MCON.NE.2)  GO TO 32
      ALPHA =  0.0
      AMIN  =  0.0
      AMAX  =  PI
      DO 30 I =  1,750
      VC2N  =  (VC1N-1.-VON)*COS(ALPHA)+1.+VON
      AIAVN =  (2.*VC1N-(VCONX+VC2N))/(ALPHA+BETA)
      IF(ABS(AIAVN-VALCON).LE.1.E-06) GO TO 58
      IF(AIAVN.LT.VALCON)  GO TO 25
      TEMP  =  ALPHA
      ALPHA =  ALPHA + (AMAX-ALPHA)*.05
      AMIN  =  TEMP
   25 IF(AIAVN.GT.VALCON)  GO TO 30
      TEMP  =  ALPHA
      ALPHA =  ALPHA - (ALPHA-AMIN)*.05
      AMAX  =  TEMP
   30 CONTINUE
   32 CONTINUE
C
```

```
C  MCON = 3  OPTIMAL TRAJECTORY CONTROL
C
      IF(MCON.NE.3)  GO TO 42
      ALPHA = 0.
      K   =  0
      IF((VC1N+1.-VON).GT.VALCON) GO TO 33
      K   =  1
      GO TO 42
  33  AMIN  =  0.
      AMAX  =  PI
      DO 40 I = 1,750
      VC2N  =  (VC1N-1.-VON)*COS(ALPHA)+1.+VON
      AIL2N =  -(VC1N-1.-VON)*SIN(ALPHA)
      DIST  =  SQRT(AIL2N**2+(VC2N+1.-VON)**2)
      IF(ABS(DIST-VALCON).LE.1.0E-06) GO TO 58
      IF (DIST.LT.VALCON) GO TO 34
      TEMP  =  ALPHA
      ALPHA =  ALPHA+(AMAX-ALPHA)*.05
      AMIN  =  TEMP
  34  IF (DIST.GT.VALCON) GO TO 40
      TEMP  =  ALPHA
      ALPHA =  ALPHA-(ALPHA-AMIN)*.05
      AMAX  =  TEMP
  40  CONTINUE
  42  CONTINUE
C
C  MCON = 4  DIODE ANGLE CONTROL
C
      IF(MCON.NE.4) GO TO 44
      ALPHA =  VALCON
  44  CONTINUE
C
C  MCON = 5  CAPACITOR VOLTAGE CONTROL
C
      IF(MCON.NE.5) GO TO 50
      IF(VC1N.GT.VALCON) GO TO 46
      ALPHA = 0.
      GO TO 58
  46  ALPHA = ARCOS((VALCON-1.-VON)/(VC1N-1.-VON))
  50  CONTINUE
C
C  MCON = 6  TRANSISTOR ANGLE CONTROL
C
      IF(MCON.NE.6) GO TO 58
      THETA1= VALCON-(PI/2)
      X     = 2*COS(THETA1)
      THETA2= ARCOS(X/(VC1N-1.-VON))
      ALPHA = PI-(THETA1+THETA2)
  58  CONTINUE
C
C  CALCULATE NEXT SWITCHING POINT INFORMATION, AIL2N AND VC2N.
C  RPRIM IS THE DIODE RADIUS AND GAMMA, AN ANGLE FOR PLOTTING
C  THE TRANSIENT TRAJECTORY.
C
      AIL2N =  -(VC1N-1.-VON)*SIN(ALPHA)
      VC2N  =  (VC1N-1.-VON)*COS(ALPHA)+1.+VON
      RPRIM =  R-2.*VON
      GAMMA =  PI-ALPHA
C
C  PLOT THE TRAJECTORY, IN TWO ARCS, DEPENDING ON ISCR VALUE.
C
      YC  =  0.
      IF (ISCR.NE.1) GO TO 60
      XC    =  1. - VON
      CALL ARC1(XC,YC,R,1,0.,BETA)
      XC    =  1. + VON
      CALL ARC1(XC,YC,RPRIM,2,GAMMA,PI)
  60  IF (ISCR.NE.2) GO TO 70
      XC    =  -1.+ VON
      CALL ARC1(XC,YC,R,2,0.,BETA)
      XC    =  -1.- VON
      CALL ARC1(XC,YC,RPRIM,1,GAMMA,PI)
C
C  IF ISCR IS 2, CHANGE POLARITY OF AIL2N AND VC2N.
C
      AIL2N = -AIL2N
      VC2N  = -VC2N
C
  70  RETURN
C
 100  IFLAG = 1
      RETURN
      END
```

Appendix B

Analysis Of SRC With Loss

In this appendix, the analysis of SRC with loss, for operation below resonant frequency, is presented. The mode boundaries and the dc characteristics are determined for each of the three modes of operation: type-1 DCM, type-2 DCM and CCM. Closed-form analytical expressions are derived for the dc characteristics in the cases of type-1 and type-2 DCMs. Computer algorithms based on the state-plane analysis were utilized to obtain steady-state results in the case of CCM. Sections B.1, B.2 and B.3 present the details of analysis. Section B.4 contains the computer programs used to generate the design curves, dc characteristics and the trajectories, shown in Chapter 3. Please refer to Secs. 2.0 and 3.0 for definitions of symbols used in this appendix.

B.1 Type - 2 DCM

Figure B.1 shows a type-2 DCM trajectory used for the analysis. First, the equations for the dc characteristics will be derived.

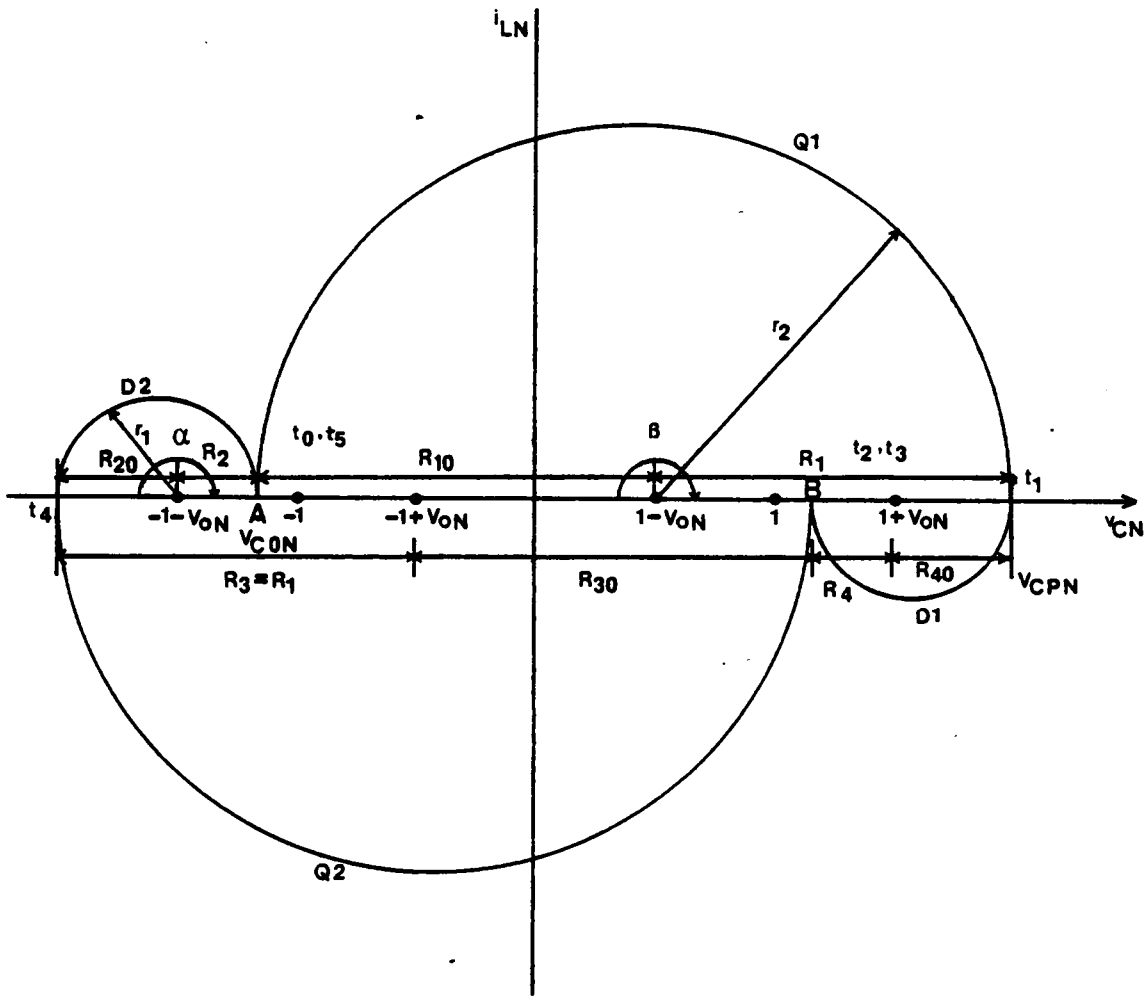

Figure B.1 Type-2 DCM operation with loss - Analysis diagram

$$\omega_N = \frac{\omega}{\omega_D} = \frac{2\pi}{T}\,\frac{1}{\omega_D} = \frac{2\pi}{T_N} \tag{B.1}$$

$$I_o = I_{LAV} = \frac{2}{T}\left[\int_{t_4}^{t_5} i_L\,dt + \int_0^{t_1} i_L\,dt\right] \tag{B.2}$$

Since $\int i_L\,dt = C\,\Delta v_C$,

$$I_o = I_{LAV} = \frac{2C}{T}\left[v_c/_{\text{at } t_5} - v_c/_{\text{at } t_4} + v_c/_{\text{at } t_1} - v_c/_{\text{at } t_0}\right] \tag{B.3}$$

Substituting for the values of v_C at the different instants from Fig. B.1 into (B.3),

$$I_o = I_{LAV} = \frac{4\,C\,V_{CP}}{T} \tag{B.4}$$

Normalizing (B.4) and using (B.1)

$$I_{oN} = I_{LAVN} = \left(2\,V_{CPN}\sqrt{1-\zeta^2}\right)\frac{\omega_N}{\pi} \tag{B.5}$$

To determine V_{CPN}, consider Fig. B.1 and (3.50).

$$\begin{aligned} R_3 = R_1 &= R_{20} + 2\,V_{oN} \\ &= \frac{R_2}{k} + 2\,V_{oN} \\ &= \frac{(2 - R_{10})}{k} + 2\,V_{oN} \\ &= \frac{\left(2 - \frac{R_1}{k}\right)}{k} + 2\,V_{oN} \end{aligned}$$

$$\text{Thus,} \quad R_1 = \frac{2\,k\,(1 + k\,V_{oN})}{1 + k^2} \tag{B.6}$$

Given ζ, parameter k in (B.6) is obtained using (3.51). Equation (B.6) determines the trajectory dimensions, given damping factor and output voltage. In [65], due to a typographical error, the term $(1 + k\,V_{oN})$ in (B.6) was written as $(1 + V_{oN})$.

From Fig. B.1,

$$V_{CPN} = 1 - V_{oN} + R_1 \tag{B.7}$$

Substituting for R_1 from (B.6) into (B.7),

$$V_{CPN} = \frac{1 - V_{oN} + 2k + k^2 + k^2 V_{oN}}{1 + k^2} \tag{B.8}$$

Substituting for V_{CPN} from (B.8) into (B.5),

$$I_{oN} = I_{LAVN} = \frac{1 - V_{oN} + 2k + k^2 + k^2 V_{oN}}{1 + k^2} \frac{2\omega_N\sqrt{1 - \zeta^2}}{\pi} \tag{B.9}$$

Equation (B.9) is the equation governing the dc characteristics of SRC in DCM-2 when losses are considered. At low ζ s, k is approximately equal to unity and (B.9) can be simplified to

$$I_{oN} = \frac{4\omega_N}{\pi} \tag{B.10}$$

which agrees with (A.78) for the lossless case.

Next, we will determine the region of occurrence of type-2 DCM. From Fig. B.1,

$$\alpha = \pi \tag{B.11}$$

$$\beta = \pi \tag{B.12}$$

In Sec. 3.2.2.1, it is shown that, for this case, the device conduction angles are also π. Thus,

$$\alpha_d = \pi \tag{B.13}$$

$$\alpha_q = \pi \tag{B.14}$$

Under CCM/DCM-2 boundary conditions the discontinuous intervals are zero and, thus, for DCM-2 operation

$$\omega_N = \frac{2\pi}{T_N} \leq \frac{2\pi}{2(\alpha_d + \alpha_q)} = 0.5 \tag{B.15}$$

Thus, DCM-2 occurs at $\omega_N \leq 0.5$ for the case with losses also.

Also, as V_{oN} is increased in Fig. B.1, the diode conduction radius R_{20} decreases. At a certain value of V_{oN} , R_{20} may be expected to become zero. Here the circuit operates in discontinuous mode without the antiparallel diode conducting at all. This, of course, is the type-1 DCM operation. From Fig. B.1,

$$R_{20} = R_1 - 2\,V_{oN} \tag{B.16}$$

Substituting for R_1 from (B.6) into (B.16),

$$R_{20} = \frac{2\,(k - V_{oN})}{1 + k^2} \tag{B.17}$$

As V_{oN} is increased, diode radius R_{20} becomes zero at $V_{oN} = k$. Thus, for DCM-2 operation

$$0 < \omega_N \leq 0.5 \text{ and} \tag{B.18}$$

$$0 \leq V_{oN} \leq k \tag{B.19}$$

B.2 Type-1 DCM

Consider the maximum energy trajectory, T_{UB} of Fig. 3.6. In this figure, the transistors are alternately switched on for conduction angles of π each and the operation frequency is ω_D. The closed trajectory contains the diode centers $(1 + V_{oN}, 0)$ and $(-1 - V_{oN}, 0)$.

Equation (3.57) indicates that radius $\hat{R}_1$ of the trajectory progressively decreases as V_{oN} increases in magnitude. Beyond a certain value of V_{oN} , which is to be determined, the trajectory in Fig. 3.6 will no longer contain the diode centers. Fig. B.2 shows such a trajectory.

In Fig. B.2, when operating frequency equals ω_D , the circuit operation is similar to that portrayed in Fig. 3.6. If, however, ω is reduced below ω_D , normal CCM operation, as in Fig. 3.4, does not occur. This is because at the end of conduction of a transistor (at point A or B of Fig. B.2), no diode trajectories are available for the circuit to automatically follow indicating that the antiparallel diode is also reverse biased. At these lower frequencies, dead times are created at points A and B with the trajectory remaining the same. As seen earlier, this corresponds to type-1 DCM operation.

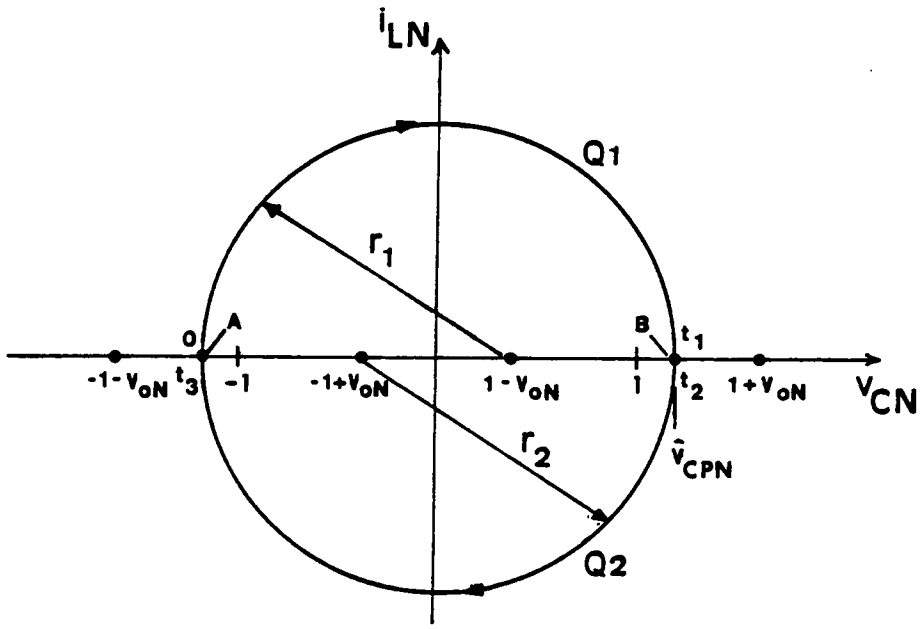

Figure B.2 Type-1 DCM operation with loss - Analysis diagram

First, let us determine the region of occurrence of this mode. From the previous discussion, the condition for type-1 DCM to occur is

$$V_{CPN} \leq 1 + V_{oN} \tag{B.20}$$

From Fig. B.2,

$$V_{CPN} = 1 - V_{oN} + R_1 \tag{B.21}$$

Thus,
$$1 - V_{oN} + R_1 \leq 1 + V_{oN} \tag{B.22}$$

Since the trajectories in Figs. B.2 and 3.6 are similar, the equation for R_1 is identical to that for $\hat{R}_1$ in (3.57). Substituting for R_1 from (3.57) into (B.22) and simplifying,

$$V_{oN} \geq k \tag{B.23}$$

In Sec. B.1 also, it was shown that the boundary between DCM-2 and DCM-1 occurs at $V_{oN} = k$ (see (B.19)). Thus, type-1 DCM occurs at all operating frequencies below ω_D, whenever V_{oN} is greater than k. For a given V_{oN} greater than or equal to k, Fig. B.2 represents all steady-state trajectories in the range $0 < \omega_N \leq 1$.

Next, we will derive the dc characteristics under this mode of operation. From Fig. B.2,

$$I_o = I_{LAV} = \frac{2}{T}\left[\int_0^{t_1} i_L \, dt + \int_{t_2}^{t_3} i_L \, dt \right] \tag{B.24}$$

By following similar steps as in Sec. B.1, it can be shown that (B.5) is valid for type-1 DCM also. Reproducing (B.5),

$$I_{oN} = I_{LAVN} = \left(2 V_{CPN} \sqrt{1 - \zeta^2}\right) \frac{\omega_N}{\pi} \tag{B.5}$$

Since Fig. B.2 and Fig. 3.6 are similar, the equation for V_{CPN} in Fig. B.2 will be the same as that for V_{CPN} in Fig. 3.6. Thus, from (3.58),

$$V_{CPN} = (1 - V_{oN}) \frac{1 + k}{1 - k} \tag{B.25}$$

Substituting for V_{CPN} from (B.25) into (B.5),

$$I_{oN} = I_{LAVN} = 2\,(1 - V_{oN})\,\sqrt{1 - \zeta^2}\,\frac{1 + k}{1 - k}\,\frac{\omega_N}{\pi} \qquad (B.26)$$

In (B.26) also, the term $\sqrt{1 - \zeta^2}$ is very close to unity and may be dropped without significantly affecting the result. Equation (B.26) shows that in type-1 DCM operation, I_{oN} linearly decreases to zero as V_{oN} approaches unity.

B.3 CCM

All trajectories in Fig. 3.4, other than the innermost one marked DCM-2, belong to CCM operation below resonance. Unlike the ideal lossless CCM analysis of Appendix A, closed-form expressions for design parameters, such as output dc current and device average currents, as functions of R and V_{oN} cannot be found in this case. A computer algorithm to numerically obtain these parameter values will be presented here. Figure B.3 shows a single CCM steady-state trajectory which will be utilized in the development of the algorithm.

First, let us determine the range of R for which Fig. B.3 is valid. As R is reduced, the type-2 DCM trajectory of Fig. B.1 is reached. For CCM operation, R is greater than R_1 of Fig. B.1. From (B.6),

$$R \geq \frac{2\,k\,(1 + k\,V_{oN})}{1 + k^2} \qquad (B.27)$$

Next, as R is increased, the trajectory T_{UB} of Fig. 3.6 is reached. For CCM operation below resonant frequency, R is less than $\hat{R}_1$ of Fig. 3.6. From (3.57),

$$R \leq \frac{2\,k\,(1 - V_{oN})}{1 - k} \qquad (B.28)$$

Thus,
$$\frac{2\,k\,(1 + k\,V_{oN})}{1 + k^2} \leq R \leq \frac{2\,k\,(1 - V_{oN})}{1 - k} \qquad (B.29)$$

for CCM operation below resonance.

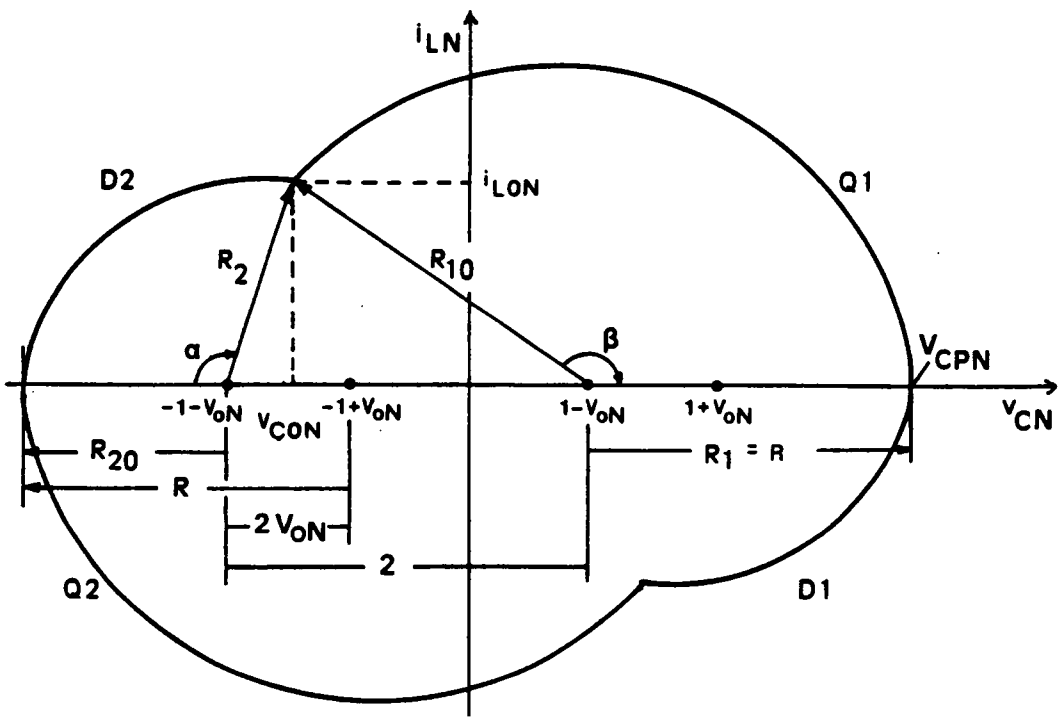

Figure B.3 CCM operation below resonance with loss - Analysis diagram

Next, we will derive equations which are used in the computer algorithm. Equations (B.30) to (B.38) are based on Fig. B.3.

$$R_{20} = R - 2\,V_{oN} \tag{B.30}$$

$$R_{10} = \sqrt{R_2^2 + 4 + 4\,R_2\,\cos\alpha} \tag{B.31}$$

$$\beta = \pi - \cos^{-1}\left(\frac{R_2^2 - R_{10}^2 - 4}{4\,R_{10}}\right) \tag{B.32}$$

$$I_{LON} = R_{10}\,\sin\beta \tag{B.33}$$

$$V_{CON} = 1 - V_{oN} + R_{10}\,\cos\beta \tag{B.34}$$

$$V_{CPN} = 1 - V_{oN} + R_1 = 1 - V_{oN} + R \tag{B.35}$$

Also, $$T_N = 2\,(\alpha_d + \alpha_q) \tag{B.36}$$

Thus, $$\omega_N = \frac{2\pi}{T_N} = \frac{\pi}{\alpha_d + \alpha_q} \tag{B.37}$$

$$\begin{aligned} I_{DAV} &= \frac{1}{T}\left[\int_0^{t_1} i_L\,dt\right] \\ &= \frac{C\,(V_{C0} + V_{CP})}{T} \end{aligned} \tag{B.38}$$

Normalizing (B.38) and using (B.36),

$$I_{DAVN} = \frac{(V_{CON} + V_{CPN})\sqrt{1 - \zeta^2}}{2\,(\alpha_d + \alpha_q)} \tag{B.39}$$

Similarly, $$I_{QAVN} = \frac{(-V_{CON} + V_{CPN})\sqrt{1 - \zeta^2}}{2\,(\alpha_d + \alpha_q)} \tag{B.40}$$

Also, $$\begin{aligned} I_{oN} = I_{LAVN} &= 2\,(I_{DAVN} + I_{LAVN}) \\ &= \frac{2\,V_{CPN}\sqrt{1 - \zeta^2}}{\alpha_d + \alpha_q} \end{aligned} \tag{B.41}$$

The factor $\sqrt{1-\zeta^2}$ in (B.39), (B.40) and (B.41), is very close to unity and may be dropped without significantly affecting the results.

The block diagram of the computer program that determines the steady-state parameters, given R, ζ and V_{oN} is shown in Fig. B.4. This computer algorithm is based on the trajectory equations of Sec. 3.2.2 and on (B.30) to (B.41). A brief description of the program is given below.

Given R, the value of R_{20} is known through (B.30). Angle α in Fig. B.3 is, then, assumed to be between 0 and π.

Knowing R_{20} and α, R_2 is calculated utilizing damped trajectory equation (3.44). From R_2 and α, R_{10} is next computed using (B.31). The value of β is then calculated from (B.32). Finally, from R_{10} and β, R_1 is calculated utilizing trajectory equation (3.44). From Fig. B.3, due to symmetry, R_1 must equal the value of given R. The value of α is iteratively adjusted by the program such that R_1 equals R within the the specified tolerance. This completes the determination of the steady-state trajectory.

From the final values of the state-plane trajectory angles α and β, the conduction angles of the diode and transistor α_d and α_q are determined by (3.41) and (3.42). The state variables at switching point, I_{L0N} andV_{C0N}, are computed using (B.33) and (B.34), respectively. The peak capacitor voltage is obtained through (B.35). Currents I_{DAVN}, I_{QAVN} and I_{LAVN} are obtained from (B.39), (B.40) and (B.41), respectively. The operating frequency ω_N corresponding to this given trajectory is obtained from (B.37) knowing the conduction angles α_d and α_q. The computer program using this algorithm is listed in Sec. B.4.

If ω_N^*, ζ and V_{oN} are the given parameters instead of R, ζ and V_{oN}, then the following procedure is adopted (Fig. B.5). The value of R is chosen within thte range specified by (B.29). The algorithm shown in Fig. B.4 is then used to obtain the solution with given ζ and V_{oN} and assumed R. The frequency ω_N is calculated for this steady-state solution and compared with ω_N^*. The value of R is iteratively adjusted such that $\omega_N = \omega_N^*$ with specified tolerance. Section B.4 lists a program which uses this algorithm.

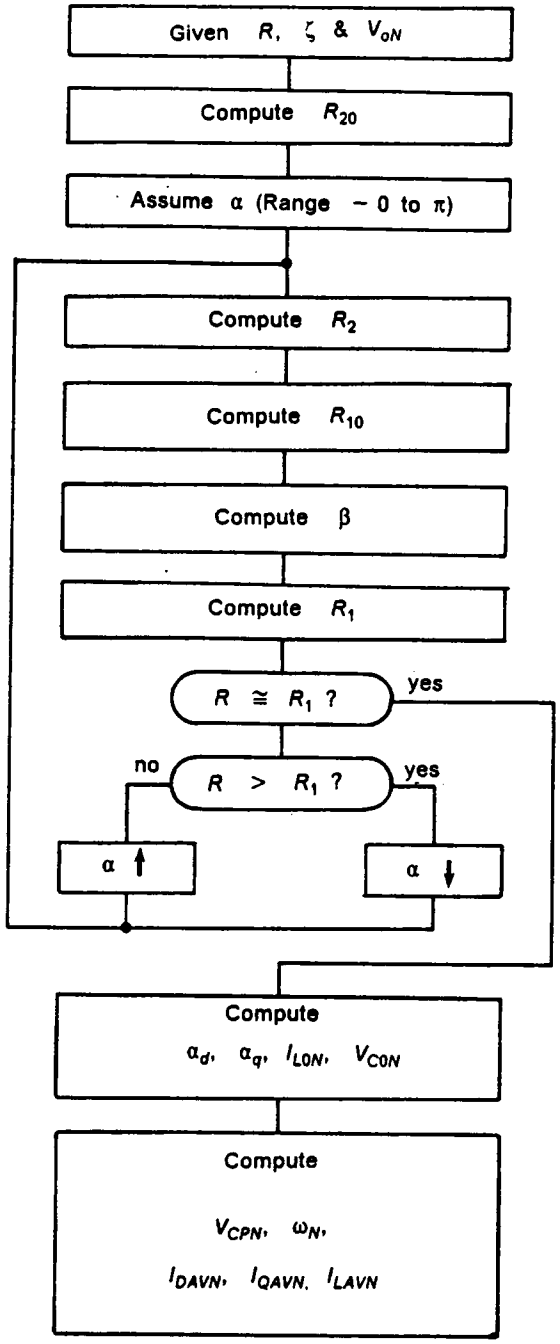

Figure B.4 CCM analysis with loss given R, ζ, and V_{oN} - computer flowchart

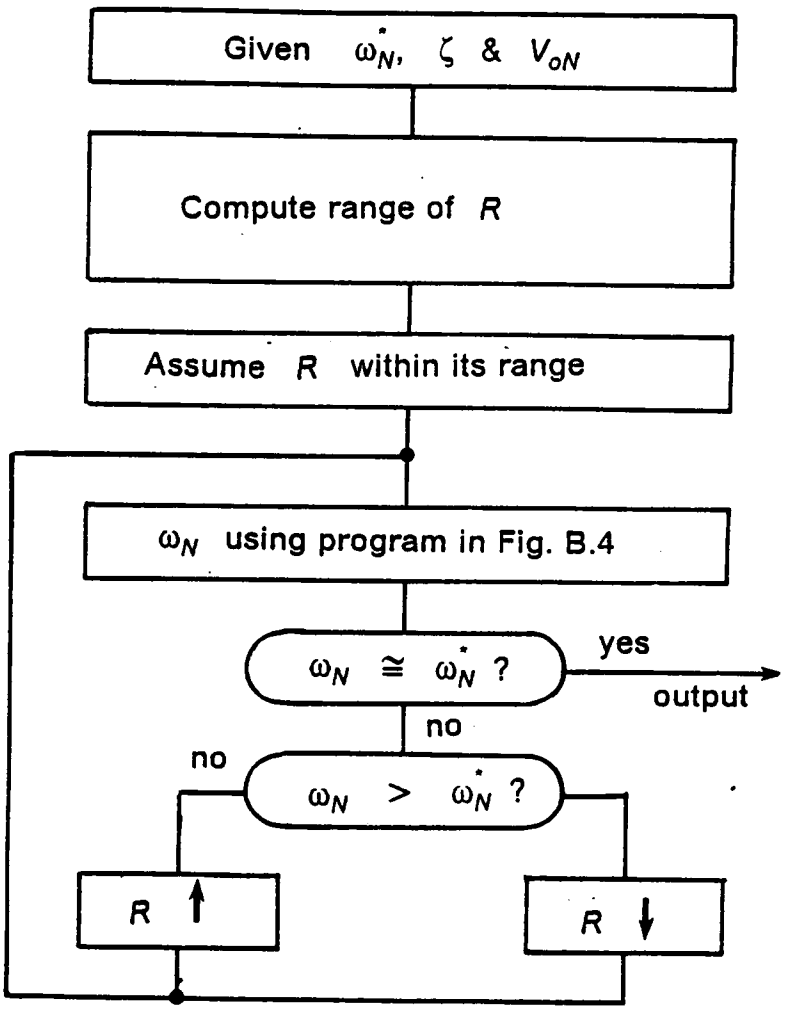

Figure B.5 CCM analysis with loss given ω_N, ζ and V_{oN} - computer flowchart

B.4 Program Listings

Please note that the symbols used for the various parameters in the programs may differ from those used in the equations of the previous sections of this appendix.

B.4.1 CCM Analysis Below Resonance

```
C  LIMITED DC ANALYSIS OF SERIES RESONANT CONVERTER WITH LOSSES
C
C  THE PROGRAM COMPUTES THE VARIOUS DESIGN PARAMETERS OF SERIES
C  RESONANT CONVERTER, SUCH AS NORMALIZED AVERAGE TRANSISTOR CURRENT,
C  AIQAVN, ETC., AS A FUNCTION OF NORMALIZED FREQUENCY, OMEGAN,
C  WITH NORMALIZED OUTPUT VOLTAGE AS A PARAMETER.
C  THE OPERATING MODE IS THE CONTINUOUS CONDUCTION MODE.
C  ONLY OPERATING FREQUENCIES LESS THAN RESONANCE ARE CONSIDERED.
C  WHEN CHOOSING THE HIGHEST VALUE OF VON, IT MUST BE ENSURED THAT
C  THE CIRCUIT IS STILL IN THE CCM MODE.
C  PROGRAM USES THE SER2 SUBROUTINE TO CALCULATE THE PARAMETERS AND
C  RANGE SUBROUTINE TO COMPUTE THE RANGE OF RADIUS, RPR.
C
C  BY RAMESH ORUGANTI
C
        VON   = .0
C
      DO 200 I = 1, 10
C
C  IF ZETA IS ZERO USE THE CC PART.
C
        ZETA = 0.025
        CALL RANGE(ZETA,VON,RPRMIN,RPRMAX)
        IF (RPRMAX.GT.20.) RPRMAX = 20.
C
CC      ZETA   = 0.
CC      RPRMIN = 1. + VON
CC      RPRMAX = 15.
        STEP   = (RPRMAX - RPRMIN)/80.
        RPR    = RPRMIN
C
      DO 100 K  = 1,81
        CALL SER2(RPR,VON,ZETA,OMEGAN,VCPN,AILAVN,AIQAVN,AIDAVN,
     *          R1PRO,VCON,AILON,ALPD,ALPQ)
        VCONMD = -VCON
        WRITE (6,9010) OMEGAN,ALPQ
 9010   FORMAT (2E14.5)
        RPR    = RPRMIN + FLOAT(K)*STEP
  100 CONTINUE
        VON  =  VON + .1
C
  200 CONTINUE
      STOP
      END
```

B.4.2 DC Characteristics Given Operating Frequency

```
C  A PROGRAM TO COMPUTE THE DC CHARACTERISTICS OF SERIES RESONANT
C  CONVERTER--OUTPUT CURRENT(AILAVN) VS OUTPUT VOLTAGE(VON) WITH
C  FREQUENCY AS PARAMETER--AT FREQUENCIES BELOW RESONANCE.  THE
C  PROGRAM TAKES INTO ACCOUNT THE LOSSES IN THE CIRCUIT(ZETA).  THE
C  TWO DCM MODES 1.WHEN OMEGAN<0.5 AND 2. WHEN VON > S ARE ALSO
C  COSNIDERED.  S IS A FACTOR DEPENDENT ON THE DAMPING FACTOR ZETA
C  AND HAS BEEN CALLED 'K' IN THE REPORT.
C
C  PROGRAMMED BY RAMESH ORUGANTI
C
        PI     =  4.*ATAN(1.)
        ZETA   =  0.025
        OMIN   =  0.1
        STEP1  =  0.1
```

```
          OMEGAR  =  0.1
          S1      =  SQRT(1.-ZETA**2)
          S       =  EXP(-ZETA*PI/SQRT(1.-ZETA**2))
C
      DO  500  I  =  1,7
          VONMIN  =  0.0
          VONMAX  =  S - 1.0E-02
          VON     =  VONMIN
          STEP2   =  (VONMAX - VONMIN)/20.
C
      DO  300  J  =  1, 21
          CALL RANGE(ZETA,VON,RPRMIN,RPRMAX)
          RPR     =  RPRMIN
          STEP3   =  (RPRMAX - RPRMIN)/2.
          IF(OMEGAR.LE.0.5)  GO TO 220
C
      DO  200  K  =  1,500
          CALL SER2(RPR,VON,ZETA,OMEGAN,VCPN,AILAVN,AIQAVN,AIDAVN,
     *                R1PRO,VCON,AILON,ALPD,ALPQ )
          ERROR   =  OMEGAR - OMEGAN
          IF (ABS(ERROR).LT.1.E-04) GO TO 240
          CALL AGAIN2(RPRMIN,RPRMAX,R1,R2,RPR,W1,OMEGAN,OMEGAR,K)
  200 CONTINUE
C
          K       =  99888
          WRITE(6,*) K
          STOP
C
  220     OMEGAN  =  OMEGAR
          AILAVN  =  ((1.-VON+2.*S+S**2+VON*S**2)*S1/(1.+S**2))
     *                    * 2. * OMEGAN/PI
  240     WRITE(6,9010) VON,AILAVN
          VON     =  VONMIN  + FLOAT(J)*STEP2
  300 CONTINUE
C
          VONMIN  =  S
          VONMAX  =  0.99999
          VON     =  VONMIN
          STEP4   =  (VONMAX-VONMIN)/20.
          OMEGAN  =  OMEGAR
C
      DO  400  L  = 1,21
          AILAVN  =  2.*(1.-VON)*S1*((1.+S)/(1.-S))*OMEGAN/PI
          WRITE (6,9010) VON,AILAVN
          VON     =  VONMIN + FLOAT(L)*STEP4
  400 CONTINUE
C
      OMEGAR      =  OMIN  +  FLOAT(I) * STEP1
  500 CONTINUE
C
 9010     FORMAT (2E14.5)
C
      STOP
      END
```

B.4.3 Trajectory Plots - State Portrait

```
C  STATE-PORTRAIT OF SRC WITH LOSSES
C
C  MAIN PROGRAM TO DRAW THE STATE-PORTRAIT FOR SERIES RESONANT
C  CONVERTER WHEN LOSSES ARE INCLUDED. PARAMETERS TO BE INPUTTED
C  ARE  OUTPUT VOLTAGE, VON AND DAMPING FACTOR, ZETA.
C  THE PROGRAM USES THE PLOTTING SUBROUTINES AVAILABLE TO ACCESS
C  VERSATEC AND CALCOMP PLOTTERS AND THE PLOT 10 PREVIEW PACKAGE
C  AND ALSO THE CIRCLE SUBROUTINE AVAILABLE AT VPI.
C  ADDITIONALLY THE PROGRAM USES THE FAMIL2 SUBROUTINE.
C
C  BY RAMESH ORUGANTI
C
      CALL PLOTS(0,0,50)
C
C  ENTER VOLTAGE, VON, DAMPING FACTOR, ZETA
C
      VON   =  0.5
      ZETA  =  1/30.
C
C  ENTER SCALE FACTOR, S
C
      S     =  0.8
```

```
      CALL FACTOR(S)
C
      CALL PLOT(1.,1.,-3)
C
C  CHOOSE PEN THICKNESS FOR THE AXES
C
      CALL NEWPEN(2)
C
C  PLOT AXES
C
      CALL AXIS(0.,5.,68H
     *                  VCN,-68,10.,0.,-10.,2.)
      CALL AXIS(5.,0.,68H
     *                  ILN,+68,10.,90.,-10.,2.)
      CALL PLOT(5.,5.,-3)
      S1    = S/2.
      CALL FACTOR(S1)
C
C  CHOOSE PEN THICNESS FOR MARKING TOPOLOGICAL CENTERS.
C
      CALL NEWPEN(5)
C
C  MARK TOPOLOGICAL CENTERS
C
      XC    = -1. - VON
      CALL CIRCLE(XC,0.,.05)
      XC    = -1. + VON
      CALL CIRCLE(XC,0.,.05)
      XC    =  1. - VON
      CALL CIRCLE(XC,0.,.05)
      XC    = 1. + VON
      CALL CIRCLE(XC,0.,.05)
C
C  CHOOSE PEN THICKNESS FOR DRAWING THE STATE-TRAJECTORIES
C
      CALL NEWPEN (2)
C
C  DRAW THE TRAJECTORIES
C
      YC    = 0.
      XC    = -1. - VON
      CALL FAMIL2(XC,YC,1,ZETA)
      XC    = -1. + VON
      CALL FAMIL2(XC,YC,4,ZETA)
      XC    =  1. - VON
      CALL FAMIL2(XC,YC,2,ZETA)
      XC    =  1. + VON
      CALL FAMIL2(XC,YC,3,ZETA)
C
      CALL PLOT(12.,0.,999)
      STOP
      END
```

B.4.4 Trajectory Plots - Steady State

```
C  STEADY-STATE TRAJECTORIES OF SRC WITH LOSSES
C
C  MAIN PROGRAM TO DRAW 1)FAMILY OF STEADY-STATE TRAJECTORIES
C  2)SWITCHING BOUNDARY FOR SRC UNDER LOSSES WHEN VON AND ZETA ARE
C  GIVEN. THE PROGRAM ALSO GENERATES THE PLOT OF THE SWITCHING
C  BOUNDARY UNDER LOSS-LESS CONDITIONS FOR COMPARISON.
C  THE PROGRAM USES THE PLOTTING SUBROUTINES AVAILABLE TO ACCESS
C  VERSATEC AND CALCOMP PLOTTERS AND THE PLOT 10 PREVIEW PACKAGE
C  AND ALSO THE CIRCLE SUBROUTINE AVAILABLE AT VPI.
C  ADDITIONALLY THE PROGRAM USES THE EQUIL2 AND RANGE SUBROUTINES
C
C  BY RAMESH ORUGANTI VPI&SU, BLACKSBURG, VA
C
      DIMENSION X(500),Y(500),X1(50),Y1(50),X2(50),Y2(50)
      CALL PLOTS(0,0,50)
C
C  ENTER VOLTAGE, VON, DAMPING FACTOR, ZETA
C
      VON   = 0.5
      ZETA  = 1/30.
C
C  ENTER SCALE FACTOR, S
C
      S     =  0.8
```

```
      CALL FACTOR(S)
C
      CALL PLOT(1.,1.,-3)
C
C  CHOOSE PEN THICKNESS FOR THE AXES
C
      CALL NEWPEN(2)
      CALL AXIS(0.,5.,68H
     *                  VCN,-68,10.,0.,-10.,2.)
      CALL AXIS(5.,0.,68H
     *                  ILN,+68,10.,90.,-10.,2.)
      CALL PLOT(5.,5.,-3)
      S1    =  S/2.
      CALL FACTOR(S1)
C
C  CHOOSE PEN THICNESS FOR MARKING TOPOLOGICAL CENTERS.
C
      CALL NEWPEN(5)
C
C  MARK TOPOLOGICAL CENTERS
C
      XC    =  -1. - VON
      CALL CIRCLE(XC,0.,.05)
      XC    =  -1. + VON
      CALL CIRCLE(XC,0.,.05)
      XC    =   1. - VON
      CALL CIRCLE(XC,0.,.05)
      XC    =  1. + VON
      CALL CIRCLE(XC,0.,.05)
C
C  COMPUTE MINIMUM AND MAXIMUM VALUES OF RADIUS, RPR
C
      CALL RANGE(ZETA,VON,RPRMIN,RPRMAX)
C
C  CHOOSE PEN THICKNESS FOR THE STEADY-STATE TRAJECTORIES
C
      CALL NEWPEN(5)
C
C  PLOT THE STEADY-STATE TRAJECTORIES
C
      RPR     =  RPRMIN
      M    =  1
      DO 100 K = 1,48
      L   =  0
      IF(M.EQ.1) L = 1
      CALL EQUIL2(RPR,VON,ZETA,OMEGAN,VCPN,AILAVN,AIQAVN,AIDAVN,
     *           R1PRO,VCON,AILON,ALPD,ALPQ,K,L)
      X1(K)  =  VCON
      Y1(K)  =  AILON
      X2(K)  =  -VCON
      Y2(K)  =  -AILON
      RPR   =  RPR + .25
      IF(K.EQ.3) RPR = 2.
      M    =  M+1
      IF(M.EQ.5) M = 1
      IF (RPR.LT.RPRMAX)  GO TO 100
      RPR = RPRMAX
  100 CONTINUE
C
C  CHOOSE PEN THICKNESS FOR SWITCHING BOUNDARIES
C
  110 CALL NEWPEN(5)
C
C  DRAW SWITCHING BOUNDARIES WITH LOSSES
C
      DO 200 L = 1,48
      IF(L.EQ.1) CALL PLOT(X1(1),Y1(1),3)
      CALL PLOT (X1(L),Y1(L),2)
  200  CONTINUE
C
      DO 210 L = 1,48
      IF (L.EQ.1) CALL PLOT(X2(1),Y2(1),3)
      CALL PLOT(X2(L),Y2(L),2)
  210  CONTINUE
C
C DRAW SWITCHING BOUNDARIES WIHOUT LOSSES
C
      RMIN   =  1.+VON
      RMAX   =  10.5
      RSTEP = 0.05
C
      DO 30 I = 1,500
      R     =   RMIN +FLOAT(I-1) * RSTEP
      IF (R.GT.(RMAX+.01)) GO TO 40
```

```
      X(I) =  -VON * (R+1.-VON)
      Y(I) =  SQRT((1.-VON**2) * ((R-VON)**2 - 1.))
      IF (I.EQ.1)  CALL PLOT(X(1),Y(1),3)
      CALL PLOT (X(I),Y(I),2)
   30 CONTINUE
C
   40 DO 50 I = 1,500
      R    =  RMIN + FLOAT(I-1) * RSTEP
      IF (R.GT.(RMAX+.01)) GO TO 60
      X(I) = -X(I)
      Y(I) = -Y(I)
      IF (I.EQ.1) CALL PLOT(X(1),Y(1),3)
      CALL PLOT (X(I),Y(I),2)
   50 CONTINUE
   60 CONTINUE
C
      CALL PLOT(12.,0.,999)
      STOP
      END
```

B.4.5 Trajectory Plots - Steady-State Given Frequency

```
C  SRC STEADY-STATE TRAJECTORY WITH LOSS GIVEN FREQUENCY
C
C  PLOTS THE CORRESPONDING CCM STEADY-STATE TRAJECTORY BELOW
C  RESONANCE WHEN FREQUENCY, OMEGAR, OUPUT VOLTAGE, VON
C  DAMPING FACTOR, ZETA ARE GIVEN.
C  THE PROGRAM USES THE PLOTTING SUBROUTINES AVAILABLE TO ACCESS
C  VERSATEC AND CALCOMP PLOTTERS AND THE PLOT 10 PREVIEW PACKAGE
C  AND ALSO THE CIRCLE SUBROUTINE AVAILABLE AT VPI.
C  ADDITIONALLY THE PROGRAM USES THE EQUIL2, RANGE AND AGAIN1
C  SUBROUTINES.
C
C  BY RAMESH ORUGANTI AT VPI&SU, BLACKSBURG, VA
C
      CALL PLOTS(0,0,50)
C
C  ENTER VOLTAGE, VON, DAMPING FACTOR, ZETA, FREQUENCY, OMEGAR
C
      VON   =  0.5
      ZETA  =  1/30.
      OMEGAR =  .7044389
C
C  ENTER SCALE FACTOR, S
C
      S     =   0.8
      CALL FACTOR(S)
C
      CALL PLOT(1.,1.,-3)
C
C  CHOOSE PEN THICKNESS FOR THE AXES
C
      CALL NEWPEN(2)
C
C  PLOT AXES
C
      CALL AXIS(0.,5.,68H
     *                  VCN,-68,10.,0.,-10.,2.)
      CALL AXIS(5.,0.,68H
     *                 ILN,+68,10.,90.,-10.,2.)
      CALL PLOT(5.,5.,-3)
      S1    =  S/2.
      CALL FACTOR(S1)
C
C  CHOOSE PEN THICKNESS FOR MARKING TOPOLOGICAL CENTERS.
C
      CALL NEWPEN(5)
C
C  MARK TOPOLOGICAL CENTERS
C
      XC   =  -1. - VON
      CALL CIRCLE(XC,0.,.05)
      XC   =  -1. + VON
      CALL CIRCLE(XC,0.,.05)
      XC   =   1. - VON
      CALL CIRCLE(XC,0.,.05)
      XC   =  1. + VON
      CALL CIRCLE(XC,0.,.05)
C
```

```
C  COMPUTE MINIMUM AND MAXIMUM VALUES OF RADIUS, RPR
C
      CALL RANGE(ZETA,VON,RPRMIN,RPRMAX)
C
C  OBTAIN PARAMETERS OF THE STEADY-STATE TRAJECTORY CORRESPONDING TO
C  OMEGAR ITERATIVELY. THE LAST ZERO ENTRY IN EQUIL SUBROUTINE
C  ENSURES THAT THESE ITERATIONS ARE NOT PLOTTED
C
      RPR    =  RPRMIN
      STEP   =  1.
      DO 120 I = 1, 30
      CALL EQUIL(RPR,VON,ZETA,OMEGAN,VCPN,AILAVN,AIQAVN,AIDAVN,
     *           R1PRO,VCON,AILON,ALPD,ALPQ,0,0)
      ERROR  =  OMEGAR -OMEGAN
      CALL AGAIN1(ERROR,RPRMIN,RPRMAX,RPR,STEP)
  120 CONTINUE
C
C  CHOOSE PEN THICKNESS FOR STEADY-STATE TRAJECTORY
C
      CALL NEWPEN(5)
C
C PLOT THE STEADY-STATE TRAJECTORY. THE LAST 1 ENTRY IN THE EQUIL
C SUBROUTINE ENABLES THE PLOTTING.
C
      CALL EQUIL(RPR,VON,ZETA,OMEGAN,VCPN,AILAVN,AIQAVN,AIDAVN,
     *           R1PRO,VCON,AILON,ALPD,ALPQ,0,1)
      CALL PLOT(12.,0.,999)
      STOP
      END
```

B.4.6 Subroutines

```
      SUBROUTINE RANGE(Z,VON,RPRMIN,RPRMAX)
C
C  SUBROUTINE RANGE DETERMINES THE RANGE OF THE RADIUS RPR (MINIMUM
C  AND MAXIMUM) WHEN THE DAMPING FACTOR, Z, AND THE NORMALIZED
C  OUTPUT VOLTAGE, VON, ARE GIVEN.
C
C  BY RAMESH ORUGANTI
C
         PI     =  4.*ATAN(1.)
         S      =  EXP(-Z*PI/SQRT(1.-Z**2))
         RPRMIN =  2.*S*(1.-VON)/(1-S)
         RPRMAX =  2*S*(1.+(S*VON))/(1.+S**)
      RETURN
      END
C
      SUBROUTINE SER2(RPR,VON,ZETA,OMEGAN,VCPN,AILAVN,AIQAVN,AIDAVN,
     *                R1PRO,VCON,AILON,ALPD,ALPQ)
C
C  THIS SUBPROGRAM CALCULATES THE VARIOUS PARAMETERS OF A CCM
C  STEADY-STATE TRAJECTORY OF SRC BELOW RESONANCE
C  WHEN RADIUS, RPR, OUTPUT VOLTAGE, VON,
C  AND DAMPING FACTOR, ZETA ARE GIVEN. THE PROGRAM RETURNS OPERATING
C  FREQUENCY, OMEGAN, PEAK CAP VOLTAGE, VCPN, INDUCTOR AV CURRENT,
C  AILAVN, TRANS AV CUR, AIQAVN, DIODE AV CUR, AIDAVN, INITIAL RADIUS,
C  R1PRO, INITIAL CAP VOLT, VCON, INITIAL IND CUR, AILON, DIODE
C  COND ANGLE, ALPD, AND TRANS COND ANGLE, ALPQ.
C  THE PROGRAM UTILIZES SUBROUTINES AGAIN1, RECT AND A.
C
C  PROGRAMMED BY RAMESH ORUGANTI
C
         PI     =  4.*ATAN(1.)
         APRMIN =  0.
         APRMAX =  PI
         ALPHPR =  APRMIN
         STEP   =  PI/2.
         S1     =  SQRT(1.-ZETA**2)
         S      =  -ZETA/SQRT(1.-ZETA**2)
         R2PRO  =  RPR - 2.*VON
C
      DO 100 I = 1,100
         R2PR   =  (R2PRO/SQRT(1.-ZETA*SIN(2.*ALPHPR)))*
     *                EXP(S*(A(ALPHPR,ZETA) - A(0.,ZETA)))
         R1PRO  =  SQRT(R2PR**2+4.+4.*R2PR*COS(ALPHPR))
         ABPR   =  (R2PR**2-R1PRO**2-4.)/(4.*R1PRO)
         IF (ABPR.LE.-1.) GO TO 70
         IF (ABPR.GE.1.) GO TO 80
         BPR    =  ARCOS(ABPR)
```

```
      GO TO 90
C
   70 BPR    =  +1.*PI
      GO TO 90
C
   80 BPR    =  0.0
C
   90 BPRO   =  PI - BPR
C
      R1PR   =  (R1PRO*SQRT(1.-ZETA*SIN(2.*BPRO)))*
     *                EXP(S*(A(PI,ZETA) - A(BPRO,ZETA)))
      ERROR  =  R1PR - RPR
      IF(ABS(ERROR).LT.1.E-6) GO TO 200
      CALL AGAIN1(ERROR,APRMIN,APRMAX,ALPHPR,STEP)
  100 CONTINUE
  200 ALPD  =  A(ALPHPR,ZETA) - A(0.,ZETA)
      ALPQ   =  A(PI,ZETA) - A(BPRO,ZETA)
      OMEGAN =  PI/(ALPD+ALPQ)
      VCPN   =  1. -VON + R1PR
      AILAVN =  2.*VCPN*S1/(ALPD + ALPQ)
      XC     =  1. - VON
      B1PRO  =  PI+BPRO
      CALL RECT(VCON,AILON,XC,0.,R1PRO,B1PRO)
      AIQAVN  = (VCPN-VCON)*S1/(2.*(ALPD+ALPQ))
      AIDAVN  = (VCPN+VCON)*S1/(2.*(ALPD+ALPQ))
C
      RETURN
      END
C
      SUBROUTINE RECT(X,Y,XC,YC,R,A)
C
C  CALCULATES RECTANGULAR COORDINATES, X, Y, GIVEN DISTANCE FROM CENTER,
C  R, AND ANGLE, A,  AND THE COORDINATES, XC, YC, OF THE CENTER.
C
C  BY RAMESH ORUGANTI
C
      X      =  XC+R*COS(A)
      Y      =  YC-R*SIN(A)
      RETURN
      END
C
      FUNCTION  A(APR,ZETA)
C
C  CALCULATES CONDUCTION ANGLE, A, ON THE TRANSFORMED PLANE
C  ((X1-X2) IN THE REPORT) GIVEN ANGLE APR ON THE VCN-ILN PLANE AND
C  DAMPING FACTOR, ZETA.
C
C  BY RAMESH ORUGANTI
C
      PI     =  4.*ATAN(1.)
      IF (ABS(APR-PI/2.).LT.1.E-03) GOTO 10
      A  =  ATAN(-ZETA/SQRT(1.-ZETA**2) + TAN(APR)/SQRT(1.-ZETA**2))
      IF (A.LT.0.AND.APR.GT.PI/4.)  A=PI+A
      SAVERETURN
   10 A      =  APR
      RETURN
      END
C
      SUBROUTINE AGAIN1(E,AMIN,AMAX,A,STEP)
C
C  THIS SUBROUTINE COMPUTES THE NEW VALUE OF THE INDEPENDENT
C  VARIABLE, A, SO THAT THE CONVERGENCE OF DEPENDENT VARIABLE, W,
C  TO THE DESIRED VALUE, WN, IS ACHIEVED IN THE MAIN PROGRAM.
C  GIVEN AMIN, AMAX THE MINIMUM AND MAXIMUM VALUES OF A, THE
C  PREVIOUS ERROR E, AND THE ABSOLUTE MAXIMUM ALLOWABLE STEP IN A,
C  STEP, AND THE CURRENT VALUE OF A, A, THE PROGRAM RETURNS THE
C  NEW VALUE OF A, A, USING SIMPLE 'HALVING' TECHNIQUE.THIS SUBROUTINE
C  IS FOUND TO TAKE MORE ITERATIONS THAN AGAIN2.
C
C  BY RAMESH ORUGANTI
      IF(E.LT.0.) GO TO 50
C
      H      =  (AMAX-A)/2.
      IF(H.GT.STEP)  H = STEP
      AMIN   =  A
      A      =  A + H
      GO TO 100
C
   50 H      =  (A-AMIN)/2.
      IF(H.GT.STEP) H = STEP
      AMAX   =  A
      A      =  A - H
C
  100 CONTINUE
```

```
      RETURN
      END
C
      SUBROUTINE AGAIN2 (RMIN,RMAX,R1,R2,R,W1,W2,WN,K)
C
C  THIS SUBROUTINE ATTEMPTS TO IMPROVE CONVERGENCE OVER AGAIN1 BY
C  CHOOSING LINEAR INTERPOLATION TECHNIQUE.
C
C  BY RAMESH ORUGANTI
C
      IF (K.EQ.1) GO TO 110
      IF(ABS(W1-W2).GT.1.0E-09) GO TO 100
      I       =   99999
      WRITE(6,*)RMIN,RMAX,R,W2,I
      STOP
  100 R       =  R2 + (R1-R2)*(WN-W2)/(W1-W2)
      STEP    =  (RMAX-RMIN)/5.
      RX      =  R2+STEP
      RY      =  R2-STEP
      IF(R.GT.RX) R = RX
      IF(R.LT.RY) R = RY
      IF (R.GT.RMAX) R = RMAX
      IF (R.LT.RMIN) R = RMIN
      R1      =  R2
      R2      =  R
      W1      =  W2
      RETURN
  110 R1      =  R
      R       =  RMIN+(RMAX-RMIN)/5.
      R2      =  R
      W1      =  W2
      RETURN
      END
C
      SUBROUTINE FAMIL2(XC,YC,IDEV,ZETA)
C
C  PLOTS A FAMILY OF TRAJECTORIES CORRESPONDING TO A DEVICE CONDUCTION
C  IN SERIES RESONANT CONVERTER WHEN LOSSES ARE INCLUDED GIVEN
C  CORRESPONDING MODE CENTER (XC, YC), THE DEVICE # IDEV AND THE
C  DAMPING FACTOR, ZETA. THE MINIMUM, MAXIMUM AND THE STEP OF THE
C  RADIUS, RPR, CAN BE ALTERED IN THE SUBPROGRAM AS REQUIRED.
C  USES SUB-ROUTINE ARC2.
C
C  BY RAMESH ORUGANTI
C
      RPRMIN =  1.
      RPRMAX =  9.
      STEP   =  1.0
      PI     =  4.*ATAN(1.)
      DO 10 I = 1,100
      RPR    =  RPRMIN + FLOAT(I-1) * STEP
      IF (RPR.GT.(RPRMAX+.1)) GO TO 20
      IF(IDEV.EQ.2.OR.IDEV.EQ.4)RPR=RPR/EXP(-ZETA*PI/SQRT(1.-ZETA**2))
      CALL ARC2(XC,YC,RPR,IDEV,0.,PI,ZETA)
   10 CONTINUE
   20 RETURN
      END
C
      SUBROUTINE ARC2(XC,YC,RPR0,IDEV,A1,A2,Z)
C
C  THE PROGRAM PLOTS AN ARC OF A DAMPED SPIRAL GIVEN THE CENTER
C  (XC,YC), INITIAL RADIUS, RPR0, BEGINNING AND END ANGLES IN RADIANS
C  (A1,A2), AND THE DEVICE # IN CONDUCTION.
C
C  BY RAMESH ORUGANTI
C
      DIMENSION  X(43),Y(43)
      X(43)    =  1.0
      Y(43)    =  1.0
      PI       =  4.*ATAN(1.0)
      H        =  (A2-A1)/40.
      DO 40 I  =  1,41
      ALPHA    =  H*FLOAT(I-1) + A1
CC    WRITE(6,*) A1,ALPHA
      RPR      =  RPR0*EXP( (-Z/SQRT(1.-Z**2))*(A(ALPHA,Z)-A(A1,Z)) ) *
     *           SQRT ((1.-Z*SIN(2.*A1))/(1.-Z*SIN(2.*ALPHA)))
CC    S        =  -Z/SQRT(1.-Z**2)
CC    X1     =  SQRT ((1.-Z*SIN(2.*A1))/(1.-Z*SIN(2.*ALPHA)))
CC    Y1       =  A(ALPHA,Z)
CC    Z1     =  A(A1,Z)
CC    WRITE(6,*) Z,S,RPR0,X1,Y1,Z1
      IF(IDEV.EQ.1.OR.IDEV.EQ.2)  ALPHA = PI + ALPHA
      CALL RECT(X(I),Y(I),XC,YC,RPR,ALPHA)
C
```

```
      IF(I.GT.1)  GO TO 30
      CALL PLOT (X(1),Y(1),3)
      GO TO 40
   30 CALL PLOT (X(I),Y(I),2)
   40 CONTINUE
      RETURN
      END
C
      SUBROUTINE EQUIL2(RPR,VON,ZETA,OMEGAN,VCPN,AILAVN,AIQAVN,AIDAVN,
     *                  R1PRO,VCON,AILON,ALPD,ALPQ,K,J)
C
C  THIS SUBPROGRAM PLOTS THE CCM STEADY-STATE TRAJECTORY OF SRC
C  WHEN RADIUS, RPR, OUTPUT VOLTAGE, VON AND DAMPING FACTOR, ZETA,
C  ARE GIVEN. THE PROGRAM ALSO RETURNS VARIOUS PARAMETERS OF THE CCM
C  TRAJECTORY, THE OPERATING FREQUENCY, OMEGAN, PEAK CAPACITOR
C  VOLTAGE, VCPN, INDUCTOR AVERAGE CURRENT, AILAVN, TRANSISTOR
C  AVERAGE CURRENT, AIQAVN, DIODE AV CUR, AIDAVN, INITIAL RADIUS,
C  R1PRO, INITIAL CAP VOLT, VCON, INITIAL IND CUR, AILON, DIODE
C  COND ANGLE, ALPD, AND TRANS COND ANGLE, ALPQ.
C  THE PROGRAM UTILIZES SUBROUTINES AGAIN1, RECT, A AND ARC2
C
C  PROGRAMMED BY RAMESH ORUGANTI
C
        PI     =  4.*ATAN(1.)
        APRMIN =  0.
        APRMAX =  PI
        ALPHPR =  APRMIN
        STEP   =  PI/2.
        S1     =  SQRT(1.-ZETA**2)
        S      =  -ZETA/SQRT(1.-ZETA**2)
        R2PRO  =  RPR - 2.*VON
C
      DO 100 I = 1,100
        R2PR   =  (R2PRO/SQRT(1.-ZETA*SIN(2.*ALPHPR)))*
     *                EXP(S*(A(ALPHPR,ZETA) - A(0.,ZETA)))
        R1PRO  =  SQRT(R2PR**2+4.+4.*R2PR*COS(ALPHPR))
        ABPR   =  (R2PR**2-R1PRO**2-4.)/(4.*R1PRO)
        IF (ABPR.LE.-1.) GO TO 70
        IF (ABPR.GE.1.) GO TO 80
        BPR    =  ARCOS(ABPR)
      GO TO 90
C
   70   BPR    =  +1.*PI
      GO TO 90
C
   80   BPR    =  0.0
C
   90   BPRO   =  PI - BPR
C
        R1PR   =  (R1PRO*SQRT(1.-ZETA*SIN(2.*BPRO)))*
     *               EXP(S*(A(PI,ZETA) - A(BPRO,ZETA)))
        ERROR  =  R1PR - RPR
        IF(ABS(ERROR).LT.1.E-6) GO TO 200
        CALL AGAIN1(ERROR,APRMIN,APRMAX,ALPHPR,STEP)
  100 CONTINUE
  200   ALPD   =  A(ALPHPR,ZETA) - A(0.,ZETA)
        ALPQ   =  A(PI,ZETA) - A(BPRO,ZETA)
        OMEGAN =  PI/(ALPD+ALPQ)
        VCPN   =  1. -VON + R1PR
        AILAVN =  2.*VCPN*S1/(ALPD + ALPQ)
        XC     =  1. - VON
        B1PRO  =  PI+BPRO
        CALL RECT(VCON,AILON,XC,0.,R1PRO,B1PRO)
        AIQAVN  = (VCPN-VCON)*S1/(2.*(ALPD+ALPQ))
        AIDAVN  = (VCPN+VCON)*S1/(2.*(ALPD+ALPQ))
C
        IF(J.EQ.0) GO TO 250
        IF(K.NE.1) GO TO 220
C
        R1PRO  =  RPR/EXP((-ZETA*PI)/SQRT(1.-ZETA**2))
        R2PRO  =  RPR - 2.*VON
        ALPHPR  =  PI
        BPRO = 0.
  220 XC       =  -(1.+VON)
      CALL ARC2 (XC,0.,R2PRO,1,0.,ALPHPR,ZETA)
      XC       =  -(1.-VON)
      CALL ARC2 (XC,0.,R1PRO,4,BPRO,PI,ZETA)
      XC       =  (1.-VON)
      CALL ARC2 (XC,0.,R1PRO,2,BPRO,PI,ZETA)
      XC       =  (1.+VON)
      CALL ARC2 (XC,0.,R2PRO,3,0.,ALPHPR,ZETA)
  250 CONTINUE
      RETURN
      END
```

Appendix C

Ideal Analysis Of PRC

In this appendix, analyses of PRC trajectories in Chapter 5 are presented. Certain results from this appendix, including plots of mode boundaries and dc characteristics, have been included in Secs. 5.3.9 and 5.4.

The boundary equations are derived in Sec. C.1. The equations for dc characteristics in each of the modes are obtained in Sec. C.2. For the CCM cases, equations for design parameters, such as average device currents, have also been obtained. Equations for design parameters can be derived for other modes also in similar fashion, if required. Section C.3 contains plots of design curves and dc characteristics obtained from the analysis. Section C.4 presents an example of PRC design to demonstrate the use of the design curves and to highlight certain features of PRC operation. Section C.5 contains computer programs based on the analytical results. Please refer to Sec. 5.0 for definitions of symbols used in this appendix.

Most of the equations in Sec. C.2 are derived in terms of intermediate parameter such as R or I_{L1N}. Given ω_N, the intermediate parameter is first determined iteratively such that the desired ω_N is reached. The value of the intermediate parameter is then used to for further calculations.

C.1 Mode Boundaries

Figure C.1 shows a set of diagrams corresponding to operation at different boundary frequencies, such as ω_{LOW} and ω_{LIMIT}. The equations for these boundaries are derived in this section based on analysis of these figures.

In the following analysis, t_{XY} refers to the time interval between points X and Y on the state-plane. Also, if T is the operating period corresponding to ω, then

$$T = \frac{2\pi}{\omega} \tag{C.1}$$

$$\text{So,} \qquad \omega_N = \frac{\omega}{\omega_0} = \frac{2\pi}{\omega_0 T} = \frac{2\pi}{T_N} \tag{C.2}$$

C.1.1 Time Intervals On State-Plane Diagrams

In this section, equations for $\omega_0 \Delta t$, normalized elapsed time during a particular topological mode (M1 through M8), will be established based on measurements on state plane. In the case of the discontinuous operation interval (M9), the system remains at a particular state throughout (Fig. 5.12(e)). Hence, time interval during this topological mode cannot be determined from measurements made on state plane.

C.1.1.1 Resonant intervals (M1, M2, M3 and M4)

From (5.4), (5.10) and (5.11),

$$\omega_0 \Delta t = \theta = \text{Angle subtended at the center} \tag{C.3}$$

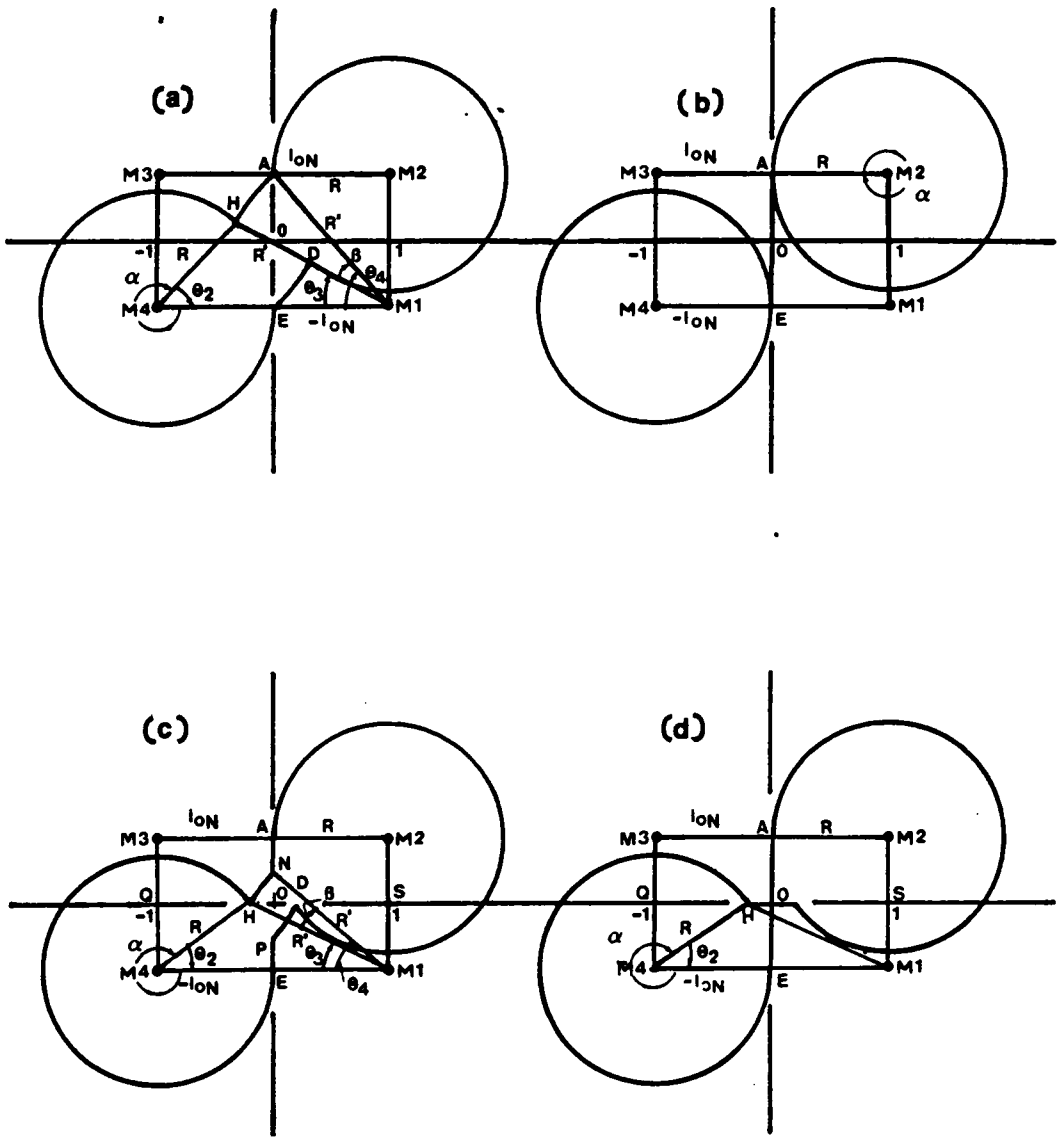

Figure C.1 Operation at boundary frequencies - Analysis diagrams

a) ω_{LOW}
b) ω_{MUL}
c) ω_{TRAN}
d) ω_{DISC}

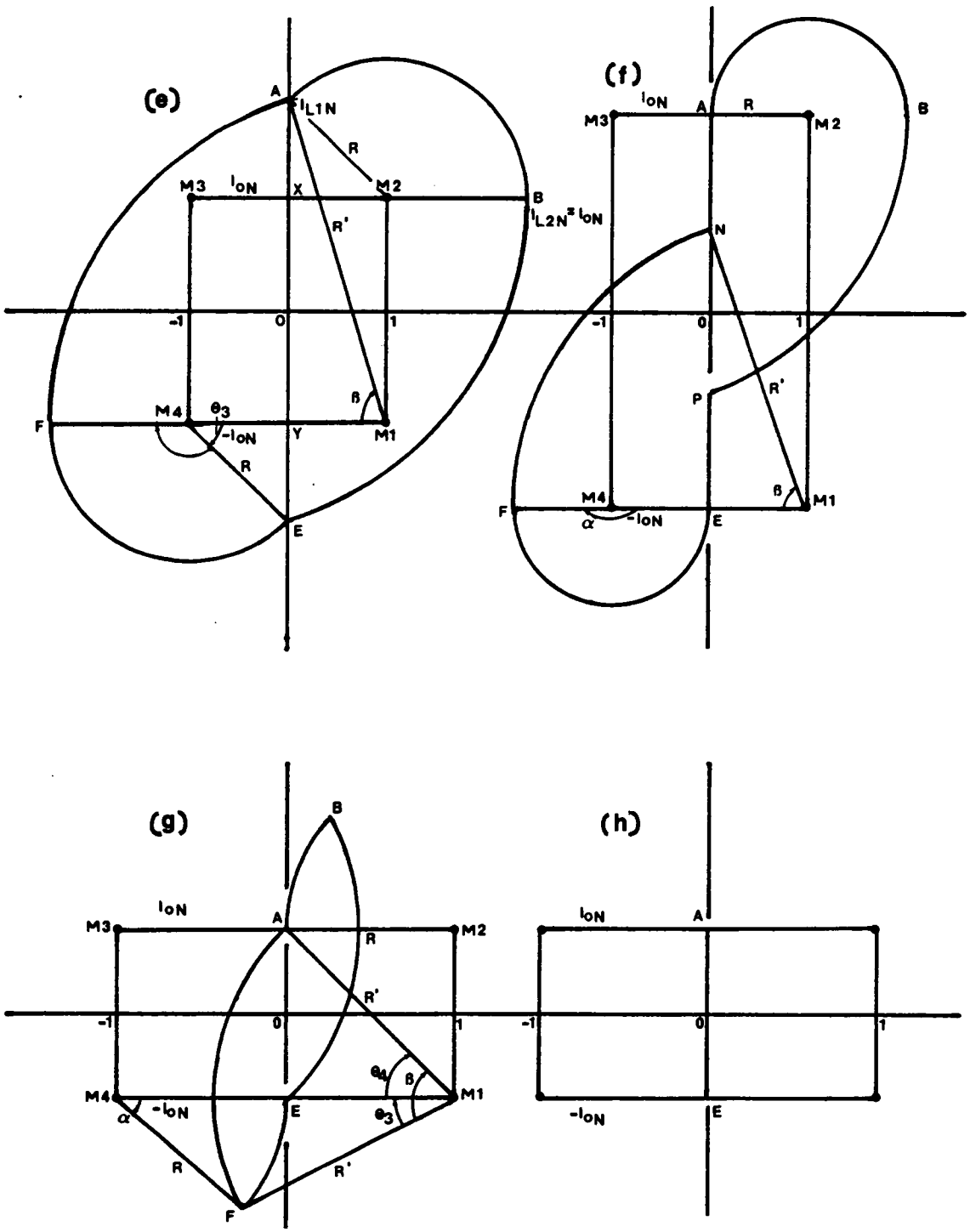

Figure C.1 (contd.)

e) ω_{MAX} $1 < I_{ON} \leq \sqrt{2}$

f) ω_{MAX} $\sqrt{2} \leq I_{ON} < \infty$

g) ω_{HIGH}

h) ω_{LIMIT}

C.1.1.2 Inductor Charging/Discharging Intervals (M5 and M6)

From Fig. 5.11(a),

$$L\frac{di_L}{dt} = V_s \tag{C.4}$$

From Fig. 5.11(b),

$$-L\frac{di_L}{dt} = V_s \tag{C.5}$$

Integrating (C.4) and (C.5) and combining,

$$V_s\,\Delta t = L\,|\Delta i_L| \tag{C.6}$$

Manipulating (C.6), (5.2) and (5.3) and then normalizing with (5.7),

$$\omega_0\,\Delta t = |\Delta i_{LN}|\,, \tag{C.7}$$

where Δi_{LN} = Normalized change in inductor current.

C.1.1.3 Capacitor Charging/Discharging Interval (M7 And M8)

From Fig. 5.11(c),

$$C\frac{dv_C}{dt} = -I_o \tag{C.8}$$

From Fig. 5.11(d),

$$C\frac{dv_C}{dt} = +I_o \tag{C.9}$$

Integrating (C.8) and (C.9) and combining,

$$I_o\,\Delta t = C\,|\Delta v_C| \tag{C.10}$$

Manipulating (C.10), (5.2) and (5.3) and then normalizing with (5.6) and (5.7),

$$\omega_0 \Delta t = \frac{|\Delta v_{CN}|}{I_{oN}} \tag{C.11}$$

C.1.2 Lower CCM Boundary

In this section, equation for ω_{LOW}, lower CCM boundary, will be derived from analysis of Fig. C.1(a). Range of applicability of Fig. C.1(a) is

$$0 \leq I_{oN} \leq \sqrt{2} \tag{C.12}$$

From Fig. C.1(a),

$$R = M2\,A = 1 \tag{C.13}$$

From Δ AEM1 in Fig. C.1(a),

$$R' = \sqrt{1 + 4I_{oN}^2} \tag{C.14}$$

$$\theta_4 = \cos^{-1}\frac{1}{R'} = \cos^{-1}\frac{1}{\sqrt{1 + 4I_{oN}^2}} \tag{C.15}$$

From Δ HM1M4 in Fig. C.1(a),

$$\theta_3 = \cos^{-1}\frac{R'^2 + 4 - R^2}{4R'} = \cos^{-1}\frac{1 + I_{oN}^2}{\sqrt{1 + 4I_{oN}^2}} \tag{C.16}$$

$$\theta_2 = \cos^{-1}\frac{R^2 + 4 - R'^2}{4R} = \cos^{-1}(1 - I_{oN}^2) \tag{C.17}$$

From Fig. C.1(a),

$$T = 2\,(t_{EH} + t_{HA}) \tag{C.18}$$

From (C.18), (C.3) and Fig. C.1(a),

$$\omega_0 T = 2(\alpha + \beta) \tag{C.19}$$

From Fig. C.1(a),

$$\alpha = 2\pi - \theta_2 \tag{C.20}$$

$$\beta = \theta_4 - \theta_3 \tag{C.21}$$

Thus, $$\omega_0 T = 2(2\pi - \theta_2 + \theta_4 - \theta_3) \tag{C.22}$$

Substituting for θ_2 from (C.17), θ_3 from (C.16) and θ_4 from (C.15) into (C.23) and then utilizing (C.2),

$$\omega_{LOW} = \text{Normalized lower CCM boundary frequency} = \frac{\pi}{2\pi - \cos^{-1}(1 - I_{oN}^2) + \cos^{-1}\frac{1}{\sqrt{1 + 4I_{oN}^2}} - \cos^{-1}\frac{1 + I_{oN}^2}{\sqrt{1 + 4I_{oN}^2}}}, \tag{C.23}$$

where $$0 \le I_{oN} \le \sqrt{2} \tag{C.12}$$

C.1.3 Multiple Region Boundary

In this section, equation for ω_{MUL}, multiple region boundary will be derived from Fig. C.1(b). Range of applicability of Fig. C.1(b) is

$$0 \le I_{oN} < \infty \tag{C.24}$$

From Fig. C.1(b),

$$R = M2\,A = 1 \tag{C.25}$$

$$\alpha = 2\pi \tag{C.26}$$

$$T = 2(t_{AA} + t_{AE}) \tag{C.27}$$

From (C.27), (C.3), (C.7) and Fig. C.1(b),

$$\omega_0 T = 2\,(\alpha + i_{LN}/_{at\ A} - i_{LN}/_{at\ E}) \tag{C.28}$$

Substituting for α from (C.26) and i_{LN} values at A and E (from Fig. C.1(b)) into (C.28) and then utilizing (C.2),

$$\begin{aligned} \omega_{MUL} &= \text{Multiple region boundary frequency} \\ &= \frac{\pi}{2(\pi + l_{oN})}, \end{aligned} \tag{C.29}$$

$$\text{where} \qquad 0 \le l_{oN} < \infty \tag{C.24}$$

C.1.4 Boundary Between TM1 And TM2

In this section, equation for ω_{TRAN}, boundary between TM1 and TM2 modes, will be derived from Fig. C.1(c). Range of applicability of Fig. C.1(c) is,

$$0 \le l_{oN} \le 1 \tag{C.30}$$

From Fig. C.1(c),

$$R = M2\,A = 1 \tag{C.31}$$

$$SH = 2 - QH = 2 - \sqrt{1 - l_{oN}^2} \tag{C.32}$$

From Δ SHM1 in Fig. C.1(c),

$$R' = \sqrt{SH^2 + SM1^2} \tag{C.33}$$

Substituting for SH from (C.32) and SM1 from Fig. C.1(c) into (C.33),

$$R' = \sqrt{5 - 4\sqrt{1 - l_{oN}^2}} \tag{C.34}$$

From Fig. C.1(c),

$$AN = AE - EN = 2\,l_{oN} - \sqrt{R'^2 - 1} = 2\,l_{oN} - 2\sqrt{1 - \sqrt{1 - l_{oN}^2}} \tag{C.35}$$

From Δ NEM1 in Fig. C.1(c),

$$\theta_4 = \cos^{-1}\frac{1}{R'} = \cos^{-1}\frac{1}{\sqrt{5 - 4\sqrt{1 - I_{oN}^2}}} \tag{C.36}$$

From Δ HM1M4 in Fig. C.1(c),

$$\theta_3 = \cos^{-1}\frac{R'^2 + 4 - R^2}{4R'} = \cos^{-1}\frac{2 - \sqrt{1 - I_{oN}^2}}{\sqrt{5 - 4\sqrt{1 - I_{oN}^2}}} \tag{C.37}$$

$$\theta_2 = \cos^{-1}\frac{R^2 + 4 - R'^2}{4R} = \cos^{-1}\sqrt{1 - I_{oN}^2} \tag{C.38}$$

From Fig. C.1(c),

$$T = 2\,(t_{EH} + t_{HN} + t_{NA}) \tag{C.39}$$

From (C.39), (C.3), (C.7) and Fig. C.1(c),

$$\omega_0 T = 2\,(\alpha + \beta + AN) \tag{C.40}$$

From Fig. C.1(c),

$$\alpha = 2\pi - \theta_2 \tag{C.41}$$

$$\beta = \theta_4 - \theta_3 \tag{C.42}$$

$$\text{Thus,} \qquad \omega_0 T = 2\,(2\pi - \theta_2 + \theta_4 - \theta_3 + AN) \tag{C.43}$$

Substituting for θ_2 from (C.38), θ_3 from (C.37), θ_4 from (C.36) and AN from (C.35) into (C.43) and then utilizing (C.2),

$$\omega_{TRAN} = \text{Normalized boundary frequency between TM1 and TM2 modes}$$

$$= \frac{\pi}{\left[2\pi - \cos^{-1}\sqrt{1 - I_{oN}^2} + \cos^{-1}\frac{1}{\sqrt{5 - 4\sqrt{1 - I_{oN}^2}}} - \cos^{-1}\frac{2 - \sqrt{1 - I_{oN}^2}}{\sqrt{5 - 4\sqrt{1 - I_{oN}^2}}} + 2I_{oN} - 2\sqrt{1 - \sqrt{1 - I_{oN}^2}}\right]} \tag{C.44}$$

where $0 \le I_{oN} \le 1$ (C.30)

C.1.5 DCM Boundary

In this section, equation for ω_{DISC}, upper boundary for DCM will be derived from Fig. C.1(d). Range of applicability of Fig. C.1(d) is

$$0 \le I_{oN} \le 1 \tag{C.45}$$

Equation for θ_2 is identical to that in Sec. C.1.4. Reproducing (C.38),

$$\theta_2 = \cos^{-1}\sqrt{1 - I_{oN}^2} \tag{C.46}$$

From Fig. C.1(d),

$$R = M2\,A = 1 \tag{C.47}$$

$$OH = 1 - QH = 1 - \sqrt{1 - I_{oN}^2} \tag{C.48}$$

$$T = 2\,(t_{EH} + t_{HO} + t_{OA}) \tag{C.49}$$

From (C.49), (C.3), (C.7), (C.11) and Fig. C.1(d),

$$\omega_0 T = 2\,(\alpha + \frac{OH}{I_{oN}} + I_{oN}) \tag{C.50}$$

From Fig. C.1(d),

$$\alpha = 2\pi - \theta_2 \tag{C.51}$$

Thus, $$\omega_0 T = 2\,(2\pi - \theta_2 + \frac{OH}{I_{oN}} + I_{oN}) \tag{C.52}$$

Substituting for θ_2 from (C.46) and OH from (C.48) into (C.52) and then utilizing (C.2),

$$\omega_{DISC} = \text{Normalized DCM upper boundary frequency}$$

$$= \frac{\pi}{2\pi - \cos^{-1}\sqrt{1 - I_{oN}^2} + \frac{1 - \sqrt{1 - I_{oN}^2}}{I_{oN}} + I_{oN}}, \tag{C.53}$$

$$\text{where} \quad 0 \le I_{oN} \le 1 \tag{C.45}$$

C.1.6 Boundary Between Intersections-1 And -2

In this section, equations for ω_{MAX}, boundary between intersection-1 and -2 trajectories will be derived. The trajectory corresponding to ω_{MAX} corresponds to the largest trajectory size for the given load current, I_{oN}. Equation for ω_{MAX} is different in three I_{oN} ranges considered in Sec. 5.3.

The first I_{oN} range (range A) is $0 \le I_{oN} \le 1$. In this range, as explained in Sec. 5.3.6, trajectory size ideally reaches infinite proportions as ω_N reaches ω_{MAX} . Value of ω_{MAX} will be determined in Sec. C.2.1.2 as a limiting frequency for CCM operation. Reproducing (C.138),

$$\omega_{MAX} = \text{Normalized boundary frequency between intersection-1 and -2 trajectories}$$
$$= 1 , \tag{C.46}$$

$$\text{for} \qquad 0 \le I_{oN} \le 1 \tag{C.47}$$

The second I_{oN} range (range B) is $1 \le I_{oN} \le \sqrt{2}$. In this range Fig. C.1(e) is applicable. Equation for ω_{MAX} in this current range will be derived now based on this diagram.

From Fig. C.1(e),

$$I_{L1N} = \sqrt{R^2 - 1} + I_{oN} \tag{C.48}$$

$$I_{L1N} = \sqrt{R'^2 - 1} - I_{oN} \tag{C.49}$$

$$R' = R + 2 \tag{C.50}$$

Solving (C.48), (C.49) and (C.50) together for I_{L1N}, R and R',

$$I_{L1N} = \frac{I_{oN}}{\sqrt{I_{oN}^2 - 1}} \tag{C.51}$$

$$R = \frac{-\sqrt{I_{oN}^2 - 1} + I_{oN}^2}{\sqrt{I_{oN}^2 - 1}} \tag{C.52}$$

$$R' = \frac{\sqrt{I_{oN}^2 - 1} + I_{oN}^2}{\sqrt{I_{oN}^2 - 1}} \tag{C.53}$$

From Δ AXM2 in Fig. C.1(e),

$$\theta_3 = \cos^{-1}\frac{1}{R} = \cos^{-1}\frac{\sqrt{I_{oN}^2 - 1}}{-\sqrt{I_{oN}^2 - 1} + I_{oN}^2} \tag{C.54}$$

From Δ AYM1 in Fig. C.1(e),

$$\beta = \cos^{-1}\frac{1}{R'} = \cos^{-1}\frac{\sqrt{I_{oN}^2 - 1}}{\sqrt{I_{oN}^2 - 1} + I_{oN}^2} \tag{C.55}$$

From Fig. C.1(e),

$$T = 2\,(t_{EF} + t_{FA}) \tag{C.56}$$

From (C.56), (C.3) and Fig. C.1(e),

$$\omega_0 T = 2\,(\alpha + \beta) \tag{C.57}$$

From Fig. C.1(e),

$$\alpha = \pi - \theta_3 \tag{C.58}$$

Thus, $$\omega_0 T = 2\,(\pi - \theta_3 + \beta) \tag{C.59}$$

Substituting for θ_3 from (C.54) and β from (C.56) into (C.59) and then utilizing (C.2),

$$\omega_{MAX} = \frac{\pi}{\pi - \cos^{-1}\dfrac{\sqrt{I_{oN}^2 - 1}}{-\sqrt{I_{oN}^2 - 1 + I_{oN}^2}} + \cos^{-1}\dfrac{\sqrt{I_{oN}^2 - 1}}{\sqrt{I_{oN}^2 - 1 + I_{oN}^2}}}, \tag{C.60}$$

$$\text{for} \qquad 1 \le I_{oN} \le \sqrt{2} \tag{C.61}$$

The third I_{oN} range (range C) is $\sqrt{2} \le I_{oN} < \infty$. For this range, applicable figure is Fig. C.1(f). Equation for ω_{MAX} in this current range will now be derived based on this diagram. From Fig. C.1(f),

$$R = M2\,A = 1 \tag{C.62}$$

$$R' = R + 2 = 3 \tag{C.63}$$

$$\alpha = \pi \tag{C.64}$$

$$\beta = \cos^{-1}\frac{1}{R'} = \cos^{-1}\frac{1}{3} \tag{C.65}$$

$$AN = 2\,I_{oN} - \text{NE} = 2\,I_{oN} - \sqrt{R'^2 - 1} = 2\,(I_{oN} - \sqrt{2}) \tag{C.66}$$

$$T = 2\,(t_{EF} + t_{FN} + t_{NA}) \tag{C.67}$$

From (C.67), (C.3), (C.7) and Fig. C.1(f),

$$\omega_0 T = 2\,(\alpha + \beta + AN) \tag{C.68}$$

Substituting for α from (C.64), β from (C.65) and AN from (C.66) into (C.68) and then utilizing (C.2),

$$\omega_{MAX} = \frac{\pi}{\pi + \cos^{-1}\dfrac{1}{3} + 2\,(I_{oN} - \sqrt{2})}, \tag{C.69}$$

$$\text{for} \qquad \sqrt{2} \le I_{oN} < \infty \tag{C.70}$$

The ω_{MAX} boundary is determined by equations (C.46), (C.60) and (C.69) in the three current ranges given by (C.47), (C.61) and (C.70), respectively.

C.1.7 Upper CCM Boundary

In this section, equation for ω_{HIGH} , upper CCM boundary, will be derived from analysis of Fig. C.1(g). Range of applicability of Fig. C.1(g) is,

$$0 \leq I_{oN} \leq \sqrt{2} \tag{C.71}$$

From Fig. C.1(g),

$$R = M2\,A = 1 \tag{C.72}$$

From Δ AEM1 in Fig. C.1(g),

$$R' = \sqrt{1 + 4\,I_{oN}^2} \tag{C.73}$$

$$\theta_4 = \cos^{-1}\frac{1}{R'} = \cos^{-1}\frac{1}{\sqrt{1 + 4\,I_{oN}^2}} \tag{C.74}$$

From Δ FM1M4 in Fig. C.1(g),

$$\theta_3 = \cos^{-1}\frac{R'^2 + 4 - R^2}{4\,R'} = \cos^{-1}\frac{1 + I_{oN}^2}{\sqrt{1 + 4\,I_{oN}^2}} \tag{C.75}$$

$$\alpha = \cos^{-1}\frac{R^2 + 4 - R'^2}{4\,R} = \cos^{-1}(1 - I_{oN}^2) \tag{C.76}$$

From Fig. C.1(g),

$$T = 2\,(t_{FA} + t_{AB}) \tag{C.77}$$

From (C.77), (C.3) and Fig. C.1(g),

$$\omega_0 T = 2\,(\alpha + \beta) \tag{C.78}$$

From Fig. C.1(g),

$$\beta = \theta_4 + \theta_3 \tag{C.79}$$

$$\text{Thus,} \qquad \omega_0 T = 2\,(\alpha + \theta_4 + \theta_3) \tag{C.80}$$

Substituting for α from (C.76), θ_3 from (C.75) and θ_4 from (C.74) into (C.80) and then utilizing (C.2),

$$\omega_{HIGH} = \text{Normalized upper CCM boundary frequency}$$

$$= \frac{\pi}{\cos^{-1}(1 - I_{oN}^2) + \cos^{-1}\dfrac{1}{\sqrt{1 + 4I_{oN}^2}} + \cos^{-1}\dfrac{1 + I_{oN}^2}{\sqrt{1 + 4I_{oN}^2}}}, \tag{C.81}$$

$$\text{where} \qquad 0 \le I_{oN} \le \sqrt{2} \tag{C.71}$$

C.1.8 Limit Boundary

In this section, equation for ω_{LIMIT} , short-circuit limit boundary, will be derived from analysis of Fig. C.1(h). Range of applicability of Fig. C.1(h) is,

$$0 < I_{oN} < \infty \tag{C.82}$$

From Fig. C.1(h),

$$T = 2\,t_{EA} \tag{C.83}$$

From (C.83), (C.7) and Fig. C.1(h),

$$\omega_0 T = 4\,I_{oN} \tag{C.84}$$

Utilizing (C.2),

$$\omega_{LIMIT} = \frac{\pi}{2\,I_{oN}}, \tag{C.85}$$

$$\text{where} \qquad 0 < I_{oN} < \infty \tag{C.82}$$

C.1.9 Results Of Mode Analysis

Section C.3 contains a computer program for computing the mode boundaries. Using this program, the mode boundaries have been plotted in Fig. C.2. Section 5.3.9 discusses the boundaries and the different regions.

C.2 Ideal DC Analysis

In the following analysis, if X and Y are two points on a state-plane trajectory, then t_{XY} is the time interval between X and Y.

$$\text{Also,} \qquad \theta_{XY} = \text{Angular interval between X and Y} = \omega_0 t_{XY} \tag{C.86}$$

C.2.1 CCM Analysis - Intersection-1

The analysis presented in this section corresponds to regions 7A and 7B of Fig. 3.26(b).

C.2.1.1 Analysis Of A Steady-State Trajectory

Reference is made to Fig. C.3 for derivation of equations in this section. Transistor trajectory radius R and normalized load current I_{oN} are assumed to be known.

In many of the following cases, desired equation for a design parameter has been written in terms of other circuit parameters. These other circuit parameters have been expressed as functions of

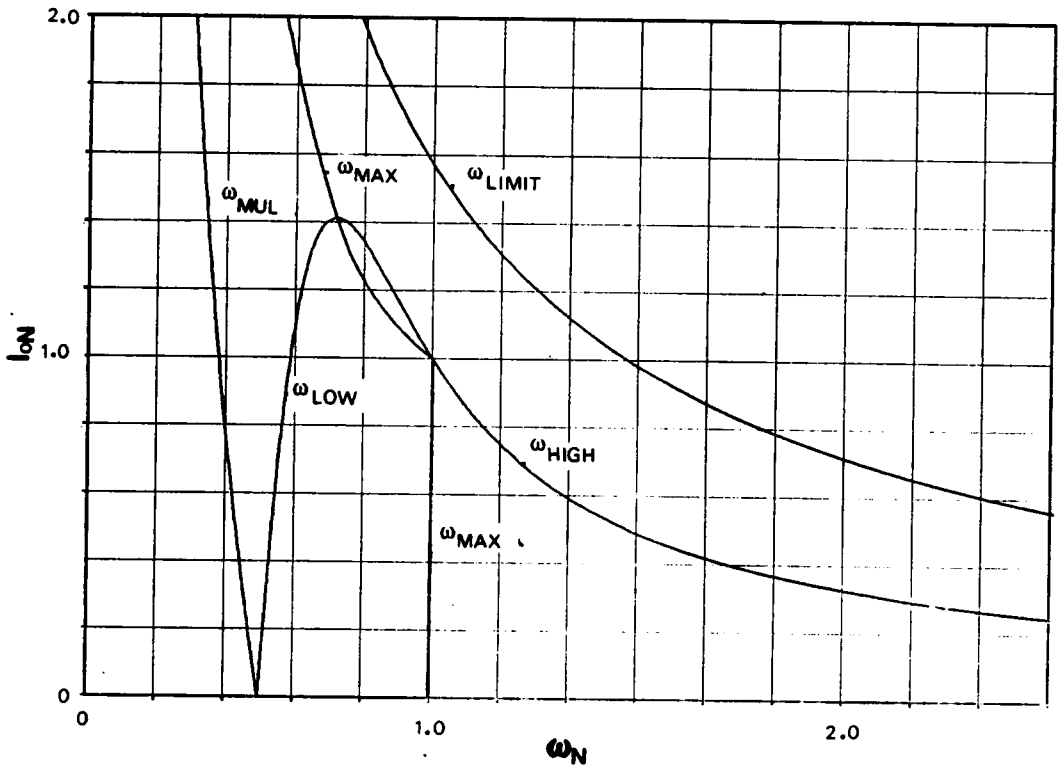

Figure C.2 PRC boundaries of operation - Strategy-1

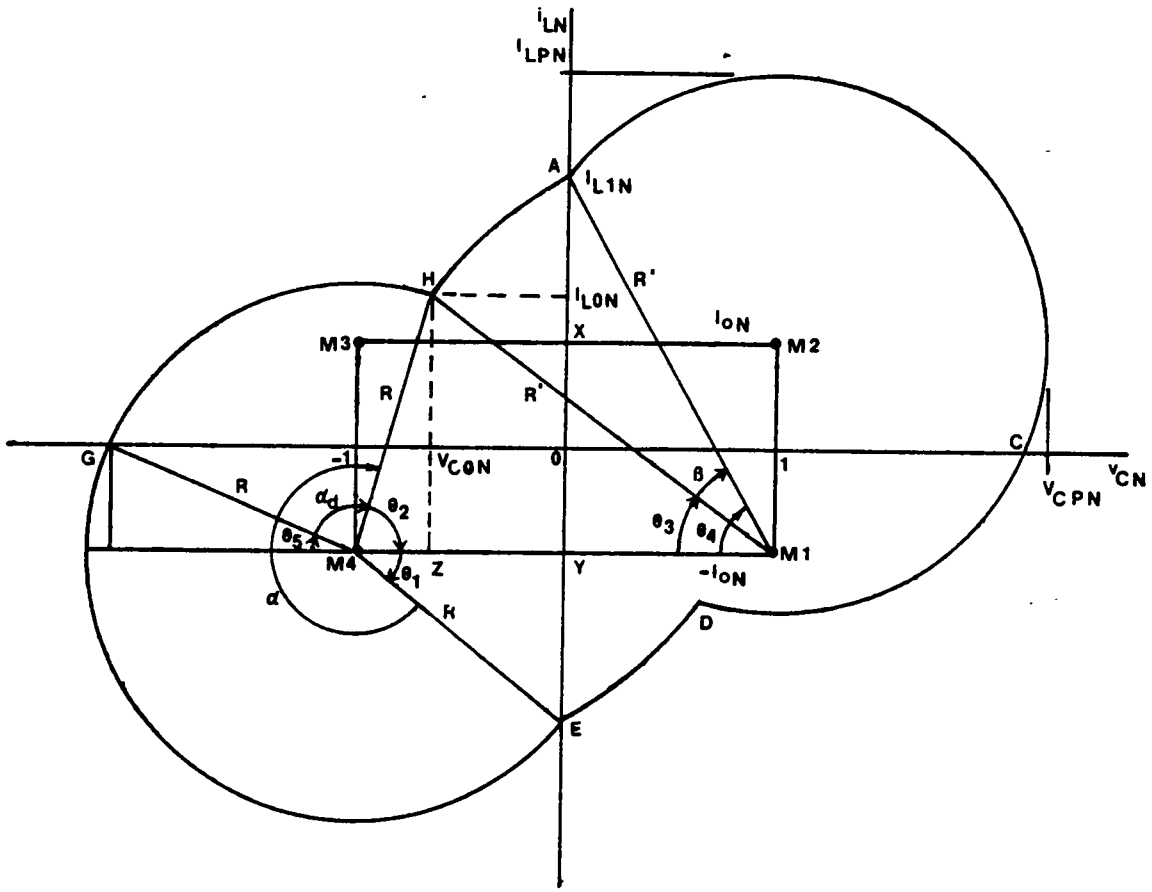

Figure C.3 CCM operation in intersection-1 - Analysis diagram

R and I_{oN} earlier. If so desired, the design parameters can be expressed solely in terms of R and I_{oN}, by appropriate substitutions.

From Fig. C.3,

$$I_{L1N} = AX + OX = \sqrt{R^2 - 1} + I_{oN} \tag{C.87}$$

$$R' = \sqrt{M1Y^2 + AY^2} = \sqrt{1 + (I_{L1N} + I_{oN})^2} \tag{C.88}$$

$$\theta_1 = \cos^{-1}\frac{1}{R} \tag{C.89}$$

$$\theta_4 = \cos^{-1}\frac{1}{R'} = \cos^{-1}\frac{1}{\sqrt{1 + (I_{L1N} + I_{oN})^2}} \tag{C.90}$$

From Δ HM4M1 in Fig. C.3,

$$\theta_2 = \cos^{-1}\frac{R^2 + 4 - R'^2}{4R} = \cos^{-1}\frac{1 - I_{oN} I_{L1N}}{R} \tag{C.91}$$

$$\theta_3 = \cos^{-1}\frac{R'^2 + 4 - R^2}{4R'} = \cos^{-1}\frac{1 + I_{oN} I_{L1N}}{\sqrt{1 + (I_{L1N} + I_{oN})^2}} \tag{C.92}$$

$$\begin{aligned}\alpha &= \text{Conduction in M2 (M4) topological mode} \\ &= 2\pi - (\theta_1 + \theta_2) = 2\pi - \cos^{-1}\frac{1}{R} - \cos^{-1}\frac{1 - I_{oN} I_{L1N}}{R}\end{aligned} \tag{C.93}$$

$$\begin{aligned}\beta &= \text{Conduction in M1 (M3) topological mode} \\ &= \theta_4 - \theta_3 = \cos^{-1}\frac{1}{\sqrt{1 + (I_{L1N} + I_{oN})^2}} - \cos^{-1}\frac{1 + I_{oN} I_{L1N}}{\sqrt{1 + (I_{L1N} + I_{oN})^2}}\end{aligned} \tag{C.94}$$

Period And Frequency Of Operation From Fig. C.3,

$$T = 2(t_{EH} + t_{HA}) \tag{C.95}$$

From (C.95), (C.3) and Fig. C.3,

$$\begin{aligned}T_N &= \text{Angular operating period} \\ &= \omega_0 T = 2(\alpha + \beta)\end{aligned} \tag{C.96}$$

Also, from (C.96) and (C.2),

$$\omega_N = \frac{\pi}{\alpha + \beta} \tag{C.97}$$

Equation (C.97) is used to determine ω_N, given R and I_{oN}. Alternatively, (C.97) can also be used to determine R, given ω_N and I_{oN}.

Diode And Transistor Conduction Angles: From Fig. C.3,

$$\theta_5 = \sin^{-1}\frac{I_{oN}}{R} \tag{C.98}$$

$$\begin{aligned} \alpha_d &= \text{Diode conduction angle} \\ &= \pi - \theta_2 - \theta_5 = \pi - \cos^{-1}\frac{1 - I_{oN}\, I_{L1N}}{R} - \sin^{-1}\frac{I_{oN}}{R} \end{aligned} \tag{C.99}$$

$$\begin{aligned} \alpha_q &= \text{Transistor conduction angle} \\ &= \alpha - \alpha_d + \beta \end{aligned} \tag{C.100}$$

$$\text{Hence,} \quad \alpha_q = \pi - \cos^{-1}\frac{1}{R} + \sin^{-1}\frac{I_{oN}}{R} + \cos^{-1}\frac{1}{\sqrt{1 + (I_{L1N} + I_{oN})^2}} - \cos^{-1}\frac{1 + I_{oN}\, I_{L1N}}{\sqrt{1 + (I_{L1N} + I_{oN})^2}} \tag{C.101}$$

Switching Point Variables: From Fig. C.3,

$$V_{C0N} = R\cos\theta_2 - 1 = -I_{oN}\, I_{L1N} \tag{C.102}$$

$$I_{L0N} = R\sin\theta_2 - I_{oN} = \sqrt{R^2 - (1 - I_{oN}\, I_{L1N})^2} - I_{oN} \tag{C.103}$$

Peak State Variables: From Fig. C.3,

$$V_{CPN} = 1 + R \tag{C.104}$$

$$I_{LPN} = I_{oN} + R \tag{C.105}$$

Peak Inductor Volt-Seconds: Reproducing (A.27),

$$(VS)_N = \Delta i_{LN} \tag{C.106}$$

From Fig. C.3,

$$(VS)_{PN} = 2 I_{LPN} = 2 (I_{oN} + R) \tag{C.107}$$

Diode Average Current: From Fig. 5.1, if t_{A1} is the start and t_{B1} the end of conduction of a device X,

$$C (V_{CB1} - V_{CA1}) = \int_{t_{A1}}^{t_{B1}} (i_L - i_I)\, dt\,, \qquad \text{where} \tag{C.108}$$

$$V_{CA1} = v_C/_{(t = t_{A1})}\,, \qquad V_{CB1} = v_C/_{(t = t_{B1})} \qquad \text{and} \tag{C.109}$$

$$\begin{aligned} i_I &= + I_o\,, \text{ Topological modes M2 and M3} \\ &= - I_o\,, \text{ Topological modes M1 and M4} \end{aligned} \tag{C.110}$$

The average device current , I_{XAV}, is,

$$I_{XAV} = \frac{1}{T} \int_{t_{A1}}^{t_{B1}} i_L\, dt = \frac{C (V_{CB1} - V_{CA1})}{T} + \frac{1}{T} \int_{t_{A1}}^{t_{B1}} i_I\, dt \tag{C.111}$$

Normalizing (C.111) with factors N_v from (5.6) and N_i from (5.7),

$$\begin{aligned} I_{XAVN} &= \text{Normalized average device current} \\ &= \frac{1}{T_N} \left[V_{CB1N} - V_{CA1N} + \int_0^{\theta_{A1B1}} i_{IN}\, d\theta \right], \end{aligned} \tag{C.112}$$

$$\text{where} \qquad \theta_{A1B1} = \omega_0 (t_{B1} - t_{A1}) \tag{C.113}$$

Parameters V_{CA1N}, V_{CB1N} and i_{IN} are normalized values of voltages V_{CA1}, V_{CB1} and i_I, respectively. Equation (C.113) is valid for all cases of PRC operation.

For antiparallel diode (considering D2), from Fig. C.3,

$$\begin{aligned} V_{CA1N} &= \text{Capacitor voltage at point G} \\ &= - 1 - \sqrt{R^2 - I_{oN}^2} \end{aligned} \tag{C.114}$$

$$V_{CB1N} = \text{Capacitor voltage at point H}$$
$$= V_{C0N} = -I_{oN} I_{L1N} \tag{C.115}$$

Also from Fig. C.3,

$$i_{IN} = -I_{oN} \qquad \text{(Topological Mode M4)} \tag{C.116}$$

$$\theta_{A1B1} = \theta_{GH} = \alpha_d \tag{C.117}$$

Substituting for V_{CA1N} from (C.114), V_{CB1N} from (C.115), i_{IN} from (C.116), θ_{A1B1} from (C.117) and T_N from (C.96) into (C.112),

$$I_{DAVN} = \frac{1}{2(\alpha + \beta)} \left[1 + \sqrt{R^2 - I_{oN}^2} - I_{oN} I_{L1N} - I_{oN} \alpha_d\right] \tag{C.118}$$

Transistor Average Current: For transistor (considering Q1), from Fig. C.3,

$$V_{CA1N} = \text{Capacitor voltage at point H}$$
$$= V_{C0N} = -I_{oN} I_{L1N} \tag{C.119}$$

$$V_{CB1N} = \text{Capacitor voltage at point C}$$
$$= 1 + \sqrt{R^2 - I_{oN}^2} \tag{C.120}$$

$$i_{IN} = -I_{oN}, \quad \text{between H and A (M1)}$$
$$= +I_{oN}, \quad \text{between A and C (M2)} \tag{C.121}$$

$$\theta_{A1C1} = \text{Angular duration in M1}$$
$$= \theta_{HA} = \beta \tag{C.122}$$

$$\theta_{C1B1} = \text{Angular duration in M2}$$
$$= \theta_{AC} = \alpha - \alpha_d \tag{C.123}$$

Substituting for V_{CA1N} from (C.119), V_{CB1N} from (C.120), i_{IN} from (C.121), θ_{A1C1} from (C.122), θ_{C1B1} from (C.123), and T_N from (C.96) into (C.112),

$$I_{QAVN} = \frac{1}{2(\alpha + \beta)} \left[1 + \sqrt{R^2 - I_{oN}^2} + I_{oN} I_{L1N} - I_{oN} (\beta - \alpha + \alpha_d)\right] \tag{C.124}$$

Inductor Average Current

$$I_{LAV} = 2\,(I_{DAV} + I_{QAV}) \tag{C.125}$$

Thus, $$I_{LAVN} = 2\,(I_{DAVN} + I_{QAVN}) \tag{C.126}$$

Substituting for I_{DAVN} from (C.118) and I_{QAVN} from (C.124) into (C.126),

$$I_{LAVN} = \frac{1}{\alpha + \beta}\left[2 + 2\sqrt{R^2 - I_{oN}^2} - I_{oN}\,(\beta - \alpha + 2\,\alpha_d)\right] \tag{C.127}$$

Output Voltage: In Fig. 3.1,

$$v_C = V_s - v_L \qquad \text{(Topological Modes M1 and M2)} \tag{C.128}$$

$$v_C = -V_s - v_L \qquad \text{(Topological Modes M3 and M4)} \tag{C.129}$$

From (C.128), (C.129) and Fig. (C.3),

$$\begin{aligned} V_o &= \text{Output DC voltage} \\ &= V_{CAV} = \text{Half-cycle average capacitor voltage} \\ &= \frac{2}{T}\left[\int_{t_A}^{t_D} (V_s - v_L)\,dt + \int_{t_D}^{t_E} (-V_s - v_L)\,dt\right] \end{aligned} \tag{C.130}$$

Normalizing the voltages and time intervals,

$$V_{oN} = V_{CAVN} = \frac{2}{T_N}\left[\alpha - \beta - \int_0^{\theta_{AD} + \theta_{DE}} v_{LN}\,d\theta\right] \tag{C.131}$$

Based on (C.106) and Fig. C.3,

$$\int_0^{\theta_{AD} + \theta_{DE}} v_{LN}\,d\theta = -2\,I_{L1N} \tag{C.132}$$

Substituting (C.132) and for T_N from (C.96) into (C.131),

$$V_{oN} = V_{CAVN} = \frac{1}{\alpha + \beta}\,(\alpha - \beta + 2\,I_{L1N}) \tag{C.133}$$

C.2.1.2 Applicable Range Of Analysis

Let us determine minimum and maximum values of transistor radius. It is possible to construct a CCM steady-state trajectory with as large a radius as we desire, whenever I_{oN} is less than unity. Thus,

$$R < R_{max} = \infty , \qquad 0 \le I_{oN} \le 1 \tag{C.134}$$

For current range $1 \le I_{oN} \le \sqrt{2}$, Fig. C.1(e) is applicable. Based on (C.52),

$$R \le R_{max} = \frac{-\sqrt{I_{oN}^2 - 1} + I_{oN}^2}{\sqrt{I_{oN}^2 - 1}}, \qquad 1 < I_{oN} \le \sqrt{2} \tag{C.135}$$

In order to determine minimum radius, R_{min}, Fig. C.1(a) is utilized. From Fig. C.1(a),

$$R \ge R_{min} = 1 , \qquad 0 \le I_{oN} \le \sqrt{2} \tag{C.136}$$

Combining inequalities (C.134), (C.135) and (C.136),

$$\begin{aligned} &1 \le R < \infty, && 0 \le I_{oN} \le 1 \\ &1 \le R \le \frac{-\sqrt{I_{oN}^2 - 1} + I_{oN}^2}{\sqrt{I_{oN}^2 - 1}}, && 1 \le I_{oN} \le \sqrt{2} \end{aligned} \tag{C.137}$$

It can be easily verifed that the operating frequency ω_N, as given by (C.97), approaches the following boundary frequencies as R approaches its minimum and maximum values.

As $R \to R_{min}$ with $0 \le I_{oN} \le \sqrt{2}$, $\omega_N \to \omega_{LOW}$.

As $R \to R_{max}$ with $0 \le I_{oN} \le 1$, $\omega_N \to \omega_{MAX}$.

As $R \to R_{max}$ with $1 \le I_{oN} \le \sqrt{2}$, $\omega_N \to \omega_{MAX}$.

In particular, when $0 \le I_{oN} \le 1$, as $R \to R_{max} (= \infty)$, α as defined by (C.93) approaches $\frac{\pi}{2} + \cos^{-1} I_{oN}$, while β as defined by (C.94) approaches $\frac{\pi}{2} - \cos^{-1} I_{oN}$. Thus, from (C.97),

$$\omega_N = \omega_{MAX} = \frac{\pi}{\alpha + \beta} = 1, \qquad 0 \le I_{oN} \le 1 \tag{C.138}$$

This confirms the validity of (C.46).

Also, the equations for ω_{MAX} for $1 \leq I_{oN} \leq \sqrt{2}$ (C.60) and for ω_{LOW} (C.22) could have been obtained by determining the limit reached by ω_N (C.97) as R approaches its minimum and maximum limits.

By using the minimum and maximum values of R, limits reached by other parameters, such as normalized device currents, can also be determined.

C.2.2 CCM Analysis - Intersection-2

The analysis presented in this section corresponds to regions 8A and 8B of Fig. 3.26(b).

C.2.2.1 Analysis Of A Steady-State Trajectory

Reference is made to Fig. C.4 for derivation of equations in this section. Once again transistor trajectory radius R and normalized load current I_{oN} are assumed to be known. Many of the steps in the following derivations are similar to those in Sec. C.2.1.1.

From Fig. C.4,

$$I_{L1N} = AX + OX = \sqrt{R^2 - 1} + I_{oN} \tag{C.139}$$

$$R' = \sqrt{M1Y^2 + AY^2} = \sqrt{1 + (I_{L1N} + I_{oN})^2} \tag{C.140}$$

$$\theta_1 = \cos^{-1}\frac{1}{R} \tag{C.141}$$

$$\theta_4 = \cos^{-1}\frac{1}{R'} = \cos^{-1}\frac{1}{\sqrt{1 + (I_{L1N} + I_{oN})^2}} \tag{C.142}$$

From Δ FM4M1 in Fig. C.4,

$$\theta_2 = \cos^{-1}\frac{R^2 + 4 - R'^2}{4R} = \cos^{-1}\frac{1 - I_{oN} I_{L1N}}{R} \tag{C.143}$$

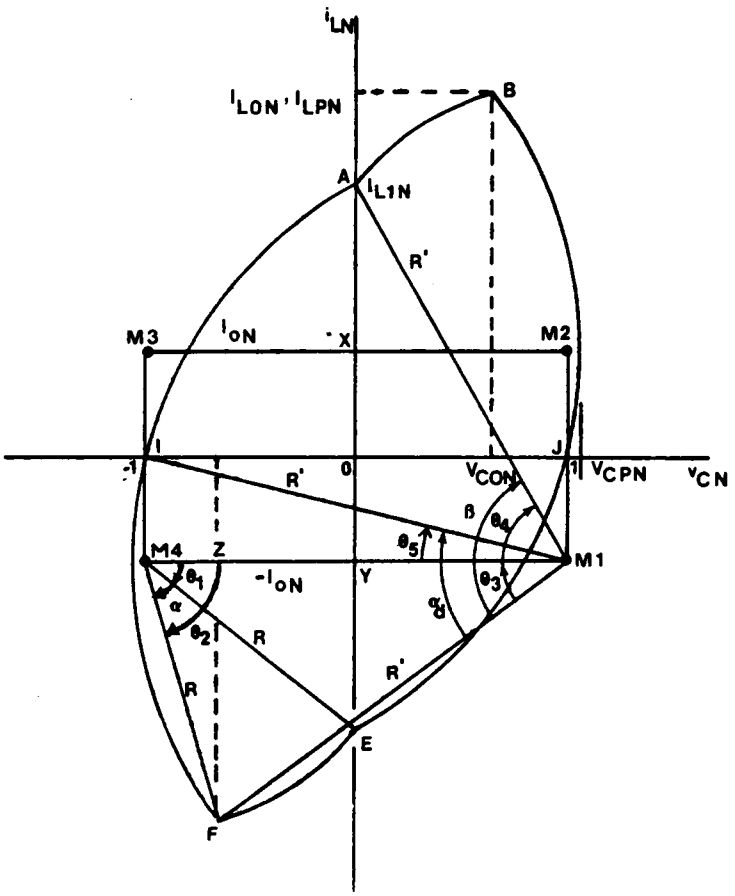

Figure C.4 CCM operation in intersection-2 - Analysis diagram

$$\theta_3 = \cos^{-1}\frac{R'^2 + 4 - R^2}{4R'} = \cos^{-1}\frac{1 + I_{oN}\,I_{L1N}}{\sqrt{1 + (I_{L1N} + I_{oN})^2}} \tag{C.144}$$

It is interesting to note that equations (C.139) through (C.144) are identical to equations (C.87) through (C.92) for CCM intersection-1 trajectories.

From Fig. C.4,

$$\alpha = \theta_2 - \theta_1 = \cos^{-1}\frac{1 - I_{oN}\,I_{L1N}}{R} - \cos^{-1}\frac{1}{R} \tag{C.145}$$

$$\beta = \theta_3 + \theta_4 = \cos^{-1}\frac{1}{\sqrt{1 + (I_{L1N} + I_{oN})^2}} + \cos^{-1}\frac{1 + I_{oN}\,I_{L1N}}{\sqrt{1 + (I_{L1N} + I_{oN})^2}} \tag{C.146}$$

Period And Frequency Of Operation: As was done in Sec. C.2.1.1, it can be shown that

$$T_N = 2(\alpha + \beta) \qquad \text{and} \tag{C.147}$$

$$\omega_N = \frac{\pi}{\alpha + \beta} \tag{C.148}$$

Equation (C.148) is used to derive ω_N, given R and I_{oN}. Alternatively, (C.148) can be used to determine R, given ω_N and I_{oN}.

Diode And Transistor Conduction Angles: From Fig. C.4,

$$\theta_5 = \sin^{-1}\frac{I_{oN}}{R'} = \sin^{-1}\frac{I_{oN}}{\sqrt{1 + (I_{L1N} + I_{oN})^2}} \tag{C.149}$$

$$\alpha_d = \theta_3 + \theta_5 = \cos^{-1}\frac{1 + I_{oN}\,I_{L1N}}{\sqrt{1 + (I_{L1N} + I_{oN})^2}} + \sin^{-1}\frac{I_{oN}}{\sqrt{1 + (I_{L1N} + I_{oN})^2}} \tag{C.150}$$

$$\alpha_q = \alpha + \beta - \alpha_d = \cos^{-1}\frac{1 - I_{oN}\,I_{L1N}}{R} - \cos^{-1}\frac{1}{R} + \cos^{-1}\frac{1}{\sqrt{1 + (I_{L1N} + I_{oN})^2}} - \sin^{-1}\frac{I_{oN}}{\sqrt{1 + (I_{L1N} + I_{oN})^2}} \tag{C.151}$$

Switching Point Variables: From Fig. C.4,

$$V_{C0N} = -(R\cos\theta_2 - 1) = I_{oN}\, I_{L1N} \tag{C.152}$$

$$I_{L0N} = R\sin\theta_2 + I_{oN} = \sqrt{R^2 - (1 - I_{oN}\, I_{L1N})^2} + I_{oN} \tag{C.153}$$

Peak State Variables: From Fig. C.4,

$$V_{CPN} = R' - 1 = \sqrt{1 + (I_{L1N} + I_{oN})^2} - 1 \tag{C.154}$$

$$\begin{aligned} I_{LPN} &= I_{L0N} \qquad \text{if} \quad \theta_2 \le \frac{\pi}{2} \\ &= R + I_{oN} \quad \text{if} \quad \theta_2 \ge \frac{\pi}{2} \end{aligned} \tag{C.155}$$

$$\text{So,} \qquad \begin{aligned} I_{LPN} &= \sqrt{R^2 - (1 - I_{oN}\, I_{L1N})^2} + I_{oN} \qquad \text{if} \quad \theta_2 \le \frac{\pi}{2} \\ &= R + I_{oN} \qquad\qquad\qquad\qquad\quad \text{if} \quad \theta_2 \ge \frac{\pi}{2}, \end{aligned} \tag{C.156}$$

where θ_2 is defined by (C.143).

Peak Inductor Volt-Seconds: Once again, the peak inductor volt-seconds is,

$$(VS)_{PN} = 2\, I_{LPN}\,, \tag{C.157}$$

where I_{LPN} is defined by (C.156).

Diode Average Current: For antiparallel diode (considering D2), from Fig. C.4,

$$\begin{aligned} V_{CA1N} &= \text{Capacitor voltage at point B} \\ &= V_{C0N} = I_{oN}\, I_{L1N} \end{aligned} \tag{C.158}$$

$$\begin{aligned} V_{CB1N} &= \text{Capacitor voltage at point J} \\ &= \sqrt{R'^2 - I_{oN}^2} - 1 = \sqrt{1 + I_{oN}\,(I_{L1N} + 2\, I_{oN})} - 1 \end{aligned} \tag{C.159}$$

$$i_{1N} = I_{oN} \qquad \text{(Topological Mode M2)} \tag{C.160}$$

$$\theta_{A1B1} = \theta_{BJ} = \alpha_d \tag{C.161}$$

Substituting for V_{CA1N} from (C.158), V_{CB1N} from (C.159), i_{IN} from (C.160), θ_{A1B1} from (C.161) and T_N from (C.147) into (C.112),

$$I_{DAVN} = \frac{1}{2(\alpha + \beta)}\left[\sqrt{1 + I_{oN}(I_{L1N} + 2I_{oN})} - 1 - I_{oN} I_{L1N} + I_{oN}\alpha_d\right] \tag{C.162}$$

Transistor Average Current: For transistor (considering Q1), from Fig. C.4,

$$\begin{aligned} V_{CA1N} &= \text{Capacitor voltage at point I} \\ &= -\sqrt{R'^2 - I_{oN}^2} + 1 = -\sqrt{1 + I_{oN}(I_{L1N}^2 + I_{oN})} + 1 \end{aligned} \tag{C.163}$$

$$\begin{aligned} V_{CB1N} &= \text{Capacitor voltage at point B} \\ &= V_{C0N} = I_{oN} I_{L1N} \end{aligned} \tag{C.164}$$

$$\begin{aligned} i_{IN} &= -I_{oN}, \quad \text{between I and A (M1)} \\ &= +I_{oN}, \quad \text{between A and B (M2)} \end{aligned} \tag{C.165}$$

$$\begin{aligned} \theta_{A1C1} &= \text{Angular duration in M1} \\ &= \theta_{IA} = \beta - \alpha_d \end{aligned} \tag{C.166}$$

$$\begin{aligned} \theta_{C1B1} &= \text{Angular duration in M2} \\ &= \theta_{AB} = \alpha \end{aligned} \tag{C.167}$$

Substituting for V_{CA1N} from (C.163), V_{CB1N} from (C.164), i_{IN} from (C.165), θ_{A1C1} from (C.166), θ_{C1B1} from (C.167) and T_N from (C.147) into (C.112),

$$I_{QAVN} = \frac{1}{2(\alpha + \beta)}\left[\sqrt{1 + I_{oN}(I_{L1N} + 2I_{oN})} - 1 + I_{oN} I_{L1N} - I_{oN}(\beta - \alpha_d - \alpha)\right] \tag{C.168}$$

Inductor Average Current

$$I_{LAV} = 2(I_{DAV} + I_{QAV}) \tag{C.169}$$

Thus,
$$I_{LAVN} = 2(I_{DAVN} + I_{QAVN}) \tag{C.170}$$

Substituting for I_{DAVN} from (C.162) and I_{QAVN} from (C.168) into (C.170),

$$I_{LAVN} = \frac{1}{\alpha + \beta}\left[2\sqrt{1 + I_{oN}(I_{L1N} + 2I_{oN})} - 2 - I_{oN}(\beta - 2\alpha_d - \alpha)\right] \quad \text{(C.171)}$$

Output Voltage From (C.128), (C.129) and Fig. (C.4),

$$V_o = V_{CAV} = \frac{2}{T}\left[\int_{t_A}^{t_B}(V_s - v_L)\,dt + \int_{t_B}^{t_E}(-V_s - v_L)\,dt\right] \quad \text{(C.172)}$$

Normalizing the voltages and time intervals,

$$V_{oN} = V_{CAVN} = \frac{2}{T_N}\left[\alpha - \beta - \int_0^{\theta_{AB} + \theta_{BE}} v_{LN}\,d\theta\right] \quad \text{(C.173)}$$

Based on (C.106) and Fig. C.4,

$$\int_0^{\theta_{AB} + \theta_{BE}} v_{LN}\,d\theta = -2I_{L1N} \quad \text{(C.174)}$$

Substituting (C.174) and for T_N from (C.147) into (C.173),

$$V_{oN} = V_{CAVN} = \frac{1}{\alpha + \beta}(\alpha - \beta + 2I_{L1N}) \quad \text{(C.175)}$$

C.2.2.2 Applicable Range Of Analysis

The maximum radius of the transistor trajectory is the same as in Sec. C.2.1.2. From (C.134) and (C.135),

$$\begin{aligned} R < R_{max} &= \infty, & 0 \le I_{oN} \le 1 \\ &= \frac{-\sqrt{I_{oN}^2 - 1} + I_{oN}^2}{\sqrt{I_{oN}^2 - 1}}, & 1 < I_{oN} \le \sqrt{2} \end{aligned} \quad \text{(C.176)}$$

For determining minimum value of R, Fig. C.1(g) is utilized. From Fig. C.1(g),

$$R \ge R_{min} = 1, \qquad 0 \le I_{oN} \le \sqrt{2} \quad \text{(C.177)}$$

Thus minimum and maximum values of R are identical to those in Sec. C.2.1.2. It can be easily verified that the operating frequency ω_N, as given by (C.148), approaches the following boundary frequencies as R approches its minimium and maximum values.

As $R \rightarrow R_{min}$ with $0 \leq I_{oN} \leq \sqrt{2}$, $\omega_N \rightarrow \omega_{HIGH}$.

As $R \rightarrow R_{max}$ with $0 \leq I_{oN} \leq 1$, $\omega_N \rightarrow \omega_{MAX}$.

As $R \rightarrow R_{max}$ with $1 < I_{oN} \leq \sqrt{2}$, $\omega_N \rightarrow \omega_{MAX}$.

In the current range $0 \leq I_{oN} \leq 1$, as $R \rightarrow R_{max} (= \infty)$, ω_N as defined by (C.148) approaches unity, which once again confirms (C.46).

Also, equations for ω_{MAX} in the current range $1 \leq I_{oN} \leq \sqrt{2}$ (C.60) and for ω_{HIGH} (C.81) could have been obtained by determining the limit reached by ω_N (C.148) as R approaches its minimum and maximum limits.

By using the minimum and maximum values of R, limits reached by other parameters, such as the normalized device currents, can also be determined.

C.2.3. TM1 Analysis - Intersection-1

The analysis presented in this section corresponds to regions 5A and 5B of Fig. 3.26(b). Please refer to Fig. C.5 for derivation of equations in this section. In this mode of operation, radius of transistor trajectory is constant ($R = 1$). Normalized current values I_{L1N} and I_{oN} are assumed to be the known variables. Equations for operating frequency ω_N and normalized output voltage V_{oN} are derived in terms of I_{L1N} and I_{oN}.

C.2.3.1 Applicable Range Of Analysis

In this section, the range of I_{L1N} for which analysis is valid will be established. Assuming that base drive strategy-1 is adopted, minimum value of I_{L1N} corresponds to value of i_{LN} at point E of Fig. C.1(b).

$$\text{Thus,} \quad I_{L1N} \geq -I_{oN}, \qquad 0 \leq I_{oN} < \infty \quad \text{Strategy-1} \tag{C.178}$$

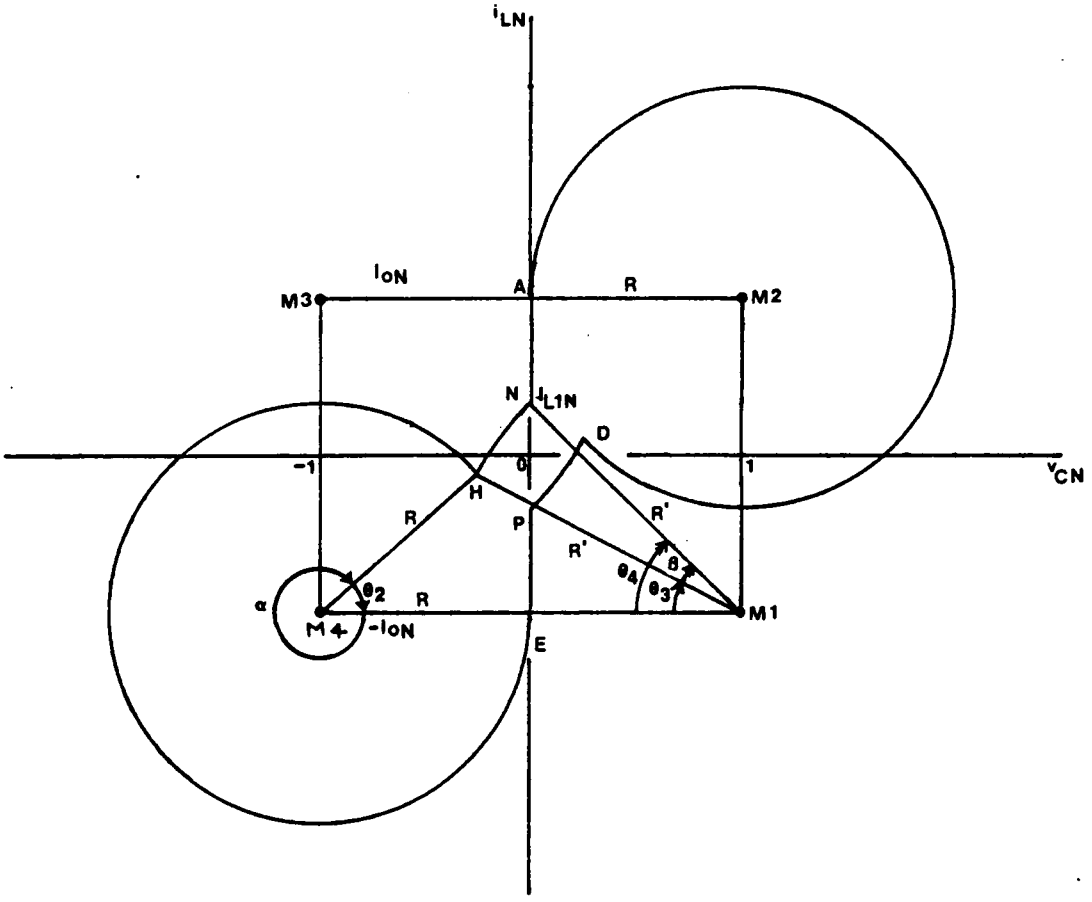

Figure C.5 TM1 operation in intersection-1 - Analysis diagram

For the range $0 \le I_{oN} \le \sqrt{2}$, maximum value of I_{L1N} corresponds to value of i_{LN} at point A of Fig. C.1(a).

$$\text{Thus,} \quad I_{L1N} \le I_{oN}, \qquad 0 \le I_{oN} \le \sqrt{2} \tag{C.179}$$

When $I_{oN} \ge \sqrt{2}$, maximum value of I_{L1N} equals value of i_{LN} at point $N(= ON)$ of Fig. C.1(f). Reproducing (C.66),

$$AN = 2\,(I_{oN} - \sqrt{2}\,) \tag{C.66}$$

From Fig. C.1(f),

$$ON = I_{oN} - AN = 2\sqrt{2} - I_{oN} \tag{C.180}$$

$$\text{Hence,} \quad I_{L1N} \le 2\sqrt{2} - I_{oN}, \qquad \sqrt{2} \le I_{oN} < \infty \tag{C.181}$$

For the case when base drive strategy-2 is adopted, only minimum value of I_{L1N} is altered for current range $0 \le I_{oN} \le 1$. Value of I_{L1N} in this case corresponds to magnitude of i_{LN} at point $N(= ON)$ of Fig. C.1(c). Reproducing (C.35),

$$AN = 2\,I_{oN} - 2\sqrt{1 - \sqrt{1 - I_{oN}^2}} \tag{C.35}$$

$$\text{Thus,} \quad ON = I_{oN} - AN = 2\sqrt{1 - \sqrt{1 - I_{oN}^2}} - I_{oN} \tag{C.182}$$

$$\text{Hence,} \quad I_{L1N} \ge 2\sqrt{1 - \sqrt{1 - I_{oN}^2}} - I_{oN}, \quad 0 \le I_{oN} \le 1 \quad \text{Strategy-2} \tag{C.183}$$

Inequalities (C.178), (C.179), (C.181) and (C.183) have been combined in the following.

$$\begin{aligned} 2\sqrt{1 - \sqrt{1 - I_{oN}^2}} - I_{oN} \le I_{L1N} \le I_{oN}, \qquad & 0 \le I_{oN} \le 1 \quad \text{Strategy-2} \\ -I_{oN} \le I_{L1N} \le I_{oN}, \qquad & 0 \le I_{oN} \le \sqrt{2} \quad \text{Strategy-1} \\ -I_{oN} \le I_{L1N} \le 2\sqrt{2} - I_{oN}, \qquad & \sqrt{2} \le I_{oN} < \infty \quad \text{Strategy-1} \end{aligned} \tag{C.184}$$

C.2.3.2 Analysis Of A Steady-State Trajectory

From Fig. C.5,

$$R = M2\,A = 1 \tag{C.185}$$

$$R' = \sqrt{M1E^2 + (ON + OE)^2} = \sqrt{1 + (I_{L1N} + I_{oN})^2} \tag{C.186}$$

$$\theta_4 = \cos^{-1}\frac{1}{R'} = \cos^{-1}\frac{1}{\sqrt{1 + (I_{L1N} + I_{oN})^2}} \tag{C.187}$$

From Δ HM4M1 in Fig. C.5,

$$\theta_2 = \cos^{-1}\frac{R^2 + 4 - R'^2}{4R} = \cos^{-1}\frac{4 - (I_{L1N} + I_{oN})^2}{4} \tag{C.188}$$

$$\theta_3 = \cos^{-1}\frac{R'^2 + 4 - R^2}{4R'} = \cos^{-1}\frac{4 + (I_{L1N} + I_{oN})^2}{4\sqrt{1 + (I_{L1N} + I_{oN})^2}} \tag{C.189}$$

Frequency Of Operation: From Fig. C.5,

$$AN = OA - ON = I_{oN} - I_{L1N} \tag{C.190}$$

$$T = 2\,(t_{EH} + t_{HN} + t_{NA}) \tag{C.191}$$

From (C.191), (C.3), (C.7) and Fig. C.5,

$$\omega_0 T = 2\,(\alpha + \beta + AN) \tag{C.192}$$

From Fig. C.5,

$$\alpha = 2\,\pi - \theta_2 \tag{C.193}$$

$$\beta = \theta_4 - \theta_3 \tag{C.194}$$

$$\text{Thus,} \quad \omega_0 T = 2\,(2\pi - \theta_2 + \theta_4 - \theta_3 + AN) \tag{C.195}$$

Substituting for θ_2 from (C.188), θ_3 from (C.189), θ_4 from (C.187) and AN from (C.190) into (C.195) and then utilizing (C.2),

$$\omega_N = \frac{\pi}{\left[2\pi - \cos^{-1}\frac{4 - (I_{L1N} + I_{oN})^2}{4} + \cos^{-1}\frac{1}{\sqrt{1 + (I_{L1N} + I_{oN})^2}} - \cos^{-1}\frac{4 + (I_{L1N} + I_{oN})^2}{4\sqrt{1 + (I_{L1N} + I_{oN})^2}} + I_{oN} - I_{L1N}\right]} \qquad \text{(C.196)}$$

Equation (C.196) is used to determine ω_N, given I_{L1N} and I_{oN}. Alternatively, (C.196) can be used to deterimine I_{L1N}, given ω_N and I_{oN}. As I_{L1N} approaches different limits as defined in (C.184), (C.196) reduces to a few of the boundary frequencies of Sec. C.1, as indicated below.

As $I_{L1N} \rightarrow 2\sqrt{1 - \sqrt{1 - I_{oN}^2}} - I_{oN}$ with $0 \leq I_{oN} \leq 1$, $\omega_N \rightarrow \omega_{TRAN}$.

As $I_{L1N} \rightarrow -I_{oN}$ with $0 \leq I_{oN} < \infty$, $\omega_N \rightarrow \omega_{MUL}$.

As $I_{L1N} \rightarrow I_{oN}$ with $0 \leq I_{oN} \leq \sqrt{2}$, $\omega_N \rightarrow \omega_{LOW}$.

As $I_{L1N} \rightarrow .2\sqrt{2} - I_{oN}$ with $\sqrt{2} \leq I_{oN} < \infty$, $\omega_N \rightarrow \omega_{MAX}$.

Equations for ω_{TRAN} (C.44), ω_{MUL} (C.29), ω_{LOW} (C.23) and ω_{MAX} in the range $\sqrt{2} \leq I_{oN} < \infty$ (C.69) could have been obtained in this manner also.

Output Voltage From (C.128), (C.129) and Fig. (C.5),

$$V_o = V_{CAV} = \frac{2}{T}\left[\int_{t_A}^{t_D}(V_s - v_L)\,dt + \int_{t_D}^{t_P}(-V_s - v_L)\,dt\right] \qquad \text{(C.197)}$$

Normalizing the voltages and time intervals,

$$V_{oN} = V_{CAVN} = \frac{2}{T_N}\left[\alpha - \beta - \int_0^{\theta_{AD} + \theta_{DP}} v_{LN}\,d\theta\right] \qquad \text{(C.198)}$$

Based on (C.106) and Fig. C.5,

$$\int_0^{\theta_{AD} + \theta_{DP}} v_{LN}\,d\theta = -AP = -(AO + OP) = -(I_{oN} + I_{L1N}) \qquad \text{(C.199)}$$

Substituting (C.199) and for T_N from (C.2), α from (C.193) and β from (C.194) into (C.198),

$$V_{oN} = V_{CAVN} = \frac{\omega_N}{\pi}(2\pi - \theta_2 - \theta_4 + \theta_3 + I_{oN} + I_{L1N}) \qquad \text{(C.200)}$$

Substituting for θ_2 from (C.188), θ_3 from (C.189), and θ_4 from (C.187) into (C.200),

$$V_{oN} = V_{CAVN} = \frac{\omega_N}{\pi}\left[2\pi - \cos^{-1}\frac{4-(I_{L1N}+I_{oN})^2}{4} - \cos^{-1}\frac{1}{\sqrt{1+(I_{L1N}+I_{oN})^2}} + \cos^{-1}\frac{4+(I_{L1N}+I_{oN})^2}{4\sqrt{1+(I_{L1N}+I_{oN})^2}} + I_{oN} + I_{L1N}\right] \quad \text{(C.201)}$$

C.2.4. TM2 Analysis

The analysis in this section corresponds to region 4 of Fig. 3.26(b). The analysis is carried out using Fig. C.6. In this mode also, I_{L1N} and I_{oN} are assumed to be known and equations for operating frequency ω_N and normalized output voltage V_{oN} are derived in terms of I_{L1N} and I_{oN}.

C.2.4.1 Applicable Range Of Analysis

Minimum value of I_{L1N} corresponds to value of i_{LN} at point O of Fig. C.1(d).

$$\text{Thus,} \quad I_{L1N} \geq 0, \qquad 0 \leq I_{oN} < 1 \quad \text{(C.202)}$$

Maximum value corresponds to point N(= ON) of Fig. C.1(c). Reproducing (C.35),

$$AN = 2I_{oN} - 2\sqrt{1-\sqrt{1-I_{oN}^2}} \quad \text{(C.35)}$$

From Fig. C.1(d),

$$ON = I_{oN} - AN = 2\sqrt{1-\sqrt{1-I_{oN}^2}} - I_{oN} \quad \text{(C.203)}$$

Hence, range of I_{L1N} is

$$0 \leq I_{L1N} \leq 2\sqrt{1-\sqrt{1-I_{oN}^2}} - I_{oN}, \quad 0 \leq I_{oN} \leq 1 \quad \text{Strategy-2} \quad \text{(C.204)}$$

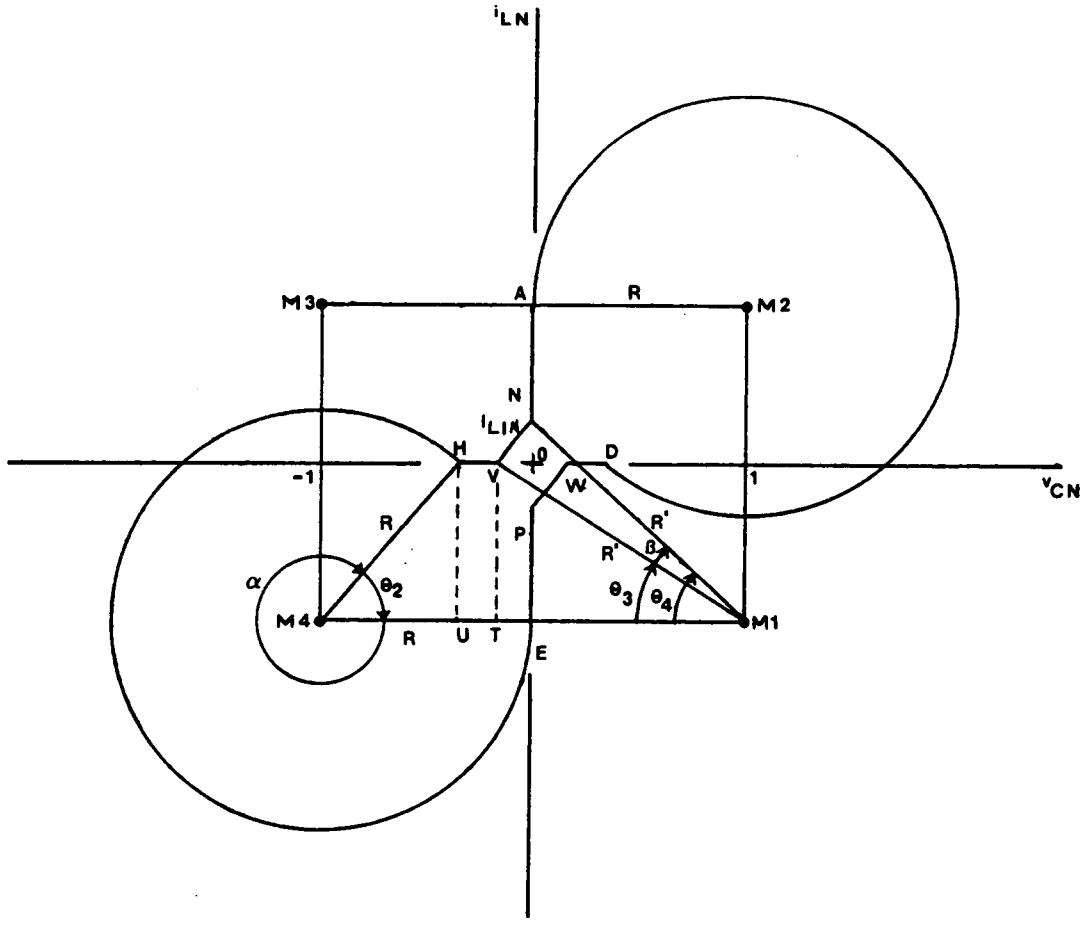

Figure C.6 TM2 operation - Analysis diagram

C.2.4.2 Analysis Of A Steady-State Trajectory

From Fig. C.6,

$$R = M2\,A = 1 \tag{C.205}$$

$$R' = \sqrt{M1E^2 + (ON + OE)^2} = \sqrt{1 + (I_{L1N} + I_{oN})^2} \tag{C.206}$$

$$M4\,U = \sqrt{R^2 - HU^2} = \sqrt{1 - I_{oN}^2} \tag{C.207}$$

$$\theta_2 = \cos^{-1}\frac{M4\,U}{R} = \cos^{-1}\sqrt{1 - I_{oN}^2} \tag{C.208}$$

$$\theta_4 = \cos^{-1}\frac{M1\,E}{R'} = \cos^{-1}\frac{1}{\sqrt{1 + (I_{L1N} + I_{oN})^2}} \tag{C.209}$$

$$M1\,T = \sqrt{R'^2 - V\,T^2} = \sqrt{1 + I_{L1N}\,(I_{L1N} + 2\,I_{oN})} \tag{C.210}$$

$$\theta_3 = \cos^{-1}\frac{M1\,T}{R'} = \cos^{-1}\frac{\sqrt{1 + I_{L1N}\,(I_{L1N} + 2\,I_{oN})}}{\sqrt{1 + (I_{L1N} + I_{oN})^2}} \tag{C.211}$$

Frequency Of Operation: From Fig. C.6,

$$AN = OA - ON = I_{oN} - I_{L1N} \tag{C.212}$$

$$\begin{aligned} H\,V &= M4\,T - M4\,U = 2 - M1\,T - M4\,U \\ &= 2 - \sqrt{1 + I_{L1N}\,(I_{L1N} + 2\,I_{oN})} - \sqrt{1 - I_{oN}^2} \end{aligned} \tag{C.213}$$

$$T = 2\,(t_{EH} + t_{HV} + t_{VN} + t_{NA}) \tag{C.214}$$

From (C.214), (C.3), (C.7), (C.11) and Fig. C.6,

$$\omega_0 T = 2\,(\alpha + \frac{H\,V}{I_{oN}} + \beta + AN) \tag{C.215}$$

From Fig. C.6,

$$\alpha = 2\,\pi - \theta_2 \tag{C.216}$$

$$\beta = \theta_4 - \theta_3 \tag{C.217}$$

$$\text{Thus,} \quad \omega_0 T = 2\,(2\pi - \theta_2 + \theta_4 - \theta_3 + \frac{H\,V}{I_{oN}} + AN) \tag{C.218}$$

Substituting for θ_2 from (C.208), θ_3 from (C.211), θ_4 from (C.209) *HV* from (C.213) and *AN* from (C.212) into (C.218) and then utilizing (C.2),

$$\omega_N = \frac{\pi}{\left[\begin{array}{l} 2\pi - \cos^{-1}\sqrt{1 - I_{oN}^2} + \cos^{-1}\dfrac{1}{\sqrt{1 + (I_{L1N} + I_{oN})^2}} \\ \qquad - \cos^{-1}\dfrac{\sqrt{1 + I_{L1N}\,(I_{L1N} + 2\,I_{oN})}}{\sqrt{1 + (I_{L1N} + I_{oN})^2}} \\ + \dfrac{2 - \sqrt{1 + I_{L1N}\,(I_{L1N} + 2\,I_{oN})} - \sqrt{1 - I_{oN}^2}}{I_{oN}} + I_{oN} - I_{L1N} \end{array}\right]} \tag{C.219}$$

Equation (C.219) is used to determine ω_N, given I_{L1N} and I_{oN}. Alternatively, (C.219) can be used to determine I_{L1N}, given ω_N and I_{oN}. The following boundary equations can be derived from (C.219).

As $I_{L1N} \to 0$ with $0 \le I_{oN} \le 1$, $\omega_N \to \omega_{DISC}$.

As $I_{L1N} \to 2\sqrt{1 - \sqrt{1 - I_{oN}^2}} - I_{oN}$ with $0 \le I_{oN} \le 1$, $\omega_N \to \omega_{TRAN}$.

Equations for ω_{DISC} (C.53) and ω_{TRAN} (C.44) could have been obtained in this manner also.

Output Voltage: During capacitor charging/discharging interval, let V_{C1} and V_{C2} (both assumed to be greater than zero) be initial and final values of capacitor voltage corresponding to instants t_1 and t_2 respectively. Then from (C.10),

$$t_2 - t_1 = \frac{C\,|V_2 - V_1|}{I_o} \tag{C.220}$$

Since the capacitor charges and discharges linearly during this interval,

$$\int_{t_1}^{t_2} v_C\,dt = \int_{t_1}^{t_2} \left[V_{C1} + \frac{V_{C2} - V_{C1}}{t_2 - t_1}\,(t - t_1)\right] dt \tag{C.221}$$

Integrating (C.221) and then substituting for $(t_2 - t_1)$ from (C.220),

$$\int_{t_1}^{t_2} v_C \, dt = \frac{C\,|V_{C2}^2 - V_{C1}^2|}{2\,I_o} \tag{C.222}$$

Normalizing (C.222),

$$\int_0^{\omega_0(t_2 - t_1)} v_{CN} \, d\theta = = \frac{|V_{C2N}^2 - V_{C1N}^2|}{2\,I_{oN}} \tag{C.223}$$

From (C.128), (C.129) and Fig. (C.6),

$$V_o = V_{CAV} = \frac{2}{T}\left[\int_{t_A}^{t_D} (V_s - v_L)\,dt + \int_{t_D}^{t_W} v_C dt + \int_{t_W}^{t_P} (-V_s - v_L)\,dt\right] \tag{C.224}$$

Normalizing the voltages and time intervals,

$$V_{oN} = V_{CAVN} = \frac{2}{T_N}\left[2\pi - \theta_2 - \theta_4 + \theta_3 - \int_0^{\theta_{AD} + \theta_{WP}} v_{LN}\,d\theta + \int_0^{\omega_0(t_W - t_D)} v_{CN}\,d\theta\right] \tag{C.225}$$

Based on (C.106) and Fig. C.6,

$$\int_0^{\theta_{AD} + \theta_{WP}} v_{LN}\,d\theta = -AP = -(AO + OP) = -(I_{oN} + I_{L1N}) \tag{C.226}$$

Based on (C.223) and Fig. C.6,

$$\int_0^{\omega_0(t_W - t_D)} v_{CN}\,d\theta = \frac{OD^2 - OW^2}{2\,I_{oN}} \tag{C.227}$$

From Fig. C.6,

$$OD = OH = 1 - M4\,U = 1 - \sqrt{1 - I_{oN}^2} \tag{C.228}$$

$$OW = OV = M1\,T - 1 = \sqrt{1 + I_{L1N}\,(I_{L1N} + 2\,I_{oN})} - 1 \tag{C.229}$$

Substituting for *OW* from (C.229) and *OD* from (C.228) into (C.229),

$$\int_0^{\omega_0(t_W - t_D)} v_{CN}\,d\theta = \frac{(1 - \sqrt{1 - I_{oN}^2})^2 - (\sqrt{1 + I_{L1N}\,(I_{L1N} + 2\,I_{oN})} - 1)^2}{2\,I_{oN}} \tag{C.230}$$

Substituting (C.226), (C.230) and for T_N from (C.2), θ_2 from (C.208) θ_3 from (C.211) and θ_4 from (C.209) into (C.225),

$$V_{oN} = V_{CAVN} = \frac{\omega_N}{\pi}\left[2\pi - \cos^{-1}\sqrt{1 - I_{oN}^2} - \cos^{-1}\frac{1}{\sqrt{1 + (I_{L1N} + I_{oN})^2}} \right.$$
$$+ \cos^{-1}\frac{\sqrt{1 + I_{L1N}(I_{L1N} + 2\,I_{oN})}}{\sqrt{1 + (I_{L1N} + I_{oN})^2}} + I_{oN} + I_{L1N} \qquad \text{(C.231)}$$
$$\left. + \frac{(1 - \sqrt{1 - I_{oN}^2})^2 - (\sqrt{1 + I_{L1N}(I_{L1N} + 2\,I_{oN})} - 1)^2}{2\,I_{oN}} \right]$$

C.2.5. DCM Analysis

The analysis in this section is carried out using Fig. C.7 and corresponds to region 1 of Fig. 3.26(b). In this mode, operating frequency ω_N and load current I_{oN} are assumed to be the known variables. Thus in this region of operation output voltage V_{oN} is conveniently expressed as an explicit function of ω_N and I_{oN}.

C.2.5.1 Applicable Range Of Analysis

Theoretically, operating frequency ω_N can be as low as desired. The maximimum operating frequency is given by boundary frequency ω_{DISC} derived in Sec. C.1.5.

$$\text{Thus,} \quad 0 < \omega_N \leq \omega_{DISC}\,, \qquad \text{(C.232)}$$

where equation for ω_{DISC} is in (C.53).

C.2.5.2 Analysis Of A Steady-State Trajectory

Since ω_N is known, only equation for V_{oN} is to be derived. From Fig. C.7,

$$R = M2\,A = 1 \qquad \text{(C.233)}$$

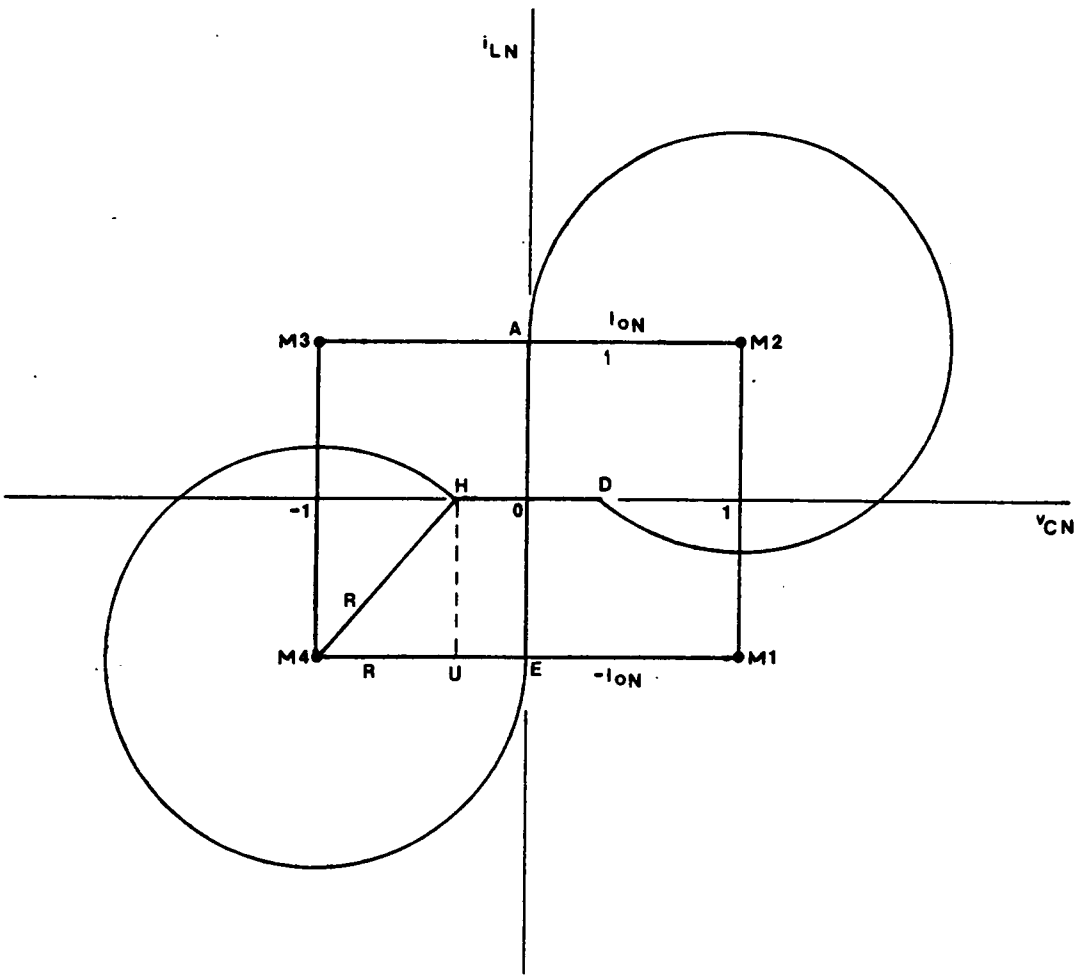

Figure C.7 DCM operation - Analysis diagram

$$OD = OH = 1 - M4\,U = 1 - \sqrt{1 - I_{oN}^2} \tag{C.234}$$

$$\alpha = 2\pi - \theta_2 = 2\pi - \cos^{-1}\sqrt{1 - I_{oN}^2} \tag{C.235}$$

From (C.128) and Fig. (C.7),

$$V_o = V_{CAV} = \frac{2}{T}\left[\int_{t_A}^{t_D} (V_s - v_L)\,dt + \int_{t_D}^{t_O} v_C dt\right] \tag{C.236}$$

Normalizing the voltages and time intervals,

$$V_{oN} = V_{CAVN} = \frac{2}{T_N}\left[\alpha - \int_0^{\theta_{AD}} v_{LN}\,d\theta + \int_0^{\omega_0(t_D - t_O)} v_{CN}\,d\theta\right] \tag{C.237}$$

Based on (C.106) and Fig. C.7,

$$\int_0^{\theta_{AD}} v_{LN}\,d\theta = -AO = -I_{oN} \tag{C.238}$$

Based on (C.223), (C.234) and Fig. C.7,

$$\int_0^{\omega_0(t_D - t_O)} v_{CN}\,d\theta = \frac{OD^2 - 0^2\,(1 - \sqrt{1 - I_{oN}^2})^2}{2\,I_{oN}} \tag{C.239}$$

Substituting (C.239), (C.238) and for T_N from (C.2) and α from (C.235) into (C.237),

$$V_{oN} = V_{CAVN} = \frac{\omega_N}{\pi}\left[2\pi - \cos^{-1}\sqrt{1 - I_{oN}^2} + I_{oN} + \frac{(1 - \sqrt{1 - I_{oN}^2})^2}{2\,I_{oN}}\right] \tag{C.240}$$

C.2.6.TM1 Analysis - Intersection-2

The analysis presented in this section pertains to region 6 of Fig. 3.26(b). The derivation of the equations are based on Fig. C.8. The steps followed are similar to those in Sec. C.2.3. Normalized current values I_{L1N} and I_{oN} are assumed to be known and equations for ω_N and V_{oN} are derived in terms of these current values.

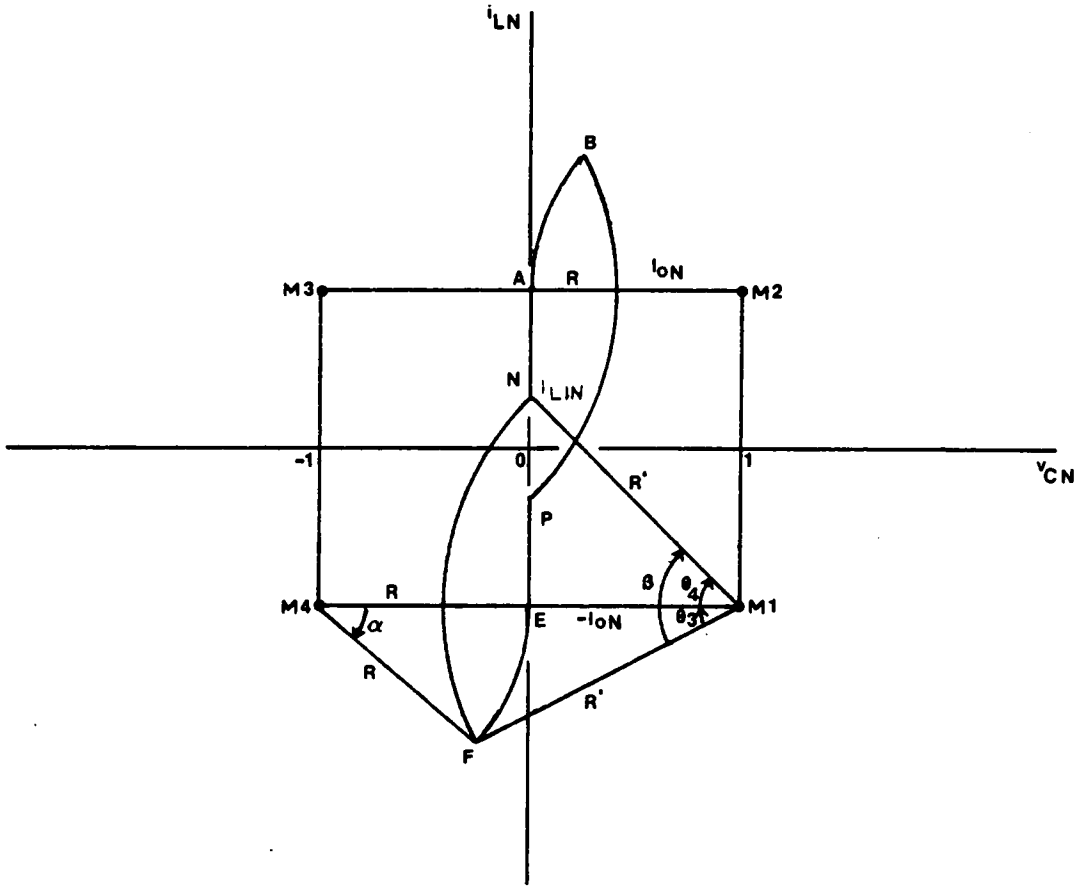

Figure C.8 TM1 operation in intersection-2 - Analysis diagram

C.2.6.1 Applicable Range Of Analysis

Minimum value of I_{L1N} corresponds to magnitude of i_{LN} at point $E(= OE)$ of Fig. C.1(h). Thus,

$$I_{L1N} \geq -I_{oN},\ 0 \leq I_{oN} < \infty \tag{C.241}$$

For range $0 \leq I_{oN} \leq \sqrt{2}$, the maximum value of I_{L1N} corresponds to magnitude of i_{LN} at point $A(= OA)$ of Fig. C.1(g). Thus,

$$I_{L1N} \leq I_{oN},\ 0 \leq I_{oN} \leq \sqrt{2} \tag{C.242}$$

When $I_{oN} \geq \sqrt{2}$, maximum value of I_{L1N} equals value of i_{LN} at point $N(= ON)$ of Fig.C.1(f), which is given by (C.181). Reproducing (C.181),

$$I_{L1N} \leq 2\sqrt{2} - I_{oN},\qquad \sqrt{2} \leq I_{oN} < \infty \tag{C.243}$$

Combining inequalities (C.241), (C.242) and (C.243),

$$\begin{aligned} -I_{oN} \leq I_{L1N} \leq I_{oN},&\qquad 0 \leq I_{oN} \leq \sqrt{2} \\ -I_{oN} \leq I_{L1N} \leq 2\sqrt{2} - I_{oN},&\qquad \sqrt{2} \leq I_{oN} < \infty \end{aligned} \tag{C.244}$$

C.2.6.2 Analysis Of A Steady-State Trajectory

From Fig. C.8,

$$R = M2\,A = 1 \tag{C.245}$$

$$R' = \sqrt{M1E^2 + (ON + OE)^2} = \sqrt{1 + (I_{L1N} + I_{oN})^2} \tag{C.246}$$

$$\theta_4 = \cos^{-1}\frac{1}{R'} = \cos^{-1}\frac{1}{\sqrt{1 + (I_{L1N} + I_{oN})^2}} \tag{C.247}$$

From Δ FM4M1 in Fig. C.8,

$$\alpha = \cos^{-1}\frac{R^2 + 4 - R'^2}{4R} = \cos^{-1}\frac{4 - (I_{L1N} + I_{oN})^2}{4} \tag{C.248}$$

$$\theta_3 = \cos^{-1}\frac{R'^2 + 4 - R^2}{4R'} = \cos^{-1}\frac{4 + (l_{L1N} + l_{oN})^2}{4\sqrt{1 + (l_{L1N} + l_{oN})^2}} \tag{C.249}$$

Frequency Of Operation: From Fig. C.8,

$$AN = OA - ON = l_{oN} - l_{L1N} \tag{C.250}$$

$$T = 2\,(t_{EF} + t_{FN} + t_{NA}) \tag{C.251}$$

From (C.251), (C.3), (C.7) and Fig. C.8,

$$\omega_0 T = 2\,(\alpha + \beta + AN) \tag{C.252}$$

From Fig. C.8,

$$\beta = \theta_4 + \theta_3 \tag{C.253}$$

$$\text{Thus,} \quad \omega_0 T = 2\,(\alpha + \theta_4 + \theta_3 + AN) \tag{C.254}$$

Substituting for α from (C.248), θ_3 from (C.249), θ_4 from (C.247) and AN from (C.250) into (C.254) and then utilizing (C.2),

$$\omega_N = \frac{\pi}{\left[\cos^{-1}\frac{4 - (l_{L1N} + l_{oN})^2}{4} + \cos^{-1}\frac{1}{\sqrt{1 + (l_{L1N} + l_{oN})^2}} + \cos^{-1}\frac{4 + (l_{L1N} + l_{oN})^2}{4\sqrt{1 + (l_{L1N} + l_{oN})^2}} + l_{oN} - l_{L1N}\right]} \tag{C.255}$$

Equation (C.255) is used to determine ω_N, given l_{L1N} and l_{oN}. Alternatively, (C.225) can be used to determine l_{L1N}, given ω_N and l_{oN}. As l_{L1N} approaches the limits defined by (C.244), different boundary frequencies of Sec. C.1 are reached as follows.

As $l_{L1N} \to -l_{oN}$ with $0 \le l_{oN} < \infty$, $\omega_N \to \omega_{LIMIT}$.

As $l_{L1N} \to l_{oN}$ with $0 \le l_{oN} \le \sqrt{2}$, $\omega_N \to \omega_{HIGH}$.

As $l_{L1N} \to 2\sqrt{2} - l_{oN}$ with $\sqrt{2} \le l_{oN} < \infty$, $\omega_N \to \omega_{MAX}$.

Equations for ω_{LIMIT} (C.85), ω_{HIGH} (C.81), and ω_{MAX} in the range $\sqrt{2} \leq I_{oN} < \infty$ (C.69) could have been obtained in this manner also.

Output Voltage: From (C.128), (C.129) and Fig. (C.8),

$$V_o = V_{CAV} = \frac{2}{T}\left[\int_{t_A}^{t_B} (V_s - v_L)\, dt + \int_{t_B}^{t_P} (-V_s - v_L)\, dt\right] \tag{C.256}$$

Normalizing the voltages and time intervals,

$$V_{oN} = V_{CAVN} = \frac{2}{T_N}\left[\alpha - \beta - \int_0^{\theta_{AB} + \theta_{BP}} v_{LN}\, d\theta\right] \tag{C.257}$$

Based on (C.106) and Fig. C.8,

$$\int_0^{\theta_{AB} + \theta_{BP}} v_{LN}\, d\theta = -AP = -(AO + OP) = -(I_{oN} + I_{L1N}) \tag{C.258}$$

Substituting (C.258) and for T_N from (C.2) and β from (C.253) into (C.257),

$$V_{oN} = V_{CAVN} = \frac{\omega_N}{\pi}(\alpha - \theta_4 - \theta_3 + I_{oN} + I_{L1N}) \tag{C.259}$$

Substituting for α from (C.248), θ_3 from (C.249) and θ_4 from (C.247) into (C.259),

$$V_{oN} = V_{CAVN} = \frac{\omega_N}{\pi}\left[\cos^{-1}\frac{4 - (I_{L1N} + I_{oN})^2}{4} - \cos^{-1}\frac{1}{\sqrt{1 + (I_{L1N} + I_{oN})^2}} - \cos^{-1}\frac{4 + (I_{L1N} + I_{oN})^2}{4\sqrt{1 + (I_{L1N} + I_{oN})^2}} + I_{oN} + I_{L1N}\right] \tag{C.260}$$

C.2.7 LIMIT Analysis

No detailed analysis is required in this region of operation. When $\omega_N \geq \omega_{LIMIT}$, the capacitor always stays at zero voltage and thus,

$$V_{oN} = V_{CAVN} = 0\,, \qquad \omega_{LIMIT} \leq \omega_N < \infty\,, \tag{C.261}$$

where the equation for ω_{LIMIT} is given by (C.85).

C.3 Design Curves

Computer programs based on equations in Secs. C.1 and C.2 are in Sec. C.5. Figures C.9 and C.10 show a set of design curves for CCM below resonance and CCM above resonance, respectively, which were generated using these programs.

The output characteristics of a PRC (V_{oN} versus I_{oN} for different ω_Ns) are shown in Fig. C.11. Using the output characteristics and the load characteristic, the operating point of a converter can be determined. Figure 12 shows the complete ideal dc characteristcs of a PRC, covering all regions of operation except the MULTIPLE region. The curves shown in Figs. C.9, C.10 and C.11 are useful in carrying out a preliminary design of a PRC.

C.4 Numerical Example

In this example, a PRC is compared with a SRC for use in a voltage regulator application. Only operation below resonant frequency is considered. This example is presented in greater detail in [73]. To simplify matters, device drops and other losses have been neglected.

Input Voltage $= V_s = 86.4$ to $115.2\ V$

Output Voltage $= V'_o = 220\ V$ (Regulated)

Load Current $= I'_o = 0$ to $10\ A$ for PRC and 3 to $10\ A$ for SRC

Maximum Operating Frequency $= f_{MAX} = 160\ kHz$

Let us assume that maximum value of ω_N ($= \omega_{NMAX}$) is limited to 0.8 for the PRC. Furthermore, let maximum value of I_{oN} ($= I_{oNMAX}$) be equal to 0.8. Likewise, let maximum value of V_{oN} ($= V_{oNMAX}$) be

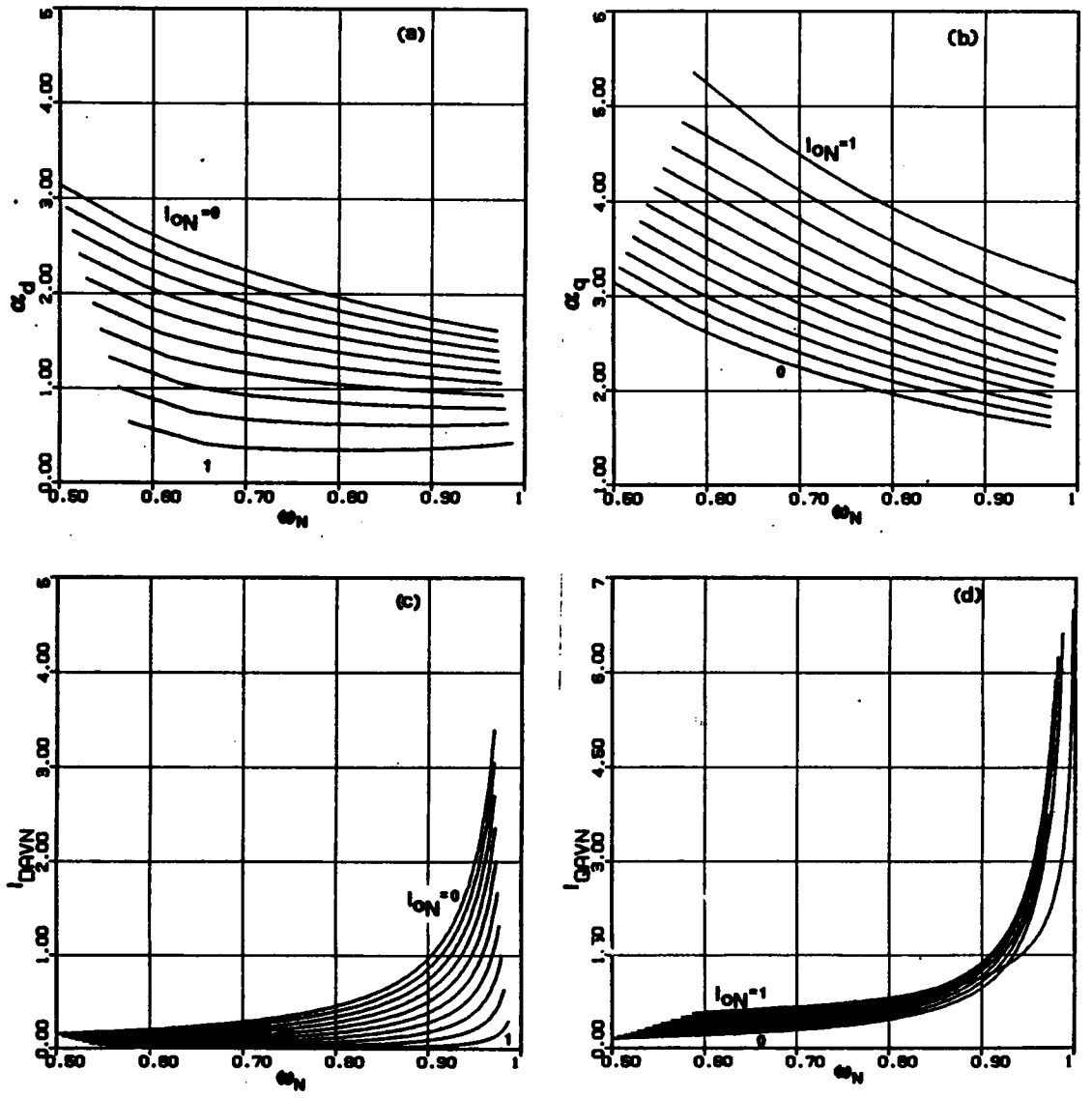

Figure C.9 Ideal design curves for a PRC - CCM below resonance ($I_{ON} \leq 1$)

a) Diode conduction angle
b) Transistor conduction angle
c) Normalized average diode current
d) Normalized average transistor current

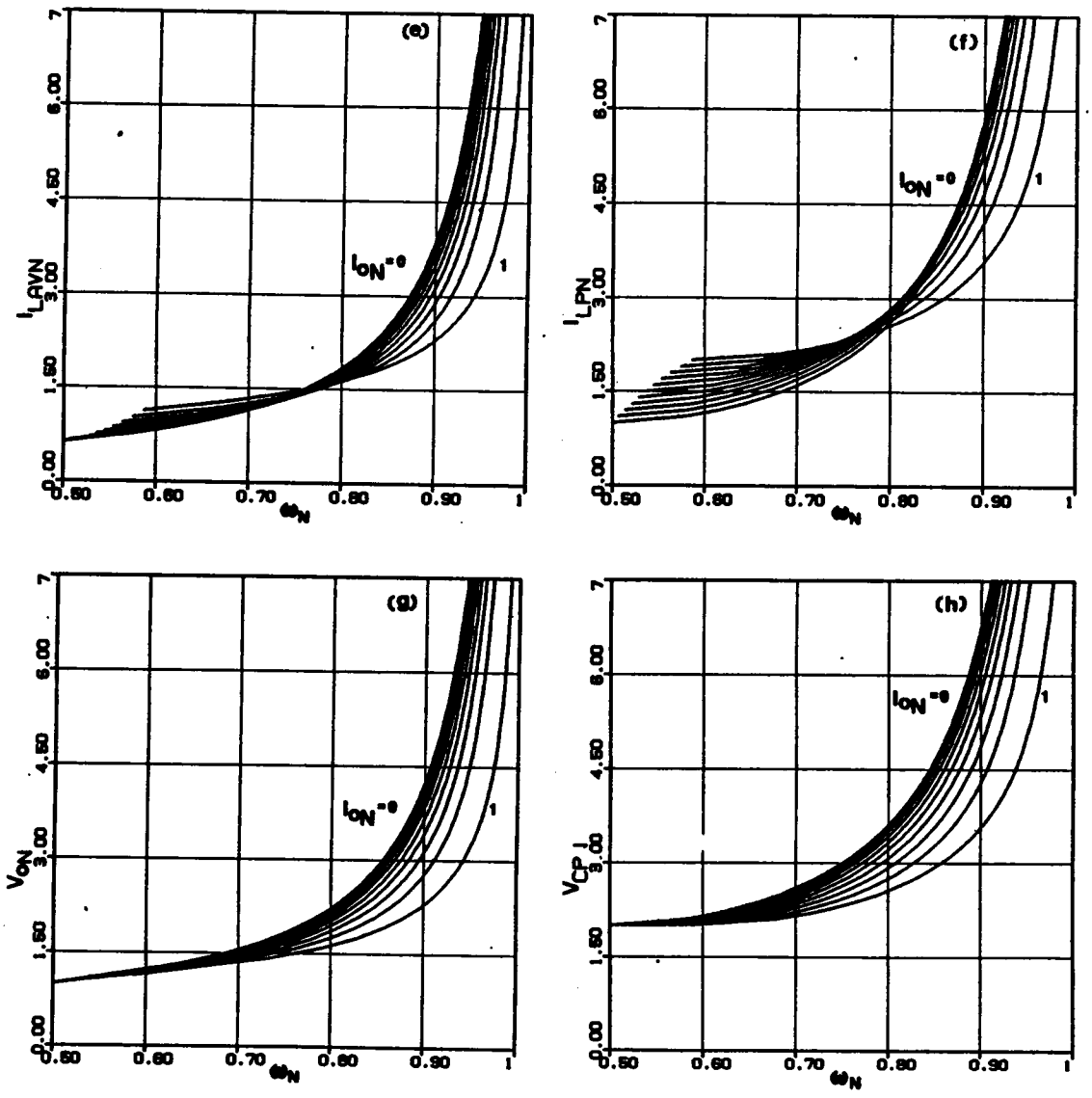

Figure C.9 (contd.)
e) Normalized average inductor current
f) Normalized peak inductor current
g) Normalized half-cycle average capacitor voltage/normalized output voltage
h) Normalized peak capacitor voltage

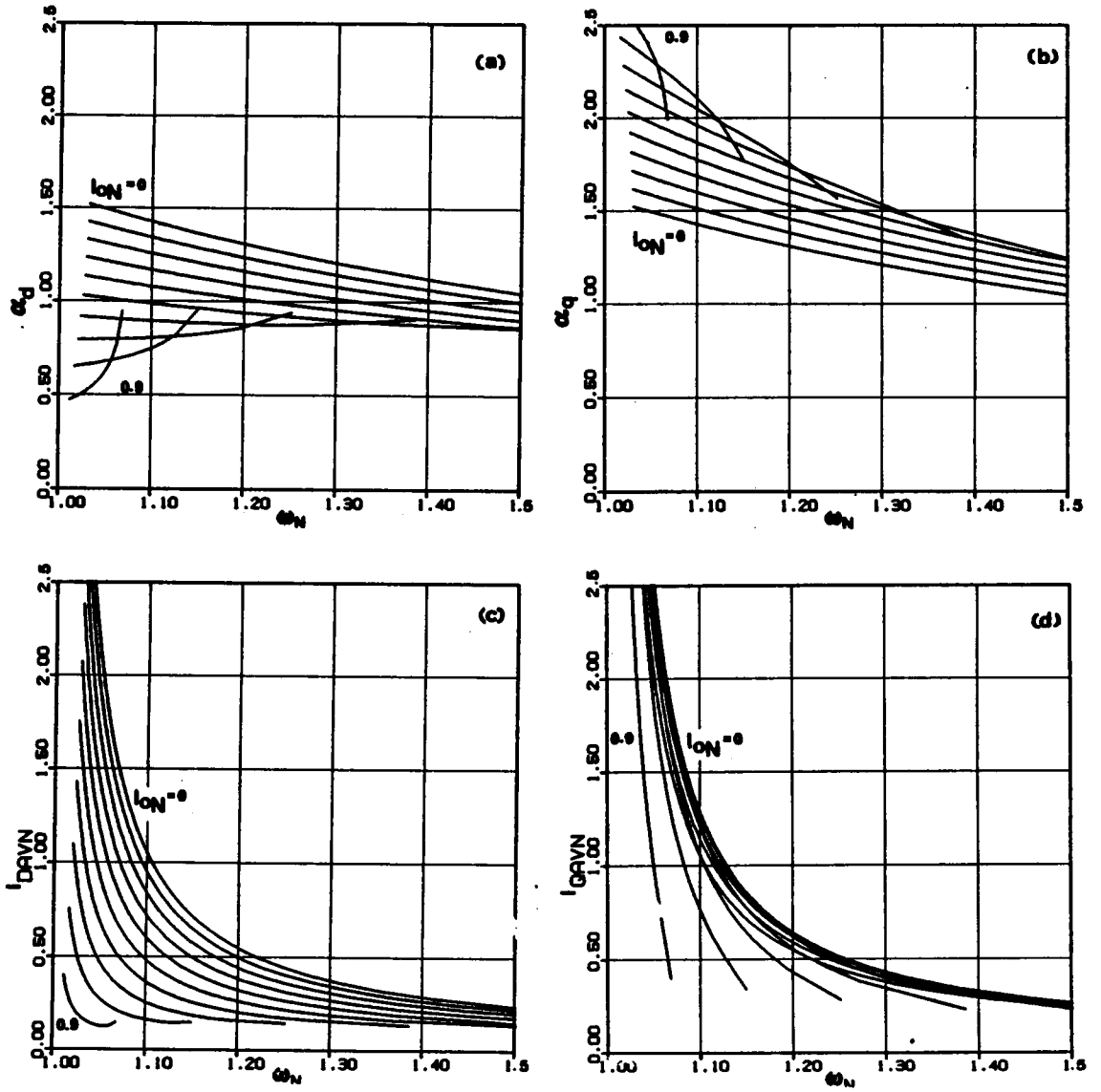

Figure C.10 Ideal design curves for a PRC - CCM above resonance ($I_{oN} < 1$)

a) Diode conduction angle
b) Transistor conduction angle
c) Normalized average diode current
d) Normalized average transistor current

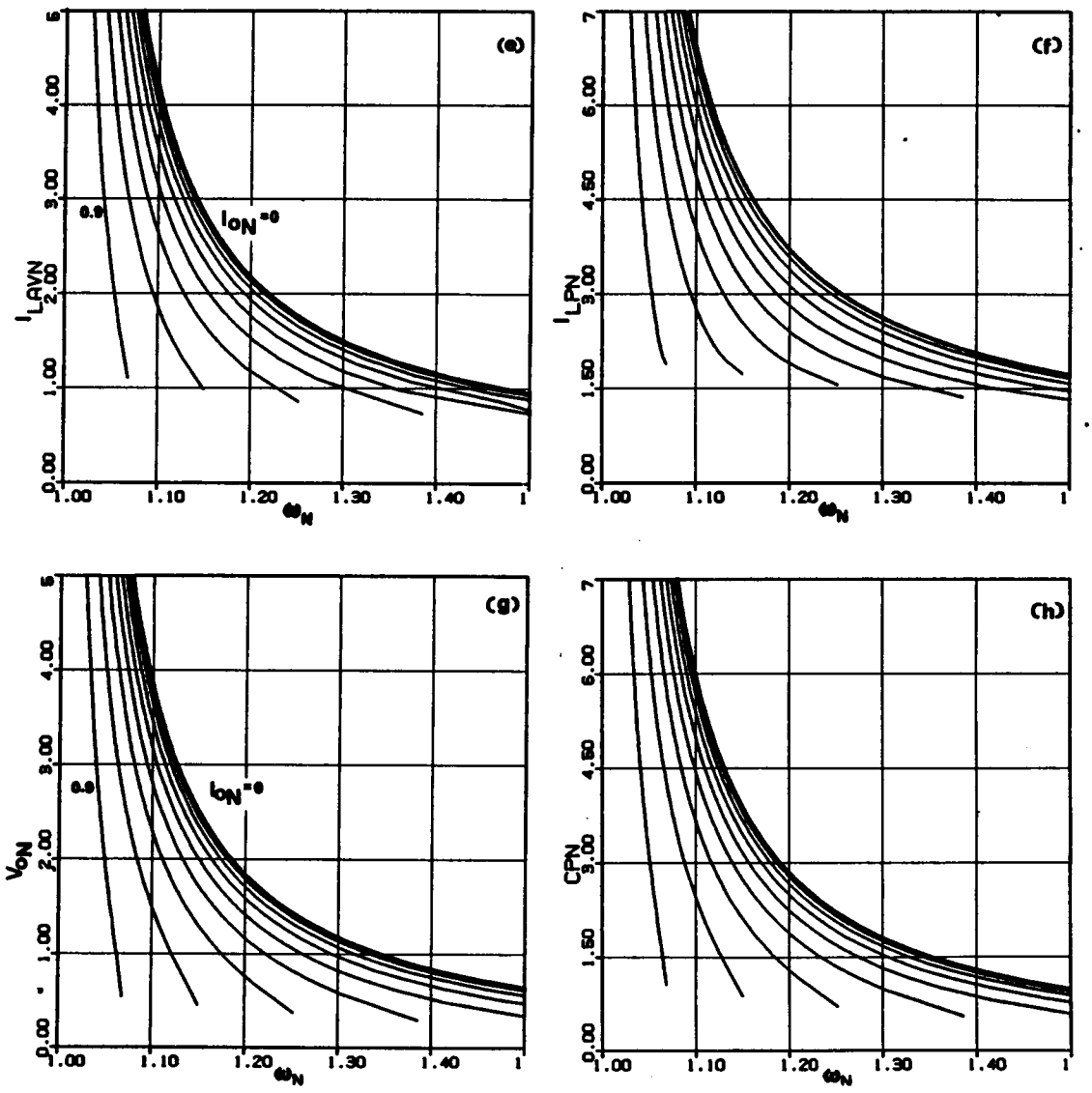

Figure C.10 (contd.)
e) Normalized average inductor current
f) Normalized peak inductor current
g) Normalized half-cycle average capacitor voltage/normalized output voltage
h) Normalized peak capacitor voltage

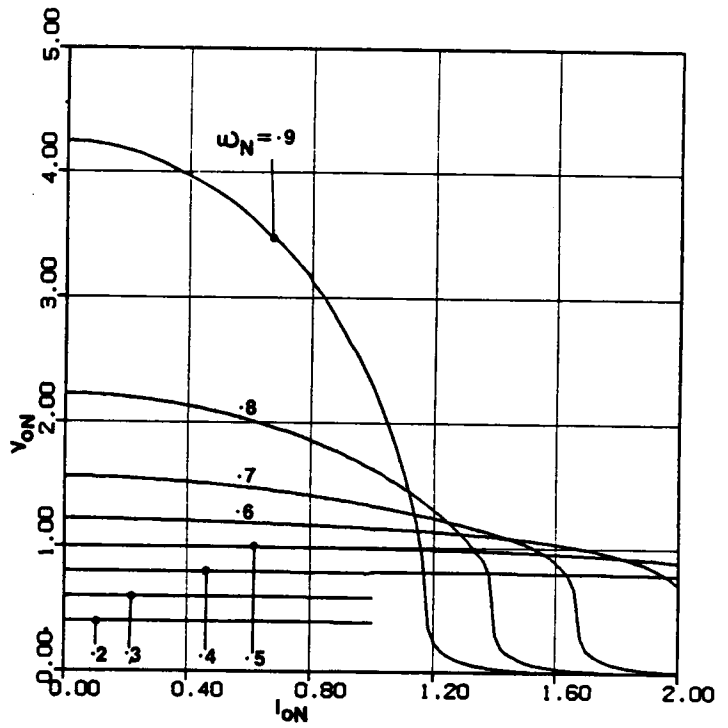

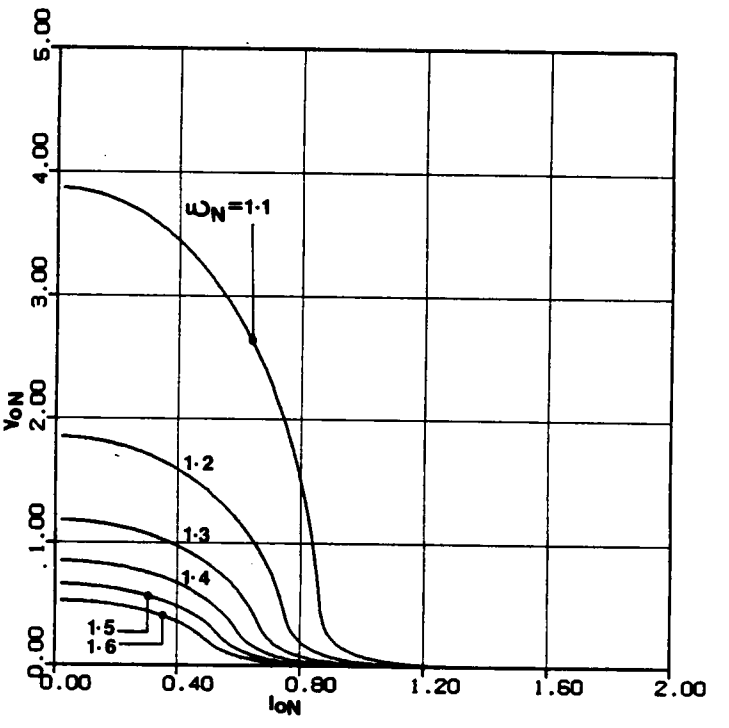

Figure C.11 Ideal DC charateristics of a PRC
a) Below resonant frequency b) Above resonant frequency

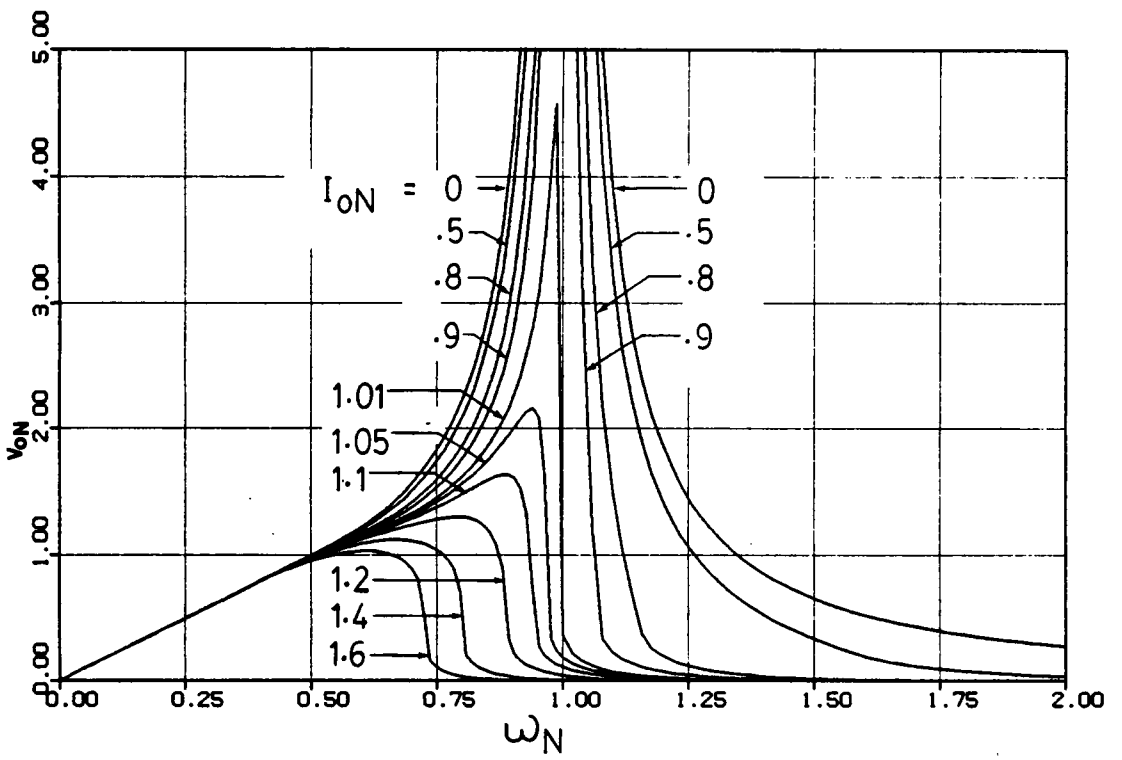

Figure C.12 Complete ideal DC characteristics of a PRC

limited to 0.8 for the SRC. These additional constraints are reasonable and have been introduced so that unique designs result in both the SRC and PRC. Also, in both cases, the output voltage has to be stepped up and, hence, a n : 1 ratio transformer is placed across the input terminals of the output bridge rectifer.

C.4.1 PRC Design

The tranformer ratio n should be such that full output voltage is developed at maximum operating frequency under worst-case operating conditions - full load current and low input supply. From Fig. C.11(a) (or Fig. C.9(g)),

$$\text{at} \quad \omega_N = 0.8 \text{ and } I_{oN} = 0.8, \quad V_{oN} = V_{oNMAX} = \frac{nV'_o}{V_{sMIN}} = 1.85$$

$$n = \frac{V_{oN} V_{sMIN}}{V'_o} = \frac{1.85 \times 86.4}{220} = 0.727$$

$$\text{Also,} \qquad I_{oNMAX} = \frac{\frac{I'_{oMAX}}{n} Z_0}{V_{sMIN}}$$

$$\text{So,} \qquad Z_0 = \frac{n I_{oNMAX} V_{sMIN}}{I'_{oMAX}} = \frac{0.727 \times 0.8 \times 86.4}{10} = 5.025\ \Omega$$

Since $\omega_{NMAX} = \frac{f_{MAX}}{f_0} = 0.8$,

$$f_0 = \frac{f_{MAX}}{\omega_{NMAX}} = \frac{160\ kHz}{0.8} = 200\ kHz$$

$$\omega_0 = 2\pi f_0 = 2\pi \times 200 \times 10^3 = 1256637.1\ \textit{radians/second}$$

From $\omega_0 = \frac{1}{\sqrt{LC}}$ and $Z_0 = \sqrt{\frac{L}{C}}$,

$$L = \frac{Z_0}{\omega_0} = \frac{5.025}{1256637.1} = 3.999\ \mu H$$

$$C = \frac{1}{Z_0\,\omega_0} = \frac{1}{5.025 \times 1256637.1} = 0.1584\ \mu F$$

Thus, in this design,

$$L = 3.999\ \mu H, \qquad C = 0.1584\ \mu F \qquad \text{and} \qquad n = 0.727$$

C.4.2 SRC Design

$$V_{oNMAX} = \frac{nV'_o}{V_{sMIN}} = 0.8$$

$$\text{So,} \quad n = \frac{V_{oNMAX}\,V_{sMIN}}{V'_o} = \frac{0.8 \times 86.4}{220} = 0.314$$

The characteristic impedance Z_0 should be such that the full output current requirement is met at maximum operating frequency under low input supply condition. From Fig. A.8(b) (or Fig. A.6(g)),

$$\text{at} \quad \omega_N = 0.8 \text{ and } V_{oN} = 0.8, \quad I_{oN} = I_{oNMAX} = \frac{\frac{I'_{oMAX}}{n} Z_0}{V_{sMIN}} = 1.4$$

$$\text{So,} \qquad Z_0 = \frac{n\,I_{oNMAX}\,V_{sMIN}}{I'_{oMAX}} = \frac{0.314 \times 1.4 \times 86.4}{10} = 3.798\ \Omega$$

As in the case of PRC, $f_0 = 200\ kHz$ and $\omega_0 = 1256637.1$ *radians/second.* From $\omega_0 = \frac{1}{\sqrt{L\,C}}$ and $Z_0 = \sqrt{\frac{L}{C}}$,

$$L = \frac{Z_0}{\omega_0} = \frac{3.798}{1256637.1} = 3.022\ \mu H$$

$$C = \frac{1}{Z_0\,\omega_0} = \frac{1}{3.798 \times 1256637.1} = 0.2095\ \mu F$$

Thus, in this design,

$$L = 3.022\ \mu H, \qquad C = 0.2095\ \mu F \qquad \text{and} \qquad n = 0.314$$

C.4.3 Operating Frequency Range

Consider operation of the PRC for $V_s = V_{sMAX} = 115.2\ V$.

$$V_{oN} = \frac{n\,V'_o}{V_s} = \frac{0.727 \times 220}{115.2} = 1.388$$

$$\text{At} \quad I'_o = I'_{oMIN} = 0\ A, \quad I_{oN} = 0$$

From Fig. C.11(a) (or Fig. C.9(g)),

$$\text{at} \quad I_{oN} = 0 \text{ and } V_{oN} = 1.388, \quad \omega_N = \omega_{N1} = 0.650$$

This corresponds to a frequency of $f = f_1 = \omega_{N1} f_0 = 0.650 \times 200\ kHz = 130\ kHz$.

$$\text{At} \quad I'_o = I'_{oMAX}, \quad I_{oN} = \frac{\frac{I'_{oMAX}}{n} Z_0}{V_{sMAX}} = \frac{\frac{10}{0.727} \times 5.025}{115.2} = 0.60$$

From Fig. C.11(a) (or Fig. C.9(g)),

$$\text{at} \quad I_{oN} = 0.6 \text{ and } V_{oN} = 1.388, \quad \omega_N = \omega_{N2} = 0.674$$

This corresponds to a frequency of $f = f_2 = \omega_{N2} f_0 = 0.674 \times 200\ kHz = 134.8\ kHz$. Thus, at $V_s = 115.2\ V$, the operating freqeucny range required to compensate for load variations is only between 130 kHz and 134.8 kHz.

Next consider the operation of the PRC for $V_s = V_{sMIN} = 86.4\ V$.

$$V_{oN} = \frac{n\,V'_o}{V_s} = \frac{0.727 \times 220}{86.4} = 1.85$$

$$\text{At} \quad I'_o = I'_{oMIN} = 0\ A, \quad I_{oN} = 0$$

From Fig. C.11(a) (or Fig. C.9(g)),

$$\text{at} \quad I_{oN} = 0 \text{ and } V_{oN} = 1.85, \quad \omega_N = \omega_{N3} = 0.753$$

This corresponds to a frequency of $f = f_3 = \omega_{N3} f_0 = 0.753 \times 200\ kHz = 150.6\ kHz$.

$$\text{At} \quad I'_o = I'_{oMAX}, \quad I_{oN} = \frac{\frac{I'_{oMAX}}{n} Z_0}{V_{sMIN}} = \frac{\frac{10}{0.727} \times 5.025}{86.4} = 0.8 \text{ as per design}$$

From Fig. C.11(a) (or Fig. C.9(g)),

$$\text{at} \quad I_{oN} = 0.8 \text{ and } V_{oN} = 1.85, \quad \omega_N = \omega_{N4} = 0.8 \text{ as per design}$$

This corresponds to the design maximum frequency of $f = f_4 = \omega_{N4} f_0 = 0.8 \times 200\ kHz = 160\ kHz$. Thus, at $V_s = 86.4\ V$, the operating freqeucny range required to compensate for load variations is only between 150.6 kHz and 160 kHz.

From the above, it is seen that for constant supply voltage condition the amount of frequency range required in the PRC to compensate for load variations is quite limited. Considering f_1, f_2, f_3 and f_4, the frequency range required to compensate for both load and supply variations is between 130 k Hz and 160 kHz, which is still quite limited.

Next, we will consider the frequency range required for the SRC. Consider operation of the SRC for $V_s = V_{sMAX} = 115.2\ V$. It is to be noted that the minimum load current of the SRC design has been limited to 3 A, unlike the PRC design.

$$V_{oN} = \frac{n V'_o}{V_s} = \frac{0.314 \times 220}{115.2} = 0.6$$

$$\text{At} \quad I'_o = I'_{oMIN} = 3\ A, \quad I_{oN} = I_{oNMIN} = \frac{\frac{I'_{oMIN}}{n} Z_0}{V_{sMAX}} = \frac{\frac{3}{0.314} \times 3.798}{115.2} = 0.315$$

From Table A.1, $I_{oN} = \frac{2}{\pi} = 0.6366$ at CCM/DCM-2 boundary. Since I_{oN} (= 0.315) < 0.6366, the SRC is in DCM-2. From (A.78),

$$\omega_N = \omega_{N1} = \frac{I_{oN} \pi}{4} = \frac{0.315 \times \pi}{4} = 0.247$$

This corresponds to a frequency of $f = f_1 = \omega_{N1} f_0 = 0.247 \times 200\ kHz = 49.4\ kHz$.

$$\text{At} \quad I'_o = I'_{oMAX}, \quad I_{oN} = \frac{\frac{I'_{oMAX}}{n} Z_0}{V_{sMAX}} = \frac{\frac{10}{0.314} \times 3.798}{115.2} = 1.050$$

From Fig. A.8(b) (or Fig. A.6(g)),

$$\text{at} \quad I_{oN} = 1.050 \text{ and } V_{oN} = 0.6, \quad \omega_N = \omega_{N2} = 0.706$$

This corresponds to a frequency of $f = f_2 = \omega_{N2} f_0 = 0.706 \times 200\ kHz = 141.2\ kHz$. Thus at $V_s = 115.2\ V$, the operating freqeucny range required to compensate for load variations for the SRC is large and is between 49.4 kHz and 141.2 kHz.

Next, consider the operation of the SRC for $V_s = V_{sMIN} = 86.4\ V$.

$$V_{oN} = \frac{n V'_o}{V_s} = \frac{0.314 \times 220}{86.4} = 0{:}8, \qquad \text{as per design.}$$

$$\text{At} \quad I'_o = I'_{oMIN} = 3\ A, \quad I'_{oN} = \frac{\frac{I'_{oMIN}}{n} Z_0}{V_{sMIN}} = \frac{\frac{3}{0.314} \times 3.798}{86.4} = 0.420$$

The operation of the SRC is in DCM-2. From (A.78),

$$\omega_N = \omega_{N3} = \frac{I_{oN} \pi}{4} = \frac{0.420 \times \pi}{4} = 0.330$$

This corresponds to a frequency of $f = f_3 = \omega_{N3} f_0 = 0.330 \times 200\ kHz = 66.0\ kHz$.

$$\text{At} \quad I'_o = I'_{oMAX}, \quad I_{oN} = I'_{oNMAX} = \frac{\frac{I'_{oMAX}}{n} Z_0}{V_{sMIN}} = \frac{\frac{10}{0.314} \times 3.798}{86.4} = 1.40$$

From Fig. A.8(b) (or Fig. A.6(g)),

$$\text{at} \quad I_{oN} = 1.4 \text{ and } V_{oN} = 0.8, \quad \omega_N = \omega_{N4} = 0.8 \text{ as per design}$$

This corresponds to a frequency of $f = f_4 = \omega_{N4} f_0 = 0.8 \times 200\ kHz = 160\ kHz$. Thus, at $V_s = 86.4\ V$, the operating freqeucny range required to compensate for load variations is again large (66.0 kHz to 160 kHz)

From the above, it is seen that even for constant supply voltage condition the amount of frequency range required for the SRC to regulate the output voltage is large. Considering f_1, f_2, f_3 and f_4, the frequency range required to compensate for both load and supply variations is even larger (49.6 Hz to 160 kHz).

Figures A.5 and A.6 can be used to estimate component stresses under different operating conditions for the SRC. Similarly, using Fig. C.9, the component stresses for the PRC can be obtained.

C.5 Program Listings

Programs for obtaining the design curves using equations in Secs. C.2.1 and C.2.2 are straightforward and are similar to those in Secs. A.7.1, A.7.2 and A.7.3 for the SRC. The mode boundaries determining the regions of operation are also obtained by directly using the equations of Sec. C.1. Also, please note that the symbols used in the following programs may differ from those used in the previous sections of this appendix.

C.5.1 Complete DC Analysis

```
C  COMPLETE DC ANALYSIS OF PARALLEL RESONANT CONVERTER - PROGRAM 1
C
C  THIS IS THE MAIN PROGRAM THAT COMPUTES THE NORMALIZED(/VS)
C  DC OUTPUT VOLTAGE, VCAVN, AS FUNCTION OF CONVERTER NORMALIZED
C  FREQUENCY, WN, FOR DIFFERENT NORMALIZED(/VS/Z0) OUTPUT
C  CURRENTS.  SUBROUTINE REGION IDENTIFIES THE PARTICULAR
C  PRC MODE OF OPERATION,IDENTIFIED BY INDEX K, FOR THE GIVEN WN AND
C  AION. SUBROUTINE OUTPUT COMPUTES VCAVN  FOR THE GIVEN WN AND AION
C  ACCORDING TO THE INDEX K.
C
C  BY RAMESH ORUGANTI
C
      AION     =   .01
C
      DO 200 I = 1,10
      IF(AION.LT.1.) WNMIN = 0.
      IF(AION.GE.1.) WNMIN = .4
      IF(AION.LE.1.) WNMAX = .98
      IF(AION.GT.1.) WNMAX = 1.0
      STEP     =  (WNMAX-WNMIN)/50.
      WN       =  WNMIN
C
      DO 100 J = 1,51
      CALL REGION(AION,WN,K)
      CALL OUTPUT(AION,WN,VCAVN,K)
      WRITE(6,9010)WN,VCAVN
 9010 FORMAT(2E14.5)
      WN       =  WN + STEP
  100 CONTINUE
C
      IF(AION.LE.1.) WNMIN = 1.02
      IF(AION.GT.1.) WNMIN = 1.0
      WNMAX    =  2.0
      STEP     =  (WNMAX-WNMIN)/50.
```

```
      WN        =  WNMIN
      DO 150 L = 1,51
      CALL REGION(AION,WN,K)
      CALL OUTPUT(AION,WN,VCAVN,K)
      WRITE(6,9010)WN,VCAVN
      WN        =  WN + STEP
  150 CONTINUE
C
      IF(I.EQ.1)  AION = .5
      IF(I.EQ.2)  AION = .8
      IF(I.EQ.3)  AION = .9
      IF(I.EQ.4)  AION = 1.01
      IF(I.EQ.5)  AION = 1.05
      IF(I.EQ.6)  AION = 1.1
      IF(I.EQ.7)  AION = 1.2
      IF(I.EQ.8)  AION = 1.4
      IF(I.EQ.9)  AION = 1.6
  200 CONTINUE
      STOP
      END
```

C.5.2 Complete DC Analysis - Given Operating Frequency

```
C  COMPLETE DC ANALYSIS OF PARALLEL RESONANT CONVERTER - PROGRAM 2
C
C  THIS IS THE MAIN PROGRAM THAT COMPUTES THE NORMALIZED(/VS)
C  DC OUTPUT VOLTAGE, VCAVN, AS FUNCTION OF NORMALIZED(/VS/ZO)
C  OUTPUT CURRENT, AION FOR DIFFERENT CONVERTER NORMALIZED
C  FREQUENCIES.  SUBROUTINE REGION IDENTIFIES THE PARTICULAR
C  PRC MODE OF OPERATION,IDENTIFIED BY INDEX K, FOR THE GIVEN WN AND
C  AION. SUBROUTINE OUTPUT COMPUTES VCAVN  FOR THE GIVEN WN AND AION
C  ACCORDING TO THE INDEX K.
C
C  BY RAMESH ORUGANTI
C
      WN        =  1.10
C
      DO 200 I = 1,6
      AION      =  0.05
      STEP      =  1.95/100.
C
      DO 100 J = 1,101
      CALL REGION(AION,WN,K)
      CALL OUTPUT(AION,WN,VCAVN,K)
      WRITE(6,9010)AION,VCAVN
 9010 FORMAT(2E14.5)
      AION      =  AION + STEP
  100 CONTINUE
C
      WN        =  WN + 0.1
C     IF(I.EQ.1) WN = 1.1
  200 CONTINUE
      STOP
      END
```

C.5.3 Subroutines

```
      SUBROUTINE OUTPUT(AION,WN,VCAVN,K)
C
C  THIS SUBROUTINE RETURNS THE NORMALIZED(/VS) OUTPUT DC AVERAGE
C  VOLTAGE, VCAVN, OF A PRC GIVEN THE NORMALIZED(/VS/ZO) LOAD
C  CURRENT, AION, THE NORMALIZED FREQUENCY, WN AND THE REGION
C  INDEX, K, AS FOUND BY SUBROUTINE REGION. DEPENDING ON K, VCAVN
C  IS COMPUTED DIRECTLY OR ITERATIVELY USING AGAIN2 (REFER PRC2
C  FORTRAN A1) SUBROUTINE.
C
C  BY RAMESH ORUGANTI
C
C  TOL1 IS THE FREQUENCY CONVERGENCE TOLERANCE WHEN THE GIVEN WN
C  IS REALIZED ITERATIVELY
C
      PI        =  4.*ATAN(1.)
      TOL1      =  1.0E-03
C
C  STOP IF OUTPUT AT RESONANCE IS TO BE CALCULATED
C
      IF(AION.GT.1..OR.WN.NE.1.) GO TO 50
```

```
      I         =  00000
      WRITE(6,*) I
      STOP
C
   50 IF (AION.LT.1.) S = SQRT(1.-AION**2)
      IF (AION.GE.1.) S = SQRT(AION**2-1.)
C
C  THE EQUATIONS FOR VCAVN DIFFERS DEPENDING ON K
C
      IF (K.EQ.1) GO TO 100
      IF (K.EQ.2) GO TO 200
      IF (K.EQ.3) GO TO 300
      IF (K.EQ.4) GO TO 400
      IF (K.EQ.5) GO TO 500
      IF (K.EQ.6) GO TO 600
      IF (K.EQ.7) GO TO 700
      IF (K.EQ.8) GO TO 800
C
C  DIRECT CALCULATION
C
  100 VCAVN   =  (2.*PI-ARCOS(S)+AION+((1.-S)**2)/(2.*AION))*WN/PI
      RETURN
C
C  WHEN K = 2, WE ARE IN THE ZONE WN < 1 AND ION > 1, WHERE MULTIPLE
C  CURRENT PEAKS OCUUR. THIS REGION IS IGNORED BY THIS SUBROUTINE.
C
  200 I       =  22222
      WRITE(6,*) I
      STOP
C
C  DIRECT CALCULATION
C
  300 VCAVN   =  0.
      RETURN
C
C  ITERATION
C
C  FOR K = 4, EQUATIONS IN TERMS OF AN INTERMEDIATE PARAMTER VCQN
C  HAVE BEEN USED IN THIS PROGRAM, WHILE THE EQUATIONS IN SEC C.2.4
C  ARE IN TERMS OF IL1N.
C  FOR CONSISTENCY, THE FOLLOWING SEGMENT CAN BE REWRIITEN IN TERMS
C  OF IL1N, IF DESIRED.
C
  400 XMIN    =  0.
C   VCQN IS EQUAL TO X.
      XMAX    =  1.-S
      X       =  XMIN
      DO 410 I = 1,100
      Q       =  SQRT((1.+X)**2+AION**2)
      T2      =  2.*(2.*PI-ARCOS(S)+(1.-S-X)/AION+ARCOS(1./Q) -
     *                  ARCOS((1.+X)/Q)+2.*AION-
     *                  SQRT((1.+X)**2+AION**2-1.))
      W2      =  2.*PI/T2
      IF(ABS(WN-W2).LT.TOL1) GO TO 420
      CALL AGAIN2(XMIN,XMAX,X1,X2,X,W1,W2,WN,I)
  410 CONTINUE
C
C  IF THE ITERATION DOES NOT CONVERGE
      I       =  44444
      WRITE(6,*) I
      STOP
C
  420 Y       =  (1.+X)**2 + AION**2
      VCAVN   =  (2.*PI-ARCOS(S)+((1.-S)**2-X**2)/(2.*AION)+SQRT(Y-1.)
     *            -ARCOS(1./SQRT(Y))+ARCOS((1.+X)/SQRT(Y)))*WN/PI
      RETURN
C
C  ITERATION
  500 IF(AION.LE.SQRT(2.)) XMAX  =  AION -1.E-06
      IF(AION.GT.SQRT(2.)) XMAX  =  2.*SQRT(2.) - AION - 1.E-06
C  IL1N IS EQUAL TO X. THE NUMBER 1.E-06 IS FOR NUMERICAL PURPOSES.
      IF(AION.LE.1.) XMIN = 2.*SQRT(1.-S) - AION + 1.E-06
      IF(AION.GT.1.) XMIN = -AION + 1.E-06
      X       =  XMIN
      DO 510 I = 1,100
      Q       =  (AION+X)**2
      T2      =  2.*(2.*PI-ARCOS((4.-Q)/4.)+ARCOS(1./SQRT(Q+1.))-
     *              ARCOS((Q+4.)/(4.*SQRT(Q+1.)))+AION-X)
      W2      =  2.*PI/T2
      IF(ABS(WN-W2).LT.TOL1) GO TO 520
      CALL AGAIN2(XMIN,XMAX,X1,X2,X,W1,W2,WN,I)
  510 CONTINUE
C
C  IF THE ITERATION DOES NOT CONVERGE
```

```
      I         =  55555
      WRITE(6,*) I
      STOP
C
  520 Y         =  (AION+X)**2
      VCAVN     =  (2.*PI-ARCOS((4.-Y)/4.)+(AION+X)-ARCOS(1./SQRT(Y+1.))
     *             +ARCOS((Y+4.)/(4.*SQRT(Y+1.))))*WN/PI
      RETURN
C
C  ITERATION
  600 XMIN      =  -AION + 1.0E-06
C  IL1N IS EQUAL TO X
      IF(AION.LE.SQRT(2.)) XMAX = AION - 1.0E-06
      IF(AION.GT.SQRT(2.)) XMAX = 2.*SQRT(2.)-AION - 1.0E-06
      X         =  XMIN
      DO 610 I = 1,100
      Q         =  (AION+X)**2
      T2        =  2.*(ARCOS((4.-Q)/4.)+ARCOS((4.+Q)/(4.*SQRT(1.+Q)))+
     *               ARCOS(1./SQRT(1.+Q))+AION-X)
      W2        =  2.*PI/T2
      IF(ABS(WN-W2).LT.TOL1) GO TO 620
      CALL AGAIN2(XMIN,XMAX,X1,X2,X,W1,W2,WN,I)
  610 CONTINUE
C
C  IF THE ITERATION DOES NOT CONVERGE
      I         =  66666
      WRITE(6,*)I
      STOP
C
  620 THETA1    =  ARCOS((4.-Q)/4.)
      RPRIM     =  SQRT(1.+Q)
      THETA2    = ARCOS((4.+Q)/(4.*SQRT(1.+Q)))
      THETA3    =  ARCOS(1./SQRT(1.+Q))
      VCAVN     =  (RPRIM*(SIN(THETA2)+SIN(THETA3))-THETA2-THETA3
     *              +THETA1-((AION+X)/4.)*SQRT(8.-Q))*WN/PI
C     WRITE(6,*) THETA1,THETA2,THETA3,X,RPRIM,VCAVN
      RETURN
C
C  ITERATION
  700 RMIN      =  1.0
      IF(AION.LE.1.) RMAX = 50.
      IF(AION.GT.1.) RMAX = (-S+AION**2)/S
      IF(RMAX.GT.50.) RMAX = 50.
      R         =  RMIN
      DO 710 I = 1, 100
      AIL1N     =  SQRT(R**2-1.)+AION
      RPRIM     =  SQRT(1.+(AIL1N+AION)**2)
      VCON      =  AION*AIL1N
      THETA2    =  ARCOS((1.-VCON)/R)
      THETA3    =  ARCOS((1.+VCON)/RPRIM)
      THETA1    =  ARCOS(1./R)
      THETA4    =  ARCOS(1./RPRIM)
      ALPHA     =  2.*PI-(THETA1+THETA2)
      BETA      =  THETA4-THETA3
      W2        =  PI/(ALPHA+BETA)
C     WRITE(6,*)THETA1,THETA2,THETA3,THETA4,ALPHA,BETA,W2
      IF(ABS(WN-W2).LT.TOL1) GO TO 720
      CALL AGAIN2(RMIN,RMAX,R1,R2,R,W1,W2,WN,I)
  710 CONTINUE
C
C  IF THE ITERATION DOES NOT CONVERGE
      I  =  77777
      WRITE(6,*)I
      STOP
C
  720 VCAVN     =  (ALPHA-BETA+2.*AIL1N)/(ALPHA+BETA)
      RETURN
C
C  ITERATION
  800 RMIN      =  1.0
      IF(AION.LE.1.) RMAX = 50.
      IF(AION.GT.1.) RMAX = (-S+AION**2)/S
      IF (RMAX.GT.50.) RMAX = 50.
      R         =  RMIN
      DO 810 I = 1,500
      AIL1N     =  SQRT(R**2-1.)+AION
      RPRIM     =  SQRT(1.+(AIL1N+AION)**2)
      THETA1    =  ARCOS(1./R)
      THETA2    =  ARCOS((1.-AION*AIL1N)/R)
      ALPHA     =  THETA2-THETA1
      THETA3    =  ARCOS((1.+AION*AIL1N)/RPRIM)
      THETA4    =  ARCOS(1./RPRIM)
      BETA      =  THETA3+THETA4
      W2        =  PI/(ALPHA+BETA)
```

```
      IF(ABS(WN-W2).LT.TOL1) GO TO 820
      CALL AGAIN2(RMIN,RMAX,R1,R2,R,W1,W2,WN,I)
C     WRITE(6,*) THETA1,THETA2,THETA3,THETA4,ALPHA,BETA,W2
  810 CONTINUE
C
C  IF THE ITERATION DOES NOT CONTINUE
      I         =  88888
      WRITE(6,*)I
      STOP
C
  820 VCAVN     =  (ALPHA-BETA+2.*AIL1N)/(ALPHA+BETA)
      RETURN
      END
C
      SUBROUTINE REGION (AION,WN,K)
C  THIS SUBROUTINE RETURNS THE REGION, BY MEANS OF THE INDEX, K,
C  IN WHICH A PARALLEL RESONANT CONVERTER IS OPERATING.  THE DIFFERENT
C  REGIONS ARE DETERMINED BY DIFFERENT CCM'S AND DIFFERENT DCM'S.
C  THE VARIOUS REGIONS ARE:
C  K = 1  :  BOTH INDUCTOR CURRENT AND CAPACITOR VOLTAGE STAY AT ZERO
C            TOGETHER FOR SOME PERIOD OF TIME. WN < WDISC, AION < 1
C  K = 2  :  THE REGION WHERE MULTIPLE CONDUCTION PEAKS OCCUR.
C            WN < WMUL, AION > 1
C  K = 3  :  OUTPUT IS ZERO.  WN > WLIMIT, AION - ANY
C  K = 4  :  BOTH INDUCTOR CURRENT AND CAPACITOR VOLTAGE STAY AT ZERO
C            FOR SOMETIME BUT NOT TOGETHER. WDISC < WN < WTRAN,AION < 1
C  K = 5  :  CAPACITOR VOLTAGE STAYS AT ZERO FOR SOMETIME BUT NOT
C            INDUCTOR CURRENT. INTERSECTION 1
C            WTRAN < WN < WLOW, AION < 1
C            WMUL  < WN < WLOW, 1 < AION < SQRT(2)
C            WMUL  < WN < WMAX, AION > SQRT(2)
C  K = 6  :  SAME AS ABOVE BUT INTERSECTION 2
C            WHIGH < WN < WLIMIT, AION < SQRT(2)
C            WMAX < WN < WLIMIT,AION > SQRT(2)
C  K = 7  :  CONTINUOUS CONDUCTION MODE - INTERSECTION 1
C            WLOW < WN < WMAX, AION < SQRT(2)
C  K = 8  :  CONTINUOUS CONDUCTION MODE - INTERSECTION 2
C            WMAX < WN < WHIGH, AION < SQRT(2)
C
C  NOTE:  THE SAME SYMBOL WDISC IS USED FOR BOTH WMUL AND WDISC.
C
C  BY RAMESH ORUGANTI
C
      IF (AION.EQ.0.)  AION = 1.E-06
      PI          =  4.*ATAN(1.)
      IF (AION.LE.1.) S = SQRT(1.-AION**2)
      IF (AION.GT.1.) S = SQRT(AION**2-1.)
C
      IF (AION.GE.1.) GO TO 100
      WDISC = PI / (2.*PI-ARCOS(S)+(1.-S)/AION+AION)
      IF ( WN.LT.WDISC) GO TO 510
      GO TO 102
C
  100 WDISC = PI /(2.*(PI + AION))
      IF ( WN.LT.WDISC) GO TO 520
C
  102 WLIMIT     =  PI/(2.*AION)
      IF ( WN.GE.WLIMIT) GO TO 530
C
      IF ( AION.GE.1.) GO TO 110
      WTRAN = PI / (2.*PI - ARCOS(S) +  ARCOS(1./SQRT(5.-4.*S)) -
     *                    ARCOS((2.-S)/SQRT(5.-4.*S)) +
     *                      2.*AION - 2.*SQRT(1.-S))
      IF (WN.LT.WTRAN) GO TO 540
C
  110 CONTINUE
      IF (AION.LT.SQRT(2.)) WLOW = PI / (2.*PI - ARCOS(1.-AION**2) +
     *                                 ARCOS(1./SQRT(1.+4.*AION**2)) -
     *                           ARCOS((1.+AION**2)/SQRT(1.+4.*AION**2)))
      IF (AION.LT.SQRT(2.)) WHIGH = PI/(ARCOS(1.-AION**2) +
     *                                 ARCOS(1./SQRT(1.+4.*AION**2)) +
     *                           ARCOS((1.+AION**2)/SQRT(1.+4.*AION**2)))
      IF (AION.LE.1.) WMAX  =  1.
      IF (AION.GT.1..AND.AION.LT.SQRT(2.))
     *    WMAX = PI / (PI-ARCOS(S/(-S+AION**2))+ARCOS(S/(S+AION**2)))
      IF (AION.GE.SQRT(2.))
     *    WMAX = PI / (PI+ARCOS(1./3.)+2.*(AION-SQRT(2.)))
C
      IF (AION.GE.SQRT(2.)) GO TO 120
      IF (WN.LT.WLOW) GO TO 550
      GO TO 122
  120 IF (WN.LT.WMAX) GO TO 550
C
  122 IF (AION.GE.SQRT(2.)) GO TO 130
```

```
      IF (WN.GE.WHIGH) GO TO 560
      GO TO 132
  130 IF (WN.GE.WMAX) GO TO 560
C
  132 IF (WN.LT.WMAX.AND.AION.LT.SQRT(2.))  GO TO 570
C
      IF (WN.GE.WMAX.AND.AION.LT.SQRT(2.))  GO TO 580
C
  510 K   =  1
      GO TO 700
  520 K   =  2
      GO TO 700
  530 K   =  3
      GO TO 700
  540 K   =  4
      GO TO 700
  550 K   =  5
      GO TO 700
  560 K   =  6
      GO TO 700
  570 K   =  7
      GO TO 700
  580 K   =  8
  700 CONTINUE
C     WRITE (6,*) K
      RETURN
      END
C
      SUBROUTINE AGAIN2 (RMIN,RMAX,R1,R2,R,W1,W2,WN,K)
C
C  THIS SUBROUTINE COMPUTES THE NEW VALUE OF THE INDEPENDENT
C  VARIABLE, R, SO THAT THE CONVERGENCE OF DEPENDENT VARIABLE, W,
C  TO THE DESIRED VALUE, WN, IS ACHIEVED IN THE MAIN PROGRAM.
C  GIVEN THE PREVIOUS TWO SETS OF VALUES, R1, W1 AND R2, W2 AND WN
C  THE PROGRAM RETURNS R USING LINEAR INTERPOLATION TECHNIQUES.
C  RMIN AND RMAX ARE THE UPPER AND LOWER BOUNDS FOR R.  SINCE
C  SINCE THE SUBROUTINE KEEPS TRACK OF R1, R2, W1 AND W2 VALUES THE
C  MAIN PROGRAM NEED NOT PROVIDE THESE VALUES TO THIS SUBROUTINE.
C  K IS THE ITERATION INDEX OBTAINED FROM THE MAIN PROGRAM'S 'DO LOOP'.
C
C  BY RAMESH ORUGANTI
      IF (K.EQ.1) GO TO 110
      IF(ABS(W1-W2).GT.1.0E-9) GO TO 100
      I       =   99999
      WRITE(6,*)RMIN,RMAX,R,W2,I
      STOP
C
  100 R       =  R2 + (R1-R2)*(WN-W2)/(W1-W2)
      STEP    =  (RMAX-RMIN)/5.
      RX      =  R2+STEP
      RY      =  R2-STEP
      IF(R.GT.RX) R = RX
      IF(R.LT.RY) R = RY
      IF (R.GT.RMAX) R = RMAX
      IF (R.LT.RMIN) R = RMIN
      R1      =  R2
      R2      =  R
      W1      =  W2
      RETURN
C
  110 R1      =  R
      R       =  RMAX
      R2      =  R
      W1      =  W2
      RETURN
      END
```

Appendix D

Ideal Analyses Of QRCs

In this appendix, ideal analyses of the QRCs based on the trajectory diagrams in Chapter 6 are carried out. Plots of characteristics of QRCs based on equations derived in this appendix have been presented in Sec. 6.7.

In the analyses, ω_{ND} , ω_{NU} and ω_{MAX} represent normalized boundary frequencies for operation between MODE 1/MODE 2, between MODE 2/MODE 3 and at the upper boundary, respectively. Section D.1 determines the durations for different intervals of operation in terms of parameters measured on state plane. The equations for the mode boundaries and normalized average diode voltage V_{D2AVN} in each mode for QRCs with half-wave ZCS, full-wave ZCS, half-wave ZVS and full-wave ZVS are derived in Secs. D.2, D.3, D.4 and D.5, respectively. Section D.6 establishes the relationship between dc gain V'_{oN} and V_{D2AVN} for each of the four types of resonant converters - buck, boost, buck-boost and boost-buck. By substituting the equations for V_{D2AVN} from Secs. D.2 through D.5 into the V'_{oN} equations of Sec. D.6, dc gains of all the sixteen types of QRCs may be obtained. Section D.7 presents the computer programs used to generate data for the plots in Chapter 6. For definitions of symbols used in this appendix please refer to Sec. 6.0. In Sec. 6.8, it has been shown that the waveform of v_C can change when a topological variation of a given QRC is considered whereas V_o and v_{D2} are among parameters that do not change. Due to this reason V_{D2AVN} has been prefered over V_{CAVN} to express the results of Secs. D.2 through D.5.

The results of the dc gain analysis under mode 2 operation have been expressed in terms of an intermediate parameter - V_{C0N} for ZCS QRCs and I_{L0N} for ZVS QRCs. Given ω_N, the intermediate parameter is first determined using the equation for ω_N, such that the desired ω_N is reached. The value of the intermediate parameter is then used to calculate the value of V_{D2AVN} (or V'_{oN}). Implicit equations relating V_{D2AVN} (or V'_{oN}), ω_N and I'_{oN} may be obtained by eliminating the intermediate parameter, if so desired.

In Chapter 6, the state plane diagrams have been drawn utilizing I_{EN} as one of the parameters. Equation (6.39) has shown that the modified normalized current I'_{oN} is equal to I_{EN} for the ideal analysis. Reproducing (6.39),

$$I_{EN} = \frac{I_E Z_0}{V_E} = \frac{I_0 Z_0}{V_s} = I'_{oN} \qquad (D.1)$$

The equations in this appendix are expressed utilizing I'_{oN} and not I_{EN}, since the load current I_o and input supply V_s are more likely to be known than current I_E and voltage V_E.

The derivations in this appendix follow the patterns of the derivations in Appendixes A, B and C. Hence, the steps of the derivation are not presented in detail.

D.1 Time Intervals On State - Plane Diagrams

Equations similar to C.1, C.2, C.3, C.7 and C.11 can be shown to be valid for QRCs also. Changing I_{oN} to I'_{oN} in (C.11) to conform to the notation used in QRC analysis, these equations are rewritten below.

$$\begin{aligned} T &= \text{Operating period} \\ &= \frac{2\pi}{\omega}, \end{aligned} \qquad (D.2)$$

where ω is the operating frequency in radians/second.

$$\begin{aligned} \omega_N &= \text{Normalized operating frequency} \\ &= \frac{\omega}{\omega_0} = \frac{2\pi}{\omega_0 T} = \frac{2\pi}{T_N}, \end{aligned} \qquad (D.3)$$

where T_N is the angular period.

$$\omega_0 \Delta t \text{ (resonant interval)} = \theta = \text{Angle subtended at center} \tag{D.4}$$

$$\omega_0 \Delta t \text{ (inductor charging/discharging interval)} = |\Delta i_{LN}| = \text{Normalized change in inductor current} \tag{D.5}$$

$$\omega_0 \Delta t \text{ (capacitor charging/discharging interval)} = \frac{|\Delta v_{CN}|}{I'_{oN}}, \tag{D.6}$$

where Δv_{CN} is the normalized change in capacitor voltage.

The value of angle $\omega_0 \Delta t$ during constant state interval cannot be determined by measurements on state plane. Equations (D.2) through (D.6) are utilized througout the rest of this appendix, as needed.

D.2 Analysis Of QRCs With Half-Wave ZCS

The analysis diagrams for this case are drawn in Fig. D.1 based on the diagrams in Fig. 6.9.

D.2.1 Boundary Equations

D.2.1.1 Boundary Between Mode 1 And Mode 2

Figure D.1 (b) is utilized to derive the equations for ω_{ND}.

$$\omega_0 T_I = I'_{oN} \tag{D.7}$$

$$\omega_0 T_{II} = \varphi = \pi + \cos^{-1}\sqrt{1 - I'^2_{oN}} \tag{D.8}$$

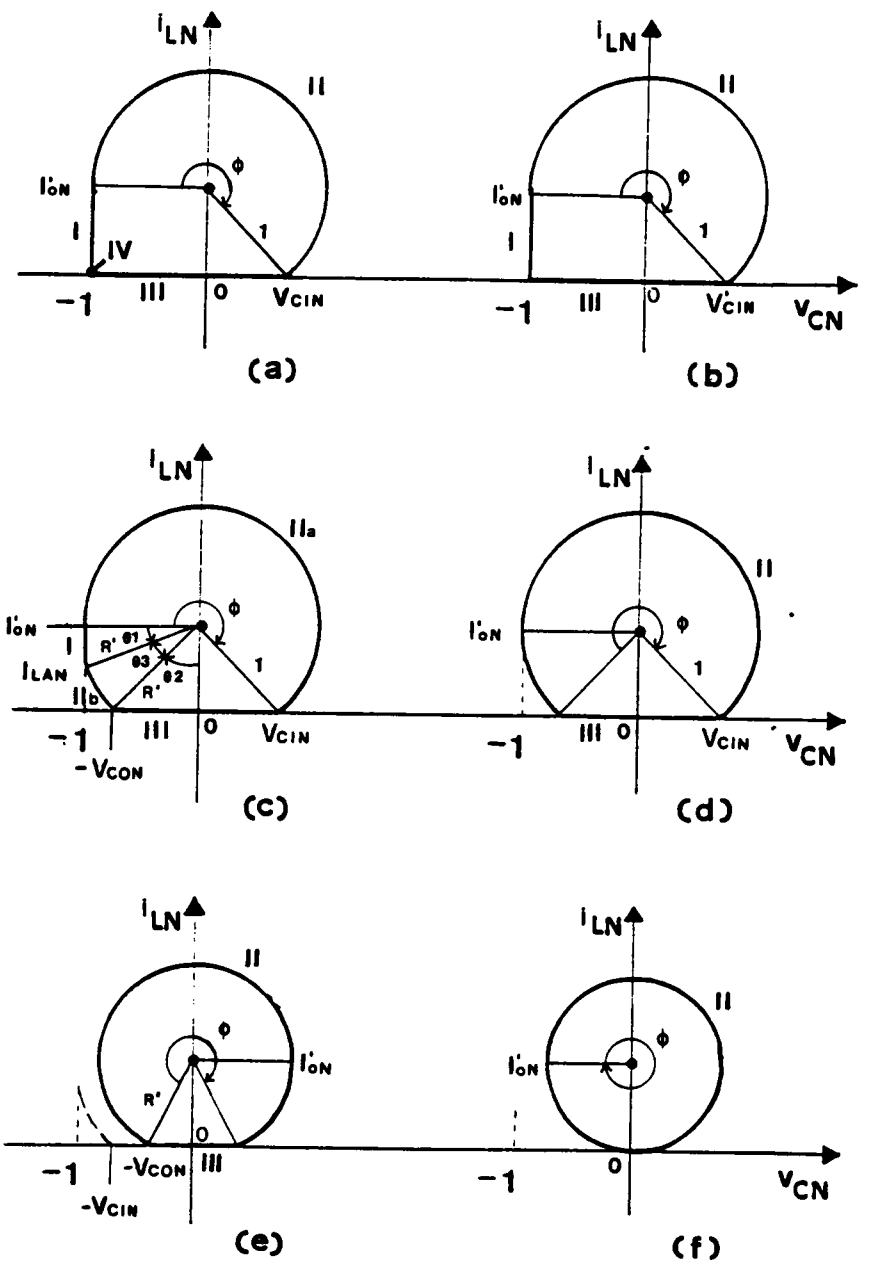

Figure D.1 QRCs with half-wave ZCS - Analysis diagrams

a) Mode 1
b) ω_{ND} boundary
c) Mode 2
d) ω_{NU} boundary
e) Mode 3
f) ω_{MAX} boundary

$$\omega_0 T_{III} = \frac{|\Delta v_{CN}|}{I'_{oN}} = \frac{1 + V_{C1N}}{I'_{oN}} = \frac{1 + \sqrt{1 - I'^2_{oN}}}{I'_{oN}}, \quad I'_{oN} \neq 0 \tag{D.9}$$

$$T_N = \frac{2\pi}{\omega_{ND}} = \omega_0 T_I + \omega_0 T_{II} + \omega_0 T_{III} \tag{D.10}$$

$$\text{Thus,} \quad \omega_{ND} = \frac{2\pi}{\pi + \cos^{-1}\sqrt{1 - I'^2_{oN}} + I'_{oN} + \dfrac{1 + \sqrt{1 - I'^2_{oN}}}{I'_{oN}}}, \quad I'_{oN} \neq 0 \tag{D.11}$$

D.2.1.2 Boundary Between Mode 2 And Mode 3

Figure D.1(d) is used to derive the equation for ω_{NU}.

$$\omega_0 T_{II} = \varphi = \pi + 2\cos^{-1}\sqrt{1 - I'^2_{oN}} \tag{D.12}$$

$$\omega_0 T_{III} = \frac{2V_{C1N}}{I'_{oN}} = \frac{2\sqrt{1 - I'^2_{oN}}}{I'_{oN}}, \quad I'_{oN} \neq 0 \tag{D.13}$$

$$T_N = \frac{2\pi}{\omega_{NU}} = \omega_0 T_{II} + \omega_0 T_{III} \tag{D.14}$$

$$\text{Thus,} \quad \omega_{NU} = \frac{2\pi}{\pi + 2\cos^{-1}\sqrt{1 - I'^2_{oN}} + \dfrac{2\sqrt{1 - I'^2_{oN}}}{I'_{oN}}}, \quad I'_{oN} \neq 0 \tag{D.15}$$

D.2.1.3 Upper Boundary

Figure D.1 (f) is used to derive the equation for ω_{MAX}.

$$T_N = \frac{2\pi}{\omega_{MAX}} = \omega_0 T_{II} = \varphi = 2\pi \tag{D.16}$$

$$\text{Thus,} \quad \omega_{MAX} = 1 \tag{D.17}$$

D.2.2 DC Analysis

For all the basic QRCs (Fig. 6.2) with ZCS, it may be observed that C, $D2$ and V_E (see equations (6.4) through (6.7) for definitions of V_E) form a circuit loop. Thus,

$$v_{D2} = -v_C - V_E \tag{D.18}$$

Normalizing over a period,

$$V_{D2AVN} = -V_{CAVN} - 1 \tag{D.19}$$

Equations (D.18) and (D.19) are valid both for the basic QRCs with half-wave ZCS and for basic QRCs with full-wave ZCS.

D.2.2.1 Analysis In Mode 1

Figure D.1(a) is used to derive equations in this subsection.

$$V_{C1N} = \sqrt{1 - I'^2_{oN}} \tag{D.20}$$

$$\omega_0 T_I = I'_{oN} \tag{D.21}$$

$$\omega_0 T_{II} = \varphi = \pi + \cos^{-1}\sqrt{1 - I'^2_{oN}} \tag{D.22}$$

$$\omega_0 T_{III} = \frac{|\Delta v_{CN}|}{I'_{oN}} = \frac{1 + V_{C1N}}{I'_{oN}} = \frac{1 + \sqrt{1 - I'^2_{oN}}}{I'_{oN}}, \qquad I'_{oN} \neq 0 \tag{D.23}$$

$$\omega_0 T_{IV} = \omega_0 T - (\omega_0 T_I + \omega_0 T_{II} + \omega_0 T_{III}) \tag{D.24}$$

During interval I,

$$v_{CN} = -1 \tag{D.25}$$

$$\text{So,} \quad \frac{1}{V_E}\int_{T_I} v_C\, dt = -T_I = \frac{1}{\omega_0}(-I'_{oN}) \tag{D.26}$$

During interval II,

$$v_{CN} = -\cos\theta \tag{D.27}$$

$$\text{So,} \quad \frac{1}{V_E}\int_{T_{II}} v_C\,dt = \frac{1}{\omega_0}\int_0^{\varphi}(-\cos\theta)d\theta = \frac{1}{\omega_0} I'_{oN} \tag{D.28}$$

During interval III,

$$v_{CN} = V_{C1N} - \frac{(V_{C1N}+1)}{T_{III}}\,t \tag{D.29}$$

$$\text{So,} \quad \frac{1}{V_E}\int_{T_{III}} v_C\,dt = \frac{1}{\omega_0}\left(\frac{-I'_{oN}}{2}\right) \tag{D.30}$$

During interval IV,

$$v_{CN} = -1 \tag{D.31}$$

$$\text{So,} \quad \frac{1}{V_E}\int_{T_{IV}} v_C\,dt = -T_{IV} = \frac{1}{\omega_0}(-\omega_0 T + \omega_0 T_I + \omega_0 T_{II} + \omega_0 T_{III}) \tag{D.32}$$

$$V_{CAVN} = \frac{1}{T}\left[\int_{T_I} v_C\,dt + \int_{T_{II}} v_C\,dt + \int_{T_{III}} v_C\,dt + \int_{T_{IV}} v_C\,dt\right] \tag{D.33}$$

Substituting for the integrals and using (D.19),

$$V_{D2AVN} = -\left[\pi + \cos^{-1}\sqrt{1 - I'^2_{oN}} + \frac{I'_{oN}}{2} + \frac{1+\sqrt{1-I'^2_{oN}}}{I'_{oN}}\right]\frac{\omega_N}{2\pi} \tag{D.34}$$

The range of operation in mode 1 is

$$0 < I'_{oN} \leq 1 \quad \text{and} \quad 0 < \omega_N \leq \omega_{ND} \tag{D.35}$$

D.2.2.2 Analysis In Mode 2

Figure D.1(c) is used to derive equations in this subsection. In expressing the equations of this subsection, V_{C0N} in Fig. D.1(c) is used as an intermediate parameter.

$$V_{C1N} = \sqrt{1 - I'^2_{oN}} \tag{D.36}$$

$$R' = \sqrt{V^2_{C0N} + I'^2_{oN}} \tag{D.37}$$

$$\theta_1 = \cos^{-1}\frac{1}{R'} = \cos^{-1}\frac{1}{\sqrt{V^2_{C0N} + I'^2_{oN}}} \tag{D.38}$$

$$\theta_2 = \cos^{-1}\frac{I'_{oN}}{R'} = \cos^{-1}\frac{I'_{oN}}{\sqrt{V^2_{C0N} + I'^2_{oN}}} \tag{D.39}$$

$$\begin{aligned}\omega_0 T_{II\,b} = \theta_3 &= \frac{\pi}{2} - \theta_1 - \theta_2 \\ &= \frac{\pi}{2} - \cos^{-1}\frac{1}{\sqrt{V^2_{C0N} + I'^2_{oN}}} - \cos^{-1}\frac{I'_{oN}}{\sqrt{V^2_{C0N} + I'^2_{oN}}}\end{aligned} \tag{D.40}$$

$$I_{LAN} = I'_{oN} - \sqrt{R'^2 - 1} = I'_{oN} - \sqrt{V^2_{C0N} + I'^2_{oN} - 1} \tag{D.41}$$

$$\omega_0 T_I = (I'_{oN} - I_{LAN}) = \sqrt{V^2_{C0N} + I'^2_{oN} - 1} \tag{D.42}$$

$$\omega_0 T_{II\,a} = \varphi = \pi + \cos^{-1}\frac{V_{C1N}}{1} = \pi + \cos^{-1}\sqrt{1 - I'^2_{oN}} \tag{D.43}$$

$$\omega_0 T_{III} = \frac{V_{C0N} + V_{C1N}}{I'_{oN}} = \frac{V_{C0N} + \sqrt{1 - I'^2_{oN}}}{I'_{oN}}, \quad I'_{oN} \neq 0 \tag{D.44}$$

$$T_N = \omega_0 T_{II\,b} + \omega_0 T_I + \omega_0 T_{II\,a} + \omega_0 T_{III} \tag{D.45}$$

$$\omega_N = \frac{2\pi}{\left[\frac{3\pi}{2} + \cos^{-1}\sqrt{1 - I'^2_{oN}} - \cos^{-1}\frac{1}{\sqrt{V^2_{C0N} + I'^2_{oN}}} - \cos^{-1}\frac{I'_{oN}}{\sqrt{V^2_{C0N} + I'^2_{oN}}} + \frac{V_{C0N} + \sqrt{1 - I'^2_{oN}}}{I'_{oN}} + \sqrt{V^2_{C0N} + I'^2_{oN} - 1}\right]}, \quad I'_{oN} \neq 0 \tag{D.46}$$

$$\sqrt{1 - I'^2_{oN}} \leq V_{C0N} \leq 1 \tag{D.47}$$

During interval IIb,

$$v_{CN} = R' \cos\theta \tag{D.48}$$

$$\frac{1}{V_E}\int_{T_{II\,b}} v_C\, dt = \frac{1}{\omega_0}\int_{\frac{\pi}{2}+\theta_2}^{\pi-\theta_1} R' \cos\theta\, d\theta = -\frac{1}{\omega_0}\left(I'_{oN} - \sqrt{V^2_{C0N} + I'^2_{oN} - 1}\right) \tag{D.49}$$

During interval I,

$$v_{CN} = -1 \tag{D.50}$$

$$\text{So,} \quad \frac{1}{V_E}\int_{T_I} v_C\, dt = -T_I = = -\frac{1}{\omega_0}\sqrt{V^2_{C0N} + I'^2_{oN} - 1} \tag{D.51}$$

During interval IIa,

$$v_{CN} = -\cos\theta \tag{D.52}$$

$$\text{So,} \quad \frac{1}{V_E}\int_{T_{II\,a}} v_C\, dt = \frac{1}{\omega_0}\int_0^{\varphi}(-\cos\theta)\, d\theta = \frac{1}{\omega_0} I'_{oN} \tag{D.53}$$

During interval III,

$$v_{CN} = V_{C1N} - \frac{(V_{C1N} + V_{C0N})}{T_{III}}\, t \tag{D.54}$$

$$\text{So,} \quad \frac{1}{V_E}\int_{T_{III}} v_C\,dt = \frac{1}{\omega_0}\left[\frac{1 - I'^2_{oN} - V^2_{C0N}}{2\,I'_{oN}}\right] \tag{D.55}$$

$$V_{CAVN} = \frac{1}{T}\left[\int_{T_{II\,b}} v_C\,dt + \int_{T_I} v_C\,dt + \int_{T_{II\,a}} v_C\,dt + \int_{T_{III}} v_C\,dt\right] \tag{D.56}$$

Substituting for the integrals and using (D.19),

$$V_{D2AVN} = -\left[\frac{1 - I'^2_{oN} - V^2_{C0N}}{2\,I'_{oN}}\right]\frac{\omega_N}{2\,\pi} - 1 \tag{D.57}$$

The range of operation in mode 2 is

$$0 < I'_{oN} \leq 1 \quad \text{and} \quad \omega_{ND} \leq \omega_N \leq \omega_{NU} \tag{D.58}$$

Given ω_N and I'_{oN} within the ranges specified by (D.58), equation (D.46) is used to determine iteratively the corresponding value of V_{C0N}. The value of V_{D2AVN} is then determined from ω_N, I'_{oN} and V_{C0N} using (D.57).

D.2.2.3 Analysis In Mode 3

Figure D.1(e) is used to derive equations in this subsection. In expressing the equations of this subsection, parameter V_{C0N} is again made use of.

$$R' = \sqrt{V^2_{C0N} + I'^2_{oN}} \tag{D.59}$$

$$\omega_0 T_{II} = \varphi = 2\,\pi - 2\,\cos^{-1}\frac{I'_{oN}}{R'} = 2\,\pi - 2\,\cos^{-1}\frac{I'_{oN}}{\sqrt{V^2_{C0N} + I'^2_{oN}}} \tag{D.60}$$

$$\omega_0 T_{III} = \frac{|\Delta\, v_{CN}|}{I'_{oN}} = \frac{2\,V_{C0N}}{I'_{oN}}, \quad I'_{oN} \neq 0 \tag{D.61}$$

$$T_N = \omega_0 T_{II} + \omega_0 T_{III} \tag{D.62}$$

$$\omega_N = \frac{\pi}{\pi - \cos^{-1}\dfrac{I'_{oN}}{\sqrt{V_{C0N}^2 + I'^2_{oN}}} + \dfrac{V_{C0N}}{I'_{oN}}}, \quad I'_{oN} \neq 0 \tag{D.63}$$

From Fig. D.1(e), it may be observed that the trajectory is symmetrical about the i_{LN} axis. Thus,

$$V_{CAVN} = 0 \tag{D.64}$$

Thus, from (D.19) $$V_{D2AVN} = -1 \tag{D.65}$$

Hence, in mode 3 the converter operation is saturated. The range of operation in mode 3 is

$$0 < I'_{oN} \leq 1 \quad \text{and} \quad \omega_{NU} \leq \omega_N \leq \omega_{MAX} \tag{D.66}$$

D.3 Analysis Of QRCs With Full-Wave ZCS

The analysis diagrams for this case are drawn in Fig. D.2 based on the diagrams in Fig. 6.10.

D.3.1 Boundary Equations

D.3.1.1 Boundary Between Mode 1 And Mode 2

Figure D.2 (b) is utilized to derive the equations for ω_{ND}.

$$\omega_0 T_I = I'_{oN} \tag{D.67}$$

$$\omega_0 T_{II} = \varphi = 2\pi - \cos^{-1}\sqrt{1 - I'^2_{oN}} \tag{D.68}$$

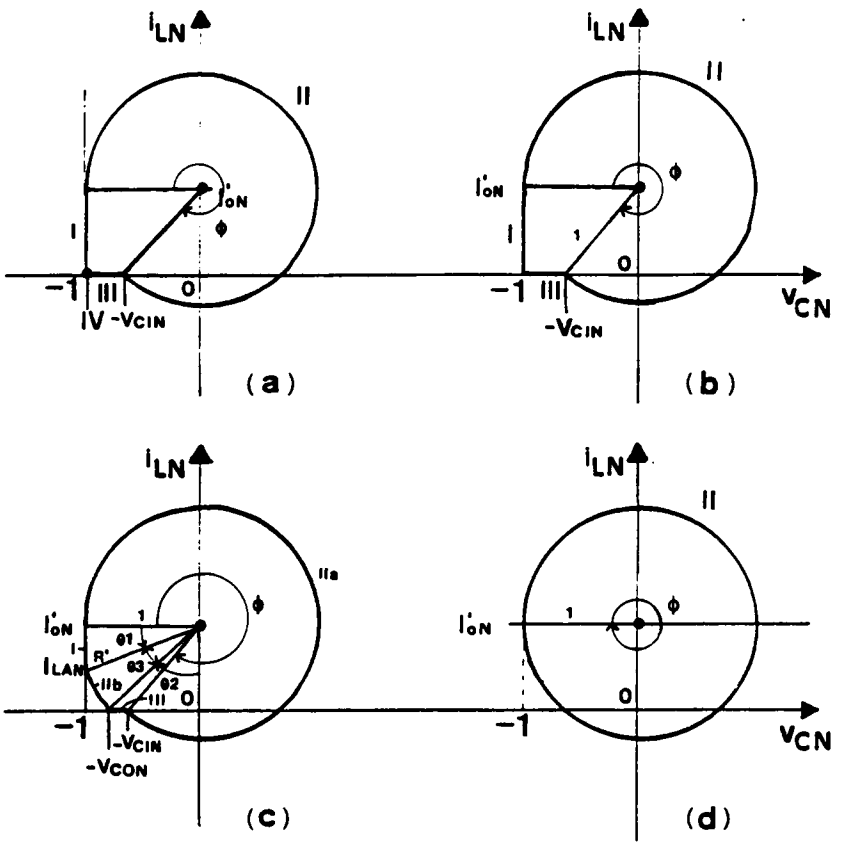

Figure D.2 QRCs with full-wave ZCS - Analysis diagrams
a) Mode 1
b) ω_{ND} boundary
c) Mode 2
d) ω_{MAX} boundary

$$\omega_0 T_{III} = \frac{1 - \sqrt{1 - I'^2_{oN}}}{I'_{oN}}, \quad I'_{oN} \neq 0$$
$$= 0, \qquad I'_{oN} = 0 \tag{D.69}$$

$$T_N = \frac{2\pi}{\omega_{ND}} = \omega_0 T_I + \omega_0 T_{II} + \omega_0 T_{III} \tag{D.70}$$

$$\omega_{ND} = \frac{2\pi}{2\pi - \cos^{-1}\sqrt{1 - I'^2_{oN}} + I'_{oN} + \frac{1 - \sqrt{1 - I'^2_{oN}}}{I'_{oN}}}, \quad I'_{oN} \neq 0$$
$$= 1, \qquad I'_{oN} = 0 \tag{D.71}$$

D.3.1.2 Upper Boundary

Figure D.2 (d) is used to derive the equation for ω_{MAX}.

$$T_N = \frac{2\pi}{\omega_{MAX}} = \omega_0 T_{II} = \varphi = 2\pi \tag{D.72}$$

$$\text{Thus, } \omega_{MAX} = 1 \tag{D.73}$$

D.3.2 DC Analysis

In this case also, (D.18) and (D.19) are valid.

D.3.2.1 Analysis In Mode 1

Figure D.2(a) is used to derive equations in this subsection.

$$V_{C1N} = \sqrt{1 - I'^2_{oN}} \tag{D.74}$$

$$\omega_0 T_I = I'_{oN} \tag{D.75}$$

$$\omega_0 T_{II} = \varphi = 2\pi - \cos^{-1}\sqrt{1 - I'^2_{oN}} \tag{D.76}$$

$$\omega_0 T_{III} = \frac{|\Delta v_{CN}|}{I'_{oN}} = \frac{1 - V_{C1N}}{I'_{oN}} = \frac{1 - \sqrt{1 - I'^2_{oN}}}{I'_{oN}}, \quad I'_{oN} \neq 0$$
$$= 0, \qquad I'_{oN} = 0 \tag{D.77}$$

$$\omega_0 T_{IV} = \omega_0 T - (\omega_0 T_I + \omega_0 T_{II} + \omega_0 T_{III}) \tag{D.78}$$

During interval I,

$$v_{CN} = -1 \tag{D.79}$$

$$\text{So,} \quad \frac{1}{V_E}\int_{T_I} v_C\, dt = -T_I = \frac{1}{\omega_0}(-I'_{oN}) \tag{D.80}$$

During interval II,

$$v_{CN} = -\cos\theta \tag{D.81}$$

$$\text{So,} \quad \frac{1}{V_E}\int_{T_{II}} v_C\, dt = \frac{1}{\omega_0}\int_0^{\varphi}(-\cos\theta)\, d\theta = \frac{1}{\omega_0} I'_{oN} \tag{D.82}$$

During interval III,

$$v_{CN} = -V_{C1N} - \frac{(-V_{C1N} + 1)}{T_{III}}\, t \tag{D.83}$$

$$\text{So,} \quad \frac{1}{V_E}\int_{T_{III}} v_C\, dt = \frac{1}{\omega_0}\left(\frac{-I'_{oN}}{2}\right) \tag{D.84}$$

During interval IV,

$$v_{CN} = -1 \tag{D.85}$$

$$\text{So,} \quad \frac{1}{V_E}\int_{T_{IV}} v_C\, dt = -T_{IV} = \frac{1}{\omega_0}(-\omega_0 T + \omega_0 T_I + \omega_0 T_{II} + \omega_0 T_{III}) \tag{D.86}$$

$$V_{CAVN} = \frac{1}{T}\left[\int_{T_I} v_C\,dt + \int_{T_{II}} v_C\,dt + \int_{T_{III}} v_C\,dt + \int_{T_{IV}} v_C\,dt\right] \tag{D.87}$$

Substituting for the integrals and using (D.19),

$$V_{D2AVN} = -\left[2\pi - \cos^{-1}\sqrt{1 - I'^2_{oN}} + \frac{I'_{oN}}{2} + \frac{1 - \sqrt{1 - I'^2_{oN}}}{I'_{oN}}\right]\frac{\omega_N}{2\pi}, \quad I'_{oN} \neq 0$$
$$= -\omega_N, \qquad I_{oN} = 0 \tag{D.88}$$

The range of operation in mode 1 is

$$0 \leq I'_{oN} \leq 1 \quad \text{and} \quad 0 \leq \omega_N \leq \omega_{ND} \tag{D.89}$$

From (D.88), under no load ($I'_{oN} = 0$), V_{D2AVN} equals $-\omega_N$. Under maximum load ($I'_{oN} = 1$), V_{D2AVN} equals $-0.989\,\omega_N$ ($\cong -\omega_N$). Thus,

$$V_{D2AVN} \cong -\omega_N \tag{D.90}$$

D.3.2.2 Analysis In Mode 2

Figure D.2(c) is used to derive equations in this subsection. In expressing the equations of this subsection, V_{C0N} in Fig. D.2(c) is used as an intermediate parameter.

$$V_{C1N} = \sqrt{1 - I'^2_{oN}} \tag{D.91}$$

$$R' = \sqrt{V^2_{C0N} + I'^2_{oN}} \tag{D.92}$$

$$\theta_1 = \cos^{-1}\frac{1}{R'} = \cos^{-1}\frac{1}{\sqrt{V^2_{C0N} + I'^2_{oN}}} \tag{D.93}$$

$$\theta_2 = \cos^{-1}\frac{I'_{oN}}{R'} = \cos^{-1}\frac{I'_{oN}}{\sqrt{V^2_{C0N} + I'^2_{oN}}} \tag{D.94}$$

$$\omega_0 T_{II\,b} = \theta_3 = \frac{\pi}{2} - \theta_1 - \theta_2$$

$$= \frac{\pi}{2} - \cos^{-1}\frac{1}{\sqrt{V_{C0N}^2 + I_{oN}'^2}} - \cos^{-1}\frac{I_{oN}'}{\sqrt{V_{C0N}^2 + I_{oN}'^2}} \tag{D.95}$$

$$I_{LAN} = I_{oN}' - \sqrt{R'^2 - 1} = I_{oN}' - \sqrt{V_{C0N}^2 + I_{oN}'^2 - 1} \tag{D.96}$$

$$\omega_0 T_I = (I_{oN}' - I_{LAN}) = \sqrt{V_{C0N}^2 + I_{oN}'^2 - 1} \tag{D.97}$$

$$\omega_0 T_{II\,a} = \varphi = 2\pi - \cos^{-1}\frac{V_{C1N}}{1} = 2\pi - \cos^{-1}\sqrt{1 - I_{oN}'^2} \tag{D.98}$$

$$\omega_0 T_{III} = \frac{V_{C0N} - V_{C1N}}{I_{oN}'} = \frac{V_{C0N} - \sqrt{1 - I_{oN}'^2}}{I_{oN}'}, \quad I_{oN}' \neq 0$$
$$= 0, \qquad I_{oN}' = 0 \tag{D.99}$$

$$T_N = \omega_0 T_{II\,b} + \omega_0 T_I + \omega_0 T_{II\,a} + \omega_0 T_{III} \tag{D.100}$$

$$\omega_N = \frac{2\pi}{\left[\frac{5\pi}{2} - \cos^{-1}\sqrt{1 - I_{oN}'^2} - \cos^{-1}\frac{1}{\sqrt{V_{C0N}^2 + I_{oN}'^2}} - \cos^{-1}\frac{I_{oN}'}{\sqrt{V_{C0N}^2 + I_{oN}'^2}} + \frac{V_{C0N} - \sqrt{1 - I_{oN}'^2}}{I_{oN}'} + \sqrt{V_{C0N}^2 + I_{oN}'^2 - 1}\right]}, \quad I_{oN}' \neq 0 \tag{D.101}$$

$$\sqrt{1 - I_{oN}'^2} \leq V_{C0N} \leq 1 \tag{D.102}$$

During interval IIb,

$$v_{CN} = R' \cos\theta \tag{D.103}$$

$$\frac{1}{V_E}\int_{T_{II\,b}} v_C\, dt = \frac{1}{\omega_0}\int_{\frac{\pi}{2}+\theta_2}^{\pi-\theta_1} R' \cos\theta\, d\theta = -\frac{1}{\omega_0}\left(I_{oN}' - \sqrt{V_{C0N}^2 + I_{oN}'^2 - 1}\right) \tag{D.104}$$

During interval I,

$$v_{CN} = -1 \tag{D.105}$$

$$\text{So,} \quad \frac{1}{V_E}\int_{T_I} v_C\,dt = -T_I = = -\frac{1}{\omega_0}\sqrt{V_{C0N}^2 + I'^2_{oN} - 1} \qquad (D.106)$$

During interval IIa,

$$v_{CN} = -\cos\theta \qquad (D.107)$$

$$\text{So,} \quad \frac{1}{V_E}\int_{T_{II\,a}} v_C\,dt = \frac{1}{\omega_0}\int_0^{\varphi}(-\cos\theta)\,d\theta = \frac{1}{\omega_0} I'_{oN} \qquad (D.108)$$

During interval III,

$$v_{CN} = -V_{C1N} - \frac{(-V_{C1N} + V_{C0N})}{T_{III}}\,t \qquad (D.109)$$

$$\text{So,} \quad \frac{1}{V_E}\int_{T_{III}} v_C\,dt = \frac{1}{\omega_0}\left[\frac{1 - I'^2_{oN} - V_{C0N}^2}{2I'_{oN}}\right] \qquad (D.110)$$

$$V_{CAVN} = \frac{1}{T}\left[\int_{T_{II\,b}} v_C\,dt + \int_{T_I} v_C\,dt + \int_{T_{II\,a}} v_C\,dt + \int_{T_{III}} v_C\,dt\right] \qquad (D.111)$$

Substituting for the integrals and using (D.19),

$$V_{D2AVN} = -\left[\frac{1 - I'^2_{oN} - V_{C0N}^2}{2\,I'_{oN}}\right]\frac{\omega_N}{2\pi} - 1 \qquad (D.112)$$

The range of operation in mode 2 is

$$0 < I'_{oN} \leq 1 \quad \text{and} \quad \omega_{ND} \leq \omega_N \leq \omega_{MAX} \qquad (D.113)$$

Given ω_N and I'_{oN} within the ranges specicified by (D.113), equation (D.101) is used to determine iteratively the corresponding value of V_{C0N}. The value of V_{D2AVN} is then determined form ω_N, I'_{oN} and V_{C0N} using (D.112). Also, although (D.57) for half-wave operation and (D.112) for full-wave operation are identical, the value of V_{C0N} used in them for a given ω_N as determined by (D.46) and (D.101) are different.

D.4 Analysis Of QRCs With Half-Wave ZVS

The analysis diagrams for this case are drawn in Fig. D.3 based on the diagrams in Fig. 6.11.

D.4.1 Boundary Equations

D.4.1.1 Boundary Between Mode 1 And Mode 2

Figure D.3 (b) is utilized to derive the equations for ω_{ND}.

$$\omega_0 T_I = \frac{|\Delta v_{CN}|}{I'_{oN}} = \frac{1}{I'_{oN}} \tag{D.114}$$

$$\omega_0 T_{II} = \varphi = \pi + \cos^{-1}\frac{\sqrt{I'^2_{oN} - 1}}{I'_{oN}} \tag{D.115}$$

$$\omega_0 T_{III} = |\Delta i_{LN}| = I'_{oN} + \sqrt{I'^2_{oN} - 1} \tag{D.116}$$

$$T_N = \frac{2\pi}{\omega_{ND}} = \omega_0 T_I + \omega_0 T_{II} + \omega_0 T_{III} \tag{D.117}$$

$$\omega_{ND} = \frac{2\pi}{\pi + \cos^{-1}\frac{\sqrt{I'^2_{oN} - 1}}{I'_{oN}} + \frac{1}{I'_{oN}} + I'_{oN} + \sqrt{I'^2_{oN} - 1}}, \quad I'_{oN} \geq 1 \tag{D.118}$$

D.4.1.2 Boundary Between Mode 2 And Mode 3

Figure D.3(d) is used to derive the equation for ω_{NU}.

$$\omega_0 T_{II} = \varphi = \pi + 2\cos^{-1}\frac{\sqrt{I'^2_{oN} - 1}}{I'_{oN}} \tag{D.119}$$

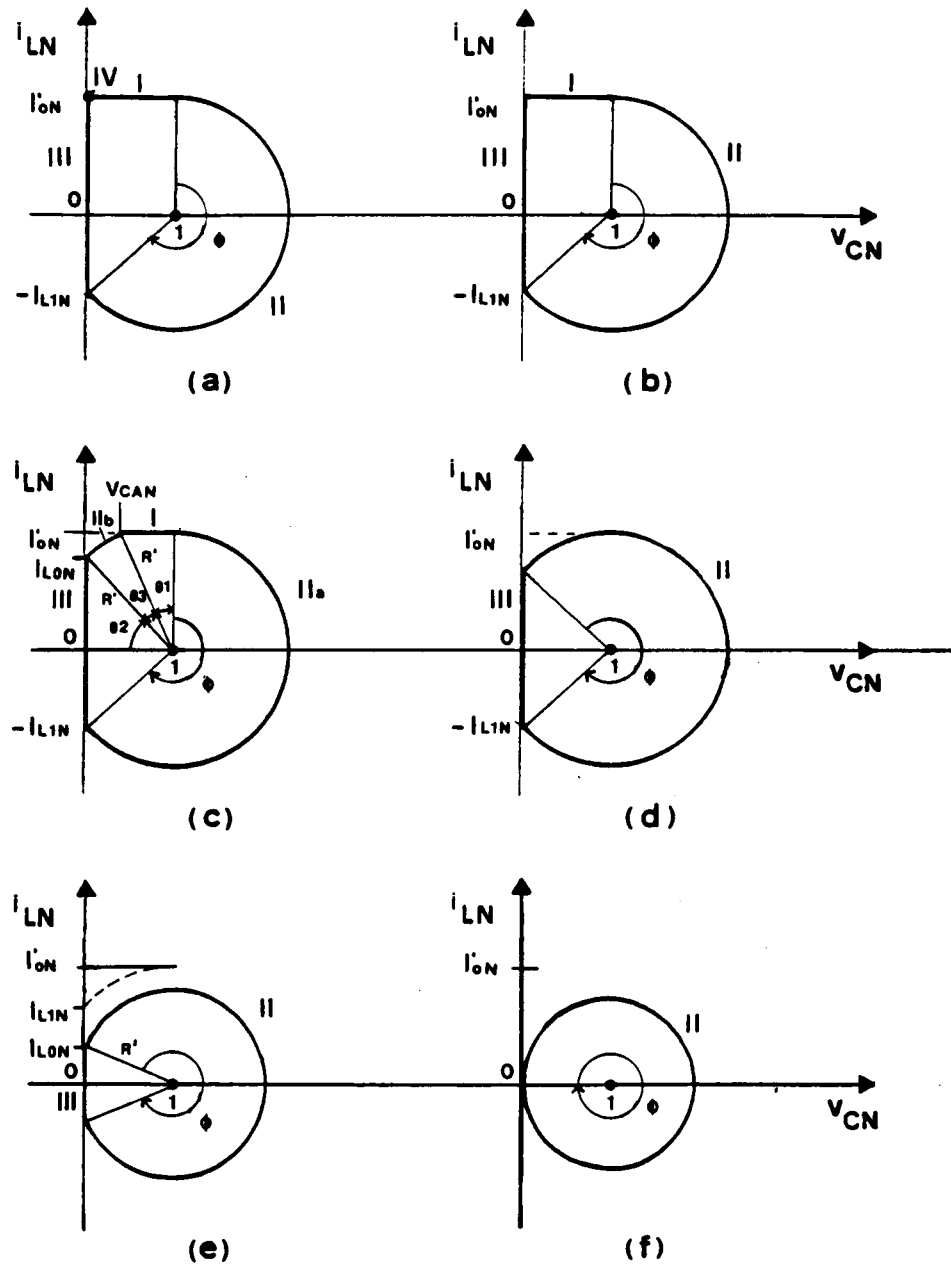

Figure D.3 QRCs with half-wave ZVS - Analysis diagrams

a) Mode 1
b) ω_{ND} boundary
c) Mode 2
d) ω_{NU} boundary
e) Mode 3
f) ω_{MAX} boundary

$$\omega_0 T_{III} = 2\sqrt{I'^2_{oN} - 1} \qquad (D.120)$$

$$T_N = \frac{2\pi}{\omega_{NU}} = \omega_0 T_{II} + \omega_0 T_{III} \qquad (D.121)$$

$$\text{Thus,} \quad \omega_{NU} = \frac{2\pi}{\pi + 2\cos^{-1}\frac{\sqrt{I'^2_{oN} - 1}}{I'_{oN}} + 2\sqrt{I'^2_{oN} - 1}}, \quad I'_{oN} \geq 1 \qquad (D.122)$$

D.4.1.3 Upper Boundary

Figure D.3 (f) is used to derive the equation for ω_{MAX}.

$$T_N = \frac{2\pi}{\omega_{MAX}} = \omega_0 T_{II} = \varphi = 2\pi \qquad (D.123)$$

$$\text{Thus,} \quad \omega_{MAX} = 1 \qquad (D.124)$$

D.4.2 DC Analysis

For all the ZVS QRCs, during the resonant interval (interval II) and inductor charging / discharging interval (interval III) the freewheel diode conducts and, hence, the value of v_{D2} is zero. During the constant state interval (interval IV), voltage of value ($-V_E$) is applied across $D2$. Finally, during the capacitor discharging/charging interval(interval I) the capacitor is charged by a constant current I_{EN} ($= I'_{oN}$) to a value of V_E. Thus, during this interval the voltage across $D2$ linearly decreases to ($-V_E$).

D.4.2.1 Analysis In Mode 1

Figure D.3(a) is used to derive equations in this subsection.

$$\omega_0 T_I = \frac{|\Delta v_{CN}|}{I'_{oN}} = \frac{1}{I'_{oN}} \tag{D.125}$$

$$\omega_0 T_{II} = \varphi = \pi + \cos^{-1}\frac{\sqrt{I'^2_{oN} - 1}}{I'_{oN}} \tag{D.126}$$

$$\omega_0 T_{III} = |\Delta i_{LN}| = I'_{oN} + \sqrt{I'^2_{oN} - 1} \tag{D.127}$$

$$\omega_0 T_{IV} = \omega_0 T - (\omega_0 T_I + \omega_0 T_{II} + \omega_0 T_{III}) \tag{D.128}$$

$$V_{D2AVN} = \frac{1}{V_E T}\left(- V_E T_{IV} - \frac{1}{2} V_E T_I \right) \tag{D.129}$$

$$V_{D2AVN} = -\left[1 - \left(\pi + \cos^{-1}\frac{\sqrt{I'^2_{oN} - 1}}{I'_{oN}} + \frac{1}{2 I'_{oN}} + I'_{oN} + \sqrt{I'^2_{oN} - 1} \right) \frac{\omega_N}{2\pi} \right] \tag{D.130}$$

The range of operation in mode 1 is

$$1 \leq I'_{oN} < \infty \quad \text{and} \quad 0 < \omega_N \leq \omega_{ND} \tag{D.131}$$

D.4.2.2 Analysis In Mode 2

Figure D.3(c) is used to derive equations in this subsection. In expressing the equations of this subsection, I_{LON} in Fig. D.3(c) is used as an intermediate parameter.

$$I_{L1N} = \sqrt{I'^2_{oN} - 1} \tag{D.132}$$

$$R' = \sqrt{I^2_{LON} + 1} \tag{D.133}$$

$$\theta_1 = \cos^{-1}\frac{I'_{oN}}{R'} = \cos^{-1}\frac{I'_{oN}}{\sqrt{I^2_{LON} + 1}} \tag{D.134}$$

$$\theta_2 = \cos^{-1}\frac{1}{R'} = \cos^{-1}\frac{1}{\sqrt{I_{LON}^2 + 1}} \tag{D.135}$$

$$\begin{aligned}\omega_0 T_{II\,b} = \theta_3 &= \frac{\pi}{2} - \theta_1 - \theta_2 \\ &= \frac{\pi}{2} - \cos^{-1}\frac{I'_{oN}}{\sqrt{I_{LON}^2 + 1}} - \cos^{-1}\frac{1}{\sqrt{I_{LON}^2 + 1}}\end{aligned} \tag{D.136}$$

$$V_{CAN} = 1 - \sqrt{R'^2 - I'^2_{oN}} = 1 - \sqrt{I_{LON}^2 + 1 - I'^2_{oN}} \tag{D.137}$$

$$\omega_0 T_I = \frac{|\Delta v_{CN}|}{I'_{oN}} = \frac{1 - V_{CAN}}{I'_{oN}} = \frac{\sqrt{I_{LON}^2 + 1 - I'^2_{oN}}}{I'_{oN}} \tag{D.138}$$

$$\omega_0 T_{II\,a} = \varphi = \pi + \cos^{-1}\frac{I_{L1N}}{1} = \pi + \cos^{-1}\frac{\sqrt{I'^2_{oN} - 1}}{I'_{oN}} \tag{D.139}$$

$$\omega_0 T_{III} = |\Delta i_{LN}| = I_{LON} + I_{L1N} = I_{LON} + \sqrt{I'^2_{oN} - 1} \tag{D.140}$$

$$T_N = \omega_0 T_{II\,b} + \omega_0 T_I + \omega_0 T_{II\,a} + \omega_0 T_{III} \tag{D.141}$$

$$\omega_N = \frac{2\pi}{\left[\begin{array}{l}\dfrac{3\pi}{2} + \cos^{-1}\dfrac{\sqrt{I'^2_{oN} - 1}}{I'_{oN}} - \cos^{-1}\dfrac{I'_{oN}}{\sqrt{I_{LON}^2 + 1}} \\ \quad - \cos^{-1}\dfrac{1}{\sqrt{I_{LON}^2 + 1}} \\ \quad + \dfrac{\sqrt{I_{LON}^2 + 1 - I'^2_{oN}}}{I'_{oN}} + I_{LON} + \sqrt{I'^2_{oN} - 1}\end{array}\right]} \tag{D.142}$$

$$V_{D2AVN} = \frac{1}{V_E T}\left[-\frac{1}{2}(V_E - V_{CA})\,T_I\right] = \frac{-1}{\omega_0 T}\frac{1}{2}(1 - V_{CAN})\,\omega_0 T_I \tag{D.143}$$

$$\text{Hence,}\quad V_{D2AVN} = -\frac{(I_{LON}^2 + 1 - I'^2_{oN})}{2\,I'_{oN}}\frac{\omega_N}{2\pi} \tag{D.144}$$

The range of operation in mode 2 is

$$1 \le I'_{oN} < \infty \quad \text{and} \quad \omega_{ND} \le \omega_N \le \omega_{NU} \tag{D.145}$$

Given ω_N and I'_{oN} within the ranges specified by (D.145), equation (D.142) is used to determine iteratively the corresponding value of I_{LON}. The value of V_{D2AVN} is then determined from ω_N, I'_{oN} and I_{LON} using (D.144).

D.4.2.3 Analysis In Mode 3

Figure D.3(e) is used to derive equations in this subsection. In expressing the equations of this subsection, parameter I_{LON} is again made use of.

$$R' = \sqrt{I_{LON}^2 + 1} \tag{D.146}$$

$$\omega_0 T_{II} = \varphi = 2\pi - 2\cos^{-1}\frac{1}{R'} = 2\pi - 2\cos^{-1}\frac{1}{\sqrt{I_{LON}^2 + 1}} \tag{D.147}$$

$$\omega_0 T_{III} = |\Delta i_{LN}| = 2I_{LON} \tag{D.148}$$

$$T_N = \omega_0 T_{II} + \omega_0 T_{III} \tag{D.149}$$

$$\omega_N = \frac{\pi}{\pi - \cos^{-1}\dfrac{1}{\sqrt{I_{LON}^2 + 1}} + I_{LON}} \tag{D.150}$$

Since intervals I and IV do not occur at all, diode $D2$ is always conducting. Thus,

$$V_{D2AVN} = 0 \tag{D.151}$$

Hence, in mode 3 the converter operation is saturated. The range of operation in mode 3 is

$$0 \le I'_{oN} < \infty \quad \text{and} \quad \omega_{NU} \le \omega_N \le \omega_{MAX} \tag{D.152}$$

D.5 Analysis Of QRCs With Full-Wave ZVS

The analysis diagrams for this case are drawn in Fig. D.4 based on the diagrams in Fig. 6.12.

D.5.1 Boundary Equations

D.5.1.1 Boundary Between Mode 1 And Mode 2

Figure D.4 (b) is utilized to derive the equations for ω_{ND}.

$$\omega_0 T_I = \frac{|\Delta v_{CN}|}{I'_{oN}} = \frac{1}{I'_{oN}} \tag{D.153}$$

$$\omega_0 T_{II} = \varphi = 2\pi - \cos^{-1}\frac{\sqrt{I'^2_{oN} - 1}}{I'_{oN}} \tag{D.154}$$

$$\omega_0 T_{III} = |\Delta i_{LN}| = I'_{oN} - \sqrt{I'^2_{oN} - 1} \tag{D.155}$$

$$T_N = \frac{2\pi}{\omega_{ND}} = \omega_0 T_I + \omega_0 T_{II} + \omega_0 T_{III} \tag{D.156}$$

$$\omega_{ND} = \frac{2\pi}{2\pi - \cos^{-1}\frac{\sqrt{I'^2_{oN} - 1}}{I'_{oN}} + \frac{1}{I'_{oN}} + I'_{oN} - \sqrt{I'^2_{oN} - 1}}, \quad I'_{oN} \geq 1 \tag{D.157}$$

D.5.1.2 Upper Boundary

Figure D.4 (d) is used to derive the equation for ω_{MAX}.

$$T_N = \frac{2\pi}{\omega_{MAX}} = \omega_0 T_{II} = \varphi = 2\pi \tag{D.158}$$

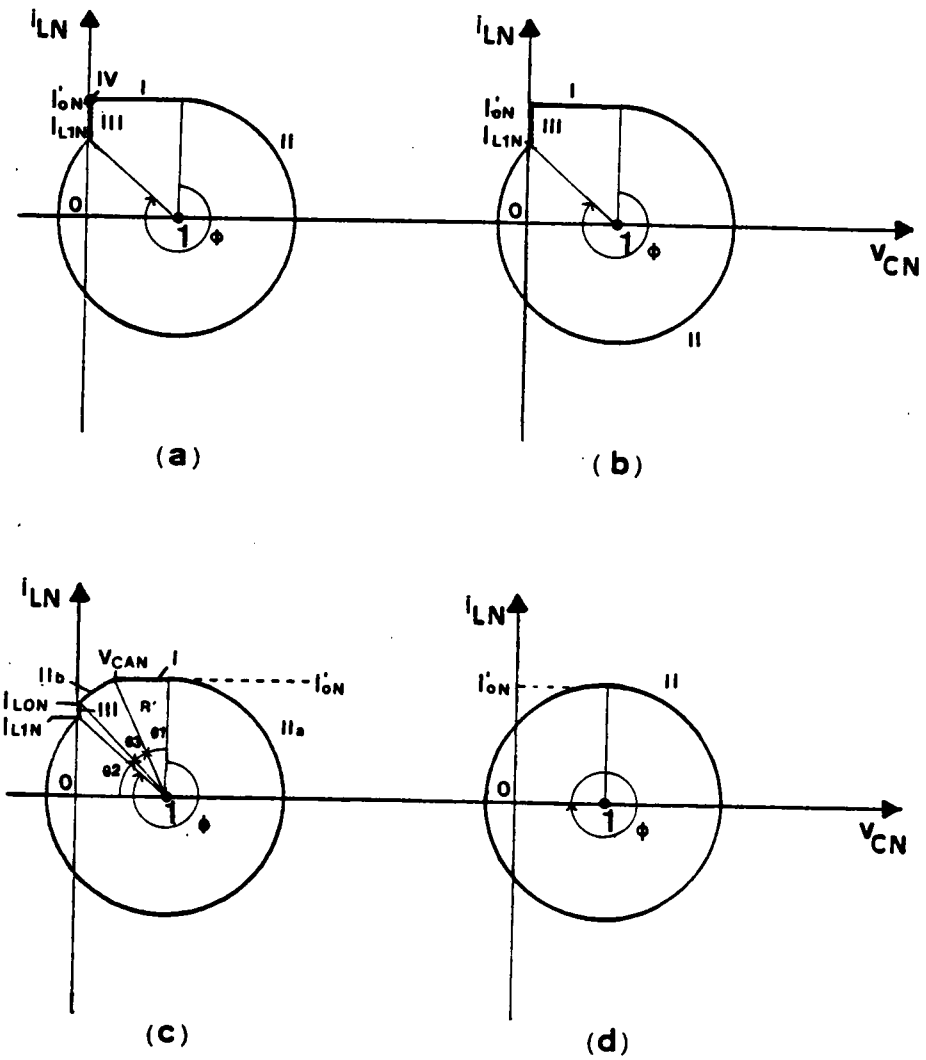

Figure D.4 QRCs with full-wave ZVS - Analysis diagrams
a) Mode 1
b) ω_{ND} boundary
c) Mode 2
d) ω_{MAX} boundary

Thus, $\omega_{MAX} = 1$ (D.159)

D.5.2 DC Analysis

D.5.2.1 Analysis In Mode 1

Figure D.4(a) is used to derive equations in this subsection.

$$\omega_0 T_I = \frac{|\Delta v_{CN}|}{I'_{oN}} = \frac{1}{I'_{oN}} \tag{D.160}$$

$$\omega_0 T_{II} = \varphi = 2\pi - \cos^{-1}\frac{\sqrt{I'^2_{oN} - 1}}{I'_{oN}} \tag{D.161}$$

$$\omega_0 T_{III} = |\Delta i_{LN}| = I'_{oN} - \sqrt{I'^2_{oN} - 1} \tag{D.162}$$

$$\omega_0 T_{IV} = \omega_0 T - (\omega_0 T_I + \omega_0 T_{II} + \omega_0 T_{III}) \tag{D.163}$$

$$V_{D2AVN} = \frac{1}{V_E T}\left(- V_E T_{IV} - \frac{1}{2} V_E T_I\right) \tag{D.164}$$

$$V_{D2AVN} = -\left[1 - \left(2\pi - \cos^{-1}\frac{\sqrt{I'^2_{oN} - 1}}{I'_{oN}} + \frac{1}{2 I'_{oN}} + I'_{oN} - \sqrt{I'^2_{oN} - 1}\right)\frac{\omega_N}{2\pi}\right] \tag{D.165}$$

The range of operation in mode 1 is

$$1 \le I'_{oN} < \infty \quad \text{and} \quad \omega_{ND} \le \omega_N \le \omega_{NU} \tag{D.166}$$

From (D.165), under minimum load ($I'_{oN} = 1$), V_{D2AVN} equals $\{ - (1 - 0.989\ \omega_N)\}$, which is approximately $\{ - (1 - \omega_N)\}$. As load current approaches maximum ($I'_{oN} \to \infty$), V_{D2AVN} equals $\{ - (1 - \omega_N)\}$. Thus,

$$V_{D2AVN} \cong - (1 - \omega_N) \tag{D.167}$$

D.5.2.2 Analysis In Mode 2

Figure D.4(c) is used to derive equations in this subsection. In expressing the equations of this subsection, I_{LON} in Fig. D.4(c) is used as an intermediate parameter.

$$I_{L1N} = \sqrt{I'^2_{oN} - 1} \tag{D.168}$$

$$R' = \sqrt{I^2_{LON} + 1} \tag{D.169}$$

$$\theta_1 = \cos^{-1}\frac{I'_{oN}}{R'} = \cos^{-1}\frac{I'_{oN}}{\sqrt{I^2_{LON} + 1}} \tag{D.170}$$

$$\theta_2 = \cos^{-1}\frac{1}{R'} = \cos^{-1}\frac{1}{\sqrt{I^2_{LON} + 1}} \tag{D.171}$$

$$\begin{aligned}\omega_0 T_{II\,b} = \theta_3 &= \frac{\pi}{2} - \theta_1 - \theta_2 \\ &= \frac{\pi}{2} - \cos^{-1}\frac{I'_{oN}}{\sqrt{I^2_{LON} + 1}} - \cos^{-1}\frac{1}{\sqrt{I^2_{LON} + 1}}\end{aligned} \tag{D.172}$$

$$V_{CAN} = 1 - \sqrt{R'^2 - I'^2_{oN}} = 1 - \sqrt{I^2_{LON} + 1 - I'^2_{oN}} \tag{D.173}$$

$$\omega_0 T_I = \frac{|\Delta v_{CN}|}{I'_{oN}} = \frac{1 - V_{CAN.}}{I'_{oN}} = \frac{\sqrt{I^2_{LON} + 1 - I'^2_{oN}}}{I'_{oN}} \tag{D.174}$$

$$\omega_0 T_{II\,a} = \varphi = 2\pi - \cos^{-1}\frac{I_{L1N}}{1} = 2\pi - \cos^{-1}\frac{\sqrt{I'^2_{oN} - 1}}{I'_{oN}} \tag{D.175}$$

$$\omega_0 T_{III} = |\Delta i_{LN}| = I_{LON} - I_{L1N} = I_{LON} - \sqrt{I'^2_{oN} - 1} \tag{D.176}$$

$$T_N = \omega_0 T_{II\,b} + \omega_0 T_I + \omega_0 T_{II\,a} + \omega_0 T_{III} \tag{D.177}$$

$$\omega_N = \frac{2\pi}{\left[\frac{5\pi}{2} - \cos^{-1}\frac{\sqrt{I'^2_{oN} - 1}}{I'_{oN}} - \cos^{-1}\frac{I'_{oN}}{\sqrt{I^2_{LON} + 1}} - \cos^{-1}\frac{1}{\sqrt{I^2_{LON} + 1}} + \frac{\sqrt{I^2_{LON} + 1 - I'^2_{oN}}}{I'_{oN}} + I_{LON} - \sqrt{I'^2_{oN} - 1}\right]} \qquad (D.178)$$

$$V_{D2AVN} = \frac{1}{V_E T}\left[-\frac{1}{2}(V_E - V_{CA})\,T_I\right] = \frac{-1}{\omega_0 T}\frac{1}{2}(1 - V_{CAN})\,\omega_0 T_I \qquad (D.179)$$

$$\text{Hence,} \quad V_{D2AVN} = -\frac{(I^2_{LON} + 1 - I'^2_{oN})}{2\,I'_{oN}}\frac{\omega_N}{2\pi} \qquad (D.180)$$

The range of operation in mode 2 is

$$1 \le I'_{oN} < \infty \quad \text{and} \quad \omega_{NU} \le \omega_N \le \omega_{MAX} \qquad (D.181)$$

Given ω_N and I'_{oN} within the ranges specicified by (D.181), equation (D.178) is used to determine iteratively the corresponding value of I_{LON}. The value of V_{D2AVN} is then determined form ω_N, I'_{oN} and I_{LON} using (D.180). Also, although (D.144) for half-wave operation and (D.180) for half-wave operation are identical, the value of V_{CON} used in them for given ω_N as determined by (D.142) and (D.178) are different.

D.6 DC Gain Relationships

In this section, equations relating the dc gain V'_{oN} to V_{D2AVN} will be derived. These equations depend only on the type of converter - buck, boost, buck-boost and boost-buck. These relationship are valid for conventional pulse-width modulated converters also.

D.6.1 Buck QRC

The voltage normalizing factor V_E for a buck QRC is V_s. In a buck QRC (Figs. 6.2(a) and (e)), since the average voltage across the output filter inductor over a cycle is zero,

$$V_0 = -V_{D2AV} \tag{D.182}$$

$$\text{Hence,} \quad V_{oN} = \frac{V_0}{V_s} = V_{oN} = -\frac{V_{D2AV}}{V_s} = -V_{D2AVN} \tag{D.183}$$

By substituting for V_{D2AVN} from Sec. D.2, D.3, D.4 or D.5 into (D.183), dc gain equations for a buck QRC with a half-wave ZCS, full-wave ZCS, half-wave ZVS or a full-wave ZVS, respectively, can be obtained. For a QRC with a full-wave ZCS, V_{D2AVN} may be approximated by (D.90). Hence,

$$V'_{oN} \cong \omega_N \qquad \text{- Buck with full-wave ZCS} \tag{D.184}$$

For a QRC with a full-wave ZVS, V_{D2AVN} may be approximated by (D.167). Hence,

$$V'_{oN} \cong 1 - \omega_N \qquad \text{- Buck with full-wave ZVS} \tag{D.185}$$

D.6.2 Boost QRC

The voltage normalizing factor V_E for a boost QRC is V_o. In a boost QRC (Figs. 6.2(b) and (f)), since the average voltage across the input filter inductor over a cycle is zero,

$$V_o = -V_{D2AV} + V_s \tag{D.186}$$

$$\text{Hence} \quad V'_{oN} = \frac{V_o}{V_s} = \frac{1}{V_{SN}} = \frac{1}{V_{D2AVN} + 1} \tag{D.187}$$

By substituting for V_{D2AVN} from Sec. D.2, D.3, D.4 or D.5 into (D.187), dc gain equations for a boost QRC with a half-wave ZCS, full-wave ZCS, half-wave ZVS or a full-wave ZVS, respectively, can be obtained. From (D.90) and (D.187),

$$V'_{oN} \cong \frac{1}{1 - \omega_N} \qquad \text{- Boost with full-wave ZCS} \qquad (D.188)$$

From (D.167) and (D.187),

$$V'_{oN} \cong \omega_N \qquad \text{- Boost with full-wave ZVS} \qquad (D.189)$$

D.6.3 Buck-Boost QRC

The voltage normalizing factor V_E for a buck-boost QRC equals $(V_o + V_s)$. In a buck-boost QRC (Figs. 6.2(c) and (g)), since the average voltage across the energy transfer inductor is zero,

$$V_o = - V_{D2AV} \qquad (D.190)$$

$$\text{Hence,} \quad V'_{oN} = \frac{V_o}{V_s} = - \frac{V_{D2AVN}}{V_{D2AVN} + 1} \qquad (D.191)$$

By substituting for V_{D2AVN} from Sec. D.2, D.3, D.4 or D.5 into (D.191), dc gain equations for a buck-boost QRC with a half-wave ZCS, full-wave ZCS, half-wave ZVS or a full-wave ZVS, respectively, can be obtained. From (D.90) and (D.191),

$$V'_{oN} \cong \frac{\omega_N}{1 - \omega_N} \qquad \text{- Buck-boost with full-wave ZCS} \qquad (D.192)$$

From (D.167) and (D.191),

$$V'_{oN} \cong \frac{1 - \omega_N}{\omega_N} \qquad \text{- Buck-boost with full-wave ZVS} \qquad (D.193)$$

D.6.4 Boost-Buck QRC

The voltage normalizing factor V_E for a boost-buck QRC equals V_i. Since the average voltage across the input and output filter inductors are zero,

$$V_i = V_s + V_o \tag{D.194}$$

$$V_o = -V_{D2AV} \tag{D.195}$$

$$\text{Hence,} \quad V'_{oN} = \frac{V_o}{V_s} = \frac{V_{oN}}{1 - V_{oN}} = -\frac{V_{D2AVN}}{V_{D2AVN} + 1} \tag{D.196}$$

The dc gain equations for the buck-boost and the boost-buck QRCs are identical. By substituting for V_{D2AVN} from Sec. D.2, D.3, D.4 or D.5 into (D.196), dc gain equations for a boost-buck QRC with a half-wave ZCS, full-wave ZCS, half-wave ZVS or a full-wave ZVS, respectively, can be obtained. From (D.90) and (D.196),

$$V'_{oN} \cong \frac{\omega_N}{1 - \omega_N} \quad \text{- Boost-buck with full-wave ZCS} \tag{D.197}$$

From (D.167) and (D.196),

$$V'_{oN} \cong \frac{1 - \omega_N}{\omega_N} \quad \text{- Boost-buck with full-wave ZVS} \tag{D.198}$$

D.7 Program Listings

D.7.1 Mode Boundaries

```
C  A PROGRAM TO COMPUTE THE BOUNDARY FREQUENCIES FOR ALL QUASI
C  RESONANT CONVERTERS
C
C     BY RAMESH ORUGANTI
C
      IMPLICIT REAL*8(A-H,O-Z)
      DIMENSION XI(201), WND(201), WNU(201)
C
```

```
C JRSW    = 1  HALF-WAVE ZCS AND HALF-WAVE ZVS
C         = 2  FULL-WAVE ZCS AND FULL-WAVE ZVS
C
C XI IS TAKEN TO BE EQUAL TO IONP FOR A ZCS AND TO BE EQUAL TO BE 1/IONP
C FOR A ZVS, WHERE IONP IS THE MODIFIED LOAD CURRENT.
C
      JRSW          =  2
      NSTEP1        =  100
      STEP1         =  1./DFLOAT(NSTEP1)
      N1            =  NSTEP1 + 1
      DO  100  K1   =  1, N1
      XI(K1)        =  DFLOAT(K1-1)*STEP1
C
      IF(JRSW.NE.1) GO TO 10
      WND(K1)       =  FNWNDH(XI(K1))
      WNU(K1)       =  FNWNUH(XI(K1))
      GO TO 100
C
   10 WND(K1)       =  FNWNDF(XI(K1))
  100 CONTINUE
C
      DO  110  K2   =  1, N1
  110 WRITE(6, 9010) WND(K2), XI(K2)
C
      IF(JRSW.NE.1) STOP
C
      DO  120  K3   =  1, N1
  120 WRITE(6, 9010) WNU(K3), XI(K3)
 9010 FORMAT(2E14.5)
      STOP
      END
```

D.7.2 DC Characteristics - Half-Wave ZCS

```
C  A PROGRAM TO COMPUTE THE DC CHARACTERISTICS OF ALL QUASI
C  RESONANT CONVERTERS WITH HALF-WAVE ZCS.
C
C  JCON = 0  COMMON FOR ALL CONVERTERS (VD2AVN OUTPUT)
C       = 1  BUCK
C       = 2  BOOST
C       = 3  BUCK-BOOST
C       = 4  BOOST-BUCK
C
C     BY RAMESH ORUGANTI
C
      IMPLICIT REAL*8(A-H,I,O-Z)
      NSTEP1        =  100
      JCON          =  0
      PI            =  4.0*ATAN(1.0)
C
      DO  300  K1   =  1, 6
      IONP          =  DFLOAT(K1-1) * 0.2
      IF(K1.EQ.1) IONP = 1.0D-06
      IF(K1.EQ.6) IONP = 1.0 - 1.0D-06
      S             =  DSQRT(1.-IONP**2)
      WND           =  FNWNDH(IONP)
C
      WNMIN         =  0.
      WNMAX         =  WND
      STEP1         =  (WNMAX-WNMIN)/DFLOAT(NSTEP1)
      N1            =  NSTEP1 + 1
C
      DO  100  K2   =  1, N1
      WN            =  WNMIN + DFLOAT(K2-1)*STEP1
      IF(K2.EQ.1) WN = WNMIN + 1.0D-06
      IF(K2.EQ.N1) WN = WNMAX - 1.0D-06
      VD2AVN        =  -(PI+DARCOS(S)+IONP/2.+(1.+S)/IONP)*WN/(2.*PI)
      VAL           =  DABS(1.+VD2AVN)
      IF(VAL.LT.1.0D-06) VD2AVN = -1.0 + 1.0D-06
      IF(JCON.EQ.0) VONP = VD2AVN
      IF(JCON.EQ.1) VONP = -VD2AVN
      IF(JCON.EQ.2) VONP = 1./(1.+VD2AVN)
      IF(JCON.EQ.3) VONP = -VD2AVN/(1.+VD2AVN)
      IF(JCON.EQ.4) VONP = -VD2AVN/(1.+VD2AVN)
      WRITE(6, 9010) WN, VONP
 9010 FORMAT(2E14.5)
  100 CONTINUE
C
      VCONMN        =  S
      VCONMX        =  1.
```

```
      STEP1       =  (VCONMX-VCONMN)/DFLOAT(NSTEP1)
C
      DO  200  K3  =  1, N1
      VCON        =  VCONMX - DFLOAT(K3-1)*STEP1
C     IF(K3.EQ.1) VCON = VCONMX - 1.0D-05
C     IF(K3.EQ.N1) VCON = VCONMN + 1.0D-05
      A           =  DSQRT(VCON**2 + IONP**2)
      B           =  DSQRT(VCON**2 + IONP**2 -1.)
      TN          =  3.*PI/2. + DARCOS(S) - DARCOS(1./A)
     *            -  DARCOS(IONP/A) + (VCON+S)/IONP + B
      WN          =  2.*PI/TN
      VD2AVN      =  -((1.-IONP**2 - VCON**2)/(2.*IONP))*WN/(2.*PI) -1.
      VAL         =  DABS(1.+VD2AVN)
      IF(VAL.LT.1.0D-06) VD2AVN = -1.0 + 1.0D-06
      IF(JCON.EQ.0) VONP = VD2AVN
      IF(JCON.EQ.1) VONP = -VD2AVN
      IF(JCON.EQ.2) VONP = 1./(1.+VD2AVN)
      IF(JCON.EQ.3) VONP = -VD2AVN/(1.+VD2AVN)
      IF(JCON.EQ.4) VONP = -VD2AVN/(1.+VD2AVN)
      WRITE(6, 9010) WN, VONP
  200 CONTINUE
C
      VCONMN      =  0
      VCONMX      =  S
      STEP1       =  (VCONMX-VCONMN)/DFLOAT(NSTEP1)
C
      DO  300  K4  =  1, N1
      VCON        =  VCONMX - DFLOAT(K4-1)*STEP1
C     IF(K4.EQ.1) VCON = VCONMX - 1.0D-06
C     IF(K4.EQ.N1) VCON = VCONMN + 1.0D-06
      A           =  DSQRT(VCON**2 + IONP**2)
      TN          =  2.*(PI - DARCOS(IONP/A) + VCON/IONP)
      WN          =  2.*PI/TN
      VD2AVN      =  -1. + 1.0D-06
      IF(JCON.EQ.0) VONP = VD2AVN
      IF(JCON.EQ.1) VONP = -VD2AVN
      IF(JCON.EQ.2) VONP = 1./(1.+VD2AVN)
      IF(JCON.EQ.3) VONP = -VD2AVN/(1.+VD2AVN)
      IF(JCON.EQ.4) VONP = -VD2AVN/(1.+VD2AVN)
      WRITE(6, 9010) WN, VONP
  300 CONTINUE
      STOP
      END
      FUNCTION FNWNDH(XI)
C
C  SUBPROGRAM TO CALCULATE THE WND BOUNDARY FREQUENCY FOR QRCS
C  WITH HALF-WAVE RESONANT SWITCHES GIVEN LOAD CURRENT PARAMETER XI.
C  XI EQUALS MODIFIED LOAD CURRENT IONP FOR ZCS AND 1/IONP FOR ZVS.
C
C  BY RAMESH ORUGANTI
C
      IMPLICIT REAL*8(A-H,O-Z)
      PI          =  4.0*ATAN(1.)
      S           =  DSQRT(1.-XI**2)
      IF(XI.EQ.0.) GO TO 10
      FNWNDH      =  2.*PI/(PI+DARCOS(S) + XI + (1./XI) +S/XI)
      RETURN
   10 FNWNDH      =  0.
      RETURN
      END
C
      FUNCTION FNWNUH(XI)
C
C  SUBPROGRAM TO CALCULATE THE WNU BOUNDARY FREQUENCY FOR QRCS
C  WITH HALF-WAVE RESONANT SWITCHES GIVEN LOAD CURRENT PARAMETER XI.
C  XI EQUALS MODIFIED LOAD CURRENT IONP FOR ZCS AND 1/IONP FOR ZVS.
C
C  BY RAMESH ORUGANTI
C
      IMPLICIT REAL*8(A-H,O-Z)
      PI          =  4.0*ATAN(1.)
      S           =  DSQRT(1.-XI**2)
      IF(XI.EQ.0.) GO TO 10
      FNWNUH      =  2.*PI/(PI+2.*DARCOS(S) + 2.*S/XI)
      RETURN
   10 FNWNUH      =  0.
      RETURN
      END
C
      FUNCTION FNWNDF(XI)
C
C  SUBPROGRAM TO CALCULATE THE WND BOUNDARY FREQUENCY FOR QRCS
C  WITH FULL-WAVE RESONANT SWITCHES GIVEN LOAD CURRENT PARAMETER XI.
C  XI EQUALS MODIFIED LOAD CURRENT IONP FOR ZCS AND 1/IONP FOR ZVS.
```

```
C
C  BY RAMESH ORUGANTI
C
      IMPLICIT REAL*8(A-H,O-Z)
      PI            =  4.0*ATAN(1.)
      S             =  DSQRT(1.-XI**2)
      IF(XI.EQ.0.) GO TO 10
      FNWNDF        =  2.*PI/(2.*PI-DARCOS(S) + XI + (1./XI) -S/XI)
      RETURN
   10 FNWNDF        =  1.
      RETURN
      END
```

D.7.3 DC Charateristics - Full-Wave ZCS

```
C  A PROGRAM TO COMPUTE THE DC CHARACTERISTICS OF ALL QUASI
C  RESONANT CONVERTERS WITH FULL-WAVE ZCS.
C
C  JCON = 0  COMMON FOR ALL CONVERTERS (VD2AVN OUTPUT)
C       = 1  BUCK
C       = 2  BOOST
C       = 3  BUCK-BOOST
C       = 4  BOOST-BUCK
C
C     BY RAMESH ORUGANTI
C
      IMPLICIT REAL*8(A-H,I,O-Z)
      NSTEP1        =  100
      JCON          =  0
      PI            =  4.0*ATAN(1.0)
C
      DO  200  K1   =  1, 6
      IONP          =  DFLOAT(K1-1) * 0.2
      IF(K1.EQ.1) IONP = 1.0D-03
      IF(K1.EQ.6) IONP = 1.0 - 1.0D-03
      S             =  DSQRT(1.-IONP**2)
      WND           =  FNWNDF(IONP)
C
      WNMIN         =  0.
      WNMAX         =  WND
      STEP1         =  (WNMAX-WNMIN)/DFLOAT(NSTEP1)
      N1            =  NSTEP1 + 1
C
      DO  100  K2   =  1, N1
      WN            =  WNMIN + DFLOAT(K2-1)*STEP1
      IF(K2.EQ.1) WN = WNMIN
      IF(K2.EQ.N1) WN = WNMAX
      VD2AVN        =  -(2.*PI-DARCOS(S)+IONP+((1.-S)**2)/(2.*IONP))
     *                                        *WN/(2.*PI)
      IF(JCON.EQ.0) VONP = VD2AVN
      IF(JCON.EQ.1) VONP = -VD2AVN
      IF(JCON.EQ.2) VONP = 1./(1.+VD2AVN)
      IF(JCON.EQ.3) VONP = -VD2AVN/(1.+VD2AVN)
      IF(JCON.EQ.4) VONP = -VD2AVN/(1.+VD2AVN)
      WRITE(6, 9010) WN, VONP
 9010 FORMAT(2E14.5)
  100 CONTINUE
C
      VCONMN        =  S
      VCONMX        =  1.
      STEP1         =  (VCONMX-VCONMN)/DFLOAT(NSTEP1)
C
      DO  200  K3   =  1, N1
      VCON          =  VCONMN + DFLOAT(K3-1)*STEP1
      IF(K3.EQ.1) VCON = VCONMN + 1.0D-06
      IF(K3.EQ.N1) VCON = VCONMX - 1.0D-02
      A             =  DSQRT(VCON**2 + IONP**2)
      B             =  DSQRT(VCON**2 + IONP**2 -1.)
      TN            =  5.*PI/2. - DARCOS(S) - DARCOS(1./A)
     *                 - DARCOS(IONP/A) + (VCON-S)/IONP + B
      WN            =  2.*PI/TN
      VD2AVN        =  -((1.-IONP**2 - VCON**2)/(2.*IONP))*WN/(2.*PI)-1.
      IF(JCON.EQ.0) VONP = VD2AVN
      IF(JCON.EQ.1) VONP = -VD2AVN
      IF(JCON.EQ.2) VONP = 1./(1.+VD2AVN)
      IF(JCON.EQ.3) VONP = -VD2AVN/(1.+VD2AVN)
      IF(JCON.EQ.4) VONP = -VD2AVN/(1.+VD2AVN)
      IF(VONP.GT.6.) VONP = 6.
  200 CONTINUE
      STOP
```

```
      END
C
      FUNCTION FNWNDH(XI)
      IMPLICIT REAL*8(A-H,O-Z)
      PI              =  4.0*ATAN(1.)
      S               =  DSQRT(1.-XI**2)
      IF(XI.EQ.0.) GO TO 10
      FNWNDH          =  2.*PI/(PI+DARCOS(S) + XI + (1./XI) +S/XI)
      RETURN
   10 FNWNDH          =  0.
      RETURN
      END
C
      FUNCTION FNWNUH(XI)
      IMPLICIT REAL*8(A-H,O-Z)
      PI              =  4.0*ATAN(1.)
      S               =  DSQRT(1.-XI**2)
      IF(XI.EQ.0.) GO TO 10
      FNWNUH          =  2.*PI/(PI+2.*DARCOS(S) + 2.*S/XI)
      RETURN
   10 FNWNUH          =  0.
      RETURN
      END
C
      FUNCTION FNWNDF(XI)
      IMPLICIT REAL*8(A-H,O-Z)
      PI              =  4.0*ATAN(1.)
      S               =  DSQRT(1.-XI**2)
      IF(XI.EQ.0.) GO TO 10
      FNWNDF          =  2.*PI/(2.*PI-DARCOS(S) + XI + (1./XI) -S/XI)
      RETURN
   10 FNWNDF          =  1.
      RETURN
      END
```

D.7.4 DC Characteristics - Half-Wave ZVS

```
C  A PROGRAM TO COMPUTE THE DC CHARACTERISTICS OF ALL QUASI
C  RESONANT CONVERTERS WITH HALF-WAVE ZVS.
C
C  JCON = 0  COMMON FOR ALL CONVERTERS (VD2AVN OUTPUT)
C       = 1  BUCK
C       = 2  BOOST
C       = 3  BUCK-BOOST
C       = 4  BOOST-BUCK
C
C     BY RAMESH ORUGANTI
C
      IMPLICIT REAL*8(A-H,I,O-Z)
      NSTEP1          =  100
      JCON            =  3
      PI              =  4.0*ATAN(1.0)
C
      DO  300  K1     =  1, 5
      IONP            =  DFLOAT(K1) * 1.0
      IF(K1.EQ.1) IONP = 1.0 + 1.0D-06
      XI              =  1./IONP
      S               =  DSQRT(IONP**2-1.)
      WND             =  FNWNDH(XI)
C
      WNMIN           =  0.
      WNMAX           =  WND
      STEP1           =  (WNMAX-WNMIN)/DFLOAT(NSTEP1)
      N1              =  NSTEP1 + 1
C
      DO  100  K2     =  1, N1
      WN              =  WNMIN + DFLOAT(K2-1)*STEP1
      IF(K2.EQ.1) WN = WNMIN + 1.0D-06
      IF(K2.EQ.N1) WN = WNMAX - 1.0D-06
      VD2AVN          =  -1. + (PI+DARCOS(S/IONP)+1./(2.*IONP)+IONP+S)
     *                                                      *WN/(2.*PI)
      VAL             =  DABS(1.+VD2AVN)
      IF(VAL.LT.1.0D-06) VD2AVN = -1.0 + 1.0D-06
      IF(JCON.EQ.0) VONP = VD2AVN
      IF(JCON.EQ.1) VONP = -VD2AVN
      IF(JCON.EQ.2) VONP = 1./(1.+VD2AVN)
      IF(JCON.EQ.3) VONP = -VD2AVN/(1.+VD2AVN)
      IF(JCON.EQ.4) VONP = -VD2AVN/(1.+VD2AVN)
      WRITE(6, 9010) WN, VONP
 9010 FORMAT(2E14.5)
```

```
  100 CONTINUE
C
      ILONMN        =  S
      ILONMX        =  IONP
      STEP1         =  (ILONMX-ILONMN)/DFLOAT(NSTEP1)
C
      DO  200  K3   =  1, N1
      ILON          =  ILONMX - DFLOAT(K3-1)*STEP1
      IF(K3.EQ.N1) ILON = ILONMN + 1.0D-09
      A             =  DSQRT(ILON**2 + 1.)
      B             =  DSQRT(ILON**2 + 1. - IONP**2)
      TN            =  3.*PI/2. + DARCOS(S/IONP) - DARCOS(IONP/A)
     *                 - DARCOS(1./A) + B/IONP + ILON + S
      WN            =  2.*PI/TN
      VD2AVN        =  -(ILON**2 + 1. - IONP**2)*(WN/(2.*PI))/(2.*IONP)
      VAL           =  DABS(1.+VD2AVN)
      IF(VAL.LT.1.0D-06) VD2AVN = -1.0 + 1.0D-06
      IF(JCON.EQ.0) VONP = VD2AVN
      IF(JCON.EQ.1) VONP = -VD2AVN
      IF(JCON.EQ.2) VONP = 1./(1.+VD2AVN)
      IF(JCON.EQ.3) VONP = -VD2AVN/(1.+VD2AVN)
      IF(JCON.EQ.4) VONP = -VD2AVN/(1.+VD2AVN)
      WRITE(6, 9010) WN, VONP
  200 CONTINUE
C
      ILONMN        =  0
      ILONMX        =  S
      STEP1         =  (ILONMX-ILONMN)/DFLOAT(NSTEP1)
C
      DO  300  K4   =  1, N1
      ILON          =  ILONMX - DFLOAT(K4-1)*STEP1
      A             =  DSQRT(ILON**2 + 1.)
      TN            =  2.*(PI - DARCOS(1./A) + ILON)
      WN            =  2.*PI/TN
      VD2AVN        =  0.
      IF(JCON.EQ.0) VONP = VD2AVN
      IF(JCON.EQ.1) VONP = -VD2AVN
      IF(JCON.EQ.2) VONP = 1./(1.+VD2AVN)
      IF(JCON.EQ.3) VONP = -VD2AVN/(1.+VD2AVN)
      IF(JCON.EQ.4) VONP = -VD2AVN/(1.+VD2AVN)
      WRITE(6, 9010) WN, VONP
  300 CONTINUE
      STOP
      END
```

D.7.5 DC Characteristics - Full-Wave ZVS

```
C  A PROGRAM TO COMPUTE THE DC CHARACTERISTICS OF ALL QUASI
C  RESONANT CONVERTERS WITH FULL-WAVE ZVS.
C
C  JCON = 0  COMMON FOR ALL CONVERTERS (VD2AVN OUTPUT)
C       = 1  BUCK
C       = 2  BOOST
C       = 3  BUCK-BOOST
C       = 4  BOOST-BUCK
C
C     BY RAMESH ORUGANTI
C
      IMPLICIT REAL*8(A-H,I,O-Z)
      NSTEP1        =  100
      JCON          =  1
      PI            =  4.0*ATAN(1.0)
C
      DO  200  K1   =  1, 5
      IONP          =  DFLOAT(K1-1) * 1.0
      IF(K1.EQ.1) IONP = 1.0 + 1.0D-06
      XI            =  1./IONP
      S             =  DSQRT(IONP**2 -1.)
      WND           =  FNWNDF(XI)
C
      WNMIN         =  0.
      WNMAX         =  WND
      STEP1         =  (WNMAX-WNMIN)/DFLOAT(NSTEP1)
      N1            =  NSTEP1 + 1
C
      DO  100  K2   =  1, N1
      WN            =  WNMIN + DFLOAT(K2-1)*STEP1
      IF(K2.EQ.1) WN = WNMIN + 1.0D-06
      IF(K2.EQ.N1) WN = WNMAX - 1.0D-06
      VD2AVN        =  -1. + (2.*PI-DARCOS(S/IONP)+1./(2.*IONP)+IONP-S)
```

```
     *                                        *WN/(2.*PI)
      VAL            =  DABS(1.+VD2AVN)
      IF(VAL.LT.1.0D-06) VD2AVN = -1. + 1.0D-06
      IF(JCON.EQ.0) VONP = VD2AVN
      IF(JCON.EQ.1) VONP = -VD2AVN
      IF(JCON.EQ.2) VONP = 1./(1.+VD2AVN)
      IF(JCON.EQ.3) VONP = -VD2AVN/(1.+VD2AVN)
      IF(JCON.EQ.4) VONP = -VD2AVN/(1.+VD2AVN)
      WRITE(6, 9010) WN, VONP
 9010 FORMAT(2E14.5)
  100 CONTINUE
C
      ILONMN         =  S
      ILONMX         =  IONP
      STEP1          =  (ILONMX-ILONMN)/DFLOAT(NSTEP1)
C
      DO  200  K3    =  1, N1
      ILON           =  ILONMX - DFLOAT(K3-1)*STEP1
      IF(K3.EQ.N1) ILON = ILONMN + 1.0D-09
      A              =  DSQRT(ILON**2 + 1.)
      B              =  DSQRT(ILON**2 + 1. - IONP**2)
      TN             =  5.*PI/2. - DARCOS(S/IONP) - DARCOS(IONP/A)
     *                  - DARCOS(1/A) + B/IONP + ILON - S
      WN             =  2.*PI/TN
      VD2AVN         =  -(ILON**2 + 1. - IONP**2)*(WN/(2.*PI))/(2.*IONP)
      VAL            =  DABS(1.+VD2AVN)
      IF(VAL.LT.1.0D-06) VD2AVN = -1. + 1.0D-06
      IF(JCON.EQ.0) VONP = VD2AVN
      IF(JCON.EQ.1) VONP = -VD2AVN
      IF(JCON.EQ.2) VONP = 1./(1.+VD2AVN)
      IF(JCON.EQ.3) VONP = -VD2AVN/(1.+VD2AVN)
      IF(JCON.EQ.4) VONP = -VD2AVN/(1.+VD2AVN)
      WRITE(6, 9010) WN, VONP
  200 CONTINUE
      STOP
      END
      FUNCTION FNWNDH(XI)
C
C  SUBPROGRAM TO CALCULATE THE WND BOUNDARY FREQUENCY FOR QRCS
C  WITH HALF-WAVE RESONANT SWITCHES GIVEN LOAD CURRENT PARAMETER XI.
C  XI EQUALS MODIFIED LOAD CURRENT IONP FOR ZCS AND 1/IONP FOR ZVS.
C
C  BY RAMESH ORUGANTI
C
      IMPLICIT REAL*8(A-H,O-Z)
      PI             =  4.0*ATAN(1.)
      S              =  DSQRT(1.-XI**2)
      IF(XI.EQ.0.) GO TO 10
      FNWNDH         =  2.*PI/(PI+DARCOS(S) + XI + (1./XI) +S/XI)
      RETURN
   10 FNWNDH         =  0.
      RETURN
      END
C
      FUNCTION FNWNUH(XI)
C
C  SUBPROGRAM TO CALCULATE THE WNU BOUNDARY FREQUENCY FOR QRCS
C  WITH HALF-WAVE RESONANT SWITCHES GIVEN LOAD CURRENT PARAMETER XI.
C  XI EQUALS MODIFIED LOAD CURRENT IONP FOR ZCS AND 1/IONP FOR ZVS.
C
C  BY RAMESH ORUGANTI
C
      IMPLICIT REAL*8(A-H,O-Z)
      PI             =  4.0*ATAN(1.)
      S              =  DSQRT(1.-XI**2)
      IF(XI.EQ.0.) GO TO 10
      FNWNUH         =  2.*PI/(PI+2.*DARCOS(S) + 2.*S/XI)
      RETURN
   10 FNWNUH         =  0.
      RETURN
      END
C
      FUNCTION FNWNDF(XI)
C
C  SUBPROGRAM TO CALCULATE THE WND BOUNDARY FREQUENCY FOR QRCS
C  WITH FULL-WAVE RESONANT SWITCHES GIVEN LOAD CURRENT PARAMETER XI.
C  XI EQUALS MODIFIED LOAD CURRENT IONP FOR ZCS AND 1/IONP FOR ZVS.
C
C  BY RAMESH ORUGANTI
C
      IMPLICIT REAL*8(A-H,O-Z)
      PI             =  4.0*ATAN(1.)
      S              =  DSQRT(1.-XI**2)
      IF(XI.EQ.0.) GO TO 10
```

```
      FNWNDF        =  2.*PI/(2.*PI-DARCOS(S) + XI + (1./XI) -S/XI)
      RETURN
   10 FNWNDF        =  1.
      RETURN
      END
```

D.7.6 Subroutines

```
      FUNCTION FNWNDH(XI)
C
C  SUBPROGRAM TO CALCULATE THE WND BOUNDARY FREQUENCY FOR QRCS
C  WITH HALF-WAVE RESONANT SWITCHES GIVEN LOAD CURRENT PARAMETER XI.
C  XI EQUALS MODIFIED LOAD CURRENT IONP FOR ZCS AND 1/IONP FOR ZVS.
C
C  BY RAMESH ORUGANTI
C
      IMPLICIT REAL*8(A-H,O-Z)
      PI            =  4.0*ATAN(1.)
      S             =  DSQRT(1.-XI**2)
      IF(XI.EQ.0.) GO TO 10
      FNWNDH        =  2.*PI/(PI+DARCOS(S) + XI + (1./XI) +S/XI)
      RETURN
   10 FNWNDH        =  0.
      RETURN
      END
C
      FUNCTION FNWNUH(XI)
C
C  SUBPROGRAM TO CALCULATE THE WNU BOUNDARY FREQUENCY FOR QRCS
C  WITH HALF-WAVE RESONANT SWITCHES GIVEN LOAD CURRENT PARAMETER XI.
C  XI EQUALS MODIFIED LOAD CURRENT IONP FOR ZCS AND 1/IONP FOR ZVS.
C
C  BY RAMESH ORUGANTI
C
      IMPLICIT REAL*8(A-H,O-Z)
      PI            =  4.0*ATAN(1.)
      S             =  DSQRT(1.-XI**2)
      IF(XI.EQ.0.) GO TO 10
      FNWNUH        =  2.*PI/(PI+2.*DARCOS(S) + 2.*S/XI)
      RETURN
   10 FNWNUH        =  0.
      RETURN
      END
C
      FUNCTION FNWNDF(XI)
C
C  SUBPROGRAM TO CALCULATE THE WND BOUNDARY FREQUENCY FOR QRCS
C  WITH FULL-WAVE RESONANT SWITCHES GIVEN LOAD CURRENT PARAMETER XI.
C  XI EQUALS MODIFIED LOAD CURRENT IONP FOR ZCS AND 1/IONP FOR ZVS.
C
C  BY RAMESH ORUGANTI
C
      IMPLICIT REAL*8(A-H,O-Z)
      PI            =  4.0*ATAN(1.)
      S             =  DSQRT(1.-XI**2)
      IF(XI.EQ.0.) GO TO 10
      FNWNDF        =  2.*PI/(2.*PI-DARCOS(S) + XI + (1./XI) -S/XI)
      RETURN
   10 FNWNDF        =  1.
      RETURN
      END
```

Appendix E

SPICE2 Simulation Of A Series Resonant Converter

In this appendix the simulation program for a series resonant converter with ASDTIC control is presented. SPICE2 is a network analysis program [48]. which was adapted to simulate the system under consideration.

The SPICE2 listing for the system is given in Sec. E.1. Devices XSCR1 and XSCR2 in the power circuit were implemented with a SPICE2 subcircuit (SUBCKT SCR), which was written to simulate the operation of an ideal latching switch with unidirectional current flow and triggered by pulse. The 10 $K\Omega$ resistors (RL, RLS1 etc.) across the inductors, the 10 $M\Omega$ resistor, RGND, and the capacitors across the diodes of the output bridge rectifier (CO1, CO2 etc.) have all been included to facilitate numerical convergence. Zero voltage source VZ7 in the power circuit model has been used to monitor output current (= absolute value of tank current), respectively.

SPICE2 has no provisions for directly implementing various system block diagram elements, such as compensators, comparators, logic gates and so on. An equivalent circuit diagram using standard SPICE2 elements, was created for each of these blocks and was then implemented as a SPICE2 subcircuit. The various subcircuits in the program, such as BISTAB, INTEG and COMP implement different circuit elements such as bistable, integrator and comparator. The sensor subcircuit (SENSOR) is included to ensure proper start of the simulation.

E.1 Program Listings

```
TEST OF SERIES RESONANT CONVERTER - ASDTIC CONTROL
*-------------------------------------------------------------------------
*A SPICE2 PROGRAM TO SIMULATE A SERIES RESONANT CONVRTER WITH
*ASDTIC CONTROL.
*THE PROGRAM INCLUDES INITIAL GATING PULES TO INSURE PROPER
*STARTING OF THE  SIMULATION.
*IREF IS THE CONTROL INPUT DETERMINING THE SET VALUE OF AVERAGE
*CURRENT. DESIRED OUTPUT CURRENT IO = 10 * IREF AMPS.
*THE PROGRAM AS SHOWN SIMULATES ASDTIC CONTROL UNDER START-UP AND
*SHOWS THE HIGH CURRENT SURGES IN THE TANK CIRCUIT WITH IRREGULAR
*SEQUENCES OF CONDUCTION.
*
*THE LOSSES IN CONVERTER CAN BE SIMULATED BY INCLUSION OF
*RLOSS RESISTOR APPROPRIATELY WHICH RESULTS IN A DAMPING
*FACTOR OF 0.025.
*
*BY REPLACING CERTAIN EXISTING STATEMENTS WITH THOSE MARKED WITH
*AN ASTERIK (*), THE INSTABILITY OF ASDTIC CONTROL
*NEAR STEADY-STATE IS SHOWN FOR AN AVERAGE CURRENT OF 37.5 A AND
*DAMPING FACTOR OF 0.025. THE INITIAL CONDITIONS FOR THE RUN
*HAVE BEEN SET AT VALUES CORRESPONDING TO THE STEADY-STATE.
*
*THE PROGRAM USES SEVERAL SUBCKTS WHICH SIMULATE CIRCUIT ELEMENTS
*SUCH AS AND GATE, COMPARATOR, OP-AMP AND INTEGRATOR IN A MANNER
*COMPATIBLE WITH SPICE2.
*SUBCKT SCR SIMULATES THE ACTION OF A SELF-LATCHING UNI-DIRECTIONAL
*SWITCH TRIGGERED BY A PULSE.
*
*RELTOL HAS BEEN SET AT 0.0001 FOR GREATER ACCURACY OF SIMULATION.
*
*BY RAMESH ORUGANTI AT VPI&SU, BLACKSBURG, VA.
*
*-------------------------------------------------------------------------
*POWER CIRCUIT
*-------------------------------------------------------------------------
 VS1 2 1 DC 300.V
 VS2 1 0 DC 300.V
* C 1 3 2.UF IC=346.05V
 C 1 3 2.UF
 XSCR1 2 205 5 205 SCR
 DAP1 6 2 D
 XSENS1 205 6 0 206 SENSOR
 CSN1 6 7 .01UF
 RSN1 7 2 50.
 LS1 6 8 2.UH
 RLS1 6 8 10.K
* RLOSS 8 100 0.3202
* L1 100 9 80.UH IC=20.6A
 L1 8 9 80.UH
* RL1 100 9 10.K
 RL1 8 9 10.K
 FF 201 0 VZ7 .1
* LS2 8 11 2.UH IC=-20.6A
 LS2 8 11 2.UH
 RLS2 8 11 10.K
 XSCR2 305 0 12 0 SCR
 DAP2 0 11 D
 XSENS2 11 305 0 306 SENSOR
 CSN2 0 13 .01UF
 RSN2 13 11 50.
 DO1 9 34 D
 DO2 3 34 D
 DO3 36 3 D
 DO4 36 9 D
 .MODEL D D
 CO1 9 34 1.PF
 CO2 3 34 1.PF
 CO3 36 3 1.PF
 CO4 36 9 1.PF
 VZ7 34 35 DC 0.V
* VO 35 36 DC 150.V
 CF 35 36 1000.UF
 RLOAD 35 36 4.OHMS
 RGND 36 0 10.MEG
 *-------------------------------------------------------------------------
```

```
*CONTROL CIRCUIT
*-----------------------------------------------------------------------
* IREF 0 201 DC 3.75A
IREF 0 201 DC 3.0A
XINT 201 0 203 0 INTEG
XCOMP1 203 0 206 0 COMP
GCOMP2 0 306 203 0 10.
ISTART1 0 206 PULSE(-10. 10. 10.US .1US .1US 1.S 1.1S)
ISTART2 0 306 PULSE(-10. 10. 10.US .1US .1US 1.S 1.1S)
XBISTAB 221 0 321 0 306 0 206 0 BISTAB
*-----------------------------------------------------------------------
XAND2 206 0 207 0 AND
XPULSE2 207 0 12 0 0 321 PULSE
*-----------------------------------------------------------------------
XAND1 306 0 307 0 AND
XPULSE1 307 0 5 205 0 221 PULSE
IGINIT1 205 5 PULSE(0. 1. 0.01US .1US .1US 10.US 1.1S)
IGINIT2 221 0 PULSE(0. 1. 0.01US .1US .1US 10.US 1.1S)
*-----------------------------------------------------------------------
*RUN CONTROLS
*-----------------------------------------------------------------------
.TRAN 2US 400US UIC
.PLOT TRAN I(VZ7) V(0,201) V(3,1)
.PRINT TRAN I(VZ7) V(0,201) V(3,1)
.OPTIONS ACCT LIMPTS=601 ITL5=25000 LVLTIM=1 RELTOL=0.0001
*-----------------------------------------------------------------------
*SUB-CIRCUITS
*-----------------------------------------------------------------------
.SUBCKT SCR 1 2 3 4
RG 3 4 1.
CT 6 2 10.PF
D1 1 5 MOD1 OFF
D2 2 6 MOD2
RT 6 2 15.K
RZ1 5 6 1.
GT 6 2 POLY(2) 5 6 3 4 -.1A 2.25 0.2 IC=0.
.MODEL MOD1 D
.MODEL MOD2 D(RS=.8)
.ENDS SCR
*-----------------------------------------------------------------------
.SUBCKT BISTAB 1 2 3 4 5 6 7 8
G1 2 1 3 4 -0.8
G2 4 3 1 2 -0.8
C1 1 2 0.2UF
C2 3 4 0.2UF
D1 1 2 D
D2 2 1 D
D3 3 4 D
D4 4 3 D
G3 6 5 1 2 10.
G4 8 7 3 4 10.
.MODEL D D(RS=0.1)
.ENDS BISTAB
*-----------------------------------------------------------------------
.SUBCKT OPAMP 1 2 3 4
E1 5 4 2 1 10.K
R1 5 3 20.
D1 6 3 D
D2 3 7 D
V1 4 6 DC 6.3V
V2 4 7 DC 3.7V
.MODEL D D
.ENDS OPAMP
*-----------------------------------------------------------------------
.SUBCKT INTEG 1 2 3 4
R1 1 2 1000.MEG
C1 1 2 25.UF
D1 1 5 D
D2 6 1 D
V1 5 2 DC 9.3V
V2 2 6 DC 9.3V
G1 4 3 1 2 10.
.ENDS INTEG
*-----------------------------------------------------------------------
.SUBCKT COMP 1 2 3 4
D1 1 2 D
D2 2 1 D
G1 4 3 1 2 10.
.MODEL D D
.ENDS COMP
*-----------------------------------------------------------------------
.SUBCKT AND 1 2 3 4
I1 1 2 27.A
D1 1 2 D
```

```
D2 2 1 D
C1 1 2 2.UF
G1 4 3 1 2 10.
.MODEL D D
.ENDS AND
*-------------------------------------------------------------------------
.SUBCKT PULSE 1 2 3 4 5 6
R1 1 2 500.OHMS
C1 1 7 10.NF IC=5000.V
R4 7 8 .1OHM
R2 8 2 .2OHM
C2 8 2 .1UF
D1 8 9 D
R3 9 2 1.K
G1 4 3 9 2 1. IC=0.A
G2 6 5 9 2 1. IC=0.A
.MODEL D D
.ENDS PULSE
*-------------------------------------------------------------------------
.SUBCKT SENSOR 1 2 3 4
VZ1 1 2 DC 0.V
F1 4 5 POLY(1) VZ1 -0.005A 1.
D1 5 4 D
D2 4 5 D
G1 4 3 5 4 10.
.MODEL D D
.ENDS SENSOR
*-------------------------------------------------------------------------
.END
```

The vita has been removed from the scanned document